PSI — PAUL SCHERRER INSTITUT

67th ICFA
Advanced
Beam Dynamics
Workshop
FLS 2023

Future Light Sources 2023

28 August – 1 September 2023
Swiss Museum of Transport
Lucerne, Switzerland

www.fls23.ch

PROCEEDINGS

Foreword

The 67th ICFA Advanced Beam Dynamics Workshop on Future Light Sources (FLS 2023) took place in Lucerne, Switzerland, from August 27 to September 1, 2023. The inception of this workshop proved particularly difficult. The Covid19 crisis forced us to cancel the event on two occasions, first from the originally planned date of March'21, and second from the rescheduled date of March'22. In both cases the IOC and LOC, driven by the realization that the inherently lively discussions were a core element of the FLS series, were adamant that a postponement was preferable to a deferred online format.

When, finally, FLS'23 did occur, it was met with great enthusiasm: over 200 participants enjoyed an exciting potpourri of excellent presentations, posters, discussions and valuable exchanges with eleven industrial exhibitors. It was gratifyingly evident that advances in light sources had not ceased during the Covid crisis, and that the FLS workshop provided a much welcome and long-awaited opportunity to present this progress to our community.

As is the tradition of the FLS series, the working-group conveners were granted the task of drafting the scientific program. This consisted of 16 invited talks, 64 contributed talks, 4 working group summary talks and 62 posters, a few of which were also presented in 4 hybrid sessions. All presentations generated much discussion that would often propagate enthusiastically into the coffee breaks. The unseasonably wet weather unwittingly helped keep participants in check and focused on the workshop topics. Thankfully, as if on cue, the rain stopped in time for the workshop dinner aboard a boat cruising the captivating lake of Lucerne, surrounded by a panorama of mountains. With 65 contributions documented in this proceeding, we have a sound record of the work presented at the workshop, and a lasting point of reference.

We thank all participants, and in particular the working group conveners and LOC members for contributing to the success of this workshop. A special thanks to the JACoW editorial team for diligently processing the manuscripts and ensuring the timely release of these proceedings. Last, but not least, we are pleased to announce, on behalf of the IOC, that the next FLS event will take place in Chicago in fall 2027 and is to be chaired by John Byrd of ANL.

Hans-Heinrich Braun
FLS'23 Workshop chair

Romain Ganter
FLS'23 LOC chair

FLS'23 was hosted by the Paul Scherrer Institut, Villigen, Switzerland, and held at the Swiss Museum of Transport, Lucerne, from 27 Aug.-1 Sep. 2023.

International Organizing Committee (IOC)

Ralph Assmann	DESY	Germany
James Clarke	STFC	UK
Marie-Emmanuelle Couprie	Soleil	France
Winfried Decking	DESY	Germany
Luca Gianessi	ELETTRA	Italy
Marc Guetg	DESY	Germany
Zhirong Huang	SLAC	USA
Andreas Jankoviac	Helmholtz Zentrum Berlin	Germany
Chan Joshi	University of California	USA
Kwang-Je Kim	Argonne National Laboratory	USA
Andreas R. Maier	DESY	Germany
Oliver Marcouille	Soleil	France
George Neil	Lawrence Berkeley National Laboratory	USA
Hideaki Ohgaki	Kyoto University	Japan
Tor Raubenheimer	SLAC	USA
Jean-Luc Revol	ESRF	France
David S. Robin	Lawrence Berkeley National Laboratory	USA
Michele Svandrlik	ELETTRA	Italy
Hitoshi Tanaka	SPring-8	Japan
Nicolay Vinokurov		
Richard Walker	Diamond	UK
Jiuqing Wang	Institute of High Energy Physics, CAS	China
Zhao Zhentang	SINAP	China

Local Organising Committee (LOC)

Hans-Heinrich Braun	Workshop Chair
Romain Ganter	LOC Chairperson
Silvia Bacher	
Jan Chrin	
Nicole Hiller	
Frank Reiser	
Elisabeth Rohrer	
Harald Shori	

JACoW Scientific Editorial Committee (JSEC)

Jan Chrin	PSI
Nicole Hiller	PSI
Michaela Marx	DESY
Volker RW Schaa	GSI

Contents

STORAGE RING BASED STEADY STATE MICROBUNCHING

Alex Chao*, Tsinghua University, Beijing, China

Abstract

Powerful light sources are highly desired tools for scientific research and for industrial applications. Electrons are the objects that most readily and easily radiate photons. A natural conclusion follows that one should pursue electron accelerators as the choice tools towards powerful light sources. How to manipulate the electron beam in the accelerator so that it radiates light most efficiently, however, remains to be studied and its physical principle and technical limits be explored and optimized for the purpose. One such proposed concepts is based on the steady state microbunching (SSMB) mechanism in an electron storage ring. We make a brief introduction of the SSMB mechanism and its recent status in this presentation.

INTRODUCTION

As we have observed in the past few decades, modern physics has evolved out of the more traditional regime of nuclei and quarks, and now has backtracked to the regime of atoms and molecules. This means the prime research means has evolved out of particles of ever higher energies and into photons of various wavelengths, and the tools have evolved out of colliders and into light sources. This trend has been a major evolution expected to continue in the next decades.

At presnt, there are two main approaches in advanced light sources, the third- (and fourth-) generation storage ring synchotron radiation sources, and free electron lasers.

In a third-generation synchrotron radiation light source, with an RF focusing, the electron bunches are separated by perhaps ∼1 m, while each bunch has a length of the order of ∼10 mm. With the electrons circulating around the storage ring in steady state, the radiation has a high repetition rate. However, with a bunch much longer than the wavelength of radiation, the radiation from the electrons is incoherent. The radiation peak power is low, proportional to N, the number of electrons in the bunch.

In a free electron laser light source, on the other hand, the electrons are provided by a linac. A single electron bunch is cleverly manipulated in such a way that it gets microbunched by the time it is about to exit a long undulator and therefore radiates coherently, with a very high peak power proportional to N^2. However, using a linac in a pulsed mode, the repetition rate is low.

The present situation is therefore that, towards the goal of high power light sources, one of our main approaches has a high repetition rate but low peak power, the other has a high peak power but low repetition rate. Since the net radiation power is the product of repetition rate and peak power, we naturally come to an idea of a somehow combined device. This device aims to have both the high repetition rate of a storage ring and a high peak power of a microbunched beam like in an FEL.

It must be quickly pointed out that a straigtforward insertion of a long undulator in a storage ring will destroy the microbunches of the electron beam — FELs always use linacs for a good reason. If an FEL linac is simply inserted into a storage ring, the storage ring will have to be operated in a pulsed mode; every time the electron beam traverses the FEL, it has to wait in the storage ring for a long time to cool down before a next passage can be made, effectively making this device a pulsed operation and the benefit of high repetion rate of the storage ring does not apply.

Such a combined device must be done while keeping the intigrity of the microbunched structure of the electron beam. The way being proposed to accomplish this is named steady state microbunching (SSMB). Once accomplished, an SSMB device aims for simultaneously a high repetition rate and a high peak power. Since N is a very large number, an SSMB ring potentially gains a large factor in the desired radiation power compared to a third-generation storage ring facility.

In terms of its operation principle, this conceived storage ring-based SSMB functions very closely to that of a conventional storage ring, except that the microwave RF is replaced by an IR laser modulator. The equilibrium beam distribution becomes microbunched with the bunch spacing given by the modulation laser wavelength λ_m instead of a conventional RF wavelength. This represents an extrapolation of six orders of magnitude in bunch spacing but the mechanism of the steady state is the same, i.e., a balance between radiation damping and quantum excitation. No FEL mechanism is invoked. To demonstrate the applicability of our resent understanding of storage rings to this six orders of magnitude extrapolation, a critical proof-of-principle test has been launched.

SSMB SCENARIOS

Before we discuss its technical design, we first need to know that there are a variety of SSMBs that one can aim for, ranging from simple to sophisticated ones. Depending on the applications, particularly depending on the targeted wavelength of the SSMB radiation, there are several different SSMB scenarios with different levels of sophistication.

To illustrate the various scenarios, we start with a conventional third-generation storage ring source. The electron beam is bunched with a Gaussian distribution with bunch length ∼10 mm. The radiation is incoherent, as mentioned. If the targeted wavelegnth is long enough, e.g., in the THz range, then by some conventional techniques, one may try to compress the bunch length toward the desired wavelength and accomplish some enhancement of the radiation. This source however remains basically a conventional design.

---

* achao@slac.stanford.edu
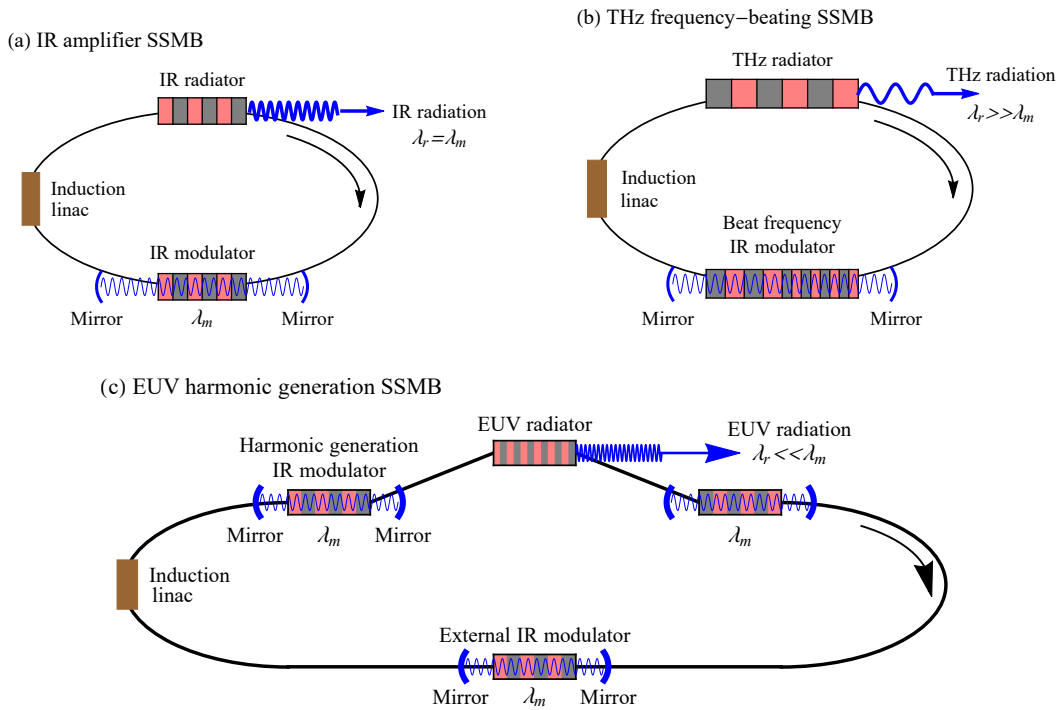
Figure 1: SSMB scenarios for different radiation wavelengths. (a) $\lambda_r = \lambda_m$; (b) $\lambda_r \gg \lambda_m$; (c) $\lambda_r \ll \lambda_m$.

Potential-well Distortion SSMB

The very simplest SSMB scenario is to start with the conventional beam and slightly modulate its equilibrium Gaussian distribution to generate a small micro-structure on top of the Gaussian. This can be accomplished by adding a laser modulator in the storage ring so that a weak laser modulation is superimposed onto the large RF waveform. The traditional quadratic potential well provided by the RF system is then ever so slightly potential-well distorted by the laser modulation. The laser wavelength is an exact k times shorter than the RF wavelength, where k is a large integer. Once modulated, this slightly micro-modulated beam will circulate around the storage ring in a steady state and will radiate coherently at the desired wavelength. Although the modulation is only very slight, its coherent radiation easily overwhelms the conventional synchrotron radiation because of the extra factor of N. This scenario is the simplest SSMB scenario and is not expectd to be difficult to implement as it requires basically only a stable conventional storage ring.

As a numerical example, consider an electron beam in a typical conventional electron storage ring. Let this beam have an average current of $I_{ave} = 0.5$ A and let its natural Gaussian bunch have a peak current $I_{peak} = 50$ A. Now let this beam be slightly modulated at 1 µm wavelength by a moderate IR modulator, so that it has a bunching factor $\mathcal{B} = 0.01$ at 1 µm. Now assume an undulator radiator with $K = 2$ and total number of radiator periods $N_u = 40$. This SSMB source will radiate at 1 µm wavelength a power of 25 W (peak power 2.5 kW),

$$P_{ave} = \frac{\pi}{\epsilon_0 c} |\mathcal{B}|^2 \xi [JJ]^2 N_u I_{ave} I_{peak}, \quad (1)$$

where $[JJ] = J_0(\xi) - J_1(\xi)$, with $\xi = K^2/(4 + 2K^2)$.

This numerical example indicates that a slightly modulated simplest SSMB is already a respectable radiator. This SSMB ring does not require any demanding momentum compaction factor and can be applied to existing conventional electron rings.

Amplifier SSMB

To increase the SSMB radiation power of a slightly potential-well modulated SSMB, naturally we want to increase the laser modulation strength. We then consider a case when the beam is fully modulated [$\mathcal{B} \to 1$ in Eq. (1)]. This beam radiates coherently at the modulation wavelength. The SSMB then serves as a very strong amplifier of the original modulation laser.

One weakness of this amplifier SSMB is that, to apply this SSMB at a certain desired wavelength, one needs to have already an existing laser of the same wavelength to be used as the modulation laser. This SSMB only amplifies the exisiting laser, although the amplification factor can be very large.

The SSMB research so far has included an important proof of principle test. This test is being carried out at the Metrology Light Source MLS, Berlin. Its phase I has been quite successful [1], and its phase II is being initiated. A successful proof of principle test is in fact already a realization of an amplifier SSMB. We will discuss more of this test experiment later in this presentation.

Harmonic Generation SSMB

A practical existing laser could be an IR laser. It is natural to consider an IR laser as the modulation laser for the SSMB scenarios. As such, the potential-well-distortion and the amplifier scenarios are readily available for IR radiation, and for them, there is not much additional accelerator technology needed beyond existing state-of-the-art. What requires additional R&D is when we consider a scenario when the desired radiation has a wavelength much shorter than IR. For those applications, there is an additional step of harmonic generation required. We refer to this scenario the harmonic generation SSMB.

One reason of a need to consider harmonic generation, in spite of the additional R&D needed, is its potential to some special industrial applications. In particular, we need to consider it if the wavelength we desire is DUV, EUV, or soft Xray. We will say more about the on-going efforts in the R&D and design of a harmonic generation SSMB later in this presentation.

THz SSMB

Considering an IR modulation laser, harmonic generation provides a way to shorten the radiation wavelength. An SSMB scenario also provides a way to lengthen the radiation wavelength to, e.g., the THz range [2]. This can be done by taking an amplifier SSMB, and simply replacing the modulator undulator by two back-to-back shorter undulators. The two undulators have slightly different resonant frequencies, with both of their resonance bandwidths covering the modulation laser, but slightly differ by a frequency split of 1 THz. The electron beam distribution then contains a strong beat frequency component at 1 THz, thus producing SSMB radiation at 1 THz.

FEL-ERL Based Scenario [3]

We have so far emphasized the role of a storage ring, and it was noted that a ring-based SSMB is not an FEL. FEL linacs are of course quite capable of producing radiation at desired wavelengths. To make them powerful light sources, however, it becomes necessary to increase substantially the linac repetition rate by adopting a superconducting gun and linac, and to add an energy recovery linac to recover the electron beam energy. Such a concept is not included in the ring-based SSMB discussed here. On the other hand, the two concepts are not too dissimilar. In the FEL-ERL scenario, the steady state is maintained not by reusing the electron beam but by reusing the electron beam energy. Other than how the steady state is maintained, the principle of SSMB and particularly the microbunching beam dynamics, including its harmonic generation, are quite similar.

Figure 1 intends to illustrate more design details of three of the SSMB scenarios. Figure 1(a) shows an amplifier version. The modulation laser is stored in a laser cavity. The radiated laser has the same wavelength (assumed to be IR) but is amplified by a large factor. Beam energy is replenished not by a conventional RF but by an induction

linac [4]. Figure 1(b) shows the conceptual design of a THz SSMB. The modulator undulator now has a design with dual resonant frequencies that split by THz. In this case, the radiation wavelength is much longer than IR. Figure 1(c) is a harmonic generation SSMB, aiming for radiating a much shorter wavelength than IR, e.g., in the EUV regime. In this case, a much more complex radiator section replaces the simple radiator undulator. On each side of the radiator, a harmonic generation modulator is installed to further compress the microbunch. The two modulators sandwiching the radiator are made to compensate each other, so that the electron beam is restored before reentering the ring arcs.

PROOF OF PRINCIPLE TEST

To test the SSMB mechanism, a proof of principle experiment is carried out at the MLS, Berlin [1, 5–7]. Figure 2 illustrates the conceived three phases in the SSMB planning. Phases I and II are proof-of-principle tests. Phase III is the design and construction of a dedicated SSMB storage ring.

Phase I, a critical proof-of-principle step, has been demonstrated [1]. A single-shot laser is used to establish the feasibility in a low momentum-compaction environment that is suitable for sustaining the microbunched beams for multiple turns. In the experiment, after the beam is stably stored in the ring, a single-shot IR laser pulse is fired to excite the beam with energy modulation. A precision semi-isochronous storage ring optics causes the beam to microbunch at its next turn. The modulating undulator then serves as the radiator in the subsequent turns of the beam. An SSMB effect is detected by the coherent radiation of the microbunched beam for multiple turns following the single-shot of the laser.

In this single-shot experiment, the fundamental 1064-nm SSMB signal is interfered from the original modulation laser, so the experiment was carried out by detecting the second
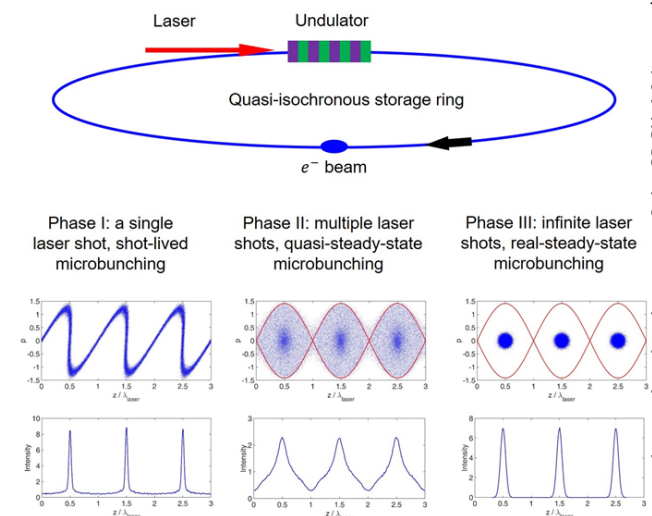
Figure 2: Conceived three SSMB phases. Phases I and II are proof-of-principle tests. Phase I has been demonstrated. Phase II is currently restarted since COVID. Phase III, presently under a design effort, is the eventual construction of a dedicated harmonic generation SSMB ring.
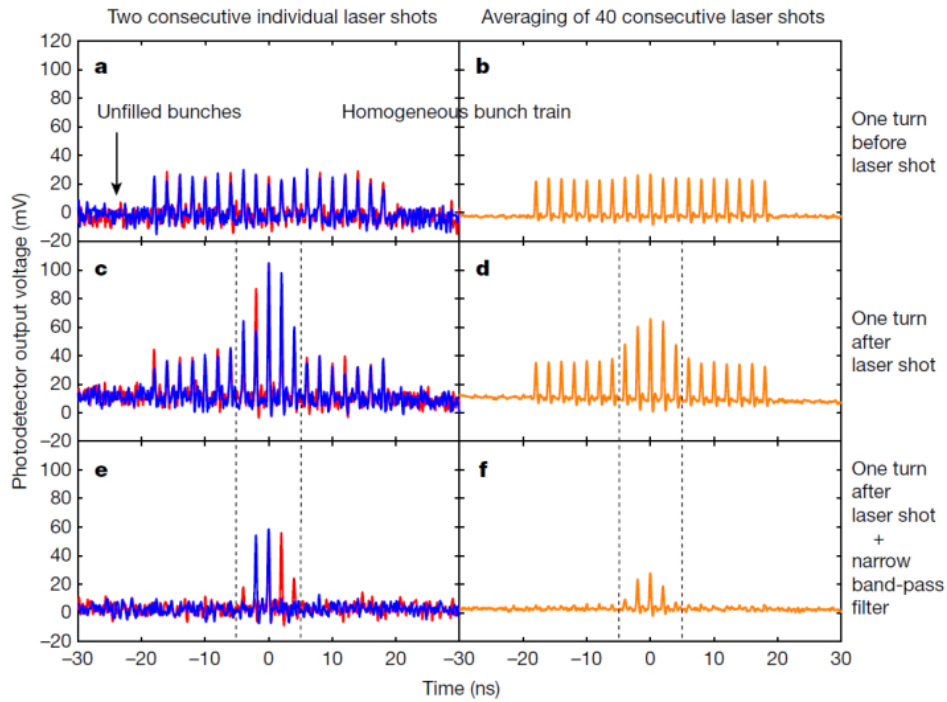
Figure 3: Coherent SSMB radiation demonstration in phase I proof of principle test at MLS.
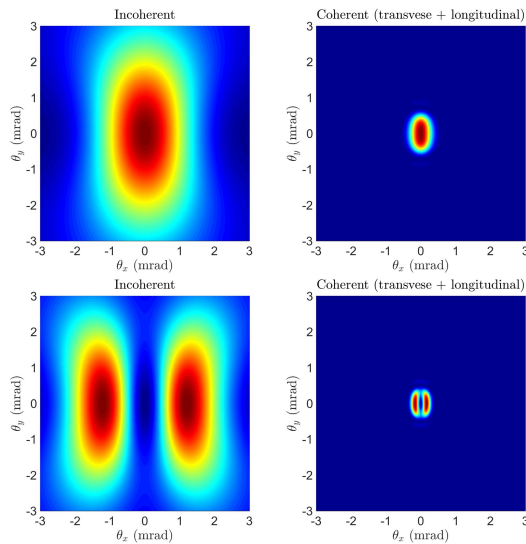
Figure 4: Angular distribution patterns of the expected SSMB radiation from the proof of principle test. The left column shows the patterns for the incoherent undulator radiation (upper figure for the fundamental 1064 nm mode, lower figure for the 532 nm second-harmonic mode). The right column shows the same for the coherent SSMB radiation. All plots have the same scales of axes.

harmonic 532-nm radiation. Robust signals were detected. One set of data is shown in Fig. 3. Before the laser shot, a 19-bunch beam is stored in the ring. Figure 3(a) shows 19 incoherent synchrotron radiation peaks. A laser shot is then fired, affecting 5 in the middle of the 19 bunches. On the next turn of the beam, these 5 bunches get microbunched. Figure 3(c) shows their enhanced radiation. When a frequency filter

is installed in front of the detector, filtering out the wide-spectrum of the incoherent radiation, Fig. 3(e) shows that only the coherent SSMB signal from the middle bunches remains, proving the enhanced radiation is truly from the microbunching mechanism. Figures 3(a), (c), (e) show the measurements of two laser shots. Figures 3(b), (d), (f) repeat (a), (c), (e) with the signals averaged over 40 consecutive shots.

In addition to the narrower frequency range, the coherent radiation is expected also to have a narrower angular spread. Figure 4 shows the expected angular pattern of the radiation in the PoP test [8]. The coherent radiation is expected to be much more collimated than the incoherent radiation. Investigation of these interesting features are being continued.

After the laser shot, the beam is microbunched and radiate coherently in its next turn. This microbunched beam can be rather robust. Its microbunching structure can last for several revolutions without additional laser shots [7]. A case with robust microbunched beam is shown in Fig. 5.

This multi-turn result is very encouraging. After a single shot of the laser, the microbunched beam is robust over several revolutions. If we continue to fire the laser, it is expected that the beam will stay microbunched circulating around the ring. This is what the phase-II experiment aims to demonstrate. The single-shot laser is to be replaced by a high repetition laser. In the phase-II experiment, the microbunches are expected to slowly leak out of the microbuckets. Its SSMB state is therefore a quasi-steady-state, as indicated in Fig. 2(b). A fully steady SSMB awaits a dedicated storage ring, currently under a design effort.
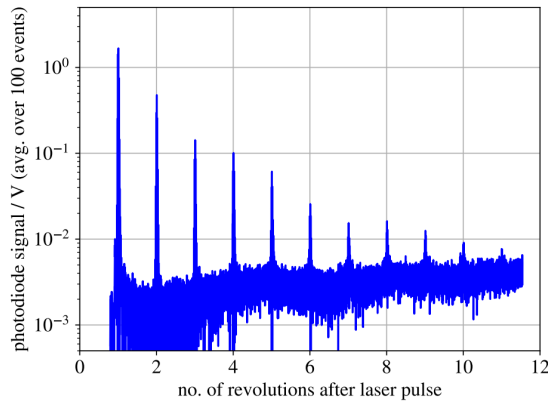
Figure 5: SSMB proof of principle signal lasts for multiple turns.

Figure 6: Present design layout of a SSMB laser system.

Figure 7: The high performance linac has included a wakefield compensation mechanism.

HARMONIC GENERATION SSMB DESIGN EFFORT

As mentioned, for applications to radiation wavelengths in the DUV, EUV and soft Xray ranges, an additional step of harmonic generation is needed. To this end, a team was organized at Tsinghua University, Beijing to investigate the technical issues involved and to make a first proposal of such a dedicated device [5,9]. The effort is continuing and preliminary designs, one aiming DUV and one aiming EUV, are in progress.

Various ways to perform the harmonic generating microbunch compression have been investigated [4, 10]. In the present design concept, two laser modulators are inserted on each side of the DUV/EUV radiator to provide an additional step of bunch compression at the radiator in the middle, as sketched in Fig. 1(c). The two modulators impose equal and opposite modulations in a reversible configuration [11, 12]. To minimize the required modulation laser power, a clever idea based on an angular dispersive modulation and longitudinal-transverse coupling mechanism [3, 13] is implemented.

The SSMB design focuses on longitudinal beam dynamics, particularly the implementation of strong focusing in the longitudinal dimension not unlike the transverse final focusing in a collider. In particular, the concept of strong focusing is further extended from 2D beam dynamics to 6D [13]. In contrast, a fouth-generation synchrotron radiation source concentrates on its transverse beam dynamics.

Various accelerator physics issues need to be addressed, including a storage ring lattice that permits a steady-state microbunched beam configuration including an insertion of harmonic generation [14, 15], in-depth understanding of various 6D single-particle dynamics [16], and various collective effects [4, 17, 18].

Other critical areas in the SSMB design effort include its laser and modulator section, and the demanding laser optical cavity [19]. A sketch if shown in Fig. 6.
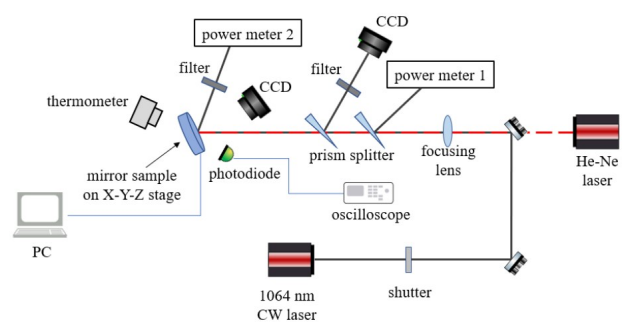
Another important technical requirement is a high performance injector, with demand of a wakefield compensated linac, sketched in Fig. 7, and a stretcher ring [20].

The design parameters vary according to the targeted radiation wavelength. The parameters evolve as the design efforts deepen. For a snapshot of the design status, Table 1 gives one recent version of parameters of two dedicated SSMB storage rings, one DUV and one EUV. More design examples aimed at other wavelengths, as well as a comprehensive set of design equations, are presented in [21]. An EUV SSMB layout is sketched in Fig. 8.

In the approach adopted in establishing Table 1, with the additional bunch compression done mostly in the reversible radiation section, the requirement on a short microbunch length in the storage ring is lifted. This also lifts the demand on an extra small momentum compaction factor α_c. The storage ring lattice is very much relaxed, while the burden of harmonic generation is taken up by the radiator insertion section. Another important implication of this design is that
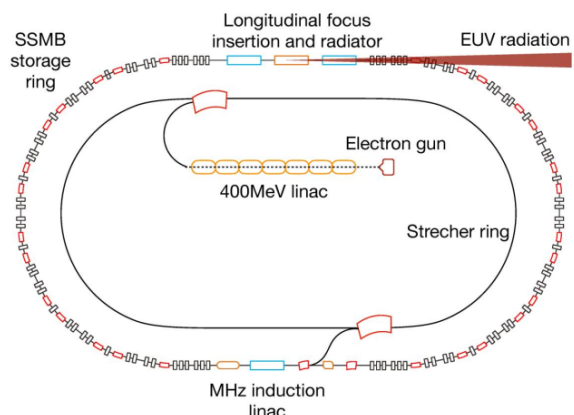
Figure 8: SSMB EUV design layout as of today.

Table 1: A sample list of parameters for a DUV and an EUV SSMB facility. Both examples require harmonic generation.

Parameter	SSMB-DUV	SSMB-EUV	Unit
C_0, circumference	100	100	m
E_0, beam energy	320	800	MeV
I_0, beam current	1	1	A
τ_δ, longitudinal damping time	92	14.7	ms
$\sigma_{\delta 0}$, energy spread	3.1	$4.85 \cdot 10^{-4}$	
σ_z(rad), bunch length at Radiator	10	2	nm
ϵ_y, vertical emittance	20	2	pm
λ_{mod}, modulation laser wavelength	1064	270	nm
h, modulation chirp slope	1000	541	m^{-1}
$L_u(\mathrm{mod})$, modulator length	1.8	1.5	m
P_{mod}, modulation laser power	326	141	kW
n, harmonic number	10	20	
λ_{rad}, radiation wavelength	106.4	13.5	nm
$L_u(\mathrm{rad})$, radiator length	3	3.2	m
$\mathcal{B}$, bunching factor	0.174	0.11	
$P_{\mathrm{rad,cw}}$, radiation power in c.w. mode	1	1	kW

intrabeam scattering and the coherent synchrotron radiation effects are also more relaxed.

SUMMARY

1. Proof of principle Phase I experiment successfully demonstrated the feasibility of the SSMB approach. Phase II experiment is being reinitiated at MLS after a 3-year COVID pause.

2. There are several scenarios of the SSMB light sources.
   - An amplifier scenario uses a conventional storage ring, readily available as a powerful IR source.
   - THz scenario requires a conventional storage ring plus a dual undulator.
   - Harmonic generation SSMB is in active R&D. Design parameters are being formulated and forthcoming.

REFERENCES

[1] X. Deng *et al.*, "Experimental demonstration of the mechanism of steady-state microbunching", *Nature*, vol. 590.7847, pp. 576–579, 2021. doi:10.1038/s41586-021-03203-0

[2] D. F. Ratner and A. W. Chao. "Steady-state microbunching in a storage ring for generating coherent radiation", *Phys. Rev. Lett.*, vol. 105, no. 15, p. 154801, 2010. doi:10.1103/PhysRevLett.105.154801

[3] C. Feng and Z. Zhao, "A storage ring based free-electron laser for generating ultrashort coherent EUV and x-ray radiation", *Sci. Rep.*, vol. 7, p. 4724, 2017. doi:0.1038/s41598-017-04962-5

[4] A. Chao, E. Granados, X. Huang, D. F. Ratner, and H. W. Luo, "High power radiation sources using the steady-state microbunching mechanism", in *Proc. IPAC'16*, Busan, Korea, May 2016, pp. 1048–1053. doi:10.18429/JACoW-IPAC2016-TUXB01

[5] C. Tang *et al.*, "First experimental demonstration of the mechanism of steady-state microbunching", presented at IPAC'20, Caen, France, May 2020, paper MOVIR08, unpublished.

[6] J. Feikes *et al.*, "Progress towards realisation of steady-state microbunching at the Metrology Light Source", presented at IPAC'21, Campinas, SP, Brazil, May 2021, paper MOXB01, unpublished.

[7] A. Kruschinski *et al.*, "Exploring the necessary conditions for steady-state microbunching at the Metrology Light Source", presented at IPAC'23, Venice, Italy, May 2023, paper MOPA176, to appear in the proceedings.

[8] X. J. Deng and A. Chao, "Why is the coherent radiation from laser-induced microbunches narrowbanded and collimated", presented at FLS'23, Lucerne, Switzerland, Aug.-Sep. 2023, paper TP4P29, this conference.

[9] C. Tang *et al.*, "An overview of the progress on SSMB", in *Proc. FLS'18*, Shanghai, China, Mar. 2018, pp. 166–170. doi:10.18429/JACoW-FLS2018-THP2WB02

[10] Y. Zhang *et al.*, "Ultralow longitudinal emittance storage rings", *Phys. Rev. Accel. Beams*, vol. 24, no. 9, p. 090701, 2021.

[11] D. Ratner and A. Chao, "Steady-state reversible seeding to drive coherent radiation in a storage ring", in *Proc. FEL'11*, Shanghai, China, Aug. 2011, paper MOPB21, pp. 53–56.

[12] C. L. Li, *et al.*, "Lattice design for the reversible SSMB", in *Proc. IPAC'19*, Melbourne, Australia, May 2019, pp. 1507–1509. doi:10.18429/JACoW-IPAC2019-TUPGW045

[13] Z. Z. Li *et al.*, "Generalized longitudinal strong focusing in a steady-state microbunching storage ring", *Phys. Rev. Accel. Beams*, 2023, to be published.

[14] Z. L. Pan *et al.*, ' 'A storage ring design for steady-state microbunching to generate coherent EUV light source", in *Proc. FEL'19*, Hamburg, Germany, Aug. 2019, pp. 700–703. doi:10.18429/JACoW-FEL2019-THP055

[15] Z. L. Pan *et al.*, "Low-alpha storage ring design for steady state microbunching to generate EUV radiation", presented

at FLS'23, Lucerne, Switzerland, Aug.-Sep. 2023, paper TU1B2, this conference.

[16] X. J. Deng *et al.*, "Single-particle dynamics of microbunching", *Phys. Rev. Accel. Beams* vol. 23, no. 4, p. 044001 and p. 044002, 2020.

[17] C.-Y. Tsai, "Theoretical formulation of multiturn collective dynamics in a laser cavity modulator with comparison to Robinson and high-gain free-electron laser instability", *Phys. Rev. Accel. Beams* vol. 25, no. 6, p. 064401, 2022.

[18] C.-Y. Tsai and X. J. Deng, "A recursive model for laser-electron-radiation interaction in insertion section of SSMB storage ring based on transverse-longitudinal coupling scheme", presented at FLS'23, Lucerne, Switzerland, Aug.-Sep. 2023, paper TU4P31, this conference.

[19] H. Wang *et al.*, "Cavity mirror development for optical enhancement cavity of steady-state microbunching light source", presented at IPAC'23, Venice, Italy, May 2023, paper MOPM123, to appear in the proceedings.

[20] X. Y. Zhang *et al.*, "Electron injector design for future steady-state microbunching high average power EUV light source', presented at IPAC'23, Venice, Italy, May 2023, paper MOPM082, to appear in the proceedings.

[21] X. J. Deng *et al.*, "Useful formulas and example parameters set for the design of SSMB storage rings", presented at FLS'23, Lucerne, Switzerland, Aug.-Sep. 2023, paper TU4P28, this conference.

REVIEW OF HARMONIC CAVITIES IN FOURTH-GENERATION STORAGE RINGS

F. J. Cullinan*, Å. Andersson, P. F. Tavares, MAX IV Laboratory, Lund, Sweden

Abstract

Several third generation light-source storage rings have used harmonic cavities to lengthen the electron bunches. With the advent of the fourth generation however, they have become an almost universal feature as the small transverse electron beam sizes make long bunches essential for increasing Touschek lifetime and reducing emittance blow-up from intrabeam scattering. Multiple technological solutions exist for the implementation of harmonic cavities and which to use and how to implement it are questions that many facilities have to tackle. This is therefore a very active area of study in which there is strong collaboration within the community. In this proceeding, the approaches taken, as determined from a survey of different projects, are summarised. Avoiding coherent collective beam instabilities is of particular concern and those that are driven by the impedance of the harmonic-cavity fundamental mode are outlined with reference to the relevant theories. Where appropriate, the discussion is complemented by a description of the observations made at the MAX IV 3 GeV ring, the first fourth generation storage ring which was commissioned with normal-conducting passive harmonic cavities already installed.

INTRODUCTION

Harmonic cavities (HCs) are used in storage rings to alter the slope of the RF voltage over the duration of the charged particle bunches. In electron storage rings used as synchrotron light sources, by far the most common aim is to lengthen the bunches in order to increase the Touschek lifetime[1]. For this reason, several third-generation light-source storage rings had harmonic cavities installed [2–6]. Now, the fourth-generation of storage rings are coming online and lengthened electron bunches are even more desirable due to the smaller transverse beam sizes, which lead to shorter Touschek lifetimes. Without bunch lengthening, fourth-generation storage rings also suffer from significant emittance blow-up due to intrabeam scattering [7]. For these reasons, harmonic cavities have become critical components in almost all fourth-generation storage rings and are included in their baseline designs. A significant amount of research has therefore been conducted to develop these harmonic cavities, better understand the beam dynamics and to decide which type and design of HC is best suited to a particular storage ring. Successful collaborations such as the recent one between HZB, DESY and ALBA [8] play a key role in how facilities overcome the technical and theoretical challenges and workshops, such as the dedicated HarmonLIP

series in Europe, provide a crucial platform for advances to be shared.

The goal of this proceeding is to present a review of this latest wave of research and the environment and context in which it is being carried out. This is done from a beam dynamics perspective so will leave out the important work that is going into the technical designs, which interested readers may find elsewhere: [8–11] and others. A survey of the world's light-source facilities that have fourth-generation storage-ring projects has been conducted and in the first part of this proceeding, the results of this survey are presented. It is hoped that the results provide a helpful guide to future projects that will be faced with the same considerations.

Of particular interest in the survey were the fill patterns to be used in the storage ring since it is well established that an uneven fill pattern can negatively impact the bunch lengthening that can be achieved and lead to a distribution of different bunch lengths over the bunch train. This aspect in particular been the subject of a lot of research. Byrd and Georgsson [4] used single-particle tracking to predict the effects of this before Bassi et al. [12] took advantage of more powerful computing techniques and employed macroparticle tracking. More recently, a semi-analytical approach was taken by Yamamoto et al [13] and Olsson et al. [14] used a matrix equation and the Newton method to iterate towards a self-consistent solution that showed good agreement with tracking using a fraction of the computational resources. Since then, other approaches have emerged [15, 16] showing improved performance and the potential to include the effects of short-range wakefields.

HARMONLIP

In October 2022, a workshop called HarmonLIP was convened at MAX IV Laboratory in Lund, Sweden [17]. This was the first in a series that is an internal project supported by the League of European Accelerator-based Photon Sources (LEAPS) Working Group 2 [18]. The hybrid workshop had delegates from eleven different synchrotron light-source facilities in Europe come in person or join remotely and was also joined remotely from South America and from Asia. The workshop photo is shown in Fig. 1. Facilities gave an update on the status of their respective harmonic-cavity systems before more general topics were discussed. These discussions included short comment talks briefly presenting the perspective of one facility or one participant. The next edition of the HarmonLIP workshop series is planned for March 2024 and will be hosted by the ESRF in Grenoble.

In preparation for the workshop, a survey was carried out of the technical specifications of the HC systems at each

---

* francis.cullinan@maxiv.lu.se

[1] Bunch shortening is also sometimes the aim [1]

Figure 1: Workshop photo of the HarmonLIP workshop at MAX IV, Lund, Sweden, 2022.

Figure 2: Bar chart of types of harmonic cavity used in fourth-generation light-source storage rings.

SURVEY

A survey was carried out of all of the projects for fourth-generation storage rings known to the authors that use or foresee the use of harmonic cavities. There is a lot of variety among the different projects, including the project status, which varies from pre-conceptual design to fully operational. As a result, some of the results are likely to change. The survey was carried out by contacting members of staff from the relevant facilities and asking them a series of questions. The storage rings included are SOLEIL-II [19], SLS 2.0 [20], the 3 GeV ring at MAX IV [21], BESSY III [22], the ESRF-EBS [23], ELETTRA 2.0 [24], DIAMOND-II [25], PETRA IV [26], ALBA II [27], the future light source at KEK [28], ALS-U [29], APS-U [30], SIRIUS [31], HEPS [32], HALF [33] and SPS II [34] (the people contacted are in the Acknowledgements section). This section presents the results of the survey's different questions alongside the interpretation of the authors.

Harmonic Cavity Type

Harmonic cavities can be made of normal or superconducting material and can either be active, with an external generator providing power to the cavity, or passive such that the power in the cavity is taken from the electron beam (indirectly from the main RF). HCs can therefore be separated into four distinct combinations of normal or superconducting and active or passive. Figure 2 shows the types of cavity used at different fourth-generation storage-rings. Normal-conducting passive harmonic cavities were opted for in the MAX IV 3 GeV ring, partly due to success in a previous MaxLab storage ring [3]. Most fourth-generation storage rings since then, however, have opted for either superconducting passive or normal-conducting active solutions. This is to limit the total R/Q so that, when running with an uneven fill pattern, the variation in bunch lengthening (and therefore lifetime) between different bunches is reduced. Even at lower R/Q, superconducting passive systems can have
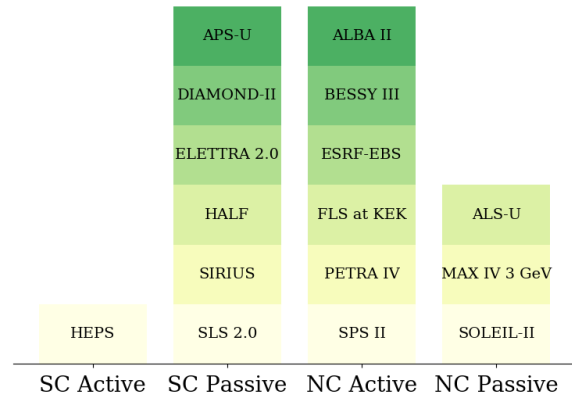
more shunt impedance than their normal-conducting passive counterparts. This allows them to be used effectively even in low-current modes of operation (although this shortcoming can be mitigated in the normal-conducting case by reducing the voltage of the main RF [35]).

Active harmonic cavities offer the most control of the total RF-voltage waveform for any beam current or energy loss to synchrotron radiation. The latter parameter can vary a lot in fourth-generation storage rings since variable sources of radiation (the insertion devices) can dominate the bare-machine magnetic lattice's fixed energy loss, which is typically lower than in third-generation storage rings of the same circumference. Once again though, set voltages can also be adjusted in passive systems to adapt to changing conditions [35]. Active cavities are also less likely than superconducting passive cavities to excite the Robinson D-mode instability when operating at low beam currents (see dedicated section below).

The majority of facilities will have harmonic cavities operating at the 3rd harmonic of the RF frequency. Three however, namely ESRF-EBS, APS-U and the SOLEIL upgrade, have opted for the fourth harmonic instead (although for SOLEIL, other options are still being considered). A higher harmonic means lower power consumption but also less bunch lengthening. However, due to the large impedances of the large APS-U and ESRF-EBS storage rings, the bunch lengthening with the beam current due to potential-well distortion is already quite high and, relative to their natural bunch lengths, these two machines actually expect the largest bunch-lengthening factors (> 6) when the harmonic cavities are engaged [36].

Bunch Lengthening

Figure 3 shows the distribution of bunch lengthening aimed for in the different storage rings. A modest bunch lengthening of around a factor of 3 can be enough to bring the Touschek and intrabeam scattering to within acceptable levels. When requesting this information from the different facilities, whether potential-well distortion should be
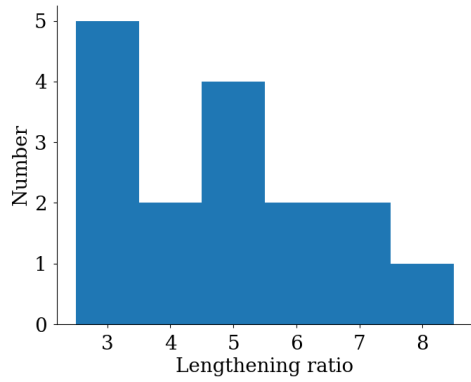
Figure 3: Histogram of bunch lengthening factors expected at each fourth-generation light-source storage ring.
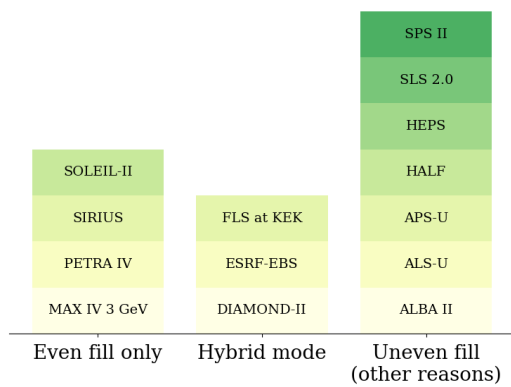

Figure 4: Bar chart of fill patterns used or to be used in fourth-generation light-source storage rings.

included was not specified so this may have led to additional variation. A range was also often given due to the use of an uneven fill pattern, which is also a limiting factor in how much lengthening that can be achieved (see next section). Facilities that can operate with an even fill pattern may decide to lengthen the bunches slightly beyond flat potential conditions as this has been shown to deliver a longer Touschek lifetime.

Fill Pattern

Although it would provide the best results in terms of bunch lengthening, running with an even filling pattern is not always possible in many fourth-generation storage rings, as shown in Fig. 4. The most common reason for using an uneven fill pattern is the need for a larger gap between two of the bunches for the clearing of ions.

Users that require x-ray pulses at reduced repetition rate may be accommodated without sacrificing too much brightness by increasing the number of empty RF buckets between evenly spaced electron bunches, as long as the repetition rates required are not too low and the machine is of sufficiently large circumference. Otherwise, uneven hybrid fill patterns must be used to achieve something similar. These

generally consist of a long train of electron bunches for brightness and a long gap with a single so-called camshaft bunch in the middle. Users of pulsed x-rays block the light from the long train using a mechanical chopper.

One project, ALS-U, cited the use of swap-out injection by trains for the need for gaps in the fill pattern. In this scheme, whole trains of bunches in the storage ring are swapped out for a fresh train coming from the injector and a gap before and after each train is required to allow for the injection kickers to reach the necessary kick strength (kicker rise time).

ESRF-EBS does foresee the use of a hybrid fill pattern but only intends to engage the harmonic cavities for higher-charge even fill patterns with fewer bunches.

It is well established that an uneven fill pattern can reduce the amount of bunch lengthening that can be achieved using harmonic cavities. Facilities are therefore considering ways in which to limit the reduction. One promising approach is to use many shorter bunch trains instead of a single long train. Calculations and simulations have shown that this leads to better average bunch lengthening [37]. In addition, the use of higher-charge 'guard' bunches at the beginning and end of a bunch train can improve the bunch lengthening of the majority of bunches in the centre. This scheme was first proposed by Milas and Stingelin [38] and it has been shown that these bunches can also improve ion clearing [39].

COLLECTIVE EFFECTS

Although the potential of harmonic cavities to damp HOM-driven longitudinal coupled-bunch instabilities has been demonstrated in the MAX IV 3 GeV ring [40], it has been decided for almost all subsequent fourth-generation storage ring projects to not rely on harmonic cavities for this purpose. The overwhelming majority of facilities prefer to use other methods such as HOM-damped cavities and longitudinal bunch-by-bunch feedback. Indeed, it is not clear that harmonic cavities are beneficial in this respect in all cases. On one hand, they introduce a spread in synchrotron frequency, either within the bunches or between the bunches for Landau damping and increase rejection of high-frequency HOMs by lengthening the bunch duration. On the other hand, they reduce the average incoherent synchrotron frequency within the bunch, and this has a destabilising effect.

A way in which harmonic cavities can impact longitudinal beam stability that cannot be solved by HOM damping is through their own impedance. If the wrong machine parameters and cavity specifications are chosen, instabilities can occur. This section briefly describes three of these instabilities. An important one that is not included is the DC Robinson instability [41].

Robinson Mode Coupling

In order to lengthen the electron bunches, passive harmonic cavities need to be detuned with respect to their RF harmonic in such a way that they drive rather than damp

67th ICFA Adv. Beam Dyn. Workshop Future Light Sources
ISBN: 978-3-95450-224-0

FLS2023, Luzern, Switzerland

JACoW Publishing

ISSN: 2673-7035

doi:10.18429/JACoW-FLS2023-M02L3

the Robinson instability. For most storage rings, which operate with a positive momentum compaction factor, this means to higher frequency. This is also the case for machines with active harmonic cavities because they must be similarly detuned in order to minimise the power reflected from the cavity. Storage rings with harmonic cavities installed must therefore be designed to avoid this instability, by ensuring that there is enough Robinson damping from the main RF cavities for example. Even if the dipole Robinson mode is stable, however, a Robinson mode coupling with the quadrupole mode can lead to an instability [42]. A measurement of this instability in the MAX IV 3 GeV ring and how it is avoided can be found in [40].

Robinson D-mode Instability

Another type of Robinson instability is the so-called D-mode instability [43]. This was observed in simulation by Gamelin [44] and also by Stingelin [45]. It was since found that by including radiation damping in the usual equation for the Robinson instability, treating each bunch as a single particle, and not linearising the equation, a second Robinson mode appears whose resonant frequency approximately follows the harmonic-cavity detuning. This mode is referred to as the D-mode. Furthermore, a reduction in the radiation damping time actually increases the growth rate of the D-mode, as does a higher quality factor of the HC. Intuitively, this can be seen as the beam motion exciting the HC on resonance while the conventional Robinson dipole mode [46], referred to in [43] as the S-mode, is the cavity exciting the beam on resonance. The relative bandwidths of the beam (in other words, the damping rate) and of the cavity determine which mode is less stable. Storage rings with superconducting harmonic cavities are therefore most prone to a D-mode instability and it is most likely to occur at low current while trying to lengthen the bunches by tuning the HC close enough to the RF harmonic that it resonantly excites motion in the beam. If the detuning is small enough to bring the coherent frequency of the D-mode close to that of the S-mode, a coupling instability can occur [43].

Mode-1 Excitation

At the other end of the scale is the mode-1 instability. This is likely to occur in storage rings with harmonic cavities of lower quality factor, excessive shunt impedance and towards higher currents. In this scenario, the HC must be detuned considerably and its impedance starts to overlap with the resonant frequency of the first coupled-bunch mode, thereby exciting it. This was a known potential issue before this latest expansion in the use of harmonic cavities [42] and has been explored more recently by Venturini [47]. It was also seen independently in simulation [48] and investigated further in [49]. An image of the instability, as observed in the MAX IV 3 GeV ring is shown in Fig. 5. One remarkable characteristic of this instability is its extremely low coherent oscillation frequency of a few Hz. It also takes on quite an asymmetric form when it saturates, which led to it also being referred to as periodic transient beam loading (PTBL) [49].
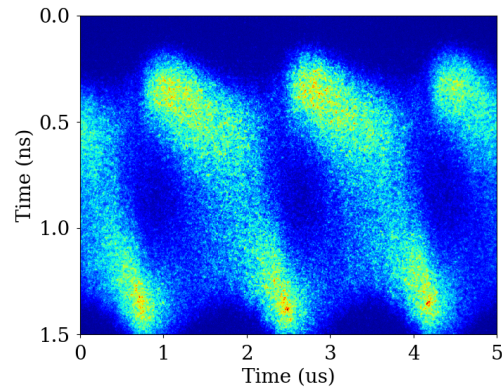
Figure 5: A single-shot streak camera image of a mode-1 instability observed in the MAX IV 3 GeV ring at a current of 200 mA and an RF voltage of 1 MV, a voltage in the passive HCs (8.25 M shunt impedance) of 335 kV, the bare lattice single-electron energy loss per turn of 363.8 keV and the machine parameters otherwise given in [50].

As it is a coupled-bunch mode, it is tempting to use simplified formulas for determining whether mode 1 is stable, as one may do with any other coupled-bunch mode. Another simplified method has come up based on the observation that, owing to its low coherent frequency of oscillation, some approaches designed to determine equilibrium bunch distributions are also capable of making predictions of the mode-1 instability as well [51]. Also readily available is an approximation from [47], although this only predicts the growth rate of the mode-1 instability in the conditions under which it is most likely to occur. However, all of these methods neglect Landau damping. In order to include it, a more comprehensive theory must be used. For a quartic potential the theory of Krinsky [52] (later extended in [53]) can be used while the complete formulation outlined in [47] covers more arbitrary longitudinal potentials but requires the use of a numerical solver.

CONCLUSION

The advantages of using harmonic cavities in fourth-generation storage rings make their use almost universal. The only fourth-generation storage ring that the authors could identify that does not foresee the use of harmonic cavities (at the very least in the conceptual design) is SPring-8-II [54]. However, harmonic cavities come in several types and which type is most suitable for a given light source is heavily dependent on the machine parameters and the user requirements. The variety in the choice of fill pattern is illustrative of the wider variety that exists between the different facilities.

The most important collective effects that come as a byproduct of using harmonic cavities have been outlined. These are caused by the impedance of the harmonic cavities themselves and can lead to beam instabilities. It must be ensured that all foreseen operational modes are within the

thresholds of these instabilities so that they do not appear. Other instabilities caused by HOMs in the cavities and the machine impedance more generally are also heavily influenced by the use of harmonic cavities and also need to be avoided. Fortunately, as evidenced by the references in this paper, a good body of research provides a strong basis for any new study and a productive and collaborative community exists to help overcome any new challenges that may arise. Successful workshops such as HarmonLIP packed with detailed presentations demonstrate that this is the case.

ACKNOWLEDGEMENTS

REFERENCES

[1] P. Jankowiak *et al.*, "Bessy vsr variable pulse length storage ring upgrade of bessy 2," Helmholtz-Zentrum Berlin, 2015. `doi:http://dx.doi.org/10.5442/R0001`

[2] G. Penco and M. Svandrik, "Experimental studies on transient beam loading effects in the presence of a superconducting third harmonic cavity," *Phys. Rev. Spec. Top. Accel. Beams*, vol. 9, p. 044 401, 4 2006. `doi:10.1103/PhysRevSTAB.9.044401`

[3] M. Georgsson, Å. Andersson, and M. Eriksson, "Landau cavities at MAX II," *Nucl. Instrum. Methods Phys. Res., Sect. A*, vol. 416, no. 2, pp. 465–474, 1998. `doi:10.1016/S0168-9002(98)00667-6`

[4] J. M. Byrd and M. Georgsson, "Lifetime increase using passive harmonic cavities in synchrotron light sources," *Phys. Rev. Spec. Top. Accel. Beams*, vol. 4, p. 030 701, 3 2001. `doi:10.1103/PhysRevSTAB.4.030701`

[5] M. Pedrozzi *et al.*, "SLS operational performance with third harmonic superconducting system," in *Proc. SRF'03*, L beck, Germany, Sep. 2003, pp. 91–94. `https://jacow.org/SRF2003/papers/MOP25.pdf`

[6] M. Georgsson, W. Anders, D. Krämer, and J. Byrd, "Design and commissioning of third harmonic cavities at BESSY II," *Nucl. Instrum. Methods Phys. Res., Sect. A*, vol. 469, no. 3, pp. 373–381, 2001. `doi:10.1016/S0168-9002(01)00783-5`

[7] S. C. Leemann, "Interplay of touschek scattering, intra-beam scattering, and rf cavities in ultralow-emittance storage rings," *Phys. Rev. Spec. Top. Accel. Beams*, vol. 17, p. 050 705, 5 2014. `doi:10.1103/PhysRevSTAB.17.050705`

[8] F. P rez *et al.*, "3HC - third harmonic normal conducting active cavity collaboration between HZB, DESY and ALBA," in *Proc. IPAC'22*, Bangkok, Thailand, 2022, pp. 1471–1474. `doi:10.18429/JACoW-IPAC2022-TUPOMS028`

[9] P. Zhang *et al.*, "Radio-frequency system of the high energy photon source," *Radiat Detect Technol Methods*, vol. 7, pp. 159–170, 2023. `doi:ttps://doi.org/10.1007/s41605-022-00366-w`

[10] M. P. Kelly *et al.*, "Superconducting harmonic cavity for the Advanced Photon Source upgrade," in *Proc. IPAC'15*, Richmond, VA, USA, May 2015, pp. 3267–3269. `doi:10.18429/JACoW-IPAC2015-WEPTY008`

[11] T. Yamaguchi, N. Yamamoto, D. Naito, T. Takahashi, and S. Sakanaka, "Design and low-power measurement of 1.5 GHz TM020-type harmonic cavity for KEK future synchrotron light source," *Nucl. Instrum. Methods Phys. Res., Sect. A*, vol. 1053, p. 168 362, 2023. `doi:10.1016/j.nima.2023.168362`

[12] G. Bassi, A. Blednykh, S. Krinsky, and J. Rose, "Self-consistent simulations of passive landau cavity effects," in *Proc. NAPAC'13*, Pasadena, CA, USA, Sep.-Oct. 2013, pp. 177–179. `https://jacow.org/PAC2013/papers/MOPBA03.pdf`

[13] N. Yamamoto, T. Takahashi, and S. Sakanaka, "Reduction and compensation of the transient beam loading effect in a double rf system of synchrotron light sources," *Phys. Rev. Accel. Beams*, vol. 21, p. 012 001, 1 2018. `doi:10.1103/PhysRevAccelBeams.21.012001`

[14] T. Olsson, F. J. Cullinan, and Å. Andersson, "Self-consistent calculation of transient beam loading in electron storage rings with passive harmonic cavities," *Phys. Rev. Accel. Beams*, vol. 21, p. 120 701, 12 2018. `doi:10.1103/PhysRevAccelBeams.21.120701`

[15] R. Warnock and M. Venturini, "Equilibrium of an arbitrary bunch train in presence of a passive harmonic cavity: Solution through coupled haïssinski equations," *Phys. Rev. Accel. Beams*, vol. 23, p. 064 403, 6 2020. `doi:10.1103/PhysRevAccelBeams.23.064403`

[16] T. He and Z. Bai, "Graphics-processing-unit-accelerated simulation for longitudinal beam dynamics of arbitrary bunch trains in electron storage rings," *Phys. Rev. Accel. Beams*, vol. 24, p. 104 401, 10 2021. `doi:10.1103/PhysRevAccelBeams.24.104401`

[17] HarmonLIP 2022. (2022), `https://indico.maxiv.lu.se/event/5098/overview`

[18] LEAPS Initiative, 2018. `www.leaps-initiative.eu`

[19] A. Nadji *et al.*, "Conceptual design report: Synchrotron soleil upgrade," Synchrotron SOLEIL, 2021. `https://www.synchrotron-soleil.fr/en/news/conceptual-design-report-soleil-upgrade`

[20] H. Braun *et al.*, "SLS-2 conceptual design report," Paul Scherrer Institut, 21-02, 2017.

[21] P. F. Tavares, S. C. Leemann, M. Sjöström, and Å. Andersson, "The MAX IV storage ring project," *Journal of Synchrotron Radiation*, vol. 21, no. 5, pp. 862–877, 2014. `doi:10.1107/S1600577514011503`

[22] P. Goslawski *et al.*, "BESSY III status report and lattice design process," in *Proc. IPAC'22*, Bangkok, Thailand, 2022, pp. 1417–1419.
`doi:10.18429/JACoW-IPAC2022-TUPOMS010`

[23] P. Raimondi *et al.*, "EBS storage ring technical report," ESRF, 2018. `https://www.esrf.fr/files/live/sites/www/files/about/upgrade/documentation/Design%20Report-reduced-jan19.pdf`

[24] F. Karantzoulis *et al.*, "Elettra 2.0 technical design report," Elettra ? Sincrotrone Trieste, internal document, ST/M-21/01, 2021.

[25] R. P. Walker, M. Abbott, C. Abraham, P. Annos, and A. R. Bainbridge, "Diamond-II technical design report," Diamond Light Source Ltd., 2022.

[26] C. G. Schroer *et al.*, "PETRA IV: Upgrade of PETRA III to the ultimate 3D x-ray microscope," Deutsches Elektronen-Synchrotron DESY, 2019.

[27] C. Biscari *et al.*, "ALBA II white paper," ALBA Synchrotron, 2023.

[28] T. Honda, "Concept of a new generation synchrotron radiation facility KEK Light Source," in *Proc. IPAC'17*, Copenhagen, Denmark, May 2017, pp. 2687–2690.
`doi:10.18429/JACoW-IPAC2017-WEPAB047`

[29] C. Steier *et al.*, "Design progress of ALS-U, the soft x-ray diffraction limited upgrade of the Advanced Light Source," in *Proc. IPAC'19*, Melbourne, Australia, May 2019, pp. 1639–1642. `doi:10.18429/JACoW-IPAC2019-TUPGW097`

[30] T. E. Fornek, "Advanced photon source upgrade project final design report," 2019. `doi:10.2172/1543138`

[31] L. Liu *et al.*, "Status of Sirius operation," in *Proc. IPAC'22*, Bangkok, Thailand, 2022, pp. 1385–1388.
`doi:10.18429/JACoW-IPAC2022-TUPOMS002`

[32] Y. Jiao *et al.*, "The HEPS project," *Journal of Synchrotron Radiation*, vol. 25, no. 6, pp. 1611–1618, 2018.
`doi:10.1107/S1600577518012110`

[33] Z. H. Bai *et al.*, "A modified hybrid 6BA lattice for the HALF storage ring," in *Proc. IPAC'21*, Campinas, Brazil, May 2021, pp. 407–409.
`doi:10.18429/JACoW-IPAC2021-MOPAB112`

[34] P. Klysubun *et al.*, "SPS-II: A 4th generation synchrotron light source in southeast Asia," in *Proc. IPAC'22*, Bangkok, Thailand, May 2022, pp. 764–768.
`doi:10.18429/JACoW-IPAC2022-MOOPLGD2`

[35] F. J. Cullinan, *Longitudinal Beam Dynamics in Ultra-low Emittance Rings*, presented at I.FAST, Karlsruhe (remote), 2022.

[36] L. R. Carver *et al.*, "Beam based characterization of the european synchrotron radiation facility extremely brilliant source short range wakefield model," *Phys. Rev. Accel. Beams*, vol. 26, p. 044 402, 4 2023.
`doi:10.1103/PhysRevAccelBeams.26.044402`

[37] T. Olsson, *Collective Effects in the Diamond-II Storage Ring*, presented at LEL, Barcelona, Spain, 2022.

[38] N. Milas and L. Stingelin, "Impact of filling patterns on bunch length and lifetime at the SLS," Kyoto, Japan, 2010. `https://api.semanticscholar.org/CorpusID:125107350`

[39] J. Calvey and M. Borland, "Simulation of incoherent ion effects in electron storage rings," *Phys. Rev. Accel. Beams*, vol. 24, p. 124 401, 12 2021.
`doi:10.1103/PhysRevAccelBeams.24.124401`

[40] F. J. Cullinan, . Andersson, and P. F. Tavares, "Longitudinal stability with landau cavities at MAX IV," in *Proc. IPAC'20*, Caen, France, 2021, p. 44.
`doi:10.18429/JACoW-IPAC2020-WEVIR05`

[41] J. Jacob, *Passive vs Active Systems, DC Robinson, DLLRF*, presented at HarmonLIP, Lund, Sweden, 2022.

[42] R. A. Bosch, K. J. Kleman, and J. J. Bisognano, "Robinson instabilities with a higher-harmonic cavity," *Phys. Rev. Spec. Top. Accel. Beams*, vol. 4, p. 074 401, 7 2001.
`doi:10.1103/PhysRevSTAB.4.074401`

[43] T. He, W. Li, Z. Bai, and W. Li, "Mode-zero robinson instability in the presence of passive superconducting harmonic cavities," *Phys. Rev. Accel. Beams*, vol. 26, p. 064 403, 6 2023. `doi:10.1103/PhysRevAccelBeams.26.064403`

[44] A. Gamelin, *Harmonic cavity studies for the SOLEIL Upgrade*, presented at I.FAST, Karlsruhe (remote), 2022.

[45] L. Stingelin, *Tracking simulations and tests results in SLS with Super-3HC*, presented at HarmonLIP, Lund, Sweden, 2022.

[46] A. W. Chao, *Physics of Collective Beam Instabilities in High Energy Accelerators*. John Wiley & Sons, Inc., 1993, pp. 162–172. `doi:ISBN0-471-55184-8`

[47] M. Venturini, "Passive higher-harmonic RF cavities with general settings and multibunch instabilities in electron storage rings," *Phys. Rev. Accel. Beams*, vol. 21, p. 114 404, 11 2018. `doi:10.1103/PhysRevAccelBeams.21.114404`

[48] A. Gamelin, *Harmonic cavities studies and applications for SOLEIL upgrade: bunch lengthening, transient beam loading and instabilities*, presented at LER, Frascati (remote), 2020.

[49] T. He, W. Li, Z. Bai, and L. Wang, "Periodic transient beam loading effect with passive harmonic cavities in electron storage rings," *Phys. Rev. Accel. Beams*, vol. 25, p. 024 401, 2 2022.
`doi:10.1103/PhysRevAccelBeams.25.024401`

[50] P. F. Tavares, Å. Andersson, A. Hansson, and J. Breunlin, "Equilibrium bunch density distribution with passive harmonic cavities in a storage ring," *Phys. Rev. Spec. Top. Accel. Beams*, vol. 17, p. 064 401, 6 2014.
`doi:10.1103/PhysRevSTAB.17.064401`

[51] T. He, "Novel perturbation method for judging the stability of the equilibrium solution in the presence of passive harmonic cavities," *Phys. Rev. Accel. Beams*, vol. 25, p. 094 402, 9 2022. `doi:10.1103/PhysRevAccelBeams.25.094402`

[52] S. Krinsky and J. M. Wang, "Longitudinal instabilities of bunched beams subject to a nonharmonic rf potential," *Part. Accel.*, vol. 17, pp. 109–139, 1985.

[53] R. R. Lindberg, "Theory of coupled-bunch longitudinal instabilities in a storage ring for arbitrary RF potentials," *Phys. Rev. Accel. Beams*, vol. 21, p. 124 402, 12 2018.
`doi:10.1103/PhysRevAccelBeams.21.124402`

[54] I. Ishikawa *et al.*, "SPring-8-II conceptual design report," RIKEN SPring-8 Center, 2014. `http://rsc.riken.jp/eng/pdf/SPring-8-II.pdf`

BEAM DYNAMICS USING SUPERCONDUCTING PASSIVE HARMONIC CAVITIES WITH HIGH CURRENT PER BUNCH

A. Gamelin*, V. Gubaidulin, A. Loulergue, P. Marchand, L. S. Nadolski, R. Nagaoka

Synchrotron SOLEIL, Gif-sur-Yvette, France

N. Yamamoto, KEK, Ibaraki, Japan

Abstract

In 4th generation synchrotron light sources, harmonic cavities (HCs) are critical components needed to achieve the required performance. They provide longer bunches, which helps to reduce statistical effects (intra-beam scattering and Touschek effect). In "timing" modes, where the bunch spacing is larger than in conventional modes and the number of particles per bunch is higher, this need is even greater. In this article, we present the beam dynamics in the high current per bunch regime and how it interacts with the single bunch collective effects. In particular, a dipole-quadrupole instability is observed above the microwave threshold and a coupling between the dipole and cavity modes is shown to limit bunch lengthening at low current. The effective gain from the use of HCs in terms of lifetime, emittance, and energy spread is also discussed.

INTRODUCTION

In this paper, we explore the beam dynamics of a double RF system with harmonic cavities (HCs) in the context of high currents per bunch. The parameters of the SOLEIL II project [1–3], which aims to replace the existing SOLEIL storage ring by a 4th generation synchrotron light source are used throughout the article.

Double RF System

For a passive unloaded cavity at the kth harmonic of the RF frequency f_{RF}, the only knob is the cavity tuning angle ψ or equivalently the cavity detuning Δf:

$$\Delta f = f_r - k f_{RF}, \qquad (1)$$

$$\tan \psi = Q \left(\frac{f_r}{k f_{RF}} - \frac{k f_{RF}}{f_r} \right) \approx 2Q \frac{\Delta f}{f_r}, \qquad (2)$$

where f_r is the cavity resonance frequency and Q is the cavity quality factor (equal to the unloaded quality factor Q_0 in that case). The beam-induced voltage V_2 in the harmonic cavity (neglecting form factors) is given by [4]:

$$V_2 = 2 I_0 R_s \cos \psi \approx I_0 \frac{R_s}{Q} \frac{k f_{RF}}{\Delta f} \sin \psi, \qquad (3)$$

where I_0 is the total current, R_s is the cavity shunt impedance (using the circuit ohm definition). For a main cavity voltage V_1, an approximate voltage of $V_2 \approx V_1/k$ is needed to get close to the near flat potential (NFP) conditions [5] and longer bunches. Using the beam voltage induced at

---

* alexis.gamelin@synchrotron-soleil.fr

resonance, one can set a lower limit on the needed shunt impedance:

$$R_s \gg \frac{V_1}{2 k I_0}. \qquad (4)$$

For $V_1 = 1.8$ MV, a 4th HC and the lowest beam current of 20 mA, the total shunt impedance of the HCs should be much larger than 11.25 MΩ. As the system should also be stable at higher currents, the total R_s/Q should not exceed 100 Ω to avoid instabilities [5, 6]. Both conditions are only possible with superconducting (SC) cavities, which typically have Q_0 around 10^8, while normal conducting (NC) cavities typically have Q_0 of a few 10^4. For these reasons, we consider in this article a double RF system using SC HCs as detailed in Table 1 and for such a SC passive system there is $\psi \approx \pi/2$ and thus $\sin \psi \approx 1$ in Eq. (3).

Table 1: RF Cavity Parameters

Parameter	NC MC	SC HC
Harmonic number k	1	3 or 4
Shunt impedance R_s (per cavity)	5 MΩ	4.5 GΩ
Unloaded quality factor Q	35 700	10^8
R_s/Q (per cavity)	140 Ω	45 Ω
Loaded quality factor	6 000	10^8
Cavity number	4	2

BEAM DYNAMICS

In this part, the beam dynamics in 8-bunch mode at 100 mA and in single bunch mode at 20 mA is studied by tracking using mbtrack2 [7]. Results for SOLEIL II main operation mode, uniform filling at 500 mA, using the same RF system but without short-range wake, were already discussed in Ref. [5].

Short Range Wake

To be able to estimate accurately the beam dynamics at a high charge per bunch, a preliminary impedance model including the most important features of SOLEIL II (resistive wall with NEG coating, tapers, BPMs, ...) is included in the simulations [8]. Figure 1 shows the relative variation of the bunch length and energy spread when the single bunch current is varied from 0 mA to 20 mA. It can be observed that the micro-wave instability (MWI) threshold, characterized by an energy spread increase, is reached at 3 mA.

Even in uniform filling mode, where the current per bunch is limited to 1.2 mA, the short-range wake effect is important
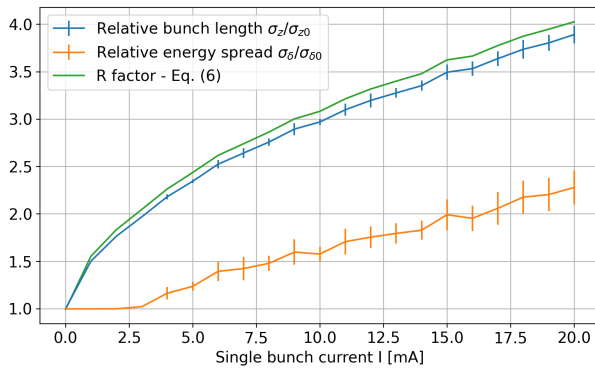
Figure 1: Relative variation of the bunch length σ_z, energy spread σ_δ and R factor (Eq. (6)) versus single bunch current. Zero current RMS values: $\sigma_{z_0} = 8.6$ ps, $\sigma_{\delta_0} = 0.09$ %.

and allows to increase the maximum bunch length by 30 % compared to what was shown in Ref. [5].

"Weak" Dipole-quadrupole Instability

In the 8-bunch mode at 100 mA, a "weak" dipole-quadrupole instability is observed in a given detuning range only when the short-range wake is included in the simulation. The instability is characterized by an in-phase oscillation of the beam center of mass and bunch length which does not lead to beam loss. The typical amplitude of the oscillations is about 20 ps for both the center of mass and the bunch length.

The coherent bunch spectrum, defined as the absolute value of the Fourier transform of the mean position of the bunch, is shown in Fig. 2 with and without the short range wake while the 3rd HC detuning is varied. In the left plot, one can see the dipole Robinson mode frequency decreasing from the unperturbed synchrotron frequency $f = f_{s_0}$ when the HC detuning decreases and the system is getting closer to the NFP conditions. In the right plot, in addition, there is the dipole synchrotron mode, from the inclusion of the short range wake, which is constant because of the (negative) incoherent tune shift compensated by the dynamic coherent frequency shift for mode $m = 1$ [9]. When the dipole synchrotron mode is reached by what we believe to be the quadrupole Robinson mode around $\Delta f \approx 20$ kHz, this "weak" dipole-quadrupole instability appears.

This instability seems remarkably similar to the fast mode coupling Robinson instability described in Ref. [10] but is driven by the dipole synchrotron mode excited by the MWI instead of the dipole Robinson mode. The instability is similarly observed for the 4th HC but closer to the NFP and in both cases it is possible to go beyond the detuning at which the modes couple and get back a stable beam.

Mode Coupling Between The Cavity and Dipole Robinson Mode

The same "weak" dipole-quadrupole instability is observed in single bunch mode at 20 mA when the impedance

model is included. In addition, very fast beam losses are observed, even without short-range wake, which are driven by the mode coupling between the dipole Robinson mode originating from $f = f_{s0}$ and the cavity mode from $f = \Delta f$.

The cavity (Robinson) mode has been introduced in Ref. [11], and recently studied in Refs. [12, 13], and is the consequence of the beam modulation at $f_{RF} \pm \Delta f$ feeding back into the main cavity. Here, this effect only originates from the HC, i.e. not from the double RF system, and thus can be described by the point bunch Robinson theory applied to the HC [9]:

$$\Omega^2 = \omega_{s0}^2 + j\frac{eI_0\alpha_c}{E_0T_0} \times \sum_{p=-\infty}^{\infty} \left[p\omega_{RF}Z(p\omega_{RF}) \right. \\ \left. - (p\omega_{RF}+\Omega)Z(p\omega_{RF}+\Omega) \right], \quad (5)$$

where Ω is the coherent mode complex frequency, $\omega_{s0} = 2\pi f_{s0}$, $\omega_{RF} = 2\pi f_{RF}$, α_c is the momentum compaction factor, E_0 is the reference energy, T_0 is the revolution period, and Z is the HC impedance.

Figure 3 shows the coherent bunch spectrum superimposed with the dipole Robinson mode and cavity mode computed numerically from Eq. (5). When the short-range wake is not included, there is a perfect agreement between the tracking and the point bunch theory. The addition of the impedance model strengthens the coupling between the modes, which lowers the instability threshold. In our case, the mode coupling is fully independent of the synchrotron damping time, differently from what is stated in Ref. [13].

This instability is a strong limitation for HC operation at low total current, the threshold is lower for lower harmonic HCs as the detuning to get the required voltage to reach NFP is lower. It explains why the 3rd HC can provide much less bunch lengthening than the 4th HC at 20 mA as shown in Table 2.

IBS AND TOUSCHEK

The reference Touschek lifetime for the SOLEIL II TDR lattice [2] is 3.0 h without errors, calculated for 1.8 MV, 1.2 mA and the zero current RMS values: bunch length $\sigma_{z_0} = 8.6$ ps, energy spread $\sigma_{\delta_0} = 0.09$ %, horizontal emittance $\epsilon_x = 84$ pm rad and vertical emittance $\epsilon_y = 25$ pm rad exited by white noise.

To compute the Touschek lifetime τ for non-Gaussian bunches including the IBS, we use the following method. Firstly, the equilibrium bunch length and energy spread are extracted from mbtrack2 tracking results including the HC and the impedance model. They are used to compute analytically, using the `ibsEmittance` command from elegant [14], new values for the equilibrium energy spread and emittances. Then the Touschek lifetime $\tau_{Piwinski}$ is computed using the Piwinski formula [15] with the IBS equilibrium values and an arbitrary bunch length σ_{z_0}. Finally the bunch profile ρ from tracking is used to compute the Touschek lifetime τ
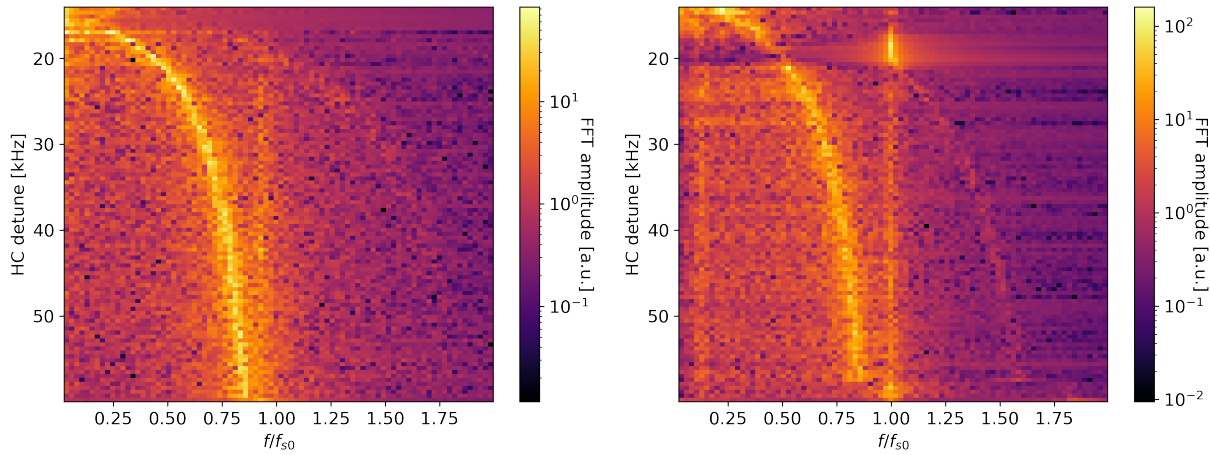
Figure 2: Coherent bunch spectrum from tracking data while the 3rd HC detuning is varied for the 8-bunch mode at 100 mA without (left) and with (right) short-range wake.
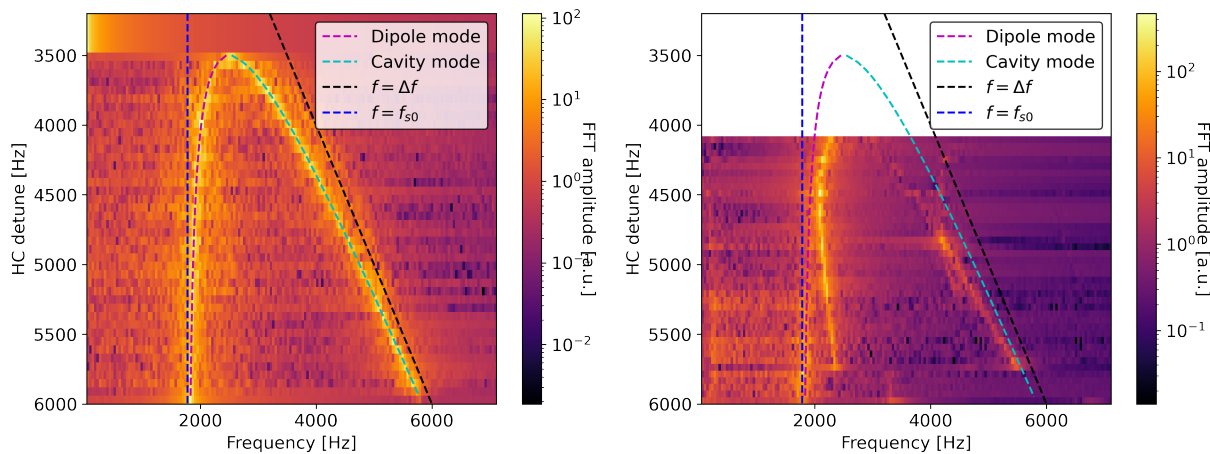
Figure 3: Coherent bunch spectrum from tracking data while the 3rd HC detuning is varied for the single bunch mode at 20 mA without (left) and with (right) short-range wake. The dipole and cavity modes shown in the dashed lines are the numerical solutions of Eq. (5).

using a scaling law [16]:

$$\tau = \tau_{\text{Piwinski}} \times \frac{\int \rho_0^2(z)\,dz}{\int \rho^2(z)\,dz} = \tau_{\text{Piwinski}} \times R, \qquad (6)$$

where ρ_0 is the longitudinal line density corresponding to a Gaussian bunch of $\sigma = \sigma_{z_0}$ and ρ is an arbitrary longitudinal line density.

This approach is not fully self-consistent, as the elegant IBS calculation assumes Gaussian bunches, and any further bunch lengthening from the IBS is neglected in the R factor. The IBS would need to be included in the tracking simulation without assuming a Gaussian shape for a fully self-consistent calculation, but the result should give a good approximation of the combined effects.

The energy spread increase from the MWI plays a significant role for the IBS and Touschek at high bunch charge. Without HC, the Touschek lifetime is quasi-constant in the

range from 10 mA to 20 mA as the current per bunch increase is compensated by the energy spread blow-up (responsible for a 60 % increase at 20 mA), the emittance increase from IBS and the bunch lengthening.

The performances, including Touschek and IBS effects, resulting from the maximum bunch lengthening found by tracking are shown in Table 2. In uniform mode at 500 mA, the 3rd HC is more effective in lengthening the bunches than the 4th HC. In 8-bunch mode at 100 mA, both harmonics give similar results while for single bunch at 20 mA the 4th HC provides better performances than the 3rd one.

Overall, the HC provides a lower lifetime gain for the high current per bunch modes (factor 2) compared to what is obtained for the uniform mode (factor 4). A first reason is that the bunches are already quite long due to the impedance without HC, and the effective lifetime gain is only the ratio $R_{\text{HC}}/R_{\text{noHC}}$. The HC bunch lengthening also reduces the energy spread, if above the MWI threshold, and the emit-

Table 2: Performance in different operation modes with and without SC HC (RMS values for σ_z and σ_δ).

Operation Mode	HC	Bunch Length	Current per Bunch	Emittance H/V	R	Lifetime	Energy Spread
Uniform	Off	13 ps	1.2 mA	103/30 pm.rad	1.6	5.1 h	1.06×10^{-3}
Uniform	3HC	64 ps	1.2 mA	90/27 pm.rad	7	22.4 h	0.95×10^{-3}
Uniform	4HC	46 ps	1.2 mA	91/27 pm.rad	5	17.0 h	0.97×10^{-3}
8 bunches	Off	27 ps	12.5 mA	126/38 pm.rad	3.4	1.5 h	1.86×10^{-3}
8 bunches	3/4HC	77 ps	12.5 mA	112/34 pm.rad	8.7	3.6 h	1.21×10^{-3}
1 bunch	Off	33 ps	20 mA	130/39 pm.rad	4	1.3 h	2.31×10^{-3}
1 bunch	3HC	41 ps	20 mA	132/40 pm.rad	5	1.7 h	1.88×10^{-3}
1 bunch	4HC	69 ps	20 mA	122/36 pm.rad	8.3	2.5 h	1.55×10^{-3}

tance blow-up from IBS which tends to reduce the lifetime improvement.

PERSPECTIVES

As shown in this paper, high current per bunch modes in ultra-low emittance rings are challenging for a double RF system, and the resulting Touschek lifetime can still be quite low despite large bunch lengthening factors. In addition, beamlines may require a limit on the maximum bunch length to maintain good resolution for "timing" mode experiments. A possible way to improve further the Touschek lifetime would be to go to a round beam, i.e. $\epsilon_x = \epsilon_y$, but it brings additional difficulties for lattice design and operation.

For the SOLEIL II project, it was decided to focus on the uniform mode at 500 mA and on a new 32-bunch mode, the other modes being kept but with lower priorities. As a consequence, we are now investigating an NC passive HC solution based on ESRF 4th HC design [17].

REFERENCES

[1] A. Nadji and L. S. Nadolski, "Upgrade Project of the SOLEIL Accelerator Complex," *Synchrotron Radiation News*, vol. 36, no. 1, pp. 10–15, 2023. doi:10.1080/08940886.2023.2186661

[2] A. Loulergue *et al.*, "TDR baseline lattice for SOLEIL II upgrade project," Venice, Italy, May 2023, presented at IPAC'23, Venice, Italy, May 2023, paper MOPM031, unpublished.

[3] "Conceptual Design Report Synchrotron SOLEIL Upgrade," Synchrotron SOLEIL, Tech. Rep., 2021. www.synchrotron-soleil.fr/fr/file/13803

[4] P. Marchand, "Hybrid normal conducting/superconducting rf system for high luminosity circular e+ e-colliders," *Part. Accel.*, vol. 36, pp. 205–222, 1992.

[5] A. Gamelin, W. Foosang, P. Marchand, R. Nagaoka, and N. Yamamoto, "Beam Dynamics with a Superconducting Harmonic Cavity for the SOLEIL Upgrade," in *Proc. IPAC'22*, Bangkok, Thailand, 2022, pp. 2229–2232. doi:10.18429/JACoW-IPAC2022-WEPOMS003

[6] T. He, W. Li, Z. Bai, and L. Wang, "Periodic transient beam loading effect with passive harmonic cavities in electron storage rings," *Phys. Rev. Accel. Beams*, vol. 25, no. 2, p. 024 401, 2022. doi:10.1103/PhysRevAccelBeams.25.024401

[7] A. Gamelin, W. Foosang, and R. Nagaoka, "mbtrack2, a Collective Effect Library in Python," in *Proc. IPAC'21*, Campinas, Brazil, May 2021, pp. 282–285. doi:10.18429/JACoW-IPAC2021-MOPAB070

[8] A. Gamelin, "SOLEIL II project review," *Proceedings of HarmonLIP 2022, Lund, MAX IV*, 2022, https://indico.maxiv.lu.se/event/5098/contributions/6752/attachments/1169/2312/HarmonLIP2022_SOLEIL.pptx.

[9] K.-Y. Ng, *Physics of intensity dependent beam instabilities*. World Scientific, 2006. doi:10.1142/5835

[10] R. A. Bosch, K. J. Kleman, and J. J. Bisognano, "Robinson instabilities with a higher-harmonic cavity," *Phys. Rev. Spec. Top. Accel Beams*, vol. 4, no. 7, p. 074 401, 2001. doi:10.1103/PhysRevSTAB.4.074401

[11] N. Towne and J.-M. Wang, "Spectrum of single bunch longitudinal dipole modes," *Physical Review E*, vol. 57, no. 3, p. 3461, 1998.

[12] T. Yamaguchi, S. Sakanaka, N. Yamamoto, D. Naito, and T. Takahashi, "Systematic study on the static Robinson instability in an electron storage ring," *Phys. Rev. Accel. Beams*, vol. 26, no. 4, p. 044 401, 2023. doi:10.1103/PhysRevAccelBeams.26.044401

[13] T. He, W. Li, Z. Bai, and W. Li, "Mode-zero Robinson instability in the presence of passive superconducting harmonic cavities," *Phys. Rev. Accel. Beams*, vol. 26, no. 6, p. 064 403, 2023. doi:10.1103/PhysRevAccelBeams.26.064403

[14] M. Borland, "Elegant: A flexible SDDS-compliant code for accelerator simulation," Argonne National Lab., IL (US), Tech. Rep. LS-287, 2000. doi:10.2172/761286

[15] A. Piwinski, "The Touschek Effect in Strong Focusing Storage Rings," Tech. Rep., 1999. doi:10.48550/arXiv.physics/9903034

[16] J. M. Byrd and M. Georgsson, "Lifetime increase using passive harmonic cavities in synchrotron light sources," *Phys. Rev. Spec. Top. Accel Beams*, vol. 4, no. 3, p. 030 701, 2001. doi:10.1103/PhysRevSTAB.4.030701

[17] A. D'Elia, J. Jacob, V. Serrière, and X. W. Zhu, "Design of 4th Harmonic RF Cavities for ESRF-EBS," in *Proc. IPAC'21*, Campinas, Brazil, May 2021, pp. 1031–1033. doi:10.18429/JACoW-IPAC2021-MOPAB332

BUNCH-LENGTHENING RF SYSTEM USING ACTIVE NORMAL-CONDUCTING CAVITIES

N. Yamamoto*, D. Naito, S. Sakanaka, T. Yamaguchi, Accelerator Laboratory, KEK, Tsukuba, Japan
A. Gamelin, P. Marchand, Synchrotron SOLEIL, Gif-sur-Yvette, France

Abstract

A normal conducting (NC) harmonic cavity (HC) bunch-lengthening system, powered with an external rf generator, is attractive for future generation synchrotron light rings. This system is expected to improve the bunch lengthening performance even at low stored currents. As a result of recent particle tracking simulations, a proper control of the external rf generator is also expected to be a countermeasure for reduction in bunch lengthening efficiency due to the transient beam loading (TBL) and for unstable beam motions in the vicinity of the "flat-potential" condition. In order to realize such a system, a low R/Q 1.5GHz-TM020 HC and a broadband kicker cavity with a bunch phase monitor integrated in the digital rf control for the TBL compensation, are being developed.

INTRODUCTION

Bunch lengthening using a double RF system with fundamental and harmonic cavities (FC and HC) [1] is essential in preserving the extremely low emittance in fourth and future generation synchrotron light rings. For these rings, the relatively low required rf voltage makes the use of normal conducting (NC) cavities quite attractive.

For more than 20 years, double rf systems with passive HCs have been used in a number of third-generation light sources to lengthen the electron bunches for improving the beam lifetime and stability [2–5]. These previous works have revealed that the transient beam loading (TBL) reduces the bunch lengthening efficiency when bunch gaps are introduced in the fill pattern, especially for systems consisting of HCs having their resonant frequency higher than 1 GHz. It has also been reported that reducing the total R/Q of the HCs is essential in mitigating such transient effects [6].

In addition, recent studies have shown that in many cases, unstable beam motions, such as the so-called "mode-0" [7, 8] and the "periodic transient beam loading (PTBL)" [9–11] instabilities, prevent one from reaching the optimum bunch lengthening condition at low and high beam current, respectively, even with symmetric filling patterns. While reducing the R/Q will help the latter, it will worsen the former.

To realize an efficient bunch lengthening system, the KEK team proposed a promising solution relying on a powered TM020 HC with RF feedbacks (RF-FBs) [12], as reported at FLS2018. Based on this concept, we are developing a HC using the TM020 resonant mode [13], a kicker cavity with a bandwidth > 5 MHz [14], a bunch phase monitor (BPhM)

_____
* naotoy@post.kek.jp

and RF-FBs. In this paper, we describe our complete bunch lengthening system including the cavity and BPhM designs.

ACTIVE NC DOUBLE RF SYSTEM

A feature of our proposed system is the use of powered TM020 HCs, also called "active HCs". The use of the higher frequency TM020 resonant mode instead of the lowest TM010 mode allows to reduce the R/Q by about 40% [13] and active HCs have some advantages over the more commonly used passive HCs:

- The external generator of an active HC can provide sufficient voltage to lengthen the bunches even at a low stored current (operation with a single or few bunches) [15]
- A proper control of the external generator by using advanced low-level rf (LLRF) techniques can mitigate the voltage fluctuations due to the TBL effect and circumvent unstable beam motions.

The first point is important to maintain a wide use of the synchrotron radiation in the future light sources by preserving all the operating modes available in third-generation light sources. New concepts of synchrotron radiation sources that emphasize flexibility are proposed by KEK [16] and SOLEIL [17].

As shown in Ref. [12], transient rf voltage compensation can be achieved by using the generators of both FC and HC or by using a separate broadband kicker cavity. Besides, particle tracking simulations, performed with the mbtrack2 code [18], have shown that an advanced feedback, such as a direct RF-FB (DRFB) loop can help to push back the PTBL instability threshold in the vicinity of the "flat-potential" condition [19].

In the following section, the development progress of hardware components, needed to realize our active NC double RF system is reviewed.

HARDWARE DEVELOPMENT STATUS

1.5GHz-TM020 Harmonic Cavity

The 508MHz-TM020 cavity was originally developed as a HOM-damped accelerating cavity for the SPring-8 II project [20], and four such cavities have already been installed as fundamental accelerating cavities at the new 3-GeV synchrotron radiation facility NanoTerasu in Japan [21].

In their design, two shallow coaxial slots are located on both end plates of the cavity, where the magnetic field of the accelerating mode vanishes (i.e., at its magnetic field node). By placing microwave absorbers on these slots, most of the harmful parasitic modes can be strongly damped without
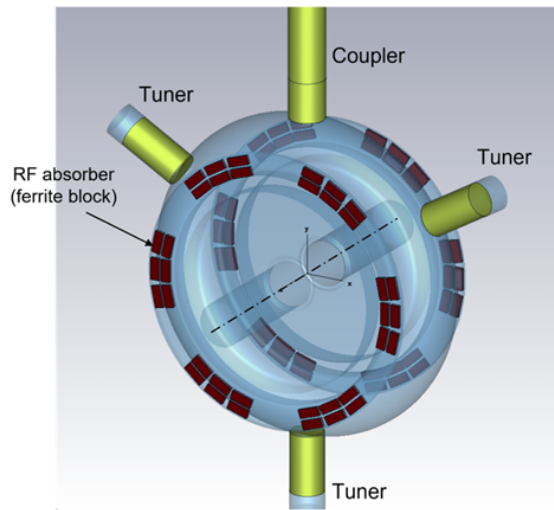
Figure 1: Inner structure of the TM020 HC.

Table 1: 1.5GHz-TM020 HC Main Parameters

Parameter	Value
Resonant frequency	1.5 GHz
R/Q, $(R_s = V_c^2/2P_c)$	34.0 Ω
Unloaded Q	31400
Tuning range, $(P_{abs}/P_{wall})^1 < 2\%$	-0.5 ∼ 0.5 MHz

Figure 2: Schematic of the broadband kicker cavity.

significantly affecting the TM020 accelerating mode and while maintaining a compact longitudinal size of the cavity.

Another advantage of this cavity is its intrinsically high unloaded Q due to the use of a higher frequency mode for the beam acceleration. Compared to a typical TM010 cavity at the same frequency of 1.5 GHz, which is the third harmonic of the KEK-PF FC, a TM020 cavity has a higher unloaded Q (by factors of 1.5–2.2) and a lower R/Q (by about 40%).

Based on these advantages, which are particularly suitable for HCs, we have been developing a 1.5GHz-TM020 HC since 2018, separately from the pioneering work described above. A similar 1.41GHz-TM020 two-cell cavity is also under development for ESRF-EBS [22].

The design work of our 1.5GHz-TM020 HC is almost completed [13]. After optimizing the cavity shape to maintain a low R/Q and a strong HOM-damping, we made a concerted effort to minimize the leakage power of the TM020 mode into the microwave absorbers over a reasonable tuning range. As a result of the numerical investigations and experimental studies with a low power cavity model, we found that maintaining the axial symmetry of the cavity is essential for minimizing the leakage power of the accelerating mode. To this end, we have symmetrically arranged three frequency tuners and designed an input coupler loop that produces only a small perturbation on the accelerating mode, as shown in Fig. 1.

The main computed parameters of our 1.5GHz-TM020 HC are listed in Table 1. The assumed total wall-loss power of 11.3 kW corresponds to an RF voltage of 155 kV. The computed parasitic mode loss factor is 0.83 V/pC at an rms bunch length of 3 mm (i.e., without HCs).

Broadband Kicker Cavity

As reported in Ref. [12], the mitigation of the voltage fluctuations due to the TBL effect can be expected by intro-

---

^{1} Ratio of the power lost into the absorbers over the cavity wall loss for the accelerating mode
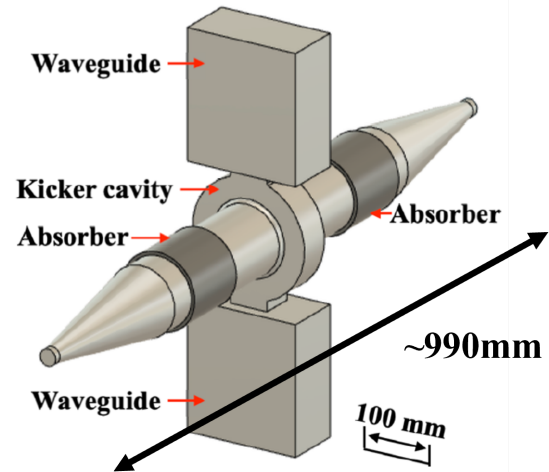
ducing an adaptive feedforward technique to both FC and HC. However, the compensation performance is limited by the narrow bandwidth of these cavities. For the purpose of increasing the bandwidth, we consider developing a dedicated kicker cavity [23] with a 3dB bandwidth of about 5 MHz, while a cavity voltage of tens of kV is sufficient. To meet these requirements, one uses a single-mode (SM) cavity concept [24], strongly loaded by means of two external wave-guides, connected through large coupling slots, as shown in Fig. 2. The harmful HOMs are attenuated by rf absorbers located on the beam pipes.

The practical design of the kicker cavity was performed using CST MW-studio and a model cavity with a resonant frequency of 1.5 GHz was fabricated to confirm the computed performance. The main parameters of the kicker cavity are listed in Table 1. Assuming a generator power of 40 kW and a beam current of 500 mA, a cavity voltage of 44 kV is obtained with a wall dissipation of 2.59 kW and a reflected power of 7.85 kW to each wave-guide, the remaining 21.7 kW being the beam loading power. The 3dB-bandwidth of the cavity is 5.1 MHz.

Bunch Phase Monitor (BPhM)

To realize the TBL compensation system, it is necessary to develop not only the dedicated cavity, but also the associated advanced digital LLRF control system. To calculate and control the additional RF voltage aimed at compensating the TBL, we use the information of the bunch center-of-mass

Table 2: Broadband Kicker Cavity Main Parameters

| Parameter	Value
Resonant frequency	1.5 GHz
R/Q, ($R_s = V_c^2/2P_c$)	30.0 Ω
Unloaded Q	17937
Loaded Q	292
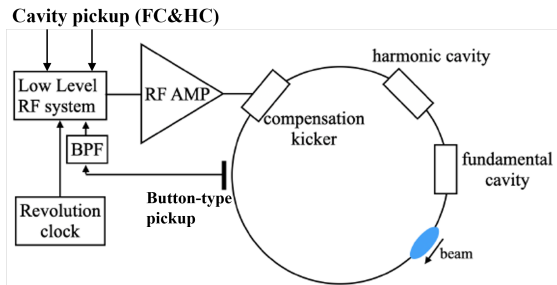
Figure 3: Schematic of the bunch phase monitor (BPhM).

phase along the bunch train together with a monitoring of the transient variations of the cavity voltage.

As shown in Fig. 3, both the FC and HC pickup signals and the bunch signal from the button-type pickup on the vacuum chamber are fed into analog inputs of the digital LLRF system. These signals are sampled by a fast ADC in synchronization with the revolution clock. For the signal sampling, we plan to measure the bunch phase by a IQ conversion applying the direct sampling method. In order to eliminate noise and harmonics, the bunch signal will be pre-processed using an appropriate band pass filter (BPF).

We intend to integrate this system in the digital LLRF system being developed for the Photon Factory upgrade project [25] to achieve a TBL compensation by measuring and feeding back the bunch phase information at a sampling frequency of more than 1 kHz.

The results of the preliminary tests of the BPhM at KEK-PF, where the HC is not yet installed, are reported hereafter. The rf and revolution frequencies at KEK-PF are 500.1 and 1.6 MHz, respectively. In the tests, a direct sampling frequency of 307.8 MHz and a BPF of 470~520 MHz were used. The IQ sampling was performed every 13 bunches, and 24 samples were obtained during one revolution period. The fill pattern was consisting of a multi-bunch train with 250 bunches and a gap of 62 unoccupied RF buckets.

The measured bunch phase with the prototype BPhM is indicated as black circles in Fig. 4, which shows the bunch phase shift due to the TBL. The results averaged over 100 turns are plotted, but no difference was observed when averaging over 100 kTurns. The significant changes in the absolute value of the bunch phase in the first part of the bunch train is suspected to be due to the frequency dispersion caused by the long transmission cable (~100 m) from the button-type pickup.

The bunch phase obtained from the BPhM prototype is compared to that from the "integrated General purpose sig-
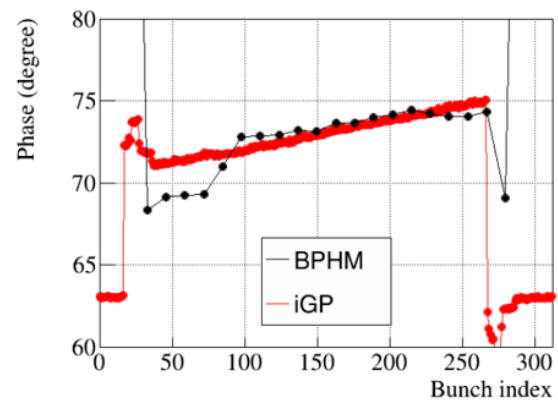
Figure 4: Measured bunch phases with the prototype BPhM (black), compared to those with iGP (red).

nal processors (iGP)" (red) [26, 27], which is averaged over 40 kTurns with a synchronous detection at 1.5 GHz. Although the measured bunch phase slopes are slightly different, we expect that it is good enough for a correct TBL compensation.

CONCLUSION

We are developing a bunch lengthening system of high performance for future synchrotron light sources. We aim to improve the bunch lengthening efficiency by using a powered NC-TM020 HC, a broadband kicker cavity and a sophisticated LLRF control system.

In the development of the TM020 HC, the symmetrical arrangement of three frequency tuners has made possible the achievement of the required operational frequency tuning range as well as the preservation of the axial symmetry, which is essential for limiting the accelerating mode power leak into the absorbers. The design of the high power model is almost completed.

The broadband kicker cavity for the TBL compensation is a SM-mode cavity concept with two rf input waveguide strongly coupled to the cavity by means of large slots in order to achieve the required wide bandwidth. The HOM attenuation is complemented by absorbers on the beam pipes.

We have also designed and confirmed the feasibility of a BPhM for bunch phase control, which is one of the required functions of the LLRF system for the TBL compensation.

We intend to further proceed with more sophisticated hardware designs and realistic tracking simulations in parallel to the design of a practical bunch lengthening system using NC active HCs.

ACKNOWLEDGEMENTS

REFERENCES

[1] A. Hofmann and S. Myers, "Beam dynamics in a double rf system," CERN-ISR-TH-RF-80-26, 1980, pp. 610–614.

[2] P. Marchand, "Possible upgrading of the SLS RF system for improving the beam lifetime," in *Proc. PAC'99 (Cat. No. 99CH36366)*, IEEE, vol. 2, 1999, pp. 989–991.

[3] J. Byrd, S. Santis, M. Georgsson, G. Stover, J. Fox, and D. Teytelman, "Commissioning of a higher harmonic RF system for the advanced light source," *Nucl. Instrum. Methods A*, vol. 455, no. 2, pp. 271–282, 2000. doi:10.1016/S0168-9002(00)00504-0

[4] M. Georgsson *et al.*, "Design and commissioning of third harmonic cavities at BESSY II," *Nucl. Instrum. Methods A*, vol. 469, no. 3, pp. 373–381, 2001.

[5] M. Pedrozzi *et al.*, "SLS operational performance with third harmonic superconducting system," in *Proc. 11th SRF Workshop*, Lübeck/Travemünder, Germany, 2003, pp. 91–94.

[6] J. M. Byrd *et al.*, "Transient beam loading effects in harmonic RF systems for light sources," *Phys. Rev. Spec. Top. Accel. Beams*, vol. 5, no. 9, paper 092001, 2002.

[7] T. He, W. Li, Z. Bai, and W. Li, "Mode-zero robinson instability in the presence of passive superconducting harmonic cavities," *Phys. Rev. Accel. Beams*, vol. 26, no. 6, p. 064 403, 2023. doi:10.1103/PhysRevAccelBeams.26.064403

[8] A. Gamelin *et al.*, "Beam dynamics using superconducting passive harmonic cavities with high current per bunch," in *Proc. FLS'23*, 2023.

[9] M. Venturini, "Passive higher-harmonic rf cavities with general settings and multibunch instabilities in electron storage rings," *Phys. Rev. Accel. Beams*, vol. 21, no. 11, paper 114404, 2018.

[10] T. He *et al.*, "Periodic transient beam loading effect with passive harmonic cavities in electron storage rings," *Phys. Rev. Accel. Beams*, vol. 25, no. 2, paper 024401, 2022.

[11] A. Gamelin *et al.*, "Beam dynamics with a superconducting harmonic cavity for the SOLEIL upgrade," in *Proc. IPAC'22*, 2022, pp. 2229–2232. https://accelconf.web.cern.ch/ipac2022/papers/wepoms003.pdf

[12] N. Yamamoto *et al.*, "Reduction and compensation of the transient beam loading effect in a double RF system of synchrotron light sources," *Phys. Rev. Accel. Beams*, vol. 21, no. 1, paper 012001, 2018.

[13] T. Yamaguchi, N. Yamamoto, D. Naito, T. Takahashi, and S. Sakanaka, "Design and low-power measurement of 1.5GHz TM020-type harmonic cavity for KEK future synchrotron light source," *Nucl. Instrum. Methods A*, vol. 1053, p. 168 362, 2023.

[14] D. Naito, S. Sakanaka, T. Takahashi, T. Yamaguchi, and N. Yamamoto, "Design consideration of a longitudinal kicker cavity for compensating transient beam loading effect in synchrotron light sources," in *Proc. IPAC'21*, Campinas, SP, Brazil, 2021, paper MOPAB331, pp. 1027–1030. doi:10.18429/JACoW-IPAC2021-MOPAB331

[15] N. Yamamoto, S. Sakanaka, P. Marchand, P. Gamelin, and R. Nagaoka, "Feasibility study of an active harmonic cavity for bunch lengthening in an electron storage ring," in *Proc. PASJ'22*, 2022, paper WEP059. http://www.pasj.jp/web_publish/pasj2022/proceedings/PDF/WEP0/WEP059.pdf

[16] K. Harada *et al.*, "Conceptual design of the Hybrid Ring with superconducting linac," *J. Synchrotron Radiat.*, vol. 29, no. 1, pp. 118–124, 2022.

[17] A. Loulergue *et al.*, "TDR baseline lattice for the upgrade of SOLEIL," in *Proc. IPAC'22*, 2022, pp. 1393–1396. https://accelconf.web.cern.ch/ipac2022/papers/tupoms004.pdf

[18] A. Gamelin, W. Foosang, and R. Nagaoka, "Mbtrack2, a collective effect library in python," in *Proc. IPAC'21*, Campinas, SP, Brazil, 2021, pp. 282–285. doi:10.18429/JACoW-IPAC2021-MOPAB070

[19] N. Yamamoto, S. Sakanaka, T. Yamaguchi, A. Gamelin, P. Marchand, and R. Nagaoka, "Stability survey of a double RF system with RF feedback loops for bunch lengthening in a low-emittance synchrotron ring," presented at IPAC'23, Venice, Italy, May 2023, paper WEPL161, to appear in the proceedings.

[20] H. Ego, J. Watanabe, S. Kimura, and K. Sato, "Design of a HOM-damped rf cavity for the SPring-8-II storage ring," in *Proc. PASJ'14*, 2014, pp. 237–241. http://www.pasj.jp/web_publish/pasj2014/proceedings/PDF/MOOL/MOOL14.pdf

[21] T. Inagaki *et al.*, "High-power tests of the compactly HOM-damped TM020-cavities for a next generation light source," presented at IPAC'23, Venice, Italy, May 2023, paper WEPL161, to appear in the proceedings.

[22] A. D'Elia *et al.*, "ESRF-EBS 352 MHz HOM Damped RF Cavities," in *Proc. IPAC'21*, 2021, pp. 1034–1036. https://jacow.org/ipac2021/papers/mopab333.pdf

[23] D. Naito, N. Yamamoto, T. Takahashi, S. Sakanaka, and T. Yamaguchi, "Low-power model tests of the wide-band cavity to compensate the transient beam loading in the next generation light sources," presented at IPAC'23, Venice, Italy, May 2023, paper WEPL161, to appear in the proceedings.

[24] T. Weiland, "Single mode cavities a possibility for fighting collective beam instabilities," DESY, Tech. Rep. DESY-83-073, 1983, DESY-83-073.

[25] D. Naito, "Adoption of the micro-tca to the next kek-pf llrf system," in *MTCA Workshop for Accelerator and Physics in Japan*, 2021. https://conference-indico.kek.jp/event/153/contributions/2791/attachments/1921/2285/mtca2021-naito-211027.pdf

[26] D. Teytelman *et al.*, "Design and testing of Gproto bunch-by-bunch signal processor," in *Proc. EPAC'06*, Edinburgh, Scotland, 2006, pp. 3038–3040. https://accelconf.web.cern.ch/e06/PAPERS/THPCH103.PDF

[27] R. Takai, M. Tobiyama, T. Obina, J. Flanagan, M. Tadano, and T. Mitsuhashi, "Bunch by bunch feedback system using iGp at KEK-PF," in *Proc. DIPAC'09*, Basel, Switzerland, 2009, pp. 59–61. https://accelconf.web.cern.ch/d09/papers/mopd08.pdf

GENERATING HIGH REPETITION RATE X-RAY ATTOSECOND PULSES IN SAPS

Weihang Liu[1], Yi Jiao*, Yu Zhao[1], Xingguang Liu[1], Xiao Li[1], Sheng Wang[1,†]

Institute of High Energy Physics, Chinese Academy of Sciences, Beijing, China

University of Chinese Academy of Sciences, Beijing, China

[1]also at Spallation Neutron Source Science Center, Dongguan, China

Abstract

Attosecond, which refers to 10^{-18} seconds, is the timescale of electron motion within an atom. Accurate observation of electron motion helps deepen the understanding of microscopic quantum processes such as charge transfer in molecules, wave packet dynamics, and charge transfer in organic photovoltaic materials. To meet the needs of relevant research, the South Advanced Photon Source (SAPS), currently in the design phase, is considering the construction of an attosecond beamline. This paper presents relevant research on achieving high-repetition-rate coherent attosecond pulses on the fourth-generation storage ring at SAPS. Realizing attosecond pulses in a storage ring requires femtosecond to sub-femtosecond-level longitudinal modulation of the beam, and the modulation scheme needs to consider multiple factors to avoid a significant impact on other users. The study shows that with high-power, few-cycle lasers, and advanced beam modulation techniques, the photon flux of attosecond pulses can be significantly enhanced with a minimal impact on the brightness of synchrotron radiation. Adopting high-repetition-rate lasers and precise time delay control, the repetition rate of attosecond pulses at SAPS can reach the megahertz level. To separate the attosecond pulse from the background synchrotron radiation, a pulse separation method was proposed. This mehtod improves the signal-to-noise ratio of attosecond pulses by more than an order of magnitude. Currently, the design wavelength range for attosecond pulses covers the water window (2.3-4.4 nm), which is "transparent" to water but strongly absorbed by elements constituting living organisms. This wavelength range has significant application value in fields such as biology and chemistry.

INTRODUCTION

Attosecond, which represents the natural time scale of electron motion in atomic and molecular systems, holds significant implications for several cutting-edge fields, such as quantum physics, biology, chemistry, and medicine. To advance scientific research in these fields, it is considered crucial to develop high-flux and high-repetition-rate Attosecond light sources [1].

The storage ring based light source is a stable, high-repetition-rate, and multi-user tool for light generation, which has been at the forefront of high-brilliance experiments. Currently, it has evolved from the third generation to

the fourth generation, also known as the diffraction-limited storage ring (DLSR), resulting in an increase in Brilliance by more than two orders of magnitude. The ability to achieve attosecond pulses in DLSR would make it highly attractive due to the aforementioned advantages. During the design phase, the Southern Advanced Photon Source (SAPS) [2], aims to provide this new attosecond tool for attosecond science study. By pursuing high Brilliance and providing high flux and high repetition rate attosecond pulses, SAPS hopes to contribute to the development of attosecond science.

The natural pulse duration of light in storage rings typically ranges from 10 to 100 ps. To effectively reduce pulse duration while maintaining a high pulse flux, various laser-based beam modulation techniques have been proposed and applied to storage rings, such as echo-enabled harmonic generation (EEHG) and angular dispersion-induced microbunching (ADM) [3]. Recently, we propose a method by combine ADM with a few-cycle laser for the generation of attosecond pulses in a DLSR [4].

In this paper, we adopt this method for SAPS to generate attosecond pulses. Potential problems related to the ADM section were discussed, such as vertical dispersion bump-induced vertical emittance growth, and DA and MA reduction. And to increase the signal-to-noise ratio of the attosecond pulse, we propose a pulse separation method. This method improves the signal-to-noise ratio of attosecond pulses by more than an order of magnitude.

PARAMETERS OPTIMIZATION OF THE ADM

The ADM structure, located within one of the straight sections of SAPS as illustrated in Fig. 1, initially couples the electron beam in both transverse and longitudinal directions using a vertical dipole. Subsequently, the beam undergoes energy modulation through interaction with a short wiggler (known as a modular) and a few-cycle laser. Finally, a dog-leg consisting of two vertical dipoles with equal strength but opposite deflection angles imparts transverse and longitudinal dispersion, which converts the energy modulation into density modulation, resulting in microbunching or a large local peak current in the electron beam. The modulated beam then passes through an undulator (known as a radiator) to generate coherent attosecond pulses. After this process, the radiated electron beam passes through four dipole magnets, which have been designed specifically in position and strength to eliminate the vertical dispersion and allow the beam to return to the ring. The design of the ADM
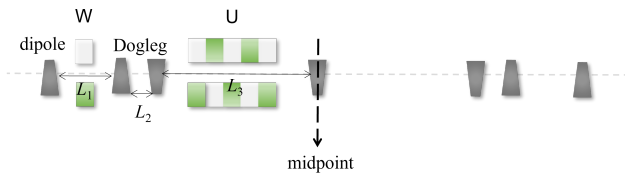
Figure 1: The layout of the ADM section in a straight section. Seven dipoles are symmetrically arranged and the center point shared by the straight and ADM sections are marked as the "midpoint".

section must meet optimal radiation performance and minimal impact on the storage ring for a given set of machine parameters. To achieve this goal, a optimization has been performed in Ref. [4] based on the SAPS parameters given in Table 1. It found that when the dogleg dispersion η is 0.48 mm, a optimal local current and local bunching factor can be achieved. All optimal parameters are presented in Table 2.

Table 1: SAPS Main Parameters

Parameters	Value	Unit
Energy	3.5	GeV
Circumference	810	m
Nature emittance	33.4	pm
Energy spread	0.11	%
Momentum compaction factor	2.5×10^{-5}	
Bunch number	405	

Impact of the Beam Dynamics

This subsection presents a study of the beam dynamics in the ring, both with and without the ADM section. We investigate the linear and nonlinear behaviors separately, starting with the linear dynamics followed by an investigation of the nonlinear dynamics.

Table 2: Optimal Parameters of ADM Elements

Parameters	Value	Unit
Dipole		
Bending angle	6.6	mrad
Dogleg		
Bending angle	7.4	mrad
Distance between dipoles	0.45	m
Modulator		
Peak field	0.52	T
Period length	0.4	m
Radiator		
Peak field	0.996	T
Period length	0.04	m

In the context of linear dynamics, we present the linear lattice function for the ADM section as shown in Fig. 2.

Corresponding detailed parameters can be found in Table 2. Upon inclusion of the ADM section, a dispersion bump with a maximum amplitude of approximately 12 mm is generated in the vertical direction. As for Twiss parameters, this ADM section only affects the vertical beta and alpha functions, with changes of less than 1%. It is important to recognize that such a low beta beating has only a small impact on the overall beta beating caused by other IDs with reasonable errors and misalignments. Therefore, it is possible to correct the root mean square (rms) beta beating of the ring to an acceptable value.

To study the nonlinear dynamic, we conducted simulations to obtain the dynamic and local momentum apertures of the SAPS, both with and without the ADM section, using the ELEGANT code. These simulations took into account the effects of radiation damping and quantum excitation.

The reduction of the on-momentum dynamic aperture (DA) by the ADM section is illustrated in Fig. 3. The DA area decreased from 29.7 mm² to 27.6 mm², with maximum horizontal and vertical size reductions of less than 2%. The MA of the ring is also reduced, particularly at the location of the ADM section, with a maximum reduction of 25%. However, given their small magnitudes, these reductions are negligible in terms of their impact on ring injection [5]. We evaluate the effect of the ADM section on the ring lifetime. The method estimates that the ring with and without the ADM section both have a lifetime of approximately 10 hours, which is sufficient for normal operation of the storage ring.
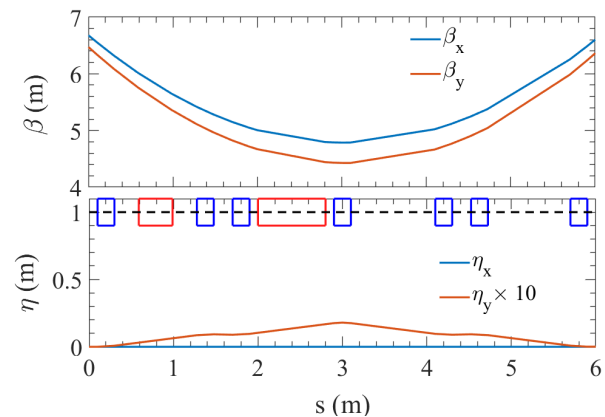
Figure 2: Lattice function for the straight section containing the ADM structure: blue squares represent the dipole, green represents the undulator.

PERFORMANCE AND REPETITION RATE

The modulated beam can generate coherent radiation pule with wavelength of 4 nm and different time duration in the radiator with different period number N. The time duration Δt are proportional to N. For short time duration one require $N < 10$, which will let $\Delta t < 100$ as. However, small N resulting lower photon flux per pulse and larger FWHM bandwidth (Bw). For instant, when $N = 4$, the time duration can be as short as 50 as, but the flux is above one order of
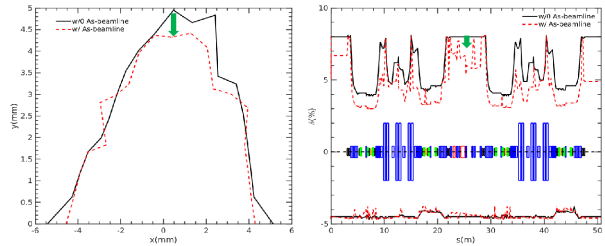
Figure 3: Dynamic and local momentum apertures comparison between different SAPS without (black line) and with ADM section (red dashed line).

magnitude lower than that of $N = 20$. Given the presence of 405 bunches in the ring, the repetition rate can reach up to 6.75 kHz, provided that each bunch is modulated only once in each recovery period (~ 60 ms) [4]. The average flux for pulses of 50 as, 122 as, and 252 as FWHM duration are 1.28×10^8, 6.4×10^8, and 2.29×10^9 photons/pulse/1%Bw, respectively.

When each bunch in the ring undergoes only one modulation during the 60 ms recovery period, the corresponding repetition frequency is 6.75 kHz. It is worth noting that during each modulation, only a small part of the beam (with beam length σ_b) is modulated by the few-cycle laser (with duration σ_l). If multiple modulations of different parts of the bunch are carried out during each recovery period, the repetition rate can be increased by approximately σ_b/σ_l times.

To consider the Gaussian longitudinal distribution of the beam, as a delay distance that is too large can result in a decrease in local current. We take delay length of 0.1 mm and 200 modulations are performed on the beam, the corresponding reduction in local current is maximally 6%, and there is a decrease in radiation power of approximately 10%. This suggests that multiple modulations generate radiation pulses with a variation magnitude of less than 10%. On average, the flux per second of the radiation pulses with pulse duration of 48, 122, and 252 as can reach 2.47×10^{10}, 1.23×10^{11}, and 4.4×10^{11} photons/s/1%Bw, respectively.

SEPARATION OF THE ATTOSECOND PULSE

For a few femtoseconds to attosecond pulses obtained by the seeding method, the signal-to-noise ratio of the ultrashort pulses is low due to the large difference in pulse length (1e-4 to 1e-2) from the storage ring synchrotron pulses, despite the large peak power due to coherence. In order to improve the signal-to-noise ratio of the attosecond pulses generated using the scheme of this paper, a pulse separation scheme with microbunches beam dynamics is given in this section.

Beam dynamics and certain FEL experiments have shown that microbunches rotate in the new direction of travel when the electron beam is kicked and defocused. This can be used for multiplexing in the FEL. Under a weak focusing kicker, the direction of the microbunches remains unchanged [6].

Inspired by this effect, we add a kicker of suitable strength at the entrance of the beam section to deflect the beam horizontally. a kicker of suitable strength to deflect the beam horizontally. As shown in Fig. 4, since the direction of the microbunch is unchanged, there will be an angular difference between the direction of the coherent radiation and the synchrotron radiation, thus realising the separation of coherent pulses.

The simulation results show (Fig. 4) that for a kicker angle of 200 μrad, placing an aperture of size [-0.4 mm, 1mm]×[-1mm, 1mm] at a distance of 10m from the source can separate out 99% of the coherent radiation, improving the signal-to-noise ratio of the attosecond pulse by a factor of 10-100.
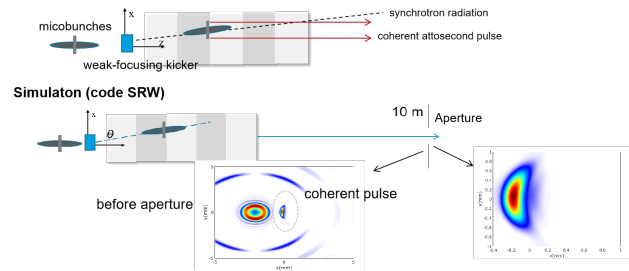
Figure 4: Layout and simulation results of the pulse separation scheme.

DISCUSSION AND CONCLUSION

We proposed a method to generate attosecond pulses in SAPS by combining ADM and few cycle laser. simulations show attosecond pulse with repetition rate of 6.75 kHz can be generated. By introducing a suitable time delay between the laser and the beam, the modulation can be performed repeatedly on a beam, thereby increasing the repetition rate to 1.35 MHz. To separate the attosecond pulse from the background synchrotron radiation, a pulse separation method was proposed. There are still some open issues with this scheme, such as the need for a large kicker angle in the pulse separation scheme. The larger the angle, the greater the degradation of the coherent radiation. In the future, a full optical beamline design will be required to see if these degradations are acceptable for the experimental requirements.

ACKNOWLEDGEMENTS

REFERENCES

[1] P. B. Corkum and F. Krausz, "Attosecond science", *Nat. Phys.*, vol. 3, pp. 381–387, 2007. `doi:10.1038/nphys620`

[2] Y. Zhao, Y. Jiao, and S. Wang, "Design study of APS-U-type hybrid-MBA lattice for mid-energy DLSR", *Nucl. Sci. Tech*, vol. 32, art. no. 71, 2021. `doi:10.1007/s41365-021-00902-1`

[3] C. Feng and Z. Zhao, "A storage ring based free-electron laser for generating ultrashort coherent EUV and X-ray radiation", *Sci. Rep.*, vol. 7, art. no. 4724, 2017. `doi:10.1038/s41598-017-04962-5`

[4] W. Liu *et al.*, "Generating high repetition rate X-ray attosecond pulses in a diffraction limited storage ring", *Sci. Rep.*, to be published.

[5] W. Liu, Y. Jiao, Y. Zhao, J. Chen, Y. Han, and S. Wang, "Multi-objective optimization of longitudinal injection based on a multi-frequency RF system for fourth-generation storage ring-based light sources", *Nucl. Instrum. Methods Phys. Res., Sect. A*, vol. 1046, art. no. 167712, 2023. `doi:10.1016/j.nima.2022.167712`

[6] J. P. MacArthur, A. A. Lutman, J. Krzywinski, and Z. Huang, "Microbunch rotation and coherent undulator radiation from a kicked electron beam", *Phys. Rev. X*, vol. 8, no. 4, art. no. 041036, 2018. `doi:10.1103/PhysRevX.8.041036`

STATUS AND PERSPECTIVES FOR THE SWISS FREE-ELECTRON LASER (SwissFEL)

T. Schietinger* on behalf of the SwissFEL team
Paul Scherrer Institut, Villigen, Switzerland

Abstract

We summarize the status of SwissFEL, the X-ray free-electron laser at the Paul Scherrer Institute. Apart from some key operational performance figures the contribution covers the state of the experimental stations, the evolution of user demand and gives a brief overview of the use of advanced operation modes beyond SASE at our facility. Furthermore we report on progress of our seeding upgrade program on the soft X-ray line. Lastly we mention our long-term upgrade plans for a third undulator beamline in the tender and hard X-ray regime.

INTRODUCTION

SwissFEL is a free-electron laser (FEL) facility at the Paul Scherrer Institute in Switzerland featuring two beamlines, Aramis for the hard X-ray regime (1.8–12.4 keV) and Athos covering the soft X-ray spectrum (0.26–1.9 keV) [1]. The accelerator consists of an S-band photoinjector gun followed by an S-band booster radiofrequency (rf) linac, which accelerates electron bunches to an energy of 300 MeV. Main acceleration to the final beam energy of up to 6.2 GeV (Aramis) is accomplished through a series of C-band rf linacs.

A schematic view of the SwissFEL facility is given in Fig. 1. The electron gun generates two bunches, separated by 28 ns, at a repetition rate of 100 Hz. The first bunch goes straight to the Aramis undulator line, while the second bunch is extracted at a beam energy of 3.17 GeV into a dog-leg beamline leading to the Athos undulator. A short tuning linac in the Athos branch allows for energy adjustments in the range ±250 MeV. The electron bunches are compressed longitudinally in two magnetic chicanes (BC1 and BC2). In the Aramis branch they may be further compressed in an energy collimator chicane before the undulator, in Athos in the dogleg and in additional chicanes present in that beamline. The Aramis undulator line consists of 13 planar in-vacuum undulator modules of 4 m length each with 15 mm period. Athos features 2×8 highly flexible APPLE-X type undulator modules, which are 2 m long and have 38 mm period. The Athos undulator modules are interspersed with small magnetic delaying chicanes. Between the two undulator halves there is a larger chicane used for tuning the delay (up to 500 fs) between two-color pulses generated individually in the two undulator halves. All undulators have adjustable deflecting parameters K through variable gaps (up to a maximum value of 1.8 in Aramis, 3.8 in Athos). For more details we refer to the "first-lasing" publications for Aramis [2] and Athos [3] and references therein.

Several deflecting rf cavities at different locations along the accelerator are used for measurements of the bunch profile or longitudinal phase space. An S-band deflecting cavity after BC1 performs such measurements with a temporal resolution of about 10 fs, whereas two C-band deflecting cavities at the end of linac-3 provide subfemtosecond resolution [4]. In 2022, a set of two X-band rf deflecting cavities for postundulator measurements in the Athos line was installed and commissioned, marking the completion of the SwissFEL baseline design. The cavities are based on the PolariX design, which arose from a collaboration between DESY, CERN and PSI [5]. The system gives time-resolved information on the lasing process with subfemtosecond resolution [6] and is indispensable for the clean setup of the many advanced operation modes available in Athos. Longitudinal phase space measurements of similar quality can also be obtained by streaking the beam passively with the wakefields from metallic corrugated structures [7].

SwissFEL ENDSTATIONS

Each of the SwissFEL undulator lines is designed to deliver FEL pulses to one out of three endstations associated with that line. Pairs of offset mirrors are set to ensure transport of the X-rays to the desired endstations. The endstations are named after Swiss mountain passes: Alvra, Bernina and Cristallina at the Aramis line, Maloja, Furka and Diavolezza at the Athos line.

At the Aramis line, Alvra and Bernina have been in operation since the beginning of FEL operation, with pilot runs in 2018 followed by the start of regular user operation in 2019. Alvra focuses on ultrafast dynamics of photochemical and photobiological systems while Bernina primarily measures ultrafast phenomena in condensed matter systems. The third endstation, Cristallina, designed for quantum science and structural biology, is currently in its pilot phase and will switch to user operation at the beginning of 2024.

The Athos undulator line was completed in the course of 2020. The first endstation, Maloja, started its pilot run at the end of that year and moved on to regular user operation in the beginning of 2022. Its focus lies on atomic, molecular and nonlinear X-ray physics and chemical dynamics. The second endstation, Furka, addresses ultrafast dynamics in quantum matter. Its pilot phase began in early 2023 and is planned to last for about one year. Finally, a third endstation, to be called Diavolezza and dealing with attosecond and nonlinear X-ray science, is in a conceptual phase and expected to become operational in a few years.

---

* thomas.schietinger@psi.ch
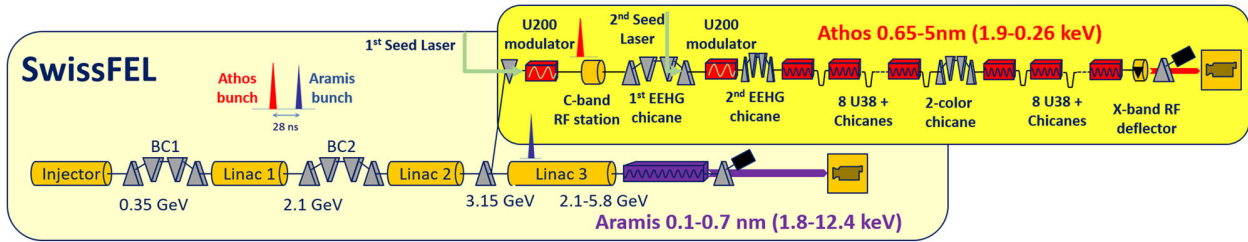
Figure 1: Schematic of SwissFEL accelerator layout (from Ref. [3]).

OPERATIONAL PERFORMANCE

For regular SASE operation, SwissFEL has achieved a level of performance that is close to the theoretically expected limit for a machine of its type. In Aramis, both electron energy and undulator K values are adjusted to reach a given photon energy. Whenever possible, the undulator is set to the maximum K value of about 1.75 to benefit from the strongest FEL coupling (with suitably tapered K values towards the end of the undulator line to compensate for electron energy loss). Only at the highest photon energies (above 9 keV), the K values are lowered to match the resonance condition with a 6-GeV electron beam. At the highest K and electron energy, a photon pulse energy of about 1.5 mJ can be extracted from the FEL at a resulting photon energy around 9 keV. This value drops to about 1.0 mJ at 2.5 keV photon energy (operating at a lower electron energy) or 0.9 mJ at 12.4 keV (operating at lower K values). In many cases, users ask for shorter pulses, which can only be achieved by either restricting the number of electrons that lase or reducing the overall number of electrons in the beam, with corresponding reductions in pulse energy.

In Athos the adjustment of the photon energy mainly hinges on the variation of the K values, since the tuning of the electron energy is limited to the ±250 MeV provided by the one C-band rf station installed between the switchyard and the undulator line. Accordingly, the photon pulse energy drops from a maximum of around 5 mJ at 0.5 keV down to below 1.2 mJ at 1.2 keV. (The FEL has not yet been optimized over the entire photon energy range.)

The achieved pulse energies are largely reproducible from one experiment to the next. The overall beam availability of the facility primarily depends on hardware failures. It is rather high for an FEL, reaching 95.8% for Aramis and 96.1% for Athos in 2022 during user operation.

USER DEMAND

Figure 2 shows the overall numbers of submitted and accepted experiment proposals at SwissFEL for the years 2018 through 2022 (top), as well as the corresponding numbers for experiment days (bottom). One experiment day equals three eight-hour shifts. A first period of euphoria is followed by a leaner period due to the Covid pandemic. In particular the low numbers of 2021 can be explained by the need to catch up the backlog of experiments granted for 2020 but

postponed during the height of the pandemic. Most recently, user numbers have been on the rise again, not least because the two new endstations Cristallina and Maloja became available to the general user community.

It is interesting to see which photon energies generate the most interest among users. Figure 3 shows the distribution of shifts in 2022 and 2023 (up to August) as a function of photon energy delivered by the FEL for Aramis and Athos, respectively.
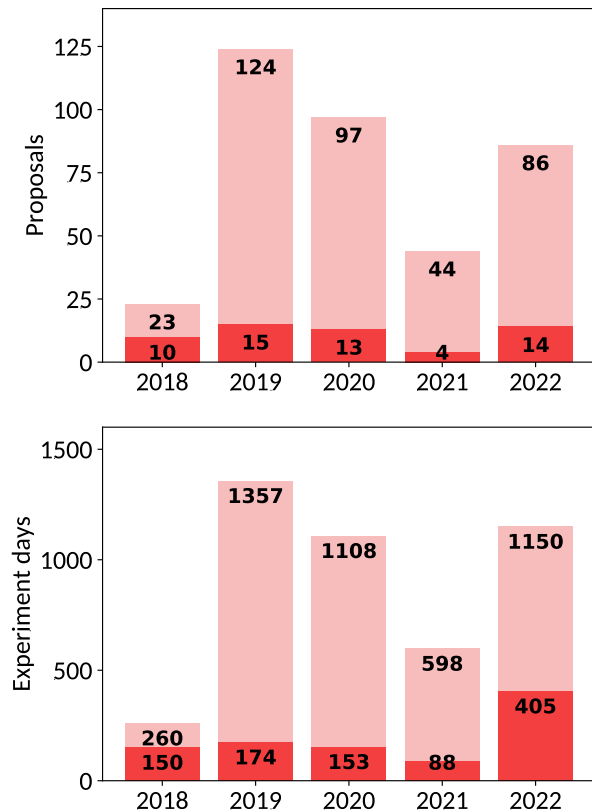
Figure 2: Evolution of the number of submitted (light red) and accepted (dark red) experiment proposals at SwissFEL (top). Corresponding evolution of the number of requested and granted experiment days (bottom, same color code). Each experiment day corresponds to three shifts of eight hours each.

The SwissFEL measurement periods lead to a steady stream of publications in a wide range of fields in science and technology. A recent highlight was the elucidation of the light-triggered structural changes of the molecule retinal inside the light-receptor protein rhodopsin with the help of data gathered at SwissFEL [8].

ADVANCED FEL OPERATION MODES – ARAMIS

At the Aramis beamline, by far the most often demanded FEL operation mode beyond SASE is a short-pulse mode in which photon pulses are shortened by applying a tilt to the electron beam, which limits the length over which the beam is aligned with the undulator axis such that it can sustain the FEL process [9]. In this way, photon pulses down to 2–3 fs duration (rms) can be generated routinely, albeit with a corresponding reduction in pulse energy. The beam tilt is typically realized by utilizing the wakefields from a set of flat parallel plates with microstructured surfaces (the same devices can be used to remove a residual energy chirp in the beam).

The Aramis line provides a large-bandwidth operation mode, which is based on a strong energy chirp in the electron beam, further enhanced by exploiting the strong wakefields arising from the C-band driving linac [10]. By leaking out dispersion into the undulator line it is possible to split up the wavelengths spatially, i.e., add a spatial chirp to the photon beam (large bandwidth with spatial chirp) [11]. Both types of large-bandwidth operation modes have been demonstrated and exploited in user experiments, with further experiments of this kind in the pipeline.

Extremely short FEL pulses, so-called "attosecond pulses" with duration well below one femtosecond can be generated by nonlinear compression of a low-charge electron beam in three stages [12]. For this operation mode the energy collimator chicane just in front of the undulator line is used as a third compression stage. The resulting FEL pulses exhibit very few individual radiation spikes, with a large fraction (about 40%) of fully coherent single-spike pulses. The operation mode was recently exploited for coherent small-angle X-ray scattering (cSAXS) measurements on quantum magnets by the Cristallina endstation and is expected to become a standard operation mode for this endstation.

ADVANCED FEL OPERATION MODES – ATHOS

We refer to Ref. [13] for an overview of the numerous advanced operation modes possible with Athos. A number of these modes have been made available to users, others are still in a commissioning phase, and some modes have not been attempted yet, either because of a lack of user demand or because further improvements to the machine are necessary before they can be tackled.

Early on, the shortening of the saturation length thanks to the optical-klystron effect could be demonstrated with the entire Athos undulator line [14]. This is of particular importance for modes where only a part of the undulator is available to reach saturation at a given wavelength, such as in the two-color mode.

Similar to Aramis, also in Athos pulses shorter than those resulting from the normal SASE process are in high demand. Again this can be achieved with a beam tilt, but in contrast to Aramis here the beam tilt is controlled by the dispersion present in the dogleg of the Athos extraction line acting on the energy-chirped beam. (In principle also in Athos the beam tilt can be generated through wakefields, but this method was found to result in higher beam losses.)

The generation of FEL pulses with variable polarization represents one of the Athos beamline's main attractions [3]. Several user experiments have already exploited the straightforward switching between circular and linear polarizations afforded by Athos.

The two-color mode in Athos makes use of a split-undulator configuration, in which each half of the undulator generates one wavelength (color). Both the standard approach, in which the full electron bunch lases, and the fresh-slice approach, in which each color is generated with a different part (slice) of the bunch, have been demonstrated successfully [15]. The latter approach, which has the ad-
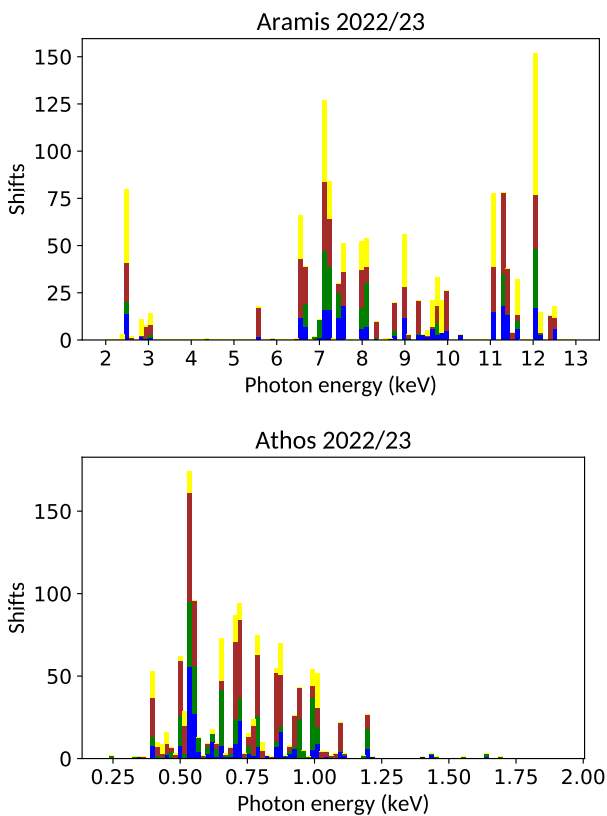

Figure 3: Number of shifts in 2022 and 2023 (until August) as a function of the set photon energy for the Aramis (top) and Athos (bottom) lines. Yellow: user experiment shifts, brown: user beamline development shifts, green: machine development shifts, blue: machine setup shifts.

vantage of delivering short pulses with the option of zero or even negative time delays between the colors, has already been applied in several user experiments.

Steady progress has been made in the very challenging high-power short-pulse mode (also known as multistage amplification mode), where the radiation pulse from a short slice of the electron bunch is further amplified, in several stages, by unspoiled electrons from new slices along the bunch, thereby exploiting the superradiant regime of the FEL. Currently about a millijoule of pulse energy can be achieved within a pulse length of a few femtoseconds [16]. The operation mode was recently applied in a test experiment at the Maloja endstation.

Last but not least we mention the recent successful demonstration of sub-femtosecond ("attosecond") pulses also in the Athos line [17]. As in Aramis, a low-charge bunch is subjected to strong nonlinear compression in three stages, but in this case the dogleg of the Athos switchyard serves as the third compression stage.

ATHOS SEEDING UPGRADE

The provision for seeding the soft X-ray line has been included in the design of building complex and associated infrastructure from the very beginning of the SwissFEL project, but was not part of the baseline design for financial reasons. The upgrade of the Athos line to enable laser-based seeding of the FEL process was then realized during the initial user operation phase, in two stages. In a first step a seed laser, with central wavelengths of 790 and 390 nm, and a 200 mm period magnetic modulator were installed in the framework of the so-called "HERO" project (named after the funding ERC project "Hidden and Entangled Resonating Order" [18]). This part of the upgrade was already sufficient to demonstrate the generation of attosecond pulse trains by energy-modulating the electron beam through overlap with the seed laser and converting the energy modulation into a density modulation in a chicane following the ESASE scheme [19]. An alternative method making use of a strong undulator taper [20] was also applied with success. The electron longitudinal phase space after energy modulation, measured with the X-band rf deflector and shown in Fig. 4, clearly exhibits the periodicity expected from the wavelength of the seed laser. In a next step, mode locking between the attosecond pulses by applying delays to the electron beam that match the laser wavelength was attempted, but no clean verification was possible at this point, given our lack of phase sensitive diagnostics.

The second stage of the upgrade comprises a second seed laser with another incoupling modulator (also 200 mm period), and a larger magnetic chicane, all necessary to put into practice echo-enabled harmonic generation (EEHG) [21]. As of this writing, all the components have been installed and tested individually. First attempts to implement and verify EEHG are planned very soon.

OUTLOOK

Midterm Improvements

SwissFEL is still in its early stages and is constantly being improved on various fronts. Here we mention two areas of further development.

A number of FEL operation modes are difficult to set up because of the inhomogeneous longitudinal electron beam profile coming out of the photoinjector. In particular head and tail of the bunch, where the charge density is lower and the energy chirp is less linear, are subject to overcompression, leading to two distinct peaks ("horns") in the current profile. These parts of the beam feature significantly different beam properties giving rise to issues associated with beam transport, diagnostics and reduced lasing performance.

The only viable solution to this problem consists in collimating away both head and tail of the bunch (as is done at LCLS). The dispersive sections in the bunch compression chicanes are ideal locations to perform such collimation. Indeed it was confirmed that collimation in the first bunch compressor essentially fixes the problem, but the associated beam loss would not allow operation at 100 Hz. A radiation-shielding enclosure of the chicane was installed recently, but needs further iteration to meet our stringent radiation safety requirements.

A second challenge to be addressed in the near future concerns the stabilization of the EEHG mode in order to turn this mode from an experimental demonstration into a work horse for regular user experiments. This will require both improvements to the seed laser systems as well as a feedback loop keeping constant the overlap between laser and electron beam, based on suitable instrumentation monitoring the difference in arrival time. The previously mentioned cleaning of the longitudinal electron current profile is also an important prerequisite for the stable operation of EEHG.

In the longer term we are considering moving the first bunch compressor further upstream in order to reduce the
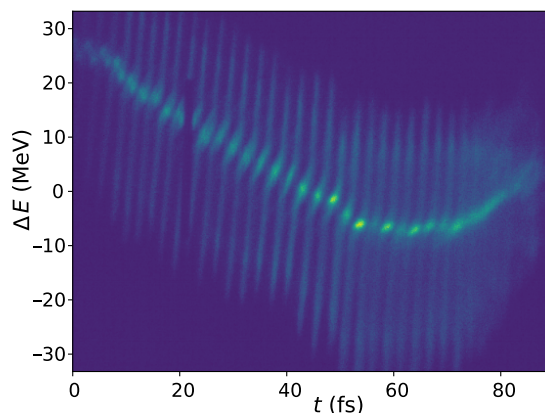

Figure 4: Electron longitudinal phase space (energy versus time) after energy modulation by a seed laser with 790 nm wavelength, as observed with the X-band rf deflector.

effects of microbunching and, in particular, intrabeam scattering on the energy spread.

Porthos Upgrade

In the longer run it is planned to expand the SwissFEL capabilities by adding a third beamline, which, in good Musketeer tradition, will go by the name of Porthos. The existing building and associated infrastructure already provide for a third beamline running in parallel to the Aramis beamline, including a beamdump. Preliminary work on the extraction line has already started in the framework of the PSI-CERN collaboration for building and testing a prototype of a positron source for the FCC-ee project [22]. Space for the experiments, however, is still missing, and a new experiment hall would have to be built for Porthos.

The science case for Porthos is still in development. A first iteration of the deliberations within the community was documented in the 2021 photon science roadmap [23] compiled by the Swiss photon community. More recent considerations suggest a photon energy range between 1 and 10 keV for Porthos, with an undulator line providing similar or even more flexibility than the existing Athos line, thus including polarization control and intra-undulator chicanes to delay the electron beam with respect to the emitted radiation.

The timescale for the implementation of Porthos is still uncertain, as PSI is strongly focused on its current flagship project, SLS-2.0, and a major upgrade of the proton facility to be realized afterwards.

CONCLUSION

After five years of user operation, SwissFEL has reached a stable level of performance, responding to the needs of a growing user community. By exploring new FEL modes, SwissFEL has established itself as one of the main drivers of FEL science, in particular in the soft X-ray regime with its extremely flexible Athos beamline. The extension of Athos to a laser-seeded FEL will make this beamline even more attractive for users. In the long term, a third beamline, probably covering the photon energy range between 1 and 10 keV and offering flexibility similar to Athos in that energy range, will further enhance the SwissFEL portfolio.

ACKNOWLEDGMENTS

REFERENCES

[1] C. J. Milne *et al.*, "SwissFEL: the Swiss X-ray free electron laser", *Appl. Sci.*, vol. 7, p. 720, 2017. `doi:10.3390/app7070720`

[2] E. Prat *et al.*, "A compact and cost-effective hard X-ray free-electron laser driven by a high-brightness and low-energy electron beam", *Nat. Photonics*, vol. 14, p. 748, 2020. `doi:10.1038/s41566-020-00712-8`

[3] E. Prat *et al.*, "An X-ray free-electron laser with a highly configurable undulator and integrated chicanes for tailored pulse properties", *Nat. Commun.*, vol. 14, p. 5069, 2023. `doi:10.1038/s41467-023-40759-z`

[4] E. Prat, A. Malyzhenkov, and P. Craievich, "Sub-femtosecond time-resolved measurements of electron bunches with a C-band radio-frequency deflector in x-ray free-electron lasers", *Rev. Sci. Instrum.*, vol. 94, p. 043103, 2023. `doi:10.1063/5.0144876`

[5] P. Craievich *et al.*, "Novel X-band transverse deflection structure with variable polarization", *Phys. Rev. Accel. Beams*, vol. 23, p. 112001, 2020. `doi:10.1103/PhysRevAccelBeams.23.112001`

[6] P. Craievich *et al.*, "Post-undulator beam measurements with PolariX TDS in SwissFEL", *Proc. of SPIE*, vol. 12581, p. 1258106, 2023. `doi:10.1117/12.2665447`

[7] P. Dijkstal *et al.*, "Self-synchronized and cost-effective time-resolved measurements at x-ray free-electron lasers with femtosecond resolution", *Phys. Rev. Res.*, vol. 4, p. 013017, 2022. `doi:10.1103/PhysRevResearch.4.013017`

[8] T. Gruhl *et al.*, "Ultrafast structural changes direct the first molecular events of vision", *Nature*, vol. 615, p. 939, 2023. `doi:10.1038/s41586-023-05863-6`

[9] P. Dijkstal, E. Prat, and S. Reiche, "Short FEL pulses with tunable duration from transversely tilted beams at SwissFEL", in *Proc. FEL'22*, Trieste, Italy, Aug. 2022, pp. 121–125. `doi:10.18429/JACoW-FEL2022-MOP51`

[10] E. Prat *et al.*, "Demonstration of large bandwidth hard X-Ray free-electron laser pulses at SwissFEL", *Phys. Rev. Lett.*, vol. 124, p. 074801, 2020. `doi:10.1103/PhysRevLett.124.074801`

[11] S. Reiche *et al.*, "Frequency and spatially chirped free-electron laser pulses", *Phys. Rev. Res.*, vol. 5, p. L022009, 2023. `doi:10.1103/PhysRevResearch.5.L022009`

[12] A. Malyzhenkov *et al.*, "Single- and two-color attosecond hard x-ray free-electron laser pulses with nonlinear compression", *Phys. Rev. Res.*, 2, p. 042018(R), 2020. `doi:10.1103/PhysRevResearch.2.042018`

[13] R. Abela *et al.*, "The SwissFEL soft X-ray free-electron laser beamline: Athos", *J. Synchrotron Radiat.*, vol. 26, p. 1073, 2019. `doi:10.1107/S1600577519003928`

[14] E. Prat *et al.*, "Demonstration of a compact x-ray free-electron laser using the optical klystron effect", *Appl. Phys. Lett.*, vol. 119, p. 151102, 2021. `doi:10.1063/5.0064934`

[15] E. Prat *et al.*, "Widely tunable two-color x-ray free-electron laser pulses", *Phys. Rev. Res.*, vol. 4, p. L022025, 2022. `doi:10.1103/PhysRevResearch.4.L022025`

[16] G. Wang, E. Prat, S. Reiche, and K. Schnorr, "Progress on fresh-slice multi-stage amplification at SwissFEL", presented at the 67th ICFA Advanced Beam Dynamics Workshop (FLS'23), Lucerne, Switzerland, Aug.-Sep. 2023, paper TH2A3, this conference.

[17] E. Prat *et al.*, "Coherent sub-femtosecond soft X-ray free-electron laser pulses with nonlinear compression", to be published.

[18] G. Aeppli, A. V. Balatsky, H. M. Rønnow, and N. A. Spaldin, "Hidden, entangled and resonating order", *Nat. Rev. Mater.*, vol. 5, p. 477, 2020. `doi:10.1038/s41578-020-0207-z`

[19] A. A. Zholents, "Method of an enhanced self-amplified spontaneous emission for x-ray free electron lasers", *Phys. Rev. Spec. Top. Accel. Beams*, vol. 8, p. 040701, 2005. `doi:10.1103/PhysRevSTAB.8.040701`

[20] E. L. Saldin, E. A. Schneidmiller, and M. V. Yurkov, "Self-amplified spontaneous emission FEL with energy-chirped electron beam and its application for generation of attosecond x-ray pulses", *Phys. Rev. Spec. Top. Accel. Beams*, vol. 9, 050702, 2006. `doi:10.1103/PhysRevSTAB.9.050702`

[21] G. Stupakov, "Using the beam-echo effect for generation of short-wavelength radiation", *Phys. Rev. Lett.*, vol. 102, p. 074801, 2009. `doi:10.1103/PhysRevLett.102.074801`

[22] N. Vallis *et al.*, "The PSI Positron Production Project", in *Proc. LINAC'22*, Liverpool, UK, Aug.-Sep. 2022, pp. 577–580. `doi:10.18429/JACoW-LINAC2022-TUPORI16`

[23] R. Abela, E. Abreu, A. Cavalieri, M. van Daalen, T. Feurer, and U. Staub, "Photon science roadmap for research infrastructures 2025–2028 by the Swiss photon community", *Swiss Academies Reports*, vol. 16, no. 5, 2021. `doi:10.5281/zenodo.4588917`

FLASH: STATUS AND UPGRADE

M. Vogt*, S. Schreiber, J. Zemella

Deutsches Elektronen-Synchrotron DESY, Germany

Abstract

FLASH, the Soft X-Ray and Extreme-UV Free Electron Laser at DESY, is undergoing a substantial upgrade and refurbishment project, called FLASH2020+. The project will finally enable external seeded and SASE FEL operation for a wavelength range down to 4 nm with the EEHG method. This is achieved in two long shutdowns from November 2021 to August 2022 and from June 2024 to August 2025. Key ingredient of the upgrade were installation of a laser heater, replacing two early TTF-type L-band SRF accelerating modules by modern, high-gradient XFEL-type modules, redesign of the 2nd bunch compressor, and complete redesign of the FLASH1 beam line for HGHG/EEHG seeding.

This talk will report on the project and the status of FLASH after the first shutdown with emphasis on beam dynamics aspects.

FLASH

This contribution is a modified version of a contribution [1] to the 21st International Conference on Radio-Frequency Superconductivity, held this June in Grand Rapids, MI, USA. There the emphasis was on the energy upgrade, while this contribution emphasizes certain beam dynamics aspects of the FLASH2020+ Upgrade.

FLASH [2–8] is a superconducting high-gain vacuum-ultraviolet (VUV) / soft X-ray free-electron laser (FEL), operated mainly as a photon user facility with up to two beam-lines operated simultaneously. FLASH is segmented into three functional beamlines: the common injector and linac FLASH0, preparing and accelerating bunch trains suitable for the FEL process, and the two FEL beamlines FLASH1 and FLASH2 which finalize and diagnose the bunch preparation, accommodate the FEL process each in their own internal undulator beamline, and finally dispose of the spent beam in a beam dump. The FLASH3 beamline is used by the plasma wake field acceleration experiment FLASHForward [9] which can be activated *alternatively* to FLASH2 by powering a DC dipole. The FLASH accelerating RF consists of 7 L-band (1.3 GHz) superconducting modules of 8 9-cell Tesla-type cavities.

At the moment FLASH is undergoing a substantial upgrade and refurbishment project, called FLASH2020+ (see next section). The first of two shutdowns started November 2021 and ended August 2022 successfully and the second scheduled to start June 2024 and to end August 2025, is being prepared now.

The original FLASH injector (before the upgrade) consisted of a normal-conducting photo-cathode 1.6-cell RF-gun (1.3 GHz), an accelerating L-band module (ACC1), a third harmonic linearizer (ACC39) operated at 3.9 GHz, a BACCA longitudinal feedback cavity [10], the first bunch compression chicane, two more L-band accelerating modules (ACC2,ACC3), and the second bunch compression chicane — at that time an S-type 6-dipole chicane.

The bunches are produced in up to three trains mapped to the three injector lasers.

In its standard setting, the RF-gun is operated with approximately 5 MW and produces a 600 μs flat top. The bunch at the exit of the gun then has a momentum of 5.6 MeV/"c" FLASH0 can therefore provide up to 6000 bunches per second (in 10 trains) at 1 MHz bunch repetition frequency and 10 Hz pulse repetition frequency. If the RF pulse is split between two sub-trains (for FLASH1 and FLASH2), a minimum of 70 μs has to be subtracted for transient effect of the extraction kicker and for interpolating between the RF parameters of the two flat tops which are otherwise within certain ranges independent.

The third harmonic linearizer ACC39 is typically operated in decelerating mode with a nominal set point is 19.5 MeV.

The first bunch compression chicane is a 4-dipole C-chicane designed for bending angles from 15° (longitudinal dispersion M_{56} =120 mm) to 15° (M_{56} =255 mm). Prior to the upgrade it used to be operated at a typical deflection angle of 18° (M_{56} =181 mm). Downstream of the chicane used to be a comfortably equipped transverse diagnostics and matching section.

Before the upgrade, the second (ACC2) and third (ACC3) L-band Module were among the weakest in FLASH. Well tuned they were capable of (together) providing an *E*-gain of 304 MeV at an off-crest angle of up to 30°, i.e. an effective total amplitude of at most 350 MeV

In addition prior to the first shutdown, the second bunch compression chicane was a 6-dipole (S-type) chicane blocking the space for proper a proper second beam re-match upstream of the "main-linac".

The FLASH0 "main-linac" consists of four L-band modules (ACC4/5/6/7). The maximum attainable energy gain of the main linac is about 800 MeV so that the maximum e^--beam energy of FLASH was ~1250 MeV

Downstream of the last module the combined collimation and switch-yard section starts. Switching between FLASH1 and FLASH2 is achieved via a kicker-septum scheme with two vertically deflecting flat top kickers, deflecting the FLASH2 sub-train into the horizontally deflecting channel of a DC Lambertson septum. In order to achieve the required stability for the kicked bunches, the gap between the bunch trains needs to be >70 μs to cover the kicker rise-time *and* the damping of the initial ringing.

* vogtm@mail.desy.de

The FLASH1 beamline was originally designed and optimized for SASE FEL operation.

The FLASH2 beamline also provides SASE FEL radiation. It consists of an extra bunch compression chicane (called FL2BC1), a transverse diagnostic section capable of performing a quad-scan, the 12 variable gap FLASH2 undulators, the PolariX TDS [11–13], the horizontal photon/electron separator dipole which also generates the dispersion for the longitudinal phase space mapping with PolariX, the vertical dump dipole and finally the dump beamline.

Downstream of the separators of FEL and electron beam, both tunnels (FLASH1/2) are equipped with photon diagnostics, i.e., screens, pulse energy detectors, and spectrometers for tuning the FEL. Then the FEL beams are delivered to the two experimental halls: Albert Einstein Hall (FLASH1), and Kai Siegbahn Hall (FLASH2). Both halls contain further photon diagnostics, hardware for photon beam manipulation [14], and of course the experimental end-stations.

The history of FLASH is nicely covered in Ref. [5, 8].

THE FLASH2020+ UPGRADE

To keep FLASH at the forefront of science, an ambitious upgrade and refurbishment project, called FLASH2020+ [15–17], was started in 2020. The goals are to replace outdated hardware, and at the same time upgrade the FLASH facility to stay attractive and competitive for at least the next 15 years.

Motivation

FLASH is currently the only superconducting FEL in the wavelength regime from VUV to soft X-ray. In its current injector configuration it can provide ~ 5000 bunches per second producing SASE FEL radiation from 60 nm down to ~4 nm with pulse durations from some tens to several hundreds of fs and with pulse energies from some μJ to ~1 mJ. Part of the motivation for the upgrade was to extend the wavelength range towards shorter wavelengths. In fact ~4 nm is just the upper end of a wavelength range, called "the water window", which is of special interest to many of the users. The energy upgrade will allow to reach higher beam energies and thus create photons of shorter wavelengths <4 nm In addition, so called *afterburner* undulators can significantly enhance the 3rd harmonic content of the FEL radiation, thereby extending the usability of the third harmonic down to ~1.3 nm.

SASE is a powerful production mechanism of FEL radiation however, it is a stochastically seeded process, with notable shot-to-shot fluctuations of the photon spectrum and potentially several uncorrelated modes (spikes) in a single bunch. Thus the longitudinal coherence of SASE FELs is rather low. The FEL process can however also be externally seeded with a highly coherent external laser pulse. It has been decided that FLASH1 should ultimately cover the wavelength range from ~4 nm to ~60 nm with external seeding in High Gain Harmonic Generation mode (HGHG) [18, 19] for

the longer wavelengths and Echo Enabled Harmonic Generation mode (EEHG) [20, 21] for the shorter wavelengths.

Many pump-probe experiments at FLASH1 make use of the THz undulator that produces radiation in the THz regime using the spent electron bunches from the FLASH1 FEL undulators. This was quite successful with bunches tweaked to be a little more spiky than necessary for standard SASE operation, but still compatible with producing useful SASE pulse energies. A beam optimized for high stability, efficient HGHG/EEHG operation however, is not likely to generate decent THz pulse energies. Therefore a post compressor chicane will almost surely be required at some stage to optimize the THz radiation.

In order to reliably provide beams with high quality and stability for seeding in FLASH1 and SASE in FLASH2, the operability of FLASH needs an upgrade too. The design includes more and improved sections with transverse diagnostics to match the incoming beam to a downstream optics which is optimized for best performance, more appropriate locations for the transverse deflecting structure LOLA [22, 23], an intra-train orbit feed forward to remove the systematic part of intra train orbit correlations, quad/skew-quad corrector packs in the new designed second bunch compression chicane for removing systematic longitudinal to transverse correlations within the bunches, a laser heater [24] to ameliorate the unwanted micro-bunching effects [25], and of course a upgraded diagnostics at all levels. All these measures will make the operation of FLASH more systematic and predictable.

The Injector Upgrade

The first shutdown 2021/22 was dedicated to upgrading and refurbishing the injector section of FLASH0. Figure 1 shows a schematic layout of FLASH *after* the first upgrade shutdown 2021/22. Installation of two new injector lasers was started. All components of the laser beamlines that require access to the accelerator tunnel have been installed during the shutdown. The new lasers are scheduled to be commissioned by the beginning of next year.

Kickers have been installed to reduce the systematic (short term reproducible) orbit slopes over the bunch train, between gun ad ACC1, and around the two chicanes. Downstream of BACCA, space has been generated to install an incoupling chicane for the laser heater laser, an undulator for the actual energy modulation process, and the necessary surrounding lattice elements (quadrupoles, steerers, screens). The laser heater installation has been completed in the shutdown and it is already commissioned to a large extent. We have achieved transverse and temporal overlap, optimized the undulator gap for the actual beam energy. We have observed the heating process, i.e., increased slice energy spread in the heated part of the bunch, directly by both LOLA and PolariX, and by observing the expected reduction of the micro-bunching gain and the FEL gain.

In order to make space for the laser heater the first Burch compression chicane (*now called FL0BC1*) had to be moved about 2 m downstream. Thereby the space for the transverse
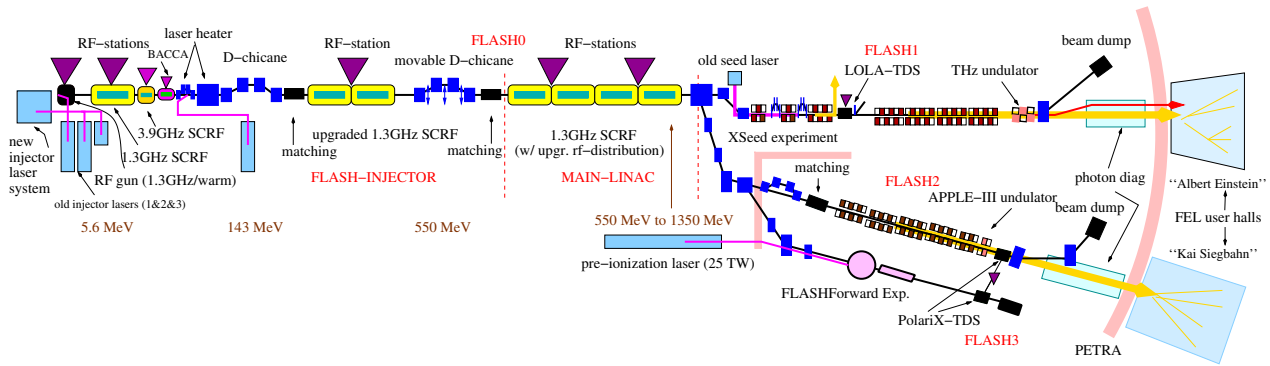
Figure 1: Schematic layout of FLASH (not to scale) after the first shutdown 2021/22.

diagnostics and matching section (between FL0BC1 and the *fixed position* of ACC2) was reduced. This required an updated concept for measuring emittance and mismatch amplitude as well as for re-matching into the design optics [26].

During the first shutdown 2021/22 two of the oldest, and weakest, TTF-type L-band modules were replaced by newly refurbished, XFEL-type modules PXM2.1 and PXM3.1 [27]. We now routinely achieve an E-gain of around 417 MeV at an off-crest phase of at most 25° which suggests an effective total amplitude of ~460 MeV. This allows to operate FL0BC2 at 560 MeV — 110 MeV more than the before the energy upgrade.
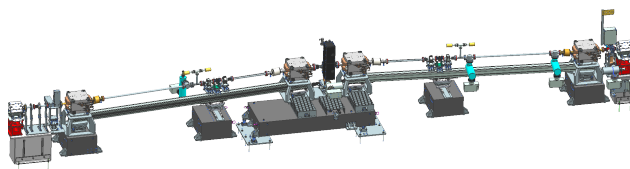
Figure 2: 3D CAD model of FLASH's 2nd bunch compression chicane FL0BC2

The section around the second bunch compressor chicane (*now called FL0BC2*) was completely redesigned in order to generate space for a proper diagnostics and re-matching section, capable of performing symmetric quads-cans and multi-quad-scans. The old (horizontal) 6-dipole S-shaped chicane with flat vacuum chamber was replaced by a new, shorter, C-shaped design with round vacuum chambers and skew-quad/BPM/quad packs in the two chicane legs [28]. Figure 2 shows at 3D CAD model of the new chicane FL0BC2. The inner dipoles are movable on rails so that the chicane is tunable from 0° to 6° (nominal 5°) with maximum a M_{56} of ~100 mm (nominal ~70 mm). The magnet packs in the chicane legs consist of a quadrupole, followed by a beam position monitor, followed by a skew-quadrupole, in one leg and the mirror image of the pack in the other leg. The goal is to employ the horizontal chicane dispersion in the quadrupole to reduce linear longitudinal-to-horizontal correlations inside the bunch, the combined action of horizontal dispersion in skew-quad and quad to reduce linear longitudinal-to-vertical correlations inside the bunch [28–30].

The new chicane could so far only be commissioned in part: Transmission with various magnet currents from 0.5° to 5° and the corresponding nominal slider positions is perfect. With the nominal deflection angle of 5° the compression factor for given bunch chirp is in the right ball park. Since mid-August the new FL0BC2 is routinely operated at 560 MeV.

In Early October 2022 commissioning with beam started for about 3.5 weeks prior to the first user run with the new injector [26]. Since then we take more and more features into operation during the regular FEL studies.[1] In the short time we managed to establish beam transport through both beamlines, commission a large part of the new updated diagnostics, match the beam from the gun to the design optics upstream of FL0BC1, correct the dispersion in injector and linac, and get the intra train orbit feed forward into operation.

The FLASH1 Upgrade Towards External (HGHG/EEHG) Seeding

The second shutdown 2024/25 was originally scheduled to convert FLASH1 into an externally seeded beamline for HGHG and EEHG operation, preserve the capability of providing also saturated SASE, and preserve the capability of producing THz radiation of high pulse energy simultaneous to seeding and/or SASE for pump-probe experiments in the Albert Einstein Hall. Figure 3 shows FLASH after this stage of the project has completely been finalized. The FLASH1 beamline is described in some detail in Ref. [31] with emphasis on the seed radiator section and in Ref. [32] with emphasis on the remaining parts. We refer to this original design as *stage-FULL*. However it turned out that in the 2024/25 shutdown, not all goals can be achieved. Instead a reduced design, called *stage-0* will be implemented at first. It enables HGHG and EEHG seeding with slightly reduced performance but in particular will not provides SASE in saturation at shortest wavelengths or high THz pulse energies.

The first new section downstream of the septum will be a transverse diagnostic and matching section. The first modulator section contains a laser incoupling chicane FL1CH1 for the first seed laser, an undulator (1st modulator) in which

---

[1] studies explicitly aiming at improving the FEL operation of FLASH.
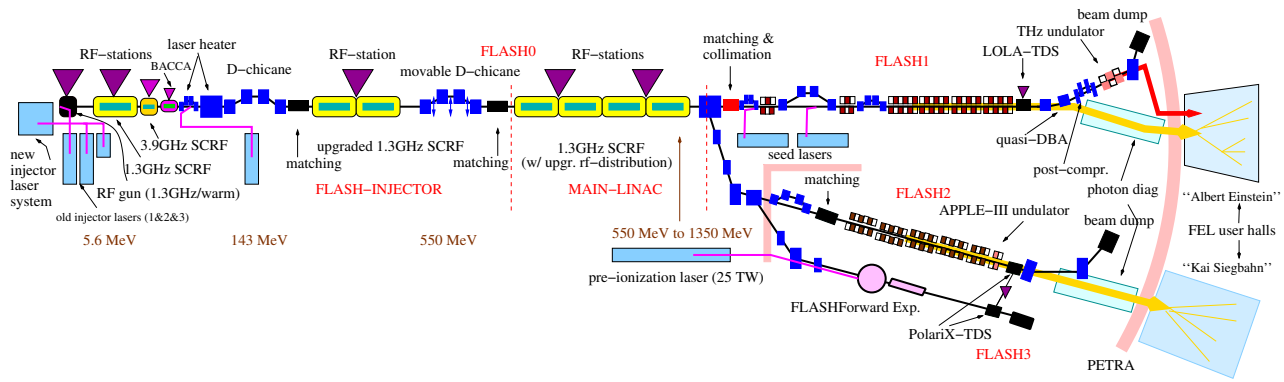
Figure 3: Schematic layout of FLASH (not to scale) after the shutdown 2024/25 (Stage-Full).
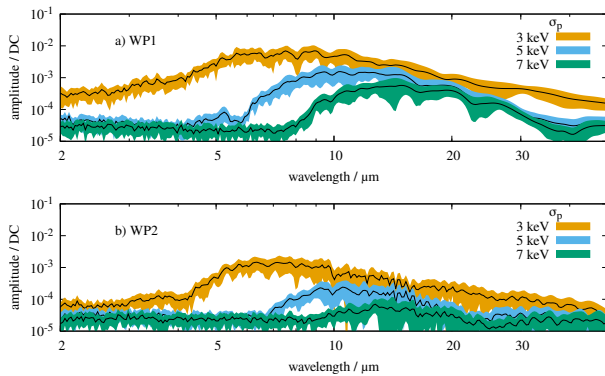

Figure 4: Microbunching simulations using a realistic shot-noise model for two compression working points with the semi-Lagrangian code SelaV$_{1D}$

the electron bunch becomes energy-modulated by laser 1, and the so-called *over-folding* chicane FL1CH2 to strongly over-fold the energy modulation from the first laser in EEHG mode. The over-folding chicane also serves for coupling seed laser 1 out and for coupling seed laser 2 in. The second modulator section contains a second undulator to modulate the incoming phase space, and the so-called *bunching* chicane FL1CH3 that is used to shear the doubly modulated structure in order to create sharp spikes in the charge distribution — with potentially very high harmonic content. Downstream follows the radiator section, with its (originally) 11 helical APPLE-III undulators.

Seeded FEL operation is much more severely perturbed by microbunching than SASE. We have performed start-to-end simulations to minimize the impact of microbunching in FLASH1. In particular we have developed a code, SelaV$_{1D}$ [33], that describes the evolution of the longitudinal phase space density by low-noise backward tracking (semi-Lagrangian method) of a tree-based grid. The tree-based grid allows extreme fine resolution for the ϵ-support of the exotic FEL densities without wasting memory on unpopulated areas. Figure 4 compares too compression working points (WPs), a heuristically designed WP and a carefully optimized WP, by means of microbunching spectra provided by SelaV$_{1D}$ simulations, starting the microbunching from

realistic shot-noise without the artifacts of macro particle tracking. Each WP shows three different slice energy spreads (intrinsic, moderate laser heater, cranked up laser heater). It becomes clear that the microbunching amplitude can be kept small ($\sim 10^{-4}$) in the relevant wavelength regime with moderate energy spread if a suitable wP is chosen.

Downstream of the radiators follows the new location for LOLA downstream of the radiators. One key aspect of the new FLASH1 beamline is to disentangle the photon beamline from the spent electron beamline, and eliminate geometrical coupling. A quasi double bend achromat structure (qDBA) will divert the beam by 5° to the port side[2]. In order to post-compress the "soft" seed beam for enhanced THz output, stage-FULL includes a 4th chicane FL1CH4 [32] between the qDBA and the actual THz undulator. Finally the beam is transported into the dump via a coupling-free beamline much alike the FLASH2 dump line.

The CDR [15] foresees for FLASH2, the installation of the PolariX TDS, the installation of a helical third harmonic afterburner undulator (APPLE-III) and not further specified modifications for advance lasing schemes. PolariX is installed and operational although not yet at full RF power (conditioning was slower than expected), the afterburner will be installed this fall.

Stage-Full vs. Stage-0

As mentioned before not all features of the FLASH1 upgrade (stage-FULL) can already be achieved in the 2024/25 shutdown. However, the so called stage-0, to be implemented 2024/25, was designed by *delaying* features in way that allows implementation at a later stage with minimal effort. Features that do not immediately affect the primary goal of external seeding were delayed. This includes the ability to saturate SASE at short wavelengths and high pulse-energy THz radiation. Only 6 of the 11 APPLE-III radiators will be installed at first, the first three radiators will be replaced by recycled planar Xseed [34] radiators as buncher, 2 more will be left empty at first. The post-compressor chicane FL1CH4 and some THz related electron beam diagnostic will be delayed. The intersections of the radiators will not equipped

---

[2] *in beam direction* left

with wire-scanners in the first implementation. The space will however be reserved.

CONCLUSION

FLASH was and is a competitive FEL user facility. The FLASH2020+ upgrade will extend the wavelength range and make FLASH the only *seeded* VUV / soft X-ray FEL capable of supplying several thousand FEL pulses per second. The first upgrade shutdown was successfully finished and user operation was established after a very short commissioning phase. The second shutdown planning is within schedule. The originally planned second stage of the upgrade will not be fully achievable after the next shutdown. However, delayed features can without exception be implemented later. We are looking forward to the next step of the FLASH2020+ upgrade.

ACKNOWLEDGMENTS

REFERENCES

[1] M. Vogt *et al.*, "The FLASH 2020+ Upgrade Project", Proc. 21st International Confrence on Radio-Frequency Superconductivity, SRF'23 Grand Rapids, MI, USA, Jun. 2023, paper TUIAA02.

[2] W. Ackermann *et al.*, "Operation of a free-electron laser from the extreme ultraviolet to the water window", *Nature Photonics*, vol. 1, pp. 336–342, 2007.
doi:10.1038/nphoton.2007.76

[3] B. Faatz and S. Schreiber, "First Lasing of FLASH2 at DESY", *Synchrotron Radiat. News* 27.
doi:10.1080/08940886.2014.970941

[4] B. Faatz *et al.*, "Simultaneous Operation of Two Soft X-Ray Free-Electron Lasers Driven by One Linear Accelerator", *New Journal of Physics* 18, 062002, 2016.
doi:10.1088/1367-2630/18/6/062002

[5] S. Schreiber and B. Faatz, "The free-electron laser FLASH", *High Power Laser Sci. Eng.*, vol. 3, p. e20, 2015.
doi:10.1017/hpl.2015.16

[6] J. Roensch-Schulenburg *et al.*, "Status of the free-electron laser user facility FLASH", presented at the 14th Int. Particle Accelerator Conf. (IPAC'23), Venice, Italy, Jun. 2023, paper TUPL020, to appear in the proceedings.

[7] K. Honkavaara, C. Gerth *et al.*, "Status of the Free-Electron Laser User Facility FLASH", presented at FEL'22, Trieste, Italy, Aug. 2022, paper MOP37, to be published.

[8] K. Honkavaara and S. Schreiber, "FLASH: The Pioneering XUV and Soft X-Ray FEL User Facility", in Proc. 39th Int. Free Electron Laser Conf. (FEL'19), Hamburg, Germany, Aug. 2019, paper THP074, pp. 734–737.
doi:10.18429/JACoW-FEL2019-THP074

[9] R. D'Arcy *et al.*, "FLASHForward: plasma wakefield accelerator science for high-average-power applicationsd", Phil. Trans. R. Soc. A, vol. 377, p. 20180392, 2019.
doi:10.1098/rsta.2018.0392

[10] B. Lautenschlager *et al.*, "Arrival Time Stabilization at FLASH Using the Bunch Arrival Corrector Cavity (BACCA)", Proc. 12th Int. Particle Acc. Conf. (IPAC'21), Campinas, SP, Brazil, 2021, paper TUPAB302.
doi:10.18429/JACoW-IPAC2021-TUPAB302

[11] B. Marchetti *et al.*, "Experimental demonstration of novel beam characterization using a polarizable X-band transverse deflection structure", *Sci. Rep.*, vol. 11, 3560, 2021.
doi:10.1038/s41598-021-82687-2

[12] P. Craievich *et al.*, "Novel X-band transverse deflection structure with variable polarization", *Phys. Rev. Accel. Beams*, vol. 23, p. 112001, 2020.
doi:10.1103/PhysRevAccelBeams.23.112001

[13] P. Gonzalez Caminal, "Beam-Based Commissioning of a Novel X-Band Transverse Deflection Structure with Variable Polarization", submitted to *Phys. Rev. Accel. Beams*.

[14] K. Tiedtke *et al.*, "The soft x-ray free-electron laser FLASH at DESY: beamlines, diagnostics and end-stations", *New J. Phys.*, vol. 11, p. 023029, 2009.
doi:10.1088/1367-2630/11/2/023029

[15] M. Beye *et al.*, "FLASH2020+, Conceptual Design Report", DESY, Hamburg, 2020.
doi:10.3204/PUBDB-2020-00465

[16] L. Schaper *et al.*, "Flexible and Coherent Soft X-ray Pulses at High Repetition Rate: Current Research and Perspectives", *Appl. Sci.*, vol. 11, p. 9729, 2021.
doi:10.3390/app11209729

[17] L. Schaper *et al.*, "FLASH2020+ Project Progress: Current installations and future plans", presented at FEL'22, Trieste, Italy, Aug. 2022, paper TUP51 to be published.

[18] L. H. Yu, "Generation of intense uv radiation by subharmonically seeded single-pass free-electron lasers", *Phys. Rev. A*, vol. 44, p. 5178, 1991. doi:10.1103/PhysRevA.44.5178

[19] E. Allaria *et al.*, "Highly coherent and stable pulses from the FERMI seeded free-electron laser in the extreme ultraviolet", *Nat. Photonics*, vol. 6, p. 699, 2012.
doi:10.1038/nphoton.2012.233

[20] D. Xiao and G. Stupakov, "Echo-enabled harmonic generation free electron laser", *Phys. Rev. Spec. Top. Accel. Beams*, vol. 12, p. 030702, 2009.
doi:10.1103/PhysRevSTAB.12.030702

[21] E. Allaria *et al.*, "Amplified Emission of a Soft-X Ray Free-Electron Laser Based on Echo-Enabled Harmonic Generation", in *Proc. IPAC'19*, Melbourne, Australia, May 2019, pp. 2230–2232. doi:10.18429/JACoW-IPAC2019-WEXXPLM1

[22] Ch. Behrens *et al.*, "Measurement and Control of the Longitudinal Phase Space at High Gain Free-Electron Lasers", presented at FEL'11, Shanghai, China, 2012, unpublished.

[23] M. Yan *et al.*, "First Realization and Performance Study of a Single-Shot Longitudinal Bunch Profile Monitor Utilizing a Transverse Deflecting Structure", in *Proc. IBIC'13*, Oxford, UK, Sep. 2013, paper TUPC36, pp. 456–459.

[24] C. Gerth *et al.*, "Layout of the Laser Heater for FLASH2020+", in *Proc. IPAC'21*, Campinas, Brazil, May 2021, pp. 1647–1650.
doi:10.18429/JACoW-IPAC2021-TUPAB111

[25] Ph. Amstutz and M. Vogt, "Microbunching Studies for the FLASH2020+ Upgrade Using a Semi-Lagrangian Vlasov Solver", in *Proc. IPAC'22*, Bangkok, Thailand, Jun. 2022, pp. 2334–2337.
doi:10.18429/JACoW-IPAC2022-WEPOMS037

[26] M. Vogt, J. Zemella, J. Roensch-Schulenburg, and S. Schreiber "Recommissioning of the FLASH Injector and Linac", presented at IPAC'23, Venice, Italy, May 2023, paper TUPL022, to appear in the proceedings.

[27] S.Barbanotti *et al.*, "Twenty Years of Cryogenic Operation of the FLASH Superconducting LINAC", presented at SRF'23, Grand Rapids, MI, USA, Jun. 2023, paper TUIAA01.

[28] M. Vogt and J. Zemella, "A New 2nd Bunch Compression Chicane for the FLASH2020+ Project", in *Proc. IPAC'21*, Campinas, Brazil, May 2021, pp. 1618–1621.
doi:10.18429/JACoW-IPAC2021-TUPAB102

[29] M. Guetg, B. Beutner, E. Prat, and S. Reiche, "Optimization of free electron laser performance by dispersion-based beam-tilt correction", *Phys. Rev. Spec. Top. Accel. Beams*, vol. 18, p. 030701, 2015.
doi:10.1103/PhysRevSTAB.18.030701

[30] M. W. Guetg, F.-J. Decker, Y. Ding, P. Emma, Z. Huang, and T. J. Maxwell, "Measurement of Advanced Dispersion-based Beam-tilt Correction", in *Proc. IPAC'16*, Busan, Korea, May 2016, pp. 813–816.
doi:10.18429/JACoW-IPAC2016-MOPOW045

[31] J. Zemella and M. Vogt, "The New FLASH1 Undulator Beamline for the FLASH2020+ Project", presented at FEL'22, Trieste, Italy, Aug. 2022, paper TUP52, to be published

[32] M. Vogt and J. Zemella, "The New FLASH1 Beamline for the FLASH2020+ Project", in *Proc. IPAC'22*, Bangkok, Thailand, Jun. 2022, pp. 1010–1013.
doi:10.18429/JACoW-IPAC2022-TUPOPT006

[33] Philipp Amstutz, Mathias Vogt, "TSelaV$_{1D}$, a semi-Lagrangian Vlasov simulation code in one degree of freedom", https://selav.desy.de

[34] S. Ackermann *et al.*, "First Demonstration of Parallel Operation of a Seeded FEL and a SASE FEL", in *Proc. FEL'22*, Trieste, Italy, Aug. 2022, pp. 236–238.
10.18429/JACoW-FEL2022-TUP41

DEVELOPMENT OF A PULSED INJECTION STRIPLINE FOR DIAMOND-II

R. Fielder*, A. Lueangaramwong, A. Morgan, Diamond Light Source, Oxfordshire, UK

Abstract

Diamond-II will use a single bunch aperture sharing injection scheme. This applies a strong kick to both the injected and the targeted stored bunch with a very short duration (ideally <3 ns, if disturbance to the adjacent bunches is to be avoided). We have developed a design for the stripline kickers that can meet these requirements while minimising internal reflections and beam impedance. We show an analysis of the electric and magnetic fields produced by the stripline and simulations of the effects on injected and stored beam, and analysis of the wakefields and impedance of the structure.

INTRODUCTION

Diamond Light Source is a third generation light source which uses a standard four kicker bump injection method. The kickers have a pulse length of 6 μs, giving some kick to the target bunch both the turn before and after injection, and affecting the entire bunch train even during single bunch injection. In theory this could have zero impact on the stored beam, but difficulty in precisely matching the full length of the four kicker pulses, plus other effects due to non-uniformity in the coating on the ceramic vessels make this difficult. Efforts have been made to reduce the measurable effects of injection on beamlines at Diamond [1, 2], but there can still be some significant impact.

The Diamond-II upgrade [3] will have greatly reduced dynamic aperture compared to Diamond, making injection even more challenging. At the same time, reduced beam size and more advanced beamline detectors and optics greatly reduce the acceptable levels of beam disturbance. Diamond-II will therefore use stripline kickers which can provide pulse lengths on the order of nanoseconds to allow true single bunch injection without disturbing the bulk of the stored beam. This allows an aperture sharing injection scheme, as described in [4, 5].

STRIPLINE DESIGN

The injection stripline design was initially based on the multibunch feedback stripline kickers and influenced by the SLS 2.0 design [6]. This has since been greatly modified to meet the requirements. A large vacuum chamber is used, with a smaller pipe with pumping grills to provide RF continuity and match radius to the incoming and outgoing beam pipe, shown in Fig. 1 with the outer vacuum chamber hidden. The stripline profile is a mix of circular arc with a flat central section to provide better field quality, but with a notch cut out to avoid synchrotron radiation (Fig. 2); a notch is

---

* richard.fielder@diamond.ac.uk

also included on the inboard side for symmetry. The gaps between the charged and grounded elements have been kept as large as possible to reduce the chance of arcing. All edges are rounded for the same reason.

There will be four stripline modules in total, at the downstream end of the mid-straight following the injection straight. The striplines are 150 mm long, with a module length of 180 mm including the surrounding structure. The curved portion of the stripline has a radius of 7 mm, while the flat part is 6.2 mm from the beam horizontally, however, the notch and hybrid shape means there is not a clearly defined gap between the striplines. The striplines are made of copper, while the rest of the chamber will be stainless steel, with ceramic spacers in the input feeds. The striplines will likely be supported inside the chamber by additional ceramic posts, but the mechanical design is not finalised yet. The total required kick of 175 μrad can be provided by a peak voltage of 12.8 kV in each module. The rise time requirement of 0.6 ns leads to a bandwidth requirement of >0.8 GHz. The voltage requirement is 20 kV, driven by the desire to be resilient against a single module failure.

The ends of the striplines are designed to minimise longitudinal field roll off and also to minimise reflections and wake impedance. Alongside tuning of the conical coaxial transitions to the ports, the best overall solution has been found with no overall tapering of the curved section combined with strong tapering of the central flat section.
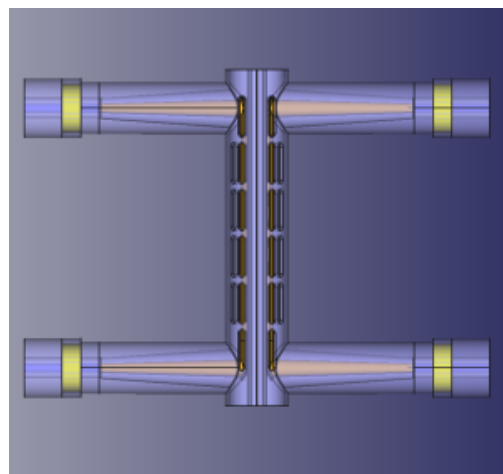

Figure 1: Top down view of stripline with vacuum vessel hidden.

Wakefield and Impedance Simulations

Wakefield and impedance simulations for the stripline were carried out using GdfidL [7] and CST Studio [8]. Impedance simulated with a 0.5 mm drive bunch is shown
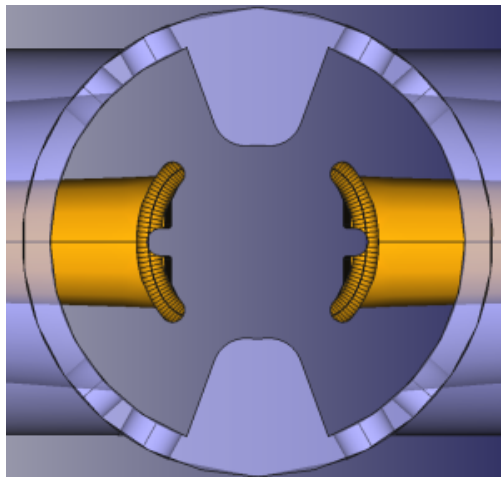
Figure 2: End view of stripline.

in Fig. 3. Impedance in the vertical and longitudinal planes is a similar magnitude to the BPM assemblies and not a cause for concern. Horizontal impedance is larger, but still comparable to other components such as dipole vessels, and likely cannot be reduced significantly without increasing the separation of the striplines. The distribution of energy loss per bunch into each component is shown in Fig. 4 and a schematic identifying these components is shown in Fig. 5. As the expected operating repetition rate is 5 Hz, the thermal load induced by the applied voltages are minimal compared to the beam induced thermal loading.
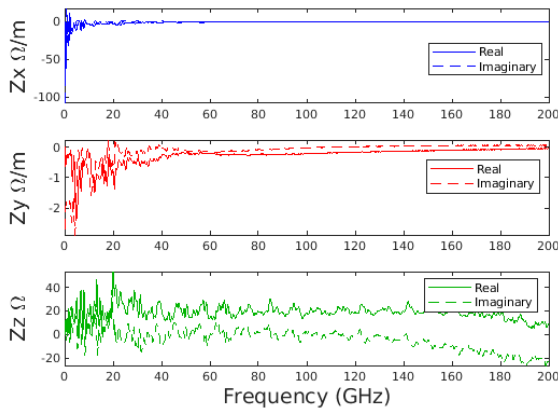

Figure 3: Real and imaginary impedance for horizontal (top), vertical (middle) and longitudinal (bottom) planes for the Diamond-II stripline module.

Field Simulations

Electric and magnetic fields were simulated in GdfidL and CST Studio. Simulations were carried out using a representative trapezoidal pulse with 0.6 ns rise time, 1.4 ns flat top and 0.7 ns fall time, shown in Fig. 6, top. $t = 0$ is defined as the moment the pulse enters the co-axial input feed. Full 3D fields, for both electric and magnetic field, resulting from this were calculated for the volume inside
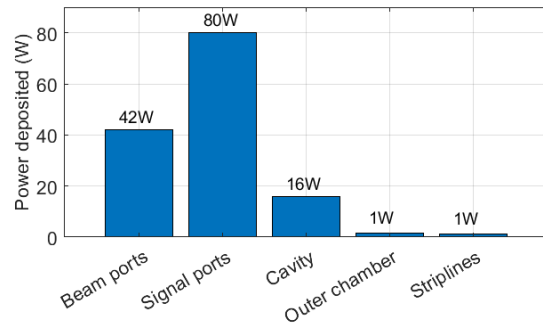

Figure 4: Power loss distribution calculated for a 300 mA full fill. Components not shown have negligible power deposited.
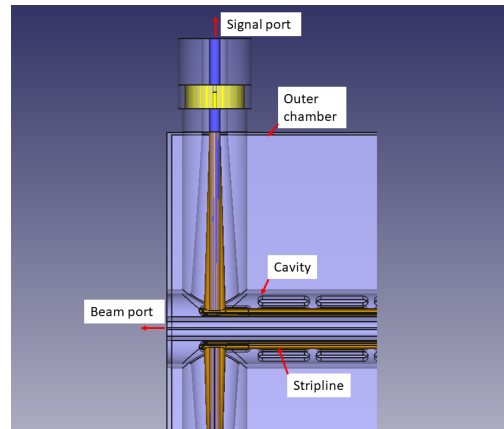
Figure 5: The main components with significant energy deposition.

the stripline radius for 5 ns from the beginning of the input pulse, along with voltage between the striplines at the centre of the beam pipe (Fig. 6, bottom). The time delay between the two plots is due to the travel time of the pulse to the location of the monitor. It can be seen that while the initial part of the pulse is closely reproduced in the voltage seen by the beam, the later part can deviate significantly due to reflections within the striplines.

Simulations were also carried out using a short pulse of 0.1 ns rise and fall time with no flat top to analyse the reflections in more detail. It was determined that these reflections primarily come from the ends of the striplines themselves, and not from a mismatch in impedance to the feedthroughs.

Particle Tracking

The field simulation results, see Fig. 7, are converted to kickmaps and used as input into particle tracking simulations using Accelerator Toolbox [9, 10]. The field is synchronized to the top-up bunch arrival time, with the particle entering the stripline module just as the peak of the voltage pulse arrives at the upstream end of the stripline, at $t = 1.74$ ns; see details in [11].

Figure 8 shows a plot of the horizontal phase space of the injected and stored beams at the middle of the injection straight for the first 50 turns after injection, using the kickmaps from the EM simulations. The grey rectangle
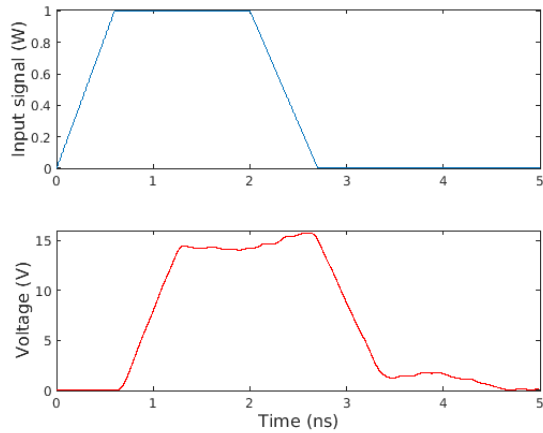
Figure 6: Top: Pulse input to stripline with rise time 0.6 ns, flat top 1.4 ns and fall time 0.7 ns, normalised to 1 W input power. Bottom: Resulting voltage between striplines at centre of module.
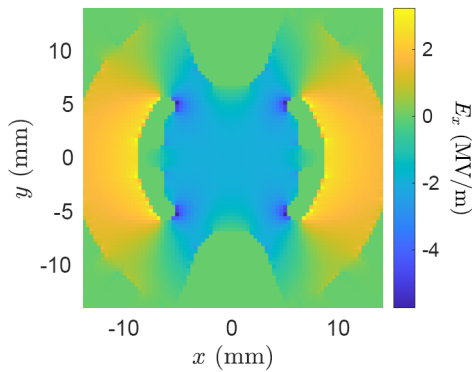
Figure 7: Slice through field map of horizontal component of E-field at centre of stripline module at 2.34 ns.

shows the injection septum plate. A static chicane is included to allow the distance between stored beam and septum plate to be adjusted [12], with a nominal offset of +2 mm.
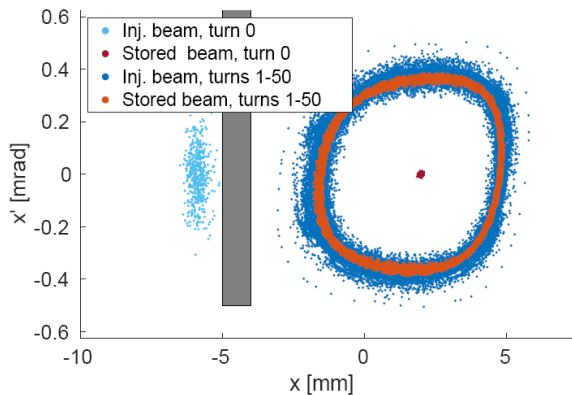

Figure 8: Horizontal phase space at the middle of the injection straight during first 50 turns after injection.

PROTOTYPE STRIPLINE

A prototype stripline with similar design has been developed for testing. This will initially be assessed on a test bench before being installed first in the Diamond booster-to-storage ring transfer line and finally in the Diamond storage ring. The prototype is rotated by 90°to allow off-axis injection and avoid synchrotron radiation, and has a larger aperture of 9.5 mm. The prototype will also allow us to validate the performance of the required high voltage, high bandwidth feedthroughs which are required for this application.

PULSER DEVELOPMENT

A pulser design is currently under development by Kentech Instruments [13]. The proposed design utilises several arrays of voltage avalanche cards, each with relatively modest voltage output. A total of 16 cards in 4 stacks would provide 5 kV per stack to meet the total 20 kV requirement. This design does not rely on a single high-voltage switching device, and would allow cards to be individually disabled or replaced, giving good fault tolerance and easy repair. Output from a proof of concept single avalanche stage is shown in Fig. 9, demonstrating the ability to produce a 1 ns pulse width at 3 kV. It is anticipated that the post-pulse ringing can be significantly reduced with passive pulse forming as part of the ongoing development work.
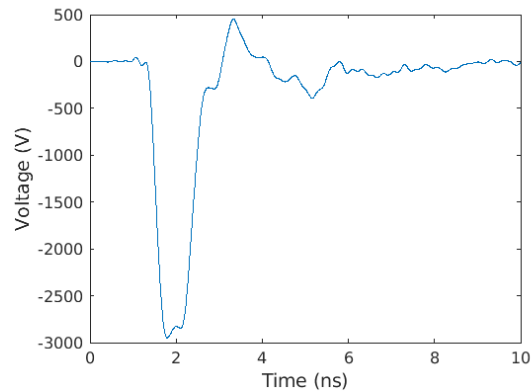
Figure 9: Output of proof of concept avalanche voltage stage.

CONCLUSION

A fast injection stripline kicker has been developed for Diamond-II. Full electromagnetic simulations have been carried out, with the output used as kickmaps for particle tracking studies. A pulser is also under development and is expected to meet the requirements for both high voltage and short pulse. A prototype will be tested at Diamond before the start of the dark period to verify simulations and perform tests in an active ring.

ACKNOWLEDGEMENTS

REFERENCES

[1] R. T. Fielder, M. Apollonio, R. Bartolini, C. Bloomer, and I. P. S. Martin, "Reduction of Stored Beam Oscillations During Injection at Diamond Light Source", in *Proc. IPAC'19*, Melbourne, Australia, May 2019, pp. 2426–2429. doi:10.18429/JACoW-IPAC2019-WEPMP042

[2] R. T. Fielder, M. Apollonio, and I. P. S. Martin, "Operational Use of Pinger Magnets to Counter Stored Beam Oscillations During Injection at Diamond Light Source", in *Proc. IPAC'21*, Campinas, Brazil, May 2021, pp. 459–462. doi:10.18429/JACoW-IPAC2021-MOPAB128

[3] *Diamond-II Technical Design Report*, R. P. Walker, Ed. Diamond Light Source, UK, https://www.diamond.ac.uk/Diamond-II.html, Accessed: 2023-08-08.

[4] J. Kallestrup, H. Ghasem, and I. P. S. Martin, "Aperture Sharing Injection for Diamond-II", in *Proc. IPAC'22*, Bangkok, Thailand, Jun. 2022, pp. 2606–2609. doi:10.18429/JACoW-IPAC2022-THPOPT018

[5] *SLS 2.0 Storage Ring. Technical Design Report*, H. Braun, T. Garvey, M. Jörg, A. Ashton, P. Willmott, R. Kobler, Eds. Paul Scherrer Institut, Villigen, Switzerland, PSI Rep. No. 21-02, Nov. 2021, https://www.dora.lib4ri.ch/psi/islandora/object/psi:39635

[6] M. Paraliev, M. Aiba, S. Dordevic, C. H. Gough, and A. Streun, "Development of Fast and Super-Fast Kicker System for SLS 2.0 Injection", in *Proc. IPAC'21*, Campinas, Brazil, May 2021, pp. 2889–2892. doi:10.18429/JACoW-IPAC2021-WEPAB122

[7] W. Bruns, "GdfidL: a finite difference program for arbitrarily small perturbations in rectangular geometries", *IEEE Trans. Magn.*, vol. 32, no. 3, pp. 453–1456, May 1996. doi:10.1109/20.497522

[8] CST Studio Suite, https://www.3ds.com/productsservices/simulia/products/cst-studio-suite/

[9] A. Terebilo, "Accelerator toolbox for MATLAB", No. SLAC-PUB-8732. Stanford Linear Accelerator Center, Menlo Park, CA (US), 2001.

[10] "Accelerator Toolbox", ATCOLLAB, version 2.0, https://atcollab.github.io/at/

[11] A. Lueangaramwong, H. Ghasem, I. Martin, and A. Morgan, "Study of aperture sharing injection scheme for Diamond-II", presented at the IPAC'23, Venice, Italy, May 2023, paper MOPM073, to appear in the proceedings.

[12] I. P. S. Martin *et al.*, "Diamond-II Storage Ring Developments and Performance Studies", in *Proc. IPAC'22*, Bangkok, Thailand, Jun. 2022, pp. 1491–1494. doi:10.18429/JACoW-IPAC2022-TUPOMS033

[13] Kentech Instruments Ltd., http://www.new1.kentech.co.uk/index.html

DEVELOPMENT OF A COMPACT LIGHT SOURCE USING A TWO-BEAM-ACCELERATION TECHNIQUE *

P. Piot[1], C. Chen, X. Lu[1], J. G. Power, E. E. Wisniewski,
Argonne National Laboratory, Lemont, IL, USA
C. Jing, S. Kuzikov, Euclid TechLabs, Solon, OH, USA
E. Frame, Northern Illinois University, DeKalb, IL, USA
[1]also at Northern Illinois University, DeKalb, IL, USA

Abstract

The recent demonstration of sub-GV/m accelerating fields at X-band frequencies offers an alternative pathway to designing compact light sources. The high fields were enabled by powering the accelerating structures using short (< 10 ns) X-band RF pulses produced via a two-beam-accelerator (TBA) scheme. In this contribution, we discuss a conceptual roadmap to scale the concept to a ∼ 0.5 GeV accelerator. We present the optimization of a photoinjector and preliminary beam-dynamics modeling of the accelerator. Finally, we discuss ongoing and planned experiments toward developing an integrated proof-of-principle experiment at Argonne National Laboratory employing the a 0.5 GeV TBA-driven accelerator to drive a free-electron laser.

INTRODUCTION

Low-emittance bunches are critical to reducing the footprint of the XFEL: for a given energy the gain length of a single-pass FEL scales with the electron-beam brightness [1]. Consequently, higher brightness translates into shorter undulator lengths. The beam emittance can only degrade between the electron source and the undulator, therefore the source "intrinsic" emittance sets the minimum emittance that can be ultimately attained in the accelerator. A pathway to producing low-emittance bunches is to subject the photocathode to an extremely high electric field as it mitigates the space-charge effect during the emission process and low-energy transport [2]. Currently, most normal-conducting RF guns operate at cathode fields $E_0 \in [80, 140]$ MV/m [3]. Operation at higher fields (∼ 200 MV/m) is currently under investigation using high-frequency [4] or cryogenically-cooled C-band [5] RF guns.

Since 2020, our group has concentrated on the development of an X-band RF (XRF) photoemission gun powered by short (nanosecond) RF pulses and operating at 11.7 GHz; see Fig. 1(a,b) [6, 7] using a two-beam acceleration (TBA) scheme [8]. This operational choice is motivated by the empirical dependence of the breakdown rate (BDR) on the applied surface field E_0 and the RF-pulse duration τ given by BDR $\propto E_0^{30}\tau^5$ [9]. Such a scaling suggests that for a given BDR, reducing the pulse duration significantly enhances the attainable electric field; see Fig. 1(c). The RF

pulse (peak forward power P_{FWD} ∼ 200 MW) was generated by passing a train of 8 high-charge (total charge of Q ∼ $8 \times 40 = 320$ nC) relativistic (∼ 60 MeV) electron bunches in a power-extraction and transfer structure (PETS) [10]. The high-charge bunches are produced in the Argonne Wakefield Accelerator (AWA) drive-beam accelerator with a time separation of 769 ps corresponding to 1.3 GHz. The developed XRF gun enabled the generation of E-field on the photocathode surface of ∼ 0.4 GV/m with a low BDR and insignificant dark current [7].

The ongoing R&D program leverages this recent accomplishment to focus on forming bright electron bunches and characterizing the associated beam parameters. We are also exploring the building blocks necessary to generate bright ultra-relativistic electron beams for linear collider and light-source applications. This paper summarizes our research program and the latest results.
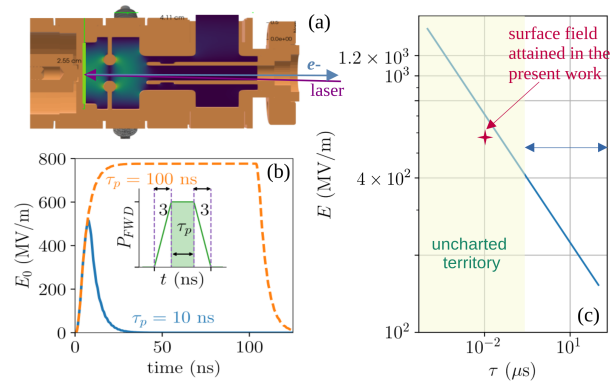
Figure 1: Schematics of the XRF gun with photocathode plane shown in green and electric-field amplitude appearing as a false-color map (a), RF-pulse envelope for short (blue) and (long) RF pulse excitation (b), and example of electric-field scaling with RF pulse duration for a given BDR constant (c). In plot (b), the inset shows the shape of the RF pulse produced from the PETS which yields the blue-trace pulse envelope.

PHOTOEMISSION IN EXTREME FIELDS

Ideally, the beam 4D brightness scales as $B \propto E_0^{\nu}$/MTE, the mean transverse energy (MTE) is related to the photocathode physical and chemical properties [2]. The brightness scaling suggests that a low-MTE photocathode combined

67th ICFA Adv. Beam Dyn. Workshop Future Light Sources
ISBN: 978-3-95450-224-0

FLS2023, Luzern, Switzerland

ISSN: 2673-7035

JACoW Publishing
doi:10.18429/JACoW-FLS2023-M04C2
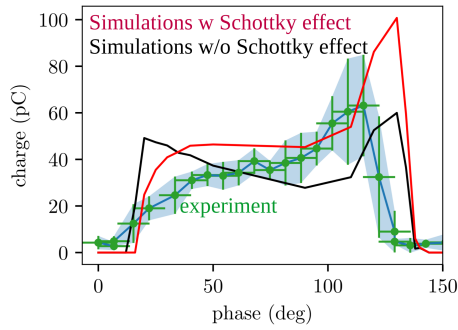
Figure 2: Example of charge emission during a laser-phase scan for $E_0 \simeq 370$ MV/m. The green circles are data points, and the solid traces correspond to numerical simulation with (red trace) and without (black trace) accounting for the Schottky effect.

with a high extraction field offers a path to increasing the brightness. In practice, large fields can affect the MTE due to physical (e.g. cathode surface roughness) or chemical (e.g. position-dependent work function) inhomogeneities [11]. Likewise, the high-field produced in the XRF gun yields a significant charge enhancement due to the effective lowering of the work function (Schottky effect) as illustrated in Fig. 2. Such effects can deteriorate the beam emittance and thus thereby modify the ideal scaling of the brightness with applied E field. A dedicated measurement campaign will investigate the dependence of transverse emittance on the applied field and on the photoemission-laser wavelength in the low-charge limit where space-charge effects are negligible. Such a parametric study will provide insight into the evolution of the MTE in the strong-field regime along with an experimental investigation of the scaling of 4D brightness. In the nominal XRF gun, the copper back plate serves as a photocathode. A future version of the gun will include a load-lock transfer system to facilitate the investigation of other photocathode materials, including low-MTE semiconductor-compound photocathodes.

GENERATION OF 10-MeV EMITTANCE-COMPENSATED BUNCHES

In a second phase, a linac will be installed downstream of the XRF gun to boost the bunch's energy to ~ 10 MeV and for phase-space control. The configuration will ideally recover the intrinsic emittance from the photocathode by implementing the emittance-compensation technique. The results of the beam-dynamics optimization of such a beamline appear in Fig. 3. The beam-dynamics simulations were performed with the program ASTRA and considered a 100-pC bunch. The photocathode-laser temporal shape is taken to be a 3-ps-duration (FWHM) plateau distribution with 300-fs rise time nominally available at AWA. The simulations assume a steady-state regime for the RF as the field variation is negligible over the time it takes for the bunch to transit through the accelerating structures (XRF gun and linac).
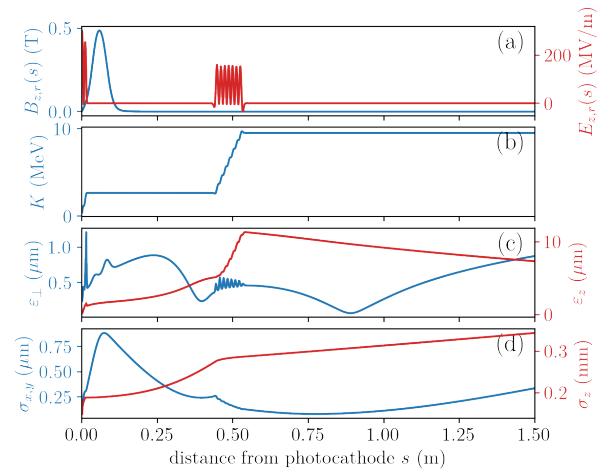
Figure 3: Evolution of beam parameters for a 100-pC beam along the XRF gun+booster beamline. Longitudinal magnetic (blue) and electric (red) fields experienced by the reference particle (a), average kinetic energy (b), rms transverse $\varepsilon_\perp$ and longitudinal ε_z emittances (c) and rms transverse beam sizes $\sigma_{x,y}$ and bunch length σ_z (d).

It should be noted that in practice the short-pulse regime can be employed to power long accelerating structures with each cell powered individually using a distributed-coupling technique [12]. The numerical simulations indicate that a transverse beam emittance of $\varepsilon_\perp \simeq 70$ nm can be attained. However, due to the low final kinetic energy $K \simeq 10$ MeV the emittance is only locally compensated reaching its minimum value at $s \simeq 0.6$ m from the photocathode; see Fig. 3(c). Additionally, the linac can be operated as a buncher to com-
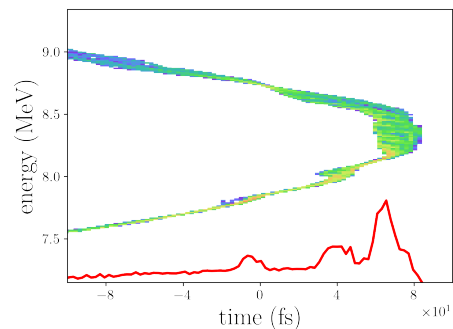
Figure 4: Ballistically bunched longitudinal phase space (false color map) and associated temporal profile (red trace) for a 100-pC bunch downstream of the linac operated off-crest (the head of the bunch is at positive times).

press the longitudinal phase space via ballistic bunching producing a bunch temporal profile with a 20-fs spike; see Fig. 4.

The beam parameters attained with this 10-MeV photoinjector are consistent with requirements associated with the production of ~ 2 keV X-ray source via inverse Compton scattering (ICS) using infrared laser pulses available from the AWA photocathode laser. Likewise, the operating param-

eters of the beamline could also be tuned to support ultrafast electron diffraction experiments. In the near term, we plan to characterize the beam phase spaces downstream of the linac for various operational parameters. Several diagnostics will be developed including a single-shot emittance measurement technique based on a pepper-pot or scanning slits. We will also examine the compression of the bunch via ballistic bunching including the possible use of an X-band deflecting cavity to characterize the longitudinal phase space [13].

PRODUCING 0.5-GeV BRIGHT BEAM

The beam dynamics modeling presented in Fig. 3 was further extended to investigate the required energy to ensure stable emittance compensation without further oscillation. The simulations indicate that accelerating the beam to $K \simeq 50$ MeV is sufficient. The attained beam parameters correspond to a 5D brightness of $B_{5d} \equiv cB/\sigma_z \simeq 3 \times 10^{15}$ A/m^2 comparable to the single-bunch brightness requirements for several next-generation free-electron lasers (FELs) currently under consideration. In order to explore possible FEL configurations based on a TBA scheme that could fit within the AWA facility, a 1-D SASE-FEL model [14] was employed to guide potential working points for SASE-FEL driven by the 0.5-GeV electron beam. In our calculations, the FEL-saturation length was restricted to 5-m (due to real-estate constraints at AWA) and we considered an undulator with period $\lambda_u = 23$ mm and undulator parameter $K = 2.5$ yielding a resonant wavelength $\lambda \simeq 50$ nm; see Fig. 5.
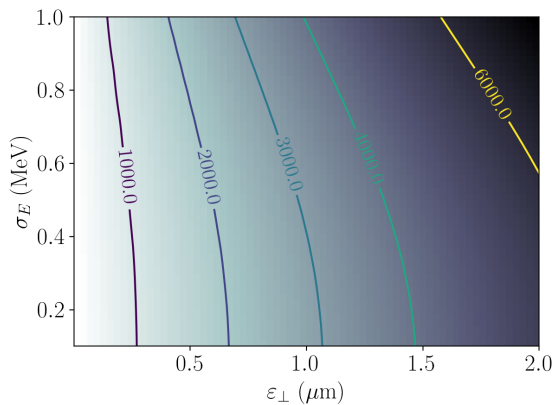
Figure 5: Required peak current (isoclines with labels in Ampère) as a function of transverse emittance $\varepsilon_\perp$ and energy spread σ_E. The saturation length is set to 5 m and the SASE FEL radiation wavelength is $\lambda = 45.9$ nm.

Given the simulated performances of the injector ($\varepsilon_\perp \leq 100$ nm), and accounting for emittance dilution during acceleration and manipulation prior to the undulator, a general accelerator architecture coupling the photoinjector to a high-energy linac was formulated. In its current implementation, we anticipate the photoinjector after further acceleration to 140 MeV would be coupled to a K-band linac operating at 26 GHz (20th harmonic of 1.3 GHz). Preliminary 1D-1V nu-

merical simulations of the longitudinal beam dynamics [15] associated with the generation of a low-emittance bunch and its acceleration to a final energy of 0.5 GeV appear in Fig. 6.
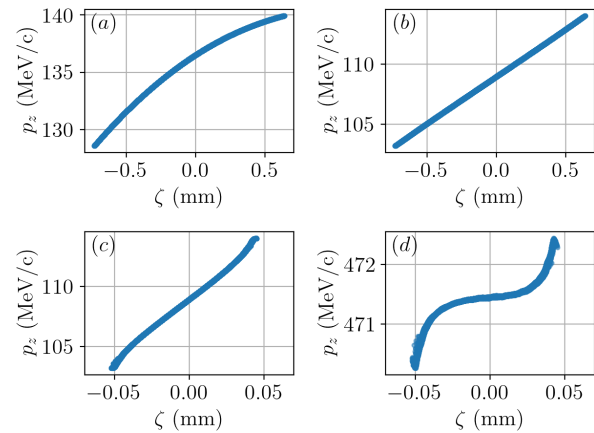
Figure 6: Evolution of the longitudinal phase space (ζ, p_z) along the X and K-band linacs. The snapshots give the distribution at the injector exit simulated from ASTRA after acceleration in the X-band linac (a), downstream of a 26-GHz linac for phase-space linearization (b), after a bunch-compression beamline (c) and after further acceleration in a 26-GHz linac to the final energy (d).

SUMMARY & OUTLOOK

Preliminary experimental tests on a TBA concept have produced high surface fields that could support the compact generation and acceleration of bright electron bunches. The design of such a compact accelerator to produce 0.5-GeV bunches is under investigation at the AWA facility. Preliminary estimates indicate the contemplated beam brightness could support the lasing of a SAFE-FEL at 50 nm using a 5-m undulator. Further numerical simulations of the beam dynamics including collective effects are underway to further optimize the accelerator design.

ACKNOWLEDGMENTS

REFERENCES

[1] S. Di Mitri, "On the importance of electron beam brightness in high gain free electron lasers," *Photonics*, vol. 2, no. 2, pp. 317–341, 2015. doi:10.3390/photonics2020317

[2] D. Filippetto, P. Musumeci, M. Zolotorev, and G. Stupakov, "Maximum current density and beam brightness achievable by laser-driven electron sources," *Phys. Rev. Spec. Top. Accel Beams*, vol. 17, p. 024 201, 2 2014.
doi:10.1103/PhysRevSTAB.17.024201

[3] Y. Ding *et al.*, "Measurements and simulations of ultralow emittance and ultrashort electron beams in the linac coherent light source," *Phys. Rev. Lett.*, vol. 102, p. 254 801, 25 2009.
doi:10.1103/PhysRevLett.102.254801

[4] R. A. Marsh, G. G. Anderson, S. G. Anderson, D. J. Gibson, C. P. J. Barty, and Y. Hwang, "Performance of a second generation X-band RF photoinjector," *Phys. Rev. Accel. Beams*, vol. 21, p. 073 401, 7 2018.
doi:10.1103/PhysRevAccelBeams.21.073401

[5] R. R. Robles, O. Camacho, A. Fukasawa, N. Majernik, and J. B. Rosenzweig, "Versatile, high brightness, cryogenic photoinjector electron source," *Phys. Rev. Accel. Beams*, vol. 24, p. 063 401, 6 2021.
doi:10.1103/PhysRevAccelBeams.24.063401

[6] S. Kuzikov *et al.*, "An X-Band Ultra-High Gradient Photoinjector," in *12th International Particle Accelerator Conference*, 2021.
doi:10.18429/JACoW-IPAC2021-WEPAB163

[7] W. H. Tan *et al.*, "Demonstration of sub-GV/m accelerating field in a photoemission electron gun powered by nanosecond *X*-band radio-frequency pulses," *Phys. Rev. Accel. Beams*, vol. 25, p. 083 402, 8 2022.
doi:10.1103/PhysRevAccelBeams.25.083402

[8] R. Corsini, "Final Results From the Clic Test Facility (CTF3)," in *Proc. of International Particle Accelerator Conference (IPAC'17), Copenhagen, Denmark, 14-19 May, 2017*, Copenhagen, Denmark, 2017, pp. 1269–1274.
doi:10.18429/JACoW-IPAC2017-TUZB1

[9] A. Grudiev, S. Calatroni, and W. Wuensch, "New local field quantity describing the high gradient limit of accelerating structures," *Phys. Rev. Spec. Top. Accel Beams*, vol. 12, p. 102 001, 10 2009.
doi:10.1103/PhysRevSTAB.12.102001

[10] M. Peng *et al.*, "Generation of High Power Short Rf Pulses using an X-Band Metallic Power Extractor Driven by High Charge Multi-Bunch Train," in *10th International Particle Accelerator Conference*, 2019, MOPRB069.
doi:10.18429/JACoW-IPAC2019-MOPRB069

[11] G. S. Gevorkyan, S. Karkare, S. Emamian, I. V. Bazarov, and H. A. Padmore, "Effects of physical and chemical surface roughness on the brightness of electron beams from photocathodes," *Phys. Rev. Accel. Beams*, vol. 21, p. 093 401, 9 2018. doi:10.1103/PhysRevAccelBeams.21.093401

[12] S. Tantawi, M. Nasr, Z. Li, C. Limborg, and P. Borchard, "Design and demonstration of a distributed-coupling linear accelerator structure," *Phys. Rev. Accel. Beams*, vol. 23, p. 092 001, 9 2020.
doi:10.1103/PhysRevAccelBeams.23.092001

[13] S. Kim *et al.*, "Longitudinal Bunch Shaping Using an X-Band Transverse Deflecting Cavity Powered by Wakefield Power Extractor at Argonne Wakefield Accelerator Facility," in *Proc. 13th International Particle Accelerator Conference (IPAC'22)*, Bangkok, Thailand, 2022, paper WEOZSP1, pp. 1655–1658.
doi:10.18429/JACoW-IPAC2022-WEOZSP1

[14] M. Xie, "Design optimization for an x-ray free electron laser driven by slac linac," in *Proceedings Particle Accelerator Conference*, vol. 1, 1995, 183–185 vol.1.
doi:10.1109/PAC.1995.504603

[15] W. H. Tan, P. Piot, and A. Zholents, "Formation of temporally shaped electron bunches for beam-driven collinear wakefield accelerators," *Phys. Rev. Accel. Beams*, vol. 24, p. 051 303, 5 2021.
doi:10.1103/PhysRevAccelBeams.24.051303

AN EFFICIENT OPTIMISATION OF A BURST MODE-OPERATED FABRY-PEROT CAVITY FOR COMPTON LIGHT SOURCES

V. Muşat[1,*], A. Latina, E. Granados, CERN, Meyrin, Switzerland
E. Cormier, G. Santarelli, LP2N, Talence, France
[1]also at The University of Oxford, Oxford, UK

Abstract

The burst mode operation of a Fabry-Perot cavity (FPC) allows for the generation of a high-intensity photon beam in inverse Compton scattering (ICS) sources. The geometry and burst mode parameters of the FPC can be optimised to maximise the scattered photon flux. A novel optimisation method is presented, significantly improving processing speed and accuracy. The FPC's dimensions, mirror requirements, and effective energy can be obtained from the electron beam parameters at the interaction point. A multi-objective optimization algorithm was used to derive the geometrical parameters of the FPC; this brought orders of magnitude increase in computation speed if compared to the nominal Monte Carlo-based approaches. The burst mode parameters of the FPC were obtained by maximizing the effective energy of the laser pulse in the FPC. The impact of optical losses and thermal lensing on the FPC parameters is addressed. Preliminary parameters of an ICS source implementing this novel optimisation are presented. The source could reach high-performance photon beams for high-energy applications.

INTRODUCTION

Fabry-Pérot cavities are widely used to generate high-intensity photons from inverse Compton scattering [1]. FPCs are operated in one of two regimes: permanent or pulsed. Most ICS setups use the first option, which matches the high repetition rate requirements for storage ring sources.

More recently, FPCs operated in the pulsed regime have been considered for linac-based ICS sources [2], since both require a lower repetition rate than storage ring or energy-recovery linac designs. In burst mode, FPCs can achieve an effective gain 2 or 3 orders of magnitude larger than for the permanent mode.

This paper addresses the optimisation of an FPC's geometry and burst-mode parameters from [3]. Significant improvements were made relating to the runtime and efficiency of the optimisation.

THEORY

The mechanism of optical enhancement in FPCs can be described in terms of the temporal patterns of the electron and laser pulses in the cavity. N_p laser pulses are stacked in the FPC and interact with N_e electron bunches. Prior to the interaction, N_0 laser pulses are injected to provide an initial circulating laser power. A schematic of the interaction

---

* vlad.musat@cern.ch

between the electron train and the laser pulses stored in the FPC is shown in Fig. 1.
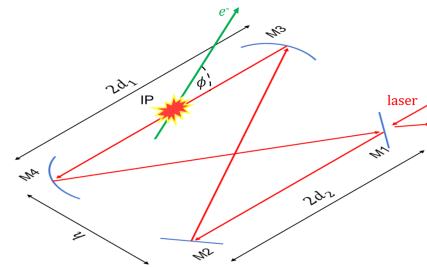
Figure 1: Layout of the ICS interaction of the input electron train with the laser pulses stored in the four-mirror planar Fabry-Pérot cavity. The electron beam enters the cavity plane with a crossing angle ϕ.

Given a small electron recoil, identical time separation between the electron and the laser pulses and no change in both the laser's pulse energy, $\mathscr{E}_0$, and the bunch charge, Q, the total scattered photon flux from ICS, $\mathscr{F}$, can be determined from

$$\mathscr{F} = \sigma_{\mathrm{C}} \frac{f_{\mathrm{rep}} Q N_b \mathscr{E}_{\mathrm{tot}}}{2\pi (ehc/\lambda)\sigma_{\gamma,y}\sqrt{\sigma_{\gamma,x}^2 + \sigma_{\gamma,z}^2 \tan^2(\phi/2)}}, \quad (1)$$

where σ_{C} is the Compton cross section, e the elementary charge, h Planck's constant, c the speed of light in vacuum, λ the laser wavelength, ϕ the crossing angle between the electron and laser beam, $\mathscr{E}_{\mathrm{tot}}$ the laser effective energy, and σ_γ the source *rms* spot size at the interaction point (IP) [3]. To maximise the total flux, the FPC should provide the maximum $\mathscr{E}_{\mathrm{tot}}$ and the smallest laser waist size at the IP. The first condition depends mainly on the optimisation of the burst mode parameters provided by the input laser, while the second depends on the optimisation of the cavity geometry.

The circulating laser-beam energy determines $\mathscr{E}_{\mathrm{tot}}$. It is a function of $\mathscr{E}_0$, N_0, N_p, N_e, and the cavity finesse, F,

$$\mathscr{E}_{\mathrm{tot}} = \epsilon\left(N_p, N_0, N_e, F\right) N_p \mathscr{E}_0, \quad (2)$$

where ϵ is the effective gain, and $N_p \mathscr{E}_0$ is the laser macropulse energy delivered to the FPC, in the following called U. The effective gain is a cavity-dependent parameter. Its linear dependence to $\mathscr{E}_{\mathrm{tot}}$ makes it relevant for the maximisation of the scattered photon flux. The optimum value for N_0 can be derived from $\partial\epsilon/\partial N_0 = 0$.

Given a high optical power, thermal lensing effects in the cavity mirrors must be considered, as they change their focal length, which can prevent the FPC from reaching a small

waist size at the IP. For standard optics used in FPCs, the main contribution to thermal lensing is from the temperature dependence of the refractive index of the mirror substrate, dn/dT. Under this condition, the thermal lensing effect can be quantified by $f_{thermal}$, the thermally-induced focal length:

$$f_{thermal} = \frac{2\pi\kappa}{1.3b\,(dn/dT)\,l}\frac{w^2}{P} = \frac{1}{m_0}\frac{w^2}{P}, \qquad (3)$$

where P and w are the laser beam power and waist incident on the mirror, b is the absorption coefficient of the material, κ the thermal conductivity, and l the thickness of the material [4]. Note that the terms in the first fraction only depend on the substrate material, and can be expressed in terms of a constant, m_0 [5].

The goal of both the previous seminal study from [3] and this paper was to optimise a burst mode FPC to provide the largest flux with state-of-the-art technology. This was achieved by optimising both the geometry and burst mode parameters of the FPC.

BURST PARAMETER OPTIMISATION

The burst mode parameters are represented by the initial and total number of laser pulses injected in the cavity, N_0 and N_p, respectively. These parameters, along with the cavity finesse were tuned to maximise $\mathscr{E}_{tot}$.

A parametric scan of F against laser-defining parameters was performed to assess the finesse's impact on the optimisation results. It was found that more laser pulses can be stored in an FPC with a large F (due to the smaller losses in the cavity). However, cavities with large F require precise laser matching and mirror tuning, which has been shown to be challenging. Nevertheless, relaxing the technical requirements of the FPC by reducing F leads to an increase in the power requirements of the input laser. The performance of FPCs with $F > 1000$ was therefore optimized and compared.

Review of the Previous Studies

In the previous study [3], ϵ was obtained from the numerical maximisation of its formula. The only input required was the number of electron bunches per train. The effective energy was obtained by multiplying ϵ with the maximum U allowed by the cavity geometry. This optimisation is adequate if the cavity round-trip length L_{RT} is fixed and $\mathscr{E}_0$ is treated as a free variable. However, e.g., in X-band-based linacs [6], where GHz repetition rates are used, the cm-long L_{RT} suggested the use of a subharmonic of the pulse repetition rate to increase the distance between the IP and the nearest mirrors, allowing for a larger U. Furthermore, $\mathscr{E}_0$ is fixed by the input laser, and was therefore treated as a constant in the present optimisation.

Novel Method

To establish a dependence between $\mathscr{E}_{tot}$ and N_p, a scan of the maximised ϵ against N_p was performed, given a maximum F. To obtain curves for $\mathscr{E}_{tot}$, each ϵ was then multiplied
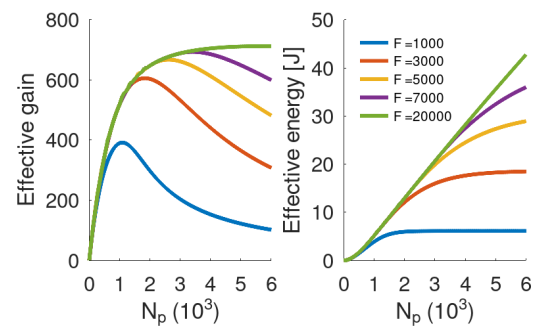
Figure 2: Scans of the optimised effective gain (left) and effective energy (right) against the total number of laser pulses injected, for a range of values of the maximum cavity finesse. The number of electron bunches per train is 1000, and the laser micropulse energy is 10 μJ.

by its corresponding N_p, and a fixed $\mathscr{E}_0$. Plots for $N_e = 1000$ and $\mathscr{E}_0 = 10\,\mu J$ are shown in Fig. 2.

A local maximum is reached for ϵ, which, for a large enough F, is constant. However, for any F, $\mathscr{E}_{tot}$ continues to increase with N_p past the point of maximum ϵ. This constitutes a major issue in the previous study. If one wants to obtain the largest possible flux $\mathscr{F}$ from the burst mode parameters of an input laser, the maximisation of ϵ will provide a smaller $\mathscr{E}_{tot}$ than the global maximum of $\mathscr{E}_{tot}$.

By setting a limit on the maximum F, one can see that $\mathscr{E}_{tot}$ plateaus with increasing N_p, with relative changes smaller than 1%. The burst mode parameters should, therefore, be taken at the onset of the plateau. One would then adjust the geometry optimisation to allow for the U obtained from the burst mode optimisation. For example, given a maximum $F = 1000$, the $\mathscr{E}_{tot}$ corresponding to the maximum ϵ is lower than the global maximum of $\mathscr{E}_{tot}$ by 40%, with a corresponding change in flux. Note that this difference in flux increases with the set maximum F.

CAVITY GEOMETRY OPTIMISATION

A planar bow-tie configuration was chosen because it provides increased stability compared to other designs [7]. A geometrical optimisation of the cavity was performed, simultaneously varying the distance between the planar ($2d_2$) and spherical mirrors ($2d_1$), the cavity height (h), and radius of curvature (R) of the spherical mirrors. The mirror diameter was set to a standard value of 0.59 cm. The dimensions are shown in Fig. 1.

The only input required for the geometry optimisation is the cavity round-trip length L_{RT}. The limits of the optimisation are three constraints: (1) prevent the optical beam on a mirror from being eclipsed by another mirror, $h - \Phi > h|d_1 - d_2| / (d_1 + d_2)$; (2) set the maximum fluence on each mirror, $2U / (\pi w_s w_t)$, smaller than the laser-induced damage threshold [8]; and (3) constrain the absolute value of the FPC's ABCD matrix's trace to be smaller than 2, to ensure stability.

Review of the Previous Studies

In the previous study, the geometrical parameters were randomly varied in the range [0, $L_{RT}/4$], and the largest flux solution within the constraints was selected. This Monte-Carlo-based technique, however, does not guarantee that a global optimum is reached. Furthermore, over 10 million iterations were required to reach convergence, corresponding to a significant computation runtime. A plot of the values for waist size at the IP and burst energy from a set of stable geometries is shown in Fig. 3a.

Novel Method

The optimisation was rewritten as a merit function minimized using the simplex algorithm. As shown in Fig. 3b, the number of iterations required to reach convergence was decreased to 100. The computation runtime was reduced by more than four orders of magnitude compared to the Monte-Carlo technique. Note that this optimisation does not claim to be global; however, a global optimum can be approached by running the algorithm in parallel from randomised starting points.

The merit function required careful weighting to fulfill the cavity constraints, e.g., maximising flux while keeping the laser waist sizes within a realistic range. Given identical constraints and objectives, the results obtained with the simplex method corresponded to those from the Monte-Carlo method.
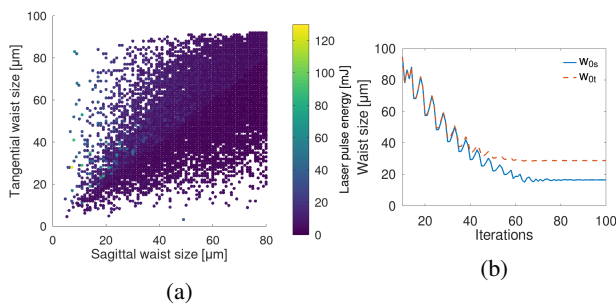

Figure 3: Representation of the Monte-Carlo (a) and simplex (b) method of optimisation. Each of the 50000 points from the Monte-Carlo optimisation corresponds to a possible FPC geometry. Less than 100 iterations were required for the simplex optimisation to converge.

IMPACT OF THERMAL EFFECTS

The thermal lensing effect was implemented in the optimization of the FPC geometry by adding the contribution from Eq. (3) to the mirror ABCD matrices. Fused silica substrates with $m_0 = 4.19 \times 10^{-12}$ m W^{-1} were assumed for the FPC mirrors [9].

A decrease of up to 83% in flux was observed when introducing thermal lensing to set-ups optimised without the effect. However, the impact from thermal lensing was cancelled when the geometrical parameters were tuned by the optimisation to account for the thermal focal lengths.

FPC PARAMETERS FOR AN ICS SOURCE

The present optimisation was used to compute the burst parameters and FPC geometry suitable for an ICS source implementing an X-band linac driven by an S-band photo-injector. The setup was optimised to provide a 240 MeV electron beam colliding with a laser with a 515 nm wavelength [6]. This promises high intensity, small bandwidth 2 MeV photon beams suitable for nuclear resonance fluorescence (NRF) experiments [10].

In the setup, the electron gun produces a multi-bunch beam with a bunch spacing equal to 3 GHz. A cavity with a round-trip length matching a 3 GHz spacing corresponds to $L_{RT} = 10$ cm, which is too small for practical use. Therefore, a sub-harmonic of the rep-rate was used to increase L_{RT} to 1 m. The geometrical parameters obtained from the optimisation allowed for a maximum U of 42.0 mJ and sagittal and tangential waist sizes at the IP of 8.6/13.4 μm. For 1000 bunches per train and a maximum $F = 1000$, $\mathcal{E}_{tot} = 6$ J was determined from the burst mode optimisation.

Considering a train repetition rate of 100 Hz, the total flux obtained from this source would be in the order of 10^{13} photons per second. This value corresponds to the requirements set by the NRF-based detection of clandestine material [11].

FURTHER WORK

A ray-tracing model of the FPC should be implemented to realistically evaluate the impact of losses and thermal effects in the cavity for different mirror materials. Another relevant study would be computing the geometry optimisation using Kostenbauder matrices, which consider dispersive effects for both the spatial and temporal coordinates [12].

CONCLUSIONS

Burst-mode FPCs perfectly match the multi-bunch operation of high-gradient linacs in the X-band, promising very high-flux ICS photon sources. A novel optimisation technique of a burst-mode-operated Fabry-Pérot cavity is presented. The optimisation is based on previous studies, of which we improved methodology and objectives, significantly increasing the efficiency and reducing the runtime. A multi-dimensional, multi-objective optimisation was set up with the primary goal of maximising the scattered photon flux of the ICS source. This was achieved by maximising the effective energy provided by the cavity, which led to an increase in the total flux by over 40%. The novel geometry optimisation was shown to be faster by more than four orders of magnitude than the initial Monte-Carlo-based approach. A theoretical study of thermal lensing concluded that standard mirror substrates and coatings can be used for burst mode FPCs, with minimal impact on the laser waist size at the IP, given that the effects are implemented in the geometry optimisation. The present considerations can be used to design high-intensity linac-based ICS sources.

REFERENCES

[1] H. Kogelnik and T. Li, "Laser Beams and Resonators," *Applied Optics*, vol. 5, no. 10, 1966.
doi:10.1364/ao.5.001550

[2] K. Sakaue *et al.*, "Observation of pulsed x-ray trains produced by laser-electron Compton scatterings," *Review of Scientific Instruments*, vol. 80, no. 12, 2009.
doi:10.1063/1.3272789

[3] P. Favier *et al.*, "Optimization of a Fabry-Perot cavity operated in burst mode for Compton scattering experiments," *Physical Review Accelerators and Beams*, vol. 21, no. 12, 2018. doi:10.1103/PhysRevAccelBeams.21.121601

[4] W. Winkler, K. Danzmann, A. Rüdiger, and R. Schilling, "Heating by optical absorption and the performance of interferometric gravitational-wave detectors," *Physical Review A*, vol. 44, no. 11, 1991. doi:10.1103/PhysRevA.44.7022

[5] C. Simonelli *et al.*, "Realization of a high power optical trapping setup free from thermal lensing effects," *Optics Express*, vol. 27, no. 19, 2019.
doi:10.1364/oe.27.027215

[6] A. Latina *et al.*, "A Compact Inverse Compton Scattering Source Based on X-band Technology and Cavity-enhanced High Average Power Ultrafast Lasers," presented at the 67th ICFA Advanced Beam Dynamics Workshop on Future Light Sources (FLS 2023), Lucerne, Switzerland, Aug. 2023, paper TH4A2, this conference.

[7] F. Zomer, Y. Fedala, N. Pavloff, V. Soskov, and A. Variola, "Polarization induced instabilities in external four-mirror Fabry - Perot cavities," *Applied Optics*, vol. 48, no. 35, 2009.
doi:10.1364/AO.48.006651

[8] L. Gallais and M. Commandré, "Laser-induced damage thresholds of bulk and coating optical materials at 1030 nm, 500 fs," *Applied Optics*, vol. 53, no. 4, 2014.
doi:10.1364/ao.53.00a186

[9] M. A. Khashan and A. Y. Nassif, "Dispersion of the optical constants of quartz and polymethyl methacrylate glasses in a wide spectral range: 0.2-3 μm," *Optics Communications*, vol. 188, no. 1-4, 2001.
doi:10.1016/S0030-4018(00)01152-4

[10] R. Hajima, T. Hayakawa, N. Kikuzawa, and E. Minehara, "Proposal of nondestructive radionuclide assay using a high-flux gamma-ray source and nuclear resonance fluorescence," *Journal of Nuclear Science and Technology*, vol. 45, no. 5, pp. 441–451, 2008.
doi:10.1080/18811248.2008.9711453

[11] J. Pruet, D. P. McNabb, C. A. Hagmann, F. V. Hartemann, and C. P. Barty, "Detecting clandestine material with nuclear resonance fluorescence," *Journal of Applied Physics*, vol. 99, no. 12, 2006. doi:10.1063/1.2202005

[12] A. G. Kostenbauder, "Ray-Pulse Matrices: A Rational Treatment for Dispersive Optical Systems," *IEEE Journal of Quantum Electronics*, vol. 26, no. 6, pp. 1148–1157, 1990.
doi:10.1109/3.108113

EVOLUTION OF THE INVERSE COMPTON SCATTERING X-RAY SOURCE OF THE ELSA ACCELERATOR*

A. Pires[1], V. Le Flanchec[1,†], R. Rosch, J. Touguet, CEA DAM DIF, Arpajon, France

N. Delerue, Université Paris-Saclay, CNRS/IN2P3, IJCLab, Orsay, France

[1]also at Université Paris-Saclay, CEA, LMCE, Bruyères-le-Châtel, France

Abstract

The Inverse Compton Scattering (ICS) X-ray source of ELSA accelerator at CEA-DAM, presents an efficient approach for generating X-rays with a compact linac. The source consists of a 30 MeV, 15 ps rms, up to 3 nC electron beam and a table-top Nd:YAG laser. X-rays are produced in the 10-80 keV range, higher X-ray energies achieved with frequency doubling of the laser. The yield is increased by a factor of 8 thanks to an optical mirror system developed at CEA, folding the laser beam path and accumulating successive laser pulses. We present a new version of the device, with improvement of mechanical constraints management, adjunction of motorized mirrors, and a new imaging system. A Chirped Pulse Amplification (CPA) system was also designed, enabling higher amplification levels without exceeding laser damage threshold. The uniqueness of this CPA system lies in its use of a short wavelength bandwidth, ±250 pm after Self-Phase Modulation (SPM) broadening, and a line density of 1850 lines/mm for the gratings of the compressor. The pulse will be stretched with a chirped fiber Bragg grating (CFBG) before amplification in Nd:YAG amplifiers, and compressed by a double pass grating compressor.

ELSA X-RAY SOURCE

ELSA Accelerator

ELSA produces X-rays for studies of detectors used in facilities like the Laser Megajoule at CEA CESTA. The ICS source will be used to produce high flux in both single-shot and recurrent modes in the 10-80 keV range. The main goal is to produce 20 ps X-ray pulses in single-shot mode, with a flux of 10^{18} ph/s/cm². First experimental results have been published in 2010 and 2016 [1, 2], still far from the ultimate goal, but showcasing potential for scaling up the X-ray flux. The accelerator (Fig. 1) is an electron linac featuring a 144 MHz photoinjector, 433 MHz accelerating cavities to reach 17 MeV, and a 1.3 GHz to reach 30 MeV, delivering 0.1 to 3 nC bunch trains typically at 1 Hz [3]. Double alpha magnets compress bunches from 80 to 28 ps before the final acceleration stage and the Inverse Compton Scattering (ICS) interaction point (IP). The accelerator can currently supply 10^4 bunches per train at 17 MeV, or 300 bunches per train at 30 MeV, and can also deliver single bunches.

Compton Laser

The laser dedicated to the ICS emits laser pulses at the same rate as the electron bunches, with similar temporal shape. It consists of a 144 MHz mode-locked Nd:YVO$_4$ oscillator at 1064 nm, a pulse selector, three Nd:YAG amplifiers, and eventually a KTP or LBO crystal for frequency doubling to 532 nm. Quadrupling can be achieved by the addition of a BBO crystal but is not implemented yet. The laser system can presently deliver up to 150 mJ per train at 1 Hz at 532 nm.

SMILE Device

At the interaction point (Fig. 2), our SMILE system (System Multipass Interaction Laser Electrons) focuses and superimposes 8 successive laser pulses going back and forth between two planes, reflecting on a series of spherical mirrors separated by a distance allowing a round trip time equal to the emission period of the laser pulses (Fig. 3). Thus eight successive pulses can interact with one electron bunch at the same time.
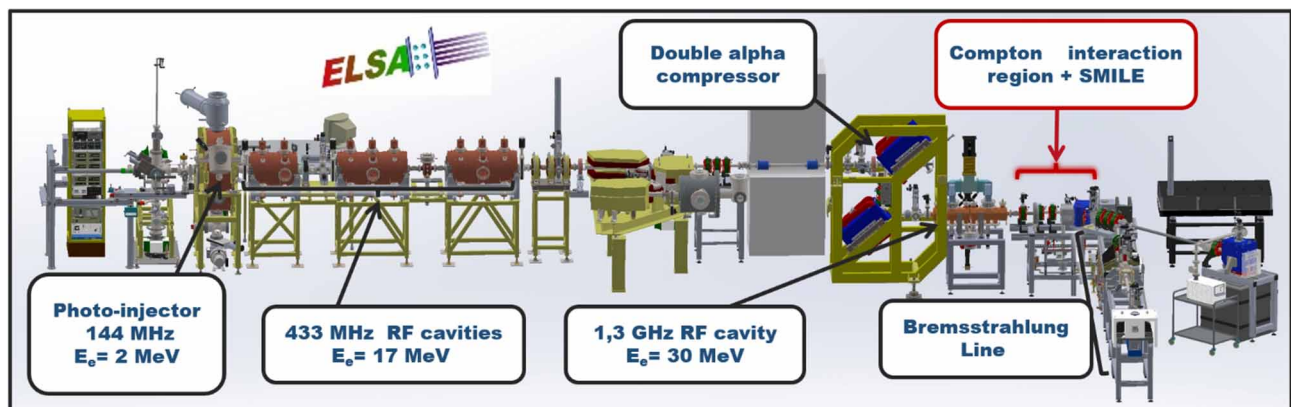

Figure 1: Layout of the ELSA Accelerator.

† Vincent.le-flanchec@cea.fr
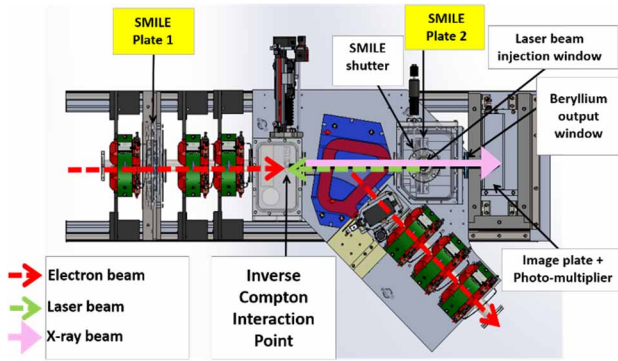
Figure 2: Top view of the Compton interaction Region.

For clarity, only forward trajectories are shown in Fig. 3. Forward paths pass through the interaction point whereas backward paths go around the interaction point (Fig. 4) therefore lying outside of the trajectory plane.
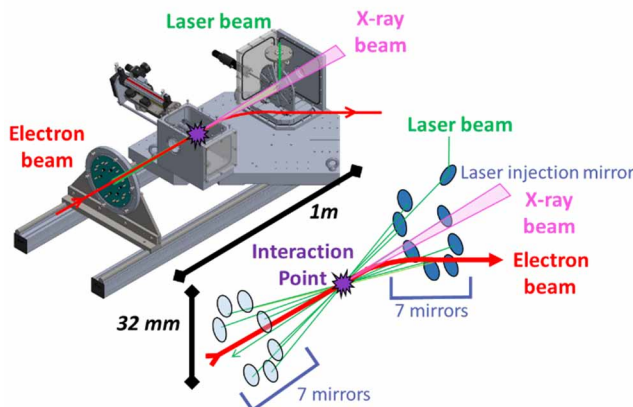
Figure 3: 3D view of the SMILE and schematic (not to scale) with highly exaggerated angle.
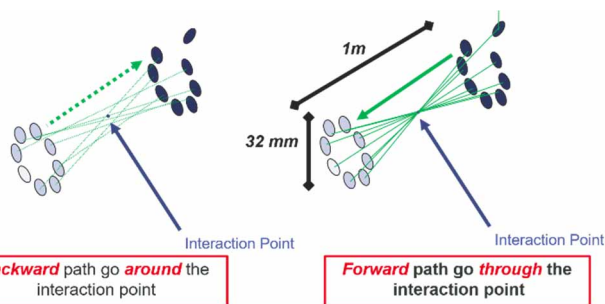
Figure 4: Trajectories of laser beams in the backward and in the forward direction.
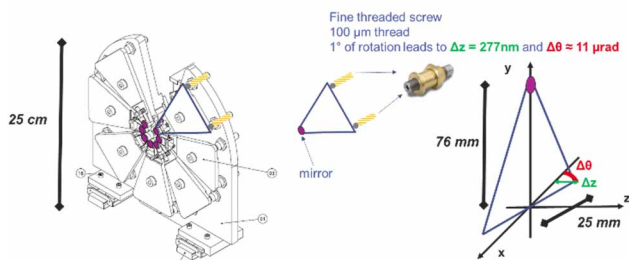
Figure 5: 3D view of the SMILE and schematic.

The SMILE device optomechanical system was designed for high angular precision. Mirrors are placed at the end of lengthy triangular metallic plates, with fine-threaded screws adjusting the plate orientation at the other two ends to achieve µrad precision (Fig. 5).

STRATEGY FOR OPTIMIZATION

A global analysis was done to bring out the pitfalls of the source and build a global strategy encompassing multiple domains. The planned improvements are: (i) a SMILE upgrade to reduce mechanical constraints including a redesign of the interaction area, (ii) the development of a remote alignment method compatible with IR laser, (iii) a Chirped Pulse Amplification (CPA) system to avoid laser damage risks in the laser amplifiers, (iv) Twiss parameters and charge optimization, (v) the linearization of the accelerating field by a decelerating 1.3 GHz cavity for bunch compression enhancement and (vi) an upgrade of the 1.3 GHz accelerating cavity and klystron system. Only the 3 first items are addressed in this article. First results for item (iv) have been published at IPAC'23 [4].

Re-designing the Interaction Area

The SMILE exhibited two key shortcomings. Firstly, the mechanical components supporting the mirrors displayed slight shifts when transitioning from atmospheric pressure to vacuum conditions and drifted along the day. The whole mechanical system was redesigned, thoroughly isolating constraints on the mirror plates (Fig. 6) and on the laser injection mirror (Fig. 7). Secondly, alignment used to be done manually, forbidding further fine adjustments and necessitating frequent disruption of vacuum conditions. The fine thread screws were replaced by piezo actuators (Fig. 7), enabling the ability to align the mirrors directly in vacuum.
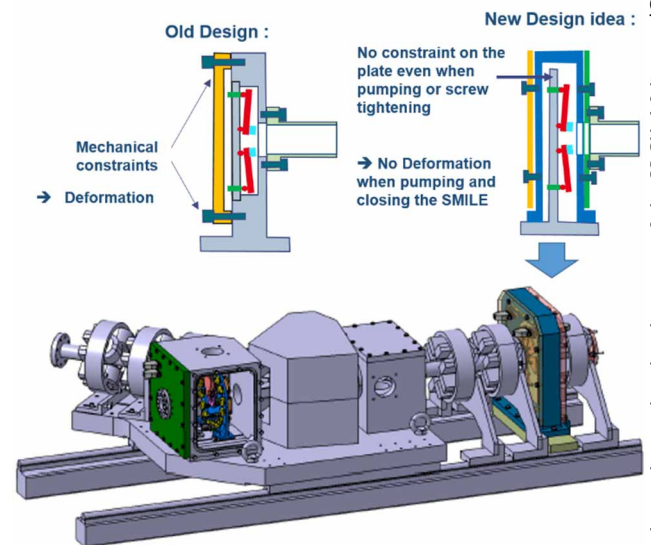
Figure 6: New mechanical design of the SMILE with better mechanical constraints management.
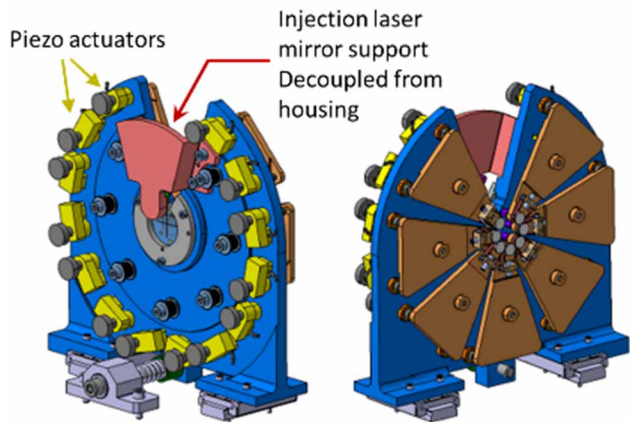
Figure 7: New design for the injection laser mirror and addition of piezo actuators

Remote Alignment Method for IR Laser (1064 nm)

It is often preferable to use IR photons (1064 nm) to maximise the X-Ray flux when using the source in the 5 – 20 keV range, as the frequency doubling yield is only about 30%. In this case alignment with direct eye observation is not possible anymore.

A new alignment method using three CCD cameras and the piezo actuators was developed, allowing, in the near future, the implementation of a real time automatic adjustment to compensate for the various environmental drifts.

## Chirped Pulse Amplification

A CPA system was designed to avoid laser induced damage in the amplifiers, limit non-linear effects, and shorten laser pulses (Fig. 8). The specificity of this design is the narrow bandwidth (0.03 nm) Nd:YAG laser chain. A similar system was designed to use as a pump for near and mid-IR OPCPA [5], but never used for an ICS source. All parts were actually delivered, and are now in the process of installation and alignment, with tests scheduled in the following weeks. The narrow bandwidth is an advantage for ICS source, as the $\Delta E/E$ is kept small.
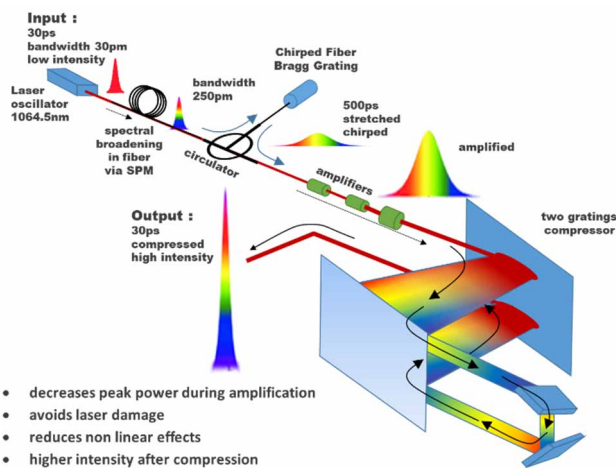
Figure 8: Principle of the new CPA system under development.

We present here the main features of the design of our CPA (Fig. 8). First the laser spectrum is broadened to 0.25 nm by self-phase modulation (SPM) in a 6.6 μm-core monomode fiber. Then the laser pulse duration is stretched to 500 ps by a Chirped Fiber Bragg Grating (CFBG) before amplification in three Nd:YAG modules. The pulse is then compressed by a double-pass gratings compressor using high line density (1850 l/mm, Fig. 9), high laser resistance high efficiency (> 96%, Fig. 10) gratings at an angle of incidence of 78°, 2° apart from the Littrow angle to enhance dispersion. The distance between the gratings is 1.7 m. These parameters were used to maximise diffraction efficiency and dispersion, in order to keep the system compact.

Average efficiency : 96,7%
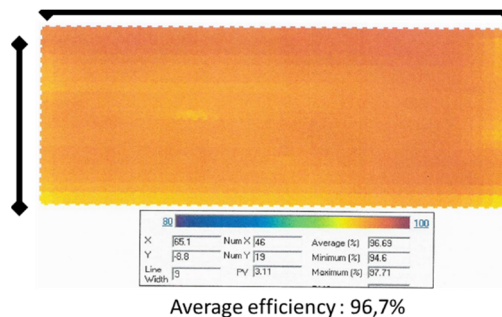
Figure 9: Scanning of the diffraction efficiency over the surface of the grating. Excellent efficiency was achieved. Courtesy: Plymouth Grating Laboratory
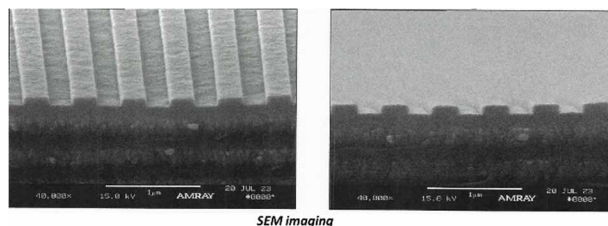
SEM imaging

Figure 10: SEM imaging of the grating. Courtesy: Plymouth Grating Laboratory

CONCLUSION

The ICS source of ELSA is undergoing deep improvements on several fronts. They include the upgrade of the laser pulses piling up system SMILE with better mechanical constraints management to improve alignment maintaining, the use of IR laser pulses which led us to develop a camera-based alignment system, and the development of a CPA system to avoid optical damage in the laser amplifiers. The main features of the design of these improvements were presented in this proceedings paper. All parts have been actually delivered and are now being installed and tested in the laboratory. Final tests on the ELSA accelerator are scheduled by the end of the year. Other optimizations are also carried out simultaneously on other aspects, namely the optimization of the electron beam Twiss parameters and current, the optimization of bunch compression by a field linearizing 1.3 GHz cavity, and an upgrade of the 1.3 GHz accelerating cavity and klystron system. All these enhancements will contribute to a more versatile, user-friendly source with significantly improved yield.

REFERENCES

[1] A. Chaleil *et al.*, "Inverse Compton scattering X-ray source yield optimization with a laser path folding system inserted in a pre-existent RF linac," *Nucl. Instrum. Meth. A*, vol. 840, pp. 113-120, 2016, `doi:10.1016/j.nima.2016.10.008`

[2] A.-S. Chauchat et *al.*, "Instrumentation developments for production and characterisation of Inverse Compton Scattering X-rays and first results with a 17 MeV electron beam, " *Nucl. Instrum. Meth. A*, vol. 622, pp. 129-135, 2010. `doi:10.1016/j.nima.2010.07.034`

[3] P. Guimbal *et al.*, "Status of the ELSA-2 Project," in *Proc. EPAC'02*, Paris, France, Jun. 2002, paper TUPRI066, pp. 1768-1770.

[4] A. Pires, A.-S. Chauchat, M. Collet, V. Le Flanchec, and N. Delerue, "Emittance growth study of an electron beam in a double-alpha magnet compressor used in an Inverse Compton Scattering X-ray source", presented at the IPAC'23, Venice, Italy, May 2023, paper TUPL172, to appear in the proceedings.

[5] T. Pinto, S. Wittte, and K. Eikema, "High-Power Nd:YAG Pump Laser System for OPCPA," in *Lasers Congress 2016 (ASSL, LSC, LAC)*, OSA Technical Digest (online), Optica Publishing Group, 2016, paper AM5A.24. `doi:10.1364/ASSL.2016.AM5A.24`

THE CXFEL PROJECT AT ARIZONA STATE UNIVERSITY

W. S. Graves* on behalf of the CXFEL collaboration[†], Arizona State University, Tempe, AZ, USA

Abstract

The CXFEL Project encompasses the Compact X-ray Light Source (CXLS) that is now commissioning in the hard x-ray energy range 2-20 keV, and the Compact X-ray Free-Electron Laser (CXFEL) designed to lase in the soft x-ray range 250 - 2500 eV. CXFEL has recently completed a 3-year design phase and just received NSF funding for construction over the next 5 years. These instruments are housed in separate purpose-built laboratories and rely on inverse Compton scattering of bright electron beams on powerful lasers to produce femtosecond pulses of x-rays from very compact linacs approximately 1 m in length. Both instruments use recently developed X-band distributed-coupling, room-temperature, standing-wave linacs and photoinjectors operating at 1 kHz repetition rates and 9300 MHz RF frequency. They rely on recently developed Yb-based lasers operating at high peak and average power to produce fs pulses of 1030 nm light at 1 kHz repetition rate with pulse energy up to 400 mJ. We present the current commissioning performance of CXLS, and review the design of the fully coherent CXFEL.

INTRODUCTION

Future light sources aim to improve performance, cost, and accessibility over today's instruments. The CXFEL project is developing femtosecond x-ray light sources at a cost and size that makes the novel time-resolved molecular science they provide accessible to many institutions including universities, medical facilities, and industrial labs. The first instrument produced and now commissioning is the CXLS that produces partially coherent synchrotron-like x-ray pulses at few hundred fs duration in the hard x-ray range. The second instrument, CXFEL, has completed design and is now under construction. It is a further development of CXLS technology that adds novel nanometer-scale electron bunching to produce fully coherent x-rays in the soft x-ray spectrum. These instruments differ from the major XFEL and synchrotron facilities as well as current laboratory scale sources, thus require development of new experimental techniques, sample delivery, detector properties, controls and data analysis methods that are matched to their novel properties. These properties include lower flux than the major facilities as well as improvements in stability and precision of beam properties, and the ability to tailor integrated accelerator, laser, and x-ray beamline operations to optimize particular experiments. We first describe the labs that house the instruments and then the 2 instruments. For illustrations of the various equipment and laboratories discussed here please see oral presentation TU1C4 in the proceedings of the 2023 FLS workshop.

___

* wsg@asu.edu
[†] see Annex A

LABORATORY ENVIRONMENT

Environmental factors have a large impact on the stability and performance of experiments at molecular length and time scales. In 2018 we constructed a new laboratory building on campus, Biodesign C, with 2 essentiallly identical groups of labs that are purpose-built for the accelerators, RF systems, lasers, and x-ray endstations used by CXFEL and CXLS. The laser, accelerator, and x-ray labs are in separate rooms each with their own safety and air-handling systems but the 3 rooms share a single 2m thick reinforced concrete foundation that is physically separated from the adjoining building spaces to provide a common stable platform for the beams. These rooms are verified to meet VC-E vibration standards similar to an electron microscope lab. The air temperature stability in the laser labs is $\pm 0.25°$ C, and is $\pm 0.5°$ C in the accelerator lab and x-ray hutch. Air humidity is at 40% $\pm$ 5%.

To mitigate electromagnetic interference we installed the RF systems including the klystrons in a Faraday cage preventing external pickup and suppressing any effects of the high power klystron pulses on sensitive x-ray experiments. The majority of equipment is water-cooled for temperature stability of high power systems. We designed and built a precision processed cooling water system that is tunable and stable to $\pm 0.05°C$ with a future goal to achieve $\pm 0.01°C$.

CXLS

The CXLS is constructed and now commissioning having produced first x-rays in February 2023. The technical components of CXLS including RF and accelerator sections, magnets, lasers, and diagnostics all serve as prototypes for the CXFEL equipment. CXLS will continue commissioning through 2023, transitioning to early science phase in 2024.

CXLS X-ray Performance

The CXLS design performance is given in Table 1. So far for commissioning we are running at lower electron bunch charge (10 - 20 pC) and laser ICS laser power (80 W) resulting in x-ray flux of 3×10^5 photons/shot at 1 kHz repetition rate. The charge is limited by damage to UV photoinjector optics that are currently being replaced with reflective optics. We are being conservative with the ICS laser power while developing automated steering software. In coming months we expect to increase UV and ICS laser powers to their full design specs. Simulations indicate that current x-ray performance (flux, emission angle, energy) is consistent with measured values. We anticipate meeting the full x-ray performance specifications as the power from both lasers is increased.

Table 1: CXLS Design Performance at 0.1% and 5% bandwidth. Brilliance units are ph/(s 0.1% mm^2 mr^2.

Parameter	0.1% BW	5% BW
Photon energy (keV)	2 - 20	2 - 20
Photons/pulse	5×10^6	1×10^8
Pulse rate (Hz)	1000	1000
Avg flux (ph/s)	5×10^9	1×10^{11}
Avg brilliance	2×10^{12}	5×10^{12}
Peak brilliance	3×10^{19}	9×10^{18}
Round RMS src size (μm)	3.0	3.0
Round RMS src angle (mrad)	4.0	4.0
RMS pulse length (fs)	< 300	< 300
RMS timing jitter (fs)	< 50	< 50

Interaction Point

The electron and laser beams meet at the interaction point (IP), crossing at an 8° angle from head-on to produce x-rays. The electron bunch length is 300 fs and the Dira is 1 ps. Timing jitter is 100 fs and is stable over timescales of hours. The Dira output is focused by a f=20 cm lens to a $\omega_0 = 10\,\mu$m spot and the electron beam is focused by a quadrupole triplet located 20 cm upstream of the IP to a 4 μm rms spot size at the IP. Spatial overlap is stable over periods of minutes at these spot sizes. We are developing steering feedback to correct slow thermal drift over longer timescales. The x-rays emerge with a 10 mrad opening angle. In current commissioning no collimating x-ray optic is present. An f = 20 cm elliptical Montel x-ray optic at fixed photon energy of 9.3 keV will be installed in coming weeks to collimate the beam. There are several YAG:Ce screens in the vicinity of the IP to image the electron/x-ray/laser beams including one insertable screen directly at the IP. Fitting short focal length optics for all of these beams within a few cm of teh IP as well as the diagnostics was an engineering challenge.

Accelerator and RF Systems

The accelerator consists of a 4.5 cell photoinjector and 3 short linac sections of 20 cells each, all powered by 2 RF transmitters. All of the accelerator structures are high efficiency standing-wave room-temperature copper structures with a repetition rate of 1 kHz and fill time of 170 ns. Peak cathode field in the photoinjector is 120 MV/m for a 3 MW input power. The cathode cell is less than a half-cell so that the laser arrival timing is close to the peak applied electric field. Exit energy is 4.0 MeV.

The linacs are innovative distributed-coupling structures [1] with a high shunt impedance 165 MOhm/m making them very efficient, gradient up to 30 MV/m and peak surface E-field of 120 MV/m. The structures are 20 cells long (32 cm), produce energy gain of 10 MeV each for 2 MW input power and a final maximum linac energy of 34 MeV. This energy is adequate to produce up to 20 keV x-rays via ICS.

The low-level RF (LLRF) system is a hybrid analog-digital system based on IQ modulation/demodulation developed at ASU. It drives 100 W solid-state power amplifiers that in turn drive a pair of L3 L-6145 klystrons to 6 MW saturated output power in 700 ns pulses. Output from klystron 1 is split with a waveguide variable phase-shifter power-divider (VPSPD) between the photoinjector (3 MW) and linac 1 (2 MW) after losses. Klystron 2 output is fed to a 3 dB hybrid that routes 2.5 MW power to each of linacs 2 and 3. We use a total of 3 VPSPDs that can shunt klystron power to water loads so that the klystrons always run at max power and constant thermal load regardless of what final beam energy is required. Scandinova K1 modulators power the klystrons, achieving 100 ppm rms voltage stability. Generally the RF systems are extremely stable over short and long terms with phase jitter of < 0.04° (12 fs) and amplitude jitter < 5×10−4. Typical operations during commissioning are to run for 8-10 hours in a day, shutdown, and then repeat the next day. The facility reaching thermal stability about 45 minutes after startup when running at 1 kHz, or within 10 minutes when running at 100 Hz. The day-to-day stability is excellent requiring only a few minutes of tuning to rephase all the structures and laser.

Lasers and Timing Systems

CXLS includes a photocathode laser that produces the electron beam and the high power ICS laser that collides with the electron beam. The photocathode laser is a Light-Conversion Pharos Yb:KGW amplifier producing 1.5 mJ pulses of 1030 nm light with FWHM 180 fs at 1 kHz repetition rate. The single-box laser has a 4th harmonic module that produces up to 100 μJ of 258 nm light that produces the electron beam at the photocathode. The Pharos oscillator is synchronized to the RF master oscillator via a Menlo Systems RRE-SYNCHRO unit resulting in 120 fs rms timing jitter between RF and UV. This unit runs stably with little tweaking required. However the fs UV pulses at 1 kHz have proved to cause nonlinear effects and damage in optical coatings on the MgF lenses used for transport. These effects limit the charge available in the accelerator to 20 pC. We are in the process of replacing the transmissive optics with reflective optics and are testing damage thresholds to increase the fluence to the cathode.

The ICS laser is a Trumpf Dira 200-1 Yb:YAG thin-disk amplifier producing 200 mJ pulses of 1030 nm light with FWHM of 1.1 ps at 1 kHz repetition rate. The Pharos oscillator sends an optical seed signal to the Dira that is amplified producing good synchronization with the cathode laser and electron beam. Trumpf has also supplied a cross-correlator that measures and corrects the timing difference between the Pharos and Dira amplifier outputs resulting in a net timing jitter of 33 fs between amplified pulses at 1 kHz rate. Pointing stability of the Dira is 4 μrad rms and power stability is 0.2% rms over 24 hours. The Dira has been tested to its full specifications but we are typically using it at 80 mJ/shot in early x-ray commissioning.

CXFEL

CXFEL is a further development of the technologies used in CXLS that is designed to produce fully coherent x-ray pulses. See the illustrations in the TU1C4 oral presentation in these proceedings. The accelerator components are nearly identical to CXLS with the addition of an electron diffaction [2] chamber and emittance exchange [3] line. The components also apply lessons learned with CXLS to improve performance. The purpose of the additional equipment is to create bunches of electrons that are short on the x-ray wavelength scale, i.e., < 1 nm in length so that when they interact with the ICS laser the output is coherent. ICS sources are generally excellent at producing hard x-ray photons with performance decreasing for softer photon energies. However the technique used by CXFEL to produce nanobunches that radiate coherently is currently limited by equipment jitter performance to lower energies (longer x-ray wavelengths) in the soft x-ray range. We believe that with further development this technique will reach hard x-rays, but the scope of CXFEL is currently limited to photon energies less than 2.5 keV with most of the development work focusing on the important energy range from 250 eV to 1.2 keV.

Producing x-rays in this lower energy range is not well suited to the head-on collision geometry of CXLS where the effective undulator period is just 515 nm. Such a short period requires an ebeam energy into the few MeV range to make soft x-rays. Such low energy electrons are subject to strong space-charge forces and difficult to focus to a small interaction spot. Instead we adopt an "overtaking" collision geometry where the electron beam and laser propagate in the same direction with a 30° angle between them resulting in an effective undulator period of $8\,\mu m$ thus raising the ebeam energy to e.g. 29 MeV to produce 1 keV photons. This geometry does however require a substantially more powerful and shorter pulse ICS laser as discussed below.

X-ray Performance

The CXFEL design performance is given in Table 2 across a range of energies. The nanobunching concept that produces coherent emission is very sensitive to space charge forces resulting in the use of very low charge (1 pC) electron bunches vs the 200 pC bunches of CXLS. Thus the flux of CXFEL with its more efficient coherent emission is similar to CXLS. However the coherent photons are emitted into a phase space volume that is orders of magnitude smaller than the incoherent CXLS and thus the brilliance of the CXFEL s orders of magnitude higher. The x-ray pulses are also much shorter, ranging from 0.5 - 10 fs.

Accelerator and RF Systems

The CXFEL accelerator reuses the CXLS photoinjector and has 3 similar linac sections. However the linacs have subtle design changes that improve the symmetry of the cells and allow operation at higher gradient up to 75 MV/m. The RF system uses the same 2 klystrons as CXLS, but combines and compresses the klystron output to make short

Table 2: CXFEL Design Performance at several photon energies. Brilliance units are ph/(s 0.1% mm^2 mr^2.

Parameter	Photon energy (eV)	
	250	1000
Photons/pulse	8×10^8	1.1×10^8
Pulse rate (Hz)	1000	1000
Avg flux (ph/s)	8×10^{11}	1.1×10^{11}
Flux/shot (nJ)	32	18
Avg brilliance	1.3×10^{15}	1.2×10^{16}
Peak brilliance	1.2×10^{28}	5.6×10^{28}
Round RMS src size (μm)	0.9	0.5
Round RMS src angle (μrad)	440	188
FWHM pulse length (fs)	9.1	4.6
FWHM bandwidth (%)	0.18	0.09
Arrival timing jitter (fs)	< 10	< 10
Electron beam energy (MeV)	14	29

pulses up to 40 MW. This power is then split among the RF structures. Combining and splitting the power produces a system with redundancy that enables operation with a single RF transmitter, as well as providing the opportunity to reduce ebeam energy and timing jitter by using the correlations in phase and amplitude jitters among the linac sections to partially cancel their effects. The transmitters are upgraded Scandinova K200 units customized with low jitter triggers and additional charging supplies with the goal to reduce high voltage jitter from 100 ppm to 10 ppm at 1 kHz. The compressed high power RF is used to drive the photoinjector cathode gradient up to 150 MV/m.

Lasers and Timing Systems

The photoinjector laser is identical to CXLS except that we will build our own harmonic module to improve the UV mode. The ICS laser is a significant upgrade over CXLS with the final multipass amplifier producing 500 mJ of 1030 nm light in 800 fs pulses at 1 kHz. This output is then spectrally broadened in a large Herriott cell and compressed to 40 fs.

The timing synchronization for CXFEL takes a different approach than CXLS, using BOM-PD components from Cycle Laser with the goal to achieve approximately 20 fs locking between RF and photoinjector and ICS lasers. We anticipate ebeam and x-ray arrival time jitter below 10 fs with proper setup of the accelerator and laser timing.

ACKNOWLEDGMENTS

REFERENCES

[1] S. Tantawi, M. Nasr, Z. Li, C. Limborg, and P. Borchard, "Design and demonstration of a distributed-coupling linear accelerator structure," *Phys. Rev. Accel. Beams*, vol. 23, no. 9, p. 092 001, 2020.
doi:10.1103/PhysRevAccelBeams.23.092001

[2] L. Malin *et al.*, "Quantitative agreement between dynamical rocking curves in ultrafast electron diffraction for x-ray lasers," *Ultramicroscopy*, vol. 223, p. 113 211, 2021. doi:10.1016/j.ultramic.2021.113211

[3] E. A. Nanni, W. S. Graves, and D. E. Moncton, "Nanomodulated electron beams via electron diffraction and emittance exchange for coherent x-ray generation," *Phys. Rev. Accel. Beams*, vol. 21, no. 1, p. 014 401, 2018. doi:10.1103/PhysRevAccelBeams.21.014401

ANNEX A: CXFEL COLLABORATION

A. Botana, S. Botha, B. Cook, O. Erten, P. Fromme, A. Gardeck, W. Graves, M. Holl, J. Houkal, S. Jachim, R. Kaindl, S. Karkare, R. Kirian, E. Lttman, B. Liebich, S. Rednour, A. Ros, K. Schmidt, D. Smith, S. Teitelbaum, T. Thornton, S. Tilton, S. Tongay, J. Vela, K. Warble, U. Weierstall, D. Winkel, Arizona State University, Tempe, AZ

H. Loos, Yorktown Heights, NY

M. Mitrano, Harvard University, Cambridge, MA

D. Rolles, A. Rudenko, Kansas State University

Y.-D. Chuang, O. Gessner, J. Qiang, S. Roy, T. Weber, Lawrence Berkeley National Laboratory, Berkeley, CA

R. Comin, K. Nelson, Massachusetts Institute of Technology, Cambridge, MA

L. DiMauro, Ohio State University

N. Shivaram, Purdue University

G. Phillips, Rice University

J. Cryan, V. Dolgashev, Z. Li, E. Nanni, S. Tantawi, M. Trigo, SLAC National Accelerator Laboratory, Stanford, CA

R. Fung, A. Hosseinizadeh, A. Ourmazd, M. Schmidt, P. Schwander, University of Wisconsin - Milwaukee, Milwaukee, WI T. Grant, University of Buffalo, Buffalo, NY

M. Brown, A. Sandhu, University of Arizona, Tucson, AZ

M. Frank, T. Kuhl, University of California Davis, Davis, CA

F. Mahmood, University of Illinois Urbana-Champagne, Urbana-Champagne, IL

M. Centurion, University of Nebraska, Nebraska

Undergraduate students: G. Babic, C. Bell, E. Boyd, T. Brown, T. Dela Rosa, R. DeMott, A. Dupre, K. Eckrosh, E. Everitt, A. Eyler, J. Falconer, R. Jaswal, R. Larson, X. Ma, A. Martinez, S. Ramkumar, E. Ros, A. Semaan, A. Staletovic, J. Stanton, S. Tripathi, D. Valentin, Arizona State University, Tempe, AZ

A HIGHLY COMPETITIVE NON-STANDARD LATTICE FOR A 4th GENERATION LIGHT SOURCE WITH METROLOGY AND TIMING CAPABILITIES

P. Goslawski*, M. Abo-Bakr, J. Bengtsson, K. Holldack, Z. Hüsges, A. Jankowiak,
K. Kiefer, B. Kuske, A. Meseck, R. Müller, M. Sauerborn, O. Schwarzkopf, J. Viefhaus, J. Völker
Helmholtz-Zentrum Berlin, BESSY, Berlin, Germany

Abstract

The PTB, Germany's national institute for standards & metrology, has relied on synchrotron radiation for metrology purposes for over 40 years and the most prominent customers are lithography systems from ASML/ZEISS. HZB is now working on a concept for a BESSY II successor, based on a 4th generation light source with an emittance of 100 pm rad @ 2.5 GeV. It is essential, that this new facility continues to serve the PTB for metrology purposes. This sets clear boundary conditions for the lattice design, in particular, the need for homogeneous bends as metrological radiation sources. Different Higher-Order-Multi-Bend-Achromat lattices have been developed, based on combined function gradient bends and homogeneous bends in a systematic lattice design approach. All lattices are linearly equivalent with the same emittance and maximum field strength. However, they differ significantly in their non-linear behavior. Based on this analysis, the choice of the BESSY III lattice type is motivated. A special focus is set also on TRIBs (Transverse Resonance Island Buckets) to operate with two orbits as a bunch separation scheme in MBAs, for different repetition rates or for the separation of short and long bunches.

HZB's AND BESSY's NEAR FUTURE

HZB is preparing for its future light source with two main projects [1]: the BESSY II+ project and BESSY III. BESSY II+ is a refurbishment and modernization project of BESSY II, to enable state-of-the-art operation for the next decade. The greenfield BESSY III project aims to establish a storage ring-based light source of the 4th generation based on a Multi-Bend-Achromat (MBA) lattice. A first sketch of the facility was recently published in a pre-CDR [2]. The initial operation of a greenfield project is not expected earlier than 2035, so a modernization of BESSY II, which has been running for 25 years, is mandatory and requested with the BESSY II+ project. It will pave the way towards BESSY III. The time schedule for BESSY II+/III is shown in Fig. 1.

Figure 1: Time schedule for BESSY II+/III project.

* paul.goslawski@helmholtz-berlin.de

VIA BESSY II+ TOWARDS BESSY III

The strategic focus points of the BESSY II+ project are *operando capabilities, modernization, and sustainability*. Overall it is a 100 M€ project, where nearly 25% will be covered by HZB, another 25% by strategic partners or third-party projects and 50% has been requested from the funding bodies. About 50% of the BESSY II+ project scope will be invested in new beamlines and endstations (25%), sample environment (12.5%), and digitalization (12.5%) to strengthen the operando capabilities of BESSY II and HZB. 35% will be used for the modernization of the accelerator complex (30%) and beamline instruments (5%), and 15% is foreseen to improve the sustainability of BESSY II.

The modernization scope for the accelerator complex will not only cover general preservation and modernization measures, but also includes technology development towards BESSY III.

A project already advanced is the development of an active normal conducting 1.5 GHz higher harmonic cavity (HHC) with HOM damper within a European collaboration between ALBA, DESY, and HZB. The prototype, designed and purchased by ALBA and RF tested at HZB, is installed in the BESSY II storage ring. Since autumn 2022, it is tested with beam and conditioned for user operation. Based on this experience, a new HHC system will be developed for BESSY II also including the option for a 1.75 GHz cavity system to generate a beating in the bunch focusing, allowing for simultaneously storing of short and long bunches.

Another important work package is the development of a BESSY II+/III digital twin as a natural interface for the efficient implementation of digitalization measures. This framework and methods are mandatory for the startup, commissioning, and efficient operation of BESSY III and already for the design process, e.g., in order to check for lattice robustness.

The work package *Permanent Magnets for Energy Efficiency* within the BESSY II+ is mainly motivated by BESSY III. In order to improve sustainability and to reduce the power consumption of BESSY III, it is discussed to replace the well-established classical iron yoke electromagnet technology with permanent magnets wherever possible, i.e., at dipoles and quadrupoles. Therefore conceptional designs, prototyping, and testing under real operating conditions are necessary. Within BESSY II+, it is foreseen to replace a very power-hungry bending electromagnet in the transferline between booster and storage ring with a permanent magnet

solution to gain experience and know-how. Since the PTB has special requirements on the bending radiation source for metrology purposes, it is also discussed to replace two main bends of one double-bend-achromat section with permanent magnets.

BESSY III PARAMETERS & OVERVIEW

The main objectives and also largest changes compared to BESSY II, as summarized in Table 1, is the increase of energy up to 2.5 GeV and the decrease of emittance down to 100 pm rad, motivated by the science case request for diffraction-limited radiation with adjustable polarisation up to 1 keV photon energy from the 1st undulator harmonics.

Table 1: Main parameters of BESSY II and BESSY III.

Parameter	BESSY II	BESSY III
Energy	1.7 GeV	2.5 GeV
Circumference	240 m	~ 350 m
# of straights	16 with 5.0 m	16 with 5.6 m
Emittance ε_0	5 nm rad	100 pm rad
$\beta_{x,y}$ in straights	(1.2, 1.2) m	~ (3, 3) m

At BESSY II 1 keV photon energy is only accessible with the 3rd or 5th harmonics using APPLE II undulators, as shown in Fig. 2. With the increase of the electron beam energy up to 2.5 GeV, the 1st harmonic with a standard period length of 40 mm will cover this range. It seems that beamline scientists and the user community will prefer the In-Vacuum-Apple type Undulator (IVUE) because the gap can be closed down to ~5 mm instead of ~12 mm for the out-of-vacuum type, enabling a wider photon energy range starting from 100 eV or even below. By the reduction of the emittance by a factor of 50, the spectral brilliance will increase by 2 orders of magnitude in the soft-X-ray regime and by 3 orders of magnitude in the tender-X-ray range.

Not only HZB's scientific infrastructure but also those of its partners as the Max-Planck-Institutes, PTB/BAM, Leib-
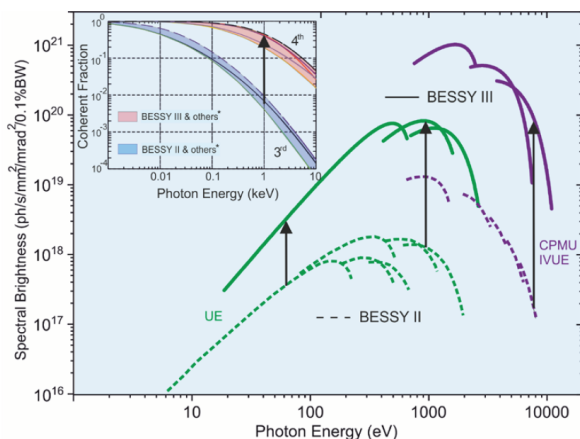

Figure 2: Spectral brightness and coherent flux of BESSY III compared to BESSY II.

niz institutes (MBI, FBH, IKZ) and the Berlin universities and high-tech companies, make Berlin-Adlershof the one and only place to be for BESSY III. There is still one free site left in Germany's biggest Science and Technology Park, which will limit BESSY III's circumference to ~350 m. With the envisaged emittance of 100 pm rad, BESSY III will rank between current and future upgrades worldwide, staying competitive for the next decades and further scientific challenges to come, see Fig. 3.
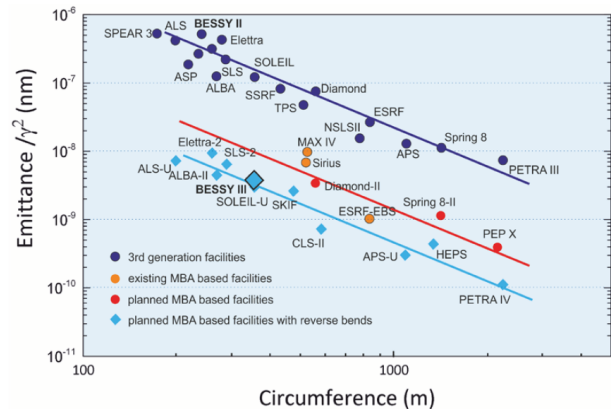

Figure 3: The BESSY facilities on the emittance-circumference landscape.

BESSY III LATTICE DESIGN PROCESS

In addition to the main target parameters, given in Table 1, the momentum compaction factor was chosen not to be too small $\alpha_c > 1.0 \times 10^{-4}$ in order to achieve a reasonable bunch length and manageable collective effects. We aim for a momentum acceptance of 3% or even higher to reach a good Touschek lifetime to keep the option for flexible operation, such as supporting time-resolved experiments. The developments of "TRIBs / Two orbit operation" over the last years motivate us to study this operation scheme for BESSY III and investigate the impact on the achievable parameters compared to a standard user mode with one orbit.

Due to the long-standing partnership with the PTB, an absolutely mandatory demand on the BESSY III facility is to provide a radiation source, usable as a primary radiation standard, i.e., an absolute, predictable, and traceable radiation source for metrology purposes. For that, the deflecting magnetic field around the source point has to be known to high precision and be accessible for an NMR probe measurement. This is best realized with a purely homogeneous dipole magnet. A combined function bend with a magnetic gradient perpendicular to the beam motion, which is often used in MBA unit cells, is therefore not a good choice. The request for the *homogeneous metrology bend* strongly influenced our lattice design process towards a first baseline lattice.

In order to deliver a robust design with good control of non-linear beam dynamics, also with regards to TRIBs operation close to a 3rd order resonance, *we chose the Higher*

TU1B1

Order Achromat (HOA) approach, fixing the phase advance between the distributed and repetitive two chromatic sextupole families within the MBA-structure. This cancels all the geometric and quadratic resonance driving terms to 2nd order.

For comparison of a metrology solution using a homogeneous bend with a "classical" combined function bend solution for an MBA lattice, we have chosen a *systematic and deterministic lattice design approach*. That means that all three building blocks of an MBA lattice: the inner MBA unit cell (UC), the dispersion suppression cell (DSC), and finally the matching cell (MC), have been investigated and optimized individually and finally combined like LEGO into a robust sector cell. All lattices designed this way use the same hardware limitations, defined in Table 2 in [3] for a fair comparison.

So far, as shown in Ref. [3] and in Fig. 4, two lattice configurations have been investigated in detail.

Figure 4: The lattices are named after the type of their bend in the UC and DSC. Top: cfsf (**c**ombined **f**unction, **s**eparate **f**unction) HOA-6MBA lattice. Bottom: sfcf HOA-6MBA.

Due to symmetry reasons, the homogeneous metrology bend was included right from the beginning in the MBA structure to have 16 completely symmetric sectors (or superperiods) as a starting point. In principle, there are then two configurations. In the upper plot the inner UC of the MBA structure is set up with combined function bends (cf), as often used in most MBA lattices. The homogeneous bend - or separated function bend (sf) - is placed at the beginning and end of the MBA structure as matching bend in the DSC. In the bottom plot the configuration is swapped. In the following, we will name the lattices first with the type of the UC bend followed by the type of the DSC bend. So the upper plot shows a cfsf lattice and the lower one an sfcf lattice. The only non-linear elements included so far in the lattice are the two chromatic sextupole families to correct the linear chromaticity to zero.

Since both lattices strongly differ in their non-linear behavior, we decided to study also the more symmetric solutions cfcf and sfsf without switching the type of the bending magnet between UC and DSC. This reduces the perturbation of the optical functions within the MBA structure, especially at the sextupoles in the DSC, and pushes the variation of the optical functions out into the MC. It is clear that the cfcf solution is without a metrology bend, which has to be included later, e.g., in one sector only.

LINEAR LATTICE TUNE FOOTPRINT

Figure 5 shows the optical functions and the magnet arrangement of different lattices for the cf-UC case (cfcf, cfsf)

and for the sf-UC case (sfcf, sfsf, sfsf4Q) and Fig. 6 shows the corresponding tune shift with momentum (TSWM). All lattices yield basically the same emittance, momentum compaction factor, working point (Q_x, Q_y) = (43.72, 12.79), maximal field strengths, drift lengths, and straight length of 5.6 m. Therefore, they are linearly equivalent. Only the circumference differs by about 10% because the magnet length has always been adapted to its maximally allowed gradient and in case of the main bend to reach the required emittance. The biggest difference is the construction of the UC, which results in the cf-case in a very strong quadratic behavior of the horizontal TSWM. In the sf-case, the quadratic behavior is reduced and the cubic starts to dominate.
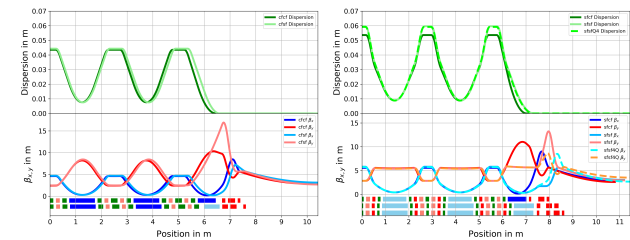
Figure 5: Lattices with optical functions of variants with a cf-UC: cfcf, cfsf (left) and a sf-UC: sfcf, sfsf, sfsf4Q (right).
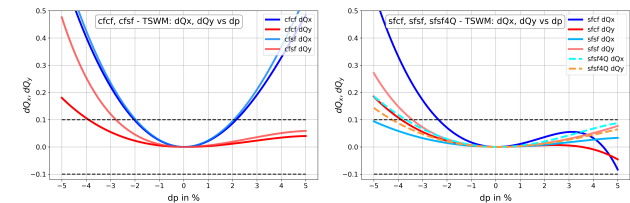
Figure 6: The TSWM for the different lattice variants: cfcf, cfsf (left) and sfcf, sfsf, sfsf4Q (right).

In order to set up a lattice with well-controlled non-linear dynamics one should keep the natural chromaticity and sextupole strength as small as possible to set up an effective chromatic correction $\xi \sim \oint [k_2(s) \cdot D(s) - k_1(s)] \, \beta(s) \, ds$ by placing the sextupoles at the best positions of the optical functions to confine the tune-footprint as good as possible, i.e., to reduce the non-linear behavior and "harmonize" the lattice. Since the chromatic sextupoles introduce the non-linear behavior in order to compensate for the natural chromaticity, we tried to optimize for a solution, where its integrated sextupole strength $\sum (k_2 \cdot L)^2$ is minimized. The most important parameters to judge the non-linear behavior of the different lattice variants are summarised in Tab. 2. To compare the tune footprint of different lattices we define *a tune confinement criterion as a maximal tune shift to be $dQ_{x,y}$ = 0.1 for TSWM and TSWA* (tune shift with amplitude).

cf-UC: cfcf, cfsf:

The lattices with cf-UC are limited in the horizontal plane at 2.0 % momentum acceptance if applying the tune confinement criterion. The vertical TSWM is dominated by the cubic order. The change from the cf- to sf-DSC reduces the

Table 2: Comparison of the different cf and sf lattice variants for the most important non-linear parameters.

Type	Circ. in m	Angle in ° UC, DSC	Main bend length in m	ε_0 (UC, DSC) in pm rad	Natural chromaticity	Sext. strength $\sum (k_2 \cdot L)^2$	TSWM, dp in % for $dQ_{x,y} = 0.1$
cfcf	327 m	4.25, 2.75	1.0	95 (98, 78)	-86, -45	292e3	2.0, 3.9
cfsf	333 m	4.25, 2.75	1.0	99 (99, 97)	-82, -60	325e3	2.1, 2.8
sfcf	346 m	4.00, 3.25	1.0	98 (99, 95)	-94, -39	110e3	2.3, 3.9
sfsf	358 m	4.375, 2.5	1.1	99 (101, 81)	-79, -47	76e3	5.0, 3.4
sfsf4Q	366 m	4.375, 2.5	1.1	99 (101, 80)	-86, -35	69e3	3.8, 4.3

cubic behavior. It mainly affects the β_y function, shifting its maximum from 10 m up to 16 m, increasing the vertical natural chromaticity from -45 to -60 and reducing the momentum acceptance in the vertical plane from 3.9% to 2.8%.

sf-UC: sfcf, sfsf, sfsf4Q:

The lattices with an sf-UC are not as limited as the cf-UC lattices by the quadratic order. The sfcf lattice shows the strongest cubic behavior and is limited in TSWM in the horizontal plane at 2.3 % (vertically at 3.9 %). The change of the DSC bend from a cf to an sf bend was only possible by introducing an additional vertical focusing quadrupole in the DSC and inverting the quadrupole triplet in the straight. This makes a strong change in the beta-functions at the end of the DSC and in the matching quadrupoles and changes the natural chromaticity from (-94, -39) to (-79, -47). In addition, the length of the main bend had to be increased by 10% to fit the emittance of 100 pm rad. The changes in the optical functions reduced the strong cubic behavior and the TSWM confinement is limited now by the vertical plane and massively relaxed in the horizontal one (5.0%, 3.4%), due to the large value of β_y in the matching quadrupoles and the small values for β_x. Following this argumentation line, it is a logical consequence to change the quadrupole triplet into a quadruplet to improve the control of both beta functions in the matching quadrupole section, which allows a careful adjustment of the non-linear behavior and tune confinement. The quadruplet solution "sfsf4Q" is shown with dashed lines and allows to equalize the TSWM behavior in both planes resulting in a TSWM confinement of (3.8%, 4.3%).

The TSWA is shown in Figs. 7 and 8 for the different lattices in the middle of a straight with $\beta_{x,y} \approx (3\,\text{m}, 3\,\text{m})$. The cfcf-lattice gives the best results with amplitudes of 4 mm to 5 mm. The worst case is the sfcf lattice with amplitudes of 1.5 mm to 2.5 mm, whereas the other three cfsf, sfsf, sfsf4Q range at 2 mm to 3.5 mm.

So far no measures have been introduced to the lattices to optimize the TSWA behavior. The inner beam pipe radius of 9 mm results in an aperture in the straights of 5 mm to 6 mm in the horizontal and 3.5 mm to 5.5 mm in the vertical plane for the different lattice candidates. First tests showed that an improvement could be possible by splitting up the chromatic sextupole families or introducing geometric/harmonic multipoles.

The direct next step is the introduction of a non-linear optimization scheme. For example, chromatic octupoles can
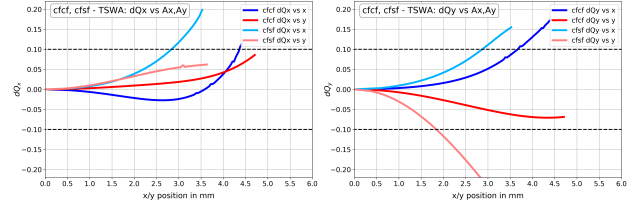

Figure 7: TSWA for lattice variants with a cf-UC: cfcf, cfsf. Left: dQ_x vs. $A_{x,y}$. Right: dQ_y vs. $A_{x,y}$.
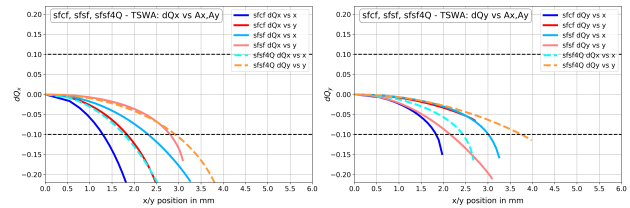
Figure 8: TSWA for lattice variants with a sf-UC: sfcf, sfsf, sfsf4Q. Left: dQ_x vs. $A_{x,y}$. Right: dQ_y vs. $A_{x,y}$.

be introduced to reduce the quadratic order, especially for the cf-UC lattices. Or the two families of sextupoles could be split up to improve the tune footprint. Discussion and work are ongoing to find a robust solution for BESSY III. Further steps are the verification of robustness, the development of an injection concept, the implementation of a simulated commissioning scheme, and a detailed analysis of collective effects.

CONCLUSION

In this paper, we have given an overview of the BESSY III project and shown how a careful setup of the linear lattice influences the non-linear beam dynamics. The choice for a different hardware realization of the UC with cf or sf bends has a big impact on the non-linear tune footprint and sets a starting point for further optimization of the non-linear behavior including higher-order multipoles.

REFERENCES

[1] O. Schwarzkopf *et al.*, "Materials discovery at BESSY", *Eur. Phys. J. Plus*, vol. 138, no. 348, 2023. doi:10.1140/epjp/s13360-023-03957-8

[2] P. Goslawski *et al.*, "BESSY III - The Materials Discovery Facility", PreCDR, 2022. doi:10.5442/r0004

[3] P. Goslawski *et al.*, "BESSY III - Status Report and Lattice Design Process", presented at IPAC'22, Bangkok, Thailand, May 2022, paper TUPOMS010. doi:10.18429/JACoW-IPAC2022-TUPOMS010

NONLINEAR OPTICS FROM HYBRID DISPERSIVE ORBITS*

Yongjun Li[†], Derong Xu, Victor Smaluk, Robert Rainer

Brookhaven National Laboratory, Upton, NY, USA

Abstract

In this paper we present an expansion of the technique of characterizing nonlinear optics from off-energy orbits (NOECO) [Olsson et al., Phys. Rev. Accel. Beams, vol. 23, p. 102803] to cover harmonic sextupoles in storage rings. The existing NOECO technique has been successfully used to correct the chromatic sextupole errors on the MAX-IV machine, however, it doesn't account for harmonic sextupoles, which are widely used on many other machines. Through generating vertical dispersion with chromatic skew quadrupoles, a measurable dependence of nonlinear optics on harmonic sextupoles can be observed from hybrid horizontal and vertical dispersive orbits. Proof of concept of our expanded technique was accomplished by simulations and beam measurements on the National Synchrotron Light Source II (NSLS-II) storage ring.

INTRODUCTION

Characterizing the nonlinear optics of storage rings is becoming more essential with the introduction of higher order multipole magnets in accelerator design. Errors from the higher order multipoles have been observed to degrade machine performance, such as reduction of dynamic aperture, energy acceptance, etc. Some efforts have been made to identify the nonlinear multipole errors by measuring local resonances [1] and distorted resonance driving terms [2], which requires a sophisticated Hamiltonian dynamics analysis. A more practical technique for measuring the nonlinear optics from off-energy closed orbits (NOECO) was reported and demonstrated on the MAX-IV ring [3]. Significant improvements on its dynamic aperture and beam lifetime were observed after correcting sextupole errors. Desired results were obtained while testing the NOECO technique on the ESRF-EBS ring as well [4]. However, the dependence of nonlinear optics on off-energy orbits is only measurable for chromatic sextupoles. This technique, however, doesn't apply to harmonic sextupoles, which do not see the first order linear dispersion. Harmonic sextupoles are used in almost every third-generation light source ring, and some fourth-generation diffraction-limited machines, such as the ALS-U ring [5]. They are even being used in the design of a future electron-ion collider ring [6]. As such, an expansion of the existing NOECO technique to correct for the harmonic sextupoles would be useful due to their common, integral use in current and future accelerator design. In the National Synchrotron Light Source II (NSLS-II) ring [7], the number of harmonic sextupoles is greater than the number of chromatic sextupoles (180:90). Therefore, correcting

harmonic sextupole errors is important for improving machine performance due to their greater influence. In this paper, we outline our expansion on the capabilities of existing sextupole correction techniques to accommodate for the harmonic sextupoles.

Some straightforward methods for calibrating harmonic sextupoles for correction would be (1) to temporarily convert them to chromatic ones; (2) to generate local orbit bumps through the sextupoles being calibrated. They are not practical when considering the limitations of routine operations of user facilities.

NONLINEAR OPTICS ON HYBRID DISPERSIVE ORBIT

When a sextupole sees vertical dispersion, its Hamiltonian reads as

$$H = \frac{p_x^2 + p_y^2}{2(1+\delta)} + \frac{K_2}{3}[x^3 - 3x(y + \eta_y\delta)^2], \qquad (1)$$

which includes a skew quadrupole component $2K_2\eta_y\delta \cdot xy$, with η_y the vertical dispersion, δ the beam momentum deviation, and sextupole strength $K_2 = \frac{1}{(B\rho)_0}\frac{\partial^2 B_y}{\partial x^2}$, normalized with the beam rigidity $(B\rho)_0$. Therefore, the nonlinear optics on off-energy orbits depend on the sextupole gradient, which can be utilized for their calibration and correction. A vertical dispersive wave can be generated through chromatic skew quadrupoles. In most light source rings, skew quadrupoles are widely equipped to control the residual vertical dispersion and linear coupling. Usually, a considerable amount of vertical dispersion can be generated, but only introduces weak coupling when the Betatron tune has sufficiently deviated from the linear difference/sum resonance. Thus, the nonlinear off-energy optics depends on not only chromatic sextupoles, but also on the original harmonic ones. In other words, horizontal harmonic sextupoles are converted into vertical chromatic ones, which makes their calibration and correction possible on hybrid dispersive orbits. In our studies, the NSLS-II ring double-bend achromat lattice was used to demonstrate these expanded capabilities.

At the NSLS-II ring, each odd-numbered cell is equipped with one 0.2 m long chromatic skew quadrupole (see Fig. 1). Their maximum gradients are $g_1 = 0.35\,\text{T}\cdot\text{m}^{-1}$, which is limited by the capacity of their power supplies. Assuming we can double their gradients to $g_1 = 0.70\,\text{T}\cdot\text{m}^{-1}$, a vertical dispersion wave with a ~ 0.1 m amplitude can be generated. The necessity for a double gradient is to increase the sensitivity of the nonlinear optics distortion to sextupoles. Although these gradients are twice as large as the maximum output of their power supplies, they are still quite weak compared to other operational quadrupoles with a maximum gradient of


$g_{1,max} = 22 \, \text{T} \cdot \text{m}^{-1}$. Under these conditions, the exact coupled optics computed with the Ripken parameterization [8,9] indicates that the linear optics remain weakly coupled. In Fig. 1, the non-dominating functions $\beta_{1,y}$ and $\beta_{2,x}$ (dashed lines) are observed as very close to zero, while the dominating $\beta_{1,x}$ and $\beta_{2,y}$ (solid lines) are almost the same as in the uncoupled case. The skew quadrupoles also cause a small amount of horizontal dispersion to be leaked into the straight sections. Although such small residual dispersion could not be solely used to measure the off-energy nonlinear optics, its effect is accounted for in our method because the exact parameterization has been used.
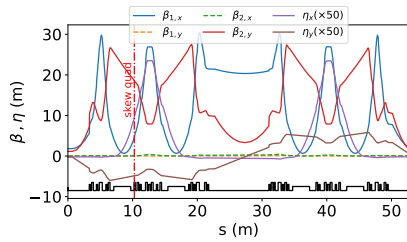

Figure 1: Coupled Twiss functions for a supercell at NSLS-II when a vertical dispersion wave is generated with chromatic skew quadrupoles. The location of the skew quadrupole is marked with a red vertical dash-dot line. Two non-dominating β-functions (dashed lines) indicate that this optics configuration remains weakly coupled.

For demonstration purposes, we choose a harmonic sextupole "SH3" and a chromatic sextupole "SM1" to compute their linear dependence on the off-energy optics, i.e., the so-called response vectors, as seen below. Only two dominating optics functions $\frac{d\beta_{1,x}}{d\delta}$ and $\frac{d\beta_{2,y}}{d\delta}$ observed at their corresponding BPMs were computed with the code MAD-X: PTC module [10] and verified with ELEGANT [11]. If no skew quadrupoles are used to excite the beam, they become the uncoupled β_x and β_y. The response vectors computed with and without the vertical dispersion are compared in Fig. 2. With horizontal dispersion, the dependence of off-energy optics on "SH3(N)" is not measurable in both the horizontal and vertical planes. On the hybrid dispersive orbits, a measurable dependence on "SH3(Y)" can be observed. Note that, for both cases, the dependence of the chromatic "SM1(Y/N)" is always measurable because it sees a large horizontal dispersion. In the meantime, the dependencies are quite similar since the optics are only slightly altered.

SIMULATIONS

In this simulation, random distributed errors on all 180 harmonic sextupoles are introduced and the distortion of off-energy optics are computed by comparing against the ideal lattice model. Then the needed sextupole correction scheme is obtained by the least squares regression,

$$\Delta \frac{d\beta}{d\delta} \approx M_{x,y} \Delta K_2, \qquad (2)$$
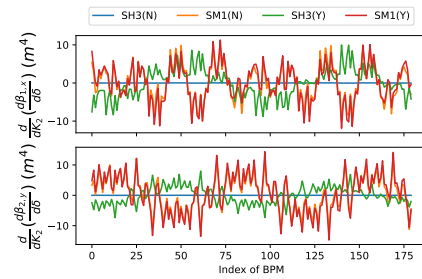
Figure 2: Comparison of the off-energy optics dependence on a chromatic sextupole "SM1" and a harmonic sextupole "SH3". With horizontal dispersion, the optics dependence on the harmonic sextupole (labeled as "SH3(N)") is too small to measure. On hybrid dispersive orbits, a measurable dependence (labeled as "SH3(Y)") is observed.

Here $M_{x,y}$ are the response matrices, which were obtained by computing the derivatives $d\beta/d\delta$ by varying sextupoles sequentially. For comparison, the optics distortions before and after correction, and the real error distributions and computed correction scheme are illustrated in Figs. 3 and 4, respectively. As seen in Fig. 4, the obtained correction schemes only approximately follow the real errors that were added in advance. This is due to the strong degeneracy that exists among sextupoles in the NSLS-II lattice.
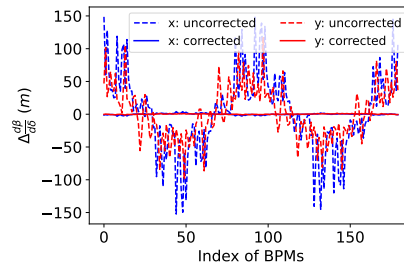
Figure 3: Distortions of the nonlinear optics with 180 randomly added errors. The dashed lines are uncorrected distortions, and the solid lines represent the distortions after correction.
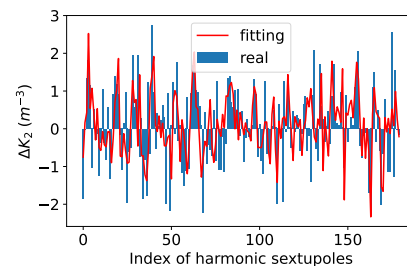

Figure 4: Comparison of the added errors (labeled as "real") on 180 harmonic sextupoles and the obtained correction scheme (shown with red lines labeled as "fitting").

The correction scheme based on the BPM observations can partially correct the optics distortion, therefore improve the dynamic aperture. To illustrate this, the dynamic apertures of the ideal machine, and uncorrected/corrected nonlinear lattices for the 2nd simulation were computed for comparison (Fig. 5). Although the degraded dynamic aperture due to sextupole errors could not be fully recovered through the correction scheme, a significant improvement was achieved. Such improvement is the main purpose of calibrating and correcting the distorted nonlinear optics. If we could distinguish between the degeneracy among the sextupoles, further improvement could be made. This topic is slightly beyond the scope of this paper, however, but worth more study.
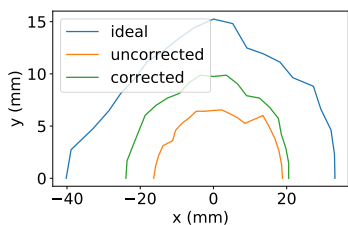

Figure 5: Comparison of the dynamic apertures for the ideal, uncorrected and corrected nonlinear lattices.

EXPERIMENTAL STUDIES

A two-stage proof-of-principle through beam-based calibration of sextupole errors was implemented at the NSLS-II storage ring. As the sextupoles are powered in series, the sextupoles lack individual configurability. Therefore, no actual nonlinear optics correction can be implemented with these limitations. For stage-1, we calibrated 90 chromatic sextupoles with with a similar technique like NOECO. First, spurious vertical dispersion was minimized using 15 chromatic skew quadrupoles, and the global linear coupling was well corrected with another 15 non-dispersive skew quadrupoles. The β seen by the BPMs were measured [12], then $\frac{d\beta}{d\delta}$ on horizontal dispersive orbits through varying the beam energy (i.e., RF frequency). By comparing the measured nonlinear optics against the design model, the chromatic sextupole errors (red bars in Fig. 6) were obtained using the model response matrices, and then incorporated into the lattice model. The updated model would be used as the reference for the stage-2 calibration.

For stage-2, a vertical dispersion wave was generated with 15 dispersive skew quadrupoles to their maximum capacity. Based on the measured dispersion, the 15 skew quadrupole settings and the vertical dispersion at the BPMs were reproduced with the lattice model as illustrated in Fig. 7. To achieve greater accuracy, a large amplitude vertical dispersion wave is preferred. However, it is limited by the capacity of the skew quadrupole power supply. Under the current configuration, ~ 0.05 m is the maximum amplitude that can be generated. The $\frac{d\beta}{d\delta}$ seen by the BPMs were re-measured,

but from hybrid dispersive orbits this time. With the updated lattice model (incorporated with skew quadrupoles and chromatic sextupole errors) as the new reference, 180 harmonic sextupole errors were obtained (blue bars in Fig. 8).
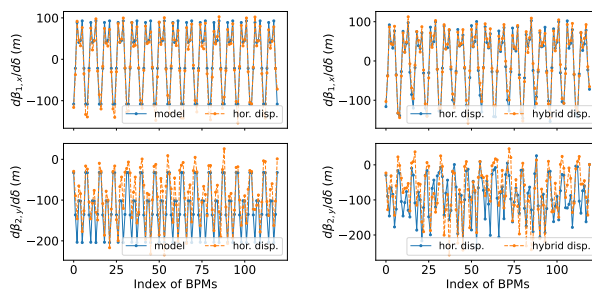
Figure 6: Off-energy optics at two stages. Left: off-energy optics of the ideal model and measurements from horizontal dispersive orbits. Bottom: measured optics from horizontal and hybrid dispersive orbits for harmonic sextupole calibration.
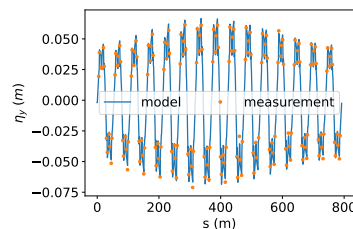
Figure 7: Vertical dispersion seen by the BPMs, and its reproduction with the lattice model.
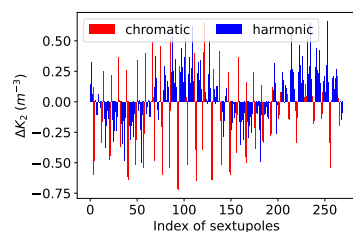
Figure 8: Sextupole errors from the two-stage measurements. The chromatic sextupoles marked with red bars are from the first stage, while the harmonic ones (blue bars) are from the second stage.

When the skew quadrupole polarities are flipped, the vertical dispersion pattern is flipped as well. It turns out that that the off-energy optics dependence on sextupoles in the flipped vertical dispersive orbit remains unchanged when the Ripken parameterization is used. This was used as the validation of the stage-2 measurement. More details can be found in the Ref. [13].

ACKNOWLEDGMENTS

REFERENCES

[1] R. Bartolini *et al.*, "Correction of multiple nonlinear resonances in storage rings", *Phys. Rev. Spec. Top. Accel. Beams*, vol. 11, no. 10, p. 104002, 2008.
doi:10.1103/PhysRevSTAB.11.104002

[2] A. Franchi *et al.*, "First simultaneous measurement of sextupolar and octupolar resonance driving terms in a circular accelerator from turn-by-turn beam position monitor data," *Phys. Rev. Spec. Top. Accel. Beams*, vol. 17, p. 074001, 2014.
doi:10.1103/PhysRevSTAB.17.074001

[3] D. Olsson *et al.*, "Nonlinear optics from off-energy closed orbits", *Phys. Rev. Accel. Beams*, vol. 23, p 102803, 2020.
doi:10.1103/PhysRevAccelBeams.23.102803

[4] S. M. Liuzzo *et al.*, "Lifetime correction using fast-off-energy response matrix measurements", in *Proc. IPAC'22*, Bangkok, Thailand, Jun. 2022, pp. 1409–1411.
doi:10.18429/JACoW-IPAC2022-TUPOMS008

[5] C. Sun *et al.* "Optimization of the ALS-U storage ring lattice" in *Proc. IPAC'16*, Busan, Korea, May 2016, pp. 2959–2961.
doi:10.18429/JACoW-IPAC2016-WEPOW050

[6] Y. Cai *et al.*, "Optimization of chromatic optics in the electron storage ring of the electron-ion collider", *Phy. Rev. Accel. Beams*, vol 25, p. 071001, 2022.
doi:10.1103/PhysRevAccelBeams.25.071001

[7] S. Dierker, "NSLS-II preliminary design report", Brookhaven National Lab, Upton, NY, USA, Tech. Rep. BNL-94744-2007, Nov. 2007.

[8] I. Borchardt *et al.*, "Calculation of beam envelopes in storage rings and transport systems in the presence of transverse space charge effects and coupling," *Zeitschrift für Physik C Particles and Fields*, vol. 39, p. 339, 1988.
doi:10.1007/BF01548283

[9] F. Willeke and G. Ripken, "Methods of beam optics", in *AIP Conf. Proc,*, vol. 184, no. 1, pp. 758–819, 1989.
doi:10.1063/1.38050

[10] F. Schmidt, "MAD-X PTC integration", in *Proc. PAC'05*, TN, USA, 2005, pp. 1272–1274, paper MPPE012.
doi:10.1109/PAC.2005.1590731

[11] M. Borland, "elegant: A flexible SDDS-compliant code for accelerator simulation", Advanced Photon Source, Argonne National Lab, IL, USA, Tech. Rep. LS-287, 2000.

[12] P. Zisopoulos, Y. Papaphilippou, A. Streun, and V. G. Ziemann, "Beam optics measurements through turn by turn beam position data in the SLS", in *Proc. IPAC'13*, Shanghai, China, May 2013, paper WEPEA067, pp. 2663–2665.

[13] Y. Li *et al.*, "Nonlinear optics from hybrid dispersive orbits", arXiv preprint, arXiv:2303.03930, 2023.
doi:10.48550/arXiv.2303.03930

MINIMIZING THE FLUCTUATION OF RESONANCE DRIVING TERMS FOR ANALYZING AND OPTIMIZING THE STORAGE RING DYNAMIC APERTURE

Zhenghe Bai[*], Bingfeng Wei
National Synchrotron Radiation Laboratory, USTC, Hefei, China
Alexandre Loulergue, Laurent S. Nadolski, Ryutaro Nagaoka
Synchrotron SOLEIL, L'Orme des Merisiers, Saint-Aubin, France

Abstract

Minimization of resonance driving terms (RDTs) of nonlinear magnets such as sextupoles and octupoles is an essential condition for enlarging the dynamic aperture (DA) of a storage ring. We recently studied the correlation between minimizing the fluctuation or variation of RDTs along the ring and enlarging the DA. It was found that minimizing the RDT fluctuations is much more effective than minimizing the commonly-used one-turn RDTs in enlarging the DA, and that reducing low-order RDT fluctuations can also help reduce both higher-order RDT fluctuations and higher-order one-turn RDTs. In this paper, the DA analysis based on minimizing RDT fluctuations is further extended. By considering the RDT fluctuations including low- and high-frequency fluctuations, some nonlinear dynamics issues can be explained. The DA optimization is also studied based on numerically minimizing RDT fluctuations using genetic algorithms. Large DAs can be obtained, and the optimization is performed very fast.

INTRODUCTION

Enlarging the dynamic aperture (DA) of a storage ring is critical for improving beam injection efficiency and beam lifetime. At present, the numerical approach based on particle tracking and evolutionary algorithms has been intensively developed and successfully applied to the DA optimization of many storage ring light sources, which can in principle obtain the global best solution. But in this approach, it is hard to provide the physics for further nonlinear analysis and feedback on linear optics adjustment. Minimization of resonance driving terms (RDTs) [1] is a widely-used analytical approach, which has been used for nonlinear analysis and optimization for decades. In this traditional analytical approach, controlling RDTs and amplitude dependent tune shifts (ADTS) can give a larger DA, but it is only a necessary condition. Just recently, we found that minimizing the fluctuation or variation of RDTs along the ring is much more effective than minimizing the commonly-used one-turn RDTs in enlarging the DA [2], which can enhance the capability of this analytical approach.

In this paper, we will first briefly describe the correlation between minimizing RDT fluctuations and enlarging DA, and the physics behind this correlation. Then taking the SOLEIL II storage ring lattice as an example, this paper studies the DA analysis with low- and high-frequency RDT fluctuations, and the DA optimization based on minimizing RDT fluctuations.

ANALYZING DA BASED ON MINIMIZING RDT FLUCTUATIONS

Correlation Between RDT Fluctuations and DA

For the hybrid multi-bend achromat (MBA) lattice and higher-order-achromat based MBA lattice, which have been adopted in many designs of 4th-generation synchrotron light sources, main nonlinear effects caused by sextupoles can be cancelled within a lattice cell. This kind of nonlinear cancellation is more effective than the nonlinear cancellation over some lattice cells, which was used in designing some 3rd-generation light sources. That is why the DAs of some 4th-generation light source designs can allow off-axis injection, even though their emittances are 1~2 orders of magnitude lower than those of 3rd-generation light sources. For the nonlinear cancellation within a lattice cell, the variation of RDTs along the longitudinal position is smaller than the case of the nonlinear cancellation over some lattice cells. This inspires us that reducing the variation or fluctuation of RDTs could be very beneficial for enlarging the DA.

Recently, we studied the correlation between minimizing RDT fluctuations and enlarging DA with different lattices [2]. In our study, the fluctuation of a RDT is quantitatively represented by the average RDT at the positions of sextupoles and octupoles. The results of DA analysis showed that minimizing RDT fluctuations is much more effective than minimizing one-turn RDTs. In other words, a nonlinear solution with smaller RDT fluctuations has a much higher probability of having a larger DA than a solution with smaller one-turn RDTs. In addition, by calculating RDT fluctuations, we can analyze which RDTs are likely to have a relatively large effect on the DA.

Physics Behind Minimizing RDT Fluctuations

We also studied the correlation between low-order RDTs and higher-order RDTs. It was found that reducing low-order RDT fluctuations can also help reduce both higher-order RDT fluctuations and higher-order one-turn RDTs [2]. By this logic, if higher-order RDT fluctuations are reduced, even higher-order RDTs can also be reduced. By using frequency map analysis, it was demonstrated that a 5th-order RDT of the SSRF lattice can be controlled if 3rd-order RDT fluctuations are reduced [2]. Besides, we also found that reducing 3rd-order RDT fluctuations can also help reduce

* baizhe@ustc.edu.cn

ADTS terms [3]. While for the commonly-used one-turn RDTs, even if the 3rd-order one-turn RDTs are smaller, the 4th-order one-turn RDTs can be larger. Figure 1 shows the schematic of the correlation between low- and higher-order RDTs, which is also the physics behind the strong correlation between minimizing RDT fluctuations and enlarging DA.
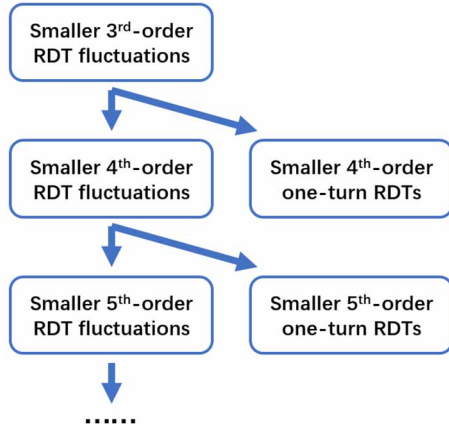

Figure 1: Schematic of the correlation between low- and higher-order RDTs.

Since reducing low-order RDT fluctuations can also reduce higher-order and even higher-order RDTs, we can mainly consider low-order RDT fluctuations if we analyze and optimize DA based on minimizing RDT fluctuations, and it would not be necessary to calculate higher-order RDTs. As we know, for RDTs higher than 4th-order, they are not only more computationally complicated but also more numerous. Note that octupoles are used in many 4th-generation light source designs, so we need to calculate the 4th-order RDT fluctuations for such designs.

Low- and High-frequency RDT Fluctuations

The RDT fluctuations are like waves, and they can be considered to include low- and high-frequency fluctuations. The low-frequency RDT fluctuations are related to the nonlinear cancellation over some lattice cells, and the high-frequency fluctuations are related to the cancellation within a lattice cell. Based on a simplified model, we can use low- and high-frequency RDT fluctuations to analyze some nonlinear dynamics.

Here we take the CDR lattice of SOLEIL II [4] as an example, which has two super-periods with the betatron tunes of 54.2/18.2 (H/V). If the tunes are chosen to be 53.2/17.2, which are close to odd numbers, there will be a rough –I transformation between the two super-periods, which is beneficial for sextupole cancellation and thus the increase in DA. Furthermore, the tunes 53.2/17.2 are smaller than 54.2/18.2, which is also beneficial for nonlinear dynamics. So it is likely that the CDR lattice with the tunes of 53.2/17.2 can have a larger DA. However, the tracking-based optimization showed an opposite result.

The low-frequency RDT fluctuations can be used to explain the above problem. As shown in Fig. 2, the nonlinear

lattice of the whole ring can basically be seen as consisting of mainly four identical parts, and these parts can be further modelled as "macro-particles" located at the middle positions of these parts. A macro-particle represents all nonlinear magnets of a part. In Figure 2, the betatron tunes between these macro-particles are also given. To calculate RDTs, each macro-particle was treated as a thin sextupole, and the values of sextupole strength and beta functions at the positions of macro-particles were all set to 1. The calculated low-frequency RDT fluctuations are shown in Figs. 3 and 4 for the tunes of 54.2/18.2 and 53.2/17.2, respectively. We see that overall the lattice with the tunes of 53.2/17.2 has larger RDT fluctuations, and this is probably why this lattice has a smaller DA in the numerical optimization.
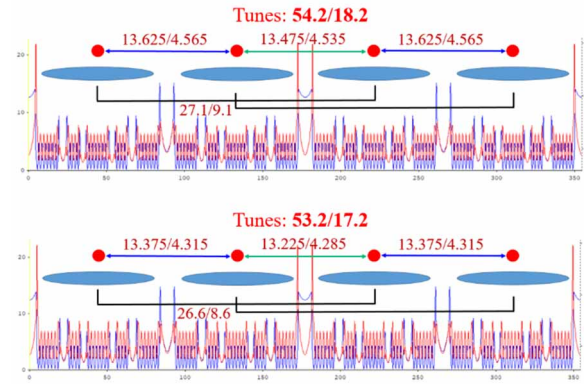
Figure 2: Simplified model for calculating low-frequency RDT fluctuations of the SOLEIL II CDR lattice with betatron tunes of 54.2/18.2 and 53.2/17.2.
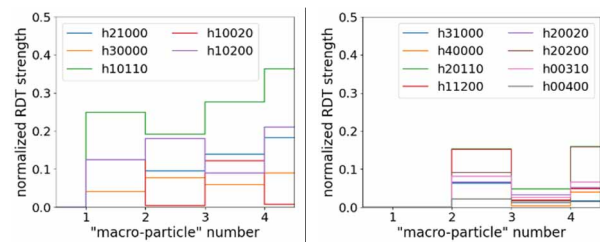
Figure 3: Low-frequency fluctuations of 3rd- and 4th-order RDTs for the betatron tunes of 54.2/18.2.
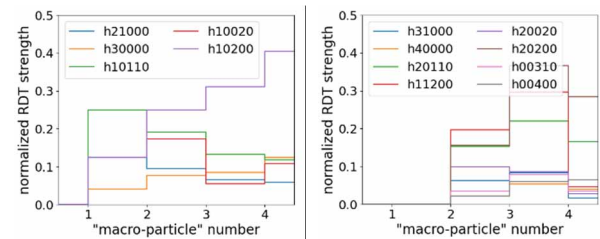
Figure 4: Low-frequency fluctuations of 3rd- and 4th-order RDTs for the betatron tunes of 53.2/17.2.

For the SOLEIL II CDR lattice, it was also found that if the horizontal beta function at the injection straight section and its symmetric straight is increased to a larger value of

about 20 m with the betatron tunes of 54.2/18.2 unchanged, surprisingly the DA is not increased in the numerical optimization. By using low-frequency RDT fluctuations, we also explained the possible reason based on the same simplified model. Note that the tunes between macro-particles are slightly changed when the horizontal beta function is increased. Here we will not show the results of low-frequency RDT fluctuations for this problem.

OPTIMIZING DA BASED ON MINIMIZING RDT FLUCTUATIONS

For the SOLEIL II TDR lattice [5], we preliminarily optimized its DA based on numerically minimizing RDT fluctuations using genetic algorithms. The result showed that large DAs can be obtained, and the optimization was performed very fast as compared to the tracking-based numerical approach. The RDT fluctuations and DA of the reference solution are shown in Figs. 5 and 6, respectively; and Figs. 7 and 8 show the corresponding results of one optimized solution. The reference solution is from Ref. [5]. It can be seen that the optimized solution has smaller RDT fluctuations and its horizontal DA is larger in the negative direction, which is also the direction of beam injection.
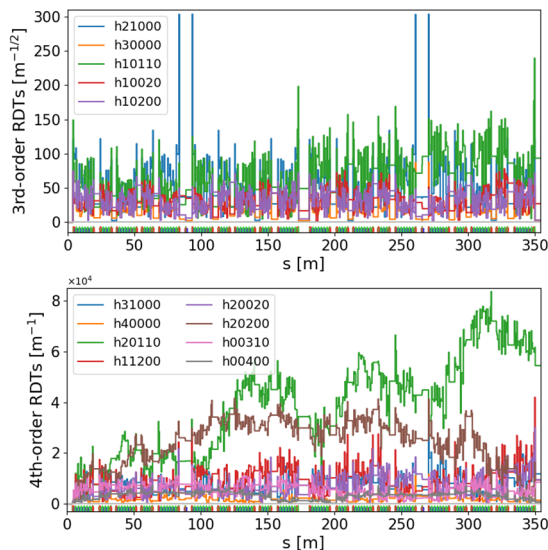

Figure 5: Fluctuation of 3rd- and 4th-order RDTs of the reference solution of the SOLEIL II TDR lattice.
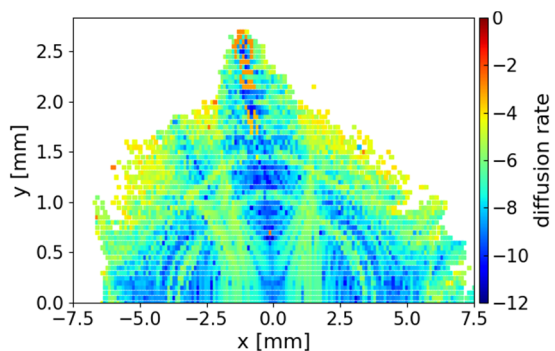
Figure 6: DA of the reference solution of the SOLEIL II TDR lattice, with colour bar indicating diffusion rate.
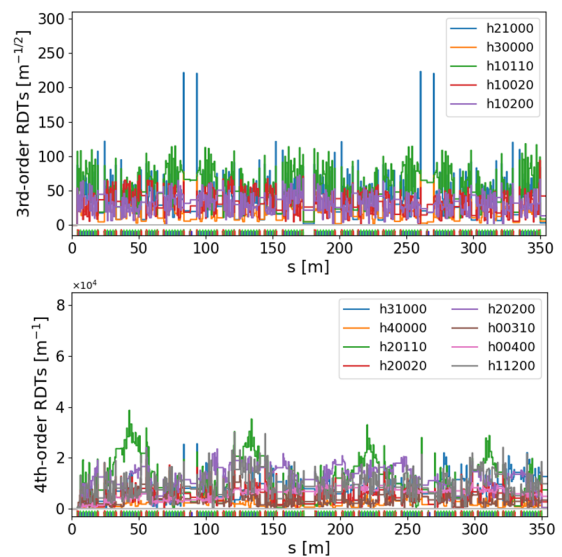
Figure 7: Fluctuation of 3rd- and 4th-order RDTs of one optimized solution.
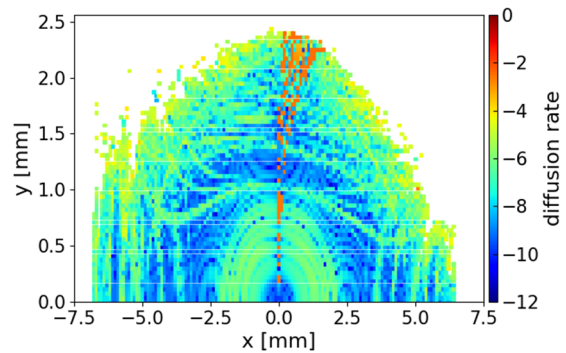
Figure 8: DA of the optimized solution.

In the nonlinear optimization, the tune shifts with momentum also need to be controlled. Based on minimizing RDT fluctuations, the nonlinear optimization of the SOLEIL II lattice, including both DA optimization and control of tune shifts with momentum, is ongoing. Of course, in the vicinity of the optimized solutions, we can further use tracking-based numerical optimization to search for better solutions.

CONCLUSION

Minimizing the fluctuation or variation of RDTs along the longitudinal position is much more effective than minimizing the commonly-used one-turn RDTs in enlarging the DA. The physical reason is that reducing low-order RDT fluctuations can also help reduce both higher-order RDT fluctuations and higher-order one-turn RDTs. The RDT fluctuations can be considered to have low- and high-frequency fluctuations. Based on a simplified model, the nonlinear dynamics problems of the SOLEIL II lattice can be explained by using low-frequency RDT fluctuations. Based on minimizing RDT fluctuations using genetic algorithms, large DA solutions of the SOLEIL II lattice can be found very fast. Further development for the approach of minimizing RDT fluctuations is ongoing.

REFERENCES

[1] J. Bengtsson, "The sextupole scheme for the Swiss Light Source (SLS): an analytic approach", PSI, Villligen, Switzerland, Tech. Note SLS 9/97, 1997.

[2] B. Wei, Z. Bai, J. Tan, L. Wang and G. Feng, "Minimizing the fluctuation of resonance driving terms in dynamic aperture optimization," *Phys. Rev. Accel. Beams*, vol. 26, p. 084001, Aug. 2023.
doi: 10.1103/PhysRevAccelBeams.26.084001

[3] B. Wei, Z. Bai, G. Feng, and J. Tan, "Analyzing and optimizing dynamic aperture based on minimizing the fluctuation of resonance driving terms", presented at the *IPAC'23*, Venice, Italy, May 2023, paper WEPL078, to appear in the proceedings.

[4] A. Loulergue *et al*., "CDR baseline lattice for the upgrade of SOLEIL", in *Proc. IPAC'21*, Campinas, Brazil, May 2021, pp. 1485-1488.
doi:10.18429/JACoW-IPAC2021-TUPAB054

[5] A. Loulergue et al., "TDR baseline lattice for SOLEIL II upgrade project", presented at the *IPAC'23*, Venice, Italy, May 2023, paper MOPM031, to appear in the proceedings.

SINGLE LONGITUDINAL MODE GENERATION IN SLIPPAGE-DOMINATED TAPERED UNDULATOR SASE SOFT X-RAY FEL

D. C. Nguyen†, C. Mayes, G. Stupakov, W. Lou, B. Dunham, xLight Inc., Palo Alto, CA, USA

Abstract

We study a short-pulsed SASE method called Slippage-dominated Tapered Undulator (STU) SASE to produce single longitudinal mode in each soft X-ray SASE pulse driven by an electron bunch with 10 fs bunch length and 16 pC bunch charge. STU-SASE uses both normal and inverse tapered undulators to select a single spike and increase its coherence length. Numerical simulations showing single-mode generation and narrow-lined spectra in a soft X-ray SASE FEL without seeding are presented.

SOFT X-RAY (BEUV) LITHOGRAPHY

A paradigm shift in light source utilization is required for the continuation of Moore's law scaling, the prediction that the number of transistors in an integrated circuit doubles every two years. To obtain smaller feature sizes, BEUV (beyond EUV) lithography at 6.x nm has been proposed [1]. SASE FELs can generate high-power soft X-rays, but they must produce spectrally narrow output to work with the narrow reflectivity curve of molybdenum-boron (MoB) multilayer mirrors [2]. While many ideas have been proposed to achieve fully coherent and narrow-band X-ray FELs [3, 4], only harmonic seeding [5] and self-seeding [6] have been experimentally demonstrated to narrow the output spectra of soft X-ray FELs. In this paper, we study a linac-based SASE FEL designed to produce substantial soft X-ray pulse energies and sufficiently narrow spectra to meet the need of BEUV lithography.

SINGLE-SPIKE SASE FEL

Slippage-dominated, Tapered Undulator SASE

It is well known that the coherence length in a SASE FEL is the slippage length over one gain length in the exponential regime. At saturation, the slippage length increases but the coherence length remains the same. In the tapered undulator where the FEL power continues to grow, the coherence length becomes longer by slippage in the tapered undulator length. Previous simulations using pC electron bunches with sub-fs electron bunch length have shown the possibility of generating a single spike (longitudinal mode) in each SASE pulse [7]. A more recent study suggests using an inverse taper to produce sub-fs X-ray pulses [8]. For many FELs, the electron bunch charge needs to be greater than a few pC and the FEL pulse energy at least 10 μJ. In this paper, we study a new method to generate single-spike SASE X-ray pulses based on slippage-induced lengthening of the coherence length, and single-mode selection via amplification and absorption in the tapered undulators of a SASE FEL without seeding.

---
† dinh@xlight.com

The single mode selection is illustrated in the 2D plot of a single SASE spike in log-scale color codes (see Fig. 1). Slippage, as measured by the tilt of the radiation spike, is $\lambda/3\lambda_u$ before the taper start and increases to the full value of λ/λ_u in the taper. A second spike appears right before the taper start but is not amplified in the tapered sections.
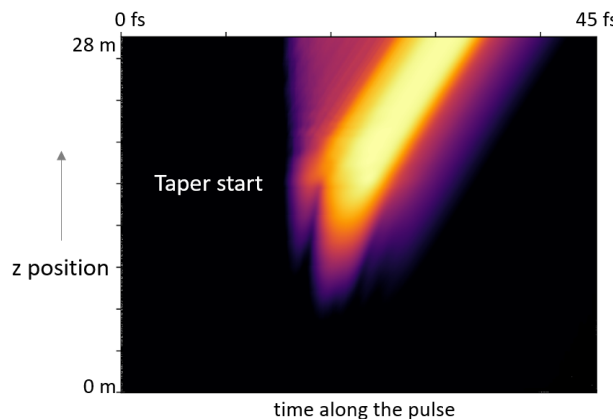
Figure 1: Evolution of a single spike along z and time.

We use the FEL code Genesis 1.3 version 4 [9] to model the STU-SASE FEL process. The electron beam, undulator and FEL parameters are listed in Table 1 below.

Table 1: STU-SASE FEL Parameters

Parameter	Value
Beam energy	1.333 GeV
Peak current	1.5 kA
Gaussian bunch FWHM	10 fs
Bunch charge	16 pC
Norm. emittance in x and y	1 μm, 0.5 μm
Undulator period	2.6 cm
Untapered undulator length	17 m
Untapered undulator K_0	2.22
Tapered undulator length	13 m
ΔK per taper section	0.02
Photon energy	186 eV
FEL ρ parameter	0.002
Average FEL pulse energy	40 μJ

Single-mode Generation in STU-SASE

Both normal and inverse tapered undulator are used in the single longitudinal mode generation. Figure 2 shows the energy phase space at the exit of the untapered undulators and the resonant energies of the untapered (black) and tapered (green=normal; red=inverse) undulator sections.
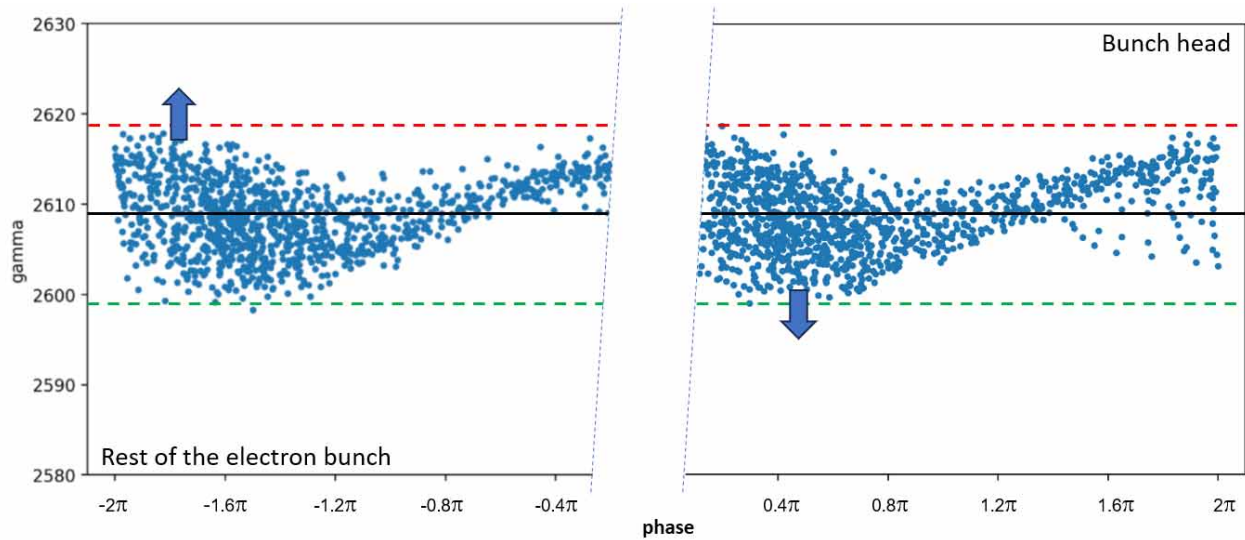
Figure 2: Energy-phase space of electrons exiting the untapered undulators. The normal taper (green) amplifies the first spike at the bunch head (right) and the inverse taper (red) attenuates the subsequent spikes in the rest of the bunch (left).

For $\Delta K \ll K_0$, the resonant energies (in gamma) of the tapered undulator sections are approximately given by

$$\gamma_{taper} \cong \sqrt{\frac{\lambda_u}{2\lambda}\left(1 + \frac{K_0^2}{2} \mp K_0 \Delta K\right)} \qquad (1)$$

where λ_u is the undulator period, λ the FEL wavelength, K_0 the untapered undulator dimensionless parameter, and the sign is – for normal or + for inverse taper. Figure 3 shows the plot of FEL pulse energy, beam radii in x and y, and the layout of the normal and inverse taper sections.

The single-mode generation occurs as the back of the first spike is amplified in the normal taper sections while the front slips ahead of the electron bunch. The spike coherence length is equal to the slippage length in the SASE exponential gain length and the taper sections, as given by

$$l_c = \frac{\lambda}{2\sqrt{3}\rho} + N_{taper}\lambda \qquad (2)$$

The inverse taper absorbs FEL power and suppresses the growth of subsequent SASE spikes in the rest of the bunch.

Simulation results for SASE with untapered undulators are shown in Fig. 4a (top) and simulations results for STU-SASE with untapered undulators followed by normal and inverse taper sections are shown in Fig. 4b (bottom). The single spike in STU-SASE (Fig. 4b) exhibits longer coherence length than any of the six SASE spikes in Fig. 4a.
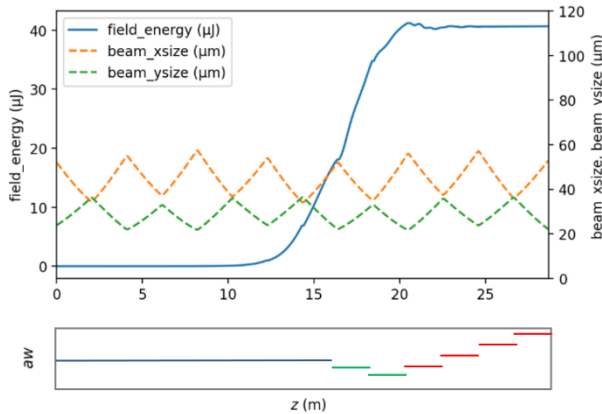
Figure 3: (top) Plots of radiation pulse energy (blue), and electron beam radii in x (orange) and y (green) along z; (bottom) a plot of the undulator K parameter along z.
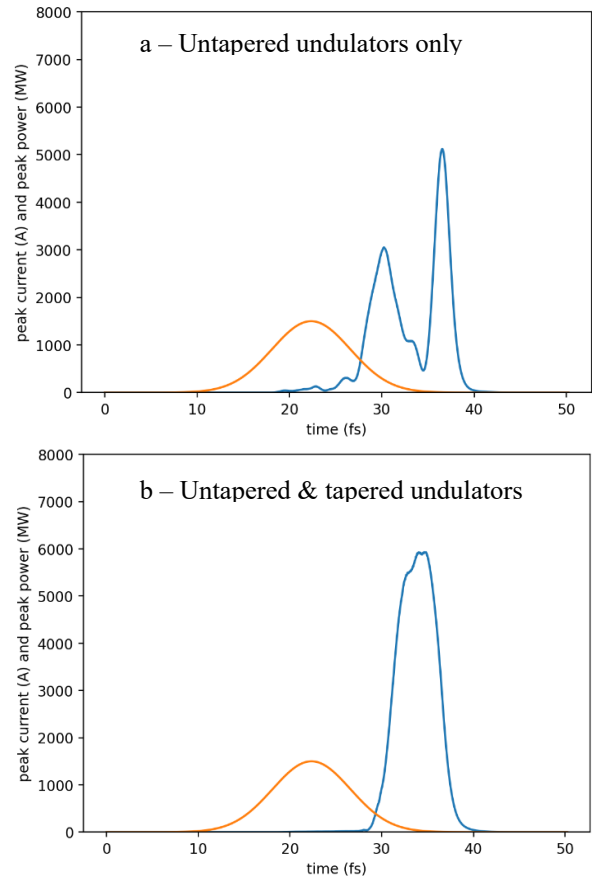
Figure 4: Plots of peak current (orange) and FEL power in MW (blue) vs. time at z = 28 m; (4a) 14 untapered sections, (4b) 8 untapered plus 2 normal and 4 inverse tapers.

Pulse-to-pulse Amplitude Fluctuations

The single-longitudinal-mode SASE is evident by the increase in amplitude fluctuations of STU-SASE pulses in the exponential region. Figure 5 plots the pulse energy as a function of z for 50 simulation runs with the same parameters but different start-up seeds. At z = 10 m, the average of pulse energy is 33 nJ with a standard deviation of 20 nJ.
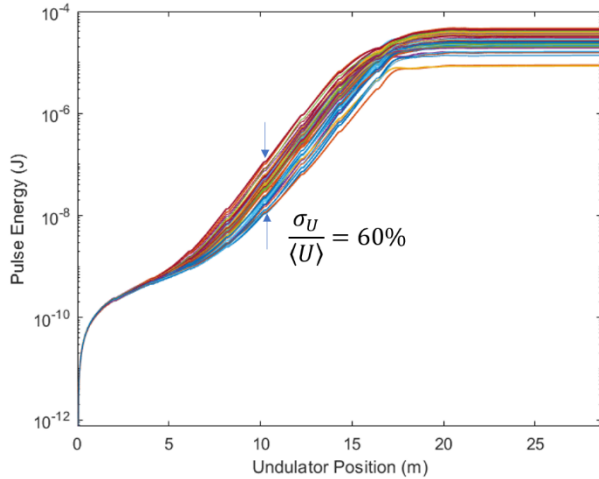
Figure 5: Semi-log plots of pulse energy of 50 simulation runs with different start-up seeds versus z position.

We analysed the amplitude of 50 simulation runs in the exponential regime and plotted the histogram of the pulse energy, superimposed with the plot of probability of these events based on Poisson statistics (Fig. 6) in the exponential regime. The plot with the best fit to the histogram is for M = 1.5, consistent with the observation of one or at most two longitudinal modes in each SASE pulse.
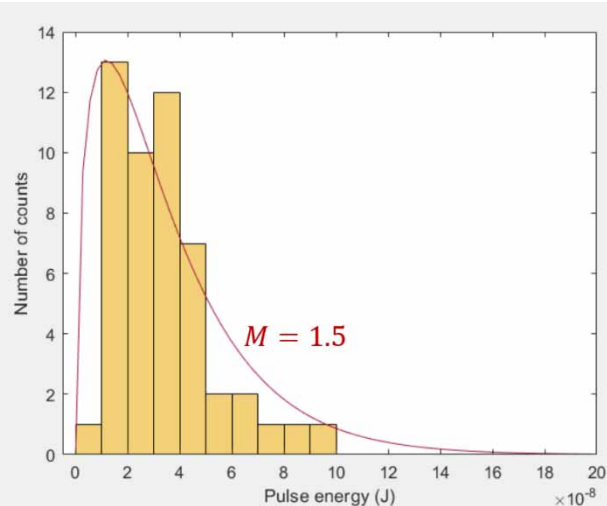

Figure 6: Histogram of pulse energy in the exponential regime at z = 10 m, superimposed with the calculated probability based on Poisson statistics with M = 1.5.

Output Spectral Linewidth

The improved temporal coherence and amplitude fluctuations between one and two longitudinal modes are also visible in the spectra of individual STU-SASE pulses. Figure 7 shows the individual spectrum and the average of

thirty STU-SASE spectra. In Fig. 8, the normalized spectra of 50 runs are plotted against the reflectivity curve of MoB (black). Most of the STU-SASE power is inside the narrow reflectivity curve of MoB multilayer mirrors.
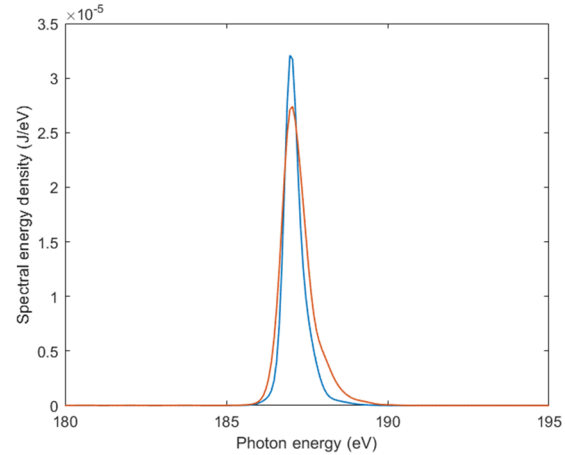
Figure 7: Output spectra from a single STU-SASE pulse (blue) and average of thirty pulses (orange).
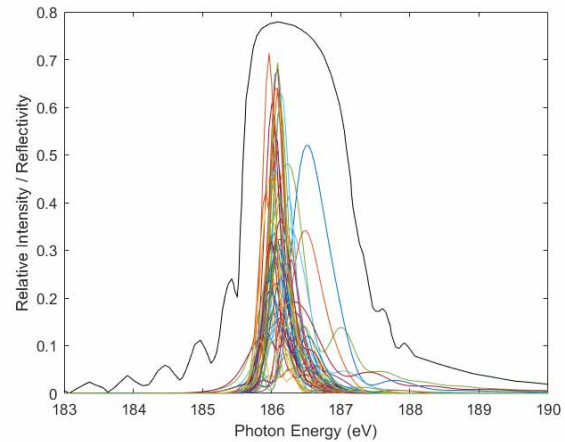
Figure 8: Normalized spectra from 50 simulation runs and a plot of MoB reflectivity vs. photon energy (black).

CONCLUSION

In conclusion, we show with Genesis simulations that the STU-SASE concept can produce a single longitudinal mode and deliver narrow spectra from a SASE FEL without seeding. Using both normal and inverse tapered undulators, the STU-SASE process can select a single longitudinal mode by amplifying the first longitudinal mode in the normal taper sections as it slips ahead of the electron bunch and suppressing the subsequent modes in the inverse tapered sections. The single longitudinal mode exhibits longer coherence length by virtue of the additional slippage length in the normal taper sections. The longer coherence length results in output spectra with spectral linewidth narrower than the SASE gain bandwidth. We show the STU-SASE spectra will fit within the reflectivity curve of the MoB multilayer mirrors.

REFERENCES

[1] N. Mojarad, J. Gobrecht, and Y. Ekinci, "Beyond EUV lithography: a comparative study of efficient photoresists' performance." *Sci. Rep.*, vol. 5, p. 9235, 2015. doi:10.1038/srep09235

[2] P. C. Uzoma, S. Shabbir, H. Hu, P. C. Okonkwo, and O. V. Penkov, "Multilayer Reflective Coatings for BEUV Lithography: A Review," *Nanomaterials*, vol. 11, no. 11, p. 2782, Oct. 2021. doi:10.3390/nano11112782

[3] B. W. J. McNeil, N. R. Thompson, and D. J. Dunning, "Transform-limited x-ray pulse generation from a high-brightness self-amplified spontaneous-emission free-electron laser," *Phys. Rev. Lett.*, vol. 110, p. 134802, Mar. 2013. doi:10.1103/PhysRevLett.110.134802

[4] D. Xiang, Y. Ding, Z. Huang, and H. Deng "Purified self-amplified spontaneous emission free-electron lasers with slippage-boosted filtering." *Phys. Rev. Spec. Top. Accel. Beams*, vol. 16 p. 010703, Jan 2013. doi:10.1103/PhysRevSTAB.16.010703

[5] E. Allaria *et al.,* "Two-stage seeded soft-X-ray free-electron laser." *Nat. Photonics*, vol. 7, pp. 913–918, 2013. doi:10.1038/nphoton.2013.277

[6] D. Ratner *et al.*, "Experimental demonstration of a soft x-ray self-seeded Free-Electron Laser." *Phys. Rev. Lett.*, vol. 114, p. 050801, 2015. doi:10.1103/PhysRevLett.114.054801

[7] S. Reiche, P. Musumeci, C. Pellegrini, J. B. Rosenzweig, "Development of ultra-short pulse, single coherent spike for SASE x-ray FELs." *Nucl. Instrum. Methods Phys. Res., Sect. A*, vol. 593 pp. 45-58, 2008. doi:10.1016/j.nima.2008.04.061

[8] E. Schneidmiller, M. Dreimann, M. Kuhlmann, J. Rönsch-Schulenburg, and H. Zacharias, "Generation of ultrashort pulses in XUV and x-ray FELs via an excessive reverse undulator taper," *Photonics*, vol. 10, no. 6, p. 653, 2023. doi:10.3390/photonics10060653

[9] Genesis, https://github.com/svenreiche/Genesis-1.3-Version4

COMPACT HOM-DAMPED RF CAVITY FOR A NEXT GENERATION LIGHT SOURCE*

H. Ego[†,1], KEK, Oho, Tsukuba, Ibaraki, Japan
T. Inagaki, H. Tanaka, RIKEN SPring-8 Center, Sayo, Hyogo, Japan
T. Asaka, N. Nishimori, QST, Sendai, Miyagi, Japan
T. Ohshima[1], T. Tomai, H. Yamaguchi[1], JASRI, Sayo, Hyogo, Japan
[1]also at QST, Japan

Abstract

A beam-accelerating RF cavity with a new HOM-damping structure was designed in order to suppress coupled-bunch instabilities in a next generation light source with an ultra-low emittance and supplying X-rays approaching their diffraction limits. The TM020 mode at 508.58 MHz is selected as a beam-accelerating mode because it has a high *Q*-value of 60,000 and a shunt impedance sufficient for beam acceleration and brings a compact HOM-damping structure to the cavity differently from massive types of cavities with waveguides or pipes extracting HOM power. Two shallow slots are cut on the cavity inner wall and materials absorbing RF waves are directly fitted into them. They work as HOM dampers without affecting the RF properties of the beam-accelerating mode. A prototype cavity of OFHC copper was fabricated to demonstrate the HOM-damping and generating an accelerating voltage of 900 kV in the cavity. Since the cavity was successful in operation up to 135 kW, the feasibility of both the high-power operation and the damping structure was proved. Four actual cavities were produced and installed to the new 3-GeV synchrotron radiation facility, NanoTerasu in Japan.

INTRODUCTION

Coupled-bunch instability (CBI) arising from high coupling impedances of higher-order modes (HOMs) in beam-accelerating RF cavities is one of the serious problems in the next generation storage ring. Therefore, RF cavities against the CBIs are indispensable for stable beam operation of the ring. We developed a new and compact type of HOM-damped cavity shown in Fig. 1 [1-3]. The beam-accelerating resonant mode of the cavity is the TM020 mode. This mode enables HOM-absorbing materials to be directly embedded into the cavity body without using special waveguides or pipes usually occupying large spaces. Our HOM-damping structure makes the cavity body extremely compact and reduces the spaces occupied with the cavities in the storage ring packed in with accelerator components.

In the next section, we show the cavity structure, its RF characteristics and the HOM-damping mechanism. The last section represents the measurements on RF characteristics of the fabricated prototype cavity and the results of its high-power tests up to 135 kW.

Figure 1: RF cavity with the compact HOM-damping structure.

HOM-DAMPING MECHANISM

Cavity Structure

Figure 2 shows the schematic cross-sectional view of the cavity with the HOM-damping structure. The cavity has an inner diameter of 1040.4 mm and a beam-gap length of 206 mm. The cavity is a reentrant type with nose cones around the beam gap on the cavity inner wall. The cavity length between the beam-pipe flanges is 452 mm and we can accommodate plural cavities in short straight sections in a storage ring.

Two slots are opened in the cavity inner wall along the nodes of the axially symmetric magnetic fields of the TM020 mode. 16 HOM dampers with 12 ferrite bars shown in Fig. 3 are directly bolted to the cavity body and the ferrite bars are exposed in the slots.
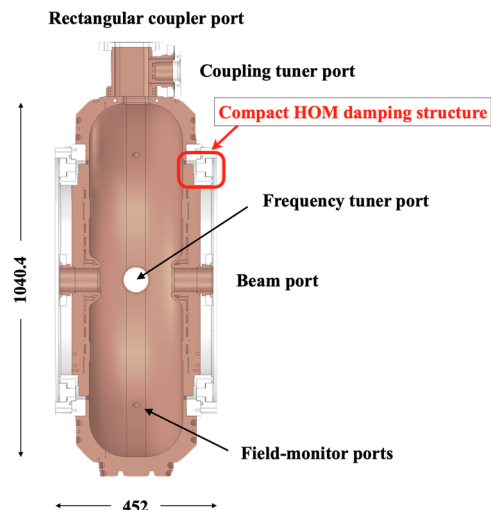

Figure 2: Cross-sectional view of the cavity.
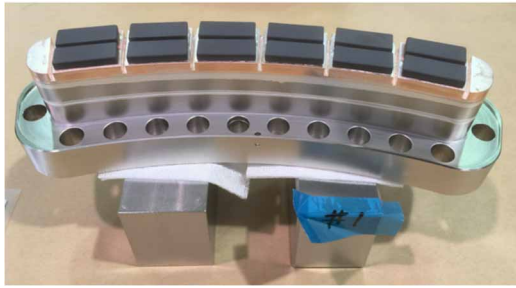
Figure 3: HOM damper with 12 ferrite bars.

Figure 4 shows the cavity assembly and cut-off view schematics. The cavity was made of class-1 OFHC copper (ASTMF68 class-1). The cavity consists of three parts: a main body and two plates with the nose cones and the beam pipes. The plate is called the nose-cone plate in this paper. The nose-cone plates have SUS flanges which are tightened to the main body by bolts and are easily detachable from the main body. Aluminum U-tight rings are used for vacuum sealing. The HOM-damping slots are formed between the nose-cone plate and the body flange as shown in Fig. 2. The flange of each nose-cone plate has eight bending slots to attach the HOM dampers by using bolts. This structure is capable of reassembling with some merits: it is easy to precisely adjust the resonant frequency of the TM020 mode by machining the inner surfaces of the nose-cone plates even after brazing the main body: the inner surface can be inspected after high-power operation: the HOM dampers can be replaced with any other ones improved. The RF coupler port is rectangular with dimensions of 381 mm x 100 mm and has a rectangular iris with dimensions of 100 mm x 75 mm in the common wall of the cavity as shown in Fig. 2. A cylindrical port with a diameter of 73 mm is opened in front of the iris. The degree of cavity coupling can be changed by using a movable cylindrical plunger installed in the port. The plunger is called a coupling tuner [4].
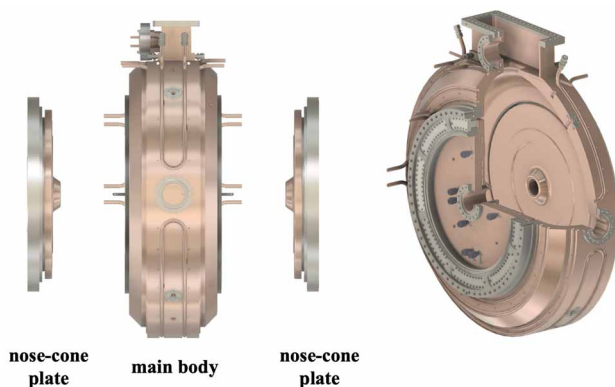
Figure 4: Schematics of the cavity assembly (left) and the cut-off view (right).

HOM-damping Structure

The RF characteristics of the cavity were estimated by using the simulation codes, MAFIA, CST STUDIO [5] and ANSYS HFSS [6]. The resonant frequency was set at 508.58 MHz because of the operating frequency of the

high-power facilities in the RIKEN SPring-8 promoting the R&D on the cavity [3, 7]. The shunt impedance, R_a, and unloaded Q-value, Q_a, are 6.8 MΩ and 60,300, respectively. The gap voltage or beam accelerating voltage, V_a, is defined in this paper as

$$V_a = \sqrt{R_a P_w} , \qquad (1)$$

where P_w is the wall-loss power in the cavity. V_a of 900 kV is assumed in our design. R_a/Q_a is set at a low value of 113 Ω and reduces the transient cavity-voltage modulation arising from bunch gaps provided to avoid beam instabilities such as ion trap in the storage ring [8, 9]. Figure 5 shows the electromagnetic field distributions in the TM020 mode. Since the HOM-damping slots are located along the nodes of the magnetic fields, there is no magnetic field near and inside the slots and only electric fields are present in front of the slots. The electric fields are parallel to the slots and are also unable to enter the slots. Therefore, the TM020 mode is not affected by the slots.
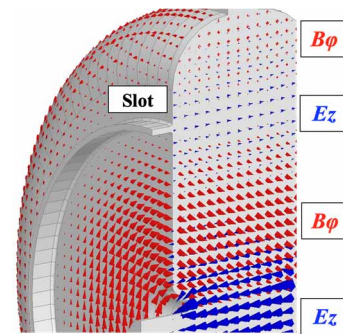
Figure 5: Field distributions of the TM020 mode. Blue and red arrows show the electric and magnetic fields, respectively.

The cavity is operated in the TM020 mode and has lower-order resonant modes (LOMs) with high coupling impedances such as TM010, TM011, TM110 and so on. Monopole and dipole HOMs and LOMs have the field distributions different from those of the TM020 mode. Figure 6 shows the electromagnetic fields of the TM110 and TM011 modes, for example. Their magnetic fields enter the slots and attenuate markedly by installing materials absorbing RF waves in the slots. Figure 7 shows the estimated distributions of coupling impedances and Q-values of the monopole and dipole modes below the beam-pipe cutoff frequency of 3.3 GHz in TM mode. The red block in Fig. 7(a) indicates the RF absorber. Black and red dots in Figs. 7(b) and (c) represent the cases without and with the RF absorber in the slot, respectively. In this estimation, the electrical conductivity of the RF absorber was assumed to be 5.8 S/m. The Q-values of the modes except the TM020 mode are markedly attenuated by the RF absorber. The coupling impedances are reduced in the similar way. Resultantly, the slot with the RF absorber becomes the compact HOM-damping structure.
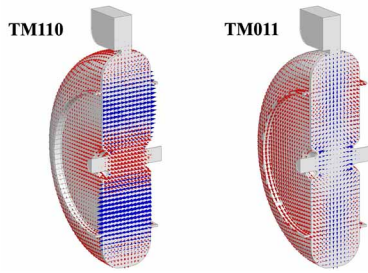
Figure 6: Field distributions of the TM110 mode (left) and the TM011 mode (right).
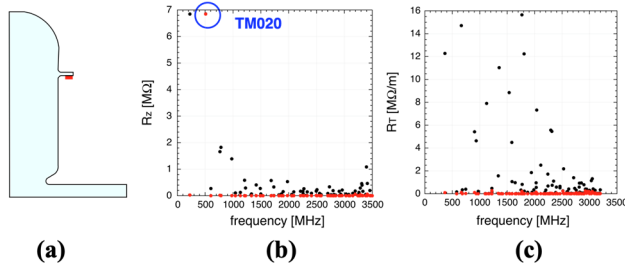
Figure 7: (a) Cavity simulation model, (b) impedance distributions of (b) monopole modes and (c) dipole modes.

DEMONSTRATIONS

HOM-damping Performance

In the actual operation of beam acceleration, we will install the HOM dampers in all slots. In the tests of the design demonstration, we mounted the four HOM dampers to each nose-cone plate. The resonant frequency and Q_a of the TM020 mode and the harmful resonant modes with high impedances were measured. Some results are shown in Table 1. The deterioration in Q_a of the TM020 mode was subtle. On the other hand, the Q-values of the harmful modes were markedly reduced. Therefore, the HOM-damping mechanism works as designed. Further attenuation is expected when all slots are full of HOM dampers.

Table 1: Measured RF Properties with the HOM Dampers

Mode	Frequency [MHz]	Q
TM020	508.3	59,100
TM010	222.4	420
TM110	363.6	760

High-power Operation

The cavity baking was processed by flowing hot water through the cooling channels of the cavity before feeding high power to the cavity. Although it was planned to raise the water temperature up to 150°C, the temperature raising was stopped at 80°C due to malfunctions of our heater unit.

RF high-power tests were performed by placing the cavity in a concrete shield of the SPring-8 RF test bench. The cavity was connected to the WR-1500 system via an E-bend vacuum waveguide, a ceramics window of plate type [10] and a waveguide transformer. At first, bending flanges without a ferrite bar were attached to the cavity and high-power tests were conducted. Vacuum deteriorations were repeated for about 12 hours at less than 1 kW. A lot of

power reflection happened around 20 kW, 70 kW, and 100 kW, but they improved as progress of RF conditioning and finally reached continuous operation of 135 kW. Since the cavity without a HOM damper became to stably operate up to a power of 135 kW, we carried out the power feeding to the cavity with the HOM dampers in four slots of each nose-cone plate. After RF conditioning for about 58 hours, the cavity with the HOM dampers was able to stably operate up to 135 kW.

SUMMARY

The RF cavity with a compact and effective HOM-damping structure using the TM020 mode was newly designed. The manufactured cavity demonstrated the RF properties of the TM020 mode as we expected. The HOM dampers with ferrite bars were installed in the cavity and markedly attenuated the Q-values of the HOMs and LOMs related to CBIs. This represents that the newly designed compact HOM damping mechanism works effectively. Four cavities revised from these research results were installed and have begun to accelerate a beam in the 3 GeV storage ring of NanoTerasu [11-13].

REFERENCES

[1] T. Watanabe and H. Tanaka, "SPring-8 upgrade project; accelerator redesigned and restarted", *Synchrotron Radiat. News*, vol. 36, no. 1, pp. 3-6, Apr. 2023. doi:10.1080/08940886.2023.2186117

[2] T. Watanabe *et al.*, "Updates on hardware developments for SPring-8-II", in *Proc. IPAC'18*, Vancouver, BC, Canada, Apr.-May 2018, pp. 4209-4212. doi:10.18429/JACoW-IPAC2018-THPMF061

[3] SPring-8-II Conceptual Design Report, RIKEN SPring-8 Center, Japan, Nov. 2014, http://rsc.riken.jp/eng/pdf/SPring-8-II.pdf

[4] H. Ego, "RF input coupler with a coupling tuner for an RF acceleration cavity", *Nucl. Instrum. Methods Phys. Res., Sect. A,* vol. 564, no. 1, pp. 74-80, 2006. doi:10.1016/j.nima.2006.04.076

[5] CST Studio Suite, https://www.3ds.com/products-services/simulia/products/cst-studio-suite/

[6] Ansys, https://ansys.com/

[7] Spring-8, http://www.spring8.or.jp/en/

[8] Y. Yamazaki, M. Kihara, and H. Kobayakawa, "Partially filled multi-bunch mode operation of the Photon Factory electron storage ring and cure of the vertical instability", KEK, Tsukuba, Ibaraki, Japan, KEK Rep. 83-17, Aug. 1983.

[9] S. Sakanaka, "Investigation of bunch-gap effects for curing ion trapping in energy recovery linacs", *Proc. ERL'07*, Daresbury, UK, May 2007, pp. 41-44.

[10] H. Ego *et al.*, *Proc. 9th Annual Meeting of Particle Accel. Soc. of Japan*, Toyonaka, Aug. 8-11, 2012, pp. 154-157.

[11] N. Nishimori, "A new compact 3 GeV light source in Japan", in *Proc. IPAC'22*, Bangkok, Thailand, Jun. 2022, pp. 2402-2406. doi:10.18429/JACoW-IPAC2022-THIXSP1

[12] T. Inagaki, *et al*, "High-power tests of the compactly HOM-damped TM020-cavities for a next generation light source", presented at IPAC'23, Venice, Italy, May 2023, paper WEODC3, to appear in the proceedings.

[13] NanoTerasu, https://www.nanoterasu.jp

Pyapas: A NEW FRAMEWORK FOR HLA DEVELOPMENT AT HEPS

Xiaohan Lu, Hongfei Ji, Yi Jiao, Jingyi Li, Nan Li, Cai Meng, Yuemei Peng,
Haisheng Xu, Daheng Ji, YuanYuan Wei, Jinyu Wan, Gang Xu, Yaliang Zhao
Institute of High Energy Physics, Chinese Academy of Sciences, Beijing, China

Abstract

The High Energy Photon Source (HEPS) is a 6 GeV, 1.3 km, 4th generation storage ring light source being built in Beijing, China. Compared to third-generation light sources, HEPS, as a fourth-generation light source, has a one to two orders of magnitude reduction in emittance. The number of magnets correspondingly increases by an order of magnitude, and there are higher demands for control precision. All of these pose new challenges for the development of HLA. The development of high-level applications (HLAs) for HEPS started in early 2021. A brand new framework named PYthon-based Accelerator Physics Application Set (*Pyapas*) was developed for HLA development. This paper will introduce the design of *Pyapas* and its application at HEPS.

INTRODUCTION

The High Energy Photon Source (HEPS) is a 6 GeV, 1.3 km, fourth-generation light source [1]. The construction started in Beijing, China, in the middle of 2019, and upon completion, it is expected one of world's brightest light source. The beam commissioning of Linac began in March 9 of this year, and the process acceptance of Linac completed three months later. Upon completion of a brief interlude for adjustments, the beam commissioning of booster started. The energy of booster successfully ramped to 6 GeV two weeks later [2]. As a fourth-generation light source, HEPS adopts a compact multi-bend achromat lattice design for the storage ring and uses a large number of combined magnets [3, 4]. The cross-talk effect between magnetic fields is significant, and the number of magnets has increased by an order of magnitude compared to the third-generation light sources, which introduce new challenges and requirements for tuning beam parameters.

Existing HLA development frameworks are mostly monolithic and not easily scalable [5, 6], which cannot meet the needs of HEPS' complex parameter tuning. And porting the existing framework is almost as much work as building it from scratch. In order to meet the requirements of HEPS, we decided to design a new HLA framework based on Python named *Pyapas* [7]. It adopts modular design philosophy to increase overall scalability. A dual-layer physical model module has been designed to meet the replaceability of online calculation models. In addition, the communication module, database module, and server module have all been specially designed to meet the needs of adjusting a large amount of parameters.

Based on *Pyapas*, we have completed the development of HLAs for the Linac [8] and successfully applied them to

---

beam commissioning [9], verifying the practicality and reliability of *Pyapas*. The development of HLAs for the booster and transfer lines [10, 11] has also been completed, and the development for the storage ring is nearing completion. This paper will briefly introduce the design of *Pyapas* and the progress of the development of HLAs for HEPS.

FRAMEWORK DESIGN

For a framework to develop HLA, the basic abilities include hardware communication, user interface development, database connection et.al. But for the high level physical application (HLPA), physical model and physical algorithm are more crucial part. Therefore the core of *Pyapas* is a dual-layer physical module. As shown in Fig. 1, there are two independent layers: device mapping layer and physical model layer. The device mapping layer corresponds to the real machine and is responsible for communicating with the machine, while the physical model [12] layer is responsible for online calculation based on the information read from the device mapping layer. The device mapping layer and the physical model layer are deeply decoupled and connected by connector, which only need to specify information such as the calculation model class name, unit conversion, and parameter name that needs to be called in the connector. This makes it very convenient to switch between different calculation models to meet the online calculation needs in different scenarios.
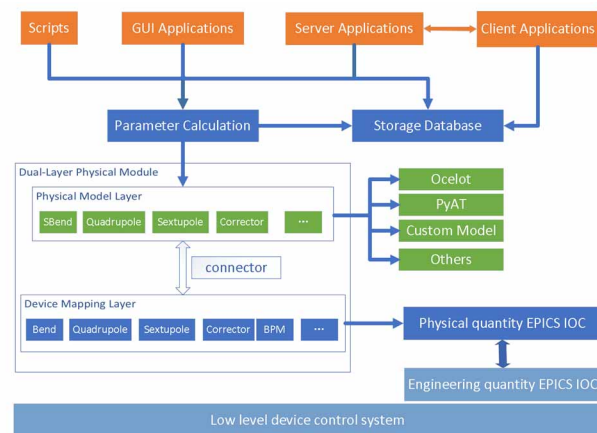
Figure 1: Pyapas framework.

In addition, to improve the scalability of the framework and reduce the development difficulty of developers, we adopt a modular design. Specifically, we analyze the functions involved in HLAs, and divide them into different modules for separate development. The modules are loosely coupled and specific application development is carried out through simple interface calls, which increases

the overall maintainability and scalability of the framework. For a framework to develop physical application, *Pyapas* is based on physical quantities, all the variables are physical quantities which make the applications more intuitive for physicists. To complement the use of physical quantities-based applications, a conversion system utilizing SoftIOCs has been implemented. In the communication module, singleton factory pattern is used to avoid duplicate creation of channel connections. In combination with Qt's signal-slot mechanism, non-blocking communication connections are established, greatly improving the ability to handle large parameter scales. Moreover, the design of C/S architecture modules and database rapid creation and management modules can help developers in physics to quickly develop complex HLAs, further enhancing the applicability of *Pyapas*.

HLAS DEVELOPMENT

Before the commencement of the specific HLAs development, a multi-user virtual accelerator (MUVA) was developed as the testing platform. As shown in Fig. 2, this is the snapshot of Linac MUVA, it can simulate the beam profile, orbit, energy, Twiss parameters etc. All the information were disseminated via a full feature EPICS IOC, acting as a real machine environment.

The MUVA system can add virous errors and unexpected scenarios to meet the testing requirements of specific HLAs. Another novel function of MUVA is the multi-user feature, that means on the same network or same server lots of VA could be launched without conflicting with each other. One HLA can connect to different VA instance with the special prefix name. This feature is very useful when a team develops HLAs on the same network area or same cluster.
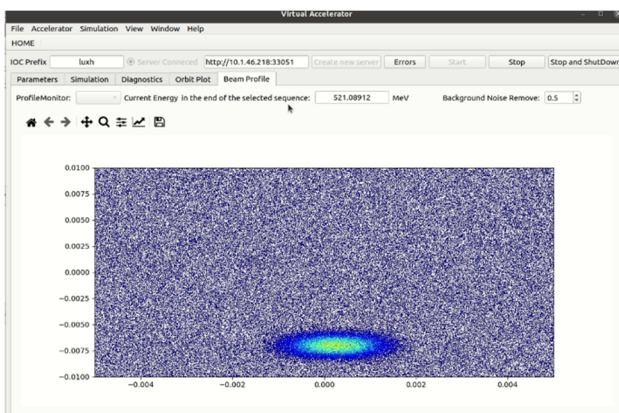
Figure 2: The virtual accelerator for testing the HLA.

The beam commissioning of the Linac started in the middle of March, 2023. All the HLAs for the Linac are based on *Pyapas*, including orbit correction, emittance measurement, energy spread and energy measurement, phase scan, and physics-based control application [13]. As a result of the previous comprehensive preparations, full beam transmission was achieved quickly, and the design energy was reached. The physics-based control program played a crucial role in this achievement.

After a brief respite, we started the beam commissioning of booster. After three days of concerted effort, we got the synchrotron light signal, two weeks later, the beam energy was ramping to 6 GeV. The beam commissioning is still underway, moving towards the machine's design objectives.
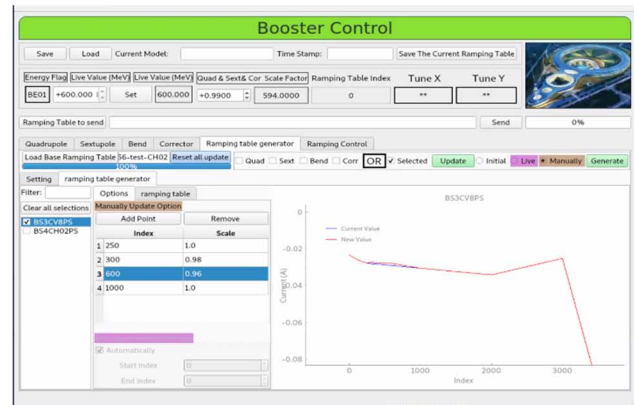
Figure 3: Booster Control based on physical quantities.

The HLAs play import role during the beam commissioning, including global orbit correction, local orbit correction, dispersion measurement, physics-based booster control (Fig. 3), chromaticity measurement, first-turn beam analysis, and more.

The HLAs for the storage ring are currently being developed and soon to be completed.

CONCLUSION

To meet the beam commissioning requirements of the HEPS, a brand framework *Pyapas* had been designed for HLA development. It is a full-featured development framework specifically designed for high level physical applications, which can significantly enhance development efficiency. Based on this framework, we have completed the HLAs development for the Linac and the booster, respectively. The HLAs for the Linac and booster have been successfully applied to beam commissioning and have achieved excellent performance, assisting beam commissioning operators in quickly achieving beam transmission throughout the entire system. The successful application of *Pyapas* demonstrates its reliability and practicality. Currently, we are developing the HLAs for the storage ring, which has a magnet data volume one order of magnitude larger than the booster and a significantly increased level of control complexity. To ensure the availability of the HLAs, more technologies need to be added to *Pyapas*, such as asynchronous communication technology and multiprocess development functions.

REFERENCES

[1] Y. Jiao, G. Xu, X. H. Cui *et al*. "The HEPS project", *J. Synchrotron Radiat.*. vol. 25, no. 6. pp. 1611-1618, Sep. 2018. doi:10.1107/s1600577518012110

[2] Y. Jiao *et al*., "Modification and optimization of the storage ring lattice of the High Energy Photon Source", *Radiat. Detection Technol. Methods*, vol. 4, pp. 415–424, 2020. doi:10.1007/s41605-020-00189-7

[3] C. Meng *et al*., "Progress of the HEPS accelerator Construction and linac commissioning", presented at FLS'23, Lucerne, Switzerland, Aug.-Sep. 2023, paper TU4P27, this conference

[4] Y. Jiao *et al*., "Progress of lattice design and physics studies on the High Energy Photon Source", in *Proc. IPAC'21*, Campinas, Brazil, May 2021, pp. 229-232. doi:10.18429/jacoW-IPAC2021-MOPAB053

[5] L. Yang *et al*., "The design of NSLS-II high level physics applications", in *Proc. ICALEPCS'13,* San Francisco, CA, USA, Oct. 2013, paper TUPPC130, pp. 890-892.

[6] I. Stevani *et al*., "High level applications for Sirius", in *Proc. PCaPAC'16,* Campinas, Brazil, Oct. 2016, pp. 47-49. doi:10.18429/JACoW-PCAPA2016-WEPOPRPO22

[7] X. H. Lu *et al*., "Status of high level application development for HEPS", in *Proc. ICALEPCS'21*, Shanghai, China, Oct. 2021. pp. 978-980. doi:10.18429/JACoW-ICALEPCS2021-THPV047

[8] C. Meng *et al*., "Physics design of the HEPS LINAC", *Radiat. Detect. Technol. Methods*, vol. 4, pp. 497–506, 2020. doi:10.1007/s41605-020-00205-w

[9] C. Meng *et al*., "Progress of the first-stage beam commissioning of High Energy Photon Source Linac", *High Power Laser Part. Beams*, vol. 35: p. 054001, 2023. doi:10.11884/HPLPB202335.230061

[10] Y. M. Peng *et al*., "Design of the HEPS booster lattice", *Radiat. Detect. Technol. Methods*, vol. 4, pp. 425–432, 2020. doi:10.1007/s41605-020-00202-z

[11] Y. Y. Guo *et al*., "The transfer line design for the HEPS project", *Radiat. Detect. Technol. Methods*, vol. 4, pp. 440–447, 2020. doi:10.1007/s41605-020-00209-6

[12] I. Agapov *et al*., "OCELOT: a software framework for synchrotron light source and FEL studies", *Nucl. Instrum. Methods Phys. Res., Sect. A*, vol. 768, p. 151, 2014. doi:10.1016/j.nima.2014.09.057

[13] Y. L. Zhao *et al.,* "The high level applications for the HEPS linac", *J. Instrum.,* vol. 18, no. 6, p. P06014, 2023. doi:10.1088/1748-0221/18/06/P06014

DESIGN OF THE TEST PLATFORM FOR HIGH AVERAGE CURRENT VHF ELECTRON GUN

Zipeng Liu[1,2], Houjun Qian[1,2], Guan Shu[1,2], Xudong Li[1,2], Zenggong Jiang[1,2], Haixiao Deng[1,2,*]
[1]Shanghai Synchrotron Radiation Facility, Shanghai, China
[2]Shanghai Advanced Research Institute, Shanghai, China

Abstract

Recently a high-average-current CW VHF electron gun is under construction at Shanghai Advanced Research Institute, which is aimed to develop the high average current and high beam quality technologies. The high average current electron source is the key component of a kW-power-order free electron laser facility. The average current and the frequency of this electron gun is 1-10 mA and 216.7 MHz, respectively. The energy of electron is over 500 kV, and repetition rate is about 1-9 MHz. To validate the performance of this instrument, a test platform has been designed. The R&D of its vacuum and diagnostics design are presented in this work.

INTRODUCTION

In recent years, several projects involving free electron lasers (FEL) and energy recovery linacs (ERL) facilities have been proposed and commissioned. These facilities require high repetition rates, low emittance, and high power. Some facilities, such as LCLS-II, SHINE, and APEX, have employed normal-conducting (NC) RF electron guns [1–4]. The electron gun (VHF) test platform in this work is under construction based on a NC continuous-wave (CW) RF photogun at the Shanghai Advanced Research Institute (SARI). The core of our photogun is a NC copper RF cavity operating at the VHF band, specifically at 216.7 MHz. This cavity generates a 22.5 MV/m accelerating field when supplied with nearly 90 kW of power. The accelerating gap measures 4 cm. To operate high quantum efficiency semiconductor photocathodes (Cs2Te), an expected vacuum level of $10^{-10} - 10^{-9}$ mbar is necessary. Beam quality, including energy, normalized emittance, beam size, beam current, and the thermal emittance of the photocathode, significantly influences the electron source. The layout of the test platform is outlined in this paper, focusing mainly on diagnostics and vacuum design. The theoretical vacuum levels for the electron gun and test line are 3×10^{-8} mbar and 1×10^{-7} mbar, respectively. The main tube diameter is 50 mm, and the entrance diameter of the dump is 80 mm.

MANUSCRIPTS

The design objectives are presented in Table 1, and the layout of the test platform is illustrated in Fig. 1. The height of the beamline is 1.3 m. The beamline comprises a load lock, electron gun, solenoids, dipole, profile monitors, ICT (Integrated Current Transformer), and BPMs (Beam Position Monitors). The positions of the main elements are indicated in Table 2.

Table 1: Design Objectives

Parameter	Value	Unit
Energy	>500	keV
Average current	>1	mA
Frequency	216.7	MHz
Repetition rate	1-9	MHz
Charge	200	pC

Table 2: Test Platform Layout

Element	Position	Unit
Electron gun	0	m
Solenoid 1,2	0.27,1.8	m
Laser injector	0.92	m
Profile 1,2,3	1.5,0.4(to the line),2.2	m
Dump	0.65(to the line)	m

Diagnostics Design

The essential characteristics of the electron gun's photocathode are crucial for the electron source. Therefore, this work includes simulations to measure beam energy, dark current, normalized emittance, and transverse momentum.

Dark current imaging Dark current is a primary focus of the electron source, particularly because superconducting linacs such as LCLS-II and SHINE require low dark currents for optimal acceleration quality and extended lifespan. Dark current imaging plays a role in enhancing the photo-cathode manufacturing process. As depicted in Equation 1, dark current emitted from the same position with varying transverse momentum should reach the same position on the profile by matching the strength of the solenoid ($M_{12} = 0$). The relationship between imaging magnification and the distance between the photo-cathode and the profile is demonstrated in Fig. 2b, where the primary emission of dark current is from the 5 mm center of the photo-cathode. As depicted in Fig. 2a, the dark current is imaged, resulting in a loss of transmission of the profile.

$$\begin{bmatrix} M_{11} & M_{12} \\ M_{21} & M_{22} \end{bmatrix} \begin{bmatrix} r_0 \\ r_0' \end{bmatrix} = \begin{bmatrix} r \\ r' \end{bmatrix} \tag{1}$$

---

* denghx@sari.ac.cn
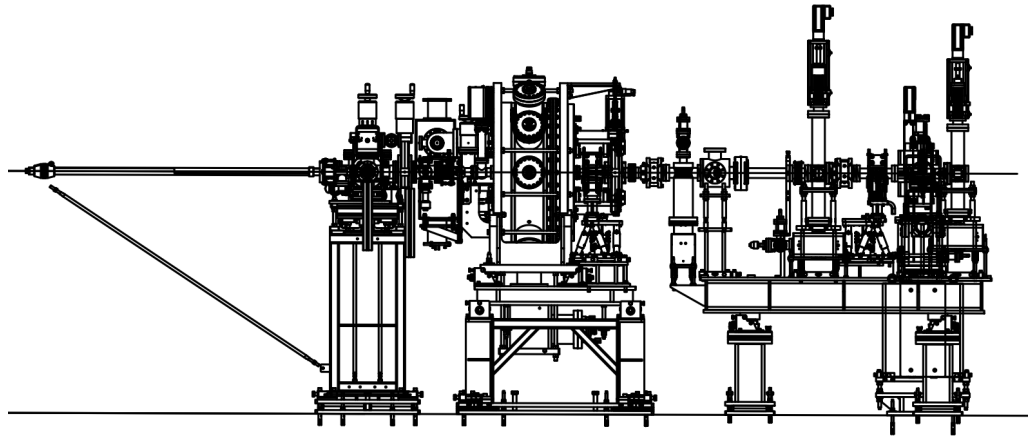
Figure 1: Layout of VHF electron gun test platform. The test line include photo-cathode system, electron gun system, diagnostics system, vacuum system, magnet system and radiapretection system. The elements include solenoids, dipole magnet, profile, ion pump, correctors, SBPMs, BBPM, ICT and dump.
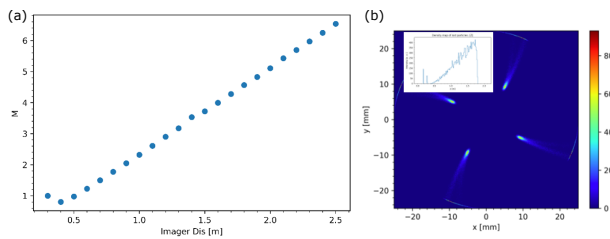
Figure 2: The simulation of dark current. (a) The relationship between position of profile and imaging magnification. (b) The dark current is imaging in profile of 1.5 m distance, and the beam transmission loss is also shown.

Figure 3: The theoretical simulation of transverse momentum imaging. (a) The influence of space charge for imaging the transverse momentum of 2.2 m profile. (b) The relationship between the imaging magnification and position of profile.

Transverse momentum imaging   Transverse momentum is the key characteristic of photo-cathode. As shown in Equation 1, the dark current emitted from the different position with same transverse momentum should arrive the same position of profile through matching the strength of solenoid ($M_{11} = 0$). The relationship between the distance between the profile and the photo-cathode and the imaging magnification was simulated using ASTRA. As shown in Fig. 3(b), the distance of the profile is 2.2 meters, in addition to the resolution of the CCD. The influence of space charge is also presented in Fig. 3(a), the space charge can be ignored when the beam charge is below 0.05 pC. Additionally, GAGG with high quantum efficiency will be chosen.

Normalized emittance measurement   The normalized emittance is significant for FEL lasing. In this work, the single-slit method was used to measure the normalized emittance. However, the space charge will increase the measured normalized emittance. As shown in Fig. 4, the space charge influence was simulated with different slit gaps. The red and blue lines represent the intensity distribution with and without space charge, respectively. Different slit gaps of 60, 100, 140, and 200 μm were simulated using ASTRA.

Additionally, the gap of slit should be below 100 μm to avoid the influence of space charge.

Vacuum Design

An excellent vacuum level is necessary for an RF cavity system, and a low vacuum level will result in radiation passing through activated air. In our test platform, the vacuum level of the RF cavity should be maintained at the order of 10^{-8}. Simultaneously, the vacuum level of the test line should achieve an order of 10^{-7}. The RF cavity maintains a high vacuum level using nine Z400 NEG pumps and a 200 L/s ion pump. To attain such a high vacuum level, four dump ports will also be utilized. Three of these consist of one 50 L/s ion pump and one Z400 NEG pump each. The pump port in front of the copper dump contains a 400 L/s ion pump. This pump will prevent the main line from experiencing a poor vacuum level resulting from the high average current. As shown in Fig. 5, the top figure depicts the 3D grid of the entire test platform in Molflow+, while the bottom figure illustrates the vacuum level distribution from the photocathode to profile 3. The vacuum level of the electron gun is nearly 3×10^{-10} mbar, and the test line measures around 2.7×10^{-9} mbar.

Figure 4: The space charge influence for measuring normalized emittance. The read line and blue line is the rms beam size without and with space charge, respectively. The slit gaps of 60, 100, 140, and 200 µm are presented. The influence of space charge can be ignored when the slit gap less than 100 µm.
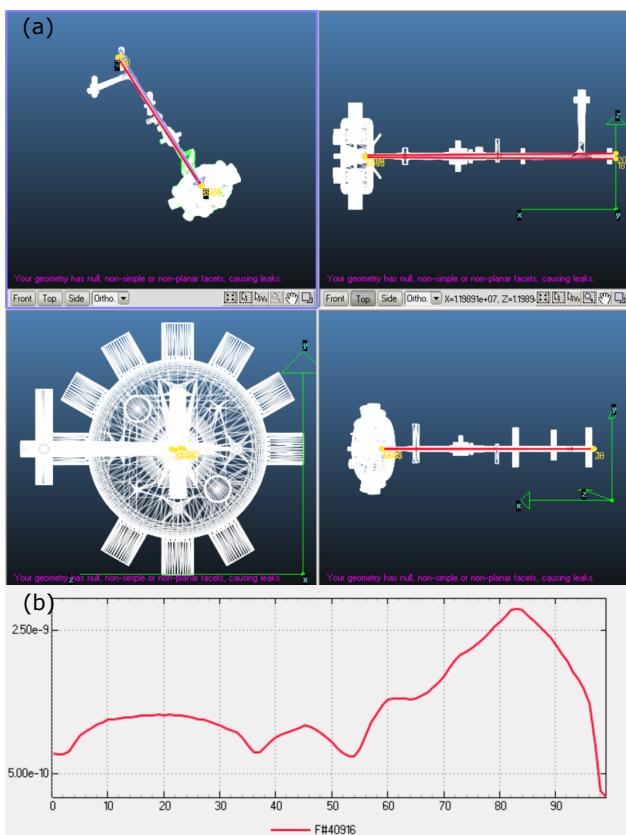
Figure 5: The simulation of vacuum. (a) The 3D grid of test platform in Molflow+. (b) The vacuum level distribution from photo-cathode to the profile 3.

SUMMARY

In this work, the electron gun test platform at SARI is described. Additionally, the diagnostic and vacuum design are presented. The test platform can be used to validate the quality of electrons by measuring dark current, average current, normalized emittance, transverse momentum, charge, and more. The theoretical vacuum level is also discussed in this work, with the vacuum level of the test line and electron gun being approximately 3×10^{-10} mbar and 2.7×10^{-9} mbar, respectively.

ACKNOWLEDGEMENTS

REFERENCES

[1] F. Zhou *et al.*, "First commissioning of LCLS-II CW injector source" in *Proc. 10th Int. Particle Accelerator Conf. (IPAC'10)*, Melbourne, Australia, May 2019, pp. 2171–2173. doi:10.18429/JACoW-IPAC2019-TUPTS106

[2] H. Chen *et al.* "Analysis of slice transverse emittance evolution in a very-high-frequency gun photoinjector", *Phys. Rev. Accel. Beams*, vol. 24, p. 124402, 2021. doi:10.1103/PhysRevAccelBeams.24.124402

[3] Z. Y. Zhu *et al.*, "SCLF: An 8-GEV CW SCRF linac-based x-ray FEL facility", *Proc. 38th Int. Free Electron Laser Conf. (FEL'17)*, Santa Fe, NM, USA, Aug. 2017, pp. 182–-184. doi:10.18429/JACoW-FEL2017-MOP055

[4] P. Emma *et al.*, "First lasing and operation of an ångstrom-wavelength free-electron laser", *Nat. Photonics*, vol. 4, pp. 641–647, 2010. doi:10.1038/nphoton.2010.176

THE EXPERIMENTAL PROGRESS FOR THE STRONG FIELD TERAHERTZ RADIATION AT SXFEL

Kaiqing Zhang[1], Yin Kang[2,3], Cheng Yu[1], Chunlei Li[1], Bin Li[1], Chao Feng[1,†]

[1]Shanghai Advanced Research Institute, Shanghai, China

[2]University of Chinese Academy of Sciences, Beijing, China

[3]Shanghai Institute of Applied Physics, Shanghai, China

Abstract

Strong field Terahertz (THz) light source has been increasingly important for many scientific frontiers, while it is still a challenge to obtain THz radiation with high pulse energy at wide-tunable frequency. In this paper, we introduce an accelerator-based strong filed THz light source to obtain coherent THz radiation with high pulse energy and tunable frequency and X-ray pulse at the same time, which adopts a frequency beating laser pulse modulated electron beam. Here, we present the experimental progress for the strong filed THz radiation at shanghai soft X-ray free-electron laser (SXFEL) facility and show its simulated radiation performance.

INTRODUCTION

Terahertz (THz) radiation, with a frequency from 0.1 THz to several tens of THz, has been increasingly significant for many scientific frontiers, such as THz‑triggered chemistry, single shot THz bioimaging and nonlinear physical [1]. The development of strong field THz radiation with a pulse energy on the order of millijoule (mJ) has provided new possibilities for studying various of new scientific phenomenon, such as strong field-novel material interactions, the high-harmonic generation of THz waves, nonlinear THz spectroscopy [2]. In recent years, the so-called THz pump and X-ray probe technique, which exciting the matter with a THz radiation and capturing the dynamic image by X-ray pulse, has been an important technique to measure the basic properties of matters such as magnetization, conductivity and even crystal lattice, or study the dynamic process of matter [3].

One main barrier for the application of strong field THz is lack of THz source with high pulse energy and tunable frequency. Currently, the strong THz radiation is mainly produced by the ultrafast laser [4], laser produced plasma [5] and electron accelerator-based techniques [6]. For the ultrafast laser and laser produced plasma techniques, it cannot generate synchronized high-power X-ray and strong field THz radiation at the same time. The electron accelerator-based technique has been treated as one reliable method to obtain strong field THz radiation, and many electron-accelerator-based THz light source also has been proposed. The electron accelerator can produce THz radiation by several methods: coherent synchrotron radiation (CSR) [7], coherent transition radiation (CTR) [8] and

undulator radiation [9]. In recent years, FEL facilities around the world, including LCLS-II, FLASH, European-XFEL and Swiss-FEL have produced high power X-ray and strong-field THz radiation at the same time by adopting an afterburner and compressing the duration of electron beam into one THz period [10]. However, generating THz radiation with a frequency above 10 THz needs to supress the electron beam duration below 100 fs, which can be a challenge for the most existing FEL facilities.

In this paper, we introduce an electron accelerator-based strong field THz radiation technique, which can produce THz radiation with high pulse energy and tunable frequency from 0.1 THz to 40 THz by using a frequency beating laser modulated electron beam. Here, we present the experimental progress, including the frequency beating laser pulse, THz undulator, THz diagnostic line, for the strong THz radiation at shanghai soft X-ray free-electron laser (FEL) (SXFEL) facility. To show the possible performance, simulation results with the basic parameters of SXFEL are also given.

WORKING PRINCIPLE

Figure 1 shows the layout of the introduced THz radiation technique [11, 12]. The working principle can be expressed as following: The electron is firstly produced from a photocathode gun with a beam energy of several keV, and then the beam is accelerated to a beam energy above 1 GeV by the LINAC, and the pulse duration of electron beam is also be supressed by the LINAC. After that, the relativistic electron beam is sent into a modulation section together with a frequency beating laser pulse. Figure 2 shows the layout of the frequency beating laser. An ultrafast laser pulse with an initial pulse length of σ is stretched by a grating pair to generate large frequency chirps, and the laser pulse undergoes a frequency-dependent modulation phase modulation, the phase can be expressed as [13]:

$$\phi(\omega) = \phi(\omega_0) + \tau_0(\omega - \omega_0) + \frac{(\omega-\omega_0)^2}{2\mu} + \cdots,$$

where τ_0 is the group delay at ω_0, μ is the carrier frequency sweep rate (linear chirp rate), $\mu = \frac{d\omega}{dt}$. At the same time, the pulse length of laser pulse is also stretched from σ to σ_n, where σ_n can be calculated by $\sigma_n = \sigma\sqrt{(1 + 4/\mu^2\sigma^4)}$. And then, a beam splitter is introduced to separate the stretched laser pulse into two pulses, one of them passes through an optical delay line, which will introduce a time delay τ. The laser pulses are recombined, which can form a quasi-sinusoidal chip modulation of the
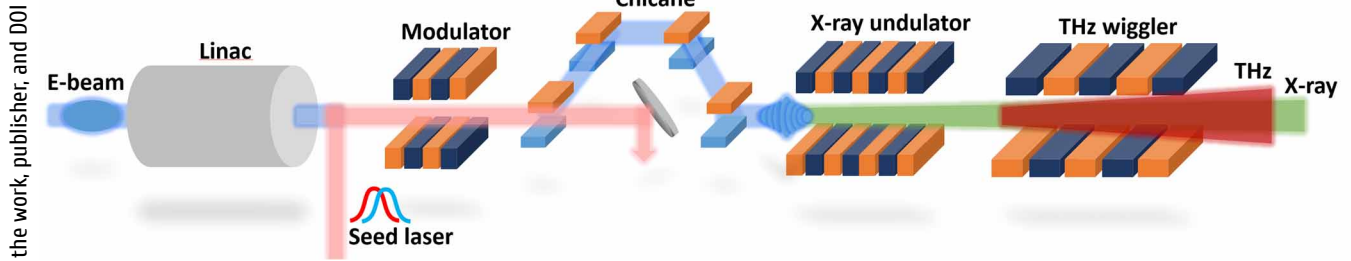
Figure 1: The basic layout of the introduced strong field THz radiation based on the frequency beating laser modulated electron beam.
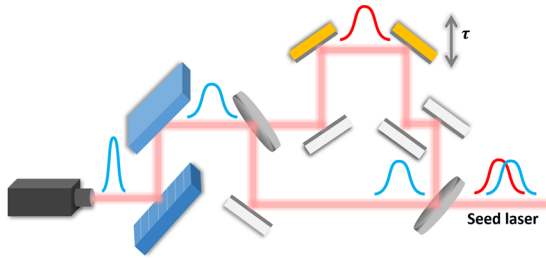
Figure 2: The layout of the frequency beating laser pulse.

light intensity considering that the frequency of the two pulses at every point in the time domain differs by a beating frequency of f, the beating frequency can be expressed by: $f = \frac{\tau}{\pi\sigma\sigma_n} \cong \frac{\mu\tau}{2\pi}$. The frequency beating laser can produce a beating frequency at THz range, and the frequency can be easily adjusted by tuning μ and τ from 0.1 to 40 THz. The frequency beating laser pulse will interact with the electron beam in the magnetic modulator, and imprint the energy modulation at the beating frequency into the beam. The electron beam then passes through a magnetic dispersion section to convert the energy modulation into density modulation at the beating frequency. The modulated electron beam is firstly sent into a undulator with a relative short magnetic period to produce X-ray radiation, and then the beam is sent into a undulator with a much longer magnetic period to THz radiation. By using the proposed technique, synchronized X-ray and THz radiation can be generated at the same time.

THE EXPERIMENTAL PROGRESS

The experiment of the introduced technique will be carried out at SXFEL. The basic parameters of SXFEL are presented in Table 1. The SXFEL can produce electron beam with a beam energy on the order of GeV, a bunch charge of 500 pC and a bunch length from 0.1 to 7 ps, the electron beam can be used to generate X-ray pulse with a peak power above 1 GW. For the SXFEL, there are two undulator beam line: SBP Line and SUD Line, the experiment will be carried out at the SBP Line. Based on the basic layout of SXFEL, there are two options to modulate the electron beam: the first option is at the laser heater section, the second option is at the existing modulator and dispersion sections before the SBP undulator. To carried out the experiment, frequency beating laser pulse, THz undulator,

THz diagnostic line are required. In this section, we will show the experimental progress for the THz radiation at SXFEL.

Table 1: The Basic Parameters of SXFEL

Parameter	Value	Unit
Energy	0.5-1.5	GeV
Bunch Charge	500	pC
Energy spread	0.005%	-
Bunch length	0.1-7	ps
Laser wavelength	800	nm
Laser pulse length	30	fs

As shown in Fig. 2, a frequency beating optical Line is required. Based on the layout of Figure 2, an actual beating frequency optical path has been built together with the laser heater optical path, which has been shown in Fig. 3 (a). To verify the performance of the optical path, the longitudinal profile at the exit of the optical path has been measured, and the results are also shown in the Fig. 3 (b). One can find a frequency beating structure at THz frequency exists along the longitudinal profile.

(a)

(b)
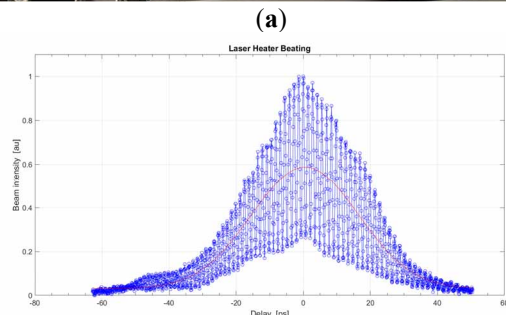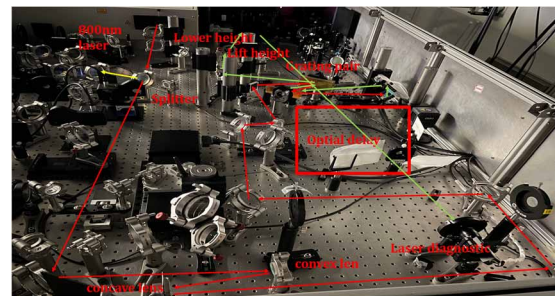
Figure 3: (a) The actual frequency beating optical path and (b) the measured longitudinal profile after the frequency beating optical path.

Besides the frequency beating laser, the THz undulator is also designed and processed. The THz undulator is shown in Fig. 4, and the THz undulator parameters are presented in Table 2. The undulator adopts an electromagnetic undulator with a changeable undulator magnetic period of 280 or 560 mm. The total length of the undulator is about 5m with about 18 magnetic of 280 mm. The THz undulator will be installed before the dump and after the X-ray undulator.
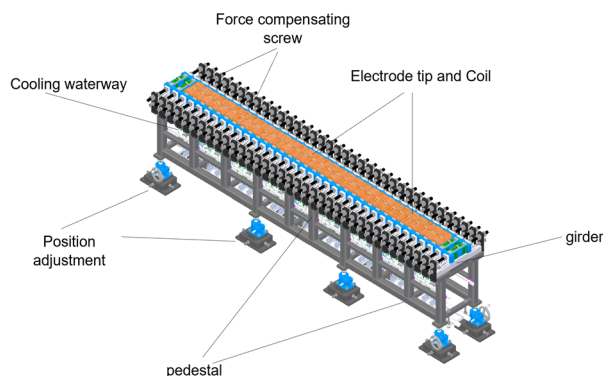
Figure 4: The THz undulator for SXFEL.

Table 2: The Basic Parameters of THz Undulator.

Parameter	Value	Unit
Type	Electromagnetic undulator	-
Period	280/560	mm
Total length	5	m
Efficient peak magnetic field	0.8-1.78	T
ΔK/K	1.4e-4	-
Phase error	<5	degree
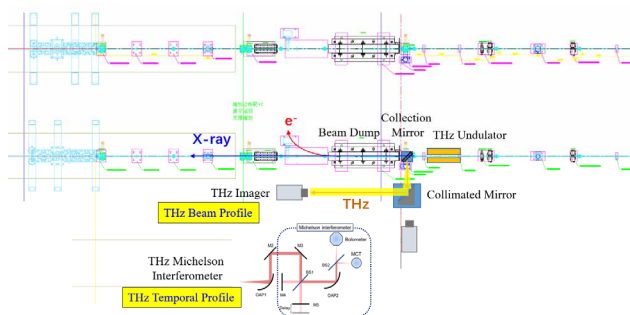
Figure 5: The layout of THz undulator and THz diagnostic line.

After the THz undulator, there will a THz mirror with a 3 mm hole to reflect the THz radiation to the downstream THz diagnostic line and transfer the X-ray to beam line. In the THz diagnostic line, a michelson interferometer will be installed to detect the pulse energy of THz radiation, and THz image and THz temporal profile will also be installed to measure the transverse and temporal image. Figure 5 shows the detail information about the layout of THz diagnostic line at SXFEL.

To show the possible performance of the introduced technique, simulations with the basic parameters of SXFEL facility are also carried out and the simulated results are shown in Fig. 6. According to Fig. 6, one can find that the peak power is about 0.58 GW and the pulse energy is below 1 mJ due to the limitation of THz undulator length.
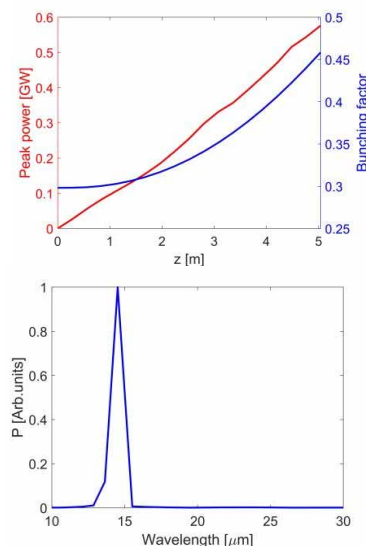
Figure 6 The peak power and bunching factor evolutions along the THz undulator, and the final spectrum of THz radiation.

CONCLUSION

In conclusion, we have introduced the strong field THz radiation technique, which can generate THz radiation with high pulse energy and tunable wavelength by using a frequency beating laser pulse modulated electron beam. The basic working principle and the experimental progress including frequency beating laser, THz undulator and THz diagnostic line are presented. The simulations of the technique are also presented, and the results show that the THz undulator with a total length of 5 m can produce THz radiation with a peak power 0.58 GW and a pulse energy below 1 mJ. The experiment will be carried out at SXFEL in the following years.

REFERENCES

[1] M. Tonouchi, "Cutting-edge terahertz technology", *Nat. Photonics*, vol. 1, pp. 97–105, 2007.
doi:10.1038/nphoton.2007.3

[2] K. Kovacs *et al.*, "Quasi-Phase-Matching High-Harmonic Radiation Using Chirped THz Pulses", *Phys. Rev. Lett.*, vol. 108, pp. 193903, 2012.
doi:10.1103/physrevlett.108.193903

[3] X.C. Zhang *et al.*, "Extreme terahertz science", *Nat. Photonics*, vol. 11, pp. 16-18, 2017, https://www.nature.com/articles/nphoton.2016.249

[4] C. Vicario *et al.*, "GV/m Single-Cycle Terahertz Fields from a Laser-Driven Large-Size Partitioned Organic Crystal", *Phys. Rev. Lett.*, vol. 112, p. 213901. doi:10.1103/PhysRevLett.112.213901

[5] K.Y. Kim *et al.*, "Coherent control of terahertz supercontinuum generation in ultrafast laser-gas interactions", *Nat. Photonics*, vol. 2, pp. 605–609. 2008, https://www.nature.com/articles/nphoton.2008.153

[6] A. Gopal *et al.*, "Observation of Gigawatt-Class THz Pulses from a Compact Laser-Driven Particle Accelerator", *Phys. Rev. Lett.*, vol. 111, p. 074802, 2014. doi:10.1103/PhysRevLett.111.074802

[7] S. Bielawski *et al.*, "Tunable narrowband terahertz emission from mastered laser-electron beam interaction", *Nat. Phys.*, vol. 4, pp. 390–393, 2008. doi:10.1038/nphys916

[8] D. Daranciang *et al.*, "Single-cycle terahertz pulses with >0.2 V/Å field amplitudes via coherent transition radiation", *Appl. Phys. Lett.*, vol. 99, p. 141117, 2011. doi:10.1063/1.3646399

[9] T. Tanaka, "Difference frequency generation in free electron lasers", *Opt. Lett.*, vol. 43, pp. 4485–4488, 2018. doi:10.1364/OL.43.004485

[10] Z. Zhang *et al.*, "A high-power, high-repetition-rate THz source for pump-probe experiments at Linac Coherent Light Source II", *J. Synchrotron Radiat.*, vol. 27, pp. 890–901, 2020. doi:10.1107/S1600577520005147

[11] K.Q. Zhang *et al.*, "A Compact Accelerator-Based Light Source for High-Power, Full-Bandwidth Tunable Coherent THz Generation", *Appl. Sci.*, vol. 11, p. 11850, 2021. doi:10.3390/photonics10020133

[12] K. Yin *et al.*, "Generating High-Power, Frequency Tunable Coherent THz Pulse in an X-ray Free-Electron Laser for THz Pump and X-ray Probe Experiments", *Photonics*, vol. 10, p. 133, 2023. doi:10.3390/app11241185

[13] A. Weling *et al.*, "Novel sources and detectors for coherent tunable narrow-band terahertz radiation in free space", *J. Opt. Soc. Am. Opt. Phys.*, vol. 13, pp. 2783–2791, 1996. doi:10.1364/JOSAB.13.002783

DESIGN OF THE BEAM DISTRIBUTION SYSTEM OF SHINE*

S. Chen[†], X. X. Fu, H. X. Deng, B. Liu, Shanghai Advanced Research Institute, Shanghai, China
B. Y. Yan, University of Chinese Academy of Sciences, Beijing, China

Abstract

For feeding the three parallel undulator lines by the CW beam of a single SRF linac simultaneously, a beam switch-yard between the linac and undulator lines is designed with the consideration of bunch-by-bunch beam separation and beam quality per. In this work, the schematic design of the beam switchyard for bunch-by-bunch beam separation of CW beam is described, and the current lattice design of the linac-to-undulator deflection branches and the start-to-end tracking simulation results are presented.

INTRODUCTION

As a high repetition rate XFEL and extreme light facility, the SHINE project is now under construction near the SSRF and ShanghaiTech campus [1,2]. High quality electron beam is generated by a VHF gun in CW mode with a repetition rate up to about 1 MHz [3]. A superconducting RF linac with two bunch compressors then accelerates the electron beam to about 8 GeV. The electron beam is used to feed the FEL undulator complex with three parallel undulator lines, referred to as FEL-I (3-15 keV), FEL-II (0.4-3 keV) and FEL-III (10-25 keV) respectively. In addition, spaces are reserved for future upgrade of more undulator lines.

For the simultaneous operation of multiple undulator lines with different parameters and operation modes in SHINE, a beam switchyard is located in between the SRF linac and the undulator lines complex. In the beam switchyard, he 1 MHz CW electron beam should be separated bunch-by-bunch in an arbitrarily programmable pattern and then delivered to each undulator line through the corresponding linac-to-undulator (LTU) branch respectively. In this work, we present the physics design of the beam switchyard for SHINE.

MAIN LAYOUT

A schematic view of the SHINE is seen in Fig. 1. Most of the beam equipment will be installed in the tunnels and shafts about 30 m underground. Electron beam starts from the injector in #1 shaft and is accelerated by the SRF linac in a 1.4 km long tunnel. The three undulator lines are installed in two of the undulator tunnels: FEL-I and FEL-II in the middle undulator tunnel and FEL-III in the west undulator tunnel. All the three undulator lines are parallel to the linac line, in the same vertical plain but not collinear. The horizontal distance between the three undulator line and the linac is about +1.85 m for FEL-II, -1.45 m for FEL-I and -8.95 m for FEL-III, where '+'('-') denotes left(right) to the linac beam direction. The linac tunnel and the undulator tunnels

---

are connected by the #2 shaft. Some key beam parameters of SHINE are listed in Table 1.

Table 1: SHINE Main Beam Parameters

Parameter	Value	Unit
Beam Energy (E_0)	8.0	GeV
Slice Energy Spread (σ_E/E_0)	~0.01	%
RMS Norm. Emittance (ε_n)	≤0.45	μm · rad
Bunch Frequency (f_{rep})	1000	kHz
Bunch Charge (Q)	10~300	pC
Bunch Length (l_b)	~100	fs
Peak Current (I_{pk})	≥1500	A

The beam switchyard section starts from the end part of the linac tunnel, passes through the #2 shaft and ends at the entrance of the undulator lines. Electron bunches from the linac should be separated and delivered either to the three undulator lines or to a 800-kW beam dump in the middle of #2 shaft. Starts from the end of the SRF linac, a linac-to-dump (LTD) line brings the undeflected bunches to the main dump. Three LTU deflection branches extract bunches from the LTD line in the sequence of LTU-2, LTU-3, and LTU-1. This arrangement avoids the conflict of the three LTU branches and reserves spaces for future extension of more LTU branches for more undulator lines.

KICKER-SEPTUM MODULE

An electron bunch that is wanted by an undulator line should be firstly extracted from the 1 MHz CW electron bunch train without affecting the bunches to other directions. Typically it is realized by pulsed kicker magnets. For maximizing the available beam modes that can be provided to the user experiments and their flexibility of switching, the kicker magnets should be able to perform a stable bunch-by-bunch kick to the electron beam and, what's more, should be programmable for arbitrary distribution pattern. Considering the beam parameter and the limited geometry, a single kicker magnet could not meet the requirements independently. Therefore, the actual scheme is based on a set of small angle vertical kicker magnets combined with a DC Lamberson septum magnet, which can be a compact scheme with high enough frequency and stability.

The configuration of the kicker-septum module is seen in Fig. 2. The fast kicker set and the DC Lamberson septum magnet are inserted in a FODO cell with about 24 m period. The fast kicker set consists of 8(+2) special designed lumped-inductance kicker magnets with a total deflection angle of about 0.8 mrad [4]. The pole of the kicker magnet is out of vacuum so that ceramic vacuum chamber should be used. To reduce the wakefields, the ceramic vacuum chamber should
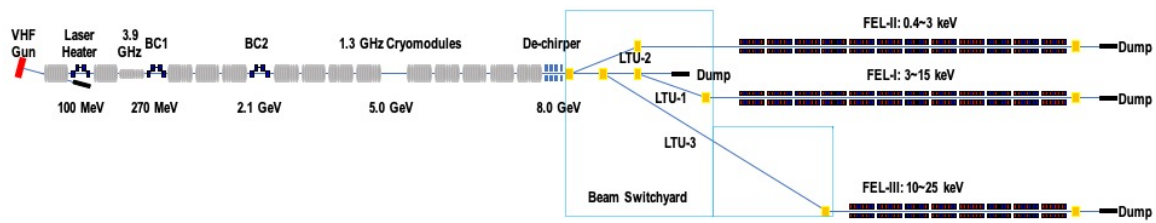
Figure 1: SHINE Schematic Layout
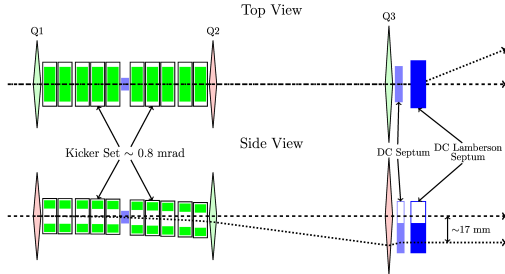
Figure 2: Schematic view of a kicker-septum module.

be coated with a conductive material and the alignment along the kicker set is slightly adjusted to prevent the beam to be too close to the chamber side. In order to ensure the relative beam trajectory stability $< 0.1\sigma_{x,y}$, it is required that the repetitive stability of the magnetic field of the kicker magnet be below 100 ppm.
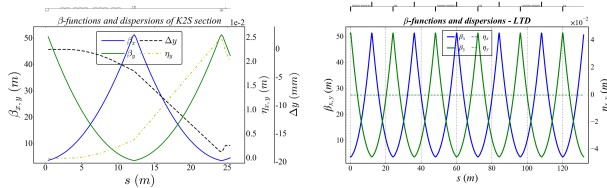
Figure 3: Lattice functions of the kicker-septum modules.

The quadrupoles of the FODO cells are aligned to be centering with the non-kicked straight bunch so that the kicked bunch experiences an extra deflection while passing them off-axis. The vertical angle of the bunch is eliminated by a small DC septum and the bunch then enters the DC Lamberson septum with ~17 mm vertical offset to the un-kicked bunch for further horizontal deflection. Because of the limited longitudinal space available for beam switchyard, the kicker-septum section is designed to be modularized so that all the three LTU branches share the same kicker-septum configuration, as is seen in the right figure of Fig. 3. For radiation safety reason, beam position monitors and beam collimators should be installed in front and behind the kicker set in order to protect the kickers and the septa. What's more, in case of emergency, all the kickers are switched off immediately to lead all the electron beam to the main dump until the beam is aborted upstream.

LINAC-TO-UNDULATOR BRANCHES

After being separated by the kicker-septum section, the electron bunches are then delivered by the three LTU branches to the corresponding undulator lines respectively. Based on the relative geometric relation between the linac and the three undulator lines, in all the three LTU branches, electron bunches should firstly be deflected to the direction of the undulator lines by a horizontal dog-leg. In this process, special concern should be given to various collective effects of high-intensity electron beam being deflected, such as the emittance growth due to dispersion effect and coherent synchrotron radiation (CSR) effect, the micro-bunching instability that may spoil the longitudinal phase space. For preserving the beam quality, several integrated optics measures are adopted for suppressing those collective effects in the lattice design of the LTU branches. The lattice functions of the three LTU branches are shown in Fig. 4.

(a) LTU-2

(b) LTU-3

(c) LTU-1
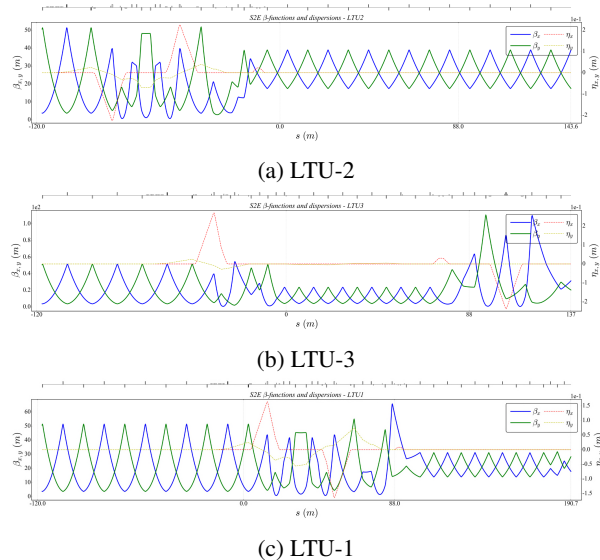
Figure 4: Lattics functions of the three LTU branches.

A direct approach of reducing the CSR effect is by reducing the deflection angle and the beam size at the bending magnet. The deflection part of each LTU branch is designed to be a dual-DBA dog-leg, i.e., replace the two reverse angle bend of the dog-leg by two reverse angle double-bend-achromatic cells for halving the deflection angle of a single bend (1.5° for LTU-2, 1.8° for LTU-3 and 1.0° for LTU-1). The optics of the dog-leg is designed to be mirror symmetrical with a

small β_x (~5 m at the middle of the DC Lamberson septa, which is determined by the FODO of kicker-septum module) at each bend. In addition, a more effective approach of further suppressing the CSR emittance growth is by matching the betatron phase advance between two adjacent dipoles to be an odd multiple of π in the deflection direction, i.e., the optics balance method [5]. To implement this method more effectively, the lattice function of the whole dog-leg is designed to be symmetrical for almost the same CSR kick in all the dipole magnets.

While deflecting the beam in the horizontal direction, the vertical offset and dispersion introduced by the kickers remain. These will be corrected by a small-angle vertical dog-leg after the horizontal dog-leg. At this point, the beam is dispersion-free both horizontally and vertically and heads towards the direction of the undulator line. A series of periodic FODO cells with 16/20 m period and $\pi/4$ phase advance then brings the beam to the entrance of undulator line. In this FODO section, the beam diagnostics instruments, such as beam profile monitors and wire scanners are inserted for emittance and twiss parameter measurement. Besides, in order to protect the radiation sensitive equipment such as the permanent magnet undulators, a final post-linac collimation should be done in advance of the beam entering the undulator lines. There will be an energy collimator inserted in the middle of the first DBA cell of the horizontal dog-leg for eliminating the large off-momentum electrons and several halo collimators inserted in the $\pi/4$-phase-advance FODO cells for removing the halo electrons that may lost in the undulator sections. All the collimators are designed to have adjustable gap to meet with different beam conditions.

START-2-END TRACKING

A collaborated start-2-end tracking simulation is done based on the baseline beam parameter of SHINE. The electron bunch is generated by the VHG gun with optimized parameters and accelerated by the injector and the SRF linac to the entrance of the beam switchyard with the longitudinal phase space distribution shown in Fig. 5. The simulation is done by the particle tracking code ELEGANT [6].
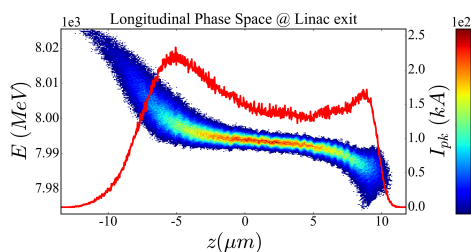
Figure 5: Longitudinal phase space at the exit of linac.

The evolution of the normalized emittance of the three LTU branches is shown in Fig. 6. With the properly designed optics for dispersion free and CSR suppression, both the horizontal and vertical normalized emittance are well preserved

after the beam passing through the beam switchyard with the maximum emittance growth less than 5%.
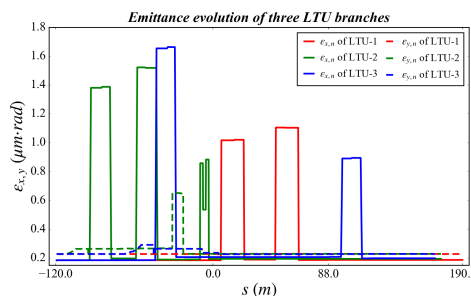
Figure 6: Evolution of emittance along the three LTU branches.

Another important beam dynamic issue of beam switchyard is the micro-bunching instability. For suppressing the micro-bunching growth in the beam switchyard of SHINE, a chicane with adjustable R_{56} is inserted in the proper position on each LTU branch. For LTU-1 and LTU-2, it is inserted in the drift space between the two quadrupoles of the FODO section after the deflection part. For LTU-3, it is inserted in the long matching section between the two DBA cells. The evolution of R56 of the three LTU branches and a comparison of the $t - x$ phase space between non-isochronous case and isochronous case of the three LTU branches are shown in Fig. 7. For the non-isochronous case, the maximum R_{56} of LTU-1, LTU-2, LTU-3 is about 100, 400, and 650 µm, respectively. Obvious micro-bunching gain can be observed in the phase space for this case, especially for the LTU-3 branch. For the isochronous case, the R_{56} is almost eliminated by the properly set chicane, micro-bunching gain in the phase space is barely observable.

Non-isochronous cases

Isochronous cases
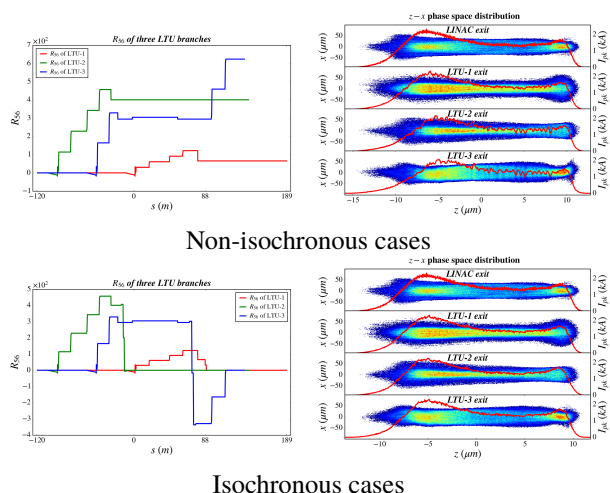
Figure 7: Comparison of the current profile at the exit of each LTU branch.

REFERENCES

[1] Z. T. Zhao, D. Wang, Z. H. Yang *et al.*, "SCLF: An 8-GeV CW SCRF linac-based x-Ray FEL facility in Shanghai, in Proc. FEL'17, Santa Fe, NM, USA, MOP055.
doi:10.18429/JACoW-FEL2017-MOP055

[2] C. Feng and H.-X. Deng, "Review of fully coherent free-electron lasers", *Nucl. Sci. Tech.*, vol. 29, p. 160, 2018.
doi:10.1007/s41365-018-0490-1

[3] H. Chen, L.-M. Zheng, and B. Gao, *et al.*, "Beam dynamics optimization of very-high-frequency gun photoinjector", *Nucl. Sci. Tech.*, vol. 33, p. 116, 2022.
doi:10.1007/s41365-022-01105-y

[4] Y. Liu, R. Wang, J. Tong, *et al.*, "Development of a high-repetition-rate lumped inductance kicker magnet prototype for beam switchyard of SHINE, *Nucl. Sci. Tech.*, to be published.

[5] S. Di Mitri, M. Cornacchia, and S. Spampinati, "Cancellation of coherent synchrotron radiation kicks with optics balance", *Phys. Rev. Lett.*, vol. 110, p. 014801, 2013.
doi:10.1103/PhysRevLett.110.014801

[6] M. Borland, *Elegant: A flexible SDDS-compliant code for accelerator simulation*, Advanced Photon Source, Argonne National Lab, IL, USA, Rep. LS-287, Sep. 2000.

DESIGN AND COMMISSIONING OF THE BEAM SWITCHYARD FOR THE SXFEL-UF*

Si Chen†, Kaiqing Zhang, Zheng Qi, Tao Liu, Chao Feng, Haixiao Deng, Bo Liu, Zhentang Zhao

Shanghai Advanced Research Institute, CAS, Shanghai, China

Abstract

A beam switchyard is designed for the Shanghai soft X-ray FEL user facility to enable parallel operation of its two FEL lines. It is designed to keep the beam properties like low emittance, high peak charge and small bunch length from being spoiled by various beam collective effects such as the dispersion, coherent synchrotron radiation and micro-bunching instability. In this work, the detailed physics design of the beam distribution system is described and the recent commissioning result is reported.

INTRODUCTION

The Shanghai soft X-ray FEL (SXFEL) user facility aims to open the way of various application fields of XFEL in China [1, 2]. It is designed to cover the whole water window range, i.e., X-ray in wavelength range of 2.3 nm ~ 4.4 nm. To accomplish this, the beam energy is accelerated to about 1.5 GeV by a normal conducting linac with a series of S-band and C-band RF structures. The bunch repetition rate is about 50 Hz. Two parallel undulator lines are installed in the undulator hall. Directly downstream of the linac it is a SASE-FEL line with radiation wavelength about 2 nm, which is named as the SBP line. A fully-coherent seeded-FEL line, which is renamed as the SUD line, is about 3 m right side of the SBP line with the radiation wavelength about 3 nm. The schematic layout of the SXFEL-UF is shown in Fig. 1. Some main beam parameters of SXFEL-UF are shown in Table 1.

Table 1: Main Parameters of SXFEL user facility Linac

Parameter	Value	Unit
E	1.5~1.6	GeV
σ_E/E (rms)	≤0.1 %	
ε_n (rms)	≤1.5	mm·mrad
l_b (FWHM)	≤0.7	ps
Q	500	pC
I_{pk}	≥700	A
f_{rep}	50	Hz

For the simultaneous operation of the two FEL lines, a beam switchyard is located between the linac and the undulator section. The electron bunch train from the linac is separated and directed in two subsequent directions: either to the SBP line or to the SUD line. Due to the high requirements of the externally seeded FEL, the beam switchyard should ensure a stable and precise transportation of the electron beam, while maintaining desirable beam quality properties such as low emittance, high peak charge, and short bunch length. In the following sections, the physics design and commissioning results of such a beam switchyard are described in detail.

BEAM SWITCHYARD DESIGN

General Layout

Since the two FEL lines lie parallel in the undulator hall, the deflection line uses a dog-leg structure to bring the kicked beam to the entrance of the seeding-FEL line. Due to the limitation of the longitudinal distance, the total deflection angle of the dog-leg is about 6°. The two reverse angle bending magnets of the dog-leg are replaced by two identical but symmetrical double-bend-achromatic(DBA) structures for reducing the deflection angle of a single bending magnet. An in-vacuum lumped-inductance kicker magnet acts as the first 3° bending magnet of the entrance DBA, with the capability of performing bunch-by-bunch beam separation and programmable for arbitrary separation pattern. To guarantee the beam trajectory stability in the SUD line, the field repetitive jitter of the kicker magnet should be less than 100 ppm.

Optics Design for CSR & MBI Suppression

Emittance growth due to coherent synchrotron radiation is a crucial beam dynamic issue of a dog-leg beam switchyard. It is necessary and possible to suppress the CSR induced emittance growth by well designed beam optics in an achromatic deflection structure. A straightforward method for mitigating emittance growth involves adjusting the beam size at the bending magnet, thereby reducing the strength of the CSR kick. Another method involves achieving mirror symmetry in the lattice of the switchyard dog-leg and adjusting the betatron phase advance between the two DBA cells to be an odd multiple of π, which is referred to as the "optics balance" method [3]. With this method, the CSR induced longitudinal dispersion and transverse kick can be well canceled at the exit of the switchyard dog-leg. The betatron functions and dispersion functions of such an optics design for SXFEL-UF are shown in Fig. 2.

Special attention should also be paid to the micro-bunching instability in the beam switchyard with multi-bend deflection line, especially for the seeded-FEL scheme which requires a smoother longitudinal phase space for more effective density modulation. For this purpose, a small bending magnet (micro-bend) is inserted in the middle of the DBA
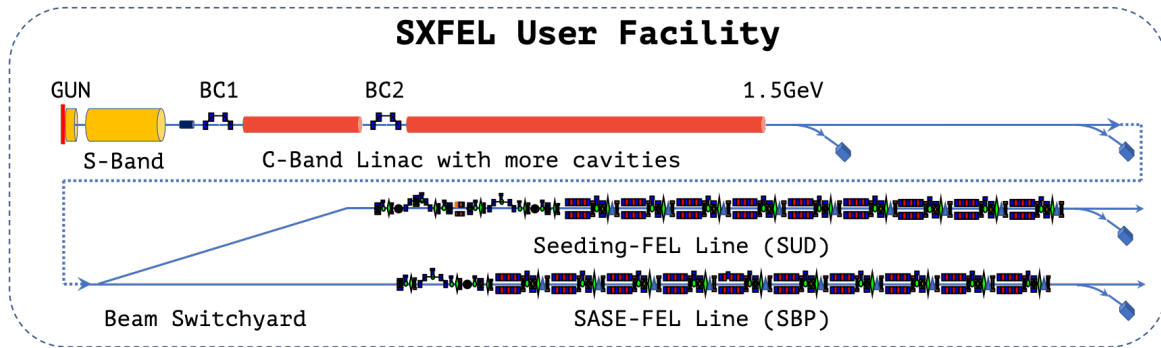
Figure 1: Schematic view of the SXFEL-UF.
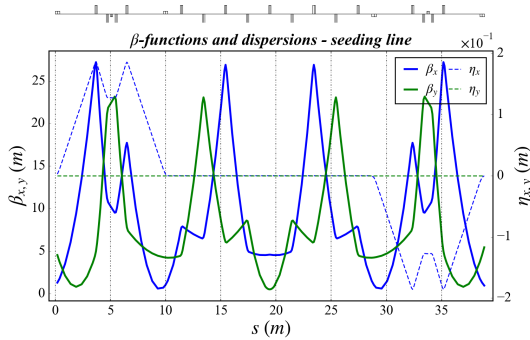
Figure 2: $\beta_{x,y}$ functions and dispersion $\eta_{x,y}$ evolution along the beam switchyard.

Figure 4: Longitudinal phase space at the linac exit.

cell with a small angle reverse to the DBA deflection angle. With this design, the R_{56} of each DBA becomes zero. Apply this design to both of the DBA cells of the switchyard, it becomes globally isochronous, as is seen in Fig. 3. With the isochronous configuration, the deflection line of the beam switchyard is substantially transparent to any incoming modulation induced by micro-bunching instability in the linac.

Figure 3: R_{56} evolution along the switchyard.

S2E Tracking Results

The start-to-end tracking from the linac end throughout the beam distribution section is performed by the code ELE-GANT [4]. The longitudinal phase space at the linac exit is shown in Fig. 4.

Figure 5 illustrates the evolution of normalized emittance (excluding the dispersion contribution) based on the S2E tracking results. These findings clearly showcase that the combined lattice design methods substantially alleviates emittance growth.
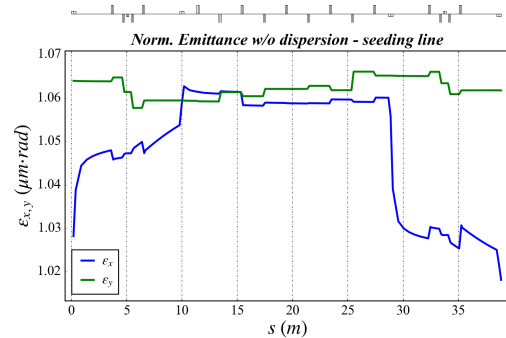
Figure 5: Normalized emittance along the beam switchyard.

For investigating the micro-bunching gain, a comparison of the t-x phase space and current profile before and after the switchyard is shown in Fig. 6. For the case that $R_{56} \neq 0$, it shows an obvious growth of the micro-bunching structure in the longitudinal phase space, especially on the head horn part. For the isochronous case with micro-bend, only imperceptible micro-bunching gain can be observed. The longitudinal phase space is well preserved after the distribution dog-leg.
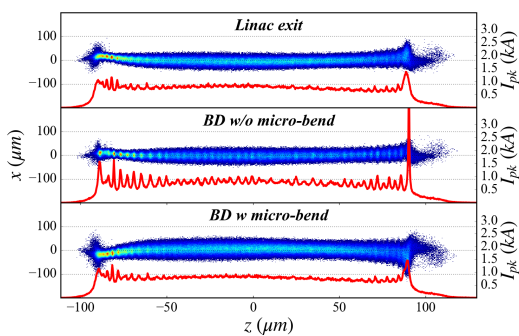
Figure 6: Comparison of the t-x phase space and the current profile at linac exit (upper), switchyard exit without micro-bend (middle) and switchyard exit with micro-bend (lower).

COMMISSIONING RESULTS

Commissioning of the Deflection Line

The commissioning of the switchyard and the Seeding-FEL line has started at the beginning of November 2021. The dispersion function is measured by fitting the orbit change slope at the beam position monitor (BPM) with different beam energy, as is shown in the upper figure of Fig. 7. It should be noted that, in this measurement, we actually did not change the beam energy directly but instead of changing the current of the bending magnets as an equivalent. Fig. 7 also shows the horizontal dispersion measured at all the BPMs from the beam switchyard to the entrance of the SUD line based on this method. The horizontal dispersion is well eliminated to be less than 1 mm at the exit of the switchyard and is well preserved downstream.
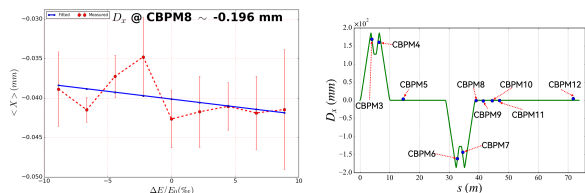
Figure 7: Horizontal dispersion measurement results.

While keeping the theoretical configuration of the magnets in the beam switchyard, the betatron matching is done by matching its entrance parameter from the linac. The emittance and twiss parameters are measured by varying the quadrupole and fitting the beam spot variation on a downstream screen. Then the beam is matched from linac exit to the entrance of beam switchyard by an automatic algorithm based on the code *Ocelot* [5]. Fig. 8 shows the comparison between the observed beam spot on each screen and the theoretical beam spot after matching, which shows a good agreement. The emittance is measured downstream of the beam switchyard and compared with the emittance in front. The results show that the emittance growth is well suppressed with less than 10 % growth.
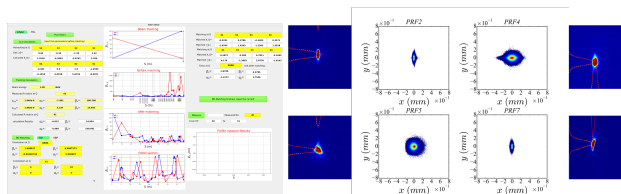
Figure 8: Automatic matching algorithm for beam switchyard.

Parallel Operation of the Two Lines

The kicker magnet has been installed online in middle of 2022, with its field stability reaching the required criteria. This enables the simultaneous commissioning and operation of the two undulator lines. Fig. 9 shows the installed kicker magnet and its high-stability-pulsed power supply in the undulator tunnel.

Figure 9: Kicker magnet and its high stability pulsed power supply installed in the undulator tunnel.

Soon afterward, a simultaneous lasing of the two FEL lines has been realized, as is seen in Fig. 10. This demonstrates the final success of the design and commissioning of the beam switchyard of SXFEL-UF.
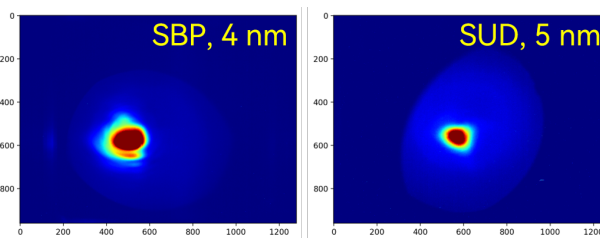
Figure 10: Simultaneous lasing of the two FEL lines.

ACKNOWLEDGMENT

study. Many useful discussions with Bart Fattz and other members of the physics and commissioning team are also gratefully acknowledged.

REFERENCES

[1] Z.T. Zhao, D. Wang, Q. Gu *et al.*, "SXFEL: A Soft X-ray Free Electron Laser in China", *Synchrotron Radiation News*, vol.30, no. 6, pp.29-33. Nov. 2017. doi:10.1080/08940886.2017.1386997

[2] B. Liu,, C. Feng, D. Gu *et al.*, "The SXFEL Upgrade: From Test Facility to User Facility", *Appl. Sci.* vol. 12, no. 1, p. 176. Dec. 2022. doi:10.3390/app12010176

[3] S. Di Mitri, M. Cornacchia, and S. Spampinati, "Cancellation of Coherent Synchrotron Radiation Kicks with Optics Balance", *Phys. Rev. Lett.* vol. 110, no. 1, p. 014801, Jan. 2013. doi:10.1103/PhysRevLett.110.014801

[4] M. Borland, "elegant: A Flexible SDDS-Compliant Code for Accelerator Simulation", in *proc. 6th International Computational Accelerator Physics Conference (ICAP 2000)*, no. LS-287, Sep. 2000. doi:10.2172/761286

[5] https://github.com/ocelot-collab/ocelot

SYMMETRIC COMPTON SCATTERING: A WAY TOWARDS PLASMA HEATING AND TUNABLE MONO-CHROMATIC GAMMA-RAYS

L. Serafini*, A. Bacci, C. Curatolo, I. Drebot, M. Rossetti Conti, S. Samsam
INFN-MI, INFN-LASA, Milan, Italy
V. Petrillo[1], A. Puppin[1], UNIMI, Milan, Italy
[1]also at INFN-MI, Milan, Italy

Abstract

We analyze the transition between Compton Scattering and Inverse Compton Scattering (ICS), characterized by an equal exchange of energy and momentum between the colliding particles (electrons and photons). In this Symmetric Compton Scattering (SCS) regime, the energy-angle correlation of scattered photons is cancelled, and, when the electron recoil is large, monochromaticity is transferred from one colliding beam to the other. Large-recoil SCS or quasi-SCS can be used to design compact intrinsic monochromatic γ-ray sources based on compact linacs, thus avoiding the use of GeV-class electron beams and powerful laser/optical systems as required for ICS sources. At very low recoil and energy collisions (about 10 keV energy range), SCS can be exploited to heat the colliding electron beam, which is scattered with large transverse momenta over the entire solid angle, offering a technique to trap electrons into magnetic bottles for plasma heating.

INTRODUCTION

The Inverse Compton Scattering (ICS) effect regards the interaction between highly relativistic electrons and laser beams, within an inverse kinematics set-up where the electron loses energy and momentum in favor of the incident photon, that is back-scattered and up-shifted to much larger energies. Compton sources are devices developed and operating in many laboratories [1] with plenty of applications. In this paper, we analyze the transition between direct Compton (DC) effect, occurring when the electron is at rest, and ICS. In this case, the colliding particles exchange an equal amount of energy and momentum, and we call this regime Symmetric Compton Scattering (SCS). Unlike in all other radiations emitted with a Lorentz boost, SCS scattered photon energy indeed no longer depends on the scattering angle, so that the back-scattered radiation beam becomes intrinsically monochromatic. SCS is characterized by the transfer of monochromaticity from one colliding beam to the other, so that when a large bandwidth photon beam collides under SCS conditions with a monoenergetic electron beam, the back-scattered photon beam results to be monochromatized. The possible applications ranges in many fields. SCS or quasi-SCS at large recoil could allow to design compact sources of intrinsic monochromatic γ-rays alimented by low energy MeV electron bunches, thus avoiding the use of GeV-class accelerators and powerful laser/optical systems, actu-

___
* luca.serafini@mi.infn.it

ally needed by ICS sources [2]. On the other hand, the SCS effect at low recoil can provide an electron heater based on X-rays.

SYMMETRIC COMPTON SCATTERING

In the Compton scattering, the photon energy ($E'_{\text{ph}} = \hbar\omega'$, with ω' being the photon angular frequency and $\hbar$ the reduced Planck constant) scattered at an angle θ is given by:

$$E'_{\text{ph}}(\theta) = \frac{(1+\beta)\gamma^2}{\gamma^2(1-\beta\cos\theta) + \frac{X}{4}(1+\cos\theta)}E_{\text{ph}}, \quad (1)$$

where the incident photon energy is $E_{\text{ph}} = \hbar\omega$, $\beta = v_e/c$ is the dimensionless electron velocity v_e (c being the speed of light), $\gamma = 1/\sqrt{1-\beta^2}$ is electron Lorentz factor and X is the electron recoil factor,

$$X = \frac{4E_e E_{\text{ph}}}{(m_0 c^2)^2} = \frac{4\gamma E_{\text{ph}}}{m_0 c^2} = 4\gamma^2 \frac{E_{\text{ph}}}{E_e}, \quad (2)$$

with m_0 the electron rest mass and $E_e = \gamma m_0 c^2$.

We call Symmetric Compton Scattering (SCS) the regime of transition between DC and ICS [3], where the energy/momentum transfer between photons and electrons is balanced. The maximum photon energy closely approaches the electron energy. Referring to Eq. (1), the dependence on θ of E'_{ph} cancels when: $\frac{X}{4} = \beta\gamma^2$, a condition valid when the photon and electron energies satisfy the relation $E_{\text{ph}} = \beta E_e$, corresponding to equal electron and photon momenta with opposite directions $\vec{p}_e = -\vec{p}_{\text{ph}}$. Moreover, we can introduce an asymmetry factor $A = \beta\gamma^2 - \frac{X}{4}$, that vanishes ($A = 0$) in SCS regime, assumes large positive values ($A \to \gamma^2$) in ICS regime (that is indeed characterized by $X \ll 4\beta\gamma^2$) and negative values in DC when $\beta = 0$.

The energy of the scattered photons is $E'_{\text{ph}} = E_{\text{ph}}$, uniformly in θ.

The asymmetry factor A is negative in DC regime, where $\beta = 0$ and $\gamma = 1$, and $A = -\lambda_C/\lambda$. In ICS regime the asymmetry factor A is positive and scales like γ^2.

Figure 1 shows the dependence of E'_0 vs. T_e and of the recoil factor X in different regimes (DC, SCS, ICS).

Another unique characteristic of Symmetric Compton Scattering, that does not occur in any other electron-photon collision, is that: $E_{\text{ph}} = \beta E_e$, $E'_{\text{ph}} = E_{\text{ph}}$ and $E'_e = E_e$, i.e., the energies of electron and photon do not change before and after SCS. This is represented by the $A = 0$ line plotted in Fig. 1.
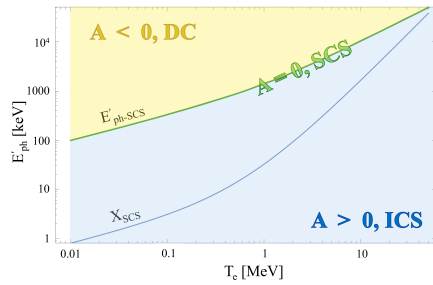
Figure 1: Plane of the scattered photon energy in SCS regime vs electron kinetic energy T_e. Direct Compton in yellow ($A < 0$), ICS in blue ($A > 0$) and in green the SCS divide line ($A = 0$).

The symmetry condition can be satisfied in a regime of low or large recoil, depending on the electron's energy. When $X \leq 1$, namely when $\gamma \leq 1.03$ or $\beta < 0.24$, the angular distribution of photons and electrons after the scattering is almost flat, with the scattered particles spread on the whole solid angle. When the recoil is strong ($X_{SC} \gg 1$), corresponding to β close to 1 and larger Lorentz factor, the angular distribution of photons and electrons is peaked close to $\theta = 0$.

Figure 2 illustrates the variation in the angular distribution of the photons as a function of the recoil factor X_{SC}. In the figure, the peak value of the zenithal angle distribution θ_{peak} (in red) and the full width half maximum θ_{FWHM} (in blue) vs X_{SC} are represented. The inner windows show the photon distribution shape for $X_{SC}=1, 5, 50$ and 250. The distribution of the scattered electrons appears to be similar to that of photons but rotated towards $\theta = \pi$.
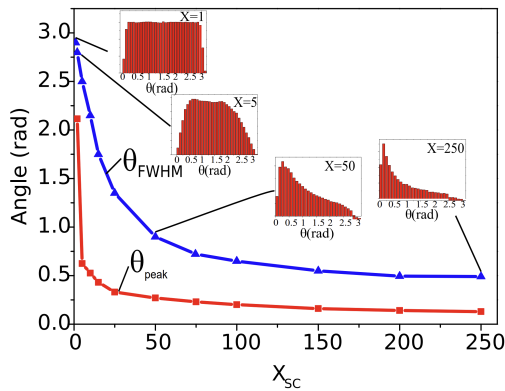
Figure 2: Peak value of the distribution of the zenithal momentum angle θ_{peak} (in red) and the full width half maximum θ_{FWHM} in SCS vs X_{SC} in the unpolarized case. The inner windows show the photon distribution shape for $X_{SC}=1,5,50$ and 250.

SYMMETRIC COMPTON SCATTERING SIMULATION

We used the WHIZARD code [4], a universal parton-level Monte Carlo event generator, to perform simulations of SCS.

An almost monochromatic (with an rms energy spread of the order of 10^{-4}) 10 MeV electron beam ($\beta \to 1$) collided

head-on with an incoming photon beam characterized by large bandwidth (20% rms spread). The recoil in this interaction is $X = 1533$. In Fig. 3 the outgoing photons showed no correlation between energy and emission angle and featured a significant narrowing of the bandwidth ($2 \cdot 10^{-4}$ rms spread, i.e., a reduction of the energy spread by about 3 orders of magnitude from incident photon beam to the scattered photon beam). The electron beam emerging from the interaction inherited an high energy spread (of the order of 10^{-1}) from the original interacting photon beam, displaying an entropy exchange.
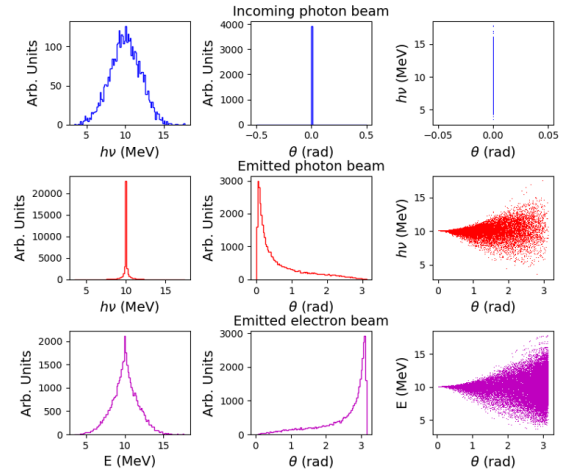
Figure 3: Simulations of SCS. First row: incident photons. Second row: outgoing photons. Third row: and outgoing electrons. First column, energy distributions. Second column, angular distributions. Third column, energy vs angle θ. Average initial photon energy $\langle E_{\text{ph}} \rangle = 10$ MeV, rms relative width of the distribution $\Delta E_{\text{ph}}/E = 0.2$. Initial electron beams with average energy $\langle E_e \rangle = 10$ MeV and $\Delta E_e/E = 0$. Recoil factor: $X = 1533$.

A home made multitasking Monte Carlo code has been also developed, validated for different type of collisions and applied to the Compton scattering process. As an additional internal feature, the code allows to consider the energy and angular (polar and azimuth) spread of both incident beams. To confirm the occurrence of the effect, we performed the same simulation of the deep recoil SCS interaction (at $X = 1533$) made with Whizard. Our findings confirm the exchange of entropy, resulting in a reduction of the bandwidth of the emitted radiation and an enlargement of the electron's bandwidth.

Furthermore, we examined the transition from the SCS regime to the ICS regime, with a particular focus on the angular distribution of the scattered radiation. To explore the transition regime, we started with the deep recoil SCS interaction ($X = 1533$) and slightly increased the energy of the incident electron bunch, while reducing the energy of the photon bunch. We investigated three cases, specifically with electron-photon energies of ($E_e \simeq E_{ph} = 10$ MeV), ($E_e = 11$ MeV, $E_{ph} = 9.08$ MeV), and ($E_e = 12$ MeV, $E_{ph} = 8.33$ MeV). The results, depicted in Fig. 4, show the

distribution shifting from an uncorrelated energy-angle pattern to a more correlated one, resembling the typical "mustache" shaped curve observed in ICS experiments, typical of the well known $(\gamma\theta)^2$ dependence shown in the denominator of Eq. (1).
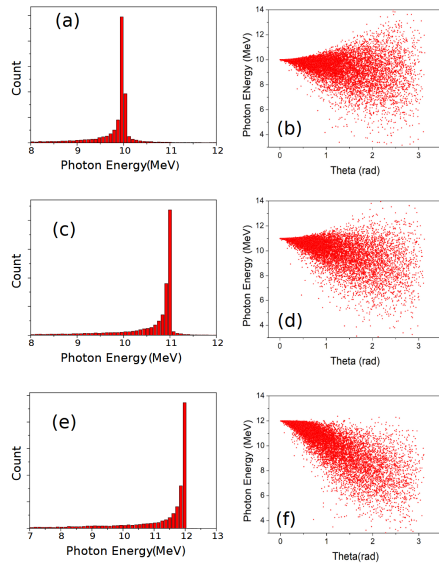
Figure 4: Transition regime between SCS and ICS for three different sets of photons and electrons energy. Left: produced photon energy distribution and right: angular photon distribution (i.e., energy as a function of emission angle) (a) and (b) initial electron energy of 10.013 MeV and initial photon energy of 10 MeV. (c) and (d) initial electron energy of 11 MeV and initial photon energy of 9.08 MeV. (e) and (f) initial electron energy of 12 MeV and initial photon energy of 8.33 MeV.

The Symmetric Compton Scattering at large recoil can transfer monochromaticity from the beam of electrons to the beam of photons, in such a way that broad band incident photon beams are transformed into narrow band photon beams by the scattering. This mechanism can be considered sort of a photon cooling effect via SCS by monoenergetic electron beams, while the electron beam is heated up to a larger energy spread. The electron energy angular distribution is peaked forward in case of large recoil, see Fig. 2, due to the angular cross section dependence, that is forward peaked when the recoil parameter X is large. On the other hand, if SCS takes place at low recoils the two scattered beams of photons and electrons are almost isotropically diffused over the entire solid angle. This is an effective heating of the transverse electron emittance, with a complete transfer of its initial dominant longitudinal momentum into prevalent transverse momentum. The part of electron beam undergoing scattering is blown all over the solid angle.

Such an effect, that does not occur in ICS, could be exploited to capture an electron beam inside a MB. SCS at a low recoil factor is the only mechanism to transfer large transverse momentum from the photon beam to the scattered electrons. A natural application of this mechanism would

be the capture of an electron beam of suitable energy into a Magnetic Bottle (MB), transforming the beam into a plasma stored inside the bottle: this would be achieved by injecting the beam on-axis and colliding it with a beam of photons under SCS conditions.

As discussed above the scattered electrons would have a dominant transverse momentum and they would comply with the well known capture condition of a MB, i.e., in terms of the angle $\theta : |\tan\theta| > \left(\frac{B_{\max}}{B_{\min}} - 1\right)^{-\frac{1}{2}}$.

We take as an example a SCS performed at the center of a MB, between an injected electron beam of 5 keV kinetic energy and a counter propagating photon beam of 72 keV (so to comply with SCS condition stated by $\frac{X}{4} = \beta\gamma^2$. Given the low β of the electrons, the differential cross section is almost flat. The recoil factor is in this case small, i.e., $X = 0.57$.

The capture condition for this MB is evaluated applying condition for $|\tan\theta|$ so to find the minimum θ angle for a captured particle $\theta_{\min} = 0.674$ rad that translates to the following percentage of electrons emitted uniformly over the solid angle: $(\pi - 2\theta_{\min})/\pi \cdot 100 \sim 57\%$.

The electrons undergoing a SCS collision in the inner region of the MB are spread all over the solid angle, converting their longitudinal momentum into transverse momentum. Tracking the scattered electrons, we find that a large majority of them (60 over 100 tracked) are trapped in the bottle. This result is in accordance with the predictions. This clearly represents a possible mechanism of plasma heating by electrons trapped into the MB generated by a SCS interaction of the injected beam into the bottle and a counter-propagating photon beam of equal momentum.

CONCLUSIONS

We explore the transition between Compton Scattering and Inverse Compton Scattering (ICS), a regime characterized by an equal exchange of energy and momentum between the colliding particles. This regime of Symmetric Compton Scattering (SCS) has the unique property of transferring monochromaticity from one beam to the other, resulting in back-scattered photons that are intrinsically monochromatic. The paper suggests that large recoil SCS or quasi SCS can be used to design compact intrinsic monochromatic γ-ray sources, thus avoiding the use of GeV-class electron beams and powerful laser/optical systems typically required for ICS sources.

The capability of SCS regime to vanish the photon energy-angle correlation, married to the large recoil beneficial effects on the scattered photon energy spread, makes possible to conceive a monochromatic gamma ray beam source based on the collision between a bremsstrahlung radiation beam (or a coherent bremsstrahlung beam from a channeling source, [5]) and a monoenergetic electron beam of similar energy, say in the 2-10 MeV range. A compact source, developed on this concept, is much more sustainable than typical ICS sources for nuclear physics/photonics like ELI-NP-GBS [6], which envisages the use of GeV-class linear accelerators.

REFERENCES

[1] V. Petrillo *et al.*, "State of the art of high-flux compton/thomson x-rays sources," *Applied Sciences*, vol. 13, no. 2, p. 752, 2023. `doi:10.3390/app13020752`

[2] C. Curatolo, I. Drebot, V. Petrillo, and L. Serafini, "Analytical description of photon beam phase spaces in inverse compton scattering sources," *Phys. Rev. Accel. Beams*, vol. 20, p. 080 701, 8 2017.
`doi:10.1103/PhysRevAccelBeams.20.080701`

[3] L. Serafini *et al.*, "Symmetric compton scattering: A way towards plasma heating and tunable mono-chromatic gamma-rays," 2023, Submitted to *Fundamentals of Plasma Physics*.

[4] W. Kilian, T. Ohl, and J. Reuter, "WHIZARD—simulating multi-particle processes at LHC and ILC," *European Physical Journal C*, vol. 71, no. 9, p. 1742, 2011.
`doi:10.1140/epjc/s10052-011-1742-y`

[5] S. B. Dabagov and N. K. Zhevago, "On radiation by relativistic electrons and positrons channeled in crystals," *La Rivista del Nuovo Cimento*, vol. 9, pp. 491–530, 2008.
`doi:10.1393/ncr/i2008-10036-x`

[6] V. Petrillo *et al.*, "Polarization of x-gamma radiation produced by a thomson and compton inverse scattering," *Phys. Rev. Spec. Top. Accel. Beams*, vol. 11, p. 110 701, 2015.
`doi:10.1103/PhysRevSTAB.11.110701`

INJECTION INTO XFELs, A REVIEW OF TRENDS AND CHALLENGES

C. Davut*,1,3, O. Apsimon1,3, S. S. Percival2,3, and B. L. Militsyn2,3
1The University of Manchester, Manchester, UK
2STFC UKRI, Daresbury, UK
3Cockcroft Institute of Accelerator Science and Technology, Daresbury, UK

Abstract

In this contribution, we review the low-energy electron injectors for the existing X-ray Free-Electron Laser (XFEL) facilities, focusing on the buncher and booster sections. The technology choices are parallel to the increasing demand for stricter six-dimensional phase space quality. The current capabilities for beam parameters and future requirements are laid out, alongside a discussion on challenges and technological bottlenecks. In light of this review, preliminary results for a high-capability injector providing a high repetition rate and continuous wave emission are presented as an option for the UK XFEL.

INTRODUCTION

XFEL facilities are an unprecedented tool for probing matter at the atomic and molecular scales. The concept of the Free-Electron Laser (FEL) was introduced in the early 1970s [1], and since then developments in FEL technology led to the construction of XFEL facilities. The first lasing in the vacuum ultra-violet range was achieved in 2005 at the Deutsches Elektronen-Synchrotron (DESY) [2]. The FLASH user facility commenced operation in the same year and extended its capabilities into the soft X-ray range. A milestone was reached in 2009 when the Linac Coherent Light Source (LCLS) at the SLAC National Accelerator Laboratory achieved X-ray lasing, starting a new era of X-ray science [3]. Since then, ongoing efforts have focused on advancing XFEL capabilities with the exploration of different concepts such as multi- colour, two-pulse X-rays, variable polarisation states, high spectral purity X-rays, higher brightness X-rays, sub-femtosecond and attosecond X-ray pulses by manipulating the electron bunch before self-amplified spontaneous emission (SASE) takes place [4]. However, increasing demand in beam quality through expanding the scope of XFEL applications leads to upgrades of existing facilities [5, 6] and motivates the construction of new ones.

One such machine, the UK XFEL, is currently undergoing the Conceptual Design and Options Analysis phase based on the published science case [7]. An exhaustive science case for UK XFEL demonstrated a community preference for high repetition rate, photon energy, energy per pulse, and some additional features such as high repetition rate laser seeding, high spectral purity X-rays, attosecond pulses across all photon energies, combining X-rays with other advanced capabilities for EUV/gammas to have a unique X-ray light source [8].

UK XFEL aims to operate across a large portion of the repetition rate-photon energy parameter space as shown in Fig. 1. In light of the science case requirements, UK XFEL has been proposed to operate at a 1 MHz repetition rate that will be likely driven by an 8 GeV beam generated using superconducting technologies. A more detailed discussion on the technologies proposed to be used based on the preliminary focus of the UK XFEL can be found in [7].

High brightness plays a central role in determining the ability of a light source to access new domains of ultra-fast X-ray science [9]. Therefore, the main design objective for the UK XFEL injector is to explore the minimum possible transverse slice emittance at the end of the injector.

The preliminary design of the UK XFEL proposes the use of a normal conducting very high frequency (VHF) gun operating either at the 6th or 7th subharmonic of the main linac RF frequency. The VHF gun will be followed by a single or 2-cell buncher operating at either harmonic or subharmonic of the main linac RF frequency to compress bunches to short lengths. Following that, a booster section will bring the beam to the emittance-dominated regime, where the energy of the beam reaches ~220 MeV after acceleration. A magnetic chicane will then perform the final bunch compression before the main linac. The design goal of the UK XFEL injector is preserving the transverse core slice emittance while compressing the bunch as much as possible and delivering it to the main linac at a high repetition rate.
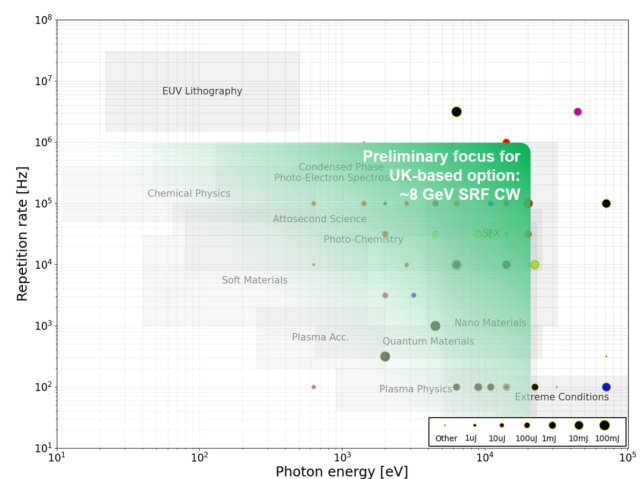

Figure 1: Research areas potentially covered by the UK XFEL, based on the preliminary repetition rate and photon energy capabilities. Figure courtesy of [7].

---

* can.davut@manchester.ac.uk

OVERVIEW OF INJECTORS FOR XFELs

The performance and the components of the injectors employed in XFELs rely on the type of electron gun used. The electron bunch is typically generated using either photoemission or thermionic emission. In RF photo guns, the distribution of the bunch is controlled by the laser pulse that drives the photoemission process when illuminating the photocathode, while the resonant RF structures of the gun generate the accelerating field to extract the emitted electrons. RF photo-guns for XFELs are generally classed in two emission types as either high-field or medium to low-field, based on their cathode accelerating field, where the transverse brightness directly depends on the beam intensity [10].

A high-field RF photo-gun enables photoemission of high peak current however delivering a very low transverse emittance can be challenging due to the space charge defocusing. In this emission type, the bunch length, σ_z, is smaller than the transverse beam size, $\sigma_{x,y}$. The transverse emittance and brightness can be estimated using 'pancake' approximation [11]. Such an emission type can be obtained using high-frequency pulsed guns (>1 GHz) to reach high cathode fields up to ~100 MV/m [12]. The beam is then matched into the main linac using solenoidal focusing as shown in Fig. 2(a). This ensures the compensation of the space charge effect and minimises the projected emittance.

(a)

(b)
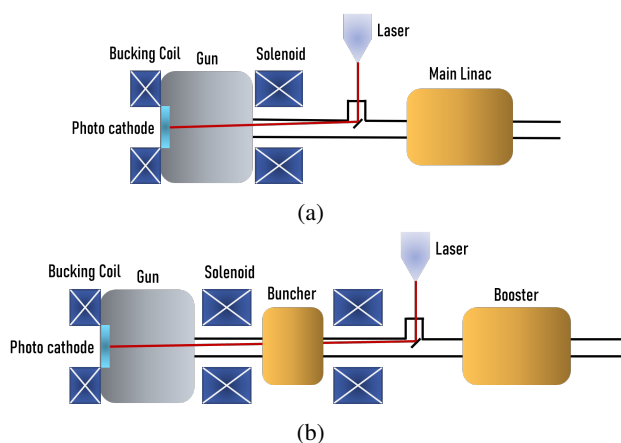
Figure 2: A simplified layout of (a) high (b) medium to low accelerating field RF photo-gun based electron injector.

Most operational XFEL facilities are based on pulsed RF photo-guns. The repetition rate is an engineering challenge and is limited by RF power dissipation on the walls of the cavity [10]. Therefore, the operation of an XFEL in Continuous Wave (CW) mode with high RF frequency and high RF field is not ideal. CW operation of normal conducting (NC) gun-based injectors can be performed either by reducing the field or the frequency, which is typically ~200 MHz [10].

An alternative technology is the superconducting RF (SRF) gun. In addition to their power efficiency, SRF guns have the advantage of reducing the migration of dislocations on the photocathode which can convert to dark current sources [13]. However, SRF gun technology is still in the

development stage and faces some challenges. SRF cavities have poor compatibility with insertable photo cathodes due to the risk of contamination as a result of frequent photo cathode changes. In addition, the use of either cryogenic or room temperature solenoids far away from the gun cavity also poses challenges, due to Meissner field exclusion which can reduce the effect on the emittance compensation [12]. Since SRF guns can operate up to 50 MV/m (as demonstrated at KEK [14], with R&D studies pursuing higher gradients) with CW operation that is lower than the limits of high-frequency NC RF guns. Different groups at HZDR-ELBE, HZB-bERLinPro, DESY (for EU-XFEL), and KEK are working on the development of L-band SRF guns to achieve CW operation under high accelerating fields [10, 12, 14, 15].

The second type of emission involves lasing the photocathode to produce electrons in an elongated, 'cigar' like pattern to reach low emittance by reducing space charge. In this case, a longer laser pulse is used to emit the electrons, therefore the bunch length is much larger than the radius of the bunch in the transverse direction, where $\sigma_z \gg \sigma_{x,y}$. The transverse emittance and brightness can be estimated using 'cigar' approximation [16]. Such an electron gun is typically operated at a subharmonic of the main linac (6th or 7th) that is sufficiently low frequency that allows to host a long bunch. The advantage of a low-frequency gun is to have negligibly small phase slippage, thus the emission field is almost the same as the cathode peak field. The long bunch is then matched (using a solenoid) into the buncher for ballistic compression before its acceleration in the booster as shown in Fig. 2(b). The UK XFEL injector is based on a VHF-band (185.7 MHz) NC CW gun to operate at 1 MHz repetition rate. Similar technology was demonstrated at LBNL for Advanced Photoinjector EXperiment (APEX) designed for the LCLS-II injector [17]. One should note that the APEX gun was then improved to the APEX2 design by increasing both the cathode launching field and the output energy to reduce RF heating and increase the cathode field [18].

There are currently two CW XFELs under construction, one is LCLS-II at SLAC, which improves the repetition rate from 120 Hz to 1 MHz compared to LCLS, and SHINE in China besides EU XFEL CW upgrade [5, 19, 20].

UK XFEL LOW ENERGY BEAM LINE

The proposed UK XFEL low energy beamline will generate a beam from a VHF gun bunched by a one or 2-cell buncher having harmonic or subharmonic of the main linac RF frequency followed by a booster linac to reach the emittance dominated regime at 220-250 MeV. The preliminary design presented here is based on a long electron bunch via 'cigar' emission, reaching slightly higher than 1 MeV energy level at the end of the gun and then compressing the bunch using a 2-cell harmonic buncher to ensure a linear longitudinal phase space before acceleration in the booster. A diagram of the injector beamline used in OPAL [21] simulations is shown in Fig. 3. This preliminary simulation study

uses field maps constructed by cylindrical single-cell field distributions for VHF gun, buncher, and booster cavities with the parameters given in Table 1 to demonstrate a ballistic compression scheme while preserving the normalised core emittance below the target 1000 nm rad.
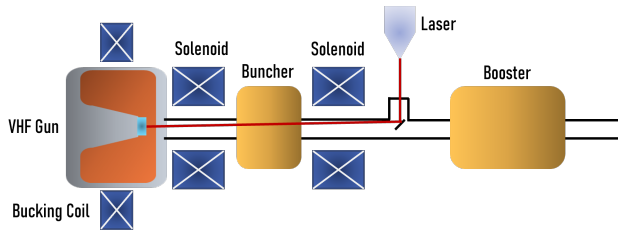
Figure 3: Diagram of the UK XFEL injector line showing the components used in the simulations. A half-cell VHF gun (operating at 185.7 MHz, 7th subharmonic of the linac RF), 2-cell 1.3 GHz buncher, and 2-cell 1.3 GHz linac (booster) were used along with the solenoids.

Table 1: OPAL simulation parameters used for the simulation study. The provided bunch parameters correspond to the initial flattop distribution.

	Parameter	Value	Unit
Bunch	Charge	300	pC
	Size	0.75	mm
	Length	150	ps
Gun	Phase	on crest	-
	Frequency	185.7	MHz
	Field	30.0	MV/m
Buncher	Phase	-90	degree
	Frequency	1300.0	MHz
	Field	10	MV/m
Booster	Phase	on crest	-
	Frequency	1300.0	MHz
	Field	100.0	MV/m

Figure 4 shows the RMS bunch length and energy spread of the electron bunch along the injector line. The ballistic bunching implemented aims to compress the bunch down to 10° of the RF frequency corresponding ~20 ps at the two-cell 1.3 GHz buncher. However, the energy spread increases in the buncher cavity due to a 90° phase shift relative to the gun phase where the energy of the tail of the bunch increases while it decreases at the head of the bunch. This is compensated in the booster during acceleration.

Normalised core emittance of the bunch (which refers to the emittance calculated using only the three slices at the center of the bunch out of 9 slices in total) was calculated along the beamline as shown in Fig. 5. The core emittance on the x- and y-axis at the end of the simulation window were found 588.5 and 576.57 nm rad, respectively. The studies of the low-energy injector will continue to investigate optimising the longitudinal phase space during the bunch compression as a function of the number of the cells, RF
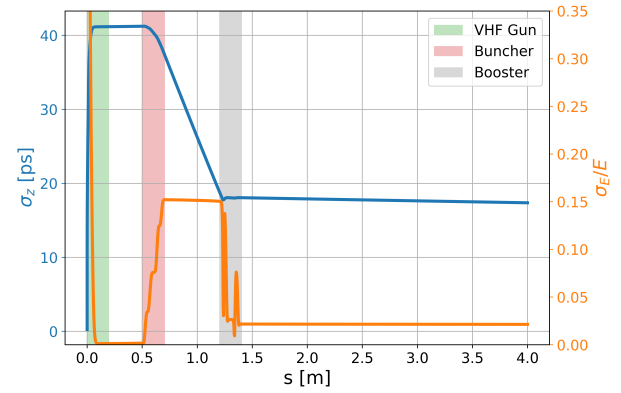
Figure 4: OPAL simulation results showing the RMS bunch length as well as the relative energy spread of the electron bunch along the beamline.
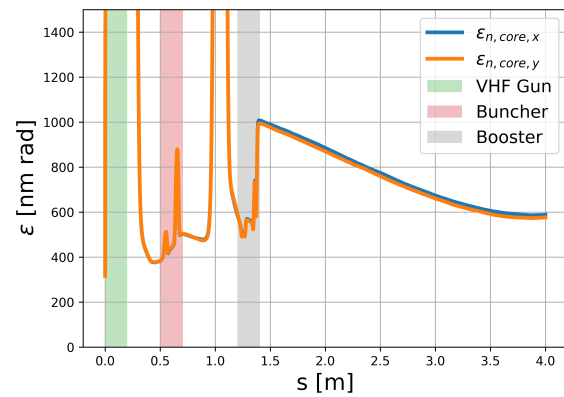
Figure 5: The variation of the normalized core emittance on the x- and y-axis along the beamline.

frequency, as well as the field in the buncher cavity; and preservation of the core emittance. The next steps include the demonstration of acceleration of the bunch using a full booster linac.

CONCLUSION

The UK XFEL conceptual design was initiated following a comprehensive science case study [7]. A possible low-energy injector design was studied to demonstrate the ballistic compression scheme using a 2-cell harmonic buncher and preserve the normalised core emittance. A single-cell buncher operating at the second subharmonic of the main linac RF frequency, along with various booster accelerating fields, is also under consideration for further simulations based on multi-objective optimisation.

ACKNOWLEDGEMENTS

REFERENCES

[1] J. M. Madey, "Stimulated emission of bremsstrahlung in a periodic magnetic field," *J. Appl. Phys.*, vol. 42, no. 5, pp. 1906–1913, 1971. doi:10.1063/1.1660466

[2] S. Schreiber, "First Lasing at 32 nm of the VUV-FEL at DESY," in *Proc. FEL'05*, Palo Alto, CA, USA, Aug. 2005, pp. 12–18. https://jacow.org/f05/papers/MOOB002.pdf

[3] P. Emma *et al.*, "First lasing and operation of an ångstrom-wavelength free-electron laser," *Nat. Photonics*, vol. 4, no. 9, pp. 641–647, 2010. doi:10.1038/nphoton.2010.176

[4] J. Duris *et al.*, "Tunable isolated attosecond X-ray pulses with gigawatt peak power from a free-electron laser," *Nat. Photonics*, vol. 14, no. 1, pp. 30–36, 2020. doi:10.1038/s41566-019-0549-5

[5] R. Brinkmann, E. Schneidmiller, J. Sekutowicz, and M. Yurkov, "Prospects for CW and LP operation of the European XFEL in hard X-ray regime," *Nucl. Instrum. Methods Phys. Res., Sect. A*, vol. 768, pp. 20–25, 2014. doi:10.1016/j.nima.2014.09.039

[6] A. Streun *et al.*, "SLS-2 – the upgrade of the Swiss Light Source," *J. Synchrotron Radiat.*, vol. 25, no. 3, pp. 631–641, 2018. doi:10.1107/S1600577518002722

[7] D. Dunning *et al.*, "An introduction to the UK XFEL Conceptual Design and Options Analysis," presented at the 67th ICFA Advanced Beam Dynamics Workshop on Future Light Sources (FLS 2023), Lucerne, Switzerland, 2023, paper TU4P13, this conference.

[8] J. P. Marangos *et al.*, "UK-XFEL science case," 2020. https://xfel.ac.uk

[9] M. Ferrario and T. Shintake, "High performance electron injectors," *Rev. Accel Sci. Technol.*, vol. 3, no. 01, pp. 221–235, 2010. doi:10.1142/S1793626810000464

[10] H. J. Qian and E. Vogel, "Overview of CW RF guns for short wavelength FELs," in *Proc. FEL'19*, Hamburg, Germany, Aug. 2019, pp. 290–296. doi:10.18429/JACoW-FEL2019-WEA01

[11] I. V. Bazarov, B. M. Dunham, and C. K. Sinclair, "Maximum achievable beam brightness from photoinjectors," *Phys. Rev. Lett.*, vol. 102, p. 104 801, 10 2009. doi:10.1103/PhysRevLett.102.104801

[12] F. Zhou, C. Adolphsen, D. Dowell, and R. Xiang, "Overview of CW electron guns and LCLS-II RF gun performance," *Front. Phys.*, vol. 11, 2023. doi:10.3389/fphy.2023.1150809

[13] F. Sannibale, "High-brightness electron injectors for high-duty cycle X-ray free electron lasers," *Front. Phys.*, vol. 11, 2023. doi:10.3389/fphy.2023.1187346

[14] T. Konomi *et al.*, "Development of high intensity, high brightness, CW SRF gun with bi-alkali photocathode," in *Proc. SRF'19*, Dresden, Germany, Jun.-Jul. 2019, pp. 1219–1222. doi:10.18429/JACoW-SRF2019-FRCAB4

[15] J. Teichert *et al.*, "Successful user operation of a superconducting radio-frequency photoelectron gun with Mg cathodes," *Phys. Rev. Accel. Beams*, vol. 24, p. 033 401, 3 2021. doi:10.1103/PhysRevAccelBeams.24.033401

[16] D. Filippetto, P. Musumeci, M. Zolotorev, and G. Stupakov, "Maximum current density and beam brightness achievable by laser-driven electron sources," *Phys. Rev. ST Accel. Beams*, vol. 17, p. 024 201, 2 2014. doi:10.1103/PhysRevSTAB.17.024201

[17] F. Sannibale *et al.*, "Advanced photoinjector experiment photogun commissioning results," *Phys. Rev. ST Accel. Beams*, vol. 15, p. 103 501, 10 2012. doi:10.1103/PhysRevSTAB.15.103501

[18] T. Luo *et al.*, "RF design of APEX2 two-cell continuous-wave normal conducting photoelectron gun cavity based on multi-objective genetic algorithm," *Nucl. Instrum. Methods Phys. Res., Sect. A*, vol. 940, pp. 12–18, 2019. doi:10.1016/j.nima.2019.05.079

[19] A. Halavanau, F.-J. Decker, C. Emma, J. Sheppard, and C. Pellegrini, "Very high brightness and power LCLS-II hard X-ray pulses," *J. Synchrotron Radiat. (Online)*, vol. 26, no. 3, 2019. doi:10.1107/s1600577519002492

[20] N. Huang, H. X. Deng, B. Liu, and D. Wang, "Physical design and FEL performance study for FEL-III beamline of SHINE," in *Proc. FEL'19*, Hamburg, Germany, Aug. 2019, pp. 199–202. doi:10.18429/JACoW-FEL2019-TUP063

[21] A. Adelmann *et al.*, "OPAL a versatile tool for charged particle accelerator simulations," *arXiv e-prints*, paper arXiv:1905.06654, 2019. doi:10.48550/arXiv.1905.06654

AN INTRODUCTION TO THE UK XFEL CONCEPTUAL DESIGN AND OPTIONS ANALYSIS

D. J. Dunning*, D. Angal-Kalinin, J. A. Clarke, J. R. Henderson, S. L. Mathisen,
B. L. Militsyn, M. D. Roper, E. W. Snedden, N. R. Thompson, D. A. Walsh, P. H. Williams,
ASTeC, STFC Daresbury Laboratory and Cockcroft Institute, Sci-Tech Daresbury, Warrington, UK
P. Aden, B. D. Fell, Tech. Dept., STFC Daresbury Laboratory, Sci-Tech Daresbury, Warrington, UK
J. L. Collier, J. S. Green, Central Laser Facility, STFC Rutherford Appleton Laboratory, Didcot, UK
J. P. Marangos, Department of Physics, Imperial College London, Blackett Laboratory, London, UK

Abstract

In October 2022, the UK XFEL project entered a new phase to explore how best to deliver the advanced XFEL capabilities identified in the project's Science Case. This phase includes developing a conceptual design for a unique new machine to fulfil the required capabilities and more. It also examines the possibility of investment opportunities at existing XFELs to deliver the same aims, and a comparison of the various options will be made. The desired next-generation capabilities include transform-limited operation across the entire X-ray range with pulse durations ranging from 100 as to 100 fs; evenly spaced high rep. rate pulses for enhanced data acquisition rates; optimised multi-colour FEL pulse delivery and a full array of synchronised sources (XUV-THz sources, electron beams and high power/high energy lasers). The project also incorporates sustainability as a key criteria. This contribution gives an overview of progress to date and future plans.

INTRODUCTION

In early 2019, the UK initiated a project to develop the science case for a UK XFEL, which was published in 2020 [1, 2]. Subsequent exercises demonstrated the support of the UK community and in June 2022, UK Research and Innovation announced funding for the next phase of the project: a 3-year conceptual design and options analysis (CDOA), which started in October 2022. This phase includes developing a conceptual design for a unique new UK machine, alongside examining investment opportunities at existing facilities e.g. [3–12], both with the aim of realising 'next-generation' XFEL capabilities (the features of which are discussed below). By the end of this phase of the project (October 2025) we will have:

- mapped out how best to deliver advanced XFEL capabilities identified in the Science Case;
- explored a conceptual design for a unique new machine that can fulfil all required capabilities;
- examined other investment options and collaborations in existing XFELs;
- updated the Science Case to feed into the process and inform future decisions;
- held multiple Townhall Meetings around the UK engaging with the user community;

---

* david.dunning@stfc.ac.uk

- investigated the socioeconomic impact of a next generation XFEL.

Year 1 has so far focused on the project launch, surveying the science requirements, preliminary engagement with overseas XFEL facilities, planning the Townhall meetings and initial conceptual design and layout work. Informed by work this year, Year 2 will focus on R&D targeting gaps in key physics and technology areas, including collaborative work with overseas XFEL facilities, and the continuation of Townhall meetings and other workshops. In Year 3, R&D activities will continue and the final CDOA report will be written, detailing the preferred options; including associated costs, socio-economic analysis, and an update to the Science Case. This paper gives an overview of progress to date.

NEXT-GENERATION XFEL CAPABILITIES

Starting from our Science Case, our project clearly sets an emphasis on enhancing XFEL capabilities and on widening access to such capabilities, defined as follows:

- Transform-limited operation across the entire X-ray range (initial focus on 0.1 - 20 keV and 100 as - 100 fs).
- High efficiency facility, with a step change in the simultaneous operation of multiple end stations.
- Evenly spaced, high rep. rate pulses to match samples & detectors.
- Improved synchronisation/timing data with external lasers to < 1 fs.
- Widely separated multiple colour X-rays to at least one end station.
- Full array of synchronised sources: XUV-THz, e-beams, high power & high energy lasers at high rep. rate.

This list of features results from both the Science Case and work in this phase, including a detailed survey of our science team, results of which are shown in Fig. 1. We are presently focusing our preliminary activities on the capabilities listed above, particularly the first two, which we consider to be the most challenging and fundamental to the machine design (see sections below). Other requested capabilities, e.g., higher photon energies will be considered beyond the preliminary focus and are briefly summarised below.

The options will ultimately be assessed on a range of criteria including the above capabilities, technology readiness level, environmental sustainability and cost.

67th ICFA Adv. Beam Dyn. Workshop Future Light Sources
FLS2023, Luzern, Switzerland
JACoW Publishing
ISBN: 978-3-95450-224-0
ISSN: 2673-7035
doi:10.18429/JACoW-FLS2023-TU4P13

PROGRESS TOWARDS A CONCEPT FOR A NEXT-GENERATION FACILITY

We are presently in the early stages of defining our concept for a next-generation facility - the preliminary designs and ideas are presented here for discussion and to highlight potential collaboration opportunities.

Photon Energy, Repetition Rate and Pulse Energy

Figure 1 shows the photon energy and repetition rate requirements identified in the Science Case (grey boxes) and survey (coloured points - pulse energy requirements are also indicated for these). For our preliminary activities, we have identified the core requirements as being photon energies from 0.1 to 20 keV (at the fundamental) and with at least 100 kHz delivered to each experiment. Meeting the repetition rate requirement implies that we must operate with superconducting RF technology. We are assuming a repetition rate of ~1 MHz to allow multiplexing to multiple experiments. The beam energy should be around 8 GeV to reach the highest photon energies with high pulse energy. This preliminary working point is indicated as the shaded region in Fig. 1. Options for higher photon energy and/or pulse energy are described in a later section.
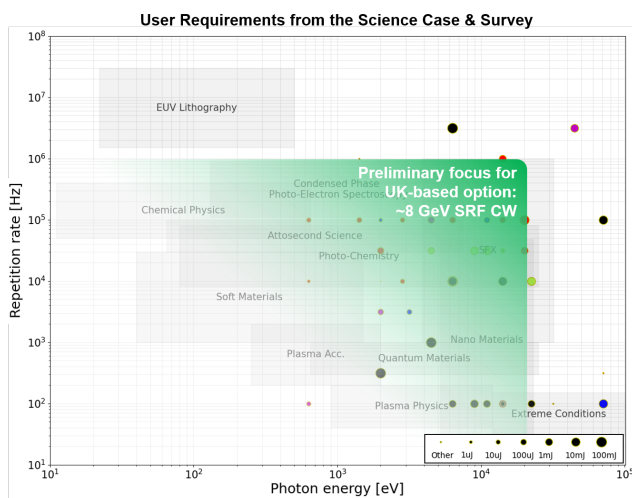
Figure 1: Photon energy, repetition rate and pulse energy requirements from the Science Case (grey boxes labelled by science area) and recent user survey (unlabelled points, colours represent different science areas), and approx. coverage provided by the proposed facility design parameters.

Transform-Limited Pulses

A key focus of our preliminary activities is the requirement for transform-limited operation across the entire X-ray range, from 0.1 - 20 keV and 100 as - 100 fs. 'Laser like X-rays' for users over such a broad range is a challenging aim that could be a distinguishing feature of a next-generation facility and R&D will be valuable to the international XFEL community. Figure 2 shows the photon energy-pulse length parameter space, with the preliminary focus region of 0.1 to

20 keV and 100 as to 100 fs indicated. The corresponding relative FWHM bandwidth for a transform-limited pulse within this space is indicated by contours, and indicative positions of some of the leading FEL techniques to meet the requirements are shown.

It is evident that several FEL techniques are required to cover such a large parameter space. Many such schemes are well established at international XFELs, however there remains much opportunity for development, e.g., to utilise advances in conventional lasers to drive external seeding as used at e.g., FERMI [5] to much higher rep. rate (~100 kHz) and to higher photon energy (potentially ~1-2 keV). Techniques for attosecond (e.g., XLEAP [13]) and narrow bandwidth (e.g., self-seeding [14, 15]) pulses are well-established and so present opportunities to pursue high rep. rate operation, increased tunability and other advanced features [16]. Techniques such as HB-SASE [17] (with potentially TW peak power, few-fs pulses at any wavelength & rep. rate [18]) and XFELO [19] are under experimental development. Furthermore, the prospect of operating multiple such techniques simultaneously is a major challenge and potentially a distinguishing feature of a next-generation machine.
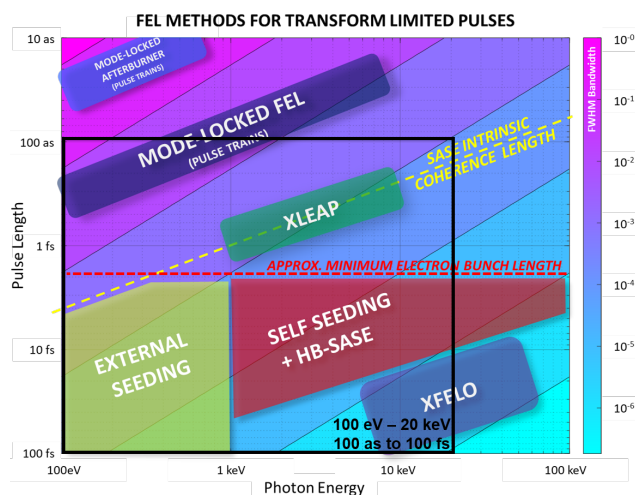
Figure 2: The project's initial aim for transform-limited pulses from 0.1 to 20 keV and 100 as to 100 fs is shown by the black box in the photon energy-pulse length parameter space. The contours show the relative bandwidth of a transform-limited pulse, along with the estimated coverage of some relevant FEL techniques.

Simultaneous Operation of Multiple FELs

Another focus of our preliminary activities is to develop a concept for a high efficiency facility with a step change in the simultaneous operation of multiple end stations. Even given the pre-eminent capabilities of existing XFELs, it is widely recognised that it would be hugely beneficial to increase the scientific output from their investment. While challenging, this is a major opportunity to differentiate the next generation of XFELs from existing machines, and is already part of the thinking for upgrades to existing facilities.

Our initial thinking is that this capability would be best achieved through operating with fixed accelerator settings up to full energy, and so multiplexing ~1 MHz bunches with fixed properties to several undulator lines, each operating at ~100 kHz, potentially using kicker magnets as shown in Fig. 3. The fixed bunch properties at the end of the linac would then be manipulated within each FEL line to deliver the varying bunch requirements of the various FEL techniques described in the previous section. Significantly more work is required on such an approach but truly independent operation of multiple high-performance FEL lines would be highly advantageous. Bunch-to-bunch variation upstream of the spreader could also be considered, e.g., by laser pulse shaping [20] in the photoinjector or laser heater.
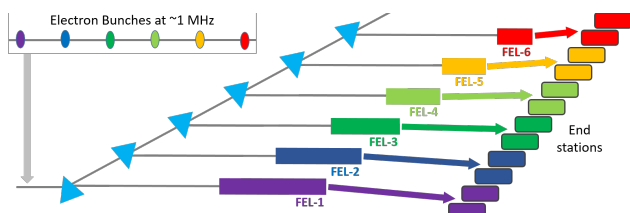
Figure 3: Initial FEL concept: electron bunches at ~1 MHz and ~8 GeV energy are divided e.g., by kicker magnets (blue triangles) to multiple independently tunable FEL lines at ~100 kHz, which each feed multiple end stations. The different bunch colours indicate which line they pass through, with different wavelengths set by the undulators parameters.

Assuming the electron beam energy to all FELs to be fixed at 8 GeV, then to cover 0.1 to 20 keV while allowing for some overlap in tuning is best covered by at least ~6 FELs as shown in Fig. 3. Potential operating ranges are shown in Fig. 4: these are indicative for ongoing discussions with our science team. Given the fixed electron beam energy, the relative width of the wavelength tuning range is narrower
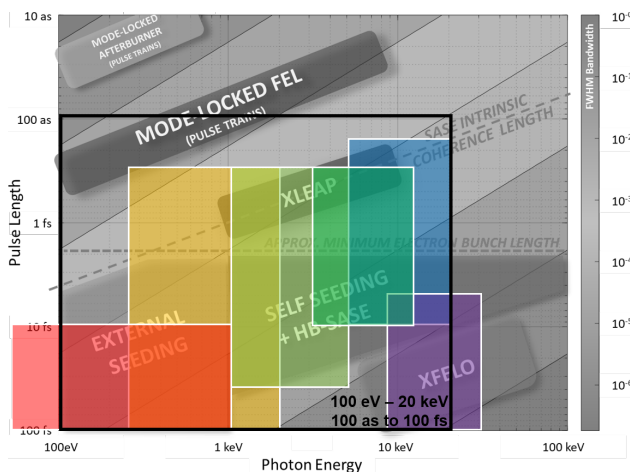
for the higher photon energy FELs to optimise performance, and can be successively broader for lower photon energies. The FEL lines would likely have some specialisms in terms of techniques, e.g., FELs-5 and 6 could feature high rep. rate seeding, while others could focus on e.g., attosecond or narrow-bandwidth schemes. The intention for the spreader is to allow an easily scalable number of lines, which could encompass both FELs and other uses of the electron beam. Figure 3 shows two end stations per line, which is again indicative and is the subject of discussion within our team.

Combining FEL Lines

A feature under consideration from an early stage due to its likely significant impact on the design is that of combining output from multiple FELs. This isn't shown in Fig. 3 but essentially builds on our concept for CompactLight [21]: the bunch pattern from the injector is adjusted to bring two bunches into adjacent RF cycles, such that they initially traverse the same FEL line, then a GHz subharmonic deflecting cavity is used to deflect one bunch onto an adjacent line. The FEL pulses can then be combined, with time of flight matching/scanning using electron delay chicanes.

Beyond the Preliminary Focus

Beyond the preliminary focus, there are several other capabilities that will be considered. Very high pulse energies of 10-100 mJ or higher have been requested in some cases, e.g., for study of matter in extreme conditions. Very high photon energies are also of interest, i.e., above 20 keV, towards 50 - 100 keV. In both cases we will consider how these could be incorporated into a UK XFEL design, potentially with a booster to increase electron beam energy and/or brightness in one of the lines post-spreader. Synchronous sources will be a major part of our proposal. The present focus is on laser-based NIR-visible sources, which are most highly demanded, and we will also consider the best way to deliver THz radiation. Calls for electrons, protons, ions and gamma sources will be explored further with our science team.

NEXT STEPS

Our present work is focused on developing the concept and analysing its implications for the main technology areas (e.g., [22]). This includes identifying key R&D areas and taking steps to undertake the required work both within the project team and in collaboration with international partners. A series of Townhall meetings is underway to extend the UK user community and to update the Science Case.

ACKNOWLEDGEMENTS

While the authorship of this paper is limited to the facility design leads and our Science Lead, we would like to recognise the innovative contributions and advice of all our team and international collaborators.

Figure 4: Indicative coverage of the photon-energy-pulse length parameter space by 6 FELs, with colours corresponding to those in Fig. 3. These ranges are in the early stages of iteration with our science team.

REFERENCES

[1] *UK XFEL Project Website*. https://xfel.ac.uk

[2] J. Marangos *et al.*, "UK XFEL Science Case," UK Research and Innovation, Science and Technology Facilities Council, Tech. Rep., 2020.

[3] W. Ackermann *et al.*, "Operation of a free-electron laser from the extreme ultraviolet to the water window," *Nat. Photonics*, vol. 1, no. 6, pp. 336–342, 2007.
doi:10.1038/nphoton.2007.76

[4] P. Emma *et al.*, "First lasing and operation of an angstrom-wavelength free-electron laser," *Nat. Photonics*, vol. 4, p. 641, 2010. doi:10.1038/nphoton.2010.176

[5] E. Allaria *et al.*, "Highly coherent and stable pulses from the FERMI seeded free-electron laser in the extreme ultraviolet," *Nat. Photonics*, vol. 6, no. 10, pp. 699–704, 2012.
doi:10.1038/nphoton.2012.233

[6] T. Ishikawa *et al.*, "A compact X-ray free-electron laser emitting in the sub-angstrom region," *Nat. Photonics*, vol. 6, p. 540, 2012. doi:10.1038/nphoton.2012.141

[7] H.-S. Kang *et al.*, "Hard X-ray free-electron laser with femtosecond-scale timing jitter," *Nat. Photonics*, vol. 11, no. 11, pp. 708–713, 2017.
doi:10.1038/s41566-017-0029-8

[8] C. J. Milne *et al.*, "SwissFEL: The Swiss X-ray Free Electron Laser," *Applied Sciences*, vol. 7, no. 7, 2017.
doi:10.3390/app7070720

[9] W. Decking *et al.*, "A MHz-repetition-rate hard X-ray free-electron laser driven by a superconducting linear accelerator," *Nat. Photonics*, vol. 14, no. 6, pp. 391–397, 2020.
doi:10.1038/s41566-020-0607-z

[10] B. Liu *et al.*, "The SXFEL Upgrade: From Test Facility to User Facility," *Applied Sciences*, vol. 12, no. 1, 2022.
doi:10.3390/app12010176

[11] R. W. Schoenlein *et al.*, "New Science Opportunities Enabled by LCLS-II X-ray Lasers," Tech. Rep., 2015, SLAC-R-1053.

[12] Z. Zhu, Z. T. Zhao, D. Wang, Z. H. Yang, and L. Yin, "SCLF: An 8-GeV CW SCRF Linac-Based X-Ray FEL Facility in Shanghai," in *Proc. FEL'17*, Santa Fe, NM, USA, Aug. 2017, pp. 182–184. doi:10.18429/JACoW-FEL2017-MOP055

[13] J. Duris *et al.*, "Tunable isolated attosecond X-ray pulses with gigawatt peak power from a free-electron laser," *Nat. Photonics*, vol. 14, no. 1, pp. 30–36, 2020.
doi:10.1038/s41566-019-0549-5

[14] G. Geloni *et al.*, "A novel self-seeding scheme for hard X-ray FELs," *J. Mod. Opt.*, vol. 58, pp. 1391–1403, 2011.
doi:10.1080/09500340.2011.586473

[15] J. Amann *et al.*, "Demonstration of self-seeding in a hard-X-ray free-electron laser," *Nat. Photonics*, vol. 6, p. 693, 2012.
doi:10.1038/nphoton.2012.180

[16] M. Coku and N. Thompson, "Investigation of attosecond pulse generation schemes for UK XFEL," Venice, Italy, May 2023, presented at IPAC'23, Venice, Italy, May 2023, paper TUPL072, to appear in the proceedings.

[17] B. W. J. McNeil, N. R. Thompson, and D. J. Dunning, "Transform-limited x-ray pulse generation from a high-brightness self-amplified spontaneous-emission free-electron laser," *Phys. Rev. Lett.*, vol. 110, p. 134 802, 2013.
doi:10.1103/PhysRevLett.110.134802

[18] N. Thompson, "Taper-enhanced high-brightness SASE for stable temporally coherent HXR FEL pulses," Venice, Italy, May 2023, presented at IPAC'23, Venice, Italy, May 2023, paper TUPL007, to appear in the proceedings.

[19] K.-J. Kim, Y. Shvyd'ko, and S. Reiche, "A proposal for an x-ray free-electron laser oscillator with an energy-recovery linac," *Phys. Rev. Lett.*, vol. 100, p. 244 802, 2008.
doi:10.1103/PhysRevLett.100.244802

[20] A. Pollard, D. Dunning, E. Snedden, and W. Okell, "Machine learning for laser pulse shaping," Venice, Italy, May 2023, presented at IPAC'23, Venice, Italy, May 2023, paper THPL034, to appear in the proceedings.

[21] G. D'Auria *et al.*, "Conceptual Design Report of the CompactLight X-ray FEL," Tech. Rep. XLS-Report-2021-010, XLS Deliverable D2.3, 2021.
doi:10.5281/zenodo.6375645

[22] C. Davut, O. Apsimon, S. S. Percival, and B. L. Militsyn, "Injection into XFELs, a Review of Trends and Challenges," presented at FLS'23, Lucerne, Switzerland, Aug 2023, paper TU4P12, this conference.

TRANSVERSE OPTICS-BASED CONTROL
OF THE MICROBUNCHING INSTABILITY

A. D. Brynes[*], E. Allaria, G. De Ninno, S. Di Mitri, D. Garzella, G. Perosa, C. Spezzani

Elettra-Sincrotrone Trieste S.C.p.A., Trieste, Italy

C.-Y. Tsai

Department of Electrotechnical Theory and Advanced Electromagnetic Technology,
Huazhong University of Science and Technology, Wuhan, China

Abstract

A number of recent experimental and theoretical studies have investigated novel techniques for suppressing the microbunching instability in high-brightness linac-based light sources. This instability has long been studied as one of the causes of reduced longitudinal coherence in these machines. It is commonly suppressed using a laser heater. This contribution presents recent developments which use an optics-based scheme to mitigate the microbunching instability in the FERMI free-electron laser, paving the way towards reversible beam heating techniques that could improve the performance of future machines.

INTRODUCTION

High-brightness electron bunches are a fundamental requirement for producing high-intensity, narrow-bandwidth free electron laser (FEL) pulses [1]. The 6D beam brightness is described by the phase space volume occupied by the beam: in the transverse plane, a bright beam has a small emittance, whereas the requirements for the longitudinal properties of the beam are a high current density and a low slice energy spread [2, 3]. One of the key factors that can reduce the brightness of the electron beam as it is accelerated on its path towards the FEL undulators is the microbunching instability [1, 4, 5], which arises due to a variety of collective interactions between particles in the beam and its environment [6]. This instability can result in a beam that has a non-uniform longitudinal density profile, and an increased slice energy spread [7, 8], thereby reducing the quality of the light produced in the FEL [9, 10].

Various methods have been proposed and tested to mitigate the development of this instability, and to preserve the beam brightness up to the entrance of the FEL [11]. The most widely used of these methods is the laser heater [12, 13], a device which increases the uncorrelated slice energy spread in the beam (to an acceptable level). However, other methods can lead to the suppression of small-scale modulations in the beam without resorting to this irreversible dilution of the beam phase space [14–23]. In this contribution, a method of controlling the microbunching content in the beam is exploited at the FERMI FEL [24]. The transverse optics functions of the beam are varied along the linac-to-FEL transfer line (also known as the 'spreader'), and it is observed that the FEL performance can be improved simply using quadrupole magnets.

* alexander.brynes@elettra.eu

THEORY

The one-dimensional bunching factor $b(k)$ [25–27] is used to characterize the depth of modulations in the electron bunch as a function of wavenumber. This parameter is given by the Fourier transform of the current profile. The ratio between the final and initial bunching factors – $b_f(k)$ and $b_i(k)$, respectively – is known as the microbunching gain $G(k) = b_f(k)/b_i(k)$. In the absence of collective effects, the final bunching factor is given by:

$$b_f(k) = b_i(k_0) \exp\left(-\frac{1}{2}\left(k_f R_{56} \sigma_{\delta,0}\right)^2\right) \times$$

$$\exp\left(-\frac{1}{2}k_f^2 \left[\epsilon_{x,0}\beta_{x,0}\left(R_{51} - \frac{\alpha_{x,0}}{\beta_{x,0}}R_{52}\right)^2 - \frac{\epsilon_{x,0}}{\beta_{x,0}}R_{52}^2\right]\right).$$

(1)

The R_{5x} parameters give the linear components of the 6×6 transfer matrix [28], and ϵ, β and α are the initial horizontal emittance and Twiss parameters of the beam. The final wavenumber k_f is given by $k_i C$, with C the compression factor of the lattice. For full derivations of the influence of the collective effects mentioned above on the microbunching gain, the reader is referred to Refs.[12, 13, 16, 25, 27, 29–32].

Coherent synchrotron radiation (CSR) [26, 27], geometric wakefields in accelerating structures [33], and longitudinal space-charge (LSC) [13, 34–36] are all examples of collective effects that can drive the microbunching instability during the electron beam acceleration and compression process.

It can be seen from Eq. (1) that the final bunching factor can be reduced by increasing either $\sigma_{\delta,0}$, R_{56}, or $\mathcal{H}_x$. The third of these terms, otherwise known as the dispersion invariant, is given by the term in square brackets within the second exponential of Eq. (1). Previous work undertaken at FERMI [18] has demonstrated that a non-isochronous spreader line ($|R_{56}| > 0$) can reduce the spectral bandwidth of the FEL pulse; in this contribution, a similar effect is observed by varying the dispersion invariant $\mathcal{H}_x$.

MEASUREMENT METHODS

While a full measurement of the electron bunch longitudinal phase space, and the modulations therein, can be captured through the use of a vertical RF deflector and a bending magnet [37], this analysis method can be complicated [7, 8]. Alternatively, as mentioned above, the microbunching
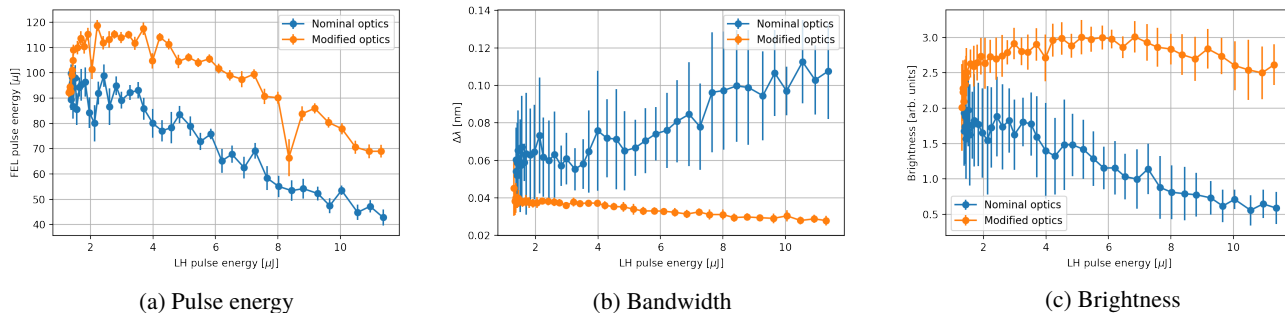
Figure 1: Performance of FEL1 as a function of laser heater pulse energy for two different transverse optics configurations in the spreader.
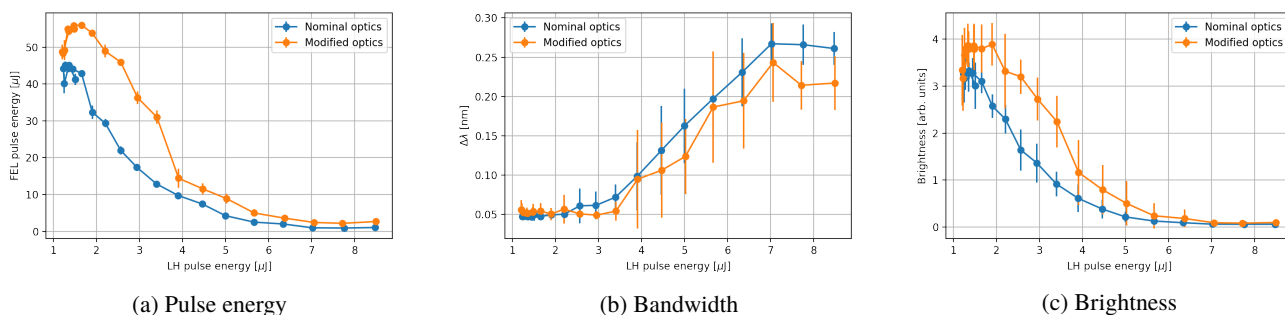
Figure 2: Performance of FEL2 as a function of laser heater pulse energy for two different transverse optics configurations in the spreader.

instability can degrade the quality of the FEL, both in terms of the pulse intensity and the bandwidth. Therefore, through the use of a laser heater, it is possible to increase the slice energy spread of the electron bunch, and thereby determine if microbunching is present in the beam [9].

A new diagnostic to measure the microbunching content in the beam, based on the generation of coherent transition radiation (CTR) and known as the Spectrometer in the InfraRed (SPIR), has recently been installed at FERMI [38–40]. CTR is generated when the electron beam passes through an aluminium foil located in the centre of the delay chicane in the FEL2 line, and the wavelength and intensity of the radiation is monitored by detectors after being dispersed through a spectrometer. The wavelength of the radiation that is generated depends on the wavelength of the modulations along the longitudinal axis of the beam, which is typically in the range 1–10 μm at this machine.

MICROBUNCHING MITIGATION IN THE SPREADER

Two sets of experiments were performed in which the dispersion invariant $\mathcal{H}_x$ was varied along the spreader (see Eq. (1)) by changing the transverse beam properties in the transfer line. This was achieved by altering the strengths of two quadrupole magnets in the section before the entrance

Table 1: Machine Setup for Experiments

Parameter	FEL1	FEL2	Unit
	LINAC		
Bunch charge		500	pC
Initial peak current		70	A
Compression factor	8	10	
Final beam energy	1240	1535	MeV
Normalized emittance	1.2	1.4	μm−rad
	FEL		
Seed wavelength	270.5	250.1	nm
Harmonic	12	8 × 5	
FEL wavelength	22.5	6.25	nm

to the spreader. The effect of varying $\mathcal{H}_x$ on the FEL performance and the microbunching instability was characterized along both FEL lines. First, the transverse emittance at the entrance to the spreader was measured using a single-quadrupole scan [41]. Next, the strengths of two quadrupole magnets were adjusted and the beam was matched into the FEL [42]. Finally, the FEL performance (and the SPIR response) was measured as a function of laser heater pulse energy. The machine setups for the experiments on both FEL lines are summarized in Table 1.

Based on the emittance measurement and the lattice parameters in the spreader, the value of the dispersion invariant was calculated for the various optics settings using the OCELOT tracking code [43, 44]. The value of $\mathcal{H}_x$ was calculated for the two different optics settings – the 'nominal' settings have two quadrupoles immediately after the emittance measurement station at the exit of the linac set to zero strength; the 'modified' settings do not. The modified optics have a larger dispersion invariant along the spreader, approximately 2 times larger in the case of FEL1, and around 40 % larger for FEL2.

By looking in detail at the performance of the FEL for both of these datasets, the impact of the transverse beam optics can be seen clearly – see Figs. 1 and 2 for measurements of the FEL pulse energy, bandwidth, and brightness as a function of laser heater pulse energy on both FEL lines. It can be seen that the modified optics functions in the spreader improved the FEL pulse energy and brightness in both cases. The fact that the microbunching instability is not fully suppressed with the laser heater switched off, observed already in Fig. 4, is confirmed here, as an increase in FEL performance can be achieved even with the modified optics settings for a non-zero laser heater pulse energy. An interesting discrepancy between the datasets for each FEL line, however, is the difference in the bandwidth curves (Figs. 1b and 2b): the former does not show the bandwidth increasing as a function of laser heater pulse energy for the modified optics, whereas in the latter plot, the two sets of beam optics resulted in similar bandwidth curves. This difference merits further study.

On FEL1, which does not have access to the SPIR, the FEL performance was used as the metric for judging the microbunching content in the beam. Figure 3 shows the average number of peaks in the FEL spectrum as a function of laser heater pulse energy for both optics settings. As discussed in Refs. [10, 18], the microbunching instability can induce sidebands in the FEL spectrum, and by finding local maxima in the measured spectra, it is possible to determine how clean the spectra are. With the modified optics settings, and a larger value of $\mathcal{H}_x$, the FEL is clearly more monochromatic, suggesting that the microbunching content has been reduced.

The second set of measurements undertaken on FEL2 provided more detailed information on the wavelength of modulations present in the bunch, thanks to the SPIR, as shown in Fig. 4. A clear peak in the intensity of the SPIR signal can be seen at around 1 μm, and the modification of the transverse optics in the spreader can reduce this signal by approximately 90 %. The signal was not entirely removed, suggesting that there was still some residual microbunching content in the beam, and that further increasing the dispersion invariant, if compatible with maintaining acceptable optics functions in the FEL, could increase the FEL performance further. However, there are other potential explanations for this: a difference in the transverse beam size at the SPIR could have an impact on the measured signal [40]. Moreover, any current spike in the beam could produce CTR
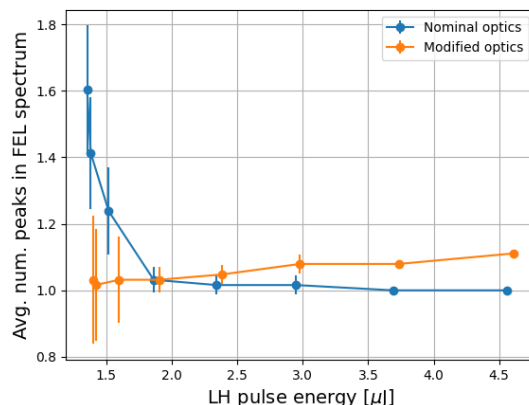
Figure 3: Average number of peaks in the spectrum of FEL1 for two different transverse optics settings in the spreader, as a function of the laser heater pulse energy. The error bars represent the standard deviation per step.
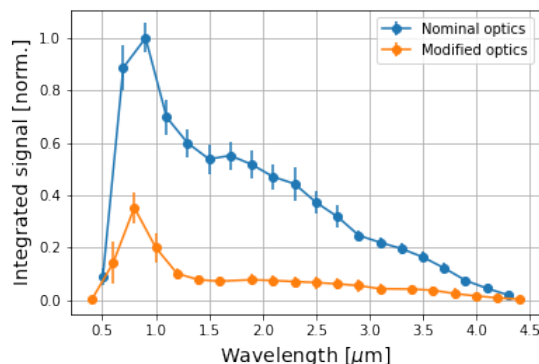
Figure 4: Integrated intensity of the SPIR as a function of IR wavelength for two different transverse optics configurations. The error bars represent the standard deviation per step.

to be observed by the IR detectors, even in the absence of any microbunching in the beam.

CONCLUSIONS

This contribution has outlined experimental work recently undertaken at FERMI to suppress the microbunching instability through transverse control of the electron beam optics in the spreader line. It has been demonstrated that the transverse beam optics – particularly in dispersive regions – can play a key role in controlling this instability. Coupled with previous theoretical and experimental work, these results could help to pave the way towards mitigation of the microbunching instability using methods based only on beam optics. Theoretical and numerical investigations to confirm the results presented herein are currently underway.

REFERENCES

[1] S. D. Mitri and M. Cornacchia, *Phys. Rep.*, vol. 539, no. 1, p. 1, 2014. `doi:10.1016/j.physrep.2014.01.005`

[2] P. Schmüser, M. Dohlus, J. Rossbach, and C. Behrens, *Free-electron lasers in the ultraviolet and x-ray regime*. Springer, 2014.

[3] Z. Huang and K.-J. Kim, *Phys. Rev. Spec. Top. Accel. Beams*, vol. 10, no. 3, p. 034 801, 2007. `doi:10.1103/PhysRevSTAB.10.034801`

[4] R. Akre *et al.*, *Phys. Rev. Spec. Top. Accel. Beams*, vol. 11, no. 3, p. 030 703, 2008. `doi:10.1103/PhysRevSTAB.11.030703`

[5] S. D. Mitri and S. Spampinati, *Phys. Rev. Spec. Top. Accel. Beams*, vol. 17, no. 11, p. 110 702, 2014. `doi:10.1103/PhysRevSTAB.17.110702`

[6] A. W. Chao, *Physics of collective beam instabilities in high energy accelerators*. Wiley, 1993.

[7] D. Ratner *et al.*, *Phys. Rev. Spec. Top. Accel. Beams*, vol. 18, no. 3, p. 030 704, 2015. `doi:10.1103/PhysRevSTAB.18.030704`

[8] A. D. Brynes *et al.*, *Sci. Rep.*, vol. 10, p. 5059, 2020. `doi:10.1038/s41598-020-61764-y`

[9] Z. Huang *et al.*, *Phys. Rev. Spec. Top. Accel. Beams*, vol. 13, no. 2, p. 020 703, 2010. `doi:10.1103/PhysRevSTAB.13.020703`

[10] Z. Zhang *et al.*, *Phys. Rev. Accel. Beams*, vol. 19, p. 050 701, 2016. `doi:10.1103/PhysRevAccelBeams.19.050701`

[11] C.-Y. Tsai, "Suppressing CSR Microbunching in Recirculation Arcs," in *Proc. IPAC'18, Vancouver, BC, Canada*, Vancouver, BC, Canada, Apr.-May 2018, pp. 1784–1789. `doi:10.18429/JACoW-IPAC2018-WEYGBE1`

[12] E. L. Saldin, E. A. Schneidmiller, and M. V. Yurkov, *Nucl. Instrum. Meth. A*, vol. 483, no. 1, p. 516, 2002. `doi:10.1016/S0168-9002(02)00372-8`

[13] Z. Huang *et al.*, *Phys. Rev. Spec. Top. Accel. Beams*, vol. 7, no. 7, p. 074 401, 2004. `doi:10.1103/PhysRevSTAB.7.074401`

[14] C. Feng *et al.*, *New J. Phys.*, vol. 17, no. 7, p. 073 028, 2017. `http://iopscience.iop.org/article/10.1088/1367-2630/17/7/073028`

[15] J. Qiang, C. E. Mitchell, and M. Venturini, *Phys. Rev. Lett.*, vol. 111, no. 5, p. 054 801, 2013. `doi:10.1103/PhysRevLett.111.054801`

[16] B. Li and J. Qiang, *Phys. Rev. Accel. Beams*, vol. 23, no. 1, p. 014 403, 2020. `doi:10.1103/PhysRevAccelBeams.23.014403`

[17] J. Qiang, *Nucl. Instrum. Meth. A*, vol. 1048, p. 167 968, 2023. `doi:10.1016/j.nima.2022.167968`

[18] G. Perosa *et al.*, *Phys. Rev. Accel. Beams*, vol. 23, no. 11, p. 110 703, 2020. `doi:10.1103/PhysRevAccelBeams.23.110703`

[19] W. Cheng *et al.*, *Nucl. Instrum. Meth. A*, vol. 1050, p. 168 145, 2023. `doi:10.1016/j.nima.2023.168145`

[20] S. D. Mitri and S. Spampinati, *Phys. Rev. Lett.*, vol. 112, no. 13, p. 134 802, 2014. `doi:10.1103/PhysRevLett.112.134802`

[21] S. Bettoni *et al.*, *Phys. Rev. Accel. Beams*, vol. 19, no. 3, p. 034 402, 2016. `doi:10.1103/PhysRevAccelBeams.19.034402`

[22] C. Behrens, Z. Huang, and D. Xiang, *Phys. Rev. Spec. Top. Accel. Beams*, vol. 15, no. 2, p. 022 802, 2012. `doi:10.1103/PhysRevSTAB.15.022802`

[23] C.-Y. Tsai *et al.*, *Phys. Rev. Accel. Beams*, vol. 20, no. 2, p. 024 401, 2017. `doi:10.1103/PhysRevAccelBeams.20.024401`

[24] E. Allaria *et al.*, *J. Synch. Rad*, vol. 22, 2015. `doi:10.1107/S1600577515005366`

[25] M. Venturini, *Phys. Rev. Spec. Top. Accel. Beams*, vol. 10, no. 10, p. 104 401, 2007. `doi:10.1103/PhysRevSTAB.10.104401`

[26] S. Heifets, G. Stupakov, and S. Krinsky, *Phys. Rev. Spec. Top. Accel. Beams*, vol. 5, no. 6, p. 064 401, 2002. `doi:10.1103/PhysRevSTAB.5.064401`

[27] Z. Huang and K.-J. Kim, *Phys. Rev. Spec. Top. Accel. Beams*, vol. 5, no. 7, p. 074 401, 2002. `doi:10.1103/PhysRevSTAB.5.074401`

[28] K. L. Brown, *SLAC-R-75*, 1982. `http://inspirehep.net/record/187522/files/slac-r-075.pdf`

[29] M. Venturini, *Phys. Rev. Spec. Top. Accel. Beams*, vol. 11, no. 3, p. 034 401, 2008. `doi:10.1103/PhysRevSTAB.11.034401`

[30] M. Venturini and J. Qiang, *Phys. Rev. Spec. Top. Accel. Beams*, vol. 18, no. 5, p. 054 401, 2015. `doi:10.1103/PhysRevSTAB.18.054401`

[31] C.-Y. Tsai *et al.*, *Phys. Rev. Accel. Beams*, vol. 23, no. 12, p. 124 401, 2020. `doi:10.1103/PhysRevAccelBeams.23.124401`

[32] C.-Y. Tsai *et al.*, *Phys. Rev. Accel. Beams*, vol. 20, no. 5, p. 054 401, 2017. `doi:10.1103/PhysRevAccelBeams.20.054401`

[33] Z. Huang, P. Emma, M. Borland, and K.-J. Kim, "Effects of linac wakefield on CSR microbunching in the linac coherent light soure," in *Proc. PAC'03*, Portland, OR, USA, May 2003, pp. 3138–3140.

[34] J. B. Rosenzweig *et al.*, *Nucl. Instrum. Meth. A*, vol. 393, no. 2, pp. 376–379, 1997. `doi:10.1016/S0168-9002(97)00516-0`

[35] E. Saldin, E. Schneidmiller, and M. Yurkov, *Nucl. Instrum. Meth. A*, vol. 490, no. 1, p. 1, 2002. `doi:10.1016/S0168-9002(02)00905-1`

[36] E. L. Saldin, E. A. Schneidmiller, and M. V. Yurkov, *Nucl. Instrum. Meth. A*, vol. 528, no. 1, p. 355, 2004. `doi:10.1016/j.nima.2004.04.067`

[37] P. Craievich *et al.*, *IEEE Trans. Nucl. Sci.*, vol. 62, no. 1, p. 210, 2015. `https://ieeexplore.ieee.org/stamp/stamp.jsp?arnumber=7024948`

[38] M. Veronese *et al.*, "Infrared spectrometer for microbunching characterization," presented at FEL'22, Trieste, Italy, Aug. 2022, paper WEP24, unpublished.

[39] A. D. Brynes, "Characterisation of microbunching instability at the FERMI Free Electron Laser," presented at IPAC'23, Venice, Italy, May 2023, paper MOOG2, to appear in the proceedings.

[40] G. Perosa *et al.*, *in preparation*,

[41] M. G. Minty and F. Zimmermann, in *Measurement and Control of Charged Particle Beams*. 2003.
doi:10.1007/978-3-662-08581-3_4

[42] A. D. Brynes *et al.*, "Upgrade to the transverse optics matching strategy for the FERMI FEL," in *Proc. FEL'22*, Trieste, Italy, Sep. 2022, pp. 362–365.
doi:10.18429/jacow-fel2022-wep04

[43] *OCELOT*, 2018-07-30. https://github.com/ocelot-collab/ocelot/

[44] I. Agapov *et al.*, *Nucl. Instrum. Meth. A*, vol. 768, p. 5, 2014.
doi:10.1016/j.nima.2014.09.057

NON-DESTRUCTIVE VERTICAL HALO-MONITORS
ON THE ESRF ELECTRON BEAM

K. Scheidt

European Synchrotron Radiation Facility, Grenoble, France

Abstract

The ESRF EBS storage ring has now among its electron beam diagnostics two independent units of vertical Halo-monitor. They use the available X-rays in a non-used Front-End, emitted from standard 0.56 T dipole magnets in the EBS lattice. These instruments measure continuously at a 2 Hz rate the so-called 'far-away' halo level, i.e. in a zone of roughly 1-3 mm away from the beam centre.

Both units are yielding excellent and well-correlated results with data of both the beam lifetime and of our 128 Beam Loss Detectors, and this as a function of the beam current, the filling-patterns, the vertical emittance, and the quality and incidents of the vacuum.

NON-DESTRUCTIVE MEASUREMENTS OF THE VERTICAL BEAM HALO

The Extreme Brilliant Source (EBS) ring at the European Synchrotron Radiation Facility (ESRF) is operational since mid-2020, generating coherent and bright X-rays for the scientific users. The X-rays are generated by an electron beam of 6 GeV and 200 mA, with horizontal and vertical emittances of 120 pm and 10 pm. A large range of diagnostics are in operation since the commissioning to measure the parameters, characteristics and behaviour of the beam [1, 2]. This 10 pm emittance implies that the beam's vertical size is in a range of roughly 4.5 to 13 um σ.

However, it is easily verified that a non-negligible beam population exists at some millimetres vertical distance from the beam-centre by inserting a vertical scraper and measuring the signal from a down-stream Beam Loss Detector (BLD). However, such method is destructive to the beam and not useable for assessing the halo population while serving normal users' operation (USM).

In 2014, in the old ESRF ring, a non-destructive vertical Halo-monitor based on imaging the X-rays from an available bending magnet beam-port was conceived and installed [3]. It was successfully operated and yielded excellent results until the disassembly of that ring for the subsequent installation of the new low emittance lattice of EBS in 2019. However, implementing a similar Halo-monitor in EBS was more complicated due to the constraints of the much smaller vacuum chamber, the weaker field strength of the available magnet source (now 0.56 T while 0.86 T before) and the longer distances between the essential components (now 6.8 m while before 4.2 m). These disadvantages were partly compensated by the availability of now non-used bending magnet Front-Ends, and this allowed a low-cost installation in cells 10 and 11 of two identical devices without any modification to the vacuum chambers in the EBS.
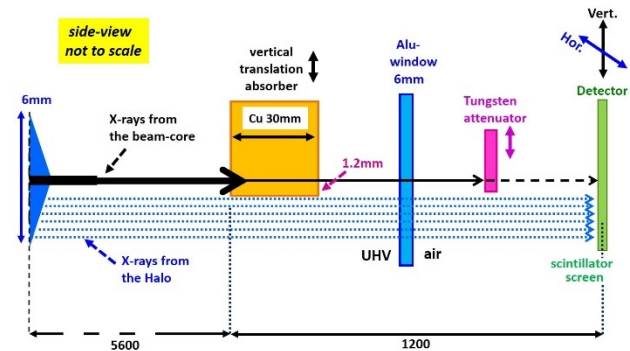
Figure 1: The main components and the paths of the X-rays of both the beam-core and that of the halo population.

Explanation of the Concept and its Components

The main components are shown in Fig. 1 in the vertical plane together with the (simplified) trajectory of the X-rays that are emitted from the electrons (at extreme left of the picture) and travel towards the detector (extreme right) which is a two-dimensional X-ray imager read-out by a standard camera. It is important to note that the X-rays from the central beam-core are many orders of magnitude stronger than those emitted from the electrons that make up the weak halo population. The specificity in our concept is to attenuate this powerful X-ray beam by an absorber that is vertically positioned so to intercept that beam.

However, the X-rays of typically 60 keV have a small but not a zero divergence as is supposed in the illustration. In fact, this divergence amplitude is 1E-9 for a divergence angle of 200 μrad. Therefore, the absorber (at roughly 6m from the source) needs to positioned at least 1.2 mm below the central axis, so to reduce this unwanted divergence signal to a negligible level compared to the weak level of the X-rays emitted by the halo. Consequently, it implies that this system can only detect the halo levels at roughly 1 to 3 mm distance from the beam-core.

The UHV of the Front-End is separated from the free air by a 6 mm thick Aluminium window. Further downstream a movable attenuator (1 mm thick Tungsten) provides flexibility in attenuation, followed by the detector that can be precisely positioned with a two-axis translation stage.

This detector is protected by a 5 mm thick lead box, and contains a 2 mm thick LYSO scintillator (15 x 15 mm), a double chicane with 3 mirrors, a set of achromat lenses and a CMOS camera and covers an 8 x 6 mm field of view.

The Fig. 2 shows a typical image (left) and its vertical profile (right). The beam-core signal there is produced by the main beam with its X-rays very strongly attenuated by the 30mm Copper, the 6 mm Aluminium and the 1 mm Tungsten. While for the halo signal beneath, the X-rays are only attenuated by the 6 mm Aluminium window. In the

67th ICFA Adv. Beam Dyn. Workshop Future Light Sources
FLS2023, Luzern, Switzerland
JACoW Publishing
ISBN: 978-3-95450-224-0
ISSN: 2673-7035
doi:10.18429/JACoW-FLS2023-TU4P17

commission period of this device, the edges of the Copper and Tungsten absorbers were optimized vertically, so to satisfy two conditions: a) let the X-rays emitted from the halo signal avoid these absorbers and b) intercept the divergent X-rays emitted from the main central beam so to ensure that these do not create a fake (background) signal in that lower zone where the system is supposed to only measure the genuine halo level. However, it implies a 'blind zone' where the system cannot measure.
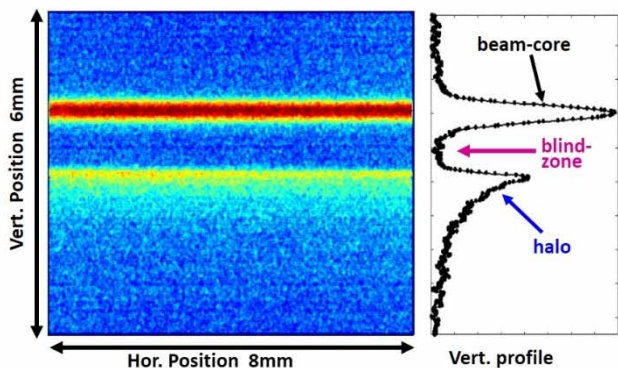
Figure 2: The typical image obtained shows clearly the beam core and the halo (below).

It is important to verify that this signal that we attribute to be the halo is not polluted by some parasitic signal by scattered X-rays, or from an incorrect positioning of the vertical absorber. In our storage ring we can use the vertical scraper to do such verification by positioning this scraper edge very close w.r.t. to the electron beam. By doing this in a relative fast scan, during which the scraper is typically put at distances of 3 to 0.3 mm in steps of 0.1 mm, and by measuring the halo levels at each step with a 1sec measurement time, we observe the progressive reduction and the final extinction of the halo level in our Halo-monitor.
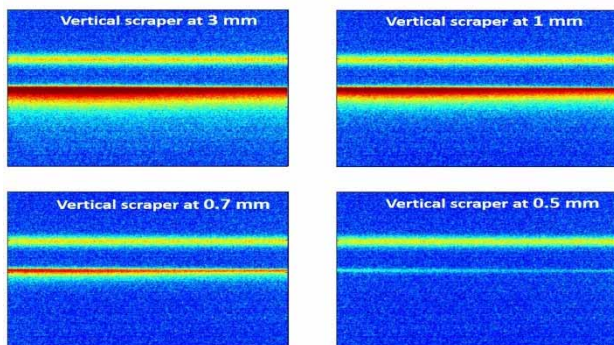
Figure 3: Verification results using the vertical scraper to check that halo signal is not polluted by a parasitic signal.

RESULTS UNDER NUMEROUS BEAM CONDITIONS AND MANIPULATIONS

These two new Halo-monitors are a useful addition to our existing scope of diagnostics systems, and their results can be directly compared with that of a) the lifetime monitor and b) the sum of all our 128 individual electron beam loss detectors. The latter we call "Losses" hereafter.

Figure 4 shows the curves of the rough data of lifetime (top), losses (middle) and the halo-levels (bottom) as a function of the beam current, up to 200 mA, with a uniform fill and a vertical emittance at 10 pm. It is emphasized that both the losses and the halo-levels are always expressed in arbitrary units.

In fact, in contrast to the beam lifetime measurement yielding an absolute and calibrated value, the BLD system, by definition, only measures a fraction of the (real total electron) losses, and the Halo-monitors only a fraction of the vertical halo-strength. However, it is now possible to normalize the results of both these losses and these halo-levels against that of the beam current and the inverse of beam lifetime. The result of this normalisation is shown in Fig. 5 over this same current range of 20 to 200 mA.
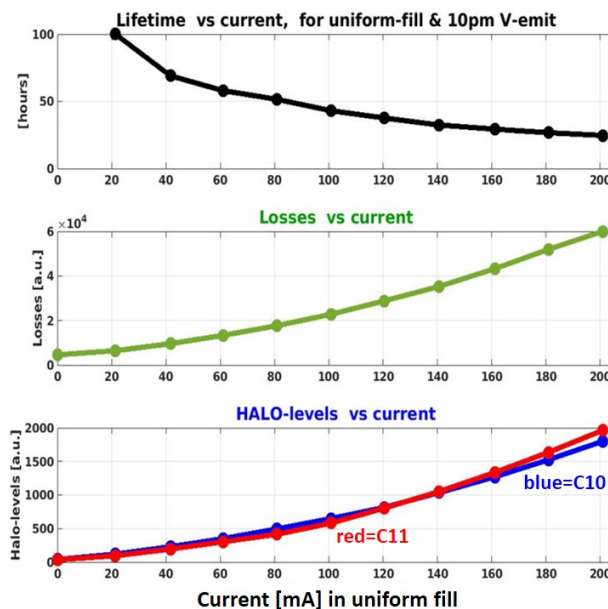
Figure 4: The signals of the beam lifetime, beam-losses, and the 2 Halo-monitors versus beam current.
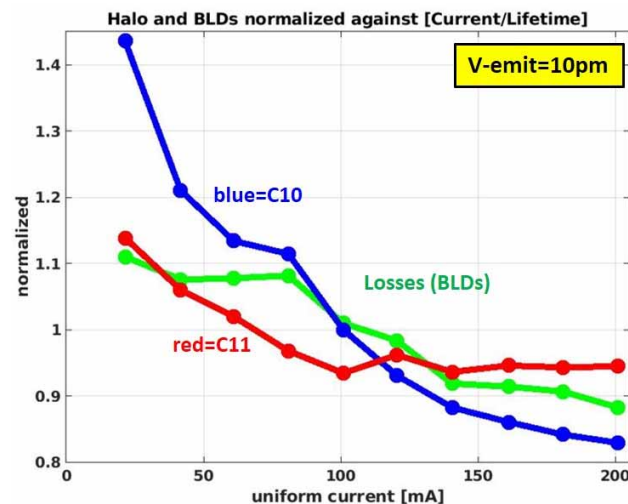
Figure 5: The normalized signals of the two Halo-monitors and of the beam-losses, versus beam current.

If all was perfect or ideal then these curves in Fig. 5 would be flat at value 1. The discrepancy is noticeable, and not further discussed or explained here, but of a reasonable low extent of about ± 10%.

Another set of data is shown in Fig. 6 in which the same values of lifetime, losses and halo-levels were recorded but this time for a stable beam current (74 mA in 16 bunch filling) while varying the vertical emittance between 1 and 50 pm. A system of adding a controlled vertical beam excitation is typically used for obtaining any wanted vertical emittance.
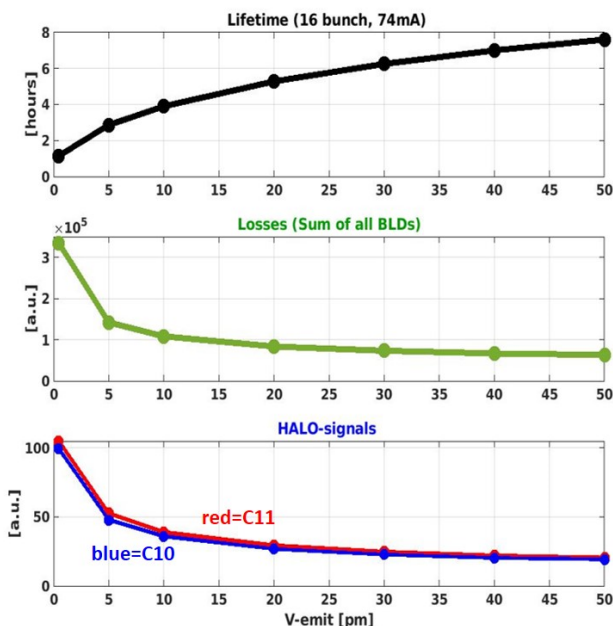
Figure 6: The signals of the beam lifetime, beam-losses, and the 2 Halo-monitors versus vertical emittance.

The same normalization is performed on this data and shown in Fig. 7 and an even better agreement (i.e. low discrepancy of ±10%) can be noted.
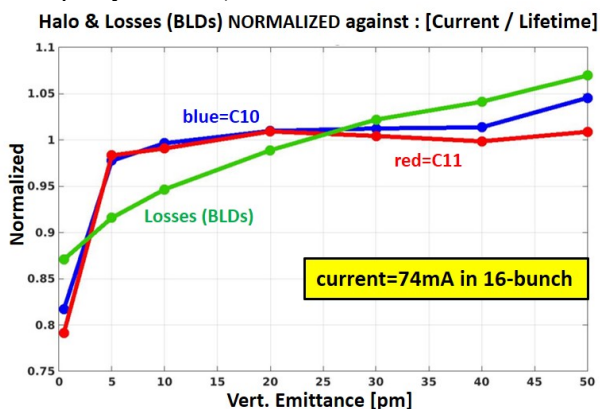
Figure 7: The normalized signals of the two Halo-monitors and of the beam-losses, versus vertical emittance.

A 3rd study was done in which the beam current in 16 bunch filling was varied up to 75 mA range, and this for a vertical emittance of 10 and 20 pm. The Fig. 8 shows the raw data while the Fig. 9 the normalized results of the BLD system and of the average of the two Halo-monitors. The

Halo-monitor here shows a marked jump at 40-50 mA which is not yet explained, and needs to be re-measured and verified later.
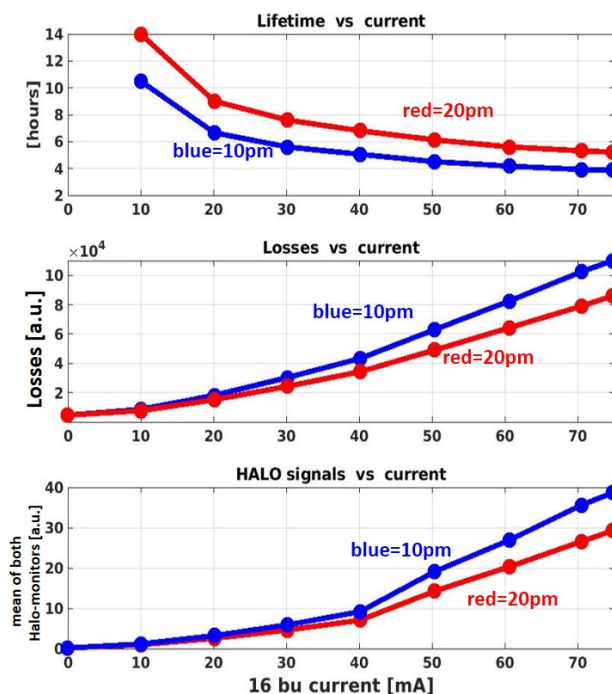
Figure 8: The signals of beam lifetime, beam-losses, and (mean of the) Halo-monitors versus beam current in 16-bunch fill, for values of 10 and 20 pm vertical emittance.
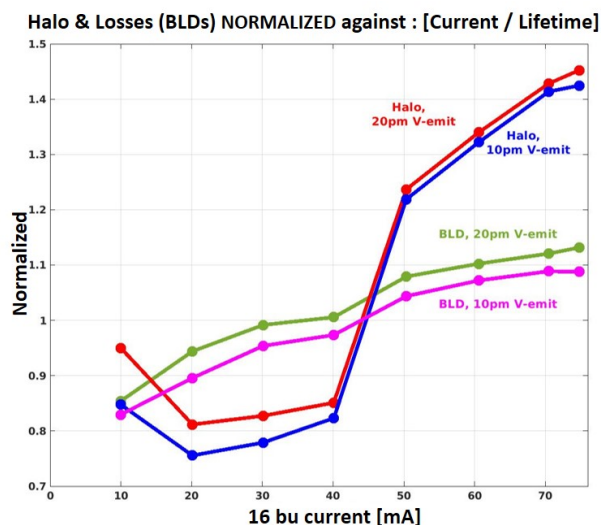
Figure 9: The normalized signals of the Halo-monitor and of the beam-losses, versus beam current, for 10 and 20 pm.

HALO SIGNALS DURING USM

The Halo-monitors provide data at 2 Hz which is stored in the database at the same rate. The same database also holds data of the beam current, beam lifetime, loss-levels of each of the 128 BLDs and the UHV pressure values of several hundreds of vacuum gauges.

67th ICFA Adv. Beam Dyn. Workshop Future Light Sources
FLS2023, Luzern, Switzerland
JACoW Publishing
ISBN: 978-3-95450-224-0
ISSN: 2673-7035
doi:10.18429/JACoW-FLS2023-TU4P17

The Fig. 10 shows a short -5% drop of the lifetime (from 5.25 to 5.0 hrs) and a +9% increase of the Losses while the Halo-monitors show both about 200% increase with much details, and an excellent signal-to-noise ratio and a quasi-perfect coherence between the two units.
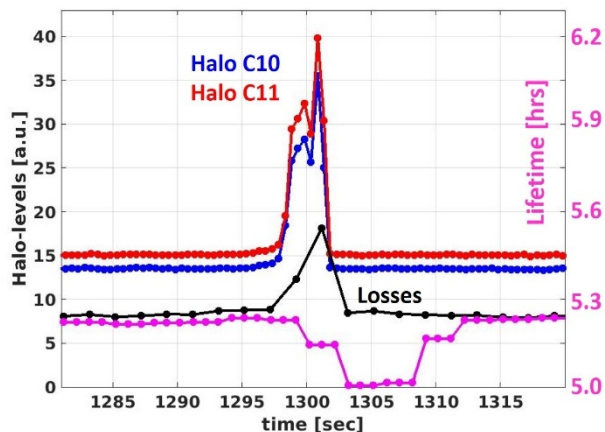
Figure 10: typical results during USM from the two Halo-monitors, the BLDs and the beam lifetime at the moment of a tiny fractional beam loss (16 bunch July 2023)

Such electron beam loss events occur rather frequently, but with very strongly varying levels, i.e. many events of the order of 1E-4 - 1E-6, while much rarer cases of >1E-3. In such latter case all related diagnostics detect and measure such event, and also the readings of the vacuum gauges can be correlated with it.

Smaller losses (e.g. 1E-4) are still easily detected by the BLDs but often not seen by the vacuum gauges, and barely detectable by the current monitor or the lifetime measurement. The two independent Halo-monitors have an extreme sensitivity to these very weak (but numerous) events. As such they constitute an 'watch-dog' to the slightest incident on the UHV vacuum quality.

The effect of, and the correlation with, the vacuum quality was assessed very neatly by creating temporarily an impaired local vacuum by switching on one of the titanium sublimators in the ring. The Fig. 11 shows the result of this manipulation.
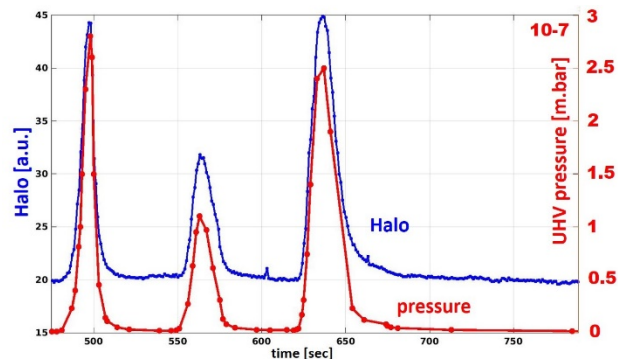
Figure 11: The excellent correlation between the halo level and the vacuum pressure on three specific events.

CONCLUSION AND PROSPECTS

The non-destructive Halo-monitor is a novice, reliable and sensitive diagnostic yielding direct information on the strength of the 'far-away' halo population of the ESRF's electron beam in its vertical plane. During USM this halo level shows to be extremely sensitive to the slightest change of beam parameters and notably to the incidence of small perturbations to the vacuum quality.

Certain accelerator studies have recently started to asses these halo levels as a function of the beam's coupling resonance, the beam's chromaticity, the minimum gap settings of our numerous in-vacuum insertion devices and the settings of our horizontal collimators. These studies will be pursued in the near future to further exploit this diagnostic.

ACKNOWLEDGMENTS

REFERENCES

[1] L. Torino *et al.*, "Overview on the diagnostics for EBS-ESRF", in *Proc. IBIC'19*, Malmö, Sweden, Sep. 2019, pp. 9-13. doi:10.18429/JACoW-IBIC2019-MOA003

[2] L. Torino *et al.*, "Beam instrumentation performances through the ESRF-EBS commissioning", in *Proc. IBIC'20*, Santos, Brazil, Sep. 2020, pp. 11-16. doi:10.18429/JACoW-IBIC2020-MOA004

[3] K. B. Scheidt, "Non-destructive vertical Halo monitor on the ESRF's 6GeV electron beam", in *Proc. IBIC'14*, Monterey, CA, USA, Sep. 2014, paper MOCYB1, pp. 2-6

[4] E. Buratin and K. B. Scheidt, "New X-rays diagnostics at ESRF: The X-BPMs and the Halo-Monitor", in *Proc. IBIC'22*, Kraków, Poland, Sep. 2022, pp. 125-128. doi:10.18429/JACoW-IBIC2022-MOP34

[5] B. K. Scheidt, "The non-destructive vertical Halo monitor on the ESRF electron beam", presented at DEELS'22, HZB Berlin, Germany, June 2022, https://events.hifis.net/event/358/contributions/2263/

NONLINEAR DYNAMICS MEASUREMENTS
AT THE EBS STORAGE RING

N. Carmignani*, L. Carver, L. Hoummi, S. Liuzzo, T. Perron, S. White
ESRF, Grenoble, France

Abstract

The Extremely Brilliance Source (EBS) is a 4th generation synchrotron light source and it has been in user operation since August 2020 at the ESRF. Several measurements to characterise the nonlinear dynamics have been performed in 2023: nonlinear chromaticity, second order dispersion and detuning with amplitude. The results of the measurements are shown and compared with simulations.

INTRODUCTION

The EBS has been in user operation since August 2020 at the ESRF [1]. The nonlinear dynamics model of the storage ring has been improved by adding the cross talk effect of some magnets to their neighbors [2]. The Touschek lifetime of the machine reached the design values already in the first year of user operation [3] and it is improved regularly by online nonlinear optimization [4]. The horizontal dynamic aperture and therefore the injection efficiency is still slightly lower than the one predicted by the model [3].

In order to better understand the disagreement with the model of the horizontal dynamic aperture, in 2023 we performed a series of nonlinear dynamics measurements and we compared them with the accelerator model.

In the next section we will show the measurements of transverse detuning with amplitude and in the following the measurements of high order chromaticity and second order dispersion. For all the cases, a comparison with the theoretical model is shown.

DETUNING WITH AMPLITUDE

Measurement Technique

In order to measure the detuning with amplitude we need to excite coherent oscillations of the beam at increasing amplitudes and measure the frequency of the free oscillations.

A kicker magnet able to excite the beam for about 1 turn, either in horizontal or vertical, will be installed in the ESRF-EBS storage ring in 2024. The four injection kickers can be used to excite horizontally the beam, but their field has a raising time of about 70 µs (see Fig. 1) [5]. The four injection kickers are usually pulsed with a current of about 1.6 to 1.9 kA.

Since the pulsed power supplies limit the minimum sent currents to a few hundreds of Amperes, we excited the beam by powering all the four kickers at full current except for the kicker K3, that was powered with reduced current. The described distribution of currents generates a bump that is not perfectly closed. In Fig. 2, the turn by turn (TBT) orbit

---

* nicola.carmignani@esrf.fr
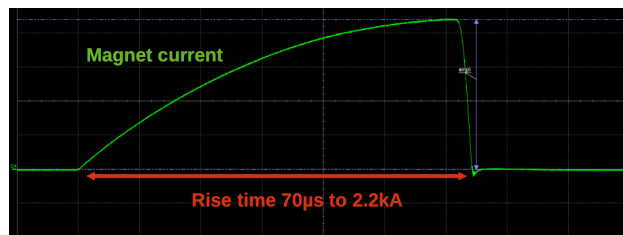
Figure 1: Pulse shape of the injection kickers.

in the first beam position monitor (BPM), which is located inside the injection bump, is shown for different current reductions of the kicker K3 power supply. The injection oscillations are dumped in about 100 turns because of the decoherence due to the high chromaticity. The radiation damping is a slower effect that lasts a few thousands turns.
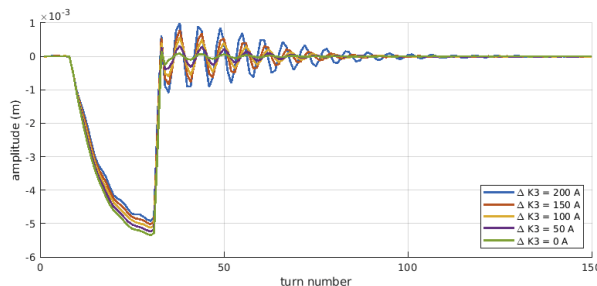
Figure 2: Orbit at the BPM number 1, which is inside the injection bump, during the ramp rise and after it goes off in about 1 turn. The oscillations are dumped quickly because of strong decoherence due to the high chromaticity.

The tune is extracted from the first 130 turns of oscillations using 5 consecutive measurements in all the 320 BPM. In order to increase the resolution of the FFT, a zero-padding of the signal with 12000 samples has been added to the measurements. A histogram of the 320 x 5 tune measurements for a single amplitude is shown in Fig. 3. The standard deviation of the histogram is about 5×10^{-4} and it is considered as the measurement error for the tune. From the peak to peak oscillation amplitude at each BPM, knowing the beta functions, we can extract the action of the beam and compute the tune shift with amplitude.

The vertical tune can be measured in the same way. Even if the injection kickers produce a horizontal excitation, some smaller vertical oscillations can be observed and can be used to measure the vertical tune as a function of horizontal amplitude of oscillations.
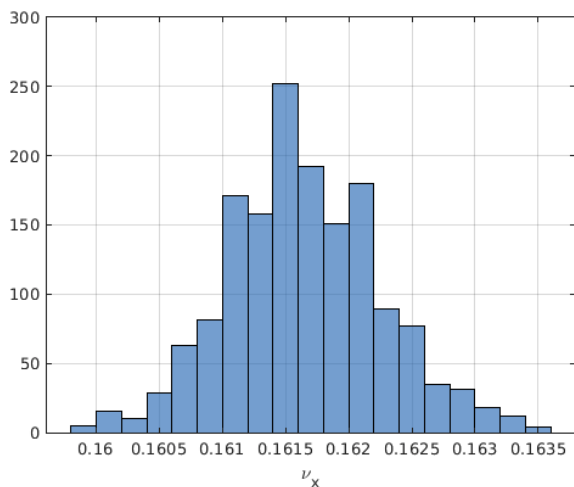
Figure 3: Histogram of the 320 x 5 measurements of the horizontal tune taken from the 320 BPMs in 5 consecutive acquisitions.

Comparison with Accelerator Model

The tune shift with amplitude has been measured for three different octupole settings: the nominal setting, which is a result of online optimizations to maximise the Touschek lifetime [4], and two settings with octupoles powered at 50% and 10% of the nominal strength.

Figures 4 and 5 show the comparison between the measured and simulated tune shift with amplitude: the first is the horizontal tune shift with horizontal amplitude and the second is the vertical tune shift with horizontal amplitude.
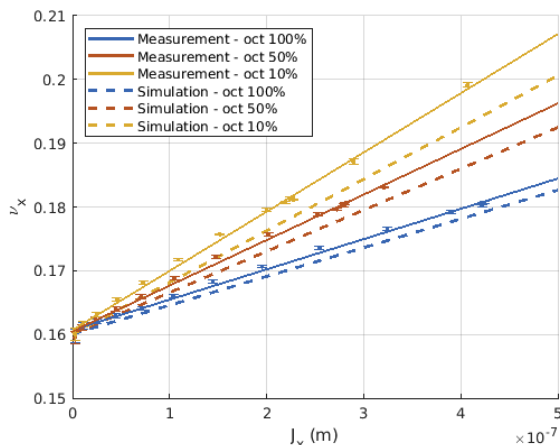
Figure 4: Horizontal tune shift with horizontal amplitude. The solid lines are the fit of the measured data, the dashed lines are from simulations.

The detuning with amplitude measurements are summarised in Tables 1 and 2. For the horizontal tune shift with horizontal amplitude, the measured value is larger than the expected by about 10%. The measurement of the vertical tune shift with horizontal amplitude disagrees with the model by about a factor 2. This disagreement is an indica-
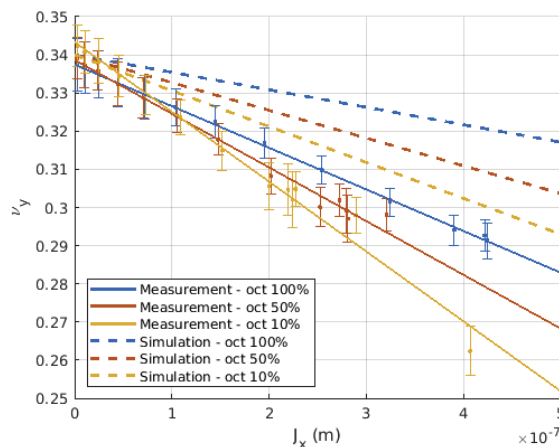
Figure 5: Vertical tune shift with horizontal amplitude. The solid lines are the fit of the measured data, the dashed lines are from simulations.

tion of a problem in the nonlinear model of the EBS storage ring.

Table 1: Measurements and simulations of horizontal detuning with amplitude.

Octupoles Fraction	Sim. dv_x/dJ_x (10^{-4} m^{-1})	Meas. dv_x/dJ_x (10^{-4} m^{-1})
10%	7.93	9.3 ± 0.3
50%	6.35	7.1 ± 0.3
100%	4.35	4.7 ± 0.2

Table 2: Measurements and simulations of vertical detuning with horizontal amplitude.

Octupoles Fraction	Sim. dv_x/dJ_x (10^{-4} m^{-1})	Meas. dv_x/dJ_x (10^{-4} m^{-1})
10%	-8.95	−18 ± 2
50%	-6.84	−14 ± 1
100%	-4.20	−10.9 ± 0.3

HIGH ORDER CHROMATICITY

The second order chromaticity can be measured by performing a third order polynomial fit of the horizontal and vertical tunes as a function of energy deviation. The energy of the machine has been changed by changing the RF frequency, using Eq. (1). The RF frequency has been changed from -300 Hz to +500 Hz.

$$\frac{dp}{p} = -\frac{1}{\alpha}\frac{df}{f} \tag{1}$$

In Fig. 6, the horizontal tunes as a function of energy deviation are shown for the three different octupole settings. The measurements are compared to the simulation, where
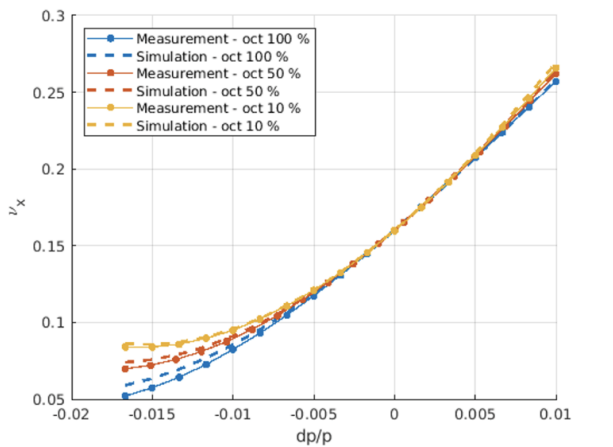
Figure 6: Horizontal tunes as a function of energy deviation. The dots are the measured point and the dashed line is the simulation.

the linear part of the chromaticity has been matched to the measured value (9.1, 9.2). All the measured and simulated values are summarised in Table 3.

Table 3: Measurements and simulations of second order chromaticities.

Octupoles Fraction	$1/2\,d^2\nu_x/d\delta^2$		$1/2\,d^2\nu_y/d\delta^2$	
	Sim.	Meas.	Sim.	Meas.
10%	117.4	98 ± 1	130.6	145 ± 2
50%	176.4	157 ± 1	89.8	101 ± 1
100%	223.7	206 ± 1	57.1	68 ± 1

The second order chromaticities disagree with the model by 10% to 20% both in horizontal and in vertical.

SECOND ORDER DISPERSION

The second order dispersion can be measured at the same time of the nonlinear chromaticity. The orbit in the 320 BPMs has been acquired for each point of energy deviation and then a third order polynomial fit has been performed for each BPM.

Figure 7 shows an example of measured and simulated orbits in a BPM. The second order dispersion is the parabolic component. The result of the fit depends on the order of the polynomial that we decide to use and can be affected by the nonlinearities of the BPMs at large amplitude.

In Fig. 8, the measured and the simulated second order dispersions are shown for the three octupole settings. In simulation, the second order dispersion does not depend on the octupole settings, while in the measurement it can change by almost a factor 2.

The disagreement between measurement and simulation is larger, more than a factor 2, when the octupoles have the full strength.
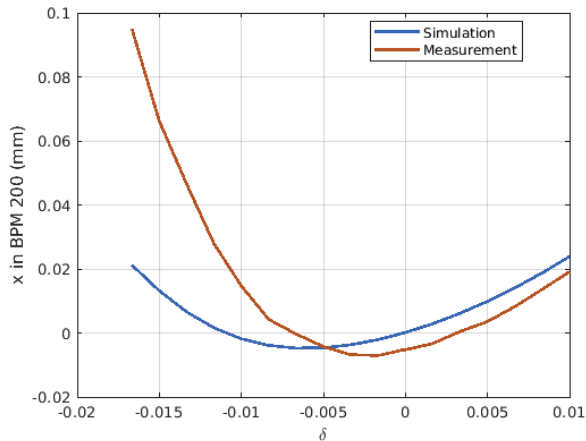
Figure 7: Horizontal orbit in BPM number 200 as a function of energy deviation with octupoles at 10% of their nominal strengths. The measured second order dispersion is about a factor 2 larger than the simulated.
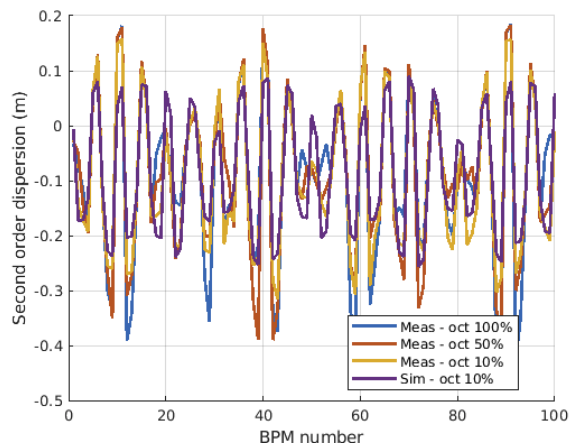
Figure 8: Measured second order dispersion for three octupole settings and simulated value.

CONCLUSION

The detuning with amplitude of the EBS storage ring is close to the predicted one for the horizontal case, within a 10% error, but the cross term is off by almost a factor 2. The vertical detuning could not be measured without a vertical kicker.

The second order chromaticities are about 10% to 20% far from the prediction of the model.

The measured second order dispersion depends unexpectedly on the octupole setting and it is in disagreement with the model by more than a factor 2 in some locations.

REFERENCES

[1] P. Raimondi *et al.*, "The extremely brilliant source storage ring of the european synchrotron radiation facility," *Communications Physics*, vol. 6, no. 1, p. 82, 2023.
`doi:10.1038/s42005-023-01195-z`

[2] G. Le Bec, J. Chavanne, S. Liuzzo, and S. White, "Cross talks between storage ring magnets at the extremely brilliant source at the european synchrotron radiation facility," *Phys. Rev. Accel. Beams*, vol. 24, no. 7, p. 072 401, 2021.
`doi:10.1103/PhysRevAccelBeams.24.072401`

[3] P. Raimondi *et al.*, "Commissioning of the hybrid multibend achromat lattice at the european synchrotron radiation facil-ity," *Phys. Rev. Accel. Beams*, vol. 24, no. 11, p. 110 701, 2021.
`doi:10.1103/PhysRevAccelBeams.24.110701`

[4] N. Carmignani *et al.*, "Online optimization of the ESRF-EBS storage ring lifetime," in *Proc. IPAC'22*, Bangkok, Thailand, 2022, pp. 2552–2555.
`doi:10.18429/JACoW-IPAC2022-THPOPT001`

[5] S. White *et al.*, "Commissioning of new kicker power sup-plies to improve injection perturbations at the ESRF," in *Proc. IPAC'22*, Bangkok, Thailand, 2022, pp. 2683–2685.
`doi:10.18429/JACoW-IPAC2022-THPOPT041`

EVOLUTION OF EQUILIBRIUM PARAMETERS RAMP INCLUDING COLLECTIVE EFFECTS IN THE DIAMOND-II BOOSTER

R. Husain[1,2,†], R.T. Fielder[1], I.P.S. Martin[1], P.N. Burrows[2]
[1]Diamond Light Source Ltd., Oxfordshire, UK
[2]John Adam Institute, University of Oxford, Oxfordshire, UK

Abstract

Efficient top-up injection into the Diamond-II storage ring will require upgrading the booster lattice for a beam emittance of < 20 nm·rad and a bunch length of < 40 ps, including when operating with high single-bunch charge. The small vacuum chamber dimensions will drive the resistive wall instability and may adversely affect equilibrium parameters along the beam energy ramp. In addition, various diagnostic and vacuum chamber components will generate geometric impedances which may further disrupt the equilibrium parameters. Based on the detailed engineering designs, impedance models of the major components have been simulated using CST Studio and included in ELEGANT tracking simulations of the booster. In addition, the effects of synchrotron radiation emission and intra-beam scattering on the equilibrium parameters during the ramp are studied.

INTRODUCTION

Diamond Light Source is to be upgraded with an advanced low emittance storage ring, Diamond-II, using a multi-bend achromat lattice [1] to provide space for more beamlines and to increase the brightness and coherence of the photon beams. For efficient beam injection into the Diamond-II storage ring, the injector system also needs to be upgraded [1, 2]. This includes a new low emittance booster synchrotron with beam emittance < 20 nm·rad and bunch length < 40 ps at the 3.5 GeV extraction energy. The lower emittance is required to achieve off-axis beam accumulation into the reduced dynamic aperture of the new storage ring. A shorter bunch length will ensure a proper matching with the storage ring RF bucket so that energy errors during synchrotron oscillations for the injected beam remain small. The major Diamond-II booster parameters are given in Table 1, more lattice details can be found in Refs. [1-3].

The Diamond-II booster should be capable of accelerating high-charge single bunches or multi-bunch trains without degradation of the equilibrium parameters such as beam emittance, bunch length and energy spread. The beam energy needs to be raised from the injection energy of 100 MeV to 3.5 GeV at extraction. During the beam energy ramp process, the equilibrium parameters change due to synchrotron radiation (SR) emission. These parameters may deviate from the equilibrium values due to high intensity collective effects [4] such as coupling impedance (resistive wall and geometric impedance) and intra-beam scattering (IBS). Another important contribution comes from

---

higher order modes (HOMs) in the RF cavities. If the beam impedance interaction become strong it may result in large disruption of the electron bunch and equilibrium parameters and could eventually lead to beam loss.

In this paper, we present simulation studies of the evolution of the equilibrium parameters during the beam energy ramp. These have been done considering a high-charge single bunch including impedances, SR and IBS effects with physical apertures applied.

Table 1: Main Parameters of the Diamond-II Booster

Parameters	At 100 MeV	At 3.5 GeV
Circumference	163.85 m	
Betatron tunes	12.41 / 5.38	
Chromaticity	+1 / +1	
Momentum comp. factor	5.65×10^{-3}	
Damping times	[156.3, 173.1, 91.5] s	[3.67, 4.04, 2.13] ms
Energy loss/turn	0.63 eV	947.5 keV
Natural beam emittance	14.1 pm·rad	17.3 nm·rad
Natural energy spread	2.5×10^{-5}	8.6×10^{-4}
Bunch length	0.55 ps	38 ps
RF Voltage	200 kV	2 MV
Energy acceptance	2.8 %	0.93 %
RF frequency	499.51 MHz	

BOOSTER RAMP PROFILE

For the present studies, the energy and voltage ramp profiles of the Diamond booster are as follows. The beam energy is raised from 100 MeV to 3.5 GeV (compared to 3 GeV in the existing booster) with a biased sinusoidal waveform at 5 Hz repetition rate. At the injection energy the RF voltage is 200 kV. This provides sufficient energy acceptance (2.8 %) for the energy errors during initial synchrotron oscillations of the injected bunch. This voltage is kept constant up to 1.93 GeV and then increases with the fourth power of energy up to 2 MV at the extraction.

BOOSTER IMPEDANCE MODEL

The Diamond-II booster consists of a large number of components which contribute to the overall impedance. Initial engineering designs of the major components have been completed and an impedance database has been generated. A vacuum vessel of stainless steel has been selected with two different circular apertures with radii 18.3 mm (in the injection/extraction sections) and 11.5 mm (in the arc sections). In addition, there are four in vacuum ferrite kickers (one for the injection and three for beam extraction). Two ceramic breaks of 10 mm length and inner radius

11.5 mm are included in each arc section to terminate the eddy currents generated due to the fast beam energy ramp rate. These are the major contributors to the overall resistive wall (RW) impedance in the booster. The impedances of these components are calculated using *Impedance-Wake2D* [5]. It was found that ferrite loaded injection/extraction kickers contribute significantly to the RW impedance. To reduce the impedance, it has been proposed to apply a 1 µm thick titanium nitride coating to the ferrite. Significant sources of geometric impedance include BPMs, screens, tapers, etc. These are simulated using *CST Studio* [6].

The impedance database in terms of the total loss and kick factors calculated for all components in the booster are given in Table 2. A bunch length of 12 mm has been used for these calculations, corresponding to the bunch length at extraction. The main contributors to the overall impedance are vacuum chambers, injection/extraction kickers, cavity tapers, pumps and BPM blocks.

Table 2: Impedance database for all booster elements showing the kick (k_x, k_y) and loss ($k_\parallel$) factors calculated for a 12 mm long Gaussian bunch. Total value of the kick and loss factor is the sum of all elements in the booster ring.

Component	No.	k_x (V/pC/mm)	k_y (V/pC/mm)	$k_\parallel$ (V/pC)
Screen	1	-7.59×10^{-3}	-5.24×10^{-3}	3.87×10^{-2}
Valve	4	-6.32×10^{-3}	-6.52×10^{-3}	3.44×10^{-3}
BPM 18.3mm	4	-4.40×10^{-4}	-3.60×10^{-4}	4.80×10^{-4}
BPM,11.5mm	44	-1.58×10^{-2}	-1.85×10^{-2}	4.40×10^{-4}
Pump	55	-8.69×10^{-2}	-8.53×10^{-2}	3.74×10^{-2}
Kicker	4	-7.50×10^{-2}	-1.92×10^{-1}	6.82×10^{-1}
Cavity taper	2	-1.91×10^{-2}	-1.91×10^{-1}	3.81×10^{-1}
RW (140 m)		-6.83×10^{-1}	-6.97×10^{-1}	1.329
Total		**-0.894**	**-1.024**	**2.476**

SIMULATION RESULTS

To calculate the equilibrium parameters during the ramp, we use the *ELEGANT* multiparticle tracking simulation code [7, 8]. In the simulations, both RW and geometric impedances, and HOMs in the main RF cavities are included. The total transverse impedance for all the components is calculated by summing the local beta function weighted impedances from the individual elements in the booster ring, whereas the total longitudinal impedance is calculated by a straight summation over all elements. In the simulations, the total transverse impedance is normalised with the beta function at the point at which it is inserted.

For these studies, an initial beam from the linac at 100 MeV is considered with two different electron gun currents 0.5 A and 1 A (corresponding to 1 nC and 2 nC charge). Considering the bunching and acceleration losses (10 %) in the linac and transmission losses (20 %) in the linac to booster transport line, a single bunch with charges of 0.72 nC and 1.44 nC has been taken for the *ELEGANT* booster tracking. The associated RMS beam emittance, bunch length and energy spread are 125 nm·rad in both the planes, 20 ps and 0.5 %, respectively.

We use 128,000 macroparticles in a bunch and tracking is performed for 182,970 turns (corresponding to the ratio

of ramp time/revolution time). The 6D tracking uses a one-turn-map with lumped SR effects. A one-turn-map using the ILMATRIX is used to describe the full ring, as an element-by-element method has a very large execution time. However, the ILMATRIX does not support the IBS effect. A single point representing the apertures in both the horizontal and vertical planes is used by scaling the 11.5 mm arc apertures to the beta functions at injection point. A horizontal-vertical emittance coupling of 10% is assumed. In the simulation, we also assume an ideal lattice without any errors. During the beam tracking, a particle is supposed to be lost in the transverse plane if its oscillation amplitude becomes comparable to the physical aperture and is lost in the longitudinal plane when the energy error becomes comparable to the energy acceptance.

Simulation results for the variation of vertical beam emittance, bunch length and vertical centroid motion along the ramp for various chromaticities (ξ) are shown in Fig. 1. The vertical centroid motion is shown for two cases which show emittance growth (ξ = 1.5, 2) and for one case without emittance growth (ξ = 0).
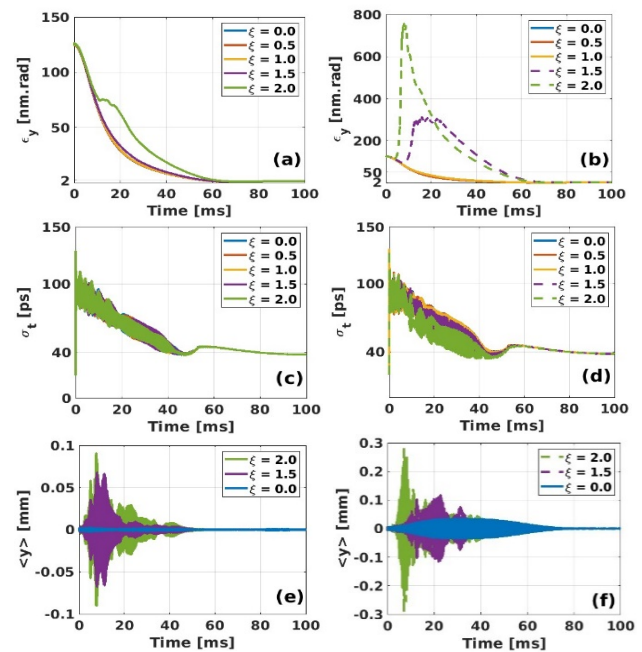
Figure 1: Variation of vertical emittance (a & b) and bunch length (c & d) vs. ramping time for a single bunch charge of 0.72 nC (left) and 1.44 nC (right) including RW impedance, geometric impedance, and RF cavity HOMs with scaled physical apertures at various chromaticities. Solid curves show the condition when there is no particle loss and dashed dotted curves with particle loss. The lower two figures show the bunch centroid motion (e & f) when there is emittance growth (ξ = 1.5, 2) and without growth (ξ = 0).

For a single bunch charge of 0.72 nC, there is no noticeable growth of the vertical emittance up to chromaticity 1. A large vertical emittance growth in the low energy regime can be observed for higher values of chromaticity. For the case of 1.44 nC charge, a significant vertical emittance growth and excitation of the vertical centroid motion are

observed for higher values of chromaticity. This also results in beam loss of ~25 % for the case with $\xi = 2$ (dashed green curve). Similar results have been reported for the HEPS booster [9] at lower energy. A fast growth of centroid motion for high chromaticity at lower energies is due to the strong beam-impedance interaction. At lower energies, the growth time of the beam-impedance interaction is small compared to the SR damping time due to weak SR effect, which is of the order of 100 s (see Table 1). Further during the ramp, the SR damping become dominant, and the vertical emittance and centroid growth are suppressed. At the final energy, the beam emittance is damped down to the natural value of ~1.57 nm·rad (10% emittance coupling).

The horizontal emittance growth is rather small compared to the vertical emittance growth. The bunch length also grows due to the longitudinal impedance and gets damped to the natural value of ~38 ps at extraction. The outcome of the studies performed for the single bunch charges considered here is that the SR effect during the energy ramping helps to supress the growth of the equilibrium parameters. In the absence of the IBS effect, the equilibrium parameters converge to the zero current equilibrium values at the extraction energy.

We have also carried out an element-by-element tracking simulation including IBS effects and distributed physical apertures in addition to the impedances. The IBS effect results in additional growth of the equilibrium parameters with increased bunch charge. The equilibrium values at the extraction energy are summarized in Table 3.

In view of future possible options including swap-out injection in the Diamond-II storage ring, we have also carried out simulations with high bunch charges to assess bunch charge thresholds in the booster. As shown in Fig. 2(a), the threshold limit on the extracted bunch charge is ~2 nC.

As mentioned, the beam centroid and emittance growths occur at low energies during the energy ramp. As such, we have also performed simulations in which the injection energy is increased to 150 MeV. As expected, the instability takes relatively longer time to build up compared to the case of 100 MeV. As a result, the bunch charge threshold limit is increased to ~3 nC (Fig. 2(b)). The SR damping is still weak at lower energy to suppress the centroid growth effectively of the single bunch with high charges.
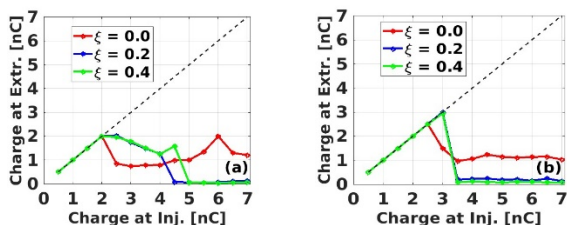
Figure 2: Extracted bunch charge thresholds with injected single bunch charges at (a)100 MeV and (b) 150 MeV.

CONCLUSIONS

Using an updated impedance model of the Diamond-II booster, ELEGANT tracking simulations have been carried out to study the variation of equilibrium parameters during

Table 3: Equilibrium parameters at extraction with collective effects including IBS effect at different single bunch charges.

Charge(nC)	ε_x(nm·rad)	ε_y(nm·rad)	σ_L(ps)	σ_ε(%)
0	17.3	1.57	38.0	0.086
0.72	19.1	1.58	42.3	0.095
1.44	21.3	1.60	44.9	0.100

the beam energy ramp. It was found that a single bunch charge of up to 0.72 nC is not of great concern for standard top-up operation; this is much higher than the required value of 0.1-0.2 nC for off-axis beam accumulation in the storage ring [1]. A significant vertical emittance growth and ~25 % beam loss was observed for a bunch charge of 1.44 nC at higher chromaticity at low energy. Without IBS effects, the equilibrium parameters were found to damp down to the zero current values at the extraction energy. The SR damping effect during energy ramping helps to supress the effect of instabilities on bunch properties. However, including the IBS effects, equilibrium parameters at extraction energy change by a small amount.

In view of the future possibility of swap-out injection in the Diamond-II storage ring, we have also carried out simulation for high-single bunch charge thresholds for the energy ramp from 100 MeV and 150 MeV. It was found that the extracted bunch charge of 3 nC can be achieved including impedance, RF cavity HOMs and physical apertures.

REFERENCES

[1] Diamond-II technical design report, Diamond Light Source Ltd., Aug. 2022,
https://www.diamond.ac.uk/Diamond-II.html

[2] I. P. S. Martin *et al.*, "Progress with the booster design for the Diamond-II upgrade", *in Proc. IPAC'21*, Campinas, SP, Brazil, May 2021, pp. 286-289.
doi:10.18429/JACoW-IPAC2021-MOPAB071

[3] I. P. S. Martin *et al.*, "Beam dynamics studies for the Diamond-II injector", *in Proc. IPAC'22*, Bangkok, Thailand, Jun. 2022, pp. 2708-2711.
doi:10.18429/JACoW-IPAC2022-THPOPT049

[4] R. Nagaoka and Karl L. F. Bane, "Collective effects in diffraction limited storage ring", J. Synchrotron Rad., 21, 937-960, 2014. doi:10.1107/S1600577514015215

[5] N. Mounet *et al.*, ImpedanceWake2D,
https://twiki.cern.ch/twiki/bin/view/ABPComputing/ImpedanceWake2D

[6] CST Studio Suite, Dassault Systemes,
https://www.3ds.com/product-services/similia/products/cst-studio-suite/

[7] M. Borland, "elegant: A flexible sdds-compliant code for accelerator simulation", APS LS-287, September 2000.
doi:10.2172/761286

[8] Y. Wang, M. Borland, "Pelegant: A parallel accelerator simulation code for electron generation and tracking", *AIP Conf. Proc.*, Vol. 877, p. 241, 2006. doi:10.1063/1.2409141

[9] H. S. Xu et al., "Studies of the single-bunch instabilities in the booster of HEPS", *in Proc. IPAC'18*, Vancouver, Canada, Apr.-May 2018, pp. 2971-2974. doi:10.18429/JACoW-IPAC2018-THPAF014

SIMULATED COMMISSIONING FOR DIAMOND-II STORAGE RING FROM ON-AXIS TO OFF-AXIS INJECTION

H.-C. Chao*, I. P. Martin, Diamond Light Source, Oxfordshire, UK

Abstract

The Diamond-II storage ring commissioning simulations have continued based on the previous results where on-axis injected beams are captured. The next goal is to enlarge the dynamic aperture so that off-axis injection can be achieved. The procedures include beam based alignment, beta-beating correction and linear optics correction. Details of the implementations are discussed and the simulation results are presented. In the end, we are able to reach off-axis injection which allows accumulation.

INTRODUCTION

The Diamond-II project [1] features a storage ring using a modified hybrid six-bend achromat lattice. The parameters of the current baseline lattice are listed in Table 1.

Table 1: Diamond-II Storage Ring Parameters

Parameter	Value	Unit
Energy	3.5	GeV
Circumference	560.56	m
Number of Straight Sections	48	
Betatron Tune (H/V)	54.14 / 20.24	
Natural Chromaticity (H/V)	-68 / -89	
Damping Partition (J_x)	1.88	
Natural Emittance	162	pm-rad
Momentum Compaction Factor	1.03	10^{-4}
Energy Loss Per Turn (w/o IDs)	723	keV
Rad. Damping Time (H/V/L)	9.7 / 18.1 / 16.0	ms
Natural Energy Spread†	9.4	10^{-4}
Natural Bunch Length†	3.5	mm
Synchrotron Tune†	0.0025	
Beta Functions (H/V)‡	8.44 / 3.41	m

† Estimated with only main RF total voltage = 1.42 MV

‡ At long straight centres

The general commissioning strategies and some preliminary simulation results were presented in the previous study [2], including initial estimates for storage ring error tolerances. Since that time, prototyping and alignment trials have begun, ensuring all sources of error are minimised within the practical engineering constraints. As such, the error specifications continue to evolve.

In the follow-up study [3], the revised error tolerances are given and some alternative methods for early-stage commissioning are discussed. Initial commissioning stages were simulated for 200 random machines, up to the phase when an on-axis injected beam is captured. The demonstrated dynamic apertures, estimated by particle tracking with more

---

* hung-chun.chao@diamond.ac.uk

than one synchrotron period, are large enough to capture on-axis injected beams efficiently.

At this stage the beam current will be low (< 1 mA), but sufficient to detect a closed orbit and betatron tunes. In addition, the RF frequencies and phases are already adjusted to minimise the synchrotron oscillation of the captured beam.

In this paper the plans for the subsequent commissioning will be discussed, together with some details of the implementation and simulation results.

COMMISSIONING RECIPES AND SIMULATIONS

The next goal of commissioning is to enlarge the dynamic aperture to switch from on-axis injection to off-axis injection for accumulation. The current subsequent commissioning recipes are as follows.

1. Very first time closed orbit correction and chromaticity correction,
2. Set up ab-initio BPM offsets,
3. Preliminary beam based alignment (BBA),
4. Preliminary beta-beating correction (BBC),
5. Integer tune correction,
6. Further iterations of BBA and linear optics correction.

During the course of commissioning a tune scan can always be performed to ensure a good beam transmission whenever needed. The tune response matrix used is constructed from the ideal lattice with 7 families of quadrupoles (excluding strong quadrupoles). Some of the commissioning procedures are detailed as follows.

First Closed Orbit Correction

The Tikhonov parameter [4] used to regularise the corrector strengths is set very weak (α = 1000). As shown in Fig. 1, the rms BPM readouts are slightly improved to a few hundreds μm and an extreme case is fixed.
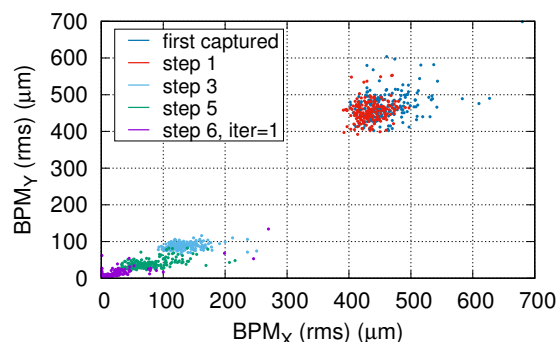
Figure 1: RMS BPM readouts at different steps.

Initial BPM Offsets and BBA

The BPM signals are weak and noisy because the intensity of captured beam is very low at this moment. We have to assign ab-initio BPM offsets to improve the closed orbit correction targets. The orbits with small quadrupole and corrector variations can be measured in order to find the most probable values of the BPM-to-quad offsets by numerical fitting. These offset values are the update values to be added to the original BPM offsets (which are initially zeros). The found values may contain some false results and extreme outliers. To reduce the harm caused by them, we can scale the updated values down by a factor and set a cap to limit the maximum change.

The closed orbits established in the first step are fragile, as any large changes of correctors may easily cause the loss of stable conditions. Therefore this step will be carried out based on the same closed orbit, i.e. no orbit corrections are applied.

After this step, the beams are still at the same position but the BPM readouts are different because the BPM offsets are changed closer to the adjacent quadrupole centres. Once these ab-initio values of BPM offsets are assigned, we can then proceed to further BPM offset refinements with frequent applications of closed orbit corrections in the first BBA routine. The BPMs have been grouped into 48 subsets based on the girders they sit on. All the subsets are visited once. The resulting rms BPM readouts are brought down from around $450\,\mu m$ to $150\,\mu m$, as Fig. 1 shows.

Beta-beating Correction

The linear optics correction can be carried out by Linear Optics from Closed Orbits (LOCO) [5] by fitting the closed orbit response matrix. However, there are some disadvantages to use this method with the on-axis injection. First of all, the accuracy of closed orbit response matrix is poor because of the large BPM noise at low current. Secondly, the measurement speed is slow due to the repetitive shot-by-shot injection. Lastly, the first LOCO solutions are not unique and depend strongly on the arbitrary choice of singular values [6]. A few trials will be needed to get a solution.

Instead, we can perform a preliminary beta-beating correction on the average beta functions. The only requirement is a beam with sufficient number of revolutions for good tune measurements. As long as the tune resolution is sufficient, the average beta function in a quadrupole can be estimated by the ratio of the tune changes and the field gradient changes $\bar{\beta}_i = 4\pi \Delta Q/(\Delta k_1 L)_i$. The corresponding beta-beating response matrix R (length weighed) is defined as

$$\frac{\bar{\beta}_i - \bar{\beta}_{0,i}}{\bar{\beta}_{0,i}} = \sum_j R_{ij} \Delta k_j,$$

where $\bar{\beta}_0$ can be calculated by the ideal model simulation. The beta-beating is then corrected by the pseudo inverse of R derived by the SVD method.

There are in total 300 pure quadrupoles therefore the dimension of R is 600×300. It takes 90,000 bi-directional

quadrupole variations to complete the R measurement. It is more time consuming than the closed orbit response matrix measurement but the problem of noisy BPM can be avoided.

Figure 2 shows the BBC results for all 200 cases simulated. The vertical beta-beatings correspond to quadrupole indices from 301 to 600. From this step on the quadrupole setpoints grouped in families are split into 300 individual setpoints.
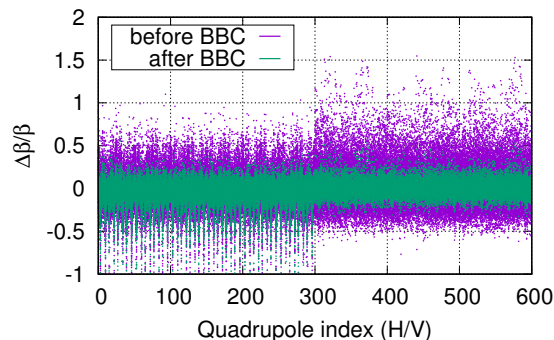
Figure 2: Beta beating improvement (200 seeds).

There are some caveats about this method. If the beta function variation in a quadrupole is large, this method may not be very effective.

Integer Tune Correction

Up to the BBC step some betatron tunes may be above the half-integer or have incorrect integer tune. The next step is to adjust the full tune to be in the correct half-integer tune window. In the simulation, it's easier to get the full tune as the phase advances can be calculated. However, in the control room, the un-corrected linear coupling and above half-integer tunes can cause the tune confusion therefore human supervision and intervention are always needed. In general the integer part of the betatron tune can be derived by counting the number of betatron oscillations. Meanwhile the fractional part of the betatron tune can be judged by observing the movement of the FFT spectrum peaks with some quadrupole change tests. In practice, trial-and-error can resolve this issue.

Figure 3 shows the tune distribution for 200-seed simulations. The corrected results are shown in the green dots.
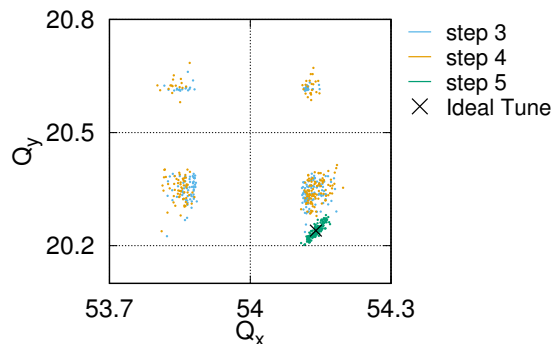
Figure 3: Full tunes at different commissioning states for 200 seeds simulations.

TU4P20

125

Some other facts are observed:

- Only about 50% of simulated seeds are in the correct half-integer tune window before correction.
- Uncorrected vertical tunes tend to be higher.
- The integer tunes do not change in the previous BBC procedure.
- The rms BPM readings do not change much in the previous BBC procedure.
- The dynamic aperture, shown by the green line in Fig. 4 (step 5), is significantly improved after the tune is adjusted.

After this step off-axis injection should be possible. If the beam can be accumulated, it will be very beneficial for the following commissioning steps in terms of BPM noise and commissioning time. LOCO can be carried out to have better linear optics corrections.

Further Corrections

We have investigated applying the LOCO for the first time at this stage but it only gets marginal improvement on dynamic apertures. A lesson learnt is the importance of improving BPM-to-quad alignment again before the application of the first LOCO for better results. Ideally we want the ability to carry out closed orbit corrections with strong corrector regularisation.

Further simulations are carried out for the second BBA and the first LOCO with all 300 independently powered quadrupoles. In the end, 95% of all generated random machines are successfully simulated and the resulting mean dynamic apertures are shown by the purple line in Fig. 4 (step 6). The chance of off-axis injection for beam accumulation is further increased.
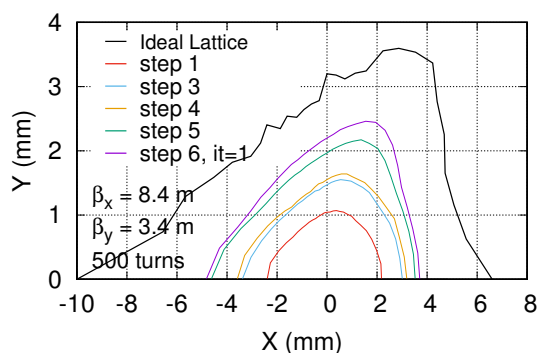
Figure 4: The average dynamic apertures at different commissioning states.

In some exceptional cases the BBA procedure results in non-converging BPM readings. These can be resolved by more careful tune control and iterative BBA. A robust BBA method is still under development. To further enlarge the dynamic aperture to improve the injection efficiency, more iterations of BBA and linear optics corrections by LOCO are necessary.

SUMMARY

The commissioning plans from on-axis to off-axis injection are outlined and the detailed procedures are explained in this study. The actual commissioning plan may still be evolving but here are some lessons we have learnt so far:

- The trick to find and set the ab-initio BPM offsets with the same closed orbit.
- Carrying out the first optics correction based on tune measurements.
- The impact of integer tune correction on dynamic apertures.
- Good BPM-to-quad alignment is essential for LOCO.

REFERENCES

[1] "Diamond-II Technical Design Report", Diamond Light Source Ltd., Aug. 2022. https://www.diamond.ac.uk/Diamond-II.html

[2] H. -C. Chao et al., "Commissioning simulations for the Diamond-II upgrade", in Proc. IPAC'22, Bangkok, Thailand, Jun. 2022, pp. 2598–2601. doi:10.18429/JACoW-IPAC2022-THPOPT016

[3] H. -C. Chao et al., "Updates to the Diamond-II storage ring error specifications and simulated commissioning procedure", in Proc. IPAC'23, Venice, Italy, May 2023. doi:10.18429/JACoW-IPAC2023-MOPA158

[4] Ph. Amstutz and T. Hellert, "Iterative trajectory-correction scheme for the early commissioning of diffraction-limited light sources", in Proc. IPAC'19, Melbourne, Australia, May 2019, pp. 353–356. doi:10.18429/JACoW-IPAC2019-MOPGW098

[5] J. Safranek, G. Portmann, and A. Terebilo, "MATLAB-based LOCO", in Proc. EPAC'02, Paris, France, Jun. 2002, paper WEPLE003, pp. 1184–1186.

[6] L. Nadolski, "LOCO fitting challenges and results for SOLEIL", in Beam Dynamics Newsletter 2007, No. 44, pp. 69–80.

SPECIAL OPERATIONAL MODES FOR SLS 2.0

J. Kallestrup*, M. Aiba, Paul Scherrer Institut, 5232 Villigen PSI, Switzerland

Abstract

The SLS 2.0 storage ring will achieve low emittance and high brightness while maintaining large dynamic aperture and lifetime comparable to the present SLS. Special operational modes are investigated to further explore the potential of the lattice. In this contribution, the first considerations on such modes for the SLS 2.0 are outlined. A promising high-brightness mode, increasing brightness by up to 25% at insertion devices with minor deterioration to dynamic and momentum aperture is presented. The use of round beams and its impact on beam dynamics and the beamlines in the SLS 2.0 portfolio is discussed.

INTRODUCTION

One of the main goals of the SLS 2.0 is to minimize the natural emittance of the machine, thereby generating significantly higher brightness than the existing SLS. This is achieved using a seven-bend achromat with longitudinal gradient bends and reverse bends [1, 2]. In this contribution we explore two possible operational modes for SLS 2.0. We investigate the option of a high-brightness mode which lowers the beta-functions at the insertion device (ID) source points. Finally, we show a possible implementation of round beams in SLS 2.0 in combination with one of the high-brightness lattice options, and evaluate the impact on both machine and beamline performance.

HIGH-BRIGHTNESS MODE

Motivation

The goal of the SLS 2.0 lattice design has been to create a lattice that provides an order-of-magnitude higher brightness and higher coherent flux than the existing SLS, without compromising with the dynamic and momentum aperture of the machine [2]. This leads to an ambitious, but realistic design. However, the brightness of IDs can be increased by optimizing the beta-functions in the straight sections further.

We follow the definitions of brightness and spatial coherence as given in [3], defined as:

$$\mathcal{B} = \frac{\Phi_{\text{ph}}}{4\pi^2 \sigma_{\text{T}x} \sigma_{\text{T}x'} \sigma_{\text{T}y} \sigma_{\text{T}y'} (d\omega/\omega)}, \quad (1)$$

and

$$\frac{\Phi_{\text{coh}}}{\Phi_{\text{ph}}} = \frac{\lambda^2}{16\pi^2 \sigma_{\text{T}x} \sigma_{\text{T}x'} \sigma_{\text{T}y} \sigma_{\text{T}y'}}, \quad (2)$$

where Φ_{ph} and Φ_{coh} are the total and spatially coherent flux, λ is the photon wavelength, $\sigma_{\text{T}u}$ and $\sigma_{\text{T}u'}$ are the effective photon source size and divergence defined as

$$\sigma_{\text{T}u} = \sqrt{\beta_u \epsilon_u + \frac{\lambda L}{8\pi}}, \quad (3)$$

_____
* jonas.kallestrup@psi.ch

and

$$\sigma_{\text{T}u'} = \sqrt{\frac{(1+\alpha_u^2)}{\beta_u}\epsilon_u + \frac{\lambda}{2L}}, \quad (4)$$

where β_u and α_u are the Twiss parameters at the ID source point. The SLS 2.0 portfolio contains IDs of several different lengths. The brightness and the coherence depends on the ID length, L, and we compute them for a range of $1 \leq L \leq 3$ m, corresponding to the actual IDs to be installed.

In the following, first the possibilities for brightness improvement without physically modifying the storage ring are investigated. Next, the option of increasing the gradient of quadrupoles will be considered.

The linear optics changes will be restricted to the straight sections to avoid modifying the optimized arc optics. This also means that the equilibrium emittances will remain unchanged.

The baseline SLS 2.0 lattice is designed such that the betatron phase advances along each straight section are the same constant values. The super-periodicity for on-momentum particles is therefore as high as the number of arcs: 12 ("pseudo symmetry"). To maintain good dynamic and momentum aperture, it is beneficial to keep the pseudo symmetry and, hence, the phase advance must be increased equally in all straight sections.

For each proposed solution, a genetic algorithm is used to optimize the nonlinear magnets in the lattice to maximize Touschek lifetime, τ_T. Piwinski's formula for the Touschek lifetime is used [4], with the nominal "flat beam emittances" $\epsilon_x = 149$ pm rad and $\epsilon_y = 10$ pm rad. All tracking simulations are performed in Accelerator Toolbox [5, 6].

We are interested in the relative increase in brightness and coherence between the baseline SLS 2.0 lattice and the new high-brightness solutions. The denominators of Eqs. (1) and (2) both scale as $(\sigma_{\text{T}x}\sigma_{\text{T}x'}\sigma_{\text{T}y}\sigma_{\text{T}y'})^{-1}$, meaning that the scaling of brightness and coherence will be the same, and we will therefore only report impacts on brightness.

Solutions-A: Unaltered Machine Layout

Two options are investigated for an unaltered machine layout: increasing the horizontal tune by a full integer ("solution A-1") or increasing the vertical tune by 0.56 ("solution A-2"). A comparison between the baseline and new Twiss parameters in the straight sections is shown in Table 1, and the relative brightness increases for IDs of the three lengths are shown in Fig. 1 for solution A-1 and A-2 as solid and dashed lines, respectively. Qualitatively, short IDs have the largest gain in brightness. Solution A-1 provides the biggest increase around the soft x-ray region of 1 keV photon energies, while solution A-2 is most beneficial around hard x-rays at 10 keV. Long straight sections benefit in a broader spectral range; for high photon energies this stems from the smaller values of α_x and α_y at the source points.

Table 1: Optics of baseline and high-brightness lattice solutions. Twiss parameters refer to the source points of short (SS), medium (MS), long straight #1 (LS#1) and long straight #2 (LS#2), respectively.

Lattice	Source	Baseline	A-1	A-2	B-1
Q_x	-	39.37	40.37	39.37	40.37
Q_y	-	15.22	15.22	15.78	15.78
β_x [m]	SS	2.5	1.4	2.5	1.5
	MS	3.4	2.0	3.5	2.0
	LS#1	9.3	7.2	9.5	7.0
	LS#2	7.8	5.0	8.0	5.3
β_y [m]	SS	1.3	1.3	0.6	0.5
	MS	2.4	2.3	1.2	1.0
	LS#1	6.5	6.4	5.4	5.9
	LS#2	5.8	5.7	3.3	3.0
α_x	SS	0.0	0.0	0.0	0.0
	MS	−0.1	0.0	−0.1	0.0
	LS#1	−0.4	0.0	−0.7	−0.1
	LS#2	0.4	0.0	0.5	0.1
α_y	SS	0.0	0.0	0.0	0.0
	MS	−0.1	−0.1	0.2	0.2
	LS#1	−0.9	−0.8	0.1	0.2
	LS#2	0.7	0.6	−0.1	−0.2
τ_T [h]	-	5.4	4.7	4.8	<1

Figure 1: Ratio of brightness between the nominal SLS 2.0 lattice and high-brightness options A-1 (solid lines), A-2 (dashed lines) and B-1 (dotted lines) in each straight section for various undulator lengths.

The results for the on- and off-momentum dynamic apertures without errors are shown in Fig. 2. The physical aperture restriction is 5.0 mm, i.e., the dynamic aperture is still outside the physical aperture of the chamber. The Touschek lifetime (with physical aperture but without third harmonic cavity) is found to be 4.7 h and 4.8 h for solutions A-1 and A-2, respectively, corresponding to a 13% and 11% reduction compared to the nominal lattice lifetime of 5.4 h.

Solutions-B: Modified Machine Layout

The potential phase advance increase is limited in the short straight sections due to the limited strength of quadrupoles in the matching sections. An option of installing stronger quadrupoles is evaluated as a hypothetical future upgrade option. We investigated a working point of [40.37, 19.78], i.e., combining the features of solutions A-1 and A-2, that requires the stronger, but still achievable, quadrupole strength 118 T m^{-1}.

The relative increase in brightness is shown as the dotted lines in Fig. 1. This solution exceeds the previous two with significant gains particularly in the tender and hard x-ray range. For one of the flagship beamlines, I-TOMCAT, a hard x-ray beamline based on a 1 m high-temperature superconducting undulator in a short straight section [1, 7], the expected increase in brightness at 10 keV is around 50%.

The nonlinear optimization of this solution has yet to yield satisfying Touschek lifetime; the working point is close to the $Q_x + 2Q_y = 72$ resonance, which is systematic for a twelve-fold symmetric machine, and is suspected to be the limitation for this lattice solution. Other modified lattices
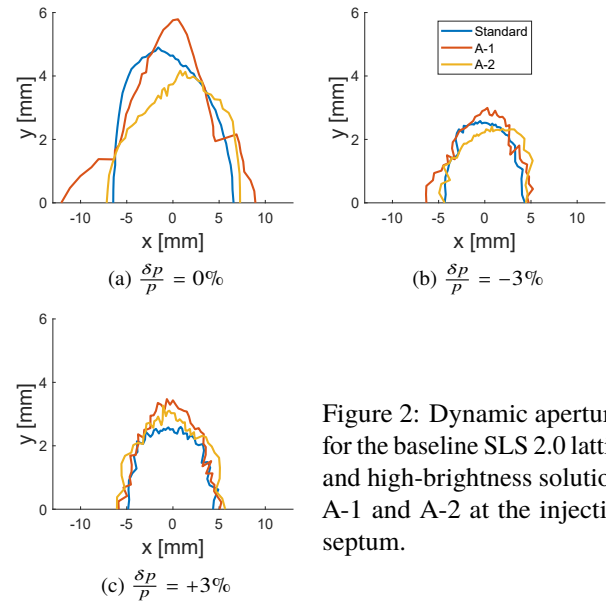
Figure 2: Dynamic apertures for the baseline SLS 2.0 lattice and high-brightness solutions A-1 and A-2 at the injection septum.

with, e.g., working points [40.37, 16.22] are currently under development.

Further Considerations

For the high-brightness lattices with increased horizontal tune, the smaller β_x at the source points comes with the increased horizontal phase advance. Due to the twelve-fold pseudo symmetry it becomes more challenging to maintain a large value of β_x at the injection point, which is used to increase the dynamic aperture for off-axis injection. Nevertheless, the nonlinear optimization provides on-momentum dynamic apertures exceeding the physical apertures.

Increasing the focusing gradient of the quadrupoles is technologically challenging, and it might therefore be simpler to install additional quadrupoles within the straight sections. This would, however, limit the available length for IDs. The trade-off between ID length and stronger focusing at the source points must be thoroughly evaluated.

ROUND BEAM MODE

Motivation

The use of round beams means redistributing the equilibrium emittance between the two transverse planes. Two benefits arise from this: the horizontal emittance is lowered, while the Touschek lifetime is increased and intrabeam scattering is reduced. Round beam operation is being considered and tested at several light source including SLS 2.0 [8–13]. The simplest way to generate the round beam is by operating the storage ring on the linear difference resonance $Q_x - Q_y = p$, where p is an integer. On the resonance the emittances will become [14]:

$$\epsilon_x = \epsilon_y = \epsilon_0 \left(\frac{J_x}{J_x + J_y} \right), \qquad (5)$$

where ϵ_0 is the natural emittance, J_x and J_y are the horizontal and vertical damping partition numbers, respectively. For SLS 2.0, with a natural emittance of 149 pm rad, $J_x = 1.85$ and $J_y = 1$, the emittances will become $\epsilon_x = \epsilon_y = 96$ pm rad.

The "A-1" high-brightness lattice setting has the attractive feature that the horizontal and vertical beta-functions at the ID source points in all sections are approximately equal. This means that, by coupling the beam transversely, it is possible to create photon beams with approximately identical sizes and divergences in both transverse planes.

Optics Options

For this purpose, a special version of the "A-1" solution is developed, henceforth called "A-1R", with the working point [40.37, 15.37]. Optical functions do not differ significantly from the values in Table 1. A coupling coefficient of $|C^-| = 0.01$ is introduced using 72 non-dispersive skew quadrupoles. This value is selected to ensure that all particles within the equilibrium bunch experience resonant coupling [13].

To quantify the effect of the coupling sources on the lattice performance, we calculate the Touschek lifetime for both the uncoupled and coupled lattices using the flat beam emittances including the physical apertures. The lifetimes become 4.3 h for the uncoupled and coupled lattice. Next, the Touschek lifetime is evaluated using the round beam emittances (Eq. (5)). This leads to $\tau_T = 10.6$ h, around a factor two larger than for the baseline SLS 2.0 lattice.

Beamline Perspective

The denominators of Eqs. (1) and (2) contain the electron beam sizes and divergences and, hence, the emittances. The larger vertical emittances will thereby lead to lowering the brightness and spatial coherent flux for the round beam mode.

(a) Short straight

(b) Medium straight

(c) Long straight #1

(d) Long straight #2
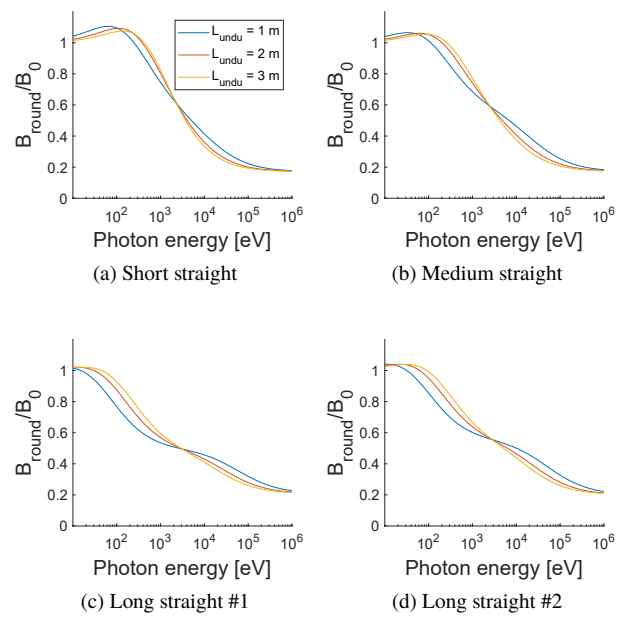
Figure 3: Ratio of brightness between the nominal SLS 2.0 lattice and round beam lattice solution A-1R with working point [40.37, 19.37] in various straight sections for different undulator lengths.

Figure 3 shows the brightness of the round beam lattice relative to the baseline lattice as a function of photon beam energy. Not all beamlines may benefit from the round beam mode, but it can be enabled upon request and by agreement with the users.

REFERENCES

[1] "SLS 2.0 Storage Ring. Technical design report", Eds. H. Braun, T. Garvey, M. Jörg, A. Ashton, P. Willmott, R. Kobler, PSI Rep. No. 21-02, Nov. 2021. https://www.dora.lib4ri.ch/psi/islandora/object/psi:39635

[2] A. Streun et al., "Swiss Light Source upgrade lattice design", to be published in Phys. Rev. Accel. Beams, 2023.

[3] A. Chao, K.H. Mess, M. Tigner and F. Zimmermann, "Handbook of accelerator physics and engineering", Singapore, World Scientific, 2013.

[4] A. Piwinski, "The Touschek Effect in strong focusing storage rings", DESY 98-179, Nov. 1998, ISSN 0418-983.

[5] A. Terebilo,"Accelerator modeling with MATLAB Accelerator Toolbox", in Proc. PAC'01, Chicago, IL, USA, Jun. 2001, paper RPAH314, pp. 3203–3205.

[6] B. Nash et al., "New functionality for beam dynamics in Accelerator Toolbox (AT)", in Proc. IPAC'15, Richmond, VA, USA, May 2015, pp. 113–116. doi:10.18429/JACoW-IPAC2015-MOPWA014

[7] "SLS 2.0 Beamline Conceptual Design Report", Eds. P. Willmott, U. Flechsig, T. Schmidt, PSI Rep. No. 21-01, Jan. 2021, https://www.psi.ch/en/media/63537/download

[8] A. Xiao, L. Emery, V. Sajaev, and B. X. Yang, "Experience with round beam operation at the Advanced Photon Source", in Proc. IPAC'15, Richmond, VA, USA, May 2015, pp. 562–564. doi:10.18429/JACoW-IPAC2015-MOPMA013

[9] Y. Hidaka, W. X. Cheng, Y. Li, T. V. Shaftan, and G. M. Wang, "Round beam studies at NSLS-II", in *Proc. IPAC'18*, Vancouver, Canada, Apr.-May 2018, pp. 1529–1532. doi:10.18429/JACoW-IPAC2018-TUPMK018

[10] T. E. Fornek, "Advanced Photon Source upgrade project preliminary design report", doi:10.2172/1423830.

[11] C. Steier *et al.*, "Status of the conceptual design of ALS-U", in *Proc. IPAC'18*, Vancouver, BC, Canada, Apr.-May 2018, pp. 4134–4137.
doi:10.18429/JACoW-IPAC2018-THPMF036

[12] "SLS-2. Conceptual design report", Ed. A. Streun, PSI Rep. No. 17-03, Dec, 2017, https://www.dora.lib4ri.ch/psi/islandora/object/psi:34977/

[13] J. Kallestrup, "Feasibility of round beams in SLS 2.0", presented at the IPAC'23, Venice, Italy, May 2023, paper MOPM021, to be published in the proceedings.

[14] A. W. Chao and M. J. Lee, "Particle distribution parameters in an electron storage ring", *J. Appl. Phys.*, vol. 47, pp. 4453-4456, 1976. doi:10.1063/1.322412

PROGRESS OF THE HEPS ACCELERATOR CONSTRUCTION AND LINAC COMMISSIONING*

C. Meng[†], J. S. Cao, Z. Duan, D. Y. He, P. He, H. F. Ji, Y. Jiao[†], W. Kang, J. Li, J. Y. Li[†], X. H. Lu, Y. M. Peng, H. M. Qu, S. K. Tian, J. Zhang, J. R. Zhang, H. S. Xu, G. Xu, W. M. Pan
Key Laboratory of Particle Acceleration Physics and Technology, Institute of High Energy Physics, Chinese Academy of Sciences, Beijing, China

Abstract

The High Energy Photon Source (HEPS) is the first fourth-generation synchrotron radiation source in China that has proceeded on the track of construction. The accelerator complex of the light source is composed of a 7BA storage ring, a booster injector, a Linac pre-injector, and three transfer lines. In order to provide high-bunch-charge beams for the storage ring, the booster was designed to be capable of both beam acceleration from low injection energy to extraction energy and charge accumulation at the extraction energy by means of accepting electron bunches from the storage ring. The Linac was built using S-band normal conducting structures, and can provide electron beam with pulse charge up to 7 nC. This paper reports the progress of the construction of the accelerators, including the installation of the storage ring, the pre-commissioning tests of the booster, and commissioning of the Linac. In particular, the beam commissioning of the Linac will be introduced in detail.

INTRODUCTION

The High Energy Photon Source (HEPS) [1, 2] is the first fourth-generation synchrotron radiation source based on a 6-GeV diffraction-limited storage ring [3, 4] that is currently under construction in China. The accelerator complex of the HEPS comprises an injector and a storage ring. The injector consists of a 500-MeV Linac [5, 6], a full-energy booster [7], a low energy transfer line connecting the Linac and booster and two high energy transfer lines that transport beams between the storage ring and booster [8]. The layout of HEPS accelerator is shown in Fig. 1 and the overall design goals of the light source are listed in Table 1.

The storage ring consists of 48 modified hybrid 7BAs, which were grouped in 24 periods with circumference of 1360.4 m. The Booster consists of 4 FODO structure lattice with circumference of 454.07 m. The optical functions and layouts of the storage ring and booster are shown in Fig. 2. The swap-out injection scheme [9] is adopted, so the booster employs the "high-energy accumulation" scheme. In order to meet the requirements of the injection and beam commissioning, a high bunch charge scheme of the Linac was adopted [5] with bunch charge of 7 nC. The layout and tunnel of the Linac are shown in Fig. 2.

Considering the long injection interval in the ring, the injector adopts an energy-saving design, the Linac operates in burst mode, and the booster adopts a novel ramping-table-controlled scheme. For the burst mode of the Linac, each macro-RF pulse has 1 to 10 RF pulse and the RF pulse repetition rate is 50 Hz. The interval time of the macro-RF pulse is decided by the injection rate. For the booster ramping-table-controlled scheme, the booster can realize the stop and start at any energy. The power supply and the cavity can be ramped according to the ramping-table, every time there is a clock trigger, take a step, and wait without the clock trigger. The schematic diagram is shown in Fig. 3. When no injection is needed, the booster is in a low-power waiting phase without repeated ramping.

In this paper, we introduce the brief construction process of the HEPS, and present the latest results of beam commissioning.
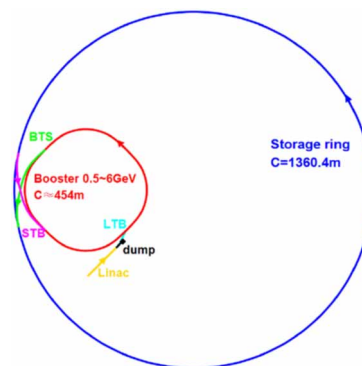
Figure 1: Layout of the HEPS accelerator.

Table 1: Main Parameters of The HEPS

Parameter	Value	Unit
Energy	6	GeV
Beam current	200	mA
Horizontal natural emittance	60	pm·rad
Brightness	>1x10^{22}	phs/s/mm^2/mrad^2/ 0.1%BW
Circumference	1360.4	m

CONSTRUCTION

Construction of the HEPS starts in June 2019 with a construction period of 6.5 years, which means it will be completed by the end of 2025. The milestone of the HEPS construction are as follows:
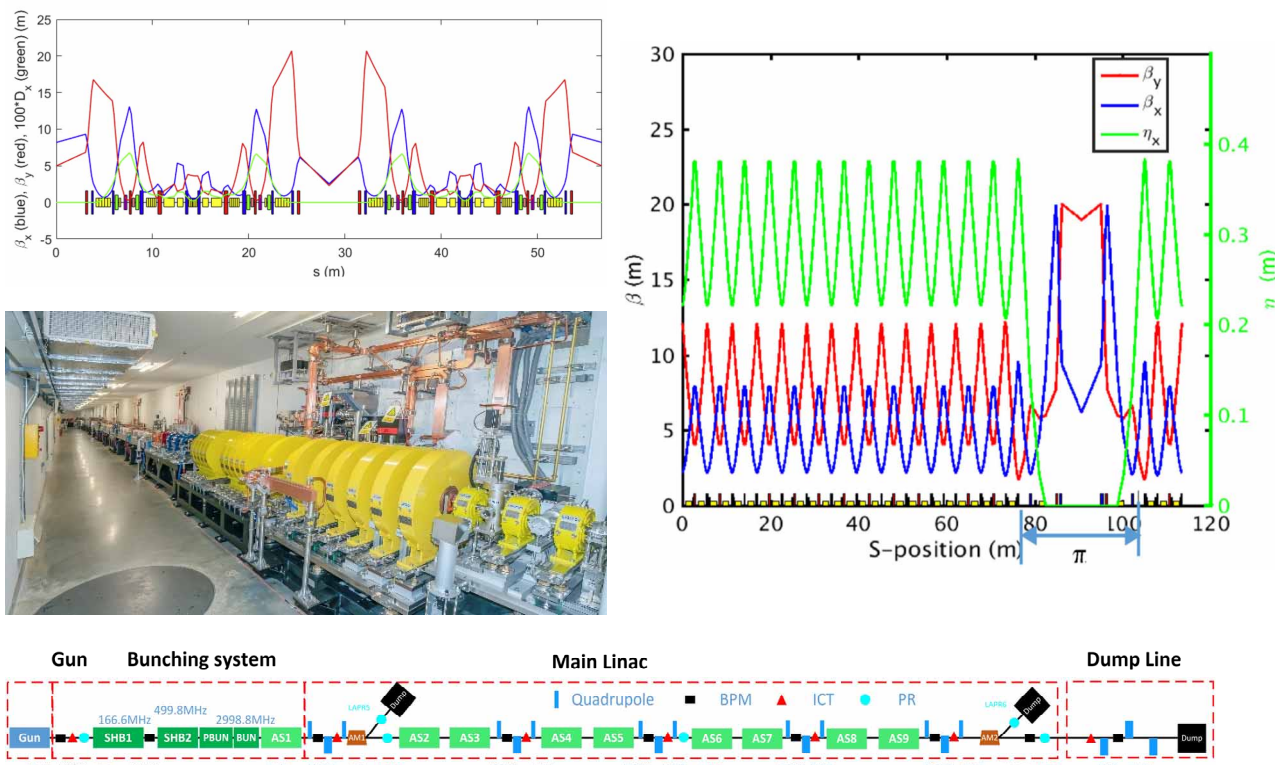
Figure 2: Optical functions and layouts of one super period of the storage ring (left-up) and booster (right-up), the tunnel (left-middle) and layout (bottom) of the Linac.
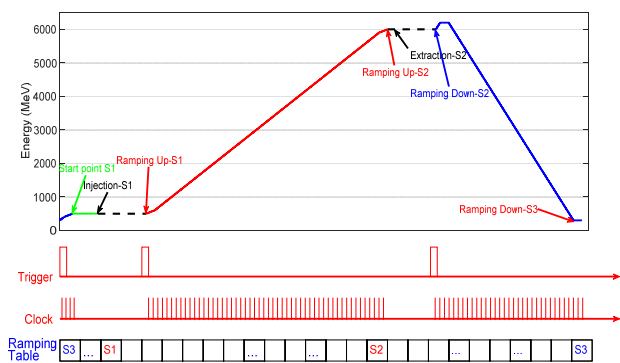
Figure 3: Schematic diagram of the booster ramping table.

- 2019.12, the physical design was frozen.
- 2021.06, installation of the first equipment.
- 2022.03, the tunnel installation of the Linac started pre-alignment installation of booster started.
- 2022.05, Linac full-line vacuum sealing was completed.
- 2022.08, the tunnel installation of the booster started.
- 2022.09, high-power online conditioning completed.
- 2023.01, booster full-line vacuum sealing was completed.
- 2023.02, the ring tunnel installation started.
- 2023.03, beam commissioning of the Linac started.

- 2023.06, completed process acceptance of the Linac.
- 2023.07, beam commissioning of the booster started.

The construction of the Linac has been completed and the process acceptance has been completed. The detailed beam commissioning will be introduced in the next part. The installation and system joint debugging of the booster has been completed and the beam commissioning is in progress, the energy has been successfully ramped to 6 GeV. The storage ring is in the intersecting process of equipment pre-alignment, tunnel installation, and tunnel alignment. At present, 60% of the tunnel alignment work of the magnet units has been completed.

COMMISSIONING

The Linac is a normal conduction S-band linear accelerator and composed of three sub-systems: an electron gun, a bunching system and the main accelerator. In terms of physical design, a complex bunching system was used to achieve a single bunch charge of up to 7 nC at the exit of the Linac. This is the highest bunch charge among linear (pre-)injectors for third and fourth generation light sources worldwide. Beam commissioning simulation of the Linac was completed in September 2021 [9]. A new platform, Python accelerator physics application set (*Pyapas*) [10] was developed and the beam commissioning applications of the Linac was completed [11].

In early March 2023, we obtained the radiation protection permit for the Linac beam commissioning, and beam commissioning started on March 9, 2023. On that day, the first electron beam was observed on the first profile monitor at 10:28 am and the electron beam was successfully transferred to the end of the Linac at 12:15 am with beam energy reaching 500 MeV[13]. The strong space charge effect and wakefield effect brought by high bunch charge bring great challenges to beam commissioning [14]. We use the beam size optimization method and the wakefield free steering method to suppress the emittance growth. The distributions before and after optimization are shown in Fig. 4 and show strong short-range and long-range wakefield effect. After 3 months of beam commissioning, the test and acceptance of the Linac was completed. The measured parameters are shown in Fig. 5 and Table 2. Due to the high performance of the IGBT based solid-state modulator with pulse repetition stability of 0.02% and LLRF, the beam energy stability is better than 0.02%, which is shown in Fig. 6.
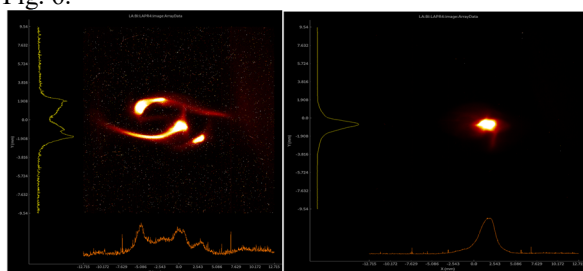
Figure 4: Beam distribution at the exit of the Linac with pulse charge of about 7 nC. Case one (left) have three bunch per pulse without optimization, Case two (right) have one bunch per pulse with optimization.
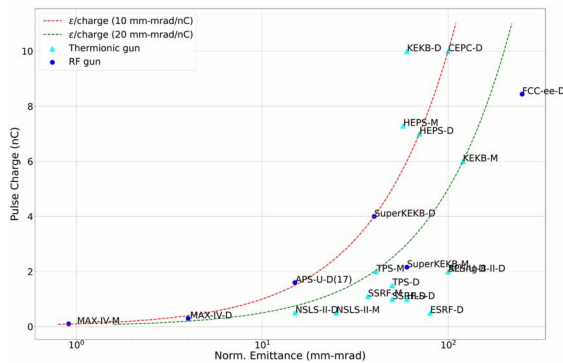
Figure 5: The bunch charge and emittance of different linear injectors.
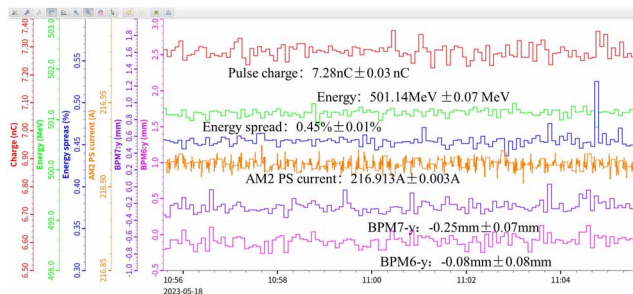
Figure 6: Stability of the Linac (mean±std).

Table 2: Measured Parameters of The HEPS Linac

Para-meter	Unit	Design		Measurement	
		Mode1	Mode2	Mode1	Mode2
Pulse charge	nC	≥2.5	≥7.0	2.84± 0.02	7.29± 0.02
Energy	MeV	≥500	≥500	501.4	501.2
Energy spread	%	≤0.5	≤0.5	0.31	0.45
Energy stability	%	±0.25	±0.25	σ=0.014 p-p=0.04	σ=0.014 p-p=0.05
Geometric emittance	nm·rad	≤41	≤70	37.2 (H) 36.9 (V)	56.4 (H) 58.5 (V)

The beam commissioning started since 25 July 2023. After 2 days injection commissioning, we saw the first synchrotron radiation light. Then we ramped the beam energy and reached to 6 GeV in 9 August, which is shown in Fig. 7.
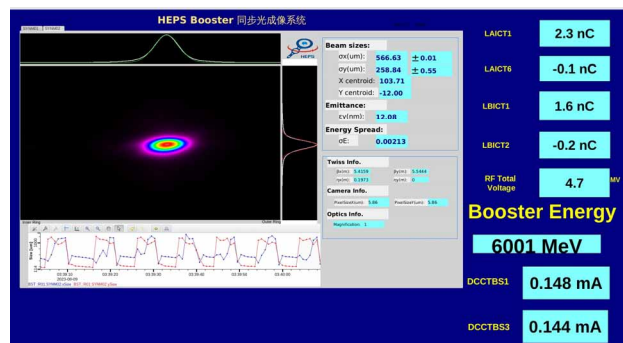
Figure 7: Synchrotron radiation light of the booster with beam energy of 6 GeV.

CONCLUSION

HEPS is the first fourth-generation synchrotron radiation source in China. The beam commissioning and process acceptance of the Linac have been completed. The beam energy has been ramped to 6 GeV and beam commissioning of the booster is in progress. The installation of the storage ring is progressing.

REFERENCES

[1] Y. Jiao *et al.*, "The HEPS project", *J. Synchrotron Radiat.* vol. 25, pp. 1611-1618, 2018.
doi:10.1107/S1600577518012110

[2] Y. Jiao, W. Pan, "High Energy Photon Source", *High Power Laser and Particle Beams,* vol. 2022, no. 34, p. 104002.
doi:10.11884/HPLPB202234.220080

[3] Y. Jiao *et al.*, "Modification and optimization of the storage ring lattice of the High Energy Photon Source", *Radiat. Detect Technol. Methods* vol. 4, pp. 415–424, 2020.
doi:10.1007/s41605-020-00189-7

67th ICFA Adv. Beam Dyn. Workshop Future Light Sources

ISBN: 978–3–95450–224–0

FLS2023, Luzern, Switzerland

ISSN: 2673–7035

JACoW Publishing

doi:10.18429/JACoW–FLS2023–TU4P27

[4] H. Xu *et al.*, "Equilibrium electron beam parameters of the High Energy Photon Source", *Radiat. Detect. Techno.l Methods*, 2023. doi:10.1007/s41605-022-00374-w

[5] C. Meng *et al.*, "Physics design of the HEPS LINAC", *Radiat Detect. Technol. Methods,* vol. 4, pp. 497–506, 2020. doi:10.1007/s41605-020-00205-w

[6] S. Zhang *et al.*, "The physics design of HEPS Linac bunching system", *Radiat. Detect. Technol. Methods* vol. 4, pp. 433–439, 2020. doi.org/10.1007/s41605-020-00200-1

[7] Y. Peng *et al.*, "Design of the HEPS booster lattice", *Radiat. Detect. Technol .Methods* vol. 4, pp. 425–432, 2020. doi:10.1007/s41605-020-00202-z

[8] Y. Guo *et al.*, "The transfer line design for the HEPS project", *Radiat. Detect. Technol. Methods* vol. 4, 4pp. 40–447, 2020. doi:10.1007/s41605-020-00209-6

[9] Z. Duan *et al.*, "The Swap-Out Injection Scheme for the High Energy Photon Source", in *Proc. IPAC'18*, Vancouver, Canada, Apr.-May 2018, pp. 4178-4181. doi:10.18429/JACoW-IPAC2018-THPMF052

[10] C. Meng *et al.*, "Development Progress of HEPS LINAC", in *Proc. IPAC'22*, Bangkok, Thailand, Jun. 2022, pp. 2472-2475. doi:10.18429/JACoW-IPAC2022-THPOST016

[11] X. H. Lu *et al.*, "Status of High Level Application Development for HEPS", in *Proc. ICALEPCS'21*, Shanghai, China, Oct. 2021, pp. 978-980. doi:10.18429/JACoW-ICALEPCS2021-THPV047

[12] Y.-L. Zhao *et al.*, "The high level applications for the HEPS Linac", *J. Instrum.*, vol. 18, p. 06014, 2023. doi:10.1088/1748-0221/18/06/P06014

[13] C. Meng *et al.*, "Progress of the first-stage beam com-missioning of High Energy Photon Source Linac", *High Power Laser and Particle Beams*, vol. 35, p. 054001, 2023 doi:10.11884/HPLPB202335.23006

[14] C. Meng *et al.*, "Beam commissioning of the HEPS Linac", presented at IPAC'23, Venice, Italy, May 2023, paper TUPL126, to appear in the proceedings.

USEFUL FORMULAS AND EXAMPLE PARAMETERS SET FOR THE DESIGN OF SSMB STORAGE RINGS

Xiujie Deng*, Alex Chao[1], Wenhui Huang, Zizheng Li, Zhilong Pan, Chuanxiang Tang

Tsinghua University, Beijing, China

[1]also at Standford University, Menlo Park, USA

Abstract

A promising accelerator light source mechanism called steady-state microbunching (SSMB) has been actively studied in recent years. Here we summarize some important formulas for the design of SSMB storage rings. Generally we group our formulas into two categories, i.e., a longitudinal weak focusing storage ring for a desired radiation wavelength $\lambda_R \gtrsim 100$ nm, and a transverse-longitudinal coupling, or a generalized longitudinal strong focusing, storage ring for a desired radiation wavelength 1 nm $\lesssim \lambda_R \lesssim 100$ nm. In each category, we have presented an example parameters set for the corresponding SSMB storage ring, to generate kW-level infrared, EUV and soft X-ray radiation, respectively.

INTRODUCTION

In Ref. [1], we have conducted indepth theoretical and experimental studies on the steady-state microbunching (SSMB) mechanism [2–18], which promises high-power narrow-band coherent radiation, with wavelength ranging from THz to soft X-ray. To make our investigations more useful for practitioners, especially concerning the parameters choice for an SSMB storage ring, here in this paper we present some important formulas and example parameters set for the design of SSMB storage rings.

LONGITUDINAL WEAK FOCUSING SSMB

The effective modulation voltage of a laser modulator using a planar undulator is [19]

$$V_L = \frac{[JJ]K}{\gamma}\sqrt{\frac{4P_L Z_0 Z_R}{\lambda_L}}\tan^{-1}\left(\frac{L_u}{2Z_R}\right). \quad (1)$$

in which γ is the Lorentz factor, $[JJ] = J_0(\chi) - J_1(\chi)$ and $\chi = \frac{K^2}{4+2K^2}$, J_n is the n-th order Bessel function of the first kind, $K = \frac{eB_0}{m_e c k_u} = 0.934 \cdot B_0[\text{T}] \cdot \lambda_u[\text{cm}]$ is the undulator parameter, determined by the peak magnetic flux density B_0 and period of the undulator λ_u, c the speed of light in free space, P_L is the modulation laser power, $Z_0 = 376.73\ \Omega$ is the impedance of free space, Z_R is the Rayleigh length of the laser, L_u is the undulator length. The linear energy chirp strength around zero-crossing phase is related to the laser and modulator undulator parameters according to $h = \frac{eV_L}{E_0}k_L$, with E_0 the particle energy, $k_L = 2\pi/\lambda_L$ the modulation laser wavenumber.

Linear stability of the longitudinal motion requires $0 < h\eta C_0 < 4$, where C_0 is the ring circumference, η is the phase

---

* dengxiujie@mail.tsinghua.edu.cn

slippage factor of the ring. In a longitudinal weak focusing ring ($\nu_s \ll 1$), the longitudinal beta function at the laser modulator is

$$\beta_{z\text{S}} \approx \sqrt{\frac{\eta C_0}{h}}. \quad (2)$$

The synchrotron tune is $\nu_s \approx \frac{\eta}{|\eta|}\frac{\sqrt{h\eta C_0}}{2\pi}$. The natural bunch length at the laser modulator is $\sigma_{z\text{S}} = \sigma_{\delta\text{S}}\beta_{z\text{S}}$, where $\sigma_{\delta\text{S}} = \sqrt{\frac{C_q}{J_s}\frac{\gamma^2}{\rho}}$ is the natural energy spread, with ρ the bending radius of dipole in the ring, $C_q = \frac{55\lambda_e}{32\sqrt{3}} = 3.8319 \times 10^{-13}$ m, $\lambda_e = \frac{\lambda_e}{2\pi} = 386$ fm is the reduced Compton wavelength of electron, J_s is the longitudinal damping partition number. The micro-bucket half-height is $\hat{\delta}_{\frac{1}{2}} = \frac{2}{\beta_{z\text{S}}k_L}$.

If there is a single laser modulator in the ring, and if longitudinal damping partition $J_s = 2$, then the theoretical minimum bunch length and longitudinal emittance in a longitudinal weak focusing ring with respect to the bending radius ρ and angle θ of each bending magnet are

$$\begin{aligned} \sigma_{z,\text{min}}[\mu\text{m}] &\approx 4.93\rho^{\frac{1}{2}}[\text{m}]E_0[\text{GeV}]\theta^3[\text{rad}], \\ \epsilon_{z,\text{min}}[\text{nm}] &\approx 8.44E_0^2[\text{GeV}]\theta^3[\text{rad}]. \end{aligned} \quad (3)$$

Coherent undulator radiation power at the odd-H-th harmonic from a transversely-round electron beam is

$$P_{H,\text{peak}}[\text{kW}] = 1.183N_u H\chi[JJ]_H^2 FF_\perp(S)|b_{z,H}|^2 I_P^2[\text{A}], \quad (4)$$

where N_u is the number of undulator periods, $[JJ]_H^2 = \left[J_{\frac{H-1}{2}}(H\chi) - J_{\frac{H+1}{2}}(H\chi)\right]^2$, with $\chi = \frac{K^2}{4+2K^2}$, and the transverse form factor $FF_\perp(S) = \frac{2}{\pi}\left[\tan^{-1}\left(\frac{1}{2S}\right) + S\ln\left(\frac{(2S)^2}{(2S)^2+1}\right)\right]$, with $S = \frac{\sigma_\perp^2 \frac{\omega}{c}}{L_u}$ and $\sigma_\perp$ the RMS transverse electron beam size, $b_{z,H}$ is the bunching factor at the H-th harmonic, and I_P is the peak current.

Based on the above formulas, here we present an example parameters set in Tab. 1 of a longitudinal weak focusing SSMB storage ring, aimed for high-power infrared radiation generation. As can be seen, such a compact SSMB storage ring can be used for high-power infrared radiation generation. The requirement on the stored laser power is easy to realize in practice. All the other parameters listed are also within practical range. A sharp reader may notice that the microbucket half-height is only twice the natural energy spread of the electron beam. Therefore, in addition to the shallow microbuckets, we need a larger bucket, for example a barrier bucket formed by an induction linac, to

Table 1: Example parameters set of a longitudinal weak focusing SSMB storage ring for infrared radiation generation.

Parameter	Value	Description
E_0	250 MeV	Beam energy
C_0	50 m	Circumeference
η	4×10^{-6}	Phase slippage factor
ρ_{ring}	0.6 m	Bending radius of dipoles in the ring
θ	$\frac{\pi}{7}$	Bending angle of each dipole
$\sigma_{\delta S}$	2.76×10^{-4}	Natural energy spread
$\sigma_{z,\text{lim}}$	86 nm	Theoretical lower bunch length limit
λ_L	1064 nm	Modulation laser wavelength
h	500 m^{-1}	Energy chirp strength
σ_{zS}	175 nm	Natural bunch length
$\delta_{\frac{1}{2}}$	5.36×10^{-4}	Microbuket half-height
$\lambda_{u\text{Mod}}$	5 cm	Modulator undulator period
$B_{0\text{Mod}}$	0.92 T	Modulator peak magnetic field
$L_{u\text{Mod}}$	1 m	Modulator undulator length
$P_L(Z_R = \frac{L_u}{3})$	24 kW	Modulation laser power
$\lambda_R = \lambda_L$	1064 nm	Radiation wavelength
b_1	0.59	Bunching factor
$\sigma_\perp$	100 μm	Transverse electron beam size at the radiator
$\lambda_{u\text{Rad}}$	5 cm	Radiator undulator period
$B_{0\text{Rad}}$	0.92 T	Radiator peak magnetic field
$L_{u\text{Rad}}$	2 m	Radiator length
P_R	1 kW @ $I_P = 0.55$ A	Radiation peak/average power

constrain the particles in the ring to ensure a large enough beam lifetime.

TRANSVERSE-LONGITUDINAL COUPLING SSMB

Transverse-longitudinal coupling (TLC) dynamics can be invoked to compress the bunch length with a shallow energy modulation strength, by taking advantage of the ultrasmall vertical emittance in a planar ring. For a TLC dynamics-based SSMB, or a generalized longitudinal strong focusing SSMB [15], using TEM00 mode laser modulator for energy modulation, we have the following important formulas.

Relation between energy chirp strength and optical functions at the modulator and radiator

$$h^2(\text{Mod})\mathcal{H}_y(\text{Mod})\mathcal{H}_y(\text{Rad}) \geq 1, \quad (5)$$

where $\mathcal{H}_y$ is a chromatic function quantifying the contribution of vertical emittance to bunch length. Bunching factor at the n-th laser harmonic in TLC SSMB at the radiator

$$b_n = \left(\sum_{m=-\infty}^{\infty} J_m(n) \exp\left[-((n-m)k_L\sigma_z(\text{Mod}))^2/2\right] \right)$$
$$\exp\left[-(nk_L\sigma_z(\text{Rad}))^2/2\right], \quad (6)$$

where $\sigma_z(\text{Mod}) = \sqrt{\epsilon_z\beta_z(\text{Mod}) + \epsilon_y\mathcal{H}_y(\text{Mod})}$ and $\sigma_z(\text{Rad}) = \sqrt{\epsilon_y\mathcal{H}_y(\text{Rad})}$ are the linear bunch length at the modulator and radiator, respectively.

Contribution of two modulators to ϵ_y from quantum excitation

$$\Delta\epsilon_y(\text{Mod}) = 2 \times \frac{55}{96\sqrt{3}} \frac{\alpha_F\lambda_e^2\gamma^5}{\alpha_V} \frac{\mathcal{H}_y(\text{Mod})}{\rho_{0\text{Mod}}^3} \frac{4}{3\pi}L_u, \quad (7)$$

where $\alpha_F = \frac{1}{137}$ is the fine-structure constant, $\alpha_V \approx \frac{U_0}{2E_0}$ is the vertical damping rate with U_0 the radiation energy loss of a particle per turn. Assuming $\epsilon_y = \Delta\epsilon_y(\text{Mod})$, which means the vertical emittance is solely from the two modulators, then the required modulation laser power and modulator length scaling are

$$P_L[\text{kW}] \approx 5.67\frac{\lambda_L^{\frac{7}{3}}[\text{nm}]E_0^{\frac{8}{3}}[\text{GeV}]B_{0\text{Mod}}^{\frac{7}{3}}[\text{T}]}{\sigma_z^2(\text{Rad})[\text{nm}]B_{\text{ring}}[\text{T}]},$$
$$L_u[\text{m}] \approx 57\frac{B_{\text{ring}}[\text{T}]\epsilon_y[\text{pm}]}{\mathcal{H}_y(\text{Mod})[\mu\text{m}]B_{0\text{Mod}}^3[\text{T}]}, \quad (8)$$

where $B_{0\text{Mod}}$ is the peak magnetic flux density of the modulator undulator, B_{ring} is the magnetic flux density of bending magnets in the ring. The above scaling laws are accurate when $K_u > \sqrt{2}$. For the more general case, refer to Ref. [1].

Based on the presented formulas, here we present an example parameters set in Tab. 2 of a TLC SSMB storage ring, aimed for high-power EUV and soft X-ray radiation. Since the bunch lengthening from vertical emittance at the modulator will be comparable or longer than the modulation laser wavelength, the difference of final bunching factor at the radiator between a pre-microbunched beam and coasting beam is negligible. To minimize the IBS effect, we choose to use

Table 2: Example parameters set of a TLC SSMB storage ring for EUV and soft X-ray radiation generation.

	Parameter	Value	Description
	E_0	800 MeV	Beam energy
	C_0	$\lesssim 100$ m	Circumference
	ρ_{ring}	2 m	Bending radius in the ring
	$\sigma_{\delta S}$	4.85×10^{-4}	Natural energy spread
	ϵ_y	2 pm	Vertical emittance
	λ_L	270 nm	Modulation laser wavelength
	$\sigma_\perp$	10 μm	Effective transverse electron beam size at the radiator
EUV (13.5 nm)	σ_z(Rad)	2 nm	Linear bunch length at the radiator
	σ_{zy}(Mod)	1.85 μm	Bunch lengthening from ϵ_y at the modulator
	h	541 m^{-1}	Energy chirp strength
	$\lambda_{u\text{Mod}}$	0.5 m	Modulator undulator period
	$B_{0\text{Mod}}$	0.039 T	Modulator peak magnetic flux density
	$L_{u\text{Mod}}$	1.5 m	Modulator length
	$P_L(Z_R = \frac{L_u}{3})$	141 kW	Modulation laser power
	$\lambda_R = \frac{\lambda_L}{20}$	13.5 nm	Radiation wavelength
	b_{20}	0.11	Bunching factor
	$\lambda_{u\text{Rad}}$	2 cm	Radiator undulator period
	$B_{0\text{Rad}}$	1.15 T	Radiator peak magnetic flux density
	$L_{u\text{Rad}}$	3.2 m	Radiator length
	P_R	1 kW @ $I_P = 1.5$ A	Radiation peak/average power
Soft X-ray (6.75 nm)	σ_z(Rad)	1 nm	Linear bunch length at the radiator
	σ_{zy}(Mod)	1.85 μm	Bunch lengthening from ϵ_y at the modulator
	h	1082 m^{-1}	Energy chirp strength
	$\lambda_{u\text{Mod}}$	0.5 m	Modulator undulator period
	$B_{0\text{Mod}}$	0.039 T	Modulator peak magnetic flux density
	$L_{u\text{Mod}}$	1.5 m	Modulator length
	$P_L(Z_R = \frac{L_u}{3})$	564 kW	Modulation laser power
	$\lambda_R = \frac{\lambda_L}{40}$	6.75 nm	Radiation wavelength
	b_{40}	0.085	Bunching factor
	$\lambda_{u\text{Rad}}$	1.5 cm	Radiator undulator period
	$B_{0\text{Rad}}$	1.11 T	Radiator peak magnetic flux density
	$L_{u\text{Rad}}$	2.4 m	Radiator length
	P_R	1 kW @ $I_P = 2.2$ A	Radiation peak/average power
Soft X-ray (2.7 nm)	σ_z(Rad)	0.5 nm	Linear bunch length at the radiator
	σ_{zy}(Mod)	2.81 μm	Bunch lengthening from ϵ_y at the modulator
	h	1423 m^{-1}	Energy chirp strength
	$\lambda_{u\text{Mod}}$	0.6 m	Modulator undulator period
	$B_{0\text{Mod}}$	0.028 T	Modulator peak magnetic flux density
	$L_{u\text{Mod}}$	1.8 m	Modulator length
	$P_L(Z_R = \frac{L_u}{3})$	1 MW	Modulation laser power
	$\lambda_R = \frac{\lambda_L}{100}$	2.7 nm	Radiation wavelength
	b_{100}	0.049	Bunching factor
	$\lambda_{u\text{Rad}}$	1 cm	Radiator undulator period
	$B_{0\text{Rad}}$	0.86 T	Radiator peak magnetic flux density
	$L_{u\text{Rad}}$	2 m	Radiator length
	P_R	1 kW @ $I_P = 5$ A	Radiation peak/average power

a coasting beam for microbunching here. It can be seen that as long as we can realize a coasting beam of 1.5 A average current, and an optical cavity stored power of $\gtrsim 100$ kW, we can realize 1 kW average power 13.5 nm EUV. Even if we can only realize an average beam current of 1 A or less, we can take advantage of the fact that $P_{\text{coh}} \propto I_P^2$ to realize an av-

erage radiation power of kW level, by decreasing the filling factor of electron beam in the ring but increasing the peak current as long as the value is below the collective instability threshold. Since there is no requirement on the longitudinal emittance for a coasting beam, the ring can be very compact, for example a circumference of 100 m or even smaller should

be feasible. This compact high-power EUV radiation source is promising to fulfill the urgent need of EUV lithography for high volume manufacture of computer chips, and also serve the future lithography like Blue-X which invokes 6.x nm-wavelength light source. Such an SSMB-based high-power high-flux soft X-ray photon source could be of great value for fundamental science like high-resolution angle-resolved photoemission spectroscopy and can also bridge the water window gap.

ACKNOWLEDGMENTS

REFERENCES

[1] X. Deng, "Theoretical and experimental studies on steady-state microbunching", PhD thesis, Tsinghua University, Beijing, China, to be published in Springer Singapore, 2023, https://link.springer.com/book/9789819957996

[2] D. F. Ratner and A. W. Chao, "Steady-state microbunching in a storage ring for generating coherent radiation", *Physical review letters*, vol. 105, no. 15, 2010. doi:10.1103/PhysRevLett.105.154801

[3] A. Chao, E. Granados, X. Huang, D. F. Ratner, and H. W. Luo, "High power radiation sources using the steady-state microbunching Mechanism", in *Proc. IPAC'16*, Busan, Korea, May 2016, pp. 1048–1053. doi:10.18429/JACoW-IPAC2016-TUXB01

[4] C.-X. Tang *et al.*, "An overview of the progress on SSMB", in *Proc. FLS'18*, Shanghai, China, Mar. 2018, pp. 166–170. doi:10.18429/JACoW-FLS2018-THP2WB02

[5] Z. Pan *et al.*, "A storage ring design for steady-state microbunching to generate coherent EUV light source", in *Proc. FEL'19*, Hamburg, Germany, Aug. 2019, pp. 700–703. doi:10.18429/JACoW-FEL2019-THP055

[6] X. J. Deng *et al.*, "Single-particle dynamics of microbunching", *Phys. Rev. Accel. Beams*, vol. 23, no. 4, pp. 044002, Apr. 2020. doi:10.1103/PhysRevAccelBeams.23.044002

[7] Y. Zhang *et al.*, "Ultralow longitudinal emittance storage rings", *Phys. Rev. Accel. Beams*, vol. 24, no. 9, pp. 090701, Sep. 2021. doi:10.1103/PhysRevAccelBeams.24.090701

[8] X. J. Deng *et al.*, "Courant-Snyder formalism of longitudinal dynamics", *Phys. Rev. Accel. Beams*, vol. 24, no. 9, pp. 094001, Sep. 2021. doi:10.1103/PhysRevAccelBeams.24.094001

[9] X. J. Deng *et al.*, "Harmonic generation and bunch compression based on transverse-longitudinal coupling", *Nucl. Instrum. Methods Phys. Res. A*, vol. 1019, pp. 165859, Dec. 2021. doi:10.1016/j.nima.2021.165859

[10] C.-Y. Tsai *et al.*, "Coherent-radiation-induced longitudinal single-pass beam breakup instability of a steady-state microbunch train in an undulator", *Phys. Rev. Accel. Beams*, vol. 24, no. 11, pp. 114401, Nov. 2021. doi:10.1103/PhysRevAccelBeams.24.114401

[11] C.-Y. Tsai, "Theoretical formulation of multiturn collective dynamics in a laser cavity modulator with comparison to Robinson and high-gain free-electron laser instability", *Phys. Rev. Accel. Beams*, vol. 25, no. 6, pp. 064401, June 2022. doi:10.1103/PhysRevAccelBeams.25.064401

[12] C.-Y. Tsai, "Longitudinal single-bunch instabilities driven by coherent undulator radiation in the cavity modulator of a steady-state microbunching storage ring", *Nucl. Instrum. Methods Phys. Res. A*, vol. 1042, pp. 167454, Nov. 2022. doi:10.1016/j.nima.2022.167454

[13] Y. J. Lu *et al.*, "Methods for enhancing the steady-state microbunching in storage rings", *Results Phys.*, vol. 40, pp. 105849, Sep. 2022. doi:10.1016/j.rinp.2022.105849

[14] X. J. Deng *et al.*, "Average and statistical properties of coherent radiation from steady-state microbunching", *J. Synchrotron Radiat.*, vol 30, part 1, pp. 35–50, Dec. 2023. doi:10.1107/S1600577522009973

[15] Z. Li, X. Deng, Z. Pan, C. Tang, and A. Chao. "Generalized longitudinal strong focusing in a steady-state microbunching storage ring" submitted to *Phys. Rev. Accel. Beams*, 2023.

[16] X. Deng *et al.*, "Experimental demonstration of the mechanism of steady-state microbunching", *Nature*, vol. 590, no. 7847, pp. 576–579, Feb. 2021. doi:10.1038/s41586-021-03203-0

[17] A. Kruschinski *et al.*, "Exploring the necessary conditions for steady-state microbunching at the Metrology Light Source", presented at the IPAC'23, Venice, Italy, May 2023, paper MOPA176, to appear in the proceedings.

[18] A. Chao, *et al.*, "Storage ring based steady state microbunching", presented at FLS'23, Lucerne, Switzerland, Aug 2023, paper MO2L2, this conference.

[19] A. Chao, "Focused laser", unpublished note, 2022.

WHY IS THE COHERENT RADIATION FROM LASER-INDUCED MICROBUNCHES NARROWBANDED AND COLLIMATED

Xiujie Deng*, Alex Chao[1], Tsinghua University, Beijing, China
[1]also at Standford University, Menlo Park, CA, USA

Abstract

There are two reasons: one is the long coherence length of radiation from microbunches imprinted by the modulation laser, the second is the finite transverse electron beam size. In other words, one is due to the longitudinal form factor, and the other the transverse form factor of the electron beam. Here we study the role of these form factors in shaping the energy spectrum and spatial distribution of microbunching radiation. The investigations are of value for cases like steady-state microbunching (SSMB), coherent harmonic generation (CHG) and free-electron laser (FEL).

GENERAL FORMULATION

For simplicity, as the first step we consider only the impacts of particle position x, y and z, but ignore the particle angular divergence x', y' and energy deviation δ, on the radiation. We will discuss the requirement of applying this approximation and the impact of beam divergence and energy spread in the end of this paper. With this simplification, the spectrum of radiation from an electron beam with N_e electrons is related to that of a single electron according to

$$\left.\frac{d^2W}{d\omega d\Omega}(\theta,\varphi,\omega)\right|_{\text{beam}} = N_e^2|b(\theta,\varphi,\omega)|^2\left.\frac{d^2W}{d\omega d\Omega}(\theta,\varphi,\omega)\right|_{\text{point}}, \tag{1}$$

with θ and φ being the polar and azimuthal angles in a spherical coordinate system, respectively, and

$$b(\theta,\varphi,\omega) = \int_{-\infty}^{\infty}\int_{-\infty}^{\infty}\int_{-\infty}^{\infty}\rho(x,y,z)$$
$$e^{-i\omega\left(\frac{x\sin\theta\cos\varphi+y\sin\theta\sin\varphi}{c}+\frac{z}{\beta c}\right)}dxdydz, \tag{2}$$

in which β is the particle velocity normalized by the speed of light in vacuum c and for relativistic beam can be approximated as 1, and $\rho(x,y,z)$ is the normalized charge density satisfying $\int_{-\infty}^{\infty}\int_{-\infty}^{\infty}\int_{-\infty}^{\infty}\rho(x,y,z)dxdydz = 1$. When the longitudinal and transverse dimensions of the electron beam are decoupled, we can factorize $b(\theta,\varphi,\omega)$ as

$$b(\theta,\varphi,\omega) = b_\perp(\theta,\varphi,\omega) \times b_z(\omega), \tag{3}$$

where

$$b_\perp(\theta,\varphi,\omega) = \int_{-\infty}^{\infty}\int_{-\infty}^{\infty}\rho(x,y)e^{-i\omega\left(\frac{x\sin\theta\cos\varphi+y\sin\theta\sin\varphi}{c}\right)}dxdy, \tag{4}$$

and

$$b_z(\omega) = \int_{-\infty}^{\infty}\rho(z)e^{-i\omega\frac{z}{\beta c}}dz. \tag{5}$$

* dengxiujie@mail.tsinghua.edu.cn

Note that $\rho(x,y)$ and $\rho(z)$ are then the projected charge density. $b_z(\omega)$ is the usual bunching factor found in literature and is independent of the observation angle. This however is not true for $b_\perp(\theta,\varphi,\omega)$. For example, for an x-y decoupled transversely Gaussian beam, we have

$$|b_\perp(\theta,\varphi,\omega)|^2 =$$
$$\exp\left\{-\left(\frac{\omega}{c}\right)^2\left[(\sigma_x\sin\theta\cos\varphi)^2 + (\sigma_y\sin\theta\sin\varphi)^2\right]\right\}, \tag{6}$$

where $\sigma_{x,y}$ are the RMS beam size in the horizontal, and vertical dimension, respectively.

In order to efficiently quantify the impact of the transverse and longitudinal distributions of an electron beam on the overall radiation energy spectrum, here we define the transverse and longitudinal form factors of an electron beam as

$$FF_\perp(\omega) =$$
$$\frac{\int_0^\pi \sin\theta d\theta \int_0^{2\pi} d\varphi |b_\perp(\theta,\varphi,\omega)|^2 \frac{d^2W}{d\omega d\Omega}(\theta,\varphi,\omega)\Big|_{\text{point}}}{\int_0^\pi \sin\theta d\theta \int_0^{2\pi} d\varphi \frac{d^2W}{d\omega d\Omega}(\theta,\varphi,\omega)\Big|_{\text{point}}}, \tag{7}$$

and

$$FF_z(\omega) = |b_z(\omega)|^2, \tag{8}$$

respectively. The overall form factor is then

$$FF(\omega) = FF_\perp(\omega)FF_z(\omega). \tag{9}$$

The total radiation energy spectrum of an electron beam is related to that of a single electron by

$$\left.\frac{dW}{d\omega}\right|_{\text{beam}} = N_e^2 FF(\omega)\left.\frac{dW}{d\omega}\right|_{\text{point}}. \tag{10}$$

LONGITUDINAL FORM FACTOR

Cleanly Separated Microbunch Train

When there are multiple microbunches cleanly separated from each other with a distance of the modulation laser wavelength λ_L, like that in some of the SSMB scenarios [1–3], the longitudinal form factor is that of the single microbunch multiplied by a macro form factor,

$$FF_{z\text{MB}}(\omega) = FF_{z\text{SB}}(\omega)\left(\frac{\sin\left(N_b\frac{\omega}{c}\frac{\lambda_L}{2}\right)}{N_b\sin\left(\frac{\omega}{c}\frac{\lambda_L}{2}\right)}\right)^2, \tag{11}$$

where the subscripts MB and SB mean multi bunch and single bunch, respectively, and N_b is the number of
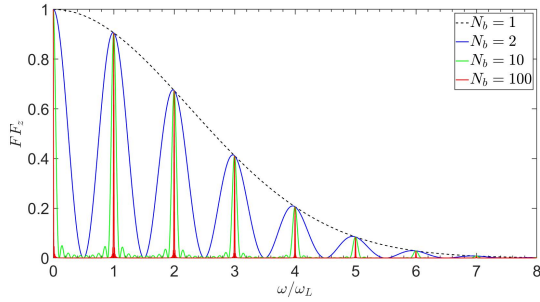
Figure 1: Example plot of the longitudinal form factor for multiple microbunches separated with a distance of laser wavelength λ_L. $\sigma_z = \frac{\lambda_L}{20}$ is used in the calculation.

microbunches. For a Gaussian microbunch we have $FF_{z\mathrm{SB}}(\omega) = \exp\left[-\left(\frac{\omega}{c}\sigma_z\right)^2\right]$, where σ_z is the RMS bunch length. The macro form factor of multi bunches is a periodic function of the radiation frequency, with a period of the modulation laser frequency. The full width at half maximum (FWHM) linewidth around each laser harmonics is

$$\Delta\omega_{\mathrm{FWHM}} = \frac{\omega_L}{N_b}. \qquad (12)$$

When N_b goes to infinity, this macro form factor will become the periodic delta function. Note that when we use the above form factor $FF_{z\mathrm{MB}}(\omega)$ to calculate the radiation energy or spectrum from N_b microbunches, the number of electrons used should be $N_b N_{e\mathrm{SB}}$, with $N_{e\mathrm{SB}}$ the number of electrons per microbunch. Figure 1 presents an example plot of the longitudinal form factor of multiple cleanly separatedly microbunches.

Continuous Bunch-based Microbunching

The longitudinal form factor for a coasting or infinite-long beam-based laser-induced microbunching is

$$FF_{z,\mathrm{coasting}}(\omega) =$$

$$\left(\sum_{n=0}^{\infty} \delta\left(\frac{\omega}{c} - nk_L\right)\right)\left|J_n\left[-\frac{\omega}{c}R_{56}A\right]\right|^2 \exp\left[-\left(\frac{\omega}{c}R_{56}\sigma_\delta\right)^2\right],$$
$$(13)$$

where $k_L = \frac{2\pi}{\lambda_L}$ is the modulation laser wavenumber, J_n is the n-th order Bessel function of the first kind and

$$\delta(x) = \begin{cases} 1, & x = 0, \\ 0, & \text{else.} \end{cases} \qquad (14)$$

Namely there is only bunching at the laser harmonics. For the more-often confronted case of a finite bunch length, like that in CHG and laser-seeded FEL, according to the convolution theorem, then each delta function line in the longitudinal form factor spectrum is broadened by

$$(\Delta\omega)_{\mathrm{FWHM}} = 2\sqrt{2\ln 2}\frac{c/\sigma_z}{\sqrt{2}} = \frac{4\sqrt{2}\ln 2}{(\Delta t)_{\mathrm{FWHM}}}, \qquad (15)$$

where we have assumed the bunch before microbuching is Gaussian with an RMS length of σ_z, and Δt is the electron
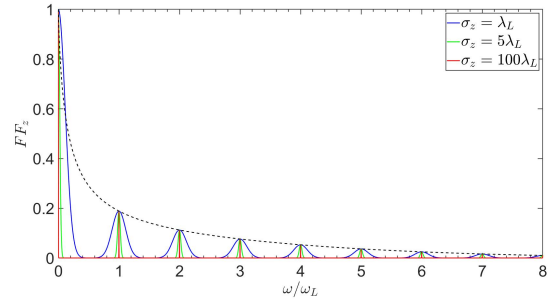
Figure 2: Example plot of the longitudinal form factor of a continuous bunch-based microbunching. The dashed line is
$$FF_z(\omega) = |J_n\left[-\frac{\omega}{c}R_{56}A\right]|^2 \exp\left[-\left(\frac{\omega}{c}R_{56}\sigma_\delta\right)^2\right].$$

bunch length in unit of time. An example plot of the longitudinal form factor of a continuous bunch-based laser-induced microbunching is given in Fig. 2. As can be seen, the longer the bunch, the narrower the bandwidth around each laser harmonic lines.

Radiation Spatial Distribution and Opening Angle

We use undulator radiation as an example. When the fundamental resonant radiation wavelength is a high harmonic of the modulation laser wavelength, $\lambda_0 = \frac{1+\frac{K^2}{2}}{2\gamma^2}\lambda_u = \frac{\lambda_L}{P}$ where K is the dimensionless planar undulator parameter, γ is the Lorentz factor, λ_u is the period of radiator undulator and P is an integer, corresponding to the peaks in the longitudinal form factor whose frequencies are lower than the on-axis radiation frequency, there will be interference rings in the spatial distribution of the coherent radiation from different microbunches. These rings corresponds to the redshifted undulator radiation, whose polar angles are determined by the off-axis resonant condition,

$$\frac{1 + \frac{K^2}{2} + \gamma^2\theta^2}{2\gamma^2}\lambda_u = \frac{\lambda_L}{Q}, \ 1 \le Q < P, \qquad (16)$$

where Q is an integer.

For the opening angle of the coherent radiation due to longitudinal form factor, we focus on the case where the relative bandwidth of form factor around the H-th harmonic of on-axis resonant frequency is much narrower than that of the incoherent radiation, $\left(\frac{\Delta\omega}{H\omega_0}\right)_{\mathrm{FWHM}} \ll \frac{1}{HN_u}$, where N_u is the number of undulator periods. The opening angle of the H-th harmonic coherent undulator radiation due to longitudinal form factor in this case is

$$\theta_{||} = \frac{\sqrt{1 + \frac{K^2}{2}}}{\sqrt{HN_u}\gamma}. \qquad (17)$$

TRANSVERSE FORM FACTOR

As can be seen from Eq. (6), when the transverse electron beam size is large, for off-axis radiation, the effective bunch
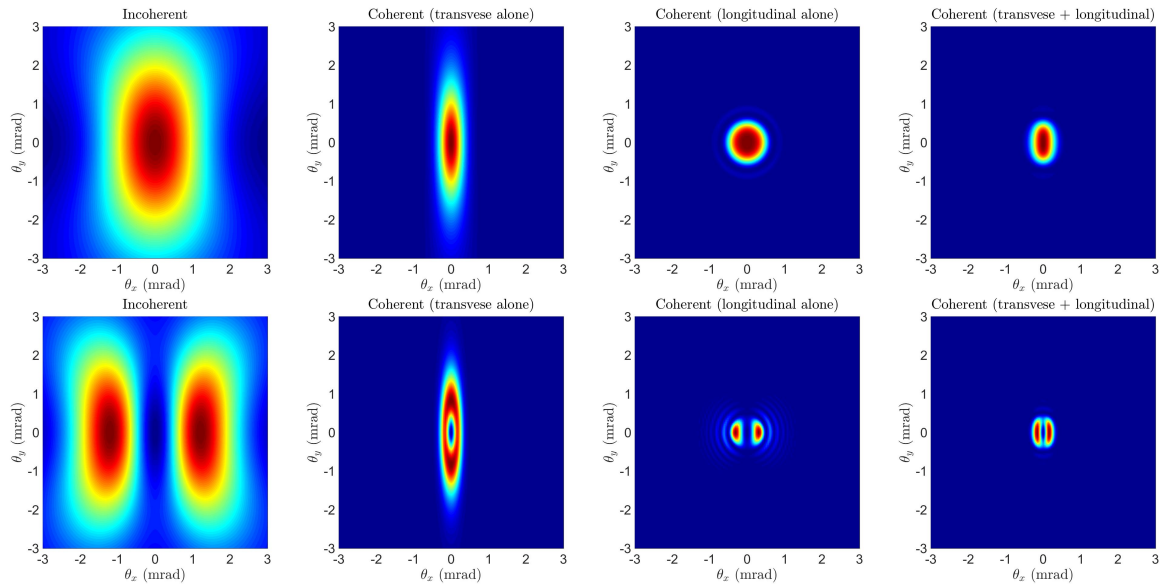
Figure 3: Spatial distribution of the fundamental mode (up) and second harmonic (bottom) coherent undulator radiation energy in SSMB PoP experiment. From left to right: 1) incoherent radiation, 2) coherent radiation but considering only the impact of transverse dimension of electron beam, 3) coherent radiation but considering only the impact of longitudinal dimension of electron beam, 4) coherent radiation considering both the transverse and longitudinal dimensions of electron beam. Parameters used: $E_0 = 250$ MeV, $\lambda_L = \lambda_0 = 1064$ nm, $\lambda_u = 0.125$ m, $N_u = 32$, $\sigma_x = 500\,\mu$m, $\sigma_y = 100\,\mu$m $\sigma_z = 30\,\mu$m (0.1 ps).

lengthening will be significant, thus decreasing the effective bunching factor. Therefore, a large transverse electron beam size will suppress the off-axis redshofted coherent radiation. Therefore, this will also makes the coherent radiation more narrowbanded and collimated in the forward direction, compared to the incoherent radiation.

Since the transverse form factor depends on the specific radiation process involved, there is not an universal formula applies in all cases. For a transversely round Gaussian beam and undulator radiation, we have the approximate transverse form factor for the H-th harmonic undulator radiation [3,4]

$$FF_\perp(H, \omega) = e^{-4N_u \pi S\left(H - \frac{\omega}{\omega_0}\right)} FF_\perp(S), \qquad (18)$$

with $FF_\perp(S) = \frac{2}{\pi}\left[\tan^{-1}\left(\frac{1}{2S}\right) + S\ln\left(\frac{(2S)^2}{(2S)^2 + 1}\right)\right]$, where $S = \frac{\sigma_\perp^2 \frac{\omega}{c}}{L_u}$. The relative bandwidth of H-th coherent radiation due to transverse form factor is

$$\left.\frac{\Delta\omega_{e^{-1}}}{H\omega_0}\right|_\perp \approx \frac{1}{2H^2\sigma_\perp^2 k_u k_0}. \qquad (19)$$

Correspondingly, the opening angle of the H-th harmonic coherent radiation due to the transverse form factor is

$$\theta_\perp \approx \frac{\sqrt{2 + K^2}}{2H\gamma\sigma_\perp\sqrt{k_u k_0}}. \qquad (20)$$

Summarizing, here we use the SSMB proof-of-principle (PoP) experiment [2,3,5] as an example for calculation to show the impact of transverse and longitudinal form factor

on the coherent undulator radiation pattern. As can be seen from Fig. 3, both the longitudinal and transverse distribution of electron beam are of relevance in determing the radiation pattern in SSMB PoP.

IMPACT OF ELECTRON BEAM DIVERGENCE AND ENERGY SPREAD

The approximation of ignoring beam divergence and energy spread of the electron beam applies when the relative change of beam size and bunch length in the radiator is small, i.e., $\beta_{x,y} > L_R$ and $\beta_z > R_{56,R}$. For undulator radiation, that is $\beta_{x,y} > L_u$, $2N_u\lambda_0\sigma_\delta < \sigma_z$, in which σ_z is the length of microbunch.

Now we take into account the impact of beam divergence and energy spread on the coherent radiation in a less rigorous way. As an example, here we assume that the beam is a 6D Gaussian one, and round in the transverse dimension. Further we assume the beam reaches its minimal in all three dimensions at the radiator undulator center, which is desired to get high-power radiation, then the effective transverse and longitudinal form factors are

$$FF_\perp(\omega) = \frac{1}{L_u}\int_{-\frac{L_u}{2}}^{\frac{L_u}{2}} FF_\perp\left(\frac{(\sigma_\perp^2 + (\sigma_{\theta_\perp}s)^2)\frac{\omega}{c}}{L_u}\right) ds,$$

$$FF_z(\omega) = \frac{1}{L_u}\int_{-\frac{L_u}{2}}^{\frac{L_u}{2}} e^{-\left(\frac{\omega}{c}\right)^2\left[\sigma_z^2 + \left(\sigma_\delta \frac{s}{L_u 2N_u\lambda_0}\right)^2\right]} ds \qquad (21)$$

$$= e^{-\left(\frac{\omega}{c}\right)^2\sigma_z^2}\frac{\sqrt{\pi}}{2}\frac{\mathrm{erf}\left(\frac{\omega}{c}\sigma_\delta N_u\lambda_0\right)}{\frac{\omega}{c}\sigma_\delta N_u\lambda_0},$$

where $\sigma_\perp$, $\sigma_{\theta_\perp}$, σ_z and σ_δ are the transverse beam size, divergence, bunch length and energy spread at the undulator center, with $\sigma_\perp \sigma_{\theta_\perp} = \epsilon_\perp$ and $\sigma_z \sigma_\delta = \epsilon_z$, and $\mathrm{erf}(x) = \frac{2}{\sqrt{\pi}} \int_0^x e^{-t^2} dt$ is the error function. The key point of considering the impact of beam divergence and energy spread is that there is an optimal choice of beam size and bunch length at the radiator center, given the transverse and longitudinal emittance of an electron beam.

ACKNOWLEDGMENTS

REFERENCES

[1] D. F. Ratner and A. W. Chao, "Steady-state microbunching in a storage ring for generating coherent radiation", *Phys. Rev. Lett.*, vol. 105, no. 15, 2010. doi:10.1103/PhysRevLett.105.154801

[2] X. Deng *et al.*, "Experimental demonstration of the mechanism of steady-state microbunching", *Nature*, vol. 590, no. 7847, pp. 576–579, Feb. 2021. doi:10.1038/s41586-021-03203-0

[3] X. Deng, "Theoretical and experimental studies on steady-state microbunching", PhD thesis, Tsinghua University, Beijing, China, to be published in Springer Singapore, 2023, https://link.springer.com/book/9789819957996

[4] X. J. Deng *et al.*, "Average and statistical properties of coherent radiation from steady-state microbunching", *J. Synchrotron Radiat.*, vol 30, part 1, pp. 35–50, Dec. 2023. doi:10.1107/S1600577522009973

[5] A. Kruschinski *et al.*, "Exploring the necessary conditions for steady-state microbunching at the Metrology Light Source", presented at the IPAC'23, Venice, Italy, May 2023, paper MOPA176, to appear in the proceedings.

OPTICAL STOCHASTIC COOLING IN A GENERAL COUPLED LATTICE

Xiujie Deng*, Tsinghua University, Beijing, China

Abstract

Here we present a formalism of optical stochastic cooling in a 3D general coupled lattice. The formalism is general, and can treat a variety of damping and diffusion mechanisms within a single framework. We expect the work to be of value for the development of future light source.

GENERAL FORMALISM OF STORAGE RING PHYSICS

Particle state vector $\mathbf{X} = (x, x', y, y', z, \delta)^T$ is used throughout this paper, with its components meaning the horizontal position, horizontal angle, vertical position, vertical angle, longitudinal position, and relative energy difference of a particle with respect to the reference particle, respectively. The superscript ^{T} means the transpose of a vector or matrix. Following Chao's solution by linear matrix (SLIM) formalism [1], we can introduce the definition of the generalized beta functions in a 3D general coupled storage ring lattice as

$$\beta_{ij}^k = 2\mathrm{Re}\left(\mathbf{E}_{ki}\mathbf{E}_{kj}^*\right), \ k = I, II, III, \tag{1}$$

where * means complex conjugate, the sub or superscript k denotes one of the three eigenmodes, Re() means the real component of a complex number or matrix, $\mathbf{E}_{ki}$ is the i-th component of vector $\mathbf{E}_k$, and $\mathbf{E}_k$ are eigenvectors of the 6×6 symplectic one-turn map $\mathbf{M}$ with eigenvalues $e^{i2\pi\nu_k}$, satisfying the following normalization condition

$$\mathbf{E}_k^\dagger \mathbf{S} \mathbf{E}_k = \begin{cases} i, \ k = I, II, III, \\ -i, \ k = -I, -II, -III, \end{cases} \tag{2}$$

and $\mathbf{E}_k^\dagger \mathbf{S} \mathbf{E}_j = 0$ for $k \neq j$, where † means complex conjugate transpose, and

$$\mathbf{S} = \begin{pmatrix} 0 & 1 & 0 & 0 & 0 & 0 \\ -1 & 0 & 0 & 0 & 0 & 0 \\ 0 & 0 & 0 & 1 & 0 & 0 \\ 0 & 0 & -1 & 0 & 0 & 0 \\ 0 & 0 & 0 & 0 & 0 & 1 \\ 0 & 0 & 0 & 0 & -1 & 0 \end{pmatrix}. \tag{3}$$

Since the one-turn map is a real symplectic matrix, for a stable motion, we have

$$\nu_{-k} = -\nu_k, \ \mathbf{E}_{-k} = \mathbf{E}_k^*. \tag{4}$$

Using the generalized beta function, we can write the eigenvector component as

$$\mathbf{E}_{kj} = \sqrt{\frac{\beta_{jj}^k}{2}} e^{i\phi_j^k}. \tag{5}$$

* dengxiujie@mail.tsinghua.edu.cn

And according to definition we have

$$\beta_{ij}^k = \sqrt{\beta_{ii}^k \beta_{jj}^k} \cos(\phi_i^k - \phi_j^k). \tag{6}$$

Similarly, here we introduce the definition of imaginary generalized beta functions as

$$\hat{\beta}_{ij}^k = 2\mathrm{Im}\left(\mathbf{E}_{ki}\mathbf{E}_{kj}^*\right), \ k = I, II, III, \tag{7}$$

where Im() means the imaginary component of a complex number or matrix. Further we can define the real and imaginary generalized Twiss matrices of a storage ring lattice corresponding to three eigen mode as

$$(\mathbf{T}_k)_{ij} = \beta_{ij}^k, \ \left(\hat{\mathbf{T}}_k\right)_{ij} = \hat{\beta}_{ij}^k, \ k = I, II, III. \tag{8}$$

Due to the symplecticity of the one-turn map, we have

$$\mathbf{T}_k^T = \mathbf{T}_k, \ \hat{\mathbf{T}}_k^T = -\hat{\mathbf{T}}_k, \tag{9}$$

where ^{T} means transpose. The generalized Twiss matrices at different places are related according to

$$\begin{aligned} \mathbf{T}_k(s_2) &= \mathbf{R}(s_2, s_1)\mathbf{T}_k(s_1)\mathbf{R}^T(s_2, s_1), \\ \hat{\mathbf{T}}_k(s_2) &= \mathbf{R}(s_2, s_1)\hat{\mathbf{T}}_k(s_1)\mathbf{R}^T(s_2, s_1), \end{aligned} \tag{10}$$

with $\mathbf{R}(s_2, s_1)$ being the transfer matrix from s_1 to s_2.

The action or generalized Courant-Snyder invariants of a particle are defined according to

$$J_k \equiv \frac{\mathbf{X}^T \mathbf{G}_k \mathbf{X}}{2}, \ k = I, II, III, \tag{11}$$

where

$$\mathbf{G}_k \equiv \mathbf{S}^T \mathbf{T}_k \mathbf{S}. \tag{12}$$

It is easy to prove that J_k are invariants of a particle when it travels around the ring, from the symplectic condition $\mathbf{R}^T \mathbf{S} \mathbf{R} = \mathbf{S}$. The three eigenemittance of a beam containing N_p particles are defined according to

$$\epsilon_k \equiv \langle J_k \rangle = \frac{\sum_{i=1}^{N_P} J_{k,i}}{N_p}, \ k = I, II, III, \tag{13}$$

where $J_{k,i}$ means the k-th mode invariant of the i-th particle.

Assume there is a perturbation $\mathbf{K}$ to the one-turn map $\mathbf{M}$, i.e., $\mathbf{M}_{\mathrm{per}} = (\mathbf{I} + \mathbf{K})\mathbf{M}_{\mathrm{unp}}$. From cannonical perturbation theory [2], the tune shift of the k-th eigen mode is then

$$\Delta\nu_k = -\frac{1}{4\pi}\mathrm{Tr}\left[\left(\mathbf{T}_k + i\hat{\mathbf{T}}_k\right)\mathbf{S}\mathbf{K}\right], \tag{14}$$

where Tr() means the trace of a matrix. This formula can be used to calculate the real and imaginary tune shifts due to symplectic (for example lattice error) and non-symplectic

(for example radiation damping) pertubations. The pertu-bation theory can also be applied to calcuate the emittance growth due to diffusion [2]. With the help of real and imag-inary generalized beta functions and Twiss matrices, the diffusion of emittance per turn can be calculated as

$$\Delta\epsilon_k = -\frac{1}{2}\oint \mathrm{Tr}\left(\mathbf{T}_k\mathbf{SNS}\right)ds = \frac{1}{2}\oint \mathrm{Tr}\left(\mathbf{G}_k\mathbf{N}\right)ds, \quad (15)$$

and the damping rate of each eigen mode is

$$\alpha_k = -\frac{1}{2}\oint \mathrm{Tr}\left(\hat{\mathbf{T}}_k\mathbf{SD}\right)ds, \quad (16)$$

where $\mathbf{N}$ and $\mathbf{D}$ are the diffusion and damping matrix, re-spectively. Note that the damping rates here are that for the corresponding eigenvectors. The damping rates for particle action or beam emittance is a factor of two larger. The equi-librium eigenemittance between a balance of diffusion and damping can be calculated as

$$\epsilon_k = \frac{\Delta\epsilon_k}{2\alpha_k} = \frac{-\frac{1}{2}\sum_{i,j}\oint \beta_{ij}^k\,(\mathbf{SNS})_{ij}\,ds}{\sum_{i,j}\oint \hat{\beta}_{ij}^k\,(\mathbf{SD})_{ij}\,ds}, \quad (17)$$

After getting the equilibrium eigenemittances, the second moments of beam can be written as

$$\Sigma_{ij} = \sum_{k=I,II,III}\epsilon_k\beta_{ij}^k, \quad (18)$$

or in matrix form as

$$\mathbf{\Sigma} = \sum_{k=I,II,III}\epsilon_k\mathbf{T}_k. \quad (19)$$

QUANTUM EXCITATION AND RADIATION DAMPING

In an electron storage ring, the intrinsic diffusion and damping are both from the emission of photons, i.e., quan-tum excitation and radiation damping. For quantum excita-tion, we have all the other components of diffusion matrix $\mathbf{N}$ zero except that

$$N_{66} = \frac{2C_L\gamma^5}{c|\rho|^3} \quad (20)$$

where c is the speed of light in free space, ρ is the benging radius of particle trajectory, γ here is the relativistic factor, $C_L = \frac{55}{48\sqrt{3}}\frac{r_e\hbar}{m_e}$ with r_e the classical electron radius, $\hbar$ the reduced Planck's constant, m_e the electron mass.

For radiation damping, we have two sources of damping, i.e., dipole magnets and RF cavity. For a horizontal dipole, we have all the matrix terms of $\mathbf{D}$ zero except that

$$D_{66} = -\frac{1}{\pi}C_\gamma\frac{E_0^3}{\rho^2},\ D_{61} = -\frac{C_\gamma E_0^3}{2\pi}\frac{1-2n}{\rho^3}, \quad (21)$$

where $C_\gamma = \frac{4\pi}{3}\frac{r_e}{(m_ec^2)^3} = 8.85\times10^{-5}\frac{\mathrm{m}}{\mathrm{GeV}^2}$, $n = -\frac{\rho}{B_y}\frac{\partial B_y}{\partial x}$ is the transverse field gradient index. For an RF cavity, we have all the matrix terms of $\mathbf{D}$ zero except that

$$D_{22} = D_{44} = -\frac{U_0}{E_0}\delta(s_{\mathrm{RF}}), \quad (22)$$

where U_0 is the radiation energy loss of a particle per turn, E_0 is the particle energy, and $\delta(s)$ means Dirac's delta function. Here we have assumed that the RF cavity is a zero-length one. Using the developed formalism, it is easy to show that for radiation damping, we have

$$\alpha_I + \alpha_{II} + \alpha_{III} = -\frac{1}{2}\oint \mathrm{Tr}(\mathbf{D})ds = \frac{2U_0}{E_0}, \quad (23)$$

which is the well-known Robinson's sum rule [3].

In a planar uncoupled electron storage ring, this general formalism reduces to the classical results of Sands, i.e., the radiation integrals formalism found in textbooks [4]. More specifically in this case we have the equilibrium emittance

$$\epsilon_x = \frac{C_L\gamma^5}{2c\alpha_I}\oint \frac{\beta_{55}^I}{|\rho(s)|^3}ds = \frac{C_L\gamma^5}{2c\alpha_I}\oint \frac{\mathcal{H}_x(s)}{|\rho(s)|^3}ds,$$
$$\epsilon_y = \frac{C_L\gamma^5}{2c\alpha_{II}}\oint \frac{\beta_{55}^{II}}{|\rho(s)|^3}ds = \frac{C_L\gamma^5}{2c\alpha_{II}}\oint \frac{\mathcal{H}_y(s)}{|\rho(s)|^3}ds, \quad (24)$$
$$\epsilon_z = \frac{C_L\gamma^5}{2c\alpha_{III}}\oint \frac{\beta_{55}^{III}}{|\rho(s)|^3}ds = \frac{C_L\gamma^5}{2c\alpha_{III}}\oint \frac{\beta_z(s)}{|\rho(s)|^3}ds,$$

with the $\mathcal{H}$-function defined as $\mathcal{H} = \gamma D^2 + 2\alpha DD' + \beta D'^2$, where α,β,γ are the classical Courant-Snyder functions [5], and the damping constants, according to Eq. (16), being

$$\alpha_I = \frac{U_0}{2E_0}\left(1 - \frac{\oint D_x\left(\frac{1-2n}{\rho^3}\right)ds}{\oint \frac{1}{\rho^2}ds}\right),$$
$$\alpha_{II} = \frac{U_0}{2E_0}, \quad (25)$$
$$\alpha_{III} = \frac{U_0}{2E_0}\left(2 + \frac{\oint D_x\left(\frac{1-2n}{\rho^3}\right)ds}{\oint \frac{1}{\rho^2}ds}\right).$$

OPTICAL STOCHATIC COOLING

Damping Rate in Linear Approximation

Now we apply the formalism to optical stochastic cool-ing (OSC) [6–9]. Denote the symplectic transfer matrix of particle state evector from the pick-up undulator to the kiker undulator as $\mathbf{R}$. Assume that the change of a particle's en-ergy induced in the kicker undulator due to its own radiation at the pick-up undulator is

$$\Delta\delta = -A\sin(k_R\Delta z) \quad (26)$$

with

$$\Delta z(s_2, s_1) = R_{51}x_1 + R_{52}x_1' + R_{53}y_1 + R_{54}y_1' \\ + R_{55}z_1 + R_{56}\delta_1 - z_1, \quad (27)$$

where we have used the subscripts 1 and 2 to represent the location of pick-up undulator and kicker undulator, respec-tively. Usually we have $R_{55} = 1$.

Linearizing the energy kick around the zero-crossing phase, we have the effective change of state vector at the pick-up undulator as

$$\Delta\mathbf{X}_1 = \mathbf{D}\mathbf{X}_1, \quad (28)$$

with the perturbation matrix at the pick-up undulator

$$\mathbf{D} = -Ak_R$$

$$
\begin{pmatrix}
-R_{51}R_{52} & -R_{52}^2 & -R_{52}R_{53} & -R_{52}R_{54} & -(R_{55}-1)R_{52} & -R_{52}R_{56} \\
R_{51}^2 & R_{51}R_{52} & R_{51}R_{53} & R_{51}R_{54} & (R_{55}-1)R_{51} & R_{51}R_{56} \\
-R_{51}R_{54} & -R_{52}R_{54} & -R_{53}R_{54} & -R_{54}^2 & -(R_{55}-1)R_{54} & -R_{54}R_{56} \\
R_{51}R_{53} & R_{52}R_{53} & R_{53}^2 & R_{53}R_{54} & (R_{55}-1)R_{53} & R_{53}R_{56} \\
-R_{51}R_{56} & -R_{52}R_{56} & -R_{53}R_{56} & -R_{54}R_{56} & -(R_{55}-1)R_{56} & -R_{56}^2 \\
R_{51}R_{55} & R_{52}R_{55} & R_{53}R_{55} & R_{54}R_{55} & (R_{55}-1)R_{55} & R_{55}R_{56}
\end{pmatrix}.
$$

$$(29)$$

Then, we have the sum rule for the OSC damping rates of three eigen modes

$$\alpha_{I,0} + \alpha_{II,0} + \alpha_{III,0} = -\frac{1}{2}\mathrm{Tr}\,(\mathbf{D}) = \frac{Ak_R R_{56}}{2}. \quad (30)$$

The subscript 0 is used to denote that the damping rates are calculated by linearizing the energy kick around the zero-crossing phase. The OSC damping rate of each eigen mode can be calculated according to Eq. (16). More specifically,

$$
\begin{aligned}
\alpha_{I,0} &= -\frac{Ak_R}{2}\left(R_{51}\hat{\beta}_{51}^I + R_{52}\hat{\beta}_{52}^I \right. \\
&\qquad \left. + R_{53}\hat{\beta}_{53}^I + R_{54}\hat{\beta}_{54}^I + R_{56}\hat{\beta}_{56}^I\right), \\
\alpha_{II,0} &= -\frac{Ak_R}{2}\left(R_{51}\hat{\beta}_{51}^{II} + R_{52}\hat{\beta}_{52}^{II} \right. \\
&\qquad \left. + R_{53}\hat{\beta}_{53}^{II} + R_{54}\hat{\beta}_{54}^{II} + R_{56}\hat{\beta}_{56}^{II}\right), \\
\alpha_{III,0} &= -\frac{Ak_R}{2}\left(R_{51}\hat{\beta}_{51}^{III} + R_{52}\hat{\beta}_{52}^{III} \right. \\
&\qquad \left. + R_{53}\hat{\beta}_{53}^{III} + R_{54}\hat{\beta}_{54}^{III} + R_{56}\hat{\beta}_{56}^{III}\right).
\end{aligned}
\quad (31)
$$

Amplitude-dependent Damping Rate

In the above analysis, we have linearized the sinusoidal energy kick around the zero-crossing phase. Without such approximation, the damping rates will be different for particles with different betatron or synchrotron amplitudes. The betatron and synchrotron oscillation-averaged damping rates in a 3D general coupled lattice are then

$$
\begin{aligned}
\alpha_I &= 2\alpha_{I,0}\frac{J_1(k_R a_I)J_0(k_R a_{II})J_0(k_R a_{III})}{k_R a_I}, \\
\alpha_{II} &= 2\alpha_{II,0}\frac{J_0(k_R a_I)J_1(k_R a_{II})J_0(k_R a_{III})}{k_R a_{II}}, \\
\alpha_{III} &= 2\alpha_{III,0}\frac{J_0(k_R a_I)J_0(k_R a_{II})J_1(k_R a_{III})}{k_R a_{III}},
\end{aligned}
\quad (32)
$$

with J_n the n-th order Bessel function of the first kind, and

$$
\begin{aligned}
a_I &= \sqrt{2J_I\left[\beta_{11}^I R_{51}^2 + 2\beta_{12}^I R_{51}R_{52} + \beta_{22}^I R_{52}^2\right]}, \\
a_{II} &= \sqrt{2J_{II}\left[\beta_{33}^{II} R_{53}^2 + 2\beta_{34}^{II} R_{53}R_{54} + \beta_{44}^{II} R_{54}^2\right]}, \\
a_{III} &= \sqrt{2J_{III}\left[\beta_{55}^{III} R_{55}^2 + 2\beta_{56}^{III} R_{55}R_{56} + \beta_{66}^{III} R_{56}^2\right]},
\end{aligned}
\quad (33)
$$

where $J_{I,II,III}$ mean the generalized Courant-Snyder invariants of the particle.

The first roots of $J_0(x)$ and $J_1(x)$ are $\mu_{01} \approx 2.405$ and $\mu_{11} \approx 3.83$. The range of betatron and synchrotron oscillation amplitude which gives a positive damping rate is called

cooling range. If we want a cooling range a factor of N larger than RMS oscillation amplitude of the particle beam in all three modos, then we need $Nk_R\bar{a}_k < \mu_{01}$, $k = I, II, III$, where $\bar{a}_k$ is a_k with $2J_k$ in the expression replaced by ϵ_k. For example, $\bar{a}_I = \sqrt{\epsilon_I\left[\beta_{11}^I R_{51}^2 + 2\beta_{12}^I R_{51}R_{52} + \beta_{22}^I R_{52}^2\right]}$. The physical meaning of $\bar{a}_k$ is the RMS lengthening of a longitudinal slice from pick-up to kicker undulator from the k-mode eigen emittance. If we only need cooling in one mode, then the cooling range can be larger, i.e., $Nk_R\bar{a}_k < \mu_{11}$.

Planar Uncoupled Ring

The above results apply for a 3D general coupled lattice. For a ring without x-y coupling and when RF cavity is placed at dispersion-free location, we can express the normalized eigenvectors using classical Courant-Snyder functions and dispersion D and dispersion angle D' [10]. Then we have

$$
\begin{aligned}
\alpha_{I,0} &= -\frac{Ak_R\left(R_{51}D_{x1} + R_{52}D'_{x1}\right)}{2}, \\
\alpha_{III,0} &= \frac{Ak_R R_{56}}{2} - \alpha_{I,0},
\end{aligned}
\quad (34)
$$

or in a more elegant form as

$$
\begin{aligned}
\alpha_{I,0} &= \frac{Ak_R}{2}\sqrt{\mathcal{H}_{x1}\mathcal{H}_{x2}}\sin\left(\Delta\psi_{x21} - \Delta\chi_{x21}\right), \\
\alpha_{III,0} &= \frac{Ak_R}{2}F,
\end{aligned}
\quad (35)
$$

where $\Delta\psi_{x21} = \psi_{x2} - \psi_{x1} = \int_{s_1}^{s_2}\frac{1}{\beta_x}ds$ is the the horizontal betatron phase advance, and $\Delta\chi_{x21} = \chi_{x2} - \chi_{x1}$ is the horizontal chromatic phase advance, from the pick-up to kicker undulator, and

$$F(s_2, s_1) = -\int_{s_1}^{s_2}\left(\frac{D_x(s)}{\rho(s)} - \frac{1}{\gamma^2}\right)ds. \quad (36)$$

To obtain the final concise result, D and D' have been expressed in terms of the chromatic $\mathcal{H}$-function and the chromatic phase χ, according to

$$D = \sqrt{\mathcal{H}\beta}\cos\chi, \quad D' = -\sqrt{\mathcal{H}/\beta}\left(\alpha\cos\chi + \sin\chi\right). \quad (37)$$

Some observations are in order based on Eq. (35). First, to induce damping on the eigen mode III, which usually corresponds to the longitudinal dimension, we need a nonzero F. Second, to induce damping on mode I, which usually corresponds to the horizontal dimension, both the pick-up and kicker undulators need to be placed at dispersive locations. Further, we need to make sure the chromatic phase advance between the two undulators is different from the corresponding betatron phase advance, and the sign of damping rate depends on the difference of chromatic and betatron phase advance. For example, if it is an achromat between pick-up and kicker undulators, which means $R_{51} = 0$ and $R_{52} = 0$, then there will be no damping on the eigen mode I.

The amplitude-dependent damping rates in this case are

$$\alpha_I = -\frac{A\left(R_{51}D_{x1} + R_{52}D'_{x1}\right)}{\sqrt{2J_x\left[\beta_{x1}R_{51}^2 - 2\alpha_{x1}R_{51}R_{52} + \gamma_{x1}R_{52}^2\right]}}$$

$$J_1\left(k_R\sqrt{2J_x\left[\beta_{x1}R_{51}^2 - 2\alpha_{x1}R_{51}R_{52} + \gamma_{x1}R_{52}^2\right]}\right)$$

$$J_0\left(k_R F\sqrt{2J_z\gamma_{z1}}\right),$$

$$\tag{38}$$

$$\alpha_{III} = \frac{A}{\sqrt{2J_z\gamma_{z1}}}$$

$$J_0\left(k_R\sqrt{2J_x\left[\beta_{x1}R_{51}^2 - 2\alpha_{x1}R_{51}R_{52} + \gamma_{x1}R_{52}^2\right]}\right)$$

$$J_1\left(k_R F\sqrt{2J_z\gamma_{z1}}\right),$$

where the horizontal and longitudinal action of a particle in a plannar uncoupled storage ring are defined as

$$J_x \equiv \frac{(x - D_x\delta)^2 + \left[\alpha_x(x - D_x\delta) + \beta_x(x' - D'_x\delta)\right]^2}{2\beta_x},$$

$$J_z \equiv \frac{\left(z - D'_x x - D_x x'\right)^2 + \left[\alpha_z(z - D'_x x - D_x x') + \beta_z\delta\right]^2}{2\beta_z}.$$

$$\tag{39}$$

In the above equation, we can also write

$$R_{51}D_{x1} + R_{52}D'_{x1} = -\sqrt{\mathcal{H}_{x1}\mathcal{H}_{x2}}\sin(\Delta\psi_{x21} - \Delta\chi_{x21}),$$

$$\beta_{x1}R_{51}^2 - 2\alpha_{x1}R_{51}R_{52} + \gamma_{x1}R_{52}^2$$

$$= \mathcal{H}_{x1} + \mathcal{H}_{x2} - 2\sqrt{\mathcal{H}_{x1}\mathcal{H}_{x2}}\cos\left(\Delta\psi_{x21} - \Delta\chi_{x21}\right).$$

$$\tag{40}$$

ACKNOWLEDGMENTS

REFERENCES

[1] A. W. Chao, "Evaluation of beam distribution parameters in an electron storage ring", *J. Appl. Phys.* vol. 50, no. 2, pp. 595-598, July 1979. doi:10.1063/1.326070

[2] X. Deng, "Storage ring physics from a modern perspective", in preparation.

[3] K. W. Robinson, "Radiation effects in circular electron accelerators", *Phys. Rev.*, vol. 111, no. 2, pp. 373–380, July 1958. doi:10.1103/PhysRev.111.373

[4] M. Sands, "The physics of electron storage rings: an introduction", Tech. Rep., Stanford Linear Accelerator Center, CA, USA, 1970. https://www.slac.stanford.edu/pubs/slacreports/reports02/slac-r-121.pdf

[5] E. D. Courant and H. S. Snyder, "Theory of the alternating-gradient synchrotron", *Ann. Phys. (N.Y.)*, vol. 3, no. 1, pp. 1–48, Jan. 1958. doi:10.1016/0003-4916(58)90012-5

[6] A. A. Mikhailichenko and M. S. Zolotorev, "Optical stochastic cooling", *Phys. Rev. Lett.*, vol. 71, no. 25, pp. 4146–4149, Dec. 1993. doi:10.1103/PhysRevLett.71.4146

[7] M. S. Zolotorev and A. A. Zholents, "Transit-time method of optical stochastic cooling", *Phys. Rev. E*, vol. 50, no. 4, pp. 3087-3091, Oct. 1994. doi:10.1103/PhysRevE.50.3087

[8] V. Lebedev *et al.*, "The design of optical stochastic cooling for IOTA", *J. Instrum.*, vol. 16, no. 05, pp. T05002, May 2021. doi:10.1088/1748-0221/16/05/T05002

[9] J. Jarvis *et al.*, "Experimental demonstration of optical stochastic cooling", *Nature*, vol. 608, no. 7922, pp. 287–292, Aug. 2022. doi:10.1038/s41586-022-04969-7

[10] X. Deng, "Theoretical and experimental studies on steady-state microbunching", PhD thesis, Tsinghua University, Beijing, China, to be published in Springer Singapore, 2023, https://link.springer.com/book/9789819957996

A RECURSIVE MODEL FOR LASER-ELECTRON-RADIATION INTERACTION IN INSERTION SECTION OF SSMB STORAGE RINGS BASED ON THE TRANSVERSE-LONGITUDINAL COUPLING SCHEME

Cheng-Ying Tsai*, Huazhong University of Science and Technology, Wuhan, China

Xiujie Deng, Tsinghua University, Beijing, China

Abstract

Recently, a mechanism of steady-state microbunching (SSMB) in the storage ring has been proposed and investigated. The SSMB aims to maintain the same excellent high repetition rate, close to continuous-wave operation, as the storage ring. Moreover, replacing the conventional RF cavity with a laser modulator for longitudinal focusing, the individual electron bunches can be microbunched in a steady state. The microbunched electron bunch train, with an individual bunch length comparable to or shorter than the radiation wavelength, can not only produce coherent powerful synchrotron radiation but may also be subject to FEL-like collective instabilities. Our previous analysis was based on the wake-impedance model. In this paper, we have developed a recursive model for the laser modulator in the SSMB storage ring. In particular, the transverse-longitudinal coupling scheme is assumed. Equipped with the matrix formalism, we can construct a recursive model to account for turn-by-turn evolution, including single-particle and second moments. It is possible to obtain a simplified analytical expression to identify the stability regime or tolerance range for non-perfect cancellation.

INTRODUCTION

Recently there has been a growing interest in the mechanism of the so-called steady-state microbunching (SSMB) in a storage ring proposed as a potential new light source [1–5]. The existing literature for the studies of electron dynamics in the laser modulators mainly focuses on single-particle dynamics, e.g., Refs. [6–9], or the radiation output characteristics based on the prescribed electron trajectories [10, 11]. The collective dynamics occurring in the laser modulators has only recently been studied [12–14] using the wake-impedance model for the case of a *single* laser modulator.

In a current design a pair of two laser modulators, where the radiator is sandwiched, is considered; see Fig. 1. In this work we propose an alternative model to study the laser-electron-radiation interaction in the laser modulators of SSMB storage rings based on the transverse-longitudinal coupling (TLC) scheme [10], by constructing a recursive model to account for multi-pass radiation dynamics in nonlinear regime to analyze multi-bunch multi-turn dynamics [9]. In the model there are two options for us to study the dynamics: non-perfect kick model and FEL-like model.
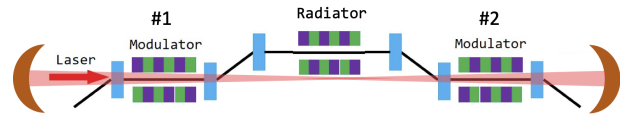
Figure 1: Conceptual schematic layout of SSMB laser modulator based on TLC scheme. The two laser modulators can be independent.

THEORETICAL FORMULATION

In the recursive formulation, the laser-electron-radiation dynamics can in principle be nonlinear. However the energy chirp is linearized; therefore the validity is limited to $\sigma_z \ll \lambda_L$. We assume the microbunch circulates clockwise. Considering the state vector $[y \ y' \ z \ \delta]^T$ at the middle of the storage ring (e.g., at RF or main-ring laser modulator), the transport from which to the insertion entrance can be formulated as a half ring $\mathbf{R}_{1/2}$, which is

$$
\begin{pmatrix}
\cos \pi \nu_y & \beta_y \sin \pi \nu_y & 0 & 0 \\
-\frac{1}{\beta_y} \sin \pi \nu_y & \cos \pi \nu_y & 0 & 0 \\
0 & 0 & \cos \pi \nu_s & \beta_z \sin \pi \nu_s \\
0 & 0 & -\frac{1}{\beta_z} \sin \pi \nu_s & \cos \pi \nu_s
\end{pmatrix},
$$

(1)

where β_y, ν_y and β_z, ν_s parametrize the transverse and longitudinal motions, respectively. The synchrotron tune ν_s is determined by the RF/laser modulator of the storage ring with the slippage factor η_{ring} and the circumference C_{ring}. Here we have implicitly assumed Courant-Snyder functions are the same at the RF, the entrance and exit of the insertion section. The insertion section begins from the vertical bending magnet

$$
\mathbf{M}_B =
\begin{pmatrix}
1 & 0 & 0 & 0 \\
0 & 1 & 0 & R_{46} \\
-R_{46} & 0 & 1 & 0 \\
0 & 0 & 0 & 1
\end{pmatrix},
$$

(2)

and the following first laser modulator

$$
\mathbf{M}_{LM}^{(1)} =
\begin{pmatrix}
1 & N_u \lambda_u & 0 & 0 \\
0 & 1 & 0 & 0 \\
0 & 0 & \cos \chi^{(1)} & \frac{R_{56,LM}}{\chi^{(1)}} \sin \chi^{(1)} \\
0 & 0 & \frac{h^{(1)}}{\chi^{(1)}} \sin \chi^{(1)} & \cos \chi^{(1)}
\end{pmatrix},
$$

(3)

with N_u, λ_u the number and period length of the undulator, $\chi^{(1)} = \sqrt{-R_{56,LM} h^{(1)}}$, $R_{56,LM}, h$ being the longitudinal

dispersion and the imposed chirp strength. The second laser modulator shall be denoted by the superscript (2). Before entering the radiator, a dogleg is used to compress the beam

$$\mathbf{M}_{DL} = \begin{pmatrix} 1 & 0 & 0 & R_{54} \\ 0 & 1 & 0 & 0 \\ 0 & R_{54} & 1 & R_{56} \\ 0 & 0 & 0 & 1 \end{pmatrix}. \tag{4}$$

The above three elements are combined to be the first half of the insertion section $\mathcal{T}_{1/2}^{(1)} = \mathbf{M}_{DL}\mathbf{M}_{LM}^{(1)}\mathbf{M}_B$. TLC scheme requires the matrix elements to satisfy [10]

$$\begin{aligned} R_{56}h + 1 &= 0, \\ R_{56} + R_{54}R_{46} &= 0. \end{aligned} \tag{5}$$

In the non-perfect kick model we will relax the first condition, considering non-perfect cancellation of the two laser modulators. The one-turn map can be constructed $O = \mathbf{R}_{1/2}\mathcal{T}_{1/2}^{(2)}\mathcal{T}_{1/2}^{(1)}\mathbf{R}_{1/2}$ around the main-ring RF, with the $\mathcal{T}_{1/2}^{(2)}$ being the reverse order of the $\mathcal{T}_{1/2}^{(1)}$. Ideally, $\mathcal{T}_{1/2}^{(2)}\mathcal{T}_{1/2}^{(1)} = \mathcal{I}$ being the identity map. When considering the radiation dynamics in the laser modulators, the above $\mathbf{M}_{LM}^{(1,2)}$ may vary turn after turn and the one-turn map perturbed, i.e., $O \rightarrow O_n$. The microbunch centroid evolves based on $X_{n+1} = OX_n$. The beam second moments evolve according to $\Sigma_{n+1} = O\Sigma_n O^T$. The bunching factor of the microbunch train is estimated as $|b_n| = e^{-\frac{1}{2}\left(\frac{2\pi}{\lambda_L}\right)^2 \sigma_{z,n}^2}$ where $\sigma_{z,n}$ can be obtained from beam sigma matrix Σ_n. Here we assume identical microbunches in the bunch train.

Non-perfect Kick Model

This is not a dynamical model but can be used to investigate to what extent the non-perfect cancellation of two laser modulators may lead to unstable operation. Here the imperfect kick is added according to $h^{(2)} \rightarrow h^{(1)}(1 + \varepsilon)$ with ε the deviation from the idealized, symmetric situation $h^{(2)} = h^{(1)}$. The first laser modulator is assumed perfect.

FEL-like Model

The turn-by-turn dependence of $\mathbf{M}_{LM}^{(1,2)}$ originates from the variation of chirp strength $h_n^{(1,2)}$. More specifically [15],

$$h_n^{(1,2)} = \frac{e[JJ]K}{\gamma^2 mc^2}\sqrt{\frac{4P_{L,n}^{(1,2)}Z_0 Z_R}{\lambda_L}}\tan^{-1}\left(\frac{L_u}{2Z_R}\right)k_L. \tag{6}$$

The turn-by-turn evolution of the laser power in the two laser modulators $P_{L,n}^{(1,2)}$, perturbed by the radiating microbunches, can be formulated using a simplified FEL model. Skipping the details, the nth-turn laser power can be evaluated as

$$P_{L,n}^{(1,2)} = P_{L,n}^{\text{ext}} + \frac{g_0}{4N_u}\left|b_n^{(1,2)}\right|^2 P_{\text{beam}}, \tag{7}$$

where $P_{L,n}^{\text{ext}}$ is the external laser, g_0 is the small-signal gain. The laser power evolves from n-th turn to $(n + 1)$-th turn as

$$P_{L,n+1} = R\left(1 + G_n\right)P_{L,n}, \tag{8}$$

with R the total mirror reflection loss and the gain per pass $G_n = G_{M,n}\frac{1 - e^{-\beta X_n}}{\beta X_n}$ with $\beta = \frac{\pi}{2}(1.0145)$, $X_n = \frac{P_{L,n}}{P_{\text{sat}}}$, $P_{\text{sat}}\left(\frac{\text{MW}}{\text{cm}^2}\right) = 6.93 \times 10^2 \left(\frac{\gamma}{N_u}\right)^4 \frac{1}{(\lambda_u(\text{cm})K[JJ])^2}$ and $G_{M,n}$ can be parameterized by [16]

$$G_{M,n} = \frac{e^{-0.132P(g_0)\mu_{\epsilon,n}^2}}{1 + 1.6Q(g_0)\,\mu_{\epsilon,n}^2}\sum_{s=1}^{3}g_0^s g_s(\kappa), \tag{9}$$

with the normalized energy spread and detuning parameter $\mu_\epsilon = 4N_u\sigma_{\delta,n}$, $\kappa = 2\pi N_u\frac{\omega_L - \omega}{\omega_L}$.

SIMULATION RESULTS

In the following simulations we assume $\beta_y \approx 10$ m at the entrance of first modulator undulator with $\nu_y \sim C_{\text{ring}}/2\pi\beta_y$. We further assume that the bunch length and energy spread are 500 nm and 3×10^{-4} around the storage ring (outside the insertion section). The R_{46} is estimated as $R_{46} \approx \sqrt{\frac{\mathcal{H}_y(\text{Mod})}{\beta_y}}$ with $\mathcal{H}_y(\text{Mod}) \approx \frac{\sigma_z^2(\text{Mod})}{\epsilon_y^G}$ [10]. Then according to Eq. (5), the remaining matrix elements can be determined in order

$$R_{56} = -\frac{1}{h}, \quad R_{54} = -\frac{R_{56}}{R_{46}}, \tag{10}$$

for the doglegs associated with two laser modulators. Other relevant beam parameters are: beam energy 360 MeV, average bunch current 1 A, vertical emittance $\epsilon_y^G = 10$ pm. The storage ring parameters: $C_{\text{ring}} = 50$ m and $\eta_{\text{ring}} = 10^{-6}$. The nominal laser modulator parameters: $\lambda_L = 1$ μm, $K_u = 3.35$, $\lambda_u = 15$ cm, $N_u = 13$, and the total mirror reflectivity $R \approx 0.99963$. The bunch length at the radiator is for the moment assumed to be 20 nm [17]. The radiation wavelength at the radiator is targeted as 200 nm.

Results Based on Non-perfect Kick Model

Figures 2 summarizes the simulation results. By scanning a range of ε, we find that the beam is stable in the range of $-0.012 \leq \varepsilon \leq 0.045$. Outside the region the beam becomes unstable; the microbunch length becomes larger than the laser modulation wavelength and the radiation power at radiator exhibits large oscillation. For the perfect-cancellation case of $\varepsilon = 0$, the bunch length remains a constant, approximately 21.3 nm. For the case with $\varepsilon \neq 0$, the bunch length disperses and becomes larger when $|\varepsilon|$ increases. This model assumes $R = 1$, i.e., no reflectivity loss.

Results Based on FEL-like Model

For simplicity, assume no initial detuning, i.e., $\kappa = 0$, of the two modulator undulators. On the first few turns we expect the results to be close to that of perfect-kick model $\varepsilon = 0$. The FEL-like model accounts for the mirror reflectivity loss. In the simulation case, for the initial laser modulation power $P_L^{(1,2)} \approx 274$ kW, meaning that we have 101 W due to the reflectivity loss. Let us assume the external injection of modulation laser power is 100 W per pass to compensate
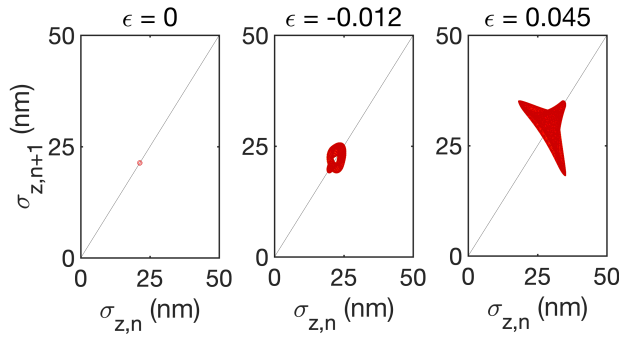
Figure 2: Turn-by-turn evolution of bunch length at the radiator for three cases. $\sigma_z \approx 21.3$ nm for perfect cancellation.
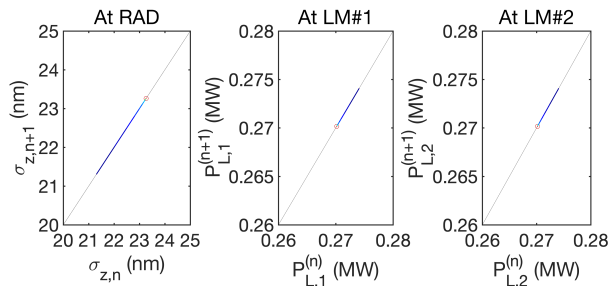

Figure 3: Turn-by-turn evolution of the bunch length and the stored radiation power in the two laser modulators. The evolution begins from blue and gradually evolve to red.

Figure 4: Turn-by-turn evolution of the microbunch length, vertical beam size at the radiator (left) and at the entrance of the first modulator (right) based on the perfect-kick model (red) and FEL-like model (blue).

Figure 5: Output radiation power at the radiator and the corresponding bunching factor based on the perfect-kick model (dashed line) and FEL-like model (solid line).

the loss. Figure 3 shows the turn-by-turn microbunch length at radiator, the laser power stored in the two modulators.

Figure 4 displays turn-by-turn evolution of the microbunch length, vertical beam size at the radiator and at the entrance of the first modulator based on the perfect-kick model and FEL-like model. At the very beginning the two models give the same prediction, as expected. As time goes by, they deviate, particularly for the microbunch length. The microbunch lengthening at the radiator is due to gradual decrease of longitudinal focusing strength, resulting from transient imbalance from cavity reflection loss, the injection compensation, and the FEL-like gain per pass. After about 2×10^4 turns the system reaches a steady state. Note that here we assume no initial detuning of the two modulator undulators. A proper detuning, together with knowledge of laser cavity design, may help retain the microbunch length at its design value at the radiator.

Figure 5 illustrates the output power at the radiator and the corresponding bunching factor based on the two models. The radiation power is targeted at 200 nm, where the microbunch length is about 20 nm in design. The slight microbunch lengthening leads to bunching factor degradation and decrease of the output power.

SUMMARY AND DISCUSSION

For perfect cancellation of the two laser modulators, the developed matrix formulation gives consistent results with the analytical estimate [17]. There are two options to con-

sider the effects of laser modulators on the beam. One is by adding a static (same for each turn) deviation parameter ε to the chirp strength at the second modulator to account for non-perfect cancellation. The other is by evaluating the turn-by-turn radiation power evolution stored in the two laser modulators based on FEL-like model. Comparing the FEL-like model with non-perfect static kick model, we find that

- Variation of microbunch length at radiator becomes larger, when using both the non-perfect kick model and the FEL-like model, see Figs. 2 and 4;
- The static and stable operation may require the chirp strength deviation within $-0.012 \leq \varepsilon \leq 0.045$, where $h_n^{(2)} = h_n^{(1)}(1 + \varepsilon)$;
- The imbalance and/or gradual decrease of longitudinal focusing strength, i.e., chirp strength $h_n^{(1,2)}$, due to cavity loss can be compensated by a proper detuning and/or re-injection of the external modulation laser power.

We have constructed a recursive model to account for turn-by-turn evolution, including beam centroid and moment stability. It is possible to obtain a simplified analytical expression to identify the stability regime or tolerance range for non-perfect cancellation. This work is ongoing.

ACKNOWLEDGMENTS

REFERENCES

[1] D. F. Ratner and A. W. Chao, "Steady-state microbunching in a storage ring for generating coherent radiation" *Phys. Rev. Lett.* vol. 105, p. 154801, 2010.
`doi:10.1103/PhysRevLett.105.154801`

[2] A. W. Chao *et al.*, "High power radiation sources using the steady-state microbunching mechanism", in *Proc. 7th Int. Particle Accelerator Conf. (IPAC'16)*, Busan, Korea, Jun. 2016, paper TUXB01, pp. 1048-1053.
`doi:10.18429/JACoW-IPAC2016-TUXB01`

[3] C. Tang *et al.*, "An overview of the progress on SSMB", in *Proc. 60th ICFA Advanced Beam Dynamics Workshop on Future Light Sources (FLS 2018)*, Shanghai, China, March 2018, paper THP2WB02, pp. 166-170.
`doi:10.18429/JACoW-FLS2018-THP2WB02`

[4] X. Deng *et al.*, "Experimental demonstration of the mechanism of steady-state microbunching", *Nature*, vol. 590, no. 7847, pp. 576-579, 2021.
`doi:10.1038/s41586-021-03203-0`

[5] A.W. Chao, "Storage ring based steady state microbunching", presented at FLS'23, Lucerne, Switzerland, Aug 2023, paper MO2L2 , this conference.

[6] Y. Zhang *et al.*, "Ultralow longitudinal emittance storage rings", *Phys. Rev. Accel. Beams*, vol 24, pp. 090701, 2021.
`doi:10.1103/PhysRevAccelBeams.24.090701`

[7] Z. Pan *et al.*, "A Storage Ring Design for Steady-State Microbunching to Generate Coherent EUV Light Source", in *Proc. 39th Int. Free-Electron Laser Conf. (FEL'19)*, Hamburg, Germany, Aug. 2019, paper THP055, pp. 700-703.
`doi:10.18429/JACoW-FEL2019-THP055`

[8] X. J. Deng *et al.*, "Single-particle dynamics of microbunching", *Phys. Rev. Accel. Beams*, vol. 23, pp. 044002, 2020.
`doi:10.1103/PhysRevAccelBeams.23.044002`

[9] Z. Li *et al.*, "Generalized longitudinal strong focusing in a steady-state microbunching storage ring". submitted for publication.

[10] X. J. Deng *et al.*, "Harmonic generation and bunch compression based on transverse-longitudinal coupling", *Nucl. Instrum. Methods Phys. Res. Sect., A*, vol. 1019 p. 165859, 2021. `doi:10.1016/j.nima.2021.165859`

[11] X. J. Deng *et al.*, "Average and statistical properties of coherent radiation from steady-state microbunching", *J. Synchrotron Radiat.*, vol. 30, pp. 35-50, 2023.
`doi:10.1107/S1600577522009973`

[12] C.-Y. Tsai *et al.*, "Coherent-radiation-induced longitudinal single-pass beam breakup instability of a steady-state microbunch train in an undulator", *Phys. Rev. Accel. Beams*, vol. 24, p. 114401, 2021.
`doi:10.1103/PhysRevAccelBeams.24.114401`

[13] C.-Y. Tsai, "Theoretical formulation of multiturn collective dynamics in a laser cavity modulator with comparison to robinson and high-gain free-electron laser instability", *Phys. Rev. Accel. Beams*, vol. 25, p. 064401, 2022.
`doi:10.1103/PhysRevAccelBeams.25.064401`

[14] C.-Y. Tsai, "Longitudinal single-bunch instabilities driven by coherent undulator radiation in the cavity modulator of a steady-state microbunching storage ring", *Nucl. Instrum. Methods Phys. Res. Sect. A*, vol. 1042, p. 167454, 2022.
`doi:10.1016/j.nima.2022.167454`

[15] A. W. Chao, "Focused laser", unpublished.

[16] G. Dattoli et al., "Booklet for FEL design: a collection of practical formulae". `https://fel.enea.it/booklet/pdf/Booklet_for_FEL_design.pdf`

[17] X. J. Deng, "10 μm and 1 μm SSMB", unpublished.

AN INVERSE-COMPTON SCATTERING SIMULATION MODULE FOR RF-TRACK

A. Latina[*], V. Mușat[1], CERN, Geneva, Switzerland
[1]also at The University of Oxford, Oxford, UK

Abstract

A simulation module implementing Inverse-Compton scattering (ICS) was added to the tracking code RF-Track. The module consists of a special beamline element that simulates the interaction between the tracked beam and a laser, making RF-Track capable of simulating a complete ICS source in one go, from the electron source to the photons. The description of the laser allows the user to thoroughly quality the laser in terms of wavelength, pulse energy, pulse length, incoming direction, M^2 parameter, aspect ratio, polarisation and whether the laser profile should be Gaussian or uniform. Furthermore, as the code implements fully generic expressions, the scattering between photons and different particles than electrons can be simulated. A benchmark against CAIN showed excellent agreement and that RF-Track outperforms CAIN in terms of computational speed by orders of magnitude.

INTRODUCTION

Light sources based on Inverse Compton Scattering are attracting growing attention due to their compactness, high brilliance, and the capability to reach a wide range of photon energies, from X-rays (few keV) to gamma rays (few MeV), the latter inaccessible to most light sources including synchrotrons.

Inverse Compton scattering takes place when a charged particle transfers a fraction of its momentum to a photon, increasing its energy. The maximum final photon energy achievable in an ICS interaction occurs in case of a *head-on* collision. If the initial energy of the photon is E_i, the final energy E_f is given by

$$E_\mathrm{f} = 4\gamma^2 E_\mathrm{i},$$

where γ is the relativistic factor of the scattering particle [1]. In the case of ultra-relativistic electrons, the photon's energy can increase by several orders of magnitude.

While designing an ICS source, the simulation of ICS is crucial to assess the scattered photons' spectral properties, bandwidth, and angular distribution. The most accredited code for simulating Inverse Compton Scattering is probably CAIN, written by Yokoya et al. [2]. CAIN is a stand-alone Monte Carlo program that simulates beam-beam interactions involving high-energy electrons, positrons, and photons. The code covers the classical and quantum domains in linear and weakly nonlinear regimes. The interaction is described as the scattering between particles and has been extensively tested and compared to experimental results.

_____
* andrea.latina@cern.ch

Despite its excellent reputation, the practical application of CAIN towards optimising an ICS-based facility is hindered by two primary limitations: (1) it operates rather slowly, and (2) as a standalone code, it requires an interface with conventional particle tracking codes that can transport electrons through the accelerator to the interaction point (IP), making integrated performance optimisation challenging.

To circumvent these limitations, the author of this paper developed a simulation module as a part of the tracking code RF-Track [3]. Since RF-Track can track particles with any charge through an accelerator while accounting for the effects of space charge, beam loading, wakefields, etc., this module enables the simulation of an ICS source from cathode to X-rays in one go. This unlocks a thorough optimisation of the source being designed.

The module was written in parallel C++ and showed simulation speed orders of magnitude faster than CAIN. This paper provides a detailed description of the implementation and two benchmarking cases.

IMPLEMENTATION

To the user, the collision point consists of a specialised lattice element called "`LaserBeam`" that simulates the scattering between the tracked beam and a laser. This element allows the user to define the key laser parameters: wavelength, pulse energy, pulse length, incoming direction (which can be arbitrarily chosen over the entire solid angle), the M^2 parameter, the aspect ratio, the degree of linear polarisation (optional), and whether the laser beam has a Gaussian or a uniform profile.

`LaserBeam` is a time-dependent element that the user can synchronise to the beam or an absolute clock. Like any other RF-Track's lattice element, it can be arbitrarily displaced by any offset and angle, allowing for misalignment imperfection studies. The element can have a length or be thin; in either case, the entire three-dimensional structure of the bunch is reconstructed during the computation.

The scattering is computed in the rest frame of the charged particle as a Monte Carlo process. When the photon's energy is much lower than the particle's rest energy, its absolute momentum and wavelength remain unchanged during the collision. In this case, the scattering is elastic and is called *Thomson scattering*. Proper *Compton scattering* occurs at higher photon energies when there is a momentum transfer between the particle and the photon, and the scattering is inelastic. After the computation of the scattering, the phase-space variables of particle and photon are updated and moved back to the laboratory frame, where tracking continues for both species.

Calculating the final state of the interacting particles requires knowledge of the total and differential cross-sections. The total cross-section is needed to determine λ, the particle's mean free path, that is, the distance a particle travels before it collides with a photon. The angular differential cross-section is needed to calculate the energy and deflection angle of the scattered photon and the recoil of the incident particle.

Since these cross-sections assume different expressions depending on whether the incoming photons are polarised, RF-Track effectively implements four scattering processes: Thomson or Compton, polarised or unpolarised. The following subsections provide the detailed expressions used in the code.

Case of Thomson Scattering

The Thomson differential cross-section of an arbitrary particle at rest with mass m and charge q elastically colliding with a photon is [4],

$$\frac{d\sigma}{d\Omega} = r^2 f\left(\theta, \varphi, P\right),$$

where $r = \frac{q^2}{4\pi\epsilon_0\,mc^2}$ is the classical radius of the particle, θ and φ correspond to the photon's incidence direction, and $d\Omega = \sin\theta\,d\theta\,d\varphi$ is the standard differential element of solid angle. The function $f\left(\theta, \varphi, P\right)$ accounts for the cross-section's dependence on the direction and polarisation of the incoming photon.

In the assumption of unpolarised photons, the function f must be averaged over all incoming polarisation angles and it reduces to [4]

$$f_{\text{unpolarized}}\left(\theta\right) = \frac{1 + \cos^2\theta}{2},$$

showing that the scattered photon is isotropic with respect to the azimuthal angle φ.

In the case of a beam of linearly polarised photons, with polarization $P = \sin\phi$ where ϕ is the polarisation angle, the angular dependence of the differential cross-section reads:

$$f_{\text{polarized}}\left(\theta, \varphi, P\right) = \left(\left(2P^2 - 1\right)\sin^2\varphi - P^2\right)\sin^2\theta + \ldots$$
$$\ldots + 2P\sqrt{1 - P^2}\cos\varphi\,\sin\varphi\,\sin^2\theta + 1,$$

and the outcoming photon is no longer isotropic in φ.

The total cross-section, needed to compute the mean free path λ, is the integration of the differential cross-section over the whole solid angle,

$$\sigma = \iint_\Omega \left(\frac{d\sigma_t}{d\Omega}\right) d\Omega = \frac{8\pi}{3}\,r^2 = \frac{8\pi}{3}\left(\frac{q^2}{4\pi\epsilon_0 mc^2}\right)^2.$$

For electrons and positrons, this is the well-known constant $\sigma_{\text{Thomson}} = 66.5\,\text{fm}^2$. In RF-Track, however, this quantity is computed event by event, allowing for the scattering simulation of any charged particle.

Case of Compton Scattering

For an incident unpolarized photon of energy E_γ, the differential cross section is given by the Klein-Nishina formula [4]:

$$\frac{d\sigma_{\text{unpolarized}}}{d\Omega} = \frac{1}{2}r^2\left(\frac{\lambda}{\lambda'}\right)^2\left[\frac{\lambda}{\lambda'} + \frac{\lambda'}{\lambda} - \sin^2\theta\right],$$

where λ/λ' is the ratio of the wavelengths of the incident and scattered photons. The angular-dependent ratio of the photon wavelengths is

$$\frac{\lambda}{\lambda'} = \frac{1}{1 + \epsilon(1 - \cos\theta)}.$$

The quantity $\epsilon = E_\gamma/(mc^2)$ is the energy of the incident photon normalised to the particle's rest energy.

For a linearly polarized photon, the differential cross section is instead given by [5]

$$\frac{d\sigma_{\text{polarized}}}{d\Omega} = \frac{1}{2}r^2\left(\frac{\lambda}{\lambda'}\right)^2\left[\frac{\lambda}{\lambda'} + \frac{\lambda'}{\lambda} - 2\sin^2\theta\cos^2\varphi\right].$$

In this case, the scattered photon is no longer isotropic in the azimuthal angle φ.

ALGORITHM

The interaction is computed over the overlap region in a user-defined number of steps, each with length ΔL. Slicing the computation enables the simulation of multiple scatterings during the collision.

For each slice and each charged particle in the beam, the simulation algorithm repeats the following seven steps until the colliding bunches no longer overlap:

1. Determine the average density and direction of the incoming photon beam at the particle's location.

2. Perform a Lorentz boost of the average photon into the rest frame of the scattered particle.

3. Check whether it is a Thomson or a Compton scattering; then, compute the total cross-section σ to evaluate the particle's mean-free path $\lambda = 1/(\rho\,\sigma)$, with ρ the volume number density of the photons.

4. Given λ and ΔL, compute the probability of scattering. If $\lambda \gg \Delta L$, force a scattering event and produce a weighted photon based on the weight of the charged particle.

5. Using a Monte Carlo method, utilise the appropriate differential cross-section to evaluate the energy and the 3D direction (θ, φ) of the scattered photon.

6. Given the scattered photon's direction and energy, resolve the kinematics of the scattering, update the particle's phase-space variables, and perform a Lorentz boost into the lab frame.

7. Add the scattered photon to the beam's data structure and advance both particle and photon through the next slice.

These computations are performed in parallel over the beam's particles.

BENCHMARK AND PERFORMANCE

The RF-Track's implementation was compared with CAIN in the ThomX and ELI-NP cases. Figure 1 compares X-ray beam-defining plots at the IP, obtained in RF-Track and CAIN for the ThomX source [6]. The expected Compton edge of 45 keV is determined from both codes. Other X-ray beam parameters obtainable in RF-Track, e.g., beam size, $\sigma_x = 58\,\mu m$, $\sigma_y = 52\,\mu m$, and beam divergence, 9 mrad, correspond to the simulations from CAIN. These results show that RF-Track and CAIN are in excellent agreement. Output photon parameters were also compared for ELI-NP-GBS [7] in Table 2. The value for the scattered photon flux is the only notable difference between the two codes.

A summary of the performance of RF-Track and CAIN is shown in Table 1. RF-Track can compute the results from Figure 1 several orders of magnitude faster than CAIN. The longer computation runtime of CAIN can be attributed to its requirement for a larger number of electron macroparticles to generate sufficient statistics, given the smallness of the scattering cross-section. RF-Track can enforce a minimum number of scattered photon macroparticles per slice, which relaxes the requirement on the number of electron macroparticles.

Table 1: Comparison Between RF-Track and CAIN in the ThomX Case

Parameter	CAIN	RF-Track
Input electron[(1)]	5×10^7	10^4
Output X-rays[(1)]	12,700	1,350,311
Runtime (s)	2,545	0.67
Total flux (10^{13} ph/s)	2.65 ± 0.02	2.50 ± 0.01

[(1)] Number of simulated macro particles

Table 2: Comparison Between RF-Track and CAIN in the ELI-NP Case (Courtesy of Gianfranco Paternò)

Parameter	CAIN	RF-Track
Mean energy (keV)	9118.63	9117.61
Peak energy (keV)	10025.00	10025.00
Max energy (keV)	10130.17	10129.02
Relative energy bandwidth[(2)]	6.74%	6.77%
Nb. of photons[(2)]	2.82×10^5	2.57×10^5
Fraction of photons[(2)]	0.2558	0.2546

[(2)] Within a cone $\theta < 0.5$ mrad

CONCLUSIONS

The capability to simulate linear Thomson and Compton scattering has been implemented in the RF-Track particle tracking code. This development enables integrated start-to-end simulations of ICS sources from cathode to X-rays. A benchmark against CAIN showed that RF-Track's results are in excellent agreement, while RF-Track outperforms CAIN's computational speed by orders of magnitude.

ACKNOWLEDGEMENTS

Figure 1: ICS beam-defining plots of ThomX, simulated using RF-Track (top) and CAIN (bottom). (a) The energy spectrum of photons travelling in all directions and through a 1 mrad and 5 mrad collection angle. (b) The transverse source size. (c) The angular emission distribution. (d) The number of ph/mrad²/s as a function of energy and collection angle.

REFERENCES

[1] G. A. Krafft and G. Priebe, "Compton Sources of Electromagnetic Radiation", *Rev. Accel Sci. Technol.*, vol. 03, no. 01, 2010. doi:10.1142/S1793626810000440

[2] P. Chen, G. Horton-Smith, T. Ohgaki, A. W. Weidemann, and K. Yokoya, "CAIN: Conglomérat d'ABEL et d'Interactions Non-linéaires", *Nucl. Instrum. Methods Phys. Res., Sect. A*, vol. 355, no. 1, 1995. doi:10.1016/0168-9002(94)01186-9

[3] A. Latina, "RF-Track Reference Manual", CERN, Tech. Rep., 2020. doi:10.5281/zenodo.3887085

[4] L. D. Landau and E. M. Lifshitz, *Mechanics and Electrodynamics (Shorter Course of Theoretical Physics)*. Pergamon, 1972, vol. 1. doi:10.1016/C2009-0-06775-0

[5] B. Badelek *et al.*, "TESLA Technical Design Report, Part VI, Chapter 1: The Photon Collider at TESLA", *Int. J. Mod. Phys. A*, vol. 19, pp. 5097–5186, 2004. doi:10.1142/S0217751X04020737

[6] A. Variola, J. Haissinski, A. Loulergue, and F. Zomer, "ThomX Technical Design Report", Tech. Rep., 2014, 164 p. https://hal.in2p3.fr/in2p3-00971281

[7] O. Adriani *et al.*, "Technical Design Report EuroGammaS proposal for the ELI-NP Gamma beam System", EuroGammaS, Research Report, 2014. https://hal.in2p3.fr/in2p3-01027561

RECENT DEVELOPMENTS OF THE cSTART PROJECT

M. Schwarz*, A. Bernhard, E. Bründermann, B. Härer, D. El Khechen, A. Malygin,
M.J. Nasse, G. Niehues, A. Papash, R. Ruprecht, J. Schäfer, M. Schuh, N. Smale,
P. Wesolowski, Ch. Widmann, A.-S. Müller
Karlsruhe Institute of Technology, Karlsruhe, Germany

Abstract

The combination of a compact storage ring and a laser-plasma accelerator (LPA) can serve as the basis for future compact light sources. One challenge is the large momentum spread (about 2 %) of the electron beams delivered by the LPA. To overcome this challenge, a very large acceptance compact storage ring (VLA-cSR) was designed as part of the compact STorage ring for Accelerator Research and Technology (cSTART) project. The project will be realized at the Karlsruhe Institute of Technology (KIT, Germany). Initially, the Ferninfrarot Linac- Und Test-Experiment (FLUTE), a source of ultra-short bunches, will serve as an injector for the VLA-cSR to benchmark and emulate LPA-like beams. In a second stage, a laser-plasma accelerator will be used as an injector, which is being developed as part of the ATHENA project in collaboration with DESY and the Helmholtz Institute Jena (HIJ). The small facility footprint, the large-momentum spread bunches with charges from 1 pC to 1 nC and lengths from few fs to few ps pose challenges for the lattice design, RF system and beam diagnostics. This contribution summarizes the latest results on these challenges.

INTRODUCTION
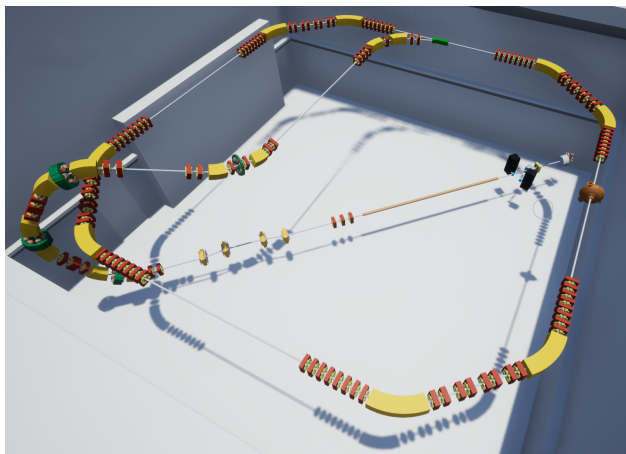
Figure 1: Artistic view of the cSTART project. The cSTART storage ring at a height of about 3.5 m is connected to the FLUTE injector by a complex 3D transfer line. The LPA (not shown) will be at the same height as the storage ring and uses the last part of the transfer line of FLUTE for injection.

Laser-based plasma acceleration can deliver electron bunches with high peak current and ultra-short bunch lengths

Table 1: Main Parameters of the cSTART Storage Ring

Parameter	Value	Unit
Circumference	43.2	m
Energy range	40 to 60	MeV
Injection rate	10	Hz
Injection type	one-turn swap-out	–
Beam storage time	100	ms
Bunch charge	1 to 1000	pC
Revolution period	144	ns
Revolution frequency	6.94	MHz
Incoherent energy loss	0.54	eV
Damping time (h, v, l)	29.5, 26.5, 12.6	s
Coherent energy loss (1 pC, 20 fs)	160	keV
Critical frequency f_{crit}	37.7	THz
Tune (h, v, l)	5.18, 1.66, 0.023	1
Momentum compaction:		
nominal	14.8×10^{-3}	1
reduced-α	3.9×10^{-3}	1
RF frequency	500	MHz
RF voltage	500	kV
Harmonic number	72	1
Vacuum pressure	1×10^{-8}	mbar

on a compact facility footprint. This makes LPAs attractive candidates for light sources, since ultra-short bunches emit intense coherent radiation in the THz regime [1]. However, their large beam divergence and energy spread require dedicated beam transport systems and insertion devices [2]. Moreover, their repetition rate is limited to a few Hz compared to MHz at storage rings.

The cSTART project develops the infrastructure and technology necessary for a compact LPA-based light source. A key component is the construction of a very-large momentum acceptance compact storage ring to inject and store sub-ps short electron bunches. One injector is a LPA developed in cooperation with DESY and HIJ [3]. The linac-based accelerator FLUTE [4] will serve also as injector to provide well-defined LPA-like bunches for benchmarking and to further explore injection of ultra-short, 10 fs-range electron bunches. An artistic view of the cSTART storage ring on top of FLUTE is shown in Fig. 1. In storing a sub-ps short bunch, the ring would act as a "multiplier" to push the few Hz injection rate to a MHz repetition rate.

With two different injectors, the beams at cSTART cover a large region in parameter space. In simulations, the LPA beam achieved a bunch charge of 20 pC with mean energy of

_____
* markus.schwarz@kit.edu

50 MeV, energy spread of ~2 % and bunch length <20 fs [5]. Meanwhile, FLUTE can cover a bunch charge range from 1 pC to 1 nC with energies between 40 MeV to 60 MeV, energy spread ~0.1 % and bunch lengths from <1 ps down to a few fs. The relatively low electron energy of ~50 MeV means that energy losses due to incoherent synchrotron radiation are negligible and that damping times are in the order of tens of seconds [6]. As a consequence, the beam remains in non-equilibrium throughout the planned storage time of 100 ms. There will be a swap-out injection of a new bunch after 100 ms, i.e. extraction of the circulating bunch into a beam dump and on-axis injection of a new bunch. Only single bunch operation is currently foreseen.

These wide ranges of beam parameters provide challenges to the lattice design [6], the transfer line from the injectors [7–9], and the beam diagnostics [10], but will also provide a plethora of measurement data and opportunities for the analysis and control of non-equilibrium beam dynamics. This paper gives an overview of the recent developments to overcome these challenges.

RING LAYOUT AND MAGNETIC LATTICE

The cSTART storage ring shall be very compact as a model for future compact light sources. This is naturally achieved by reusing the existing FLUTE hall, which leads to space constraints with a footprint of 15 m × 14.5 m. In addition, the ring will be mounted at a height of about 3.5 m. For the LPA-injector, the storage ring must have a sufficiently large momentum acceptance to accommodate its beam. The complex 3D shape of the transfer line from FLUTE (see Fig. 1) arises from a) spatial constraints and b) the need to compress the bunch, so that it is ultra-short at injection [7].

Several layouts of the storage ring have been studied, see Ref. [6] and references therein. The parameters of the final design are listed in Table 1. The ring has a circumference of 43.2 m and consists of four identical DBA arcs with a length of 6.95 m and four straight sections with a length of 3.85 m. One straight section is used as the injection section, while the other three sections are available for an RF cavity, advanced diagnostic systems, and accelerator physics experiments.

The magnet layout of one arc is shown in Fig. 2. Five families of quadrupoles (Qn) and two families of sextupoles (Sn) for chromaticity correction are foreseen. Space is reserved for four additional sextupole families and one family of octupoles, e.g., in-between the quadrupoles of the straight sections. The beam position will be measured by button beam position monitors and corrected by dedicated horizontal and vertical corrector magnets. The lattice functions of one cell are shown in Fig. 3 for the operation mode with nominal momentum compaction. The magnetic layout is very flexible to support other operation modes, e.g., with reduced momentum compaction where the dispersion leaks into the straight sections.
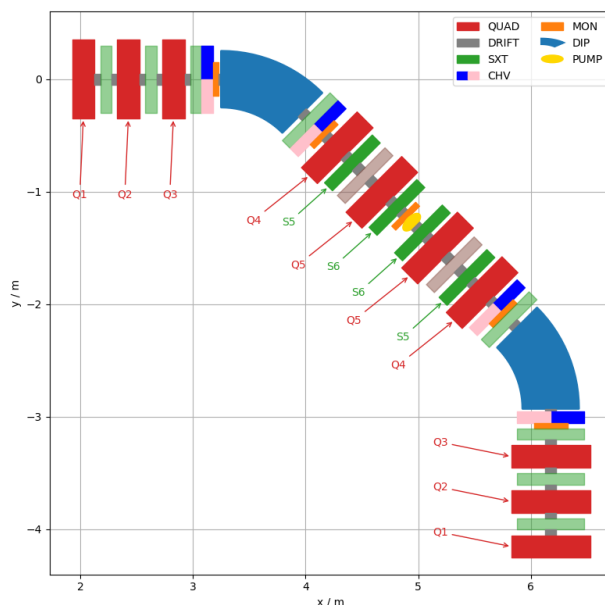
Figure 2: Magnet layout of the DBA lattice in one arc.
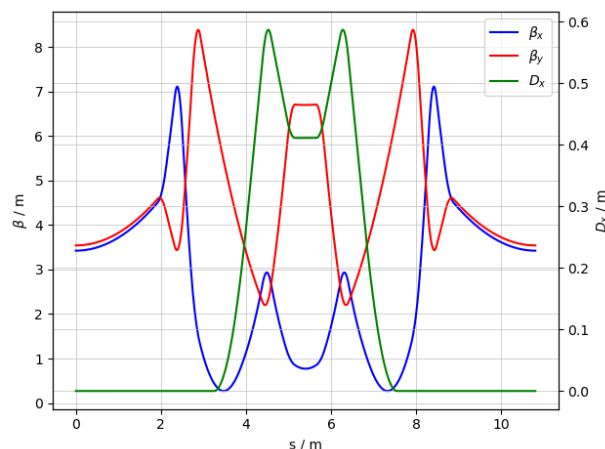
Figure 3: Lattice functions in one cell for an operation mode with nominal momentum compaction of 14.8×10^{-3}. The dispersion is located between the dipoles and does not exceed 0.6 m, while the momentum acceptance is about ±4 %.

RF SYSTEM

An RF cavity will be placed in one of the straight sections. Several considerations affected the choice of the RF frequency: 1) A large RF acceptance requires a low RF frequency, which increases the length of the cavity; 2) A small equilibrium bunch length favors a high RF frequency; 3) The cavity must be able to provide a large accelerating voltage to increase the RF acceptance and to reduce non-linear effects. Finally, a cavity frequency of 500 MHz was chosen as a good compromise [11]. Available cavities at this frequency can provide an acceleration voltage of 500 kV for an input power of 50 kW [12, 13]. With a harmonic number of 72, this yields an RF energy acceptance of ~8 %.

BEAM DYNAMIC SIMULATION RESULTS

The Touschek lifetime of a bunch depends non-trivially on the bunch and machine parameters. Due to the large range in bunch charge and bunch lengths, the Touschek lifetime at cSTART varies by two orders of magnitude [6]. It is above 1 s for a bunch charge of 1.5 pC, but varies between 12 s to 1 s for a bunch with 150 pC and bunch length between 1 ps to 0.06 ps, respectively. Intrabeam scattering (IBS) is also non-negligible at the energy of 50 MeV. The IBS growth rates have been estimated [6] to be $0.12\,\mathrm{s}^{-1}$ for a bunch of 1.5 pC and $12\,\mathrm{s}^{-1}$ for 150 pC. The latter corresponds to a time scale of 83 ms and is, thus, shorter than the storage time of 100 ms and necessitate the on-axis swap-out injection. Keep in mind that these computations assume equilibrium conditions (especially for the bunch length).

While incoherent synchrotron radiation is negligible at energies of about 50 MeV, the ultra-short bunch lengths mean that the synchrotron radiation is emitted coherently. Since the intensity of coherent synchrotron radiation (CSR) scales quadratically with the number of electrons, it is not negligible. Especially after injection, when the bunch length is only a few femtoseconds, the energy loss per electron due to CSR can be as high as 160 keV [11]. The bunch starts to filament and, after a few ms, reaches a filamented RMS bunch length of about 15 ps [14]. However, about 40 % of the electrons are contained in sub-bunches with bunch lengths below 1 ps, see Fig. 4. These sub-bunches are surrounded by a halo of electrons, which increases the RMS bunch length. Note that these simulations only include the longitudinal dynamics.

These first results show the necessity to perform full 6D simulations that include not only the CSR but also Touschek and Intrabeam scattering.
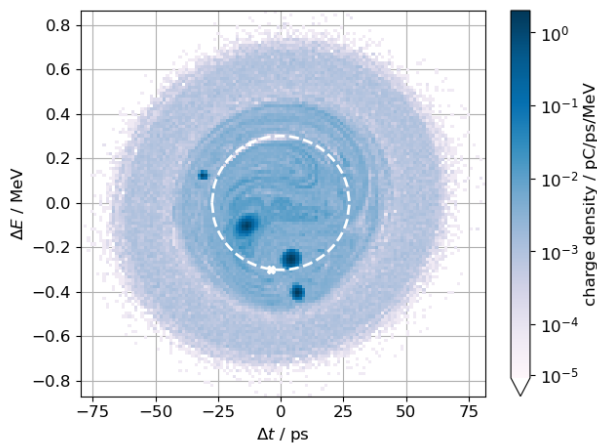

Figure 4: Simulated longitudinal phase space density after 100 ms for a 1 pC bunch. About 40 % of the particles are contained in four sub-bunches, each with $\sigma_{\mathrm{RMS}} \leq 1\,\mathrm{ps}$ [14].

SUMMARY

The cSTART project develops the infrastructure and technology necessary for a compact LPA-based light source. A key part is the construction of a compact storage ring to capture and store sub-ps short bunches. The cSTART storage ring will have a circumference of 43.2 m, and a large momentum acceptance suitable for the injection of LPA-generated beams. Its two injectors will be the linac-based accelerator FLUTE and a laser-plasma accelerator. Three out of four straight sections are available to accommodate advanced diagnostic systems and accelerator physics experiments. The DBA lattice is flexible enough to provide operation modes with different momentum compaction factors. The RF system at 500 MHz will consist of a single cavity that provides an acceleration voltage of 500 kV at a power of 50 kW.

The low beam energy of 50 MeV leads to long damping times and the bunch remains in non-equilibrium throughout the 100 ms of storage time. After filamentation, the bunch length can increase to several ps, while several sub-bunches, containing about 40 % of the particles, form with an RMS bunch length below 1 ps. Touschek scattering, intra-beam scattering, and coherent synchrotron radiation all play an important role in the beam dynamics. To study all these effects together requires the simulation in 6D phase space and may also require to define additional or new figures of merit for describing non-equilibrium beams in the future.

REFERENCES

[1] S. Hillenbrand, R. Assmann, A.-S. Müller, O. Jansen, V. Judin, and A. Pukhov, "Study of laser wakefield accelerators as injectors for synchrotron light sources," *Nucl. Instrum. Methods Phys. Res., Sect. A*, vol. 740, pp. 153–157, 2014. doi:10.1016/j.nima.2013.10.081

[2] A. Bernhard *et al.*, "Progress on experiments towards LWFA-driven transverse gradient undulator-based FELs," *Nucl. Instrum. Methods Phys. Res., Sect. A*, vol. 909, pp. 391–397, 2018. doi:10.1016/j.nima.2017.12.052

[3] E. Panofski *et al.*, "Status report of the 50 MeV LPA-based injector at ATHENA for a compact storage ring," in *Proc. IPAC'22*, Bangkok, Thailand, 2022, paper WEPOST032, pp. 1768–1771.
doi:10.18429/JACoW-IPAC2022-WEPOST032

[4] M. J. Nasse *et al.*, "FLUTE: A versatile linac-based THz source," *Review of Scientific Instruments*, vol. 84, p. 022 705, 2013. doi:10.1063/1.4790431

[5] E. Panofski *et al.*, "Developing a 50 MeV LPA-based injector at ATHENA for a compact storage ring," in *Proc. IPAC'21*, Campinas, SP, Brazil, 2021, paper TUPAB163, pp. 1765–1768. doi:10.18429/JACoW-IPAC2021-TUPAB163

[6] A. Papash *et al.*, "Flexible features of the compact storage ring in the cSTART project at Karlsruhe Institute of Technology," in *Proc. IPAC'22*, Bangkok, Thailand, 2022, paper THPOPT023, pp. 2620–2623.
doi:10.18429/JACoW-IPAC2022-THPOPT023

[7] J. Schäfer, "Lattice design of a transfer line for ultra-short bunches from FLUTE to cSTART," M.S. thesis, Karlsruher Institut für Technologie (KIT), 2019, 81 pp. doi:10.5445/IR/1000105061

[8] B. Härer *et al.*, "Non-linear features of the cSTART project," in *Proc. IPAC'19*, Melbourne, Australia, 2019, paper TUPGW020, pp. 1437–1440. doi:10.18429/JACoW-IPAC2019-TUPGW020

[9] B. Härer *et al.*, "Development of a transfer line for LPA-generated electron bunches to a compact storage ring," in *Proc. IPAC'22*, Bangkok, Thailand, 2022, paper TH-POPT059, pp. 2730–2733. doi:10.18429/JACoW-IPAC2022-THPOPT059

[10] D. E. Khechen *et al.*, "Beam diagnostics for the storage ring of the cSTART project at KIT," in *Proc. IPAC'22*, Bangkok, Thailand, 2022, paper MOPOPT026, pp. 300–303. doi:10.18429/JACoW-IPAC2022-MOPOPT026

[11] M. Schwarz *et al.*, "Longitudinal beam dynamics and coherent synchrotron radiation at cSTART," in *Proc. IPAC'21*, Campinas, SP, Brazil, 2021, paper TUPAB255, pp. 2050–2053. doi:10.18429/JACoW-IPAC2021-TUPAB255

[12] M. Bocciai, A. Fabris, D. Lachi, C. Pasotti, M. Rinaldi, and M. Svandrlik, "Operational experience with the ELETTRA RF system," in *Proc. EPAC'98*, 1998, pp. 1758–1760. http://accelconf.web.cern.ch/e98/PAPERS/TUP12C.PDF

[13] F. Marhauser and E. Weihreter, "First tests of a HOM-damped high power 500 MHz cavity," in *Proc. EPAC'04*, Luzern, Switzerland, 2004, paper TUPKF011, pp. 979–981. https://accelconf.web.cern.ch/e04/PAPERS/TUPKF011.PDF

[14] M. Schwarz, S. Braner, B. Härer, A.-S. Müller, and J. Schäfer, "Longitudinal beam dynamics for different initial distributions at cSTART," presented at IPAC'23, Venice, Italy, May 2023, paper WEPL167, to appear in the proceedings.

OPERATING LIQUID METALJET X-RAY SOURCES FOR MATERIALS RESEARCH

Mirko Boin, Roland Mainz, Manuela Klaus, Daniel Apel, Paul H. Kamm, Robert C. Wimpory,
Francisco García-Moreno, Guido Wagener, Christoph Genzel,
Helmholtz-Zentrum Berlin für Materialien und Energie GmbH, Berlin, Germany

Abstract

Even on the 100th anniversary of the death of Wilhelm Conrad Röntgen the demand for applications of his discovery of X-rays is not diminishing. On the contrary, both academic and industrial research and development need X-ray generating devices with ever-improving properties to meet the current challenges of science and technology. For this reason, the development of next-generation synchrotrons is being driven forward and made available to users worldwide. Nevertheless, the availability of synchrotron beamtime will always remain limited, even with the most brilliant sources for ultra-fast and high-throughput experiments. That is why the operation of and research with decentralized laboratory equipment becomes just as important. In this context, Helmholtz-Zentrum Berlin (HZB) has commissioned Excillum's MetalJet X-ray devices providing photon energies in the hard X-ray regime. Technical specifications of these sources, the HZB diffractometer lab installations and selected examples are shown. A comparison to synchrotron measurements is made to benchmark the performance of the available setups.

INTRODUCTION

Non-destructive testing methods utilizing conventional laboratory (desktop) X-ray sources have become a successful tool for more and more academic and industrial research purposes, such that their physical limits, for example according to the material's penetration depths, have been extended using high-energy synchrotron photons. Furthermore, high-brilliance synchrotron photons have made fast in-situ and in-operando experiments possible.

However, the increasing demand for measurement time at such facilities contrasts with their availability – the beamtime at synchrotron sources is very limited. Moreover, as a rule, the access to the beamlines cannot be obtained promptly. Waiting times of half a year or longer are quite common in this field. Synchrotron beamlines are usually overbooked many times. Hence, it seems sensible and necessary in several ways to use suitable laboratory X-ray sources as well. With their help, numerous questions can be answered which do not necessarily require the use of expensive and in their availability mostly very limited large-scale facilities.

It is the motivation of this work to address the lack of beamtime with the development of tailored measurement and evaluation methods including the implementation of appropriate experimental hardware using laboratory X-ray sources. Here, novel X-ray sources are presented that help to transport a number of applications from the synchrotron to decentralized laboratories and thus make the analysis of microstructural properties available to a larger community.

LIQUID METALJET X-RAY SOURCES

Inside laboratory and desktop X-ray devices electrons are extracted from a cathode and accelerated within an electric field into the direction of an anode, where their deceleration leads to an energy conversion into heat and X-rays. In general, the X-ray power of all electron-impact X-ray sources is limited by the thermal power loading of the anode. In solid-anode technology, the surface temperature of the anode must be cooled down and stay well below its melting point to avoid damage. Consequently, the yield in terms of photon flux of conventional fixed-anode X-ray tubes is rather low compared to synchrotron radiation. Although the X-ray output can be increased significantly with the use of rotating-anode tubes, the melting limitation of the solid anode material remains.
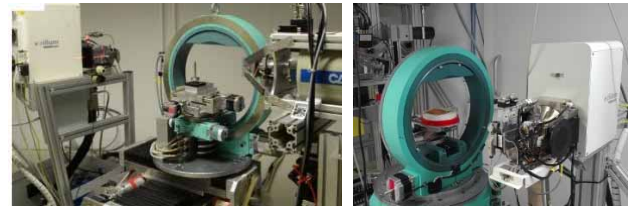
Figure 1: Photographs of the LIMAX-70 (left) and LIMAX-160 (right) laboratories.

In contrast, a liquid metal anode changes this condition since the limitation to maintain the target at well below the melting point is inexistent – the material is already molten. This approach is implemented by the MetalJet products available from the Swedish company Excillum. Two of their MetalJet D2 X-ray sources have been installed at HZB to equip a suite of the so-called LIMAX laboratories (see Fig. 1) for microstructural, residual stress and imaging characterizations. These sources continuously supply fresh target material. The liquid anode, composed of a Ga-In alloy liquid already at room temperature, is provided via a closed high-pressure circuit at 190 bars. A very fine liquid metal jet of a diameter of about 180 μm is formed with the help of a nozzle. The electrons are released by a LaB_6 cathode and accelerated into the direction of the liquid anode under a voltage of 70 kV and 160 kV respectively. With the help of focusing optics a very well-defined electron spot of down to 5 μm × 5 μm is created at the edge of the metal jet. The X-ray spectrum emitted consists of a broad range of Bremsstrahlung (the white beam) up to 70 keV and 160 keV respectively, depending on the excitation voltage. In addition, and due to the extremely high-power loading,

two very intense K_α-emission lines occur at E = 9.2 keV for Ga and E = 24.2 keV for In, depending on the alloy composition (Fig. 2).
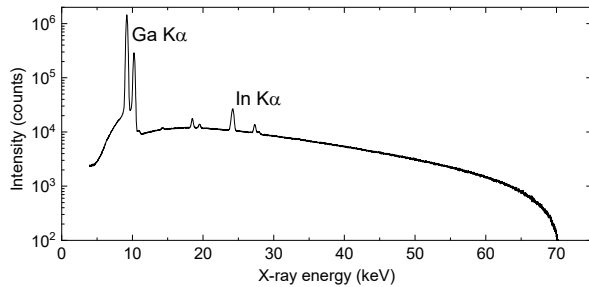

Figure 2: X-ray emission spectrum of the MetalJet D2 measured with LIMAX-70.

Utilizing the so-called Ex-Alloy-I1 target alloy (Ga: 68 wt %; In: 22 wt %; Sn: 10 wt%) the absolute photon fluxes per solid angle have been verified by photon scattering for Ga K_α and In K_α to be $6.0(5)\times10^{12}$ s^{-1} sr^{-1} and $3.8(4)\times10^{11}$ s^{-1} sr^{-1}, respectively [1] at 200 W emission power and 70 kV acceleration voltage. This agrees very well with the specifications given by Excillum.

The output X-ray windows of the MetalJet devices provide a 10° open cone beam. To shape the beam for diffraction experiments, for example, one obvious way is to cut out the size of your gauge volume with the help of a slit system, collimators and Soller slits. However, to make the most use of the incident intensity, third-party primary optics are available instead. Polycapillary optics are used to guide a large fraction of the emitted photons up to about 40 keV onto the sample by total external reflection from the walls of the thin glass tubes. Higher energies are not guided by such capillary optics such that their detected intensities are significantly lower. To provide monochromatic X-rays so-called Montel-optics are used to select very precisely the Ga K_α line, e.g. for angle-dispersive diffraction measurements. Both can be tailored to the needs of a specific experiment setup, i.e. their focus lengths can be either a few centimeters or some meters, for example. At both sources, LIMAX-70 and LIMAX-160, the primary optics – either polycapillary or Montel type – can be aligned by a 6-axis PI H811.I2 hexapod in all directions and orientations to meet the optimum beam conditions, e.g. the maximum intensity.

The LIMAX-70 is equipped with a diffractometer consisting of two Huber 480 goniometer circles, each with a diameter of 800 mm, to realize angle-dispersive diffraction and the rotation of a sample setup respectively. For sample manipulation a large x-y-z stage with a translation range of 250 mm in each direction also allows for heavier setups, such as a stress rig, furnaces or a Huber 512 Euler cradle, for example. In a similar manner, the LIMAX-160 laboratory is modular to change between an Euler cradle based diffractometer setup with integrated x-y-z translation table and other stages, such as a deposition chamber, furnaces and stress-rigs.

A set of detectors with a large range of specifications provide the opportunity for a number of diffractrion, radiographic and tomographic experiments. A Dectris Pilatus3 S 1M with an X-ray detection area of 169 x 179 mm^2 divided into 981 × 1043 pixels, consisting of 10 Si sensor modules each with a size of 83.8 × 33.5 mm^2 and 1000 μm thickness, is available for angle-dispersive X-ray diffraction. Complementary, two energy-resolving LN2-cooled Canberra Ge detectors with a sensor size of 10 ×10 mm^2 are available for energy-dispersive diffraction measurements. A PCO 1200 hs CMOS camera with a 1280 × 1024 pixel resolution and short exposures times is used with scintillators to convert X-rays into visible light. Additionally, an Advacam WidePIX detector with a CdTe sensor of 70 mm × 28 mm and an Advacam MiniPIX detector with a Si Sensor of 14 × 14 mm^2 – both with a pixel size of 55 × 55 μm^2, as well as a Hamamatsu flat panel detector with a 120 ×120 mm^2 scintillator plate and 50 × 50 μm^2 pixel size – are available for imaging experiments. A summary of the setup specifications and available instrument options is given in Table 1. Both laboratories are available for external and in-house users as well as for industrial applications.

Table 1: MetalJet Experimental Setups At HZB

	LIMAX-70	LIMAX-160
Anode alloy	Ga-rich alloy G1	In-enriched alloy I1
Excitation voltage	max. 70 keV	max. 160 keV
X-ray optic options	slits, collimators, capillary optics, Montel optics	
Sample stage	Huber-480 2-circle goniometer of 800 mm diameter with x-y-z stage and optional Euler cradle	Huber-440 goniometer of 500 mm diameter with optional Euler cradle
Sample environment options	(Cryo-)Furnace Load frame PVD chamber Extra rotation stage	
Detector options	Imaging PCO camera WidePIX + MiniPIX detectors Dectris Pilatus 1M Hamamatsu flat panel Canberra Ge-detectors	

APPLICATIONS

Taking advantage of the unique features of the X-ray spectrum emitted by the liquid metal jet source, i.e. the characteristic K_α-emission lines of Ga and In, as well as the white beam, allows for a multitude of applications and different types of measurements, such as angle- and energy-dispersive diffraction and transmission imaging, for instance.

Energy-Dispersive X-ray Stress Analysis (ED-XSA)

The basic principles of X-ray residual stress analysis rely on the correlation between lattice strain measured in any direction with respect to the sample coordinate system and the components of the stress tensor which is given by the fundamental equation for stress analysis using diffraction methods [2] and the so-called $\sin^2\psi$ method [3]. For the analysis of residual stress depth gradients an extension, taking the exponential attenuation of the X-ray intensity by the investigated material into account, is available [4, 5] and the application to the energy-dispersive case of diffraction has been implemented and used at synchrotron beamlines, such as EDDI@BESSY-II [6, 7], taking advantage of the available white and hard X-ray beam spectrum. The same practice is transferred to the LIMAX labs to make it available to a broader community without the restrictions of the limited access to a synchrotron beamline.
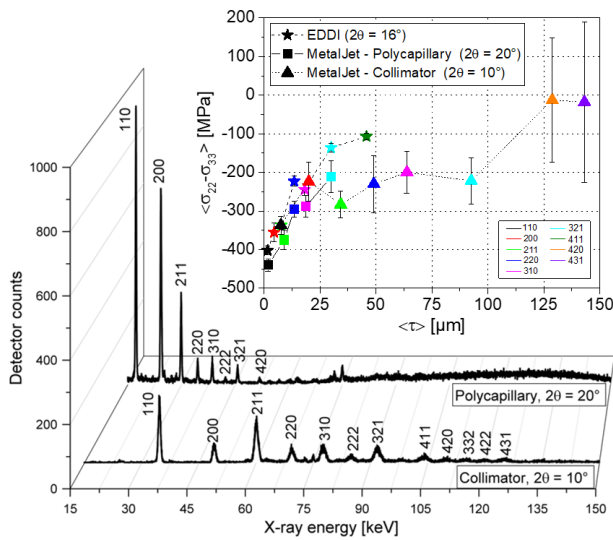

Figure 3: Diffractograms (bottom), measured with the Canberra Ge detector, of a ground steel sample measured at LIMAX-160 with two different settings – and the corresponding residual stress evaluation (top) in comparison to synchrotron results with significantly smaller error bars.

Here, the measurement of a ground C-80 steel sample at the LIMAX-160 source is shown and compared with synchrotron results. The sample surface was measured under two settings with the LIMAX-160 – with polycapillary optics (scattering angle of $2\theta = 20°$) as well as with collimator optics and a scattering angle of $2\theta = 10°$. The measured lattice plane reflections in the diffractograms in Fig. 3 (bottom) are indicated with the *hkl* Miller indices. The position of the diffraction lines depends on the choice of the selected, but fixed, scattering angle 2θ – with smaller 2θ leading to a broader distribution in the detected energy spectrum. The diffractograms as well as the residual stress depth profiles obtained with the two optics clearly reveal their advantages and drawbacks. The polycapillary lens provides sharp and intense diffraction lines within rather short measuring times up to about 40 keV. Then the glass becomes transparent losing the effect of total reflection.

The collimator, on the other hand, also guides the high energy photons without attenuation, resulting in evaluable diffraction lines up to about 125 keV, which allows to extend the information depth of the residual stress profiles considerably. However, due to the comparably low photon flux (no collimation effect) the counting times per spectrum are very long. The results achieved in both configurations are in good agreement with those obtained before at the EDDI synchrotron beamline.

ED-XSA in Complex Geometries

Nevertheless, the extreme high photon flux and brilliance of modern synchrotron beamlines provides further advantages. Diffraction measurements are possible with even very small gauge volumes and – considering the above-described energy-dispersive method – allow for residual stress experiments on surfaces difficult to access, e.g. on the inside of boreholes in complex-shaped industrial components. Such measurements are not feasible with conventional laboratory X-ray equipment, since the reduction of the X-ray spot size on the sample leads to a very small signal-to-background ratio difficult to analyze.
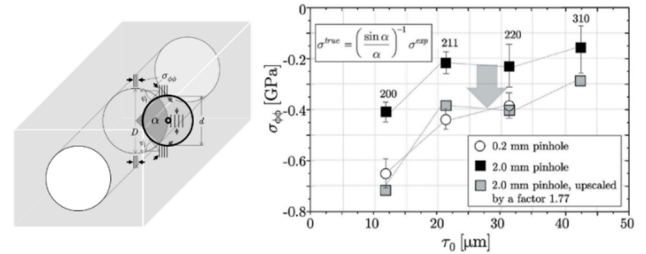
Figure 4: Influence of the X-ray beam size on curved surface (left) on the magnitude of a measured residual stress gradient (right) as taken from [8].

For example, the non-destructive access of the tangential stress component on the inside of a borehole with a large L/D ratio (length-over-diameter) is only feasible with the energy-dispersive diffraction method under small scattering angles, which must be chosen small enough to 'thread-through' the incident and diffracted X-ray beam during a $\sin^2\psi$-scan.

Despite the higher flux of a MetalJet D2, as compared to conventional X-ray sources, a reduction of the beam size is still at the costs of the signal to be evaluated for residual stress depth gradients in the frame of such applications. In the below example the LIMAX-160 was used to measure the tangential stresses at the inner wall of a borehole with a diameter of 2 mm and 10 mm length. For the comparison of two different measurements polycapillary optics were utilized in combination with a 2 mm and a 0.2 mm pinhole. Counting times of 300 s per orientation were used for the larger pinhole and 3600 s for the small pinhole. On the secondary side an equatorial Soller slit with of $\delta = 0.15°$ was installed in front of the detector for both setups. The resulting beam sizes on the inner borehole surface are sketched in Fig. 4 (left). Both beam diameters, as defined by the pinholes, are drawn as bold circles on the inner wall of the borehole.

The influence of the beam diameter on the residual stress evaluation under the effect of such a curved surface is discussed in detail in [8]. It leads to a systematic scaling of the evaluated stress gradient towards lower absolute stresses. The authors have further developed a correction method by putting the geometrical constraints of the borehole and beam diameters into the equations for strain and stress evaluation. In the example in Fig. 4 (right) a correction factor of 1.77 was derived for the measurement with the 2 mm pinhole. Its application onto the evaluated stress gradient finally leads to a perfect match of the evaluated stress curve measured with the 0.2 mm pinhole and to earlier measurements at the synchrotron beamline.

Phase Transitions in Photovoltaic Materials
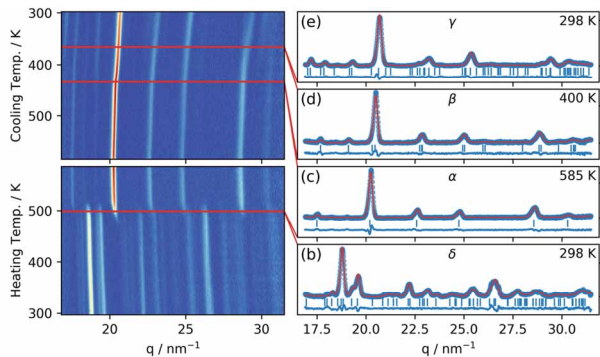
Figure 5: Integrated diffraction pattern measured with the Pilatus detector as a function of temperature for $CsPb(Br_xI_{1-x})_3$ with x = 0.23 taken from [9].

The high X-ray flux of the MetalJet sources further enables high-throughput in-situ experiments for the investigation of phase transitions, for example in photovoltaic materials. In this example Grazing-Incidence Wide-Angle X-ray Scattering (GIWAXS) measurements have been conducted to resolve all transition temperatures for a phase diagram from 300 K to 585 K of $CsPb(Br_xI_{1-x})_3$ with a composition range of $0 \leq x \leq 0.68$ in a single heating process [9]. $CsPb(Br_xI_{1-x})_3$ is utilized as a so-called perovskite solar cell material with a beneficial microstructure for high solar energy conversion efficiencies. The MetalJet source was used at 70 kV with an angle-dispersive diffraction setup, polycapillary optics, a 2D detector and a heating stage. The setup allows for fast acquisition of the samples' diffraction patterns on the detector during thermal annealing during formation of the perovskite structure. Preliminary studies have shown that Bromine helps to stabilize a metastable gamma phase structure at room temperature, but the necessary phase diagrams were unexplored before. The measurements with the MetalJet source helped to identify the transition temperatures for all phases. Fig. 5 shows the integrated GIWAXS patterns as a function of temperature during heating up and cooling down. As a result, the transition temperatures decrease with an increasing Bromium content and are in accordance with theoretical calculations.

These findings and experimental confirmations help in the design and the processing of solar cell materials, and this example has demonstrated, that fast phase diagram studies are feasible with a lab-based setup.

White-beam Imaging

Driven by X-ray tomoscopy, time-resolved tomography, activities at the BESSY II and SLS synchrotron sources [10-12] and the high-flux potential of the Excillum sources, the MetalJet devices and the experimental equipment brings further X-ray imaging opportunities to the user community. The radiographic measurements are conducted with the original cone beam geometry provided by the sources and without primary beam optics.
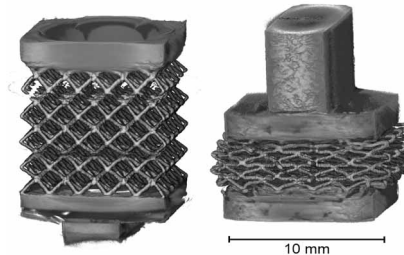
Figure 6: A tomographic reconstruction of an additive-manufactured steel sample.

The photon energies of up to 160 keV allow for the investigation of thicker components and denser materials. The use of the full white beam spectrum gives rise to fast measurements with short acquisition times. Fig. 6, for example, shows the tomographic reconstruction of an additive-manufactured test specimen made of steel in the original and in a compressed state.
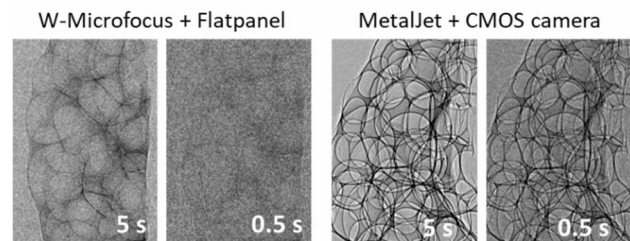
Figure 7: Radiographic images of soft matter foams [13] with different contrast and exposure times measured with a conventional tungsten microfocus tube and a flat panel detector (left) as well as with a MetalJet at 70 kV and the CMOS camera (right).

Depending on the right choice of the available detectors fast measurements of soft matter materials are also feasible within short time ranges – especially in the energy regime of the very intense Ga-Ka emission line. The detectors' energy sensitivity varies with their sensor material and leads to different image contrasts [13] such as shown in Fig. 7.

FURTHER DEVELOPMENTS & UPGRADE ACTIVITIES

The above-mentioned applications and methods are constantly being advanced. For the imaging option a new Photonics camera with 4.5 µm pixel size and a 15 µm-thick scintillator has been purchased and will be tested with the

aim to achieve higher spatial resolution for imaging experiments.

A setup for parallel white beam X-ray diffraction and imaging experiments has been realized at the BESSY II synchrotron beamline EDDI [14]. The potential of the MetalJet sources and the available equipment at HZB are currently aiming at a similar approach to make such a method available in decentralized labs.

HZB has further invested in Excillum's latest development – the MetalJet E1+. The new X-ray source uses the same technique of a liquid anode material, but with a total power of 1000 W. The source will extend the HZB activities and the throughput of applications.

CONCLUSION

The MetalJet sources and the HZB equipment described herein demonstrate a wide range of applications to be investigated with hard X-rays by academic users as well as for industrial research in the field of material science. Measurements of energy-resolved residual stress depth-gradients are feasible within complex geometry such as components with boreholes and with information depth comparable to experiments at synchrotron beamlines. Likewise, long-term experiments can be conducted without the restriction of limited beamtime. The high X-ray flux in combination with appropriate measurement and detection methods allows for in-situ investigation which have had been performed earlier at synchrotrons.

The installation, operation, and maintenance of the MetalJet sources are accompanied by higher complexity as compared to conventional X-ray tubes. The need for a 24/7 setup constantly providing high-flux X-rays over a long period requires careful handling of the devices and planning of service intervals. The new equipment at HZB is available to external user and will further bridge the gap between high-flux and high-energy synchrotron photons and conventional desktop-like low-flux X-ray tubes.

REFERENCES

[1] M. Wansleben *et al.*, "Photon flux determination of a liquid-metal jet X-ray source by means of photon scattering," *J. Anal. At. Spectrom.*, vol. 34, no. 7, pp. 1497–1502, 2019. doi: 10.1039/C9JA00127A

[2] V. Hauk, *Structural and Residual Stress Analysis by Nondestructive Methods: Evaluation - Application - Assessment*. Amsterdam: Elsevier Sience, 1997.

[3] E. Macherauch and P. Müller, "Das sin2psi-Verfahren der röntgenographischen Spannungsmessung," *Z. Angew. Phys.*, vol. 13, pp. 305–312, 1961.

[4] H. Ruppersberg, I. Detemple, and J. Krier, "Evaluation of strongly non-linear surface-stress fields σxx(z) and σyy(z) from diffraction experiments," *Phys. Status Solidi*, vol. 116, no. 2, pp. 681–687, Dec. 1989. doi:10.1002/PSSA.2211160226

[5] C. Genzel, "Formalism for the evaluation of strongly non-linear surface stress fields by X-ray diffraction performed in the scattering vector mode," *Phys. Status Solidi*, vol. 146, no. 2, pp. 629–637, Dec. 1994. doi:10.1002/PSSA.2211460208

[6] C. Genzel, I. A. Denks, J. Gibmeier, M. Klaus, and G. Wagener, "The materials science synchrotron beamline EDDI for energy-dispersive diffraction analysis," *Nucl. Instrum. Methods Phys. Res., Sect. A.*, vol. 578, no. 1, pp. 23–33, Jul. 2007. doi:10.1016/j.nima.2007.05.209

[7] M. Klaus and F. Garcia-Moreno, "The 7T-MPW-EDDI beamline at BESSY II," *J. Large-scale Res. Facil. JLSRF*, vol. 2, Jan. 2016. doi:10.17815/jlsrf-2-63

[8] C. Genzel, M. Meixner, D. Apel, M. Boin, and M. Klaus, "Nondestructive residual stress depth profile analysis at the inner surface of small boreholes using energy-dispersive diffraction under laboratory conditions," *J. Appl. Crystallogr.*, vol. 54, no. 1, pp. 32–41, Feb. 2021. doi:10.1107/S1600576720014508

[9] H. Nässtrom *et al.*, "Dependence of phase transitions on halide ratio in inorganic CsPb(Br x I 1− x) 3 perovskite thin films obtained from high-throughput experimentation," *J. Mater. Chem. A*, vol. 8, no. 43, pp. 22626–22631, 2020. doi:10.1039/D0TA08067E

[10] F. García-Moreno, P. H. Kamm, T. R. Neu, and J. Banhart, "Time-resolved in situ tomography for the analysis of evolving metal-foam granulates," *J. Synchrotron Radiat.*, vol. 25, no. 5. Wiley-Blackwell, pp. 1505–1508, Sep. 01, 2018. doi:10.1107/S1600577518008949

[11] F. García-Moreno *et al.*, "Using X-ray tomoscopy to explore the dynamics of foaming metal," *Nat. Commun.*, vol. 10, no. 1, p. 3762, Dec. 2019. doi:10.1038/s41467-019-11521-1

[12] F. García-Moreno *et al.*, "Tomoscopy: Time-Resolved Tomography for Dynamic Processes in Materials," *Adv. Mater.*, vol. 33, no. 45, p. 2104659, Nov. 2021. doi:10.1002/ADMA.202104659

[13] C. Jiménez *et al.*, "Possibilities for In-Situ Imaging of Metallic and Polymeric Foams using Laboratory Liquid Metal Jet and Microfocus X-Ray Sources," in *Metfoam, 9th Int. Conf. on Porous Metals and Metallic Foams*, 2015. doi:10.13140/RG.2.1.3563.9281

[14] C. Jiménez *et al.*, "Simultaneous X-ray radioscopy/tomography and energy-dispersive diffraction applied to liquid aluminium alloy foams," *J. Synchrotron Radiat.*, vol. 25, no. 6, pp. 1790–1796, Nov. 2018. doi:10.1107/S1600577518011657

MULTI-FELOs DRIVEN BY A COMMON ELECTRON BEAM

C.-Y. Tsai*, Huazhong University of Science and Technology, Wuhan, China
Y. Zhang†, Thomas Jefferson National Accelerator Facility, Newport News, VA, USA

Abstract

Generating a free-electron laser (FEL) requires a high-brightness electron beam. To produce multiple FELs, the linac beam must be shared to enable one beam driving an undulator. This leads to a reduced average current and compromised FEL performance. Recently, a concept of multiple FELs driven by one electron beam was proposed, which enables reduction of equipment and improvement of productivity. We present here a simulation study based on an extended 1-D FEL oscillator model to demonstrate this concept. The system consists of two FEL oscillators arranged side-by-side and one electron beam passing through them. As such, the second, downstream oscillator is driven by bunches already been used once, while the first oscillator always receives fresh bunches from the linac. The study shows lasing could be achieved for both oscillators, their radiation intensities at saturation are comparable, thus meet needs of users. The concept also enables a potential application using a circulator ring such that an oscillator can be driven alternately by fresh linac bunches and from used bunches in the circulator ring. Extending the concept to cases of more than two FEL oscillators driven by one beam is also explored.

CONCEPT OF THE SCHEME

In 1984 Colella and Lucio [1] proposed the feasibility of a low-gain FELO emitting at 2 ~ 3 Å using silicon single crystal diffraction around a right angle. With significant advance in accelerator technologies over the past 40 years, an electron beam with multi-GeV energy, multi-pC bunch charge, lower than 1 μm of the normalized emittance, and smaller than 10^{-4} of the energy spread can now be produced. In 2008 K.-J. Kim et al. [2] re-evaluated the idea and proposed using an FEL oscillator mode based on a high-repetition rate ERL-SRF and GeV electron beam to produce coherent radiation at 1 Å. Currently, the FEL community is actively investing in the development of x-ray FELO construction.

XFELO is a small-gain FEL, its undulator is much shorter compared to those used for SASE-like single-pass FELs, thus the radiation fields are built up slowly through many rounds in the optical cavity. Therefore, it is expected that the backreactions, namely interaction of the radiation fields on electrons, are usually much weaker, at least before the radiation fields reach saturation, and likely so after. As a consequence, perturbation on electrons, i.e., distortion of bunch phase space distribution, over each pass of individual short undulator is relatively small. This fact suggests that these lightly used bunches might be undegraded enough for driving next XFELOs in serial [3]. With proper design beam

---
* jcytsai@hust.edu.cn
† yzhang@jlab.org

parameters, the electron bunches could be reused multiple times before being extracted and sent to beam dump. There will be a small reduction of gain for used bunches due to backreactions, but that could be compensated by lower losses in the optical cavity and it may also take more rounds of the light pulse to grow in the optical cavity. Eventually the radiation fields will reach a similar level of laser intensity at saturation, since the latter is determined by a balance of gain in undulator and combined loss of reflective crystal mirrors and radiation outcoupling.

MODEL DESCRIPTION

In this paper, we use a simple two-XFELO system to illustrate the concept, similar to the model used in Ref. [4]. The FELOs are arranged side-by-side as shown in Fig. 1. The driving electron beam from the source and SRF linac passes through undulators of the two XFELOs while interacting with and amplifying the radiation fields in both undulators. The spent electron bunch is extracted and goes to a beam dumper. At meantime, the next fresh bunch from the SRF linac enters the dual undulator system.
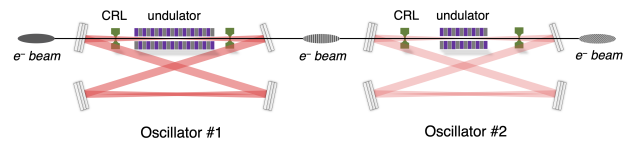
Figure 1: Conceptual schematic layout for the two-oscillator scheme. Bragg mirrors, consisting of three high-reflectivity mirrors and one mirror used for outcoupling, and two Be compound refractive lenses (CRLs) used for focusing are employed to form the oscillator. This design allows two independent users to conduct experiments.

The overall performance of the two x-ray FEL oscillators in serial is analyzed using an extended 1-D FEL model

$$\frac{d\theta_j}{d\tau} = p_j, \quad \frac{dp_j}{d\tau} = -\left(Ae^{i\theta_j} + c.c.\right), \quad \frac{dA}{d\tau} = \left\langle e^{-i\theta_j}\right\rangle + i\delta A \quad (1)$$

where τ is the scaled time along the undulator $\tau = 2\omega_u \rho t$, $\omega_u = c\beta_z k_u$, β_z is the longitudinal electron velocity along the undulator, $k_u = 2\pi/\lambda_u$ with λ_u the undulator period. The Pierce parameter $\rho = \left[\frac{1}{\gamma_r^3}\frac{I_b}{I_A}\frac{K^2[JJ]^2}{32\pi}\frac{\lambda_u^2}{2\pi\sigma_\perp^2}\right]^{\frac{1}{3}}$ with $[JJ] = J_0(\chi) - J_1(\chi), \chi = \frac{K^2}{4+2K^2}, K \approx 0.934\lambda_u[\text{cm}]B_u[\text{T}], J_{0,1}$ being the 0th and 1st order of Bessel functions of the first kind. Here (θ_j, p_j) for $j = 1, 2, ..., N_e$ are the j-th electron phase space coordinate, with $p_j = \frac{\gamma_j - \gamma_r}{\rho\gamma_r}$. γ_r is the resonant electron energy (in unit of electron rest mass energy) satisfying the resonance condition $\lambda_r = \frac{\lambda_u}{2\gamma_r^2}\left(1 + \frac{K^2}{2}\right), \omega_r = ck_r,$

$k_r = 2\pi/\lambda_r$. $A = |A|e^{i\phi}$ is the complex scaled slow-varying radiation field amplitude with $|A|^2 = \frac{\epsilon_0 |E|^2}{\rho n_e \gamma_r m c^2}$. The energy detuning parameter $\delta \equiv \frac{\langle\gamma_j\rangle_0 - \gamma_r}{\rho\gamma_r}$ where $\langle\gamma_j\rangle_0 = \langle\gamma_j\rangle (\tau = 0)$ and $b = \langle e^{-i\theta_j}\rangle$ is the bunching factor.

On each pass, within the undulator the electrons and radiation field evolve according to the above set of equations. To quantify the gain process inside the undulator, we define the following *gain parameter* [5] as $G \equiv 4\pi\rho N_u$. Note that this parameter is *not exactly* equivalent to the more familiar *intensity gain*, defined as $\mathcal{G} \equiv \left(|A_G|^2 - |A_0|^2\right)/|A_0|^2$, with $A_G = A(\tau = G)$ and $A_0 = A(\tau = 0)$. The radiation power outside the cavity, with the outcoupling coefficient α, can be related to the electron beam power as $P_{\text{out}} = \rho|A|^2 P_b \frac{\alpha}{\mathcal{L}}$, with $\mathcal{L} = \alpha + (1 - R)$ the total loss and α the outcoupling ratio [6]. To simulate two oscillators connected in serial, we extend the 1-D FEL model as follows. The subscript 1 is denoted to the quantities of the first oscillator and the subscript 2 to those of the second downstream oscillator. First, the electron beam will leave the first oscillator and serve the second one after transport $\theta_j \to \theta_j + k R_{56}\rho_1 p_j$, with $k R_{56} = 2\pi R_{56}/\lambda_r$ and R_{56} being the momentum compaction factor between the oscillators. For simplicity here we assume the in-between section is isochronous ($k R_{56} = 0$). The radiation fields will bounce back and forth inside the cavity. In the 1-D model, the first-oscillator radiation field on next pass is updated by $A_{1,0}^{(n+1)} = r_1 A_{1,G}^{(n)}$ with $r_1 = \sqrt{R_1}$, assuming the reflectivity coefficient is real, same applies for the second oscillator. The superscript (n) means the n-th pass.

For $n = 0$, the initial shot noise is given by $A_0 = \sqrt{\frac{6\sqrt{\pi}\rho}{N_\lambda \sqrt{\ln \frac{N_\lambda}{\rho}}}}$ with $N_\lambda = \frac{I_{\text{peak}}\lambda_r}{ce}$ and I_{peak} the peak current [5].

Because the second oscillator adopts the used electron beam, we have to include the effects due to beam quality degradation. While 3-D FEL model is much more complicated, there is one way to approximately take into account the effects of beam transverse finite emittance ϵ_{nx} and energy spread $\sigma_{\delta0}$, so that we can simply replace ρ by ρ_{eff} [6], i.e., $\rho_{\text{eff}} = \rho \left(F_{\text{inh}} F_f\right)^{\frac{1}{3}}$, with $F_{\text{inh}} = \frac{1}{\left(1+1.7\mu_\gamma^2\right)\left(1+\mu_\epsilon^2\right)}$, $\mu_\gamma = 4N_u\sigma_\delta$, $\mu_\epsilon = \frac{\sqrt{2}N_u\epsilon_{nx}K}{\lambda_u\left(1+\frac{K^2}{2}\right)}$ and $F_f = \frac{1}{1+\left(\frac{\bar{w}}{2\sigma_b}\right)^2}$. Here $\sigma_b \approx \sqrt{\beta_{x,\text{ave}}\frac{\epsilon_{nx}}{\gamma_0}}$, using $\beta_{x,\text{ave}}^{\text{opt}} \approx \frac{L_u}{2\pi}$. $\bar{w}$ is the mean optical mode size, assuming $\bar{w} = \sqrt{2}\sigma_b$. When considering the effect of energy spread on the second oscillator, $\mu_\gamma \leq 1$. The effect of transverse emittance is relatively small ($\mu_\epsilon \approx 10^{-3}$) and can be neglected here.

When the electron beam enters the second oscillator, we should re-normalize the electron beam parameters according to the design of the second oscillator, i.e., $p_j (\tau_2 = 0) = \left(\frac{\rho_{\text{eff},1}}{\rho_{\text{eff},2}}\right) p_j (\tau_1 = G_1)$.

The Pierce parameter of the second oscillator should be updated every pass, because the input beam properties may change significantly before the first oscillator reaches an equilibrium. This update $\rho_2 \to \rho_{\text{eff},2}$ is necessary in order to take into account the change of beam properties, especially the beam energy spread. The Pierce parameter reflects how effective the electron-radiation interaction will be; that is, $\rho_{\text{eff},2}$ is a function of both the second oscillator and of the first oscillator. The insightful idea of using a common electron beam to drive multiple x-ray FELOs really appreciates the re-use of Pierce parameter. When the FELO reaches equilibrium for each oscillator, the intensity gain $\mathcal{G}$ and loss are balanced, and the radiation field in the oscillator no longer increases or decreases when the electron beam passes through it. For simplicity, the average net energy loss of the electron beam in the first oscillator is ignored here, assuming it can be compensated by proper detuning in the second oscillator. We use the standard numerical methods to solve Eqs. (1). Here we note that the above 1-D FELO oscillator model makes the steady-state approximation. Time-dependent and 3-D effects will inevitably degrade the design performance.

Table 1: Electron Beam and Undulator Parameters

Name	Value	Unit
Resonant electron energy E	5.7	GeV
Bunch length, rms σ_t	0.55	ps
Bunch charge Q	380	pC
Bunch current I_b	300	A
Normalized emittance ϵ_{nx}	0.3	μm
Energy spread σ_δ	0.3×10^{-4}	
Undulator period λ_u	1.88	cm
No. of undulator periods N_{u1}, N_{u2}	100/68	
Undulator parameter K	1.5	
Resonant wavelength λ_r	1.6	Å
Round-trip reflectivity R	0.8	
Outcoupling ratio α	0.04	

MAIN RESULTS

We use a set of preliminary design to demonstrate the feasibility of the proposed scheme. The linac beam and undulator parameters are summarized in Table 1. Because the number of undulator periods in our design is relatively small, a pulse length of 0.55 ps is required to ensure that the bandwidth of the undulator radiation generated per pass is narrow enough to fall within the range of the Bragg crystal mirror's reflectivity curve. Assuming a crystal reflectivity width of approximately 10^{-6}, a pulse length of 0.55 ps can accommodate approximately 10^6 wavelengths. Therefore, the rms pulse length of 0.55 ps can generate undulator radiation with a bandwidth sufficient to meet the requirements.

Despite the shorter undulator, we utilize the high bunch charge of the CEBAF injector and a higher current to achieve a proper single-pass gain G, which is approximately 1.4 for the first oscillator and 0.8 for the second oscillator. The value of G should be chosen to be moderate, not too small to compensate for round-trip losses, but also avoiding being too large, which could cause the electron beam to undergo synchrotron oscillations in the undulator and saturate too

early. For the second oscillator, it is recommended to appropriately reduce the number of undulator periods because the driving electron beam is already microbunched. The total reflectivity (or round-trip reflectivity) is approximately $0.96^3 \times 0.997^2 \times 0.92 = 0.8$ for the two XFELOs.

Due to the operation of the oscillator in the low-gain regime, the initial energy offset of p_0 depends on the initial detune δ and the resonant energy. For the first oscillator, we apply the well-known result of $p_0 = \delta \approx 2.6/G_1$, where $G_1 = 4\pi\rho_1 N_{u1}$. For the second oscillator, although the electron beam may have been a bit modulated, we still choose $p_0 = \delta \approx 2.6/G_2$, where $G_2 = 4\pi\rho_2 N_{u2}$, as an acceptable choice for a preliminary feasibility demonstration. We calculate the rms energy spread before entering the second oscillator each turn and then update the Pierce parameter of the second oscillator each turn.

Figure 2 presents the numerical results based on Table 1. The output power of the first FELO is consistent with the rough estimate formula $P_{\text{sat}} \approx \frac{\alpha P_{\text{beam}}}{N_u(1-R)} \approx 3.4$ GW. In this example, the gain parameters $G_{1,2}$ of the two oscillators are 1.42 and 0.96, respectively, corresponding to the initial Pierce parameters of approximately 1.126×10^{-3}. The ideal detune is chosen the way just mentioned. We note that the choice of G is recommended to be between 1 and 1.5. If it is too small, the efficiency may be poor; if it is too large, the undulator may quickly saturate. For simplicity, we assume that the in-between transport section between the two FELOs is isochronous, i.e., $kR_{56} = 0$.
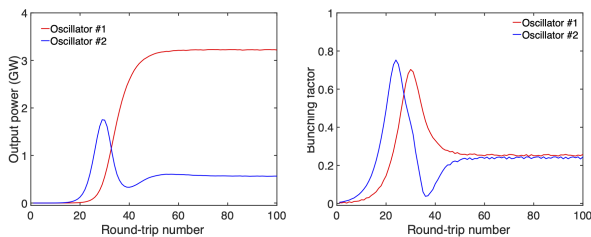

Figure 2: Evolution of output power (left) and bunching factor (right) for the two oscillators.

In the early stage of the first oscillator reaching saturation, the radiation field amplitude in the oscillator starts to accumulate with each passing round, modulating the electron beam. Note that the electron beam is modulated by the radiation field before the radiation field amplitude is enhanced. As seen in Fig. 2, the bunching factor on the right panel grows earlier than the radiation field amplitude on the left. Moreover, for the almost (but not exactly) optimal electron beam modulation in the first oscillator, it reaches the optimum bunching factor after passing through a certain distance of the undulator in the second oscillator. This explains why the peak of the blue line in Fig. 2(b) always occurs before the peak of the red line.

Figure 3 displays the evolution of the energy spread at the entrance of the second oscillator and the modified Pierce parameter $\rho_{\text{eff},2}$ of the second oscillator. It can be observed that the energy spread of the electron beam inevitably in-

creases after driving the first oscillator, leading to a decrease in $\rho_{\text{eff},2}$. It has been conventionally believed that the excitation efficiency would be compromised when the energy spread exceeds the Pierce parameter. However, when the first oscillator saturates, the disturbance on the electron beam is relieved, and most of the electrons located at the bottom of the potential well can still be effectively modulated in the second oscillator, despite the overall energy spread exceeding the Pierce parameter. Since only a fraction of the electrons in the second oscillator participate in lasing, the output power is relatively lower, but still appreciable.
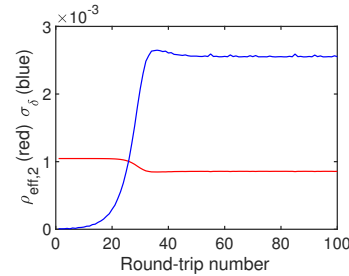

Figure 3: Beam energy spread and Pierce parameter at the entrance of the second oscillator.

SUMMARY AND DISCUSSION

We have investigated the feasibility of using the same electron beam to drive two XFELOs by extending the 1-D FEL analysis, which builds on the previous work of driving a single XFELO. The proposed scheme assumes a high repetition rate, high brightness electron beam with the energy of 5.7 GeV and the peak current of 300 A, to drive two fully coherent hard x-ray lasers, each with the light pulse length comparable to the electron bunch duration 0.5 ps. The two x-ray lasers have output powers of approximately 3.2 GW and 0.6 GW, peak brightnesses of 2×10^{32} and 0.4×10^{32} photons/sec/(mm mr)$^2 \times$(0.1% BW), and average brightnesses of 10^{27} and 2×10^{26} photons/sec/(mm mr)$^2 \times$(0.1% BW), respectively, assuming a repetition rate of 0.462 MHz [3]. This proposal has practical value, as it reduces the cost for both the facility and each user to some extent, while providing peak brightness comparable to that of the currently under construction LCLS-II, and average brightness at the same photon energy comparable or even higher by about an order of magnitude than the planned LCLS-II-HE [7]. The concept also enables a potential application using a circulator ring such that an oscillator can be driven alternately by fresh linac bunches and from used bunches in the circulator ring. In such operation, the high-brightness electron beam traversing multiple bends may induce the coherent synchrotron radiation (CSR) effect [8, 9] or other possibly undesired collective effects [10], which are beyond the scope of this analysis but will be considered in future studies. The present analysis is mostly based on numerical simulations. Further analytical [11] or semi-analytical analysis is necessary to better understand the performance of downstream oscillators in a serial FELO configuration.

ACKNOWLEDGMENTS

REFERENCES

[1] R. Colella and A. Luccio, "Proposal for a free electron laser in the x-ray region", *Opt. Commun.*, vol. 50, p. 41, 1984. doi:10.1016/0030-4018(84)90009-9

[2] K.-J. Kim, Y. Shvyd'ko, and S. Reiche, "A Proposal for an x-ray free-electron laser oscillator with an energy-recovery linac", *Phys. Rev. Lett.*, vol. 100, p. 244802, 2008. doi:10.1103/PhysRevLett.100.244802

[3] Y. Zhang *et al.*, "Future ring photon source at Jefferson Lab", unpublished.

[4] G. Dattoli *et al.*, "The tandem FEL dynamic behavior", *IEEE J. Quantum Electron*, vol. 31, p.1584, 1995. doi:10.1109/3.400416

[5] B. W. J. McNeil, "A simple model of the free-electron-laser oscillator from low into high gain", *Nucl. Instrum. Methods Phys. Res., Sect. A*, vol. 296, p. 388, 1990. doi:10.1016/0168-9002(90)91237-6

[6] B. W. J. McNeil, D. J. Dunning, G. R. M. Robb, and N. Thompson, "FELO: A One-Dimensional Time-Dependent FEL Oscillator Code", in *Proc. FEL'06*, Berlin, Germany, Aug.-Sep. 2006, paper MOPPH011, pp. 59–62.

[7] T.O. Raubenheimer, "LCLS-II-HE conceptual design report," SLAC National Lab., CA, USA, Tech. Rep. SLAC-R-1098, 2018.

[8] R. Li and C.-Y. Tsai, "CSR impedances for non-ultrarelativistic neams", in *Proc. 6th Int. Particle Accelerator Conf. (IPAC'15)*, Richmond, Virginia, USA, May 2015, pp. 709-712. doi:10.18429/JACoW-IPAC2015-MOPMN004

[9] R. Li and C.-Y. Tsai, "Entrance and exit CSR impedance for non-ultrarelativistic beams", in *Proc. 8th Int. Particle Accelerator Conf. (IPAC'17)*, Copenhagen, Denmark, May 2017, pp. 3214-3217. doi:10.18429/JACoW-IPAC2017-WEPIK113

[10] C.-Y. Tsai *et al.*, "Theoretical formulation of phase space microbunching instability in the presence of intrabeam scattering for single-pass or recirculation accelerators", *Phys. Rev. Accel. Beams*, vol. 23, p. 124401, 2020. doi:10.1103/PhysRevAccelBeams.23.124401

[11] C.-Y. Tsai *et al.*, "Analytical study of higher harmonic bunching and matrix formalism in linear high-gain free-electron laser model", *Nucl. Instrum. Methods Phys. Res., Sect. A*, vol. 1048, p. 167974, 2023. doi:10.1016/j.nima.2022.167974

HEAT LOAD AND RADIATION PULSE OF CORRUGATED STRUCTURE AT SHINE FACILITY

Junjie Guo[1], Duan Gu[2], Zhen Wang[2], Meng Zhang[2,*], Qiang Gu[2], Haixiao Deng[2,†]

[1]Zhangjiang laboratory, Shanghai, China

[2]Shanghai Advanced Research Institute, Chinese Academy of Sciences, Shanghai, China

Abstract

Corrugated structure modules are being proposed for installation after the end of the linac and before the undulator regions of SHINE facility, where it has been used for energy chirp control and as a fast kicker for two color operation of the FEL.When ultra-relativistic bunch of electrons passing through corrugated structure will generate strong wakefield, we find most of the wake power lost by the beam is radiated out to the sides of the corrugated structure in the form of THz waves, and the remaining part casue Joule heating load on the corrugated structure wall. In this paper, we estimate the Joule power loss and radiation pulse power of the corrugated structure in SHINE facility.

INTRODUCTION

In order to eliminate residual energy chirps in superconducting linear accelerator (linac)-driven X-ray FEL facilities, there are currently two traditional ways: one involves exploiting the resistive-wall wakefield induced by the beam pipe; another option, which involves running the beam 'off-crest,' is inefficient and costly, especially for ultrashort bunches in FEL facilities [1]. As far as SHINE linac [2, 3] is concerned, the electron bunch length is less than 10 lm after passing through the second bunch compressor. Therefore, the beam energy spread cannot be effectively compensated by chirping the RF phase of the main linac. The SHINE linac adopts the corrugated structure (Fig. 2) to dechirp the energy spread [4].

When an ultra-short electron bunch passing through very small gap corrugated structure, strong wake effect be generated to manipulate the phase space of the electron bunch. Most of the power radiates out along the opening of the corrugated structure, and only a small amount of power causes a heat load on the metal wall of the corrugated structure. The paper is organized as follows. In the 2nd section, the main parameters of corrugated structure in Shine Facility are introduced briefly, and the distribution wake power lost by the beam through the corrugated structure is also described. In the 3rd section total wake power lost by beam are investigated, and the heat load and distribution of the corrugated structure are calculated by numerical simulation. The 4th section introduces a radiation pulse generated by corrugated structure, and calculate the centre frequency and length of the pulse at the outlet of the corrugated structure, as well as the length of the required cooling water pipe. The final section summarizes the results and significance of this paper.

---

* zhangmeng@sari.ac.cn

† denghx@sari.ac.cn

THE DISTRIBUTION OF WAKE POWER LOST BY THE BEAM THROUGH THE CORRUGATED STRUCTURE

Schematic diagram of the corrugated structure is shown in the Fig. 1, the red ellipse indicates the on-axis bunch. The transverse directions are denoted x and y, with x pointing into the page, and z represents the longitudinal direction. The corrugated structure parameters are the radius a, the depth h, the period p and the gap width t. The parameters for the corrugated structure and for the exciting bunch to be used in simulations presented below are given in Table 1
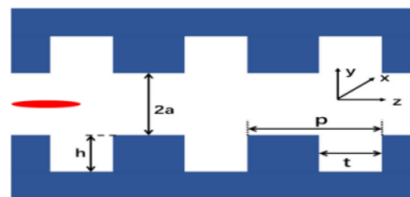
Figure 1: Schematic diagram of the corrugated structure.

Table 1: Parameters for the corrugated structure and for the exciting bunch.

Parameter	Value
Plate length, L (m)	2
Gap, a (mm)	0.7
Depth, h (mm)	0.5
Period, p (mm)	0.5
Longitudinal gap, t (mm)	0.25
Width, w(mm)	12.7
W/2a	9.07
Energy, E (GeV)	8
Charge per bunch, Q (pC)	100
Beam current, I (kA)	1.5
Bunch length (RMS), σ (μm)	5

According to the previous work by K. Bane [5–7], in a flat corrugated structure of a finite length, the wakefield energy loss experienced by a relativistic beam of charged particles is partly absorbed in the walls as Joule heat and partly generates a THz pulse that leaves the structure just behind the driving particle. The energy per unit length lost by the beam to the wake is then given by the sum:

$$P_w = P_h + (P_{\text{rad}})_z + (P_{\text{rad}})_x \qquad (1)$$

with P_h the energy generating Joule heating in the metal walls, $(P_{rad})_z$ the energy in the THz pulse that leaves the end of the structure following the driving particle, and $(P_{rad})_x$ the energy radiating out the sides of the structure.

Through the comparison of analytical estimate and numerical simulation [5], $P_h/P_w \sim 10\%$, $(P_{rad})_z/P_w \sim 80\%$, $(P_{rad})_x/P_w \sim 10\%$, when the beam pass through the two-plate flat corrugated structure on the axis and w/2a = 8.5.

HEAT LOAD OF CORRUGATED STRUCTURE

We firstly need to calculate the total wake power lost by beam $Pw = Q^2 * K_{loss} * f_{rep}$, where K_{loss} is loss factor. For a bunch with Gaussian distribution, the loss factor [8–10] is given by

$$K_{loss} = \int \lambda(s)w_z(s)ds \qquad (2)$$

Where $w_z(s)$ is short-range, point charge wake of a beam on the axis of a flat corrugated structure:

$$w_z(s) = \frac{\pi^2}{4a^2}e^{-\sqrt{s/s_0}} \qquad (3)$$

with $s_0 = 9a^2t/\left[8\pi\alpha(t/p)^2p^2\right]$ and $\alpha(x) \approx 1 - 0.465\sqrt{x} - 0.07x$. For the parameters of table 1, the loss factor and wake power lost by beam is obtained : K_{loss} = 20.44 (KV/pC/m), P_w = 204.4073 W/m, P_h = 20.4 W/m.

When the beam passes close to the side of the corrugated structure, the short-range, point charge wake of a beam passing by a single plate of a flat dechirper at offset b is

$$w_z(s) = \frac{1}{b^2}e^{-\sqrt{s/s_{0l}}}, \qquad (4)$$

with $s_{0l} = 2b^2t/\left(\pi\alpha^2p^2\right)$ and $\alpha \approx 1 - 0.465\sqrt{(t/p)} - 0.07(t/p))$. According to Ref. [5], $P_h/P_w \sim 5.5\%$ when the beam passes close to the side of the corrugated structure. For the parameters of table 1, the loss factor and wake power lost by beam at offset b = 0.25 mm is obtained : K_{loss} = 58.067 (KV/pC/m), P_w = 580.67 W/m, P_h = 31.93 W/m.

THE DISTRIBUTION OF HEAT LOAD IN CORRUGATED STRUCTURE

Although the heat load of the corrugated structure accounts for only 10 % of the total wake power, for the 2 m corrugated structure of shine, the heat load has reached 40 W. With such a high heat load, a water cooling system on the corrugated structure is required. Considering the layout of the water cooling system on the surface of the corrugated structure, we need to know the heat load distribution of the corrugated structure. Simulations were carried out using the numerical simulation software CST [11] to simulate the power of each section by dividing the corrugated structure into n sections of the same length and material along the Z-direction. The 2-metre long corrugated structure is divided into six pieces of the same length and material, and the simulation results show that the Joule power of each piece is the

same, as shown in Fig. 2, which implies that the heat load inside the corrugated structure is uniformly distributed.
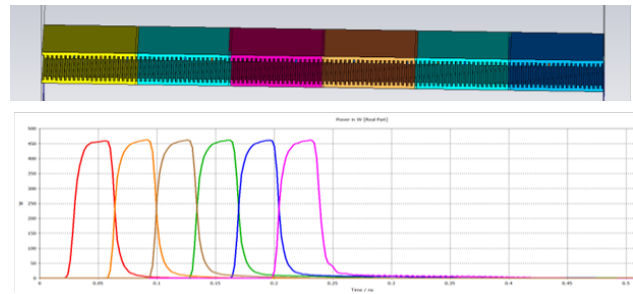

Figure 2: The 2-metre long corrugated structure is divided into six pieces of the same length and material with different colours(Top plot), Joule power of six piece (Bottom plot).

A RADIATION PULSE GENERATED BY CORRUGATED STRUCTURE

When the beam pass through the corrugated structure, most of the power will be in the form of radiated pulse that continue to propagate forward along the Z-axis with the direction of the beam. Outside the corrugated structure is a beam pipe with a radius of 35 mm, into which the radiation pulses generated by the beam after the exit of the pleated structure are spread. Now we need to know how far the radiation pulse spreads to this beam pipe and how long the cooling water pipe needs to be arranged. Therefore, a corrugated structure with Table 1 parameters was modelled with a 35 mm diameter beam pipe using CST simulation, as shown in Fig. 3(a).
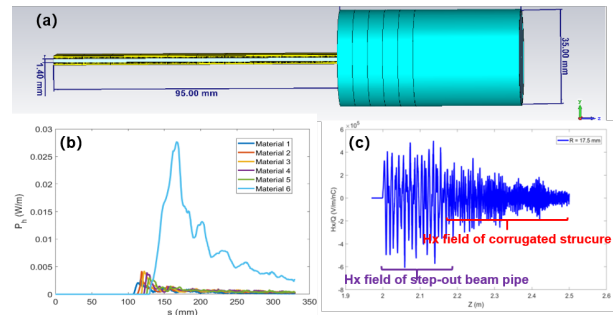
Figure 3: (a): the geometry of corrugated Structure and step-out 35 mm diameter beam pipe which created by CST; (b):Joule power calculations of 35 mm diameter beam pipe obtained by CST time-domain simulation; (c):Hx field calculation 35 mm diameter geometry by ECHO simulation [12].

Figure 3(b) shows the simulation results of Joule heating for a 35 mm diameter beam pipe where the beam pipe is divided into six sections, the first five being of the same 10 mm length and material. It can be noticed that the Joule heating of the first five sections shows the heat load of the first section rising first, the heat load of the middle three sections is uniform, and the heat load of the fifth section begins to decay. Figure 3(c) shows the Hx field distribution on the wall

of the beam pipe simulated with ECHO [12], and it is clear that the Hx field consists of the Hx field due to the corrugated structure immediately following the beam and the Hx field due to the step-out structure of the beam pipe. Combining the results of Fig. 3, we can conclude that the pulses radiated by the beam through the corrugated structure to the step-out structure of the beam pipe spread over a distance of roughly 30-50 cm, and thus require cooling-water system of about 50 cm.

Next, a Fourier analysis of the radiation pulse caused by the folded structure was done, yielding a pulse with a frequency around 100 GHz, as shown in Fig. 4. According to $f = kc/\sqrt{(ah)}$, the parameter a or h can be reduced to obtain 1 THz.
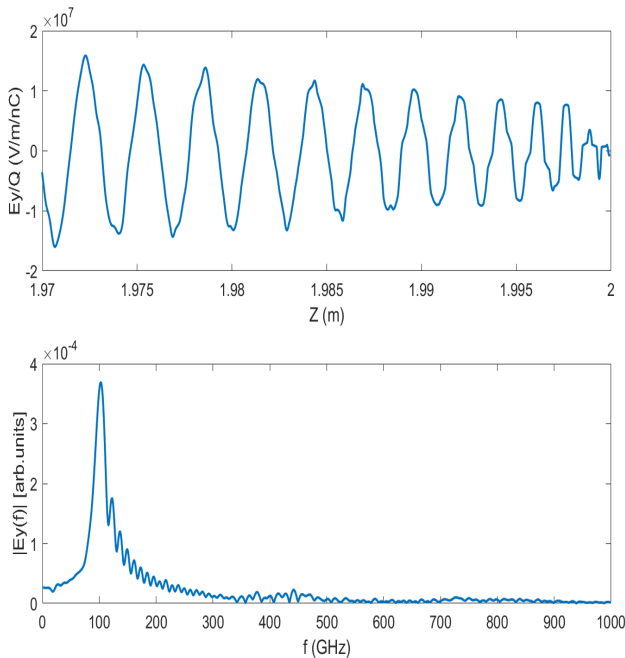

Figure 4: The radial electric field Ey at y = 0.7 mm at a monitor located at the downstream end of corrugated strucure as function of time t (Top plot);The absolute value of the Fourier transform of this function, Ey, as function of frequency (Bottom plot) .

CONCLUSION

We have performed heat load calculations and radiation pulse for the SHINE corrugated structure in this paper. We find that 204 W/m (80%) most of the wake power lost by the beam is radiated out to the sides of SHINE corrugated structure, and only 20.4 W/m (10%) a small part of the power caused heat load of metal wall. Most of the wake power is radiated downstream along the Z-axis of corrugated structure in the form of pulse, which can cause severe downstream heat load effect. Calculations and analyses show that the radiation

pulses generated by the corrugated structure will spread on the walls of the 35 mm radius circular beam pipe 30 ~50 cm from the exit of the pleated structure, so additional cooling water pipes are required. At the same time, in order to avoid damage to downstream components from radiation pulses, the photon absorber might be considered to be mounted to the downstream.

REFERENCES

[1] K. L. F. Bane and G. Stupakov, "Corrugated pipe as a beam dechirper", *Nucl. Instrum. Methods A*, vol. 690, pp. 106–110, 2012. doi:10.2172/1038704

[2] Jun-Jie Guo, Qiang Gu, Meng Zhang, Zhen Wang, Jian-Hao Tan, "Power losses caused by longitudinal HOMs in 1.3 GHz cryomodule of SHINE", *Nucl. Sci. Tech.*, vol. 30, no. 7, p. 573, 2019. doi:10.1007/s41365-019-0628-9

[3] Junjie Guo, Qiang Gu, Jianhao Tan and Zhen Wang, "Power losses caused by longitudinal HOMs in 3.9 GHz SHINE cryomodule", *J. Phys.: Conf. Ser.*, vol. 1350. p.012116 2019, doi:10.1088/1742-6596/1350/1/012116

[4] Y. W. Gong, M. Zhang, W. J. Fan, *et al.*, "Beam performance of the SHINE dechirper", *Nucl. Sci. Tech.*, vol. 32, p. 29, 2021. doi:10.1007/s41365-021-00860-8

[5] K. Bane, G. Stupakov, and E. Gjonaj, "Joule heating in a flat dechirper", *Phys. Rev. Accel. Beams*, vol. 20, no. 5, p. 054403, 2017. doi:10.1103/PhysRevAccelBeams.20.054403

[6] K. L. F. Bane and G. Stupakov, "Terahertz radiation from a pipe with small corrugations", *Nucl. Instrum. Methods in Phys. Res., Sect. A*, vol. 677, pp. 67–73, 2012. doi:10.1016/j.nima.2012.02.028

[7] K. Bane, G. Stupakov, S. Antipov, *et al.*, "Measurements of terahertz radiation generated using a metallic, corrugated pipe", *Nucl. Instr. Methods Phys. Res., Sect. A*, vol. 844, p. 121–128, 2017. doi:10.1016/j.nima.2016.11.041

[8] L. Palumbo, V. G. Vaccaro, and M. Zobov, "Wake fields and impedance", in *Proc. CAS CERN Accelerator School*, CERN, Geneva, Switzerland, Rep. CERN 95-06, pp. 331–390, 1995. doi:10.48550/arXiv.physics/0309023

[9] T. Weiland and R. Wanzenberg, "Wake fields and impedances", in *Frontiers of Particle Beams: Intensity Limitations*, Springer, pp. 39–79, 1992.

[10] M. Dohlus and R. Wanzenberg, "An introduction to wake fields and impedances", in *Proc. CAS-CERN Accelerator School on Intensity Limitations in Particle Beams*, Geneva, Switzerland, Nov. 2015. CERN Yellow Reports, vol. 3, 2017. doi:10.23730/CYRSP-2017-003.15

[11] CST Studio Suite 2011, Computer Simulation Technology AG, 2014.

[12] I. Zagorodnov, "Wakefield code ECHO", presented at the Second Topical Workshop on Instabilities, Impedance and Collective Effects (TWIICE2), Abingdon, Oxon., UK, Feb. 2016

UPGRADES OF HIGH LEVEL APPLICATIONS AT SHANGHAI SOFT X-RAY FEL FACILITY

H. Luo, D. Gu, Z. Wang, K.-Q. Zhang, T. Liu,
Shanghai Advanced Research Institute (SARI-CAS) Chinese Academy of Sciences, Shanghai, China

Abstract

The Shanghai soft X-ray free-electron laser(SXFEL) facility has made significant progress in recent years with the rapid, upgraded iterations of the high level software, including but not limited to energy matching, orbit feedback and load, beam optimization, etc. These tools are key components in operation and experiment of free electron laser facility. Some key applications are presented in this paper.

INTRODUCTION

Based on the principle of the free-electron lasers [1], the output of the free-electron laser drifts and fluctuates with the instability of the electron beam energy, the instability of the angle and position of the electron beam, the instability of each device due to environmental changes, and the instability of the device itself. A stable electron beam is the key to obtaining a stable free-electron laser. The commissioning of the e SXFEL user facility started in spring of 2021 [2], and in 2023, the SXFEL facility has been opened to the public and user experimental research has been carried out, placing a higher demand on the stability of the entire device. In order to maintain the long-term high-quality operation of the SXFEL facility, with the joint efforts of our team, through the interaction and access of applications and hardware systems implemented by the Experimental Physics and Industrial Control System (EPICS [3]), we developed and put online a set of processed beam-tuning high-level applications (SXFEL HLA) written in python language in 2022. Based on these applications, we can achieve rapid recovery and long-term stable operation of SXFEL, and practice has confirmed the reliability and sophistication of this software, which has played an indispensable role in the tuning and operation of SXFEL. This article will report on some key applications. The main window of SXFEL's high level applications is shown in Fig. 1
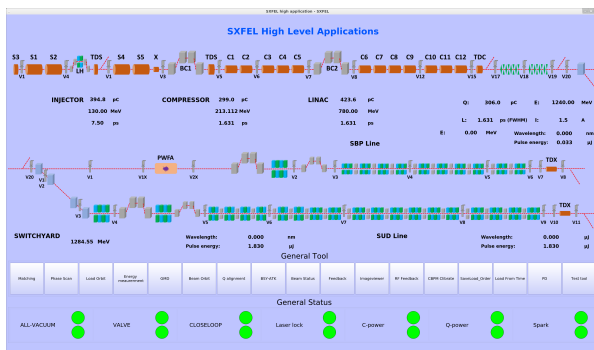
Figure 1: The main window of SXFEL's high level applications.

MATCHING

We all know that the focusing of the electron beam in the transverse direction is crucial to the stability of the beam and the amplification of the FEL, and through theoretical simulation calculations, we can get the target reasonable focusing state of the beam. Therefore, in order to get the focusing state we want, we design and develop the Matching module (shown in Fig. 2), which divides the matching of the beam into linear section, beam distribution section, SBP oscillator section and SUD oscillator section. The Energy Measurement module measures the energy and Emittance Measurement module measures the Twiss parameters, and the measurement results are placed in the background through the soft IOC for the Matching module to call. The inverse solution of the inlet parameters by this Twiss parameter is then solved by the theoretical simulation method of the Matching module.
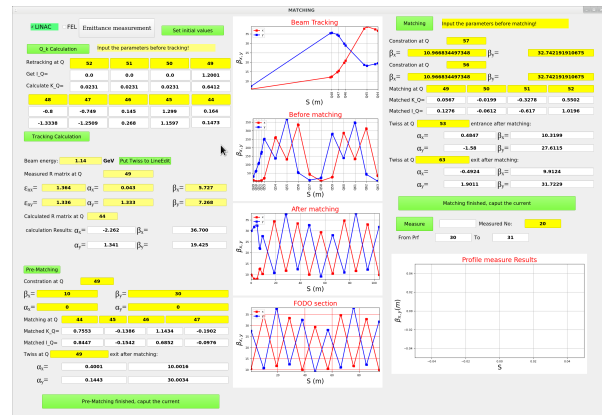
Figure 2: Matching Window.

ORBIT CONTROL MODULES

Combined with these applications: LoadOrbit, Orbit, ImageViewer and BPM Calibrate, orbit feedback (shown in Fig. 3) is one of the key feedbacks to maintain high quality and long term stability of the SXFEL facility. For the consideration of the flexibility, ease of use and reliability of the application, we have linked the orbit feedback with the newly developed tuning tools: LoadOrbit, Orbit, ImageViewer and BPM Calibrate.

The BPM may drift in phase with changes in ambient temperature and humidity. In order to ensure the accuracy of the beam position measured by the BPM, we regularly use the high-level application BPM Calibrate (shown in Fig. 4) to detect and calibrate the phase drift of the BPM, which
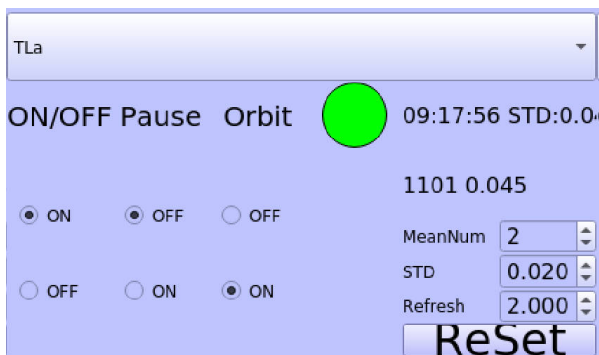
Figure 3: Orbit Feedback Window
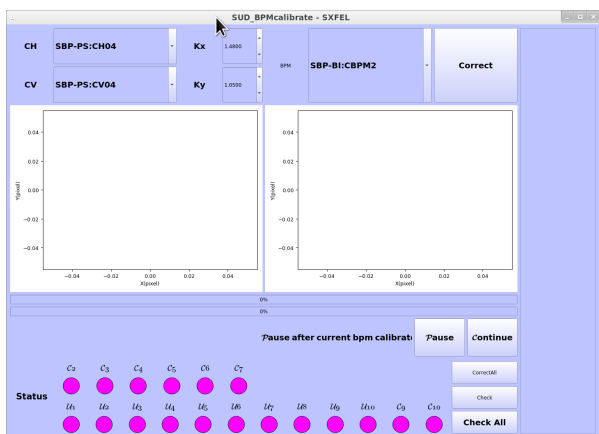
Figure 4: BPMCalibrate Window

Figure 5: Orbit Window

Figure 6: ImageViewer Window

provides a guarantee for SXFEL to carry out subsequent work related to the orbit.

SXFEL runs two oscillator lines SBP and SUD at the same time, according to the real distance of the BPM, we have developed a new version of high level application of Orbit (shown in Fig. 5) to display the beam's current orbit and jitter in real time, however, a BPM may be faulty during the work, and the position of the beam current can't be detected, so we have added the ByPass function for each BPM in the application. In the commissioning process of the FEL, the beam orbits and jitters are of great significance, and the light-emitting orbit saved by the Orbit app can not only be used as the reference orbit for the next FEL commissioning, but also be used for another high level app LoadOrbit to recover the orbit, and at the same time, it can be used as the target orbit for the orbit feedback.

Obviously, due to the dithering nature of the FEL, the beam orbit saved manually may not be exactly the light-emitting orbit, for this reason, SXFEL in the optimisation of the FEL as well as the commissioning process, the high level application of ImageViewer (shown in Fig. 6) will save the orbit corresponding to the value of the integral value that is larger than the previous one, as a more reliable light-emitting beam orbit.

The stability of the beam is different at different positions. In order to make the orbit feedback based on the response

matrix algorithm more flexible and reliable, we have segmented the orbit and assigned the BPM and corrector to each segment as the default pairing for the response matrix measurements in the high level application LoadOrbit (shown in Fig. 7). Depending on the current state of the beam, the commissioner is free to replace the pairing in the application Loadorbit with the one he thinks is better, and the orbit feedback application and the LoadOrbit application default to use the latest measured response matrix. orbit Feedback and LoadOrbit are two high level applications that share a common set of segmentation, response matrix, and light-emitting orbit data, and LoadOrbit supports kicking the orbit to a light-emitting orbit or other custom orbit.

With the LoadOrbit module, we can easily find the radiated light and even restore it to the supplied light level by simple commissioning. In addition to expert commissioning for restoration, we can also use the General FEL Opimize module for algorithmic optimisation to restore the FEL. However, there is no guarantee that the commissioning and optimisation process is going in exactly the right direction, and using the application may also lead to worse results. As a result of this, we can use the LoadFromTime module (shown in Fig. 8) to restore the magnet parameters to the time we set by setting a historical time.

67th ICFA Adv. Beam Dyn. Workshop Future Light Sources
FLS2023, Luzern, Switzerland
JACoW Publishing
ISBN: 978-3-95450-224-0
ISSN: 2673-7035
doi:10.18429/JACoW-FLS2023-WE4P12
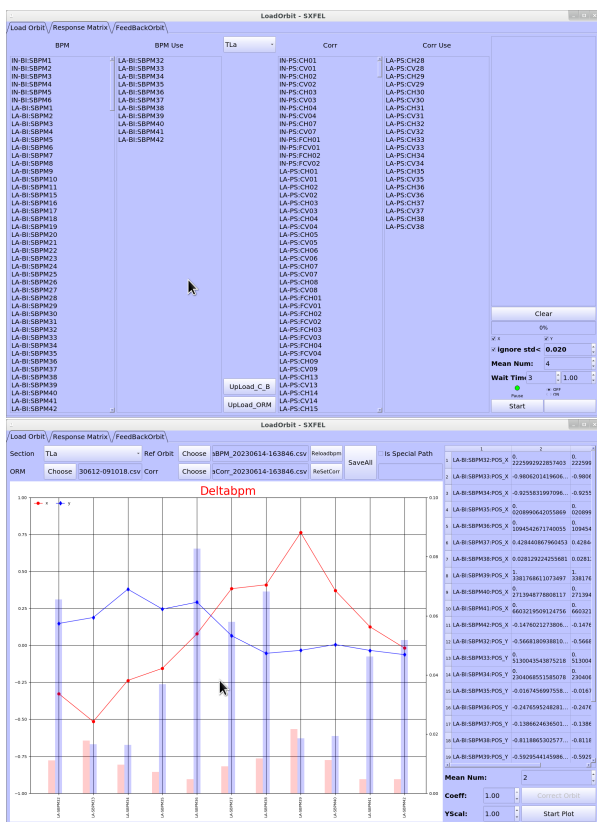
Figure 7: LoadOrbit Window
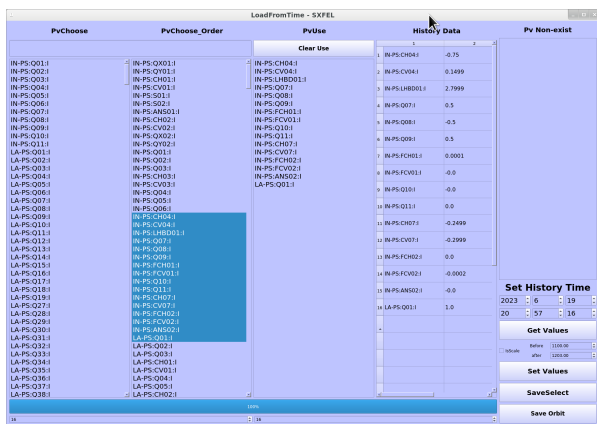
Figure 8: LoadFromTime Window

FEEDBACK

The output of the free electron laser will drift and fluctuate with the instability of the electron beam energy, the instability of the angle and position of the electron beam, the instability of each device due to environmental changes, and the instability of the device itself. Stable electron beam quality is the key to obtaining a stable free electron laser, and

is also an important factor in maintaining the long-term high-quality operation of the SXFEL facility. In order to maintain the stable operation of the free electron laser facility, based on the response matrix algorithm:

$$\triangle Y = M^{-1} \cdot \triangle X \qquad (1)$$

SXFEL has a lot of feedbacks (shown in Fig. 9), including feedbacks on charge, beam energy, beam length, injector energy, drive laser position, BAM and orbit, which play a vital role in the stable light supply of SXFEL.

Figure 9: FeedBack Window

SUMMARY

After repeated verification in practice, the high-level application of SXFEL HLA has been able to achieve efficient and standardised FEL commissioning, which plays an important role in SXFEL's rapid commissioning recovery and long-term stable, high-quality running.

ACKNOWLEDGEMENTS

REFERENCES

[1] R. Bonifacio, C. Pellegrini, L. M. Narducci, "Collective instabilities and high-gain regime in a free electron laser", *Optics Communications*, vol. 50, no. 6, pp. 373–378, 1984. doi:10.1016/0030-4018(84)90105-6

[2] Liu, Bo, Chao Feng, Duan Gu *et al.*, "The SXFEL upgrade: from test facility to user facility" *Applied Sciences*, vol. 12, no. 1, 176, 2022. doi:10.3390/app12010176

[3] https://epics-controls.org/

PHYSICS DESIGN AND BEAM DYNAMICS OPTIMIZATION OF THE SHINE ACCELERATOR

Duan Gu*, Xuan Li, Zhen Wang, Meng Zhang,

Shanghai Advanced Research Institute, Chinese Academy of Sciences, Shanghai, China

Abstract

Shanghai HIgh Repetition Rate X-ray Free Electron Laser and Extreme Light Facility (SHINE) is a hard X-ray FEL facility which is driven by a 1.3 km superconducting Linac, aims to provide high repetition rate pulses up to 1 MHz. We present the physics design of the SHINE accelerator and considerations of beam dynamics optimizations. Start-to-end simulation results show that, a high brightness electron beam with over 1500 A quasi-flat-top current can be attained which fully meet the requirements of FEL lines. Furthermore, the design of bypass line is discussed.

INTRODUCTION

In recent years, high-repetition-rate XFEL based on superconducting Linac draws increasing attention due to its unique capability of providing Ångström performance at high average power. Several facilities have been built in the world such as EXFEL [1] and LCLS-II [2].

The SHINE facility currently under construction at SARI aims to deliver FEL pulses between 0.4 keV and 25 keV, which enable research in various fields, including biology, chemistry, and material science. To meet the requirements of FEL performance, the Linac of SHINE should provide 8 GeV high brightness electron beam up to 1 MHz, with normalized emittance of < 0.5 μm at nominal 100 pC and peak current over 1500 A. In this paper, we describe the beam dynamics studies including longitudinal working point optimization and lattice matching. Then the detailed start to end simulation results are presented. Finally, the design of a bypass line design is also discussed.

LAYOUT AND MAIN PARAMETERS

At the end of the injector, the bunch length is 1 mm and the peak current is about 10 A. In the Linac section, the beam will be further accelerated to 8 GeV in four acceleration sections (L1, L2, L3 and L4) which consist of seventy-five 1.3 GHz superconducting cryomodules. To obtain the desired peak current, the beam will be compressed to over 1500 A in two bunch compression sections (BC1 and BC2). In addition, two 3.9 GHz cryomodules are used before BC1 as linearizer.

Two beam collimation sections (COL0 and COL1) are placed before L1 and after BC1 to remove undesired stray electrons which can make the serious damages to the sensitive part of the machine. And a metallic corrugated structure section (DCP) is designed to cancel the linear chirp

* gud@sari.ac.cn

of the electron beam at the exit of the Linac. The transverse magnetic focusing is carefully optimized to minimize the emittance dilution due to transverse wakes, momentum dispersion and coherent synchrotron radiation in bending magnets. The layout of the SHINE Linac is shown in Fig. 1. The main parameters are listed in Table 1.

Table 1: Main parameters of the SHINE Linac

Parameter	Value	Unit
Beam energy	8	GeV
Bunch charge	100	pC
Max Rep-rate	1	MHz
Projected emittance	<0.5	μm
Peak current	>1500	A
Sliced energy spread	<0.015	%,rms

LONGITUDINAL BEAM DYNAMICS

The electron beam is generated by a VHF gun and then accelerated to about 100MeV then the beam is transported in to the L1 (two cryomodules) where the beam will be accelerated to 326 MeV. Off-crest acceleration creates the desired correlated energy spread along the bunch in the first compressor BC1. The two 3.9 GHz cryomodules tuned at the 3rd harmonic of 1.3 GHz frequency is placed right before the first bunch compressor BC1. The function of the structure is to provide cubic corrections of the correlated momentum distribution along the bunch in presence of the sinusoidal RF time curvature and the magnetic compressors non-linearity, which also decelerates the beam to 265 MeV. The beam is compressed in BC1 from 1 mm to 0.13 mm, the peak current is increased to 80 A accordingly.

The L2 structure (18 cryomodules) is located between the first and second bunch compressor, which accelerates the electron beam from 265 MeV to 2.2 GeV. It also provides the residual energy chirp needed for the second compressor BC2, in which the peak current will be further increased to over 1500 A. After BC2 the beam is accelerated to its final 8 GeV energy in the L3 and L4 structure (54 cryomodules).

The X-ray FEL refers using an electron beam with low emittance, small energy spread and a high core current to generate coherent radiation through the undulator, it's critical to avoid the single-spike or double-horn type beam current distribution. the final beam current profile is preferred to be a so-called "flat-top" distribution [3].

Meanwhile, the beam jitters including peak current, beam energy and beam arrival time also sensitive to longitudinal parameters such as RF settings. To achieve this, the
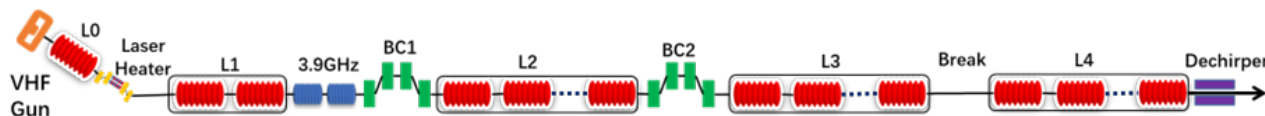
Figure 1: Schematic layout of the SHINE Linac.

working point of the Linac should be chosen carefully including the RF cavity amplitudes and phases of each accelerating section and configuration of bunch compressors. So, a global longitudinal beam dynamics optimization is studied. Some physical objectives including maximum core peak current and the flatness of beam current distribution need to be optimized simultaneously. By integrating the advanced Multi-Objective Evolutionary Algorithm (MOEA) into LiTrack code, the Linac beam dynamics optimization is demonstrated to be effective and reliable. Fig. 2 shows the Pareto front of the two objectives (length of flat-top current profile and peak current). As an illustration, we choose a solution from these Pareto front solutions where the peak current is around 1500 A.
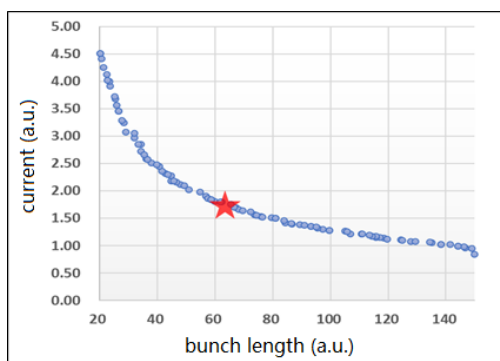

Figure 2: Pareto front of Linac longitudinal optimization.

During the optimization of Linac working point, take into consideration of potential failure of super conducting cavities, 6% of total cavities are not powered but available as a spare (one cavity for every two modules). The accelerating gradient of cryomodule is set to be 16 MV/m for TESLA-style 1.3 GHz cavities, the maximum beam energy can reach 8.7 GeV, which has near 10% energy margin. Fig. 3 shows the optimal longitudinal phase and beam current profile.
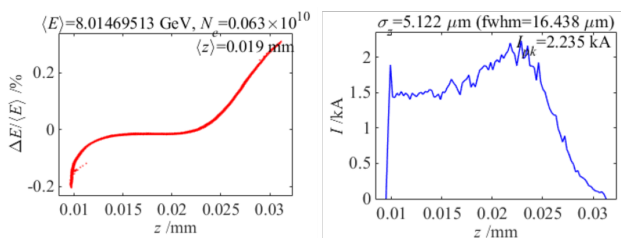
Figure 3: Longitudinal phase space (left) and beam current profile at the exit of Linac through MOEA.

TRANSVERSE BEAM DYNAMICS

The main considerations in the optics design are to minimize the transverse emittance dilution due to components misalignment during beam transportation and CSR effect during bunch length compression, and finally, to transport the electron beam to the undulator section.

The focusing lattice along the main Linac sections (L1, L2, L3 and L4) is set using cold quadrupole magnets at the end of each CM. Some warm quadrupoles are used around the bunch compressors to match the Twiss functions. The Linac lattice was studied and designed in detail using the computer code MAD and Elegant for particle tracking as shown in Fig. 4.
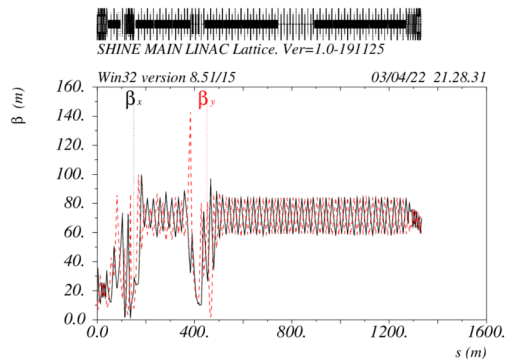
Figure 4: Beta function of the SHINE main Linac.

START TO END SIMULATIONS

Start to End (S2E) simulation including the injector and Linac, bunch compression is performed for the designed optics. In the injector section, the beam energy is relatively low where the space charge dominates, so the space charge tracking code Astra was adopted. When the beam energy is higher in Linac, the collective effects became main issue, the 6D particle tracking code ELEGANT was used, and further confirmed with IMPACT-Z.

As shown in Fig. 5, the results of longitudinal phase space at Linac exit from two codes are compared. Fig. 6 shows the final current distribution, sliced energy spread and normalized sliced emittance.

LINAC BYPASS LINE

Take in consideration of generating soft x-ray FEL lasing with relative low energy, we propose a design that extract the beam from BREAK section between L3 and L4. With this bypass line, the 4–5 GeV beam can be delivered into FEL-II undulator.

67th ICFA Adv. Beam Dyn. Workshop Future Light Sources

ISBN: 978–3–95450–224–0

FLS2023, Luzern, Switzerland

ISSN: 2673-7035

JACoW Publishing

doi:10.18429/JACoW-FLS2023-WE4P13
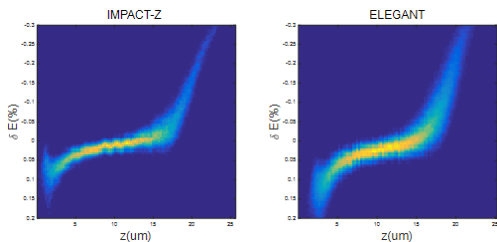
Figure 5: Phase space at exit of Linac with IMPACT-Z (left) and ELEGANT (right).
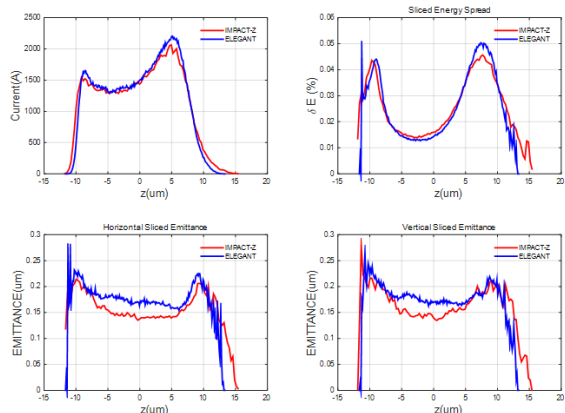
Figure 6: Final current distribution, sliced energy spread and normalized sliced emittance.

There are some requirements of bypass line:

- beam horizontal offset is 1.85 m.
- the beam is kicked out vertically, then bend back to original height.
- considering the CSR effect, the phase advance between BX2 and BX3 is close to π.
- dispersion in both planes should be cancelled, which means $R_{16}, R_{26}, R_{36}, R_{46} = 0$, and $\eta_{xy} = 0, \eta'_{xy} = 0$.
- no additional compression, which means $R_{56} = 0$.

In vertical plane, the beam separation is provided by 5 fast kickers, a set of three vertical septum and deflection by two quadrupoles. In horizontal plane, a set of four septum is used. At the exit of bypass line, a small chicane is adopted for R_{56} compensation. The layout of bypass line is shown in Fig. 7.

Start to end simulation based on layout described above shows that after the bypass line, all the requirements are fulfilled and there is no significant emittance growth or micro bunching instability observed. The beam parameters at entrance and exit of bypass line are shown in Fig. 8. The longitudinal phase space distribution is shown in Fig. 9.
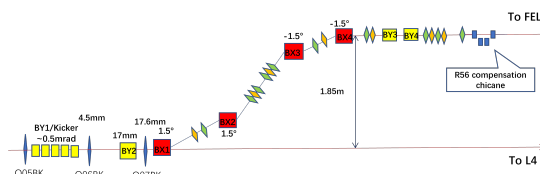
Figure 7: Layout of the bypass line.
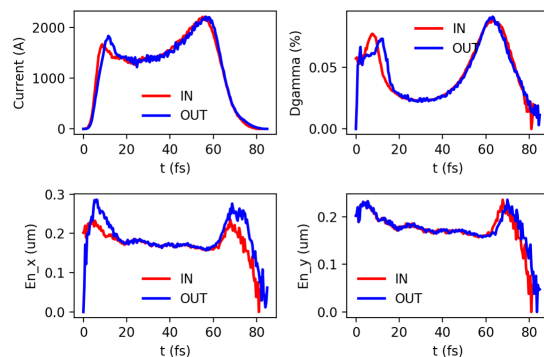
Figure 8: Comparison of beam parameters at entrance and exit of the bypass line.
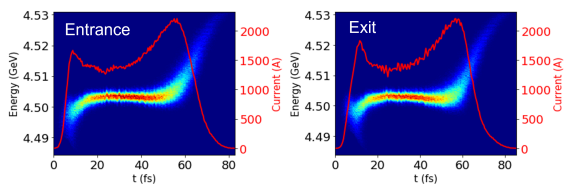
Figure 9: Phase space at entrance (left) and exit (right) of the bypass line.

CONCLUSION

In this paper, we present the physics design and optimization of the SHINE Linac. The start to end simulation results illustrate an 8 GeV high brightness beam with 1500 A flattop current distribution as expected. The bypass line based on fast kicker and septum enables the beam extraction at lower energy.

ACKNOWLEDGEMENTS

REFERENCES

[1] M. Altarelli, *et al.*, "The European x-ray free electron laser: Toward an ultra-bright high repetition-rate x-ray source", in *High Power Laser Science and Engineering*, vol. 3, p. e18, 2015. doi:10.1017/hpl.2015.17

[2] J. N. Galayda, *et al.*, "The Linac Coherent Light Source-II Project", in *Proc. IPAC'14*, Dresden, Germany, Jun. 2014, pp. 935–937. doi:10.18429/JACoW-IPAC2014-TUOCA01

[3] Zihan Zhu, *et al.*, "Inhibition of current-spike formation based on longitudinal phase space manipulation for high-repetition-rate X-ray FEL", in *Nucl. Instrum. Methods Phys. Res., Sect. A*, vol. 1026, p. 166172, 2022. doi:10.1016/j.nima.2021.166172

LAYOUT OF THE UNDULATOR-TO-DUMP LINE AT THE SHINE*

Tao Liu†, Zheng Qi, Zhangfeng Gao, Si Chen, Haixiao Deng, Bo Liu
Shanghai Advanced Research Institute, Chinese Academy of Sciences, Shanghai, China
Nanshun Huang, Zhangjiang Lab, Chinese Academy of Sciences, Shanghai, China

Abstract

The Shanghai HIgh repetitioN rate XFEL and Extreme light Facility as the first hard X-ray free-electron laser (FEL) facility in China, is currently under construction in the Zhangjiang area, Shanghai. It aims to deliver X-ray covering photon energy range from 0.4 to 25 keV, with electron beam power up to 800 kW. Downstream of the undulator line, the beam transport design of the undulator-to-dump line is critical which is mainly used for realization of FEL diagnostics based on transverse deflecting structure and beam absorption in the dump. In this manuscript we describe the current layout of this system.

INTRODUCTION

In recent years, the high-repetition-rate XFEL based on superconducting LINAC attracts increasing attention due to its ability to generate radiation pulse with higher average brightness and plays an important role in many research fields. The Shanghai HIgh repetitioN rate XFEL and Extreme light facility (SHINE) aims to join the exclusive XFEL club as one of the most advanced user facilities by delivering femtosecond X-ray pulses with high repetition rate. It is designed to deliver photons between 0.4 keV and 25 keV with repetition rate up to 1 MHz using a superconducting LINAC [1,2]. It consists of an 8 GeV continuous-wave superconducting RF Linac, 3 undulator lines, 3 X-ray beamlines and 10 experimental stations in phase-I, which has started its construction from April of 2018.

For the nominal parameters of the electron beam output at the SHINE, the operating beam energy is 8 GeV with repetition rate up 1 MHz and bunch charge of 100 pC, so that it would provide electron with beam power up to 800 kW. According to the current design requirements, there are four beam dump lines at 8 GeV, as shown in Fig. 1. One of them is the linac-to-dump (L2D) line, which is mainly used for the beam energy and energy spread measurements. The other three are the undulator-to-dump (U2D) lines, ensuring that the electron beam transport into and absorbed in the dumps. To take the commissioning and operation into consideration at the SHINE, the design of the three U2D lines mainly meets the following three basic abilities. The first one is absorbing electron beam power up to 800 kW in the dump, the second one is measurements of the incoming beam en-
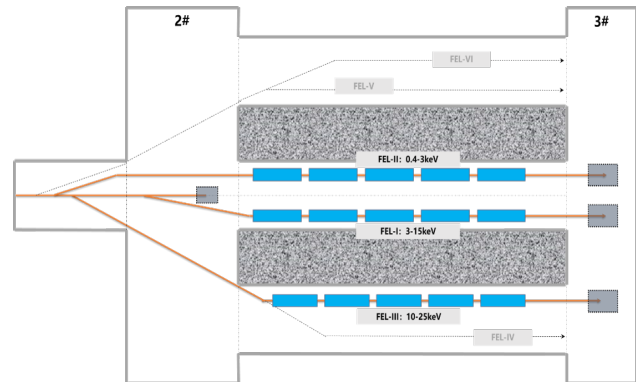
Figure 1: Undulator system at the SHINE. Main dump is located at the beam switch-yard system in the tunnel 2♯, and the other three dumps are at the downstream of the undulator systems in the tunnel 3♯.

ergy and energy spread, and the third one is measuring the longitudinal phase space of the electron beam. It is worth mentioning that beam expanding and rotation are required for dump absorbing, together with beam longitudinal phase space measurement online. The total length of the U2D line is approximately 90 m, in which the distance from the analyzing magnets to the dump is less than 20 m. This means the beam transport design of the line is great challenging under severe spatial constraints. Besides, the magnets are also specified to operate within the beam energy range from 4.0 to 10.0 GeV.

LAYOUT OF THE U2D LINE

The electron beam specifications at the SHINE are given in Table 1. On the one hand, due to such high beam power up to 800 kW, the specific dump design is essential associated with beam expanding and rotation. On the other hand, beam longitudinal phase space measurement should be operated online and the time resolution should be the femtosecond level since the bunch length is about 30 fs.

The design of the three U2D lines are very similar with slightly different arrangement in details. Therefore, we take the U2D line of the FEL-I undulator beamline as an example. As shown in Fig. 2, the scheme design is as follows:

1) A set of quadrupoles is required upstream of the transverse deflection structure (TDS) to match the beta functions of the electron beam at the center of the TDS, which aims to achieve ultra-high time resolution.

2) X-band TDS introducing transverse-to-longitudinal correlation is to present the longitudinal phase space of the electron beam and the measurement of several related beam and FEL parameters.

Table 1: SHINE Baseline Beam Parameters

Parameter	Value	Unit
Electron beam energy	8	GeV
Sliced energy spread (rms)	0.01-0.02	%
Total charge	100	pC
Peak current	1.5	kA
Bunch length (rms)	8	μm
Transverse emittance	0.45	mm·mrad
Repetition rate	1.0	MHz

3) A small angular deflection magnet is located in front of the main analyzing bending magnets, causing the electron beam to deflect slightly towards the dump tunnel, thereby ensuring that the synchronous radiation generated by the electron beam in the main bending magnet is tilted downwards to minimize transmission to the beamline station downstream.

4) Two main bending magnets are used to deflect the electron beam to the beam dump and analyze the beam energy and energy spread.

5) A set of quadrupoles downstream of the TDS are adopted to optimize the transverse dispersion, the beam envelope and the phase advance between the TDS and the measurement point.

6) Scanning dipoles and additional quadrupoles are to rotate the beam periodically together with beam expanding in the front of the beam dump.

7) A beam dump is capable of absorbing all the power of the 800 kW electron beams.

8) Beam measurement devices such as CBPMs, SBPMs, and imaging profiles are also required to observe and measure the characteristics of the electron beam.

For our scheme, the beam is designed to be deflected vertically by 15° using two 3 m long bending magnets and a small bending magnet with a length of 0.5m. The small one has a deflection of 0.2° with 0.19 T, and therefore its synchronous radiation power is only 3% of that of the large two. During the high repetition rate operation, to achieve beam diagnosis online with repetition rate less than 50 Hz, it is necessary to operate such 50 Hz beam off axis. And matching requires a large beam size at the position of the TDS, phase advance of 90° from the TDS to the measurement point, and a small beam size at the measurement point [3]. Meanwhile, facing the problem of beam power up to 800 kW, radiation protection requires high repetition rate beams to achieve a beam expansion of 0.2 mm×2 mm at the dump entrance and rotation with scanning radius of 15 cm.
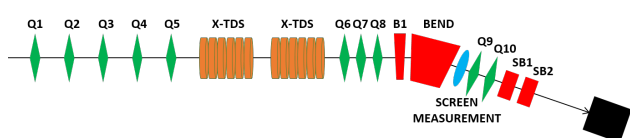
Figure 2: layout of the U2D line at the SHINE.

According to the TDS basic theory, the temporal resolution can be calculated as

$$\Delta_s = \frac{cE}{e\omega V_0} \frac{\sqrt{\varepsilon_x}}{\sqrt{\beta_x \sin \Delta\phi \cdot \gamma}} \quad (1)$$

where β_x is β function at the center of the TDS, $\sin \Delta\phi$ is the phase advance from the TDS to the measurement point. And the energy resolution can be expressed as

$$\Delta_\delta = \frac{\sqrt{\beta_y \varepsilon_y}}{\eta_y} \quad (2)$$

with η_y energy dispersion. The lattice design of the U2D line is shown in Fig. 3. The TDS phase is 1.5°, and the β functions are 400 m and 15 m at the TDS and measurement point, respectively. The phase advance from the TDS to measurement point is $\pi/2$. Therefore the time resolution of the TDS is less than 1 fs and the energy resolution is 2.4e-5, which can be used for phase space diagnostics and FEL pulse reconstruction. Besides, due to the 1.5° phase of the TDS, the horizontal deviation of the 50 Hz beam is about 9 mm far from the high repetition beam on axis, as shown in Fig. 4.
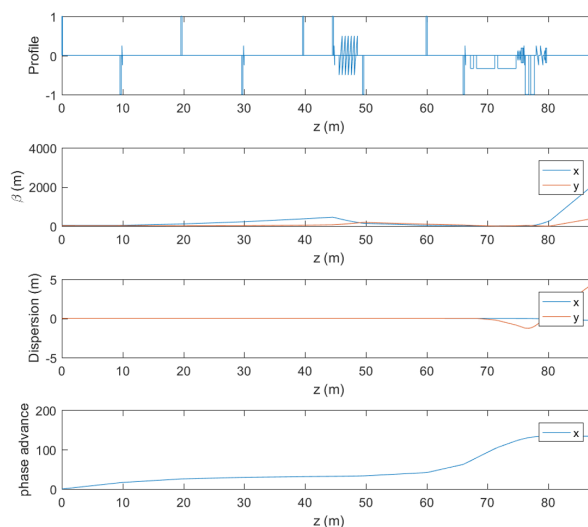
Figure 3: Lattice design of the U2D line at the SHINE, including lattice profile, β functions of x and y, y dispersion, and phase advance in the line.
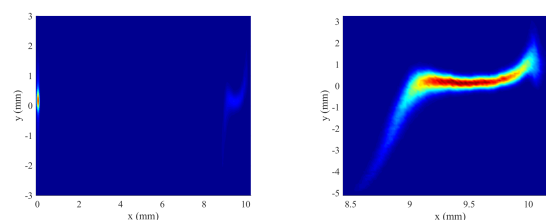
Figure 4: Beam profiles on the screen switching on/off the TDS.

To meet the requirements of dump absorbing, two quadrupoles with length of 0.6 m are arranged downstream of the measurement point, and the beam size can be expanded at 100 µm-level horizontally and vertically, and meanwhile the vertical dispersion is reserved intentionally, so that the beam size requirement of 0.2 mm × 2 mm can be achieved. The scanning dipoles in both horizontal and vertical directions with a scanning angle of 1.0° can achieve rotation with a radius of 15 cm, also meeting the needs of radiation protection. The high repetition beam profile after expanding and rotation is presented in Fig. 5, and the spot at the measurement point is also presented with a same scale as as a comparison.
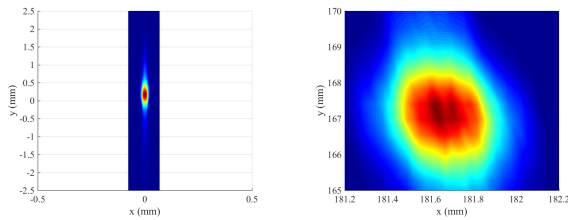
Figure 5: Beam profiles without TDS at the measurement point and the dump.

BEAM CLEAR APERTURE

According to the physical scheme design, we have provided the beam area aperture of the U2D line, as shown in Fig. 6. The top two show the beam clear apertures of the entire line in both horizontal and vertical directions, where the main beam with high repetition rate (blue) surrounds the axis center and reaches at the range of ±15 cm at the entrance of the dump, and while the horizontal distribution of the off axis beam (red) considering both off axis and phase jitter of the TDS, reaches at the range from -10 to 30 cm, which also puts additional requirements for radiation protection. The bottom two show partial enlarged views of the analysis magnets, the beam measurement point and downstream. It can be seen that the beam clear aperture inside the analysis magnet is (-10, 12) mm, and the positive horizontal side of the beam measurement point is beyond 15 mm, posing new requirements for beam measurement. The beam clear aperture at the position of the beam expanding magnets is (-10, 28) mm. The first scanning magnet performs vertical scanning, followed by horizontal scanning since the beam clear aperture of the vertical scanning position is (-10, 30) mm, and while the horizontal scanning position is beyond 30 mm. The horizontal scanning magnet can achieve larger horizontal free space to meet the beam clear area requirements. The beam clear aperture for the beam measurement area downstream of the scanning magnets will be expanded continuously, which also puts forward high requirements for beam measurement and vacuum chamber.
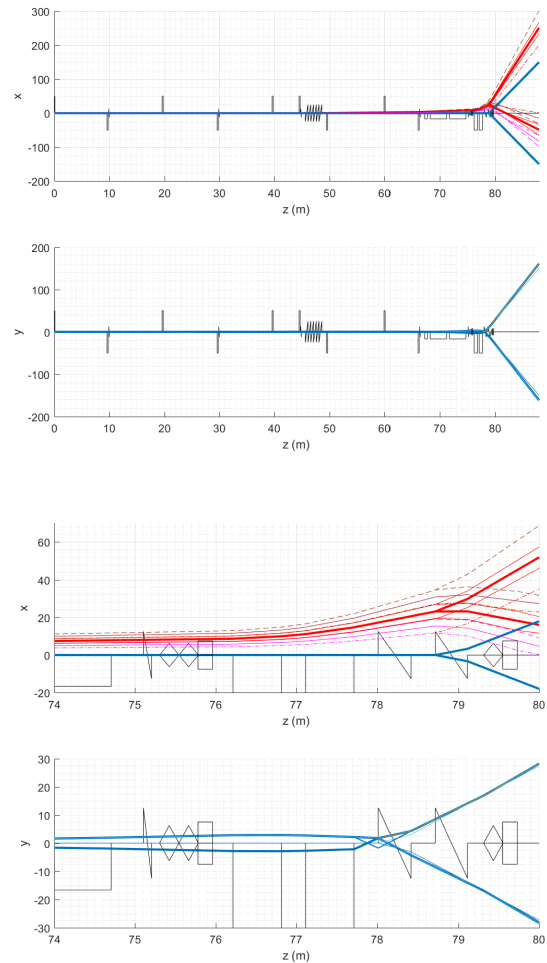
Figure 6: Beam clear aperture at the U2D line. The top two are the entire U2D line in both x and y directions. And the bottom two are the partial enlarged views for on-axis beam (blue) and off-axis beam (red).

CONCLUSION

The layout and optics design of the U2D line at the SHINE are presented in this manuscript, consisting of high precision time resolution based on the TDS, phase space diagnostics online of the 50 Hz off-axis beam, beam expanding and rotation and the corresponding beam clear aperture. The results satisfy the geometrical constraints and requirements coming from the beam dynamics, and ensures flexible operation of the system. Accompanied by the advancement of the process design of the dump, the layout will be updated through the iterative optimization.

REFERENCES

[1] Z. Y. Zhu *et al.*, "SCLF: An 8-GeV CW SCRF linac-based x-Ray FEL facility in Shanghai", in *Proc. FEL'17*, Santa Fe, NM, USA, Aug. 2017, pp. 182–184.
doi:10.18429/JACoW-FEL2017-MOP055

[2] Tao Liu *et al.*, "Status and future of the soft X-ray free-electron laser line at the SHINE", *Front. Phys.*, vol. 13, 2023. doi:10.3389/fphy.2023.1172368

[3] J. W. Yan, H. X. Deng, B. Liu, and D. Wang, "Transverse Deflecting Structure Dynamics for Time-Resolved Machine Studies of Shine", in *Proc. FEL'19*, Hamburg, Germany, Aug. 2019, pp. 632–634. doi:10.18429/JACoW-FEL2019-THP018

[4] M. Borland, "ELEGANT: A flexible SDDS-compliant code for accelerator simulation", Advanced Photon Source, Argonne National Laboratory, IL, USA, Rep. No. LS-287, 2000.

MULTICHROMATIC FREE-ELECTRON LASER GENERATION THROUGH FREQUENCY-BEATING IN A CHIRPED ELECTRON BEAM

Zheng Qi[1,*], Chao Feng[1,2]

[1]Shanghai Advanced Research Institute, Chinese Academy of Sciences, Shanghai, China

[2]University of Chinese Academy of Sciences, Beijing, China

Abstract

We propose a simple method to generate mode-locked multichromatic free-electron laser (FEL) through a longitudinal phase space frequency-beating in a chirped electron beam. Utilizing the two stage modulator-chicane setups in Shanghai Soft X-ray FEL facility, together with a chirped electron beam, we are going to imprint a frequency-beating effect into the electron beam. Hence periodic bunching trains can be formed and can be used to generate mode-locked FEL radiation pulses. Theoretical analysis and numerical simulations are given out to demonstrate the performance of the method. The results indicate that mode-locked FEL in temporal and frequency domain can be formed at the 18th harmonic of the seed laser, with the central wavelength being about 14.58 nm and the peak power over 2 GW.

INTRODUCTION

Mode locking is an essential concept and technique in conventional lasers. It's of great importance in the generation of ultrashort laser pulses and in the stable control of the laser phase. For the state-of-the-art X-ray free electron lasers, mode-locked lasing has also been proposed and pursued for the last decade [1, 2]. Mode-locked XFELs could provide new opportunities for high resolution x-ray spectroscopy and attosecond sciences. The FEL community has proposed and studied several methods for mode-locked FEL lasing. Generally mode-locked FEL lasing requires an initial energy modulation or density modulation with fixed phase relation imprinted into the electron beam. And then mode locking amplifiers with undulator and delay-chicane modules are needed for the amplification.

In this study, we propose a simple method to generate mode-locked multichromatic FEL through a longitudinal phase space frequency-beating in a chirped electron beam. The schematic layout is show in Fig 1. The layout mainly consists of two modulator-chicane setups and a radiator. The electron beam is coming from the upstream beam switchyard, and it is manipulated to have an energy chirp in the head and tail of the electron beam. Two seed lasers with identical wavelength are employed in the two modulator. The chirped electron beam first get an energy modulation in modulator-1, the chicane-1 with a relatively small dispersion will then slightly change the imprinted energy modulation wavelength since the whole electron beam has an energy chirp. The electron beam will then get an energy modulation in modulator-2, and in chicane-2 the energy modulation

* qiz@sari.ac.cn

is converted into density modulation. Through proper optimizations of the parameters, periodic bunching trains can be formed in the electron beam, and high harmonic bunching can also be formed. And then the electron beam will go through the radiator for mode-locked high-gain harmonic generation (HGHG) FEL radiation.

We will give a brief analysis of the electron beam phase space evolution in the scheme. First of all, we need to define some variables. The dimensionless energy deviation of a particle is defined as $p = (E - E_0)/\sigma_E$, where E_0 is the central energy of the electron beam and σ_E is the rms energy spread. The initial longitudinal beam distribution can be written as

$$f(p) = \frac{1}{\sqrt{2\pi}} exp(-p^2/2) \tag{1}$$

with a linear energy chirp and an energy modulation, the electron beam energy becomes

$$p_1 = p + c\frac{E_0}{\sigma_E \sigma_s} z + A_1 \sin(k_1 z) \tag{2}$$

where c is the relative linear energy chirp, A_1 is the energy modulation strength, k_1 is the wavenumber of the seed laser. After DS1, the electron longitudinal position becomes

$$z_1 = z + R_{56}^1 p_1 \sigma_E/E_0 \tag{3}$$

and the beam distribution now is

$$
\begin{aligned}
f(p, z) &= \frac{1}{\sqrt{2\pi}} exp\{-\frac{1}{2}[p - c\frac{E_0}{\sigma_E \sigma_s}(z - R_{56}^1 p\sigma_E/E_0) \\
&\quad - A_1 \sin(k_1(z - R_{56}^1 p\sigma_E/E_0))]^2\} \\
&= \frac{1}{\sqrt{2\pi}} exp\{-\frac{1}{2}[p - \frac{cE_0}{\sigma_E \sigma_s}z + cR_{56}^1 p/\sigma_s \\
&\quad - A_1 \sin(k_1 z - R_{56}^1 k_1 p\sigma_E/E_0)]^2\}
\end{aligned}
\tag{4}
$$

define $C = \frac{cE_0}{\sigma_E \sigma_s}, \xi = k_1 z, B_1 = R_{56}^1 k_1 \sigma_E/E_0$, we can simplify the formula as follows

$$
\begin{aligned}
f(p, \xi) &= \frac{1}{\sqrt{2\pi}} exp\{-\frac{1}{2}[p - C\xi/k_1 + CB_1 p/k_1 \\
&\quad - A_1 \sin(\xi - B_1 p)]^2\}
\end{aligned}
\tag{5}
$$

through the second energy modulation and the second dispersion section, the electron beam energy and the electron longitudinal positions are now

$$
\begin{aligned}
p_2 &= p_1 + A_2 \sin \xi \\
z_2 &= z_1 + R_{56}^2 p_2 \sigma_E/E_0
\end{aligned}
\tag{6}
$$
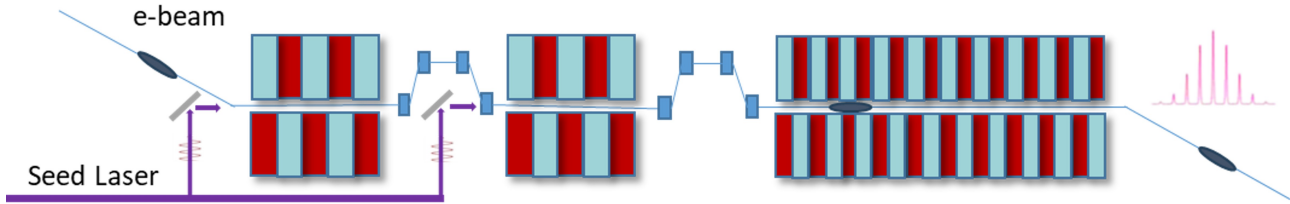
Figure 1: Schematic layout of the method

and the beam distribution is now

$$f(p, \xi) = \frac{1}{\sqrt{2\pi}} exp\{-\frac{1}{2}\{p - A_2 \sin(\xi - B_2 p)$$
$$- C/k_1[\xi - (B_1 + B_2)p + A_2 B_1 \sin(\xi - B_2 p)]$$
$$- A_1 \sin[\xi - (B_1 + B_2)p + A_2 B_1 \sin(\xi - B_2 p)]\}^2\} \tag{7}$$

in which $B_2 = R_{56}^2 k_1 \sigma_E / E_0$. Integration of this formula over p gives the beam density N as a function of ξ, $N(\xi) = \int_{-\infty}^{\infty} dp f(\xi, p)$, and the bunching factor of the nth harmonic can be written as

$$b_n = |\langle e^{-in\xi} N(\xi) \rangle| \tag{8}$$

SIMULATION

Using the main paramters in Tab. 1, we demonstrate the 3-dimentional electron beam and FEL simulation results. Firstly we can see the longitudinal phase space distribution in Fig 2 from Eq 7. One can find out that the frequency-beating effect is formed in the electron beam. And there exits three beating peaks and valleys respectively. We derived the high harmonic bunching of this longitudinal phase space distribution. The 18th harmonic bunching factor at the entrance of the undulator is shown in Fig 3. We can see three bunching peaks in the electron beam. And the maximum bunching factor is about 0.12, which is sufficient enough for the HGHG FEL radiation.

Table 1: Main Parameters

Parameter	Value	Unit
Electron beam energy	1000	MeV
Beam energy chirp	0.5	%
Slice energy spread	40	keV
Peak current	1500	A
Emittance	1.0	mm·mrad
Seed laser wavelength	264	nm
Modulation-1 amplitude	4	-
Chicane-1 dispersion	160	μm
Modulation-2 amplitude	5.5	-
Chicane-2 dispersion	30	μm

We conducted FEL simulation using Genesis 1.3. FEL radiation power and spectra results are shown respectively in Fig 4 and Fig 5. We can see the FEL radiation has three
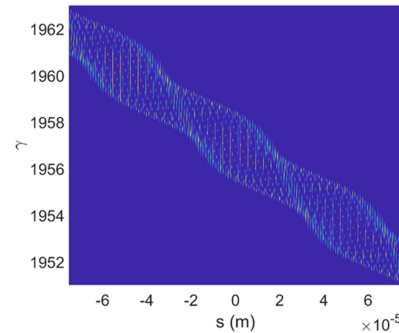
Figure 2: Electron beam longitudinal phase space distribution at the entrance of the radiator.
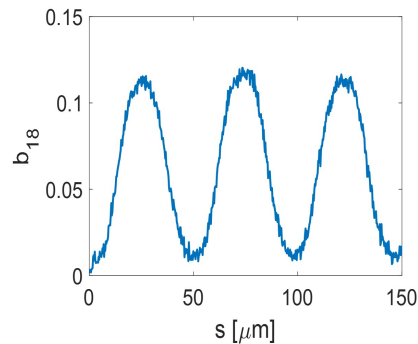
Figure 3: The 18th harmonic bunching factor at the entrance of the radiator.

correspondent peaks in the temporal domain. And the peak power can reach above 2 GW. Due to the energy chirp of the electron beam, the radiation processes of the three peaks are slight different. So the power profiles of the three peaks are not the same. We can also see the mode-locked properties of the FEL in Fig 5. The central wavelength is about 14.58 nm, which is a little bit shorter than the 18th harmonic of the seed laser. That is due to the decreased K-tuning of the undulator field for the amplification of all the three bunching peaks. The mode-locked FEL spectra also show several sideband, that is mainly due to the slippage effect.

CONCLUSION

We studied a simple method to generate mode-locked multichromatic FEL radiation pulses. Using the two modulator-chicane setups in SXFEL and a chirped electron beam, we
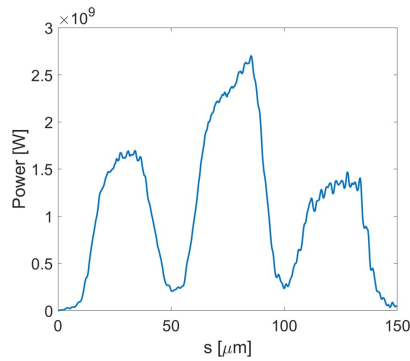
Figure 4: FEL radiation power.
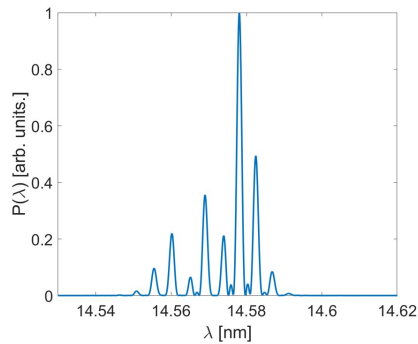
Figure 5: FEL radiation spectra.

can imprint periodic bunching trains into the electron beam. And then we can get mode-locked multichromatic FEL radiation. The simulation results demonstrate that high harmonic bunching up to 18th harmonic of the seed laser can be achieved, and mode-locked FEL lasing with a peak power of above 2 GW can be generated. We want to mention that the method we proposed here can be easily implemented in FEL facilities with two modulator-chicane setups. And the method is also quite suitable for high energy Terahertz FEL radiation since the frequency-beating structure is at the same scale of the Terahertz wavelength.

ACKNOWLEDGEMENTS

REFERENCES

[1] N. R. Thompson, and B. W. J. McNeil, "Mode locking in a free-electron laser amplifier", *Phys. Rev. Lett.*, vol. 100, no. 20, p. 203901, 2008.
doi:10.1103/PhysRevLett.100.203901

[2] P. K. Maroju *et al.*, "Attosecond pulse shaping using a seeded free-electron laser", *Nature* vol. 578, no. 7795, pp. 386-391, 2020. doi:10.1038/s41586-020-2005-6

PRELIMINARY DESIGN OF HIGHER-ORDER ACHROMAT LATTICE FOR THE UPGRADE OF TAIWAN PHOTON SOURCE

N. Y. Huang*, M. S. Chiu, P. J. Chou, H. J. Tsai, H. W. Luo, F. H. Tseng, G. H. Luo

National Synchrotron Radiation Research Center, Hsinchu, Taiwan

Abstract

We study the upgrade of Taiwan Photon Source (TPS) with energy saving as the prime objective. The upgrade design is dubbed TPS-II. To accommodate the constraints imposed by the existing TPS tunnel, we choose the higher-order achromat (HOA) lattice configuration which is composed of the 5BA and 4BA cells. This HOA lattice produces a natural beam emittance about 131 pm·rad for a 3 GeV, 518.4 m storage ring. The on-momentum dynamic aperture is about 8 mm and the estimated Touschek life time reaches around 5.7 hours at total beam current of 500 mA. As a result of the ultralow beam emittance, the brightness and coherence fraction (CF) of the photon beam are improved with a factor of several tens especially in the photon wavelength around 0.1 nm. The challenges and preliminary results of this HOA lattice design will be presented.

INTRODUCTION

The present trend of development for storage ring light sources is steering towards the design of diffraction-limited storage rings (DLSRs), a trend that has been substantiated by the successful establishment and operation of prominent facilities such as MAX-IV, SIRIUS, and ESRF-EBS [1-3]. In the continuum of this evolution, TPS as one of the bright third-generation storage rings since 2015 [4], we plan to upgrade the machine toward DLSR for a brighter synchrotron radiation light source and a green energy-oriented facility.

Globally, several advanced technologies are undergoing examination to propel the development of green energy particle accelerator. These innovations encompass diverse strategies, including the substitution of permanent magnets for electromagnets, the design of a compact accelerator with higher gradient accelerating structures, the reduction of unnecessary power consumption, the enhancement of electric power transfer efficiency and so on. Among these, a storage ring lattice configuration capable of producing an electron beam emittance toward the diffraction limit is one of the keys for energy saving. Directly impact to the users is the increase of coherent photon numbers and brightness which enable the shorter experiment sampling time and reduction of waste heat.

According to the analytical estimation, the relative brightness and CF with respect to the present TPS operation conditions improves by a factor of few tens as the electron beam emittance is reduced to one hundred pm·rad from the current TPS lattice (Fig. 1). There are several possible schemes under study such as H7BA, H6BA, 5BA and

* huang.ny@nsrrc.org.tw
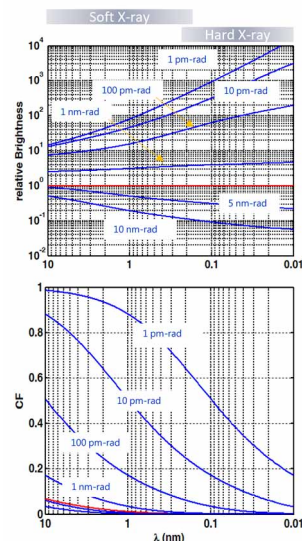
Figure 1: The estimated improvements from TPS to TPS-II on the relative brightness and CF. The red line represents the present operation conditions of TPS (ε_0 =1.6 nm·rad, 500 mA). This calculation employs undulator with the same magnet length and period numbers, optics function of (β_x, β_y) =(5.353, 1.73) m, and $\eta_x = 0$ m.

HOA for TPS upgrade [5]. In this report, we delve into the initial design stages of a HOA lattice configuration bounded by the constraints and challenges we are facing.

TPS TOWARD TPS-II

TPS is a 3 GeV, 518.4 m storage ring with the 4-DBA lattice configuration per super-period. There are totally 24 straight sections available for insertion devices (IDs). To use the existing infrastructure of accelerating tunnel, the upgrade design must keep all the source points of ID beamlines fixed. The current long straight section (LSS) to short straight section (SSS) length ratio is large, at 12:7, making it challenging to keep identical unit cells in a super cell while preserving the same source points for the insertion devises and sufficient SSS lengths. Therefore, we have adopted the HOA configuration that is based on the combination of 5-4-4-5 Multi-Bend-Achromat lattice. It is a similar strategy that proposed by SOLEIL-U to overcome the existing constraints in the tunnel [6].

The linear optics function of one TPS-II supercell is shown in Fig. 2. The number of dipole magnets in the ring is increased from 48 to 108. As predicted by the scaling law, $\varepsilon_0 \propto \theta^3$, the beam emittance of the basic HOA scheme is estimated about 430 pm·rad due to the reduction in bending angle. Additionally, the inclusion of combined dipole
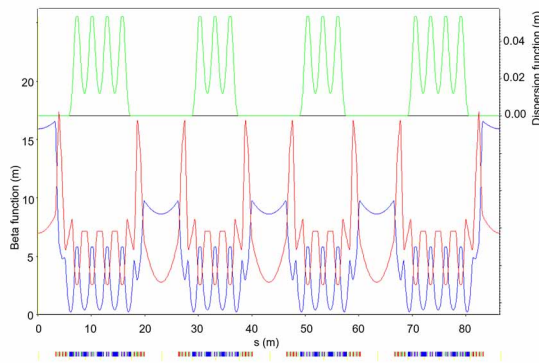
Figure 2: Optics function of TPS-II HOA scheme. The green line represents the dispersion function, while the blue line and the red line denote the β_x and β_y function respectively.

magnets and reverse dipole magnets further improves the horizontal damping and reduces the beam emittance [7]. After the careful adjustment of the length between the central dipole and the matching dipole magnet [8], the natural emittance is reduced to 131 pm·rad that is more than 12 times smaller than the current TPS beam emittance.

The inclusion of reverse dipole magnet primarily enhances the flexibility of dispersion control. The equilibrium HOA beam emittance (which is ~ 1.5 times emittance reduction compared to a lattice scheme without reverse dipoles) and the transverse damping time can be improved further due to the increasing of radiation loss. In our case, the reduction in the horizontal damping time due to reverse dipole magnets is ~ 1.4 times while the vertical damping time is reduced ~ 1.1 times. Nevertheless, the alignment issues of reverse dipole magnets need to be examined carefully.

The main parameters of TPS and TPS-II are summarized in Table 1. The ratio between straight section and circumference for TPS-II is 29 % and the length of each straight section is longer than 6 m. It is adequate to provide sufficient space for the insertion devices, the required vacuum and diagnostic components.

PRELIMINARY RESULTS

The lattice setup and the nonlinear dynamics optimization are performed by OPA [9]. To simplify the system configurations, the octupole magnets which may bring unwanted side effects such as the deterioration of dynamic aperture are not included. A pair of chromatic sextupoles is used to correct the chromaticities around 1.0 in operation. The phase and amplitude of both sextupole and quadrupole magnets are adjusted carefully to minimize the nonlinear Hamiltonian driving terms and the integral of sextupole strengths. Meanwhile, the off-momentum resonances terms are monitored during the iteration processes.

As shown in Fig. 3, the on-momentum dynamic aperture reaches about 8 mm in the horizontal direction and it retains more than 5 mm for the off-momentum case at ± 5 %. A single nonlinear magnetic kicker is considered for the

injection scheme to mitigate the injection difficulties due to a small dynamic aperture.

Table 1: Main parameters of TPS and TPS-II

Parameters	TPS	TPS-II
Circumference	518.4 m	518.4 m
Energy	3 GeV	3 GeV
Lattice	4 DBA	HOA
LSS	12 m × 6	6.43 m × 6
SSS	7 m × 18	6.31 m × 18
η_x @ SS center	0.088 m	0 m
Natural emittance	1.6 nm·rad	131 pm·rad
Energy spread	0.886×10^{-3}	1.043×10^{-3}
Tune (ν_x, ν_y)	(26.19, 13.25)	(49.23, 16.32)
Natural chromaticity (ξ_x, ξ_y)	(-75, -27)	(-92, -59)
Momentum compaction factor (α_1, α_2)	(2.4×10^{-4}, 2.1×10^{-3})	(1.2×10^{-4}, 4.0×10^{-4})
Radiation damping time	(12.2, 12.2, 6.1) ms	(9.2, 20.3, 25.6) ms
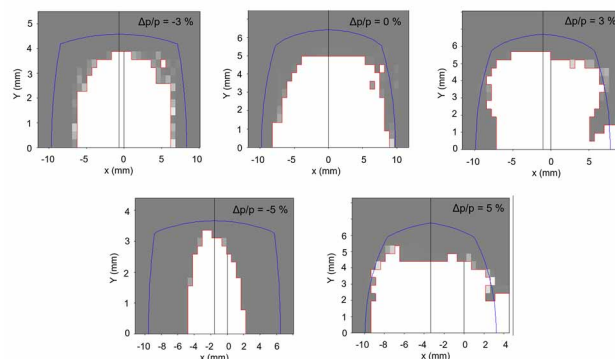
Figure 3: Performance of dynamic aperture for the error-free lattice, $(\xi_{x,ope}, \xi_{y,ope}) = (0.94, 0.93)$.
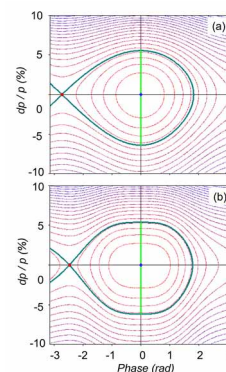
Figure 4: Contour of RF bucket of TPS-II. (a) The considered RF accelerating voltage is assumed to be 2.5 MV, and RF frequency is 499.654 MHz that the harmonic number is 864. (b) With inclusion of a 3rd harmonic cavity.

In the DLSR lattice, generally, the low momentum compaction factor will lead to a short bunch length. This operation will lead to excessive heat load on vacuum chambers and strong intrabeam scattering (IBS) effects. Hence the first order momentum compaction factor α_1 is controlled to be around 10^{-4} during the optimization of the linear lattice. The second order momentum compaction factor α_2 is also carefully examined to keep the lower possible ratio of α_2/α_1 to mitigate the deformation of RF bucket. Figure 4 (a) is the calculated RF bucket that includes the high order momentum compaction factors. The momentum acceptance ranges from -6.4 % to +5.5 %.

The nominal rms bunch length is 2.8 mm assuming an RF voltage of 2.5 MV, which could cause serious heat load in the in-vacuum IDs operating at the minimum gap [10]. It is planned to install a passive superconducting 3rd harmonic cavity for bunch lengthening. As shown in Fig. 4 (b), the phase diagram of RF bucket potential is flattened with a 3rd harmonic cavity and the estimated bunch length could be increased by about a factor of 2.
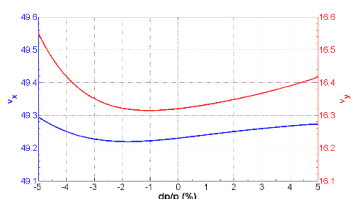
Figure 5: The tracking off-momentum tune-shift.
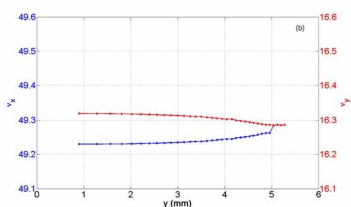
Figure 6: The simulated ADTS. (a) horizontal excitation (b) vertical excitation.
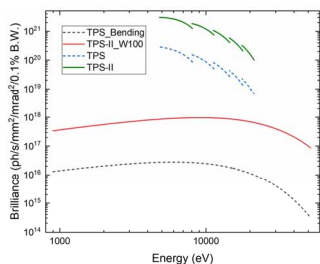
Figure 7: The improvement of spectral brilliance from TPS to TPS-II. Bending: $B\sim$ 1.2 T, W100: λ_u =100 mm, N_u=4, B_{max} ~1.8 T, IU22: λ_u =22 mm, N_u=140, B_{max} ~0.76 T.

The off-momentum tune shifts in both the horizontal and vertical directions remain less than 0.1 for $\pm$ 4 % off momentum particles (Fig. 5). The amplitude dependent tune shift (ADTS) is shown in Fig. 6. With 70 % of the RF buckets filled, the Touschek life time reaches 5.7 hours at 500 mA when the coupling strength is 1% and the total RF cavity voltage is 2.5 MV. With the 3rd harmonic cavity, the estimated Touschek life time is expected to exceed 10 hours.

To accommodate the existing bending magnet users who need the wider spectrum for experiments, we plan to install wigglers in a three-bump chicane in the straight section. The spectral brilliance achieved with the existing ID IU22, and wiggler magnet W100, is depicted in Fig. 7 [11]. The wiggler radiation is able to provide the brilliance that is more than 40 times of the current bending radiation. The increase of brilliance for IDs is more than one order of magnitude for the hard X-ray spectrum in TPS-II.

CONCLUSION

We propose the design of an HOA lattice for the TPS-II upgrade, tailored to fit the existing TPS tunnel and ID source points. This lattice configuration is composed of 24 straight sections with a length of about 6.3 m. The current TPS insertion devices could be adopted without hardware modification. The preliminary analysis indicates that this lattice design can achieve at least tenfold improvement in natural beam emittance, resulting in enhanced radiation brightness, spectral coherent flux and CF. The on-going design efforts encompass the implementation of a passive harmonic cavity and a nonlinear kicker to ensure a better and stabler beam operation. The analysis for the effects of IDs, multipole error, alignment error, further optimization of nonlinear dynamics, and IBS effect are underway.

REFERENCES

[1] Pedro F. Tavares et al., "The MAX IV storage ring project", J. Synchrotron Radiat., vol. 21, pp. 862-877, 2014. doi:10.1107/S1600577514011503

[2] L. Liu and H. Westfahl Jr, "Towards Diffraction Limited Storage Ring Based Light Sources", in Proc. IPAC'17, Copenhagen, Denmark, May 2017, pp. 1203-1208. doi:10.18429/JACoW-IPAC2017-TUXA1

[3] The European Synchrotron, "EBS Storage Ring Technical Report", September, 2018. https://www.esrf.fr/files/live/sites/www/files/about/upgrade/documentation/Design%20Report-reduced-jan19.pdf

[4] C.-C. Kuo et al., "Commissioning of the Taiwan Photon Source", in Proc. IPAC'15, Richmond, VA, USA, May 2015, pp.1314-1318. doi:10.18429/JACoW-IPAC2015-TUXC3

[5] M.S. Chiu et al., "Multi-Bend Achromat Lattice Design for the Future of TPS Upgrade", J. Phys.: Conf. Ser., vol. 1350, 012033, 2019. doi:10.1088/1742-6596/1350/1/012033

[6] A. Loulergue et al., "CDR BASELINE LATTICE FOR THE UPGRADE OF SOLEIL", in Proc. IPAC'21, Campinas, Brazil, May 2021, pp. 1485-1488. doi:10.18429/JACoW-IPAC2021-TUPAB054

[7] A. Streun, "SLS-2 Conceptual Design Report", Paul Scherrer Institut, Villigen, Switzerland, PSI Rep. No. 17-03, Dec. 2017. https://www.dora.lib4ri.ch/psi/islandora/object/psi:34977/

[8] S. Y. Lee, "Emittance optimization in three- and multiple-bend achromats", Phys. Rev. E, vol. 54, 2, 1996.

[9] A. Streun, "OPA User Guide", Paul Scherrer Institut, Villi-
     gen, Switzerland, June, 2022.
     https://ados.web.psi.ch/opa/opa4.pdf

[10] Z.-K. Liu *et al.*, "Design and Optimization of the High Or-
     der Modes Damper for a 1.5 GHz Superconducting Har-
     monic Cavity", *IEEE Trans. Appl. Supercond.*, vol. 31, Au-
     gust 2021. doi:10.1109/TASC.2021.3064532

[11] T. Tanaka, "Major upgrade of the synchrotron radiation cal-
     culation code SPECTRA", *J. Synchrotron Radiat.*, 28, 1267,
     2021. doi:10.1107/S160057752100410

SIMULATION STUDY OF ORBIT CORRECTION BY NEURAL NETWORK IN TAIWAN PHOTON SOURCE

M. S. Chiu†, C Felix, Y. S. Cheng, F. H. Tseng, H. J. Tsai, G. H. Luo

National Synchrotron Radiation Research Center, Hsinchu, Taiwan

Abstract

Machine learning has been applied in many fields in recent decades. Many research articles also presented remarkable achievements in either operation or designing of the particle accelerator. This paper focuses on the simulated orbit correction by neural networks, a subset of machine learning, in Taiwan Photon Source. The training data for the neural network is generated by accelerator toolbox (AT).

INTRODUCTION

The Taiwan Photon Source (TPS) [1,2] is designed as a 3 GeV synchrotron light source, encompassing a 518.4 m circumference. The lattice structure of the storage ring consists of 24 Double-Bend Achromat (DBA) cells, providing 18 short straight sections (7m) and 6 long straight sections (12 m). Three long straight sections, located at 3-fold symmetric position, adopt symmetrical double mini-β_y lattice in which a set of quadrupole triplet is installed in the middle of the long straight section to accommodate double undulators. Figure 1 shows the optical functions of the double mini-β_y lattice for 1/3 TPS.
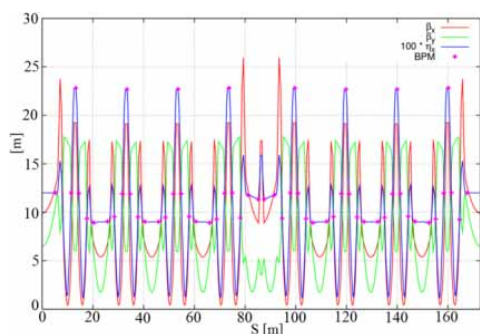
Figure 1: Optical functions of the double mini-β_y lattice for 1/3 TPS storage ring.

Each DBA cell is outfitted with 7 beam position monitors (BPMs). Two BPMs installed in the injection section are unused. There are six additional BPMs installed in three double mini-β_y sections. The TPS storage ring employs 72 horizontal and 96 vertical corrector magnets to define the electron golden orbit, which is monitored by 172 BPMs. In routine operation for user experiments and maintaining long-term orbit stability, each insertion device is equipped with orbit feed-forward table to compensate itself 1st and 2nd order residual integral fields, while gap or phase of the insertion device are moving. Additionally, TPS storage ring is also equipped with a fast

___
† chiu.ms@nsrrc.org.tw

orbit feedback systems involving 96 fast correctors (FC) in horizontal and vertical direction, and the RF feedback system.

Figure 2 shows the positions of BPMs, slow orbit corrector magnets (trim coil wound on the sextupoles) and fast orbit corrector magnets in a DBA cell.
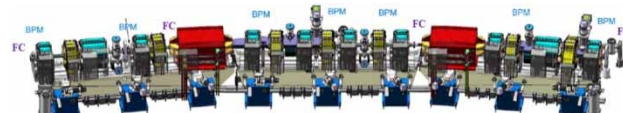
Figure 2: DBA cell in TPS storage ring. Dipole is printed in red colour. Quadrupole is in blue colour. Sextupole is in yellow. Slow orbit corrector magnets are the trim coils wound on the sextupole magnets.

In daily operation for user experiments, the orbit correction and control uses a measured orbit response matrix and singular value decomposition (SVD) algorithm. BPMs are used to monitor the electron beam's orbit, apply SVD to calculate the pseudoinverse of the orbit response matrix, the desired strengths of the corrector magnets can be derived, then apply the calculated current to corrector magnets to bring the electron orbit closer to the target orbit. This traditional method is rooted in physics and well-established principles of beam dynamics in particle accelerators. However, applying machine learning to particle accelerators is growing. D. Schirmer [3, 4] published a paper talking about orbit correction with machine learning at the synchrotron light source DELTA. We also try to create a neural network model to do orbit correction to explore the benefits and drawbacks of utilizing machine learning for orbit correction in TPS storage ring.

MACHINE LEARNING

Machine learning (ML) is a subset of artificial intelligence (AI). It can enable computers to learn from large amounts of data and make predictions or decisions without being explicitly programmed. ML can be roughly classified into three types: supervised learning, unsupervised learning, and reinforcement learning. In supervised learning, the model is trained on labeled datasets, meaning that the input data is paired with output or target values. The goal of supervised learning is to search for a mapping from inputs to outputs. Once adeptly trained, the model can make precise predictions or classifications when encountered with new or unseen data. In unsupervised learning, the model works with unlabeled data and learns patterns without predefined outcomes. It's often used for clustering and dimension reduction. In reinforcement learning, agents learn by interacting with an environment to achieve specific goals.

67th ICFA Adv. Beam Dyn. Workshop Future Light Sources
FLS2023, Luzern, Switzerland
JACoW Publishing
ISBN: 978–3–95450–224–0
ISSN: 2673–7035
doi:10.18429/JACoW–FLS2023–WE4P19

Neural network, a subset of machine learning, is a computational model inspired by the human brain's structure. It can assist us to find out the rules or relationships between the input and output of a nonlinear or complex system. A typical architecture of the feedforward neural network is shown in Fig. 3. For simplicity, we will use one hidden layer as an example. The circles in each layer stand for neurons, called nodes. The linking arrows in-between layers show the signal transduction pathways. The input layer is used to feed data. The output layer gives us the predictions by the neural network. The hidden layer is the main processing units in the neural network to process the data. Usually in each neuron, it executes two things: (a) sum the data passed from the previous layer multiplied by a weight matrix W and then add a bias value B, (b) pass the weighted sum of the data to an activation function f to make a transformation. After that, the transformed data is sent to next layer.
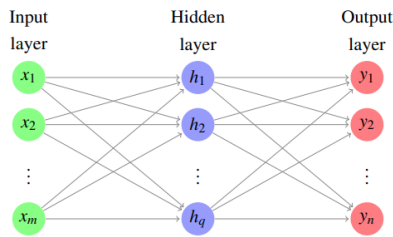
Figure 3: Scheme of a typical feedforward neural network model, considering input, output and one hidden layer

The signal transduction from input layer to the hidden layer can be formulated as the following equation:

$$H = \begin{bmatrix} h_1 \\ h_2 \\ \vdots \\ h_q \end{bmatrix} = f(W_1 X + B_1) = f\left(\begin{bmatrix} w_{11} & w_{12} & \cdots & w_{1q} \\ w_{21} & w_{22} & \cdots & w_{2q} \\ \vdots & \vdots & \ddots & \vdots \\ w_{q1} & w_{q2} & \cdots & w_{qm} \end{bmatrix} \times \begin{bmatrix} x_1 \\ x_2 \\ \vdots \\ x_m \end{bmatrix} + \begin{bmatrix} b_1 \\ b_2 \\ \vdots \\ b_m \end{bmatrix} \right),$$

resulting from the following equation to give the prediction of Y.

$$Y = \begin{bmatrix} y_1 \\ y_2 \\ \vdots \\ y_n \end{bmatrix} = W_2 H + B_2 = \begin{bmatrix} w_{11} & w_{12} & \cdots & w_{1q} \\ w_{21} & w_{22} & \cdots & w_{2q} \\ \vdots & \vdots & \ddots & \vdots \\ w_{n1} & w_{n2} & \cdots & w_{nq} \end{bmatrix} \times \begin{bmatrix} h_1 \\ h_2 \\ \vdots \\ h_q \end{bmatrix} + \begin{bmatrix} b_1 \\ b_2 \\ \vdots \\ b_n \end{bmatrix},$$

where X is the input data, Y is the output of the neural network. H stands for the output from the hidden layer. W_1 and W_2 are weight matrices. B_1 and B_2 are bias vectors. The subscript m, q, and n are the neuron number in the input layer, hidden layer, and output layer, respectively. f is an activation function. Here, we assume the activation in the output layer is linear. Figure 4 shows commonly used activation functions.

Neural Network Workflow

The flow chart of the neural network application is the following:

1. *Data collection:* Scaling and normalizing data, then splitting data into training, validation and test sets
2. *Build a neural network:* Select an appropriate neu-

ral network architecture (e.g. feedforward, recurrent, convolution) based on problem type (e.g. regression, classification, *et al.*), and assign the number of layers, neuron number in each layer, activation function (e.g. sigmoid, tanh, ReLu, *etc.*);

3. *Compile the model:* Specify the loss function (e. g. mean square error, etc.), optimizer (e.g. adam, sgd, *etc.*) that adjusts the model's weights and bias, evaluation metrics (e.g. accuracy, mean absolute error) to monitor during training;
4. *Train the model:* Specify the batch size, the number of epochs (training iteration times), and using training set of data;
5. *Evaluate the model:* Evaluate the model's performance by using validation data set;
6. *Visualize the training progress:* Plot training and validation loss over epochs to assess how well the model is learning.
7. *Hyperparameter tuning:* Training model with different learning rates (step size during training), batch size (number of data sets used in each iteration of training, epoch (training times of passing data sets through network model) to avoid underfitting and overfitting, number of layers, neurons per layer;
8. *Make predictions:* Use the trained model to make prediction on new data.
9. *Model deployment:* If the trained model performs well, save it for deployment.

Name	Function	Derivative	Figure
sigmoid	$f(x) = \frac{1}{1+e^{-x}}$	$f'(x) = f(x)(1 - f(x))^2$	
tanh	$f(x) = \frac{e^x - e^{-x}}{e^x + e^{-x}}$	$f'(x) = 1 - f(x)^2$	
ReLU	$f(x) = \begin{cases} 0 & \text{if } x < 0 \\ x & \text{if } x \geq 0. \end{cases}$	$f'(x) = \begin{cases} 0 & \text{if } x < 0 \\ 1 & \text{if } x \geq 0. \end{cases}$	
softmax	$f(x) = \frac{e^x}{\sum_i e^x}$	$f'(x) = \frac{e^x}{\sum_i e^x} - \frac{(e^x)^2}{(\sum_i e^x)^2}$	

Figure 4: Basic activation function used in neural network

Neural Network Training

Before starting the training process, the weight matrix elements are randomly assigned. During the training process, the optimizer will update the weight matrix and bias values to minimize the loss function, which is defined as the square of the difference between the outputs of the neural network and target values.
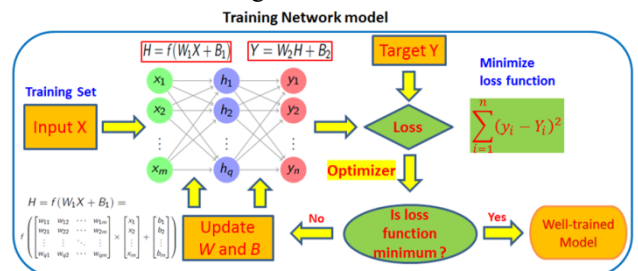
Figure 5: Flow chart for training neural network model.

67th ICFA Adv. Beam Dyn. Workshop Future Light Sources
ISBN: 978-3-95450-224-0

FLS2023, Luzern, Switzerland

JACoW Publishing
ISSN: 2673-7035
doi:10.18429/JACoW-FLS2023-WE4P19

SIMULATION DETAIL

Accelerator Toolbox (AT) [5] is used to generate training data. Three-thousand sets of 72 horizontal correctors (HC) strengths within ± 2.5 μrad are randomly assigned with the matlab [6] command `rand`. Using a for-loop selects a set of 72 random numbers to assign the strengths of 72 corrector magnets respectively, followed by using the MML command $getx$ to get the orbit. Eventually, we have 3000 different orbits associated with 3000 sets of different strengths of the 72 corrector magnets.

Python is used to develop the machine learning application. Tensorflow [7] and keras [8], machine learning packages, are used to build the neural network model. Scikit-learn [9], data mining toolbox, is used to pre-process data, e. g. normalization and split data into training and validation sets of data. For TPS orbit correction in the horizontal plane, the number of input neurons is 172 BPMs, number of output neurons is 72, number of hidden neurons is 172. Figure 6 shows the loss function for training and validation sets of data. The loss function of the training and validation sets of data converges after several training iterations. That means no overfitting and underfitting phenomenon is observed. After training, the trained model is saved with the keras package. Figure 7 shows the accuracy of the trained neural network.
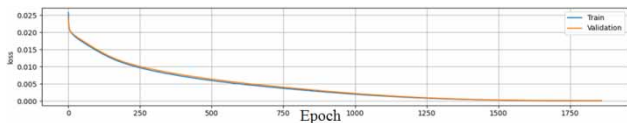
Figure 6: Loss function for training and validation sets of data during training process.
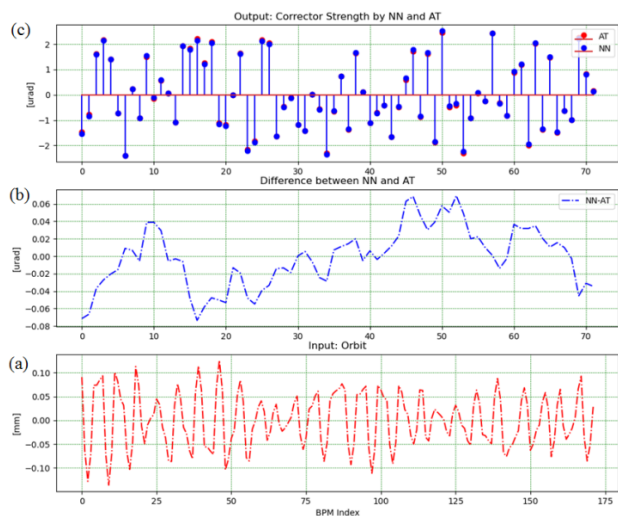
Figure 7: Accuracy of the trained neural network. (a) Test set of input data (172 BPMs' data), (b) Difference of the corrector strength between the prediction from the trained neural network (NN) and AT simulation. (c) Corrector strength: Red is by AT simulation; blue is the prediction by the trained neural network (NN).

In the following, we are going to verify the performance of the trained neural network on orbit correction in AT simulator. Figure 8 shows the implementation of the neural network on orbit correction. The unknown orbit distortion shown in red color in Fig. 9 (b), generated by shifting 249 quadrupoles randomly within ± 3 μm in horizontal plane with the AT command 'setshift', is feed into the trained neural network. The trained network will predict one set of 72 corrector strengths. Using the predicted corrector strengths to correct the orbit distortion in AT simulator and iterate three times. The corrected orbit by the trained neural network is shown in Fig. 9 (b).
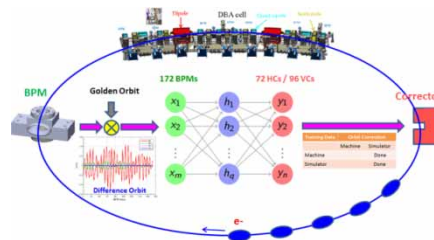
Figure 8: Implement neural network for orbit correction.
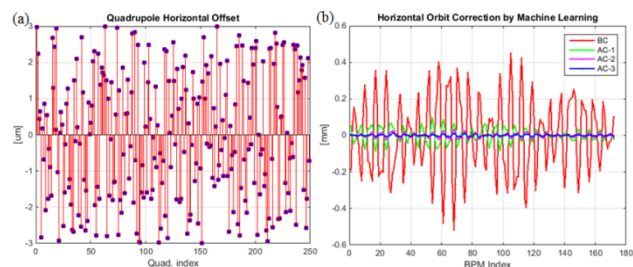
Figure 9: (a) Misalignment quantities of 249 quadrupole magnets within ± 3 μm to generate orbit distortion in TPS storage ring simulated by AT. (b) Orbit correction by neural network: Red is the orbit before correction (BC), green, magenta, and blue are the orbit after correction (AC), iterate 3 times (AC-1, AC-2, AC-3).

SUMMARY

This paper demonstrates the preliminary results of the machine learning application for the orbit correction at TPS storage ring by AT simulator. Even though there is minor residue of orbit distortion after orbit correction by the neural network, it did show great potential to use a neural network for orbit correction. There is still room for improving the performance of the neural network. The next step will to be to apply machine learning on the real machine. Detailed machine studies need to verify the performance of the neural network for orbit correction at TPS storage ring.

REFERENCES

[1] C.C. Kuo *et al.*, "Commissioning of the Taiwan Photon Source", in *Proc. IPAC'15*, Richmond, VA, USA, May 2015, paper TUXC3, pp. 1314-1318.
doi:10.18429/JACoW-IPAC2015-TUXC3

[2] M.S. Chiu *et al.*, "Double mini-betay lattice of TPS storage ring", in *Proc. IPAC'11*, San Sebastián, Spain, May 2011, paper WEPC035, pp. 2082-2084.

[3] D. Schirmer, "Orbit correction with machine learning techniques at the synchrotron light source DELTA", in *Proc. ICALEPCS'19*, paper WEPHA138, pp. 1426-1430.
doi:10.18429/JACoW-ICALEPCS2019-WEPHA138

[4] D. Schirmer, "A machine learning approach to electron orbit control at the 1.5 GeV synchrotron light source DELTA", in *Proc. IPAC'22*, Bangkok, Thailand, May 2022, paper TUPOPT058, pp. 1137-1140.
doi:10.18429/JACoW-IPAC2022-TUPOPT058

[5] https://atcollab.github.io/at/

[6] https://www.mathworks.com/

[7] https://www.tensorflow.org/

[8] https://keras.io/

[9] https://scikit-learn.org/stable/

THE ALIGNMENT RESULTS OF THE TANDEM EPU AT TAIWAN PHOTON SOURCE

F. H. Tseng, T. Y. Chung, H.-Y. Huang, C. M. Cheng, C.-Y. Hua, Y. M. Hsiao, Y. C. Liu[†]
National Synchrotron Radiation Research Center,
Hsinchu Science Park, Hsinchu, Taiwan, R. O. C.

Abstract

Since its inauguration for user applications in 2016, the Taiwan Photon Source (TPS) has facilitated numerous research endeavors. The current investigation focuses on the alignment results of a tandem Elliptically Polarizing Undulator (EPU) situated within an extended double minimum beta y long straight section. The objective is to augment the photon flux of the synchrotron light generated by the tandem EPU via accurate alignment and using a phase shifter to attain temporal coherence. A cross-correlation function is employed to scrutinize the beam parameters associated with the source points to evaluate the temporal coherence of the two light sources emitted from the tandem EPU.

INTRODUCTION

The TPS is a 3 GeV storage ring with a 6-fold symmetry Double Bend Achromat (DBA) lattice structure [1]. Spanning a circumference of 518.4 m, it comprises 24 cells, 18 six-meter-long straights, and six 12-meter-long straights. Tandem undulators are allocated to three 12-meter-long straights, which separate eight cells to maintain the symmetry of optical functions. A quadrupole triplet is positioned in the center of the 12-meter-long straight to minimize the beta y at the core of each undulator [2]. Figure 1 compares optical functions with and without the quadrupole triplet. The tandem undulator beamline was designed to double its flux. However, since TPS began user operation in 2016, only one undulator has been accessible to the three beamlines.
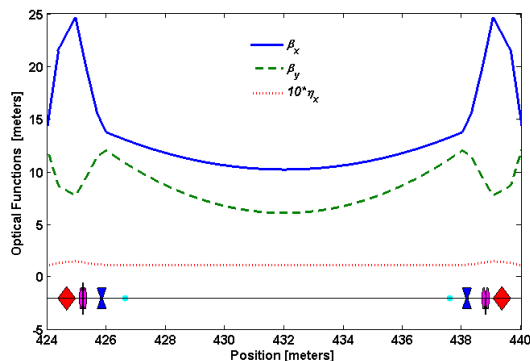
Figure 1a: Optical functions without the quadrupole tripole in the 12-meter-long straight.

† email address yichihl@nsrrc.org.tw
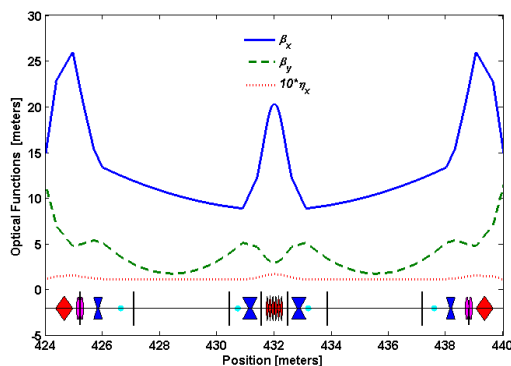
Figure 1b: Optical function with the help of qudrupole triplet to minimize the β_y at the core of each EPU.

Beamline 41A at the TPS consists of two branches [3]: high-resolution resonant inelastic X-ray scattering (RIXS) and coherent soft X-ray scattering. Both branches share the same equipment, such as the monochromator, slits, and front-end focusing optics. The light source comes from two elliptically polarized undulators (EPU) placed one after another in a 12-meter-long straight with a unique design to double the light's brilliance. Each EPU is 3.2 m long with a 48 mm period. Figure 2 presents the tandem EPUs and quadrupole triplet configuration and shows the locations of beam position monitors (BPM) and the pairs of correctors for local orbit feedback.
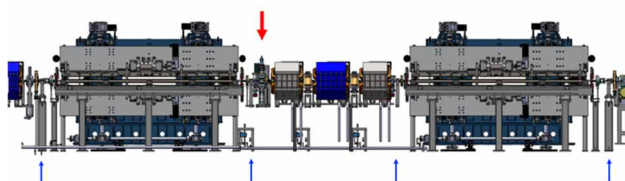
Figure 2: Tandem EPUs and quadrupole triplet configuration, locations of four BPMs (small blue arrow) and the pairs of correctors (black dot) for local orbit feedback, the red arrow indicates the location of the phase shifter.

The EPU tandem is designed to achieve a brilliance greater than 1×10^{20} photons per second per mrad^2 per mm^2 with a 0.1% bandwidth in the energy range from 400 to 1200 eV. In this range, the photon flux in the central cone is over 1×10^{15} photons per second. The calculated beam sizes are roughly 386 um horizontally and 28-35 um vertically at the full width at half-maximum (FWHM). Based on the photon energy range, the beam divergences are 42-61 μrad horizontally and 33-52 μrad vertically at FWHM.

We were initially unable to align the synchrotron light emitted from the tandem undulator due to a lack of monitoring equipment. However, after installing screen monitor 2 in the front end, we began the alignment process for the synchrotron light emitted from the tandem undulator to maximize the photon flux for the beamline. Figure 3 depicts the relative positions of screen monitors 1 and 2 and the XBPMs 1 and 2 in the front end. We also implemented a local orbit feedback to ensure consistent alignment performance.
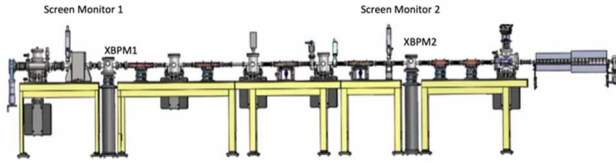
Figure 3: Relative positions of screen monitors 1 and 2 and the XBPMs 1 and 2 in the front end.

ALIGNMENT PROCEDURE

To align the photon trajectory from the upstream EPU, we used the photon trajectory emitted from the accessible downstream EPU projected on the front-end screens 1 and 2 as the target. We determined the appropriate storage beam current to be 30 mA for orbit correction, while we dumped the beam and re-injected it to 0.5 mA to locate the target on front-end screens 1 and 2. This was necessary due to the low signal-to-noise ratio of the electron BPMs at lower beam currents.

In Fig. 4, a comparative analysis of electron beam trajectories at varying beam currents is presented, illustrating discernible deviations which suggest that both the superconducting radiofrequency (SRF) systems and the induced noise have an impact on the beam position monitors (BPMs) located on either side when the beam current is set at 0.4 mA.
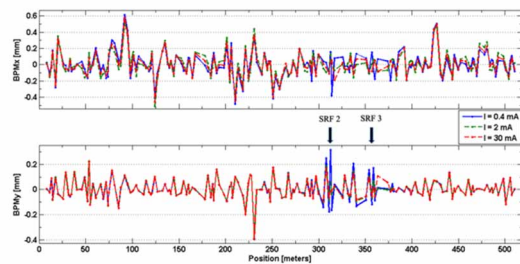
Figure 4: Comparison of the electron beam orbits for different beam currents, with apparent deviations indicating that the superconducting RF system and induced noise affect both-sides BPMs at 0.4 mA beam current.

We designed a local orbit feedback control system based on the original fast orbit feedback (FOFB) constraints [4]. We measured the response matrix of tandem EPU's corrector and both side BPMs when starting the FOFB. Therefore, the response matrix $R_{x_{ij}}, R_{y_{ij}}$, are a 4 x 4 matrix in the x and y direction, respectively. The inverse response matrix $R_{x_{ij}, y_{ij}}^{+}$ links $\Delta B_{x_{ij}, y_{ij}}$ and $\Delta x_{ij}, y_{ij}$:

$$\Delta B_{x_{ij}, y_{ij}} = R_{ij}^{+} \Delta x_{ij}, y_{ij} \qquad (1)$$

This new system helps maintain the alignment of synchrotron lights emitted from tandem EPUs. When integrating the new feedback system, it is essential to ensure that the original feedback remains continuously active to maintain stability and performance. In Fig. 4, the stability of the local orbital trajectory is demonstrated to effectively preserve the alignment of the two light sources. Measurements were consistently conducted with the implementation of local orbital feedback control mechanisms.
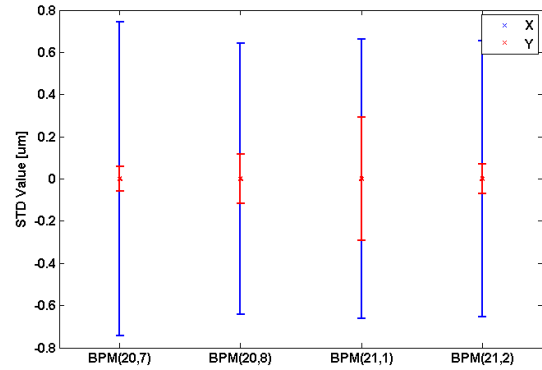

Figure 5: Stability of the local trajectories.

Figure 5 illustrates that the stability of the local trajectories contributes significantly to maintaining the alignment of two distinct light sources. A detailed examination during the gap fully opened and closed reveals that the horizontal peak-to-peak fluctuation, corresponding to the 95% confidence interval, remains confined to a 4 μm range. Similarly, the vertical peak-to-peak fluctuation is observed to be constrained within a 2 μm range, further emphasizing the effectiveness of local trajectory stability in preserving light source alignment.

ALIGNMENT RESULTS

During the alignment experiment, it was observed that the vertical entrance slit experienced an increase in temperature. Upon re-evaluation and recalculation of the beamline optics, it was determined that the primary cause of the heating issue at the vertical entrance slit was the disparate focal points of the emitted photon beam originating from the upstream and downstream EPU. Following the distance from the upstream EPU center and downstream EPU center to the horizontal focusing mirror (VFM), they are 32.555 m and 25.805 m. The emitted photon flux from the tandem is EPU quantified by measuring the current on the sample holder with fully open slits. A detailed schematic of the RIXS branch is illustrated in Fig. 6. This constrain impedes the ability to accurately measure the spatial coherence of the two photon beams.

In the present study, the primary objective is to quantify the temporal coherence of dual photon beams by employing a phase shifter [5] positioned downstream of the upstream EPU, as depicted in Fig. 2. The utilized phase shifter, composed of permanent magnets, incorporates an anti-symmetric magnet end pole configuration to mitigate

multipole errors and the influence of fringe field effects across a range of gap widths. In its design, the phase shifter exhibits a maximum gap width of 130 mm, at which point the magnetic field effectively approaches zero.
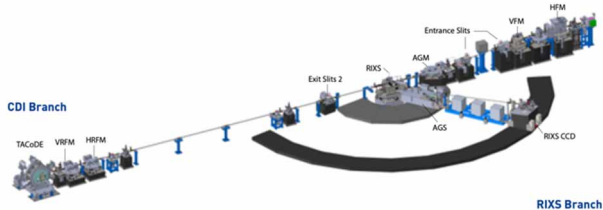
Figure 6: Detailed schematic of the RIXS branch.

The electron beam trajectory varies with the gap of the phase shifter and produces a difference in path length to its maximum gap. The path length difference of e-beam introduces a phase delay to the photon with wavelength λ propagating straight along the phase shifter can be written as:

$$\frac{L - L_0}{\lambda} = \frac{\Delta\phi}{2\pi} \qquad (2)$$

We employed a phase shifter to assess the temporal coherence of two monochromatic light sources emitted from the tandem EPU. Figures 7 and 8 present the variations in normalized flux as a function of the phase shifter gap at two distinct photon energies.
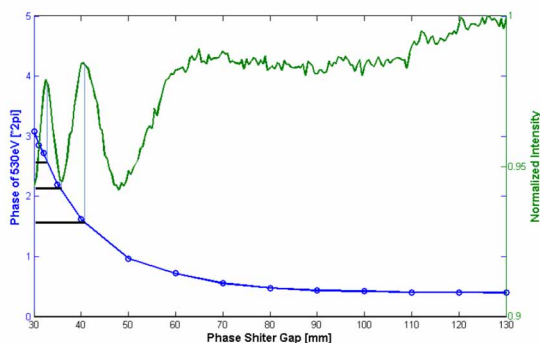
Figure 7: Variations in normalized flux as a function of the phase shifter gap with photon energies at 531.8 eV and a wavelength of 2.33 nm.
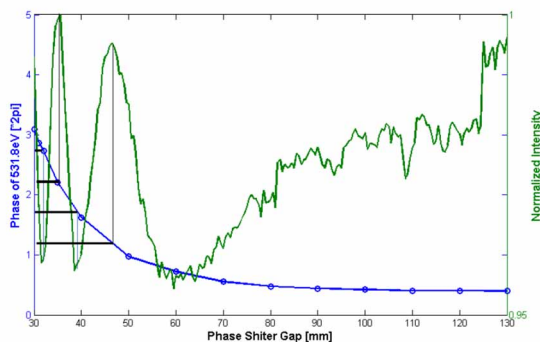
Figure 8: Fluctuations in normalized flux, contingent upon the phase shifter gap, in association with photon energies of 530 eV and a wavelength of 2.34 nm.

Based on the results, we can calculate the cross-correlation function to quantify the degree of temporal coherence

of the two monochromatic light sources and determine the visibility [6] V, a measurement of contrast of the interference pattern shown in Figs. 7 and 8, define as:

$$V = \frac{I_{max} - I_{min}}{I_{max} + I_{min}} \qquad (3)$$

In the observed visibility spectrum, the magnitude lies within 0.016 to 0.022, indicative of weak temporal coherence between the two light sources under investigation. This finding suggests that the emission originating from the EPU constitutes incoherent synchrotron radiation. A graphical representation of the incoherent synchrotron light emissions from an electron bunch is provided in Fig. 9.
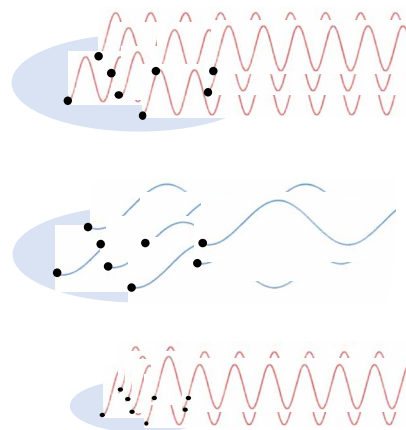
Figure 9: Emission of incoherent synchrotron light from an electron bunch. The top figure displays a highly incoherent synchrotron light, evident when the photon wavelength is significantly shorter than the electron bunch length. Conversely, the middle and bottom figures exhibit a more coherent synchrotron light, which occurs when the photon wavelength is comparable to the electron bunch length.

Constructive interference can be achieved by emitting two monochromatic light sources from the tandem EPU. To accomplish this, the phase delay of the phase shifter and the phase difference ϕ_0 between the centers of the two EPUs must be an integer multiple of 2π. Under these conditions, the normalized intensity (A) can be expressed as follows:

$$A = \frac{1 + v\cos(\Delta\phi + \phi_0)}{2} \qquad (4)$$

For Figs. 7 and 8, the phase difference ϕ_0 is determined to be $0.607 \cdot 2\pi$ and $0.404 \cdot 2\pi$, respectively. Additionally, the experimentally measured phase delay of the phase shifter demonstrates agreement with the anticipated phase delay.

In Figs. 7 and 8, the interference pattern exhibits prominent peaks, the exhibiting positive and negative slope of which is of particular interest in the current investigation. To elucidate the nature of this slope, we introduce R_{56}, R_{56} is a fundamental parameter in accelerator physics to quantify the relationship between changes in longitudinal path length and energy deviations. In the 6-dimensional matrix, the fifth coordinate represents the longitudinal coordinate,

while the sixth coordinate represents the particle's energy. In case of large momentum deviation (δ), the electron beam's longitudinal slippage (Δz) to its momentum deviation and its square of energy deviation (δ^2) can be written as:

$$\Delta z \approx R_{56}\delta + T_{566}\delta^2 \approx R_{56}\delta - \frac{3}{2}R_{56}\delta^2 \quad (5)$$

T_{566} represents the ratio of the change in longitudinal path length to the square of the energy deviations. Under the 0.1% energy spread, the R_{56} value of the phase shifter spans a range of -12.57 nm to -0.72 nm, corresponding to a gap variation between 30 mm and 70 mm. Compared to the electron bunch length of 5.28 mm observed at a stored beam current of 500 mA, the influence of bunch compression can be considered negligible. The observed phenomena of both position and negative slopes cannot be fully accounted for by equation 5.

The Tandem EPU functions as a type of optical klystron [7, 8], wherein the upstream EPU induces energy modulation, while the phase shifter generates density modulation. Subsequently, the downstream EPU amplifies the harmonic energy of the photons.

In this context, we present the spontaneous emission, denoted as $\frac{d^2I}{d\omega d\Omega}$ representing the energy emitted per electron during each pass through the EPU, per unit solid angle, and per frequency in the forward direction. The expression for spontaneous emission in the case of the tandem EPU can be formulated as follows:

$$\frac{d^2I}{d\omega d\Omega}(the\ tandem\ EPU) = 2\frac{d^2I}{d\omega d\Omega}(1 + cos\alpha) \quad (6)$$

Here, α denotes the cumulative alteration of $t - \frac{\vec{n}\vec{r}}{c}$ in single EPU and throughout the phase shifter. The unit vector $\vec{n}$ corresponds to the direction of $\frac{d^2I}{d\omega d\Omega}$ is computed. The position vector of the electron at a specific time t is denoted by $\vec{r}$. The spontaneous emission spectrum of the tandem EPU exhibits no substantial interference characteristics. The positive and negative slopes of the pronounced peaks in the interference patterns observed in Figs. 7 and 8 currently lack a convincing explanation. Further investigation is required to elucidate the underlying cause.

CONCLUSION

The findings of this investigation underscore a notable deficiency in the temporal coherence of alignment results obtained from the tandem EPU, which is attributable to an erroneous measurement procedure. Specifically, the beamline slits were found to be completely open. Consequently, an excessive overlap of the diffraction patterns was observed, leading to the obliteration of the interference. Nevertheless, the introduction of an innovative local orbit feedback control mechanism has proven to be considered adequate. This research explores the beam properties of the TPS storage ring by examining interference patterns generated by two separate light sources when the electron beam passes through a phase shifter with a variable gap. The experiments substantiate that the antisymmetric permanent-magnet phase shifter meets its design specifications, providing valuable insights for future developments in this field.

REFERENCES

[1] C. C. Kuo *et al.*, "Progress report of TPS lattice design," in *proc. PAC'09*, Vancouver, BC, Canada, 2009.

[2] M. S. Chiu *et al.*, "Double mini-betay lattice of TPS storage ring," in *proc. IPAC'11*, San Sebastián, Spain, 2011

[3] . A. Singh *et al.*, "Development of the soft X-ray AGM-AGS RIXS beamline at the Taiwan Photon Source," *J. Synchrotron Radiat.,* vol. 28, 2021, pp. 977-986.
   doi:10.1107/S1600577521002897

[4] P. C. Chiu *et al.*, "Beam commissioning of TPS fast orbit feedback system, " *proc. IBIC'16*, Barcelona, Spain, 2016.
   doi:10.18429/JACoW-IBIC2016-MOPG11

[5] T. Y. Chung, J.-C. Huang, H. Luo, Y. Chu, J. Jan, and C. Hwang*,* "An antisymmetric design of a permanent-magnet phase shifter for a tandem EPU at TPS," *IEEE Trans. Appl. Supercond.*, vol. 26, no. 4, Jun. 2016.
   doi:10.1109/TASC.2016.2524525

[6] Emil Wolf, *Introduction to the theory of coherence and polarization of light*, University of Rochester, NY., USA, Cambridge University press, 2007

[7] R. Coisson, "Optical klystrons", *Part. Accel.*, vol. 11, pp. 245-253, 1981.
   http://cds.cern.ch/record/1107994

[8] P. Elleaume, "Optical klystrons", *Journal de Physique Colloques*, vol. 44, pp. C1333-C1352, Feb. 1983.
   doi:10.1051/jphyscol:1983127

SOME BEAM DYNAMIC ISSUES IN THE HALF STORAGE RING

Jingyu Tang*, Penghui Yang, Gangwen Liu, Yihao Mo, Anxing Wang, Zhouyu Zhao, Tianlong He
Zhenghe BaiUniversity of Science and Technology of China, Hefei, China

Abstract

HALF (Hefei Advanced Light Facility) is a fourth-generation synchrotron light source that just started construction in 2023. With 2.2 GeV in energy, 350 mA in beam current and 86 pm.rad in emittance, the HALF storage ring faces several beam dynamics challenges. This presentation gives the recent study on some of these issues, in particular the beam collimation and the influence and compensation of the insertion devices. For beam collimation, different beam loss mechanisms have been studied, and the Touschek scattering and beam dumping are considered the two major effects in designing the collimation system. Then two collimators with movable horizontal blades and fixed passive vertical blades are being designed, with the main focus on the collimation efficiency and impedance. For the influence of the insertion devices, it is found that some of the long-period undulators have a high impact on the beam dynamic aperture due to low beam energy and originally small dynamic aperture. The local compensation methods for both linear and non-linear effects have been studied. Instead of the traditional compensation method by electrical wires, the method of using two combined magnets with quadrupole and octupole fields at the two ID ends in restoring the dynamic aperture is also studied and compared.

INTRODUCTION

HALF is a fourth-generation synchrotron light source. After many years of design study and R&D efforts, now it enters the construction phase of 2023-2028 [1-2]. The accelerator complex consists of a full-energy linac of 2.2 GeV and a storage ring of 20 periods with a circumference of 480 m. Figure 1 shows the lattice functions of one period. The main design parameters of the storage ring are listed in Table 1.
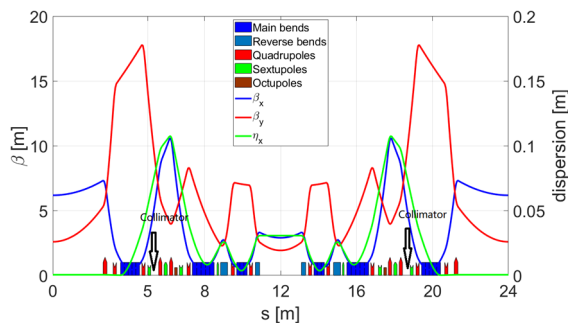
Figure 1: The lattice functions and magnet layout of the HALF storage ring (with collimator positions marked).

Table 1: Main Parameters of the HALF Storage Ring

Parameter	Value
Energy [GeV]	2.2
Current [mA]	350
Circumference [m]	479.86
Number of cells	20
Natural emittance [pm·rad]	85.8
Transverse tunes (H/V)	48.19/17.19
$\beta x/\beta y/\eta$ @ long straight [m]	6.78/2.55/0.00
$\beta x/\beta y/\eta$@ mid-straight [m]	2.51/1.95/0.03
Arc lattice	modified hybrid 6BA
Straight sections [m]	20*5.5, 20*2.2
RF frequency [MHz]	499.8

With a relatively low beam energy of 2.2 GeV, a modest beam current of 350 mA and a very small beam emittance of 86 pm.rad, the HALF storage ring faces several beam dynamics challenges. In this paper, we present the preliminary study results of some beam dynamics issues, including beam loss mechanisms, beam collimation, influences of the insertion devices (ID) on the beam dynamics and compensation methods.

BEAM LOSS MECHANISMS IN THE HALF STORAGE RING

Beam losses become much more important in fourth-generation synchrotron light sources, as compared to third-generation light sources, mainly due to the much higher loss rate and much smaller beam size. The beam loss knowledge is not only important for the design of the tunnel shielding but also for the safe operation of the machine, since a critical beam loss may damage the accelerator devices. A study on the loss mechanisms in the HALF storage ring was conducted. The following beam loss mechanisms are considered the most important: the Touschek scattering loss, beam loss during the injection, beam loss or dumping when the abnormal functions of the facility occur and intentional shutdown is launched, and beam losses in the non-standard operation modes.

The Touschek Scattering Loss

The Touschek scattering loss is the most important beam loss in the HALF storage ring. Due to that both the beam size and momentum aperture (MA) in fourth-generation light sources are significantly smaller than those in third-generation light sources, the Touschek scattering as the principal beam loss mechanism leads to a significant reduction in beam lifetime. In the normal operation mode

---

* jytang@ustc.edu.cn

of the HALF storage ring, the Touschek lifetime is about two hours. The beam losses appear almost uniformly in twenty periods. Figure 2 shows the major locations in each period with superpositions from the whole ring).
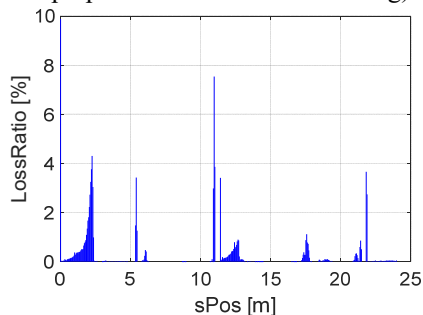
Figure 2: Distribution of the beam loss caused by the Touschek scattering effect (superpositioned into one period).

Injection Loss

Due to a small beam lifetime in the HALF storage ring, it requires frequent beam injection to maintain the quasi-constant beam current by the top-up injection mode. The beam dynamic aperture (DA) is very small here, about 6-7 mm after applying errors and corrections. The current injection scheme is the off-axis injection, with the injecting beam situated at the edge of the DA. For the two electron guns planned, the thermal-cathode gun that will be the baseline scheme delivers a much larger emittance than the photon-cathode gun, which leads significant reduction in the injection efficiency, e. g., 50-80%. The beam loss pattern is defined by the transverse acceptance around the ring, which is more uniform than that due to the Touschek loss. The fluctuation of the injecting beam due to the temporal errors in the linac and the transport beamline will have a similar effect to a larger beam emittance.

Another injection loss mechanism comes from the abnormal function of the injection devices (kickers or septa), which happens very rarely. In this case, both the stored beam and injecting beam are lost mainly in the downstream arc of the injection section.
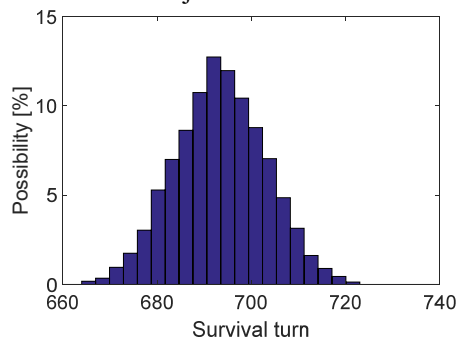
Figure 3: Beam loss pattern when the RF is turned off.

Beam Dumping

When one of the key devices in the storage ring or the beamline front-ends has a critical failure, the whole stored beam should be dumped to allow human intervention to fix the problem. Another scenario is the intentional shutdown of the machine, and there one also needs to dump the stored

beam. In both cases, we will have time to trigger the beam dumping mode when both the RF system and the orbit correction system are turned off. The stored beam will be lost in less than 1000 turns, see Fig. 3.

Beam Loss in the Non-standard Operation Modes

The storage ring will work in different operation modes, such as the commissioning mode, high bunch charge mode and hybrid mode with one isolated bunch for high time resolution. In these modes, we will meet different beam loss patterns than in the normal mode. For the commissioning mode, the circulating beam current is increased step by step, thus a much larger beam loss rate can be tolerated according to the beam current. For the two other operation modes, the loss pattern is similar to the normal operation mode, but they have different beam lifetimes.

BEAM COLLIMATION

Collimation Scheme

To protect the IDs that are vulnerable to radiation damage, localize the beam losses for better shielding design, and alleviate critical heat deposition in the devices intercepting the dumping beam, a collimation system in the HALF storage ring has been designed. The current design scheme uses two collimators in two of the 20 periods. The first one will be placed in the upstream dispersion bump of the first period and the second one in the downstream dispersion bump of the 11th period, as shown in Fig. 2, where beta and dispersion functions are relatively large and there are enough spaces left for hosting the collimators. Both of them have movable horizontal blades and fixed passive vertical blades. The collimator with a small gap has a good collimation efficiency but may limit the DA and MA. Besides, it will lead to an increase in impedance such as resonance modes and resistive wall impedance, and may result in beam instability problems. Thus, the gaps of the two collimators have to be carefully considered.

Collimation Efficiency

As mentioned earlier, Touschek scattering occurs continuously around the storage ring. The ELEGANT code based on the Monte Carlo method is applied to simulate the particle loss caused by the Touschek scattering effect [3]. The collimation efficiency and the effects on DA and MA with different values of horizontal gaps were studied. The simulation results show that a half gap of 6 mm is considered a compromised setting, which gives a collimation efficiency of larger than 70% and causes a reduction in the lifetime lower than 10%. Besides, the physical aperture from the collimator has almost no further limitation to the DA if the error effects and IDs are included. Figure 4 shows the distribution of beam loss with the horizontal collimators of ±6 mm in aperture, and it shows that the beam losses at the injection septum and all IDs are reduced to be lower than 5% and 15% of the total loss, respectively.
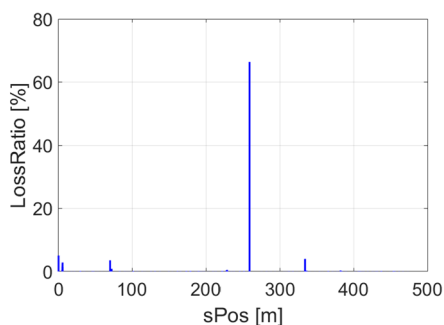
Figure 4: Distribution of beam losses caused by Touschek scattering with ±6 mm horizontal collimators in the normal operation mode.

For the case of beam dumping, the RF cavities are switched off first, and the collimation efficiency is about 50%, and the other 50% of the particles will be lost at the twenty photon masks near the mid-straight sections due to the large local distortion of the beam distribution in the phase spaces with a large momentum deviation. The large beam losses at the masks are considered acceptable since it does not happen frequently. However, due to the very small beam size, there is a concern about the heat deposition density in the interception devices. One should include this effect in designing the interception surface and cooling system of the collimators and masks.

Monte Carlo Simulations of the Lost Particles in the Collimator

The impinging of electrons of 2.2 GeV in energy on the collimator blades will produce secondary particles, which lead to serious heat deposition and radiation effects. The Geant4 code is employed to simulate the interaction between the electrons and the collimator materials. The major secondary particles are the bremsstrahlung gamma rays, then secondary electrons, positrons and also some neutrons, which are strongly dependent on the blade material. At the moment, copper is found a good compromise for being good electrical and heat conductivity, modest stopping power, and production of secondary particles, especially neutrons. The design of the blade profile along the optics axis, the heat dissipation or cooling, and the local shielding will be based on the simulation results.

Collimator Structure and the Impedance Issue

From the study of beam loss mechanisms, the particle losses are almost in the horizontal blades of the collimators. To have good flexibility that allows the collimation in the different operation modes and acts as a measurement tool for the Touschek lifetime and DA, the gap between the blades is adjustable, with a nominal ±6 mm, thus a mechanical driving system is needed. There are water-cooling channels in the blades to bring out the heat load. The collimators are in-vacuum devices, thus it introduces a concern about the coupling impedance that is caused by the discontinuity of the vacuum duct and the cavity structure. The calculation of impedance shows that the impedance issue is very serious, concerning both the

resonance modes and resistive wall impedance. The optimization of the structure is in the course, which focuses on the tapering of the two longitudinal ends and applying the upper and lower plates with a fixed aperture.

INFLUENCE OF THE INSERTION DEVICES ON THE BEAM DYNAMICS AND COMPENSATION METHODS

The IDs in the HALF Phase-I include 6 elliptically polarized undulators (EPU), one helical undulator (HU), 4 linearly polarized undulators (LPU and IVU) and 2 damping wigglers [4], and most of them have a length of about 4 m. Among these IDs, the long–period undulators of EPU54, EPU102, and HU115 have relatively strong effects on the beam dynamics of the storage ring mainly due to a relatively low beam energy of 2.2 GeV. The two damping wigglers with high dipole fields have an obvious effect on linear optics but a weak impact on the DA. The EPU102 and HU115 result in both large beta-beatings and the deterioration of nonlinear dynamics.

Taking the vertical polarization mode (16 mm gap) of EPU102 as an example, based on the kickmap model, the beta-beating reaches several hundred percent and the horizontal DA reduces from about 9 mm to about 4 mm without considering the errors. The beta-beatings can be corrected to about 2% or less by using the neighboring quadrupoles, but the DA is restored only modestly. To compensate for the dynamic field integrals of the EPUs, the active shimming method with current strips has been used in several labs to minimize undesirable nonlinear beam dynamics effects [5]. At EPU102, the dynamic multipoles of the kick map can be suppressed with 28 current strips. The beta-beatings are reduced to about several percent and the DA is recovered to about 6 mm, as shown in Fig. 5. However, very small beam size and vacuum ducts in fourth-generation light sources have an important impact to apply this method due to the high strip currents, which is the case here.
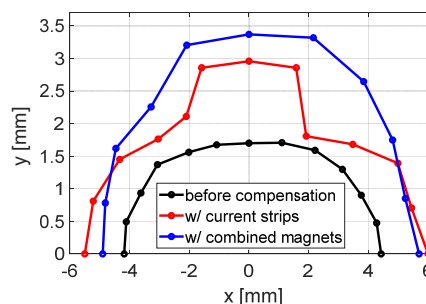
Figure 5: With the EPU102 vertical polarization mode, DAs before compensation and after compensation with current strips and combined magnets are compared.

The analysis of the kickmap shows that it contains linear and nonlinear (especially octupolar) components. Thus another kind of compensation method by using combined magnets with quadrupole and octupole fields was also studied. We place one combined field magnet on each side of the ID. The quadrupole field can effectively correct the beta-beatings and the octupole field helps to recover the

nonlinear dynamics performance, as shown in Fig. 5. Further study is still ongoing to better recover the nonlinear dynamics performance.

SUMMARY

As a fourth-generation synchrotron light source, the design of the HALF storage ring meets beam dynamic challenges, and some of them are discussed in this paper. After the Touschek scattering and beam dumping are considered the key beam loss mechanisms, a collimation system that consists of two adjustable collimators are designed to protect the ID devices and localize the radiation sources. Some of the IDs with long periods especially those EPUs have an important impact on the beam optics and dynamic aperture. Both the compensation methods of using electrical wires and combined multipole magnets are used to restore the machine's performance. Although effective, more efforts are needed to obtain satisfying solutions for all the IDs in different working modes.

ACKNOWLEDGMENT

REFERENCES

[1] Lin Wang *et al*., "Hefei advanced light source: a future soft-X diffraction limited storage ring at NRSL, " in *Proc. of IPAC'18*, Vancouver, BC, Canada, 2018, pp. 4097-4099 `doi:10.18429/JACoW-IPAC2018-THPMK120`

[2] Z. Bai *et al.*, "Progress on the storage ring physics design of Hefei Advanced Light Source (HALF), " in *Proc. IPAC'23*, Venice, Italy, 2023, paper MOPM038, to appear in the proceedings.

[3] Xiao A, Borland M. "Monte Carlo simulation of Touschek effect." *Phys Rev. Spec. Top. Accel. and Beams*, vol. 13, no. 7 p. 074201, 2010. `doi:10.1103/PhysRevSTAB.13.074201`

[4] Z. Zhao, Y. Xu, and H. Li, "Preliminary design of insertion devices at Hefei Advanced Light Facility, " in *Proc. IPAC'23*, Venice, Italy, 2023, paper MOPM115, to appear in the proceedings.

[5] Y. Hidaka, O. Chubar, *et al.*, "Commissioning of current strips for elliptically polarizing undulators at NSLS-II," in *Proc. IPAC'21*, Campinas, Brazil, 2021, pp. 4160-4163. `doi:10.18429/JACoW-IPAC2021-THPAB198`

OPTICS FOR AN ELECTRON COOLER FOR THE EIC BASED ON AN ELECTRON STORAGE RING*

J. Kewisch†, A. Fedotov, X. Gu, Y. Jing, D. Kayran, I. Pinayev, S. Seletskiy
Brookhaven National Laboratory, Upton, NY, USA

Abstract

An electron cooler based on a storage ring is one of the options to improve the luminosity in the Electron-Ion Collider (EIC). The transverse emittance of the electrons in the cooler is driven by the quantum excitation in dipoles and wigglers, as well as by both beam-beam scattering with the ions and intra-beam scattering of the electrons in the regions with a non-zero dispersion. The resulting demand to minimize a dispersion conflicts with the need of a sufficient dispersion in sextupoles for chromaticity correction. In this report we discuss our studies of several approaches to electron ring lattice, including those typically used in light sources, and present resulting compromise between various requirements.

INTRODUCTION

The Electron-Ion Collider is being designed at the Brookhaven National Laboratory, with an anticipated start of construction in 2025. This machine will allow colliding 10 GeV electrons with 275 GeV protons. An important feature of this accelerator will be a luminosity of 10^{34}cm^{-2}sec^{-1}. After injection the beam emittance of the ions, and therefore the luminosity, will degrade because of intra-beam scattering (IBS). In order to maintain a high integrated luminosity the ion beams must be cooled.

In the current design of the EIC Micro-bunched Electron Cooling (MBEC) [1] is selected as a promising new technique for cooling dense hadron beams. An alternative method is the traditional electron cooling, invented by Gersh Budker at INP, Novosibirsk, in 1966. Electron cooling has been tested in many applications and has been proven to work well with bunched beams in the LEReC cooler [2] at BNL. However, the EIC would be the first application with hadron energies greater than 10 GeV. The EIC operates at 100 GeV and 275 GeV.

The cooling rate of an electron cooler with bunched beams is proportional to:

$$\frac{1}{\tau} \propto \frac{r_e^2 m_e c Z^2 \Lambda_c}{A m_p} \frac{1}{\gamma^2} \frac{N_e}{\epsilon_{xn}\epsilon_{yn}\sigma_z\sigma_\delta} \frac{L_{cs}}{C_{ring}} \qquad (1)$$

where N_e is the number of electrons, L_{cs} is the length of the cooling section, C_{ring} is the ring circumference, Λ_c is the Coulomb log, $\epsilon_{xn}, \epsilon_{yn}$ are the normalized electron beam emittances, and γ is the Lorenz factor. The cooler becomes less effective with higher energies and we must increase the length and the electron current as well as maintain low emittances to achieve sufficient cooling rates.

The choices for the electron accelerator are a linac or a storage ring. When a photo-cathode is used in a linac the beam emittance is small, since each bunch is used only once for cooling the ions, but the electron current is limited by the life time of the cathode.

In a storage ring the beam current can be higher, but the emittance results from the equilibrium of heating of the beam by radiation excitation, intra-beam scattering of the electrons, heating by the ions (beam-beam scattering), and the radiation damping. It turns out that the IBS comprises a significant portion of the heating and strongly influences the design of the ring. Everywhere where the dispersion function is non-zero IBS couples the higher longitudinal temperature into the transverse direction and increases the emittance.

In an electron cooler the central velocity of the electrons and ions must be the same. With an ion energy of 275 GeV the required electron energy is only 150 Mev. As the radiated power is proportional to the 4th power of the energy it is therefore necessary to increase the radiation damping with wiggler magnets.

LAYOUT

The layout of the ring is shown in Fig. 1. It is shaped like a racetrack, with the cooling section being located in one straight section and the wigglers located in the other. Figure 2 shows the Twiss functions.

The arcs comprise only a small fraction of the circumference. It is not practical to concentrate the sextupoles for chromaticity correction in the arcs. We opted to eliminate the sextupoles from the arcs and use a tightly focused FODO lattice. Doing that allows keeping the dispersion small and minimizing IBS. We tried to use a double-bend-achromat lattice, but that did not decrease the beam emittance and increased the natural chromaticity significantly. The sextupoles are placed in the cooling section and the wiggler section.

In the cooling section the electrons overlay the ion bunch. It is 190 m long to maximize the interaction between electrons and ions. There are no magnetic focusing elements which results in large beta functions. An optical telescope reduces the beta functions at both ends to the small beta functions in the arcs. The non-zero dispersion in the cooling section allows redistributing longitudinal cooling into the horizontal direction [3]. It also allows placing sextupoles in the cooling section. However, since the phase advance over the whole cooling section is less than 90 degrees, placing many sextupoles would be detrimental to the dynamic aperture.
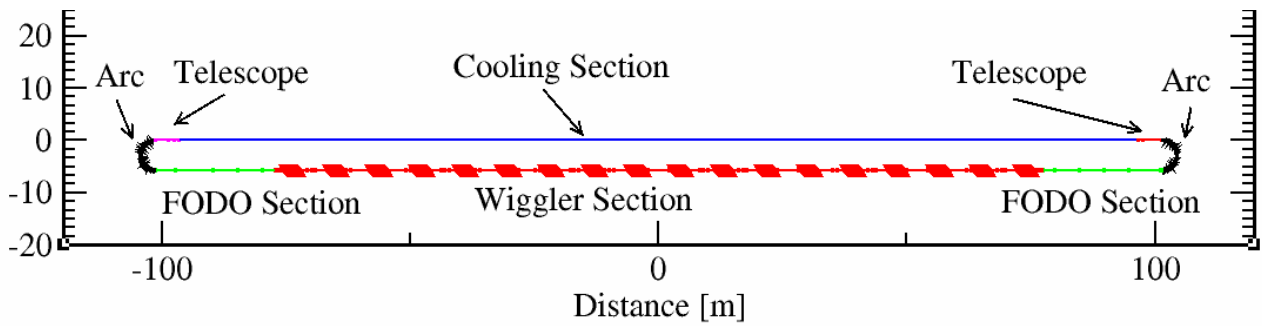
Figure 1: Layout of the ring cooler. The scale is the same in x and y. The arcs (black) have a diameter of 6 m. An optical telescope (red) connects the small beta functions in the arc to the large ones in the cooling section (blue). The other straight section has the wiggler section (red) with 18 vertical wigglers and 2 FODO sections (green) which allow setting the tunes and accommodate the RF and injection.
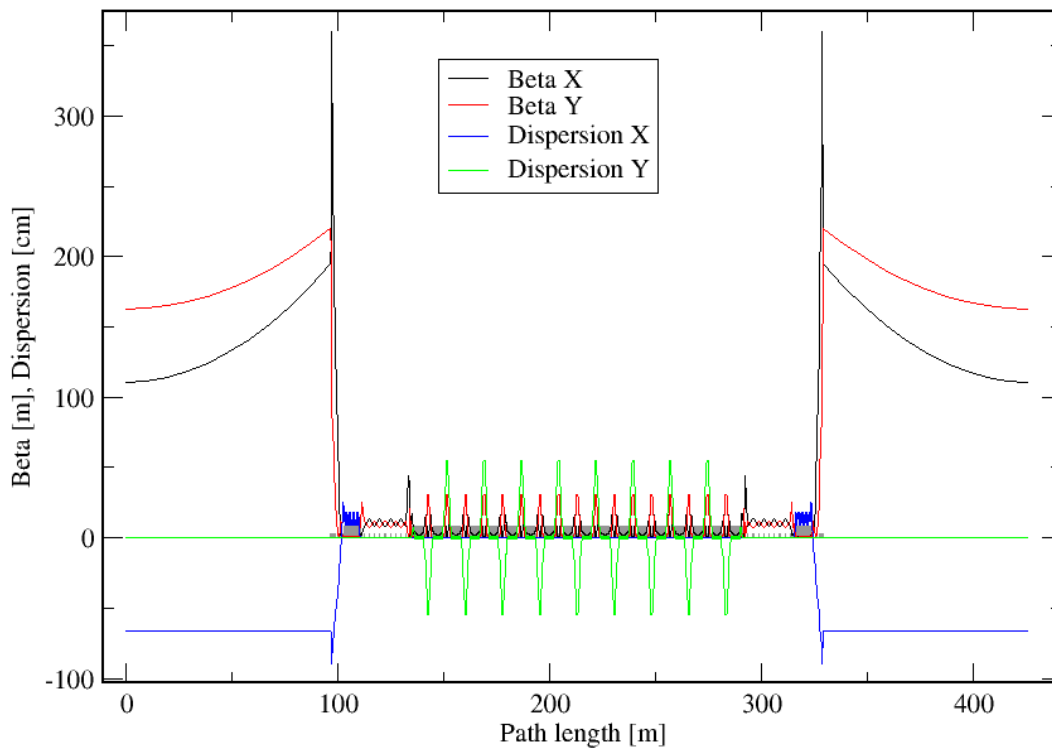
Figure 2: Optics function of the ring cooler, starting in the center of the cooling section.

The remaining location for the sextupoles is the wiggler section. We use 18 wigglers with a peak field of 2.4 T, which can be reached with Hybrid-Vanadium permanent magnets [4] . The gap is 2 cm and a wiggler period of 20 cm. Since the arcs and cooling section heats the beam in the horizontal direction and we want a round beam to cool the ions we use vertical wigglers.

The heating of the electrons from radiation excitation and (to a large degree) from IBS depends on the H-function:

$$H = \gamma D^2 + 2\alpha DD' + \beta D'^2 \qquad (2)$$

We use a gradient in the wigglers, so that they focus in the wiggler plane, so that the H-function in the wiggler is minimized.
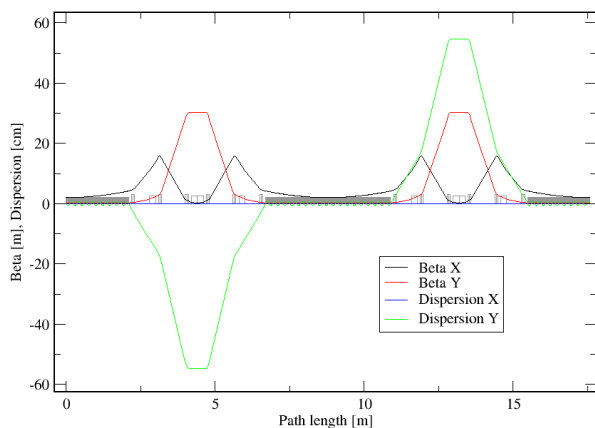
Figure 3: The optics between wigglers is similar to a DBA
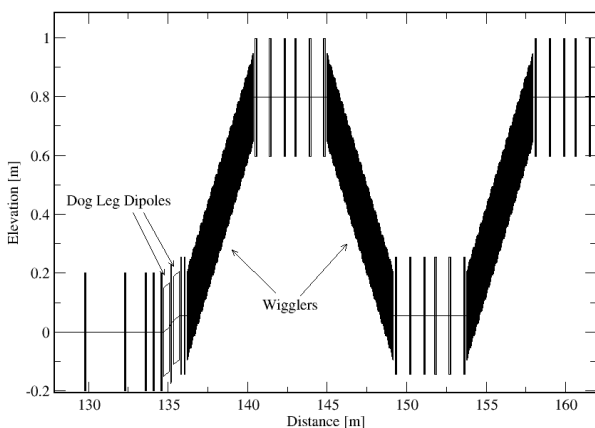
Figure 4: Side view of the wiggler section.

Since the H-function is constant outside dipoles it stays small between the wigglers and IBS is minimized. The optics between wigglers is similar to a DBA lattice(shown in Fig. 3), where the wigglers take the role of the dipoles. Unlike usual wigglers, which have half-strength poles at the ends to enter and exit on axis, we use full length poles and tilt the wiggler, as shown in Fig. 4. Using a dipole dog leg we create a vertical dispersion in front of the first wiggler. The dispersion exits with the same angle and is amplified to create a large dispersion between the wigglers, where the sextupoles are located.

In a previous design [5] we integrated a sextupole component into the wiggler field, so that the sextupoles are spread out over the whole length of the wigglers. Our new design has a factor of 2 and 3 lower emittances while taking advantage of cooling redistribution.

RESULTS

The emittances and cooling times are calculated with the GETRAD program. The program includes radiation excitation and damping and calculates the heating of the beam from IBS and from the cooling of the ion beam (Beam-

beam scattering, BBS). Starting from initial emittances it iterates until equilibrium is reached. The cooling times of the ions is then calculated from the final emittances. The results can be seen in Table 1.

Table 1: Electron Cooler Emittances and Ion Cooling Times

Parameter	Value
ϵ_x	6.3 nm
ϵ_y	11.9 nm
σ_p	$1.23 \cdot 10^{-3}$
τ_x	147 min
τ_y	368 min
τ_p	210 min

The achieved cooling times are sufficient to prevent the degradation of the luminosity from intra-beam scattering of the ions.

By locating the sextupoles in the wiggler section we calculated a momentum aperture of 7 sigma, enough to operate the ring with frequent top-up injection.

CONCLUSION

An electron cooler based on a storage ring is an alternative to the Micro-bunched Electron Cooling. Such cooler is based on proven technologies and is capable of achieving sufficient cooling to combat intra-beam scattering in the ion beam.

We have developed a ring design which provides the required emittances and cooling times. We found a compromise between the need for small dispersion to minimize IBS and the need for larger dispersion for chromaticity correction.

REFERENCES

[1] G. Stupakov, "Cooling rate for microbunched electron cooling without amplification", *Phys. Rev. Accel. Beams*, vol. 21, no. 11, p. 114402, 2018.
    doi:10.1103/PhysRevAccelBeams.21.114402

[2] A.V. Fedotov, X. Gu, D. Kayran, J. Kewisch, and S. Seletskiy, "Experience and challenges with electron cooling of colliding ion beams in RHIC", in *Proc. NAPAC'22*, Albuquerque, NM, USA, Aug. 2022, pp. 325–328.
    doi:10.18429/JACoW-NAPAC2022-TUZD5

[3] H. Zhao and M. Blaskiewicz, "Rate redistribution in dispersive electron cooling", *Phys. Rev. Accel. Beams*, vol. 24, no. 8, p. 083502, 2021.
    doi:10.1103/PhysRevAccelBeams.24.083502

[4] P. Elleaume, J. Chavanne , and Bart Faatz, "Design considerations for a 1 Å SASE undulator", *Nucl. Instrum. Methods Phys. Res., Sect. A*, vol. 455, no. 3, pp. 503–523, 2000.
    doi:10.1016/S0168-9002(00)00544-1

[5] H. Zhao, J. Kewisch, M. Blaskiewicz, and A. Fedotov, "Ring-based electron cooler for high energy beam cooling", *Phys. Rev. Accel. Beams*, vol. 24, no. 4, p. 043501, 2021.
    doi:10.1103/PhysRevAccelBeams.24.043501

DETERMINISTIC LATTICE APPROACH FOR BESSY III*

B. Kuske†, P. Goslawski, Helmholtz-Zentrum Berlin, Berlin, Germany

Abstract

Since 2021, HZB pursues the design of a 2.5 GeV storage ring as a successor of BESSY II in Berlin. The user's demand for diffraction-limited radiation at 1 keV corresponds to an emittance of 100 pm, making an MBA lattice indispensable. The envisaged location limits the circumference to ≈350 m. MBA lattices are composed of smaller substructures that can be analyzed and optimized separately, before combining them into one super period. The prerequisite for this approach is a clear idea of the goal parameters and their prioritization, as the design process is dominated by permanent decisions between different options. The resulting generic baseline lattice for BESSY III is a simple structure with few non-linear elements, already fulfilling all goal parameters and showing a very compatible non-linear behavior. This is our starting point for further optimizations including swarm or MOGA approaches.

INTRODUCTION

Multi-bend achromat lattices utilize many bending magnets with low deflection angles to reduce the emittance. Usually, these bends are placed at the center of repetitive unit cells, UCs. Multi-bend achromat lattices were pioneered by MAX LAB, Sweden. MAX IV, [1], was successfully commissioned in 2016. Sirius in Brazil followed in 2021, [2]. The ESRF, France, followed with the hybrid MBA in 2021, [3]. Nowadays, practically every new machine design or upgrade utilizes this type of lattice.

In 2014, A. Streun, PSI, added the concept of reverse bends (RB) to the MBA unit cell, UC, [4]. RBs are focusing quadrupoles placed off-axis to achieve negative bending. They detach the dispersion- and beta-function matching and significantly reduce the emittance.

In 2017, J. Bengtsson contributed the Higher-Order-Achromat approach to MBA-lattices [5, 6], where the linear lattice is constructed such, that all 1st and 2nd order resonance driving terms are suppressed by phase cancellation.

HZB now proposes a deterministic lattice design approach based on both, RB and HOA. The repetitive structure of MBA lattices is exploited to optimize small substructures, the UC, the dispersion suppression cell (DSC), and the straight section separately before they are composed into one generic super period. An important goal is to minimize non-linear effects by the set-up of the linear lattice structure. This approach leads to lattices close to the achievable optimum under the given boundary conditions, including fundamental decisions on a promising sextupole scheme. Opposed to generic optimizations this approach leads to

a clear understanding of the parameter space and optional trade-offs.

An indispensable prerequisite of this approach is a clear definition of the design goals and their priorities. For BESSY III [7], these are listed in Tables 1 and 2.

Table 1: BESSY III Goal Parameters

Parameter	Value
Energy	2.5 GeV
Super Periods	16
Circumference	≈350 m
Emittance	100 pm
Momentum Compaction Factor, α_c	> 1e-4
Momentum Acceptance	> 3 %

Table 2: Design Priorities

	Goal	Reason
1	MBA lattice	emittance
1	realization of HOA	non-linear behaviour
1	usage of reverse bends	emittance, circumference
2	low sextupole strength	non-linear behaviour
2	short circumference	site, costs
3	DSC as close as possible to half UC	non-linear behaviour

CONSTRUCTION OF THE UC

The half UC minimally consists of a central, main bend, MB, the reverse bend, RB, the defocusing quadrupole, QD, and 2 sextupoles, SF and SD. Initially, all drifts are 0.1 m.

HOA Condition for UC
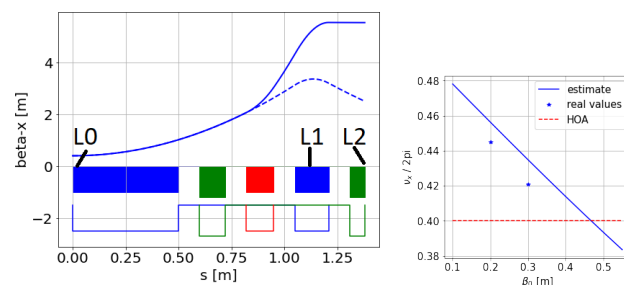
Figure 1: Left: β_x in half UC, regular (line) and for QD=0 (dashed line); magnet color code: MB: blue; RB: purple; QD: red, SF, SD: green. Right: ν_x, analytic estimate (blue line), exact phase advance (stars), and option for HOA (red).

The HOA condition on the phase advances $\nu_{x,y}$ in the UC is given by $n \cdot \nu_{x,y} = N$, where n is the number of UC in the arc and N is a lower integer. An upper limit for the horizontal phase advance in the UC is given for zero vertical focusing, QD = 0. β_x then develops like in a drift space from the center of the MB, β_0 at s=0, to β_1 at s=L1, at the RB. It can be assumed constant to the end of the UC at s=L2, see Fig. 1, left. An upper limit for ν_x is then given by

$$\nu_x < \int_0^{L1} \frac{\beta_0}{\beta_0^2 + s^2} ds + \int_{L1}^{L2} \frac{1}{\beta_1} = \arctan\left(\frac{L_1}{2\pi\beta_0}\right) + \frac{L_2 - L_1}{2\pi\beta_1}$$

Figure 1, right, shows this estimate for a wide range of β_0. The only option in this range to fulfill the HOA condition in the horizontal plane is indicated by the red line: $5 \cdot 0.4 = 2$.

Emittance Minimization

For fixed dipole parameters, the emittance is determined by β_0, η_0, at the center of the UC and the damping partition number, J_x. In the HOA-UC, β_0 is determined by the horizontal phase advance. For fixed phase advance, η_0 is determined by the RB angle. The bending gradients (MB and RB) determine the damping partition number, J_x.

$$J_x = 1 - \frac{I4}{I2} = 1 - \frac{\int_0^C \frac{\eta_x}{\rho^3} + \frac{2k\eta_x}{\rho} ds}{\int_0^C \frac{1}{\rho^2}}$$

Clearly, k and η_x at the RB are much larger than at the MB, while the bending radius, ρ, is in the same order of magnitude.

Figure 2 shows the impact on the damping partition number (left) and on the emittance (right) of a gradient in the MB (blue line) and that of an angle of the RB (green line), starting from a homogeneous bend and a pure focusing quadrupole. In all cases, the UC is fitted to phase advances of $\nu_{x,y}/2\pi = 0.4, 0.1$.
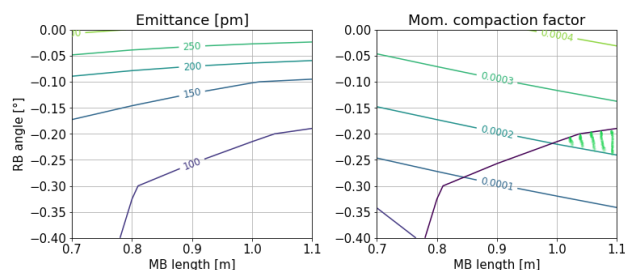
Figure 2: Left: J_x as a function of the MB gradient, blue, and the RB angle, green. Right: emittance for the same cases. Dashed line: $\epsilon * J_x$, i.e. the effect of the changing β-functions.

The much larger emittance reduction by the RB is caused by its superior β-functions and the larger gradient. Combining both effects, the gradient in the MB would worsen these conditions and enlarge the emittance. Therefore, the utilization of an RB is a better choice than a gradient MB.

The length of the MB (for fixed angle), also impacts the emittance, as well as the momentum compaction factor, α_c.

Figure 3 shows the emittance (left) and α_c (right) as a function of the RB angle and the length of MB for a fixed deflection angle. The demand for an emittance of 100 pm sets clear limits for the RB angle, as well as for the dipole length. If, in addition, also $\alpha_c > 2 \cdot 10^{-4}$ is demanded for the UC (corresponding to $\alpha_c > 1 \cdot 10^{-4}$ for the complete lattice), only the green shaded area fulfills both design goals.
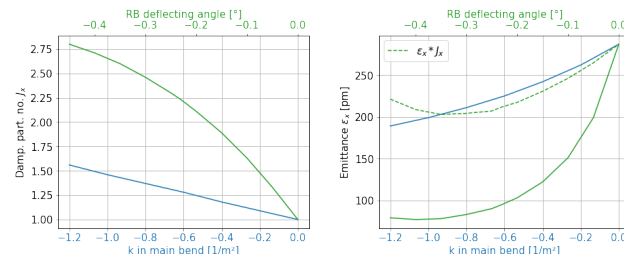
Figure 3: Left: emittance as a function of the RB angle and the MB length for fixed deflection angle. Right: α_c for the same cases.

Magnet Sorting and Angle Distribution

The different options for sorting the magnets in the UC have been discussed in [8]. There are 4 possible magnet configurations of the UC with a homogeneous MB, all similar in emittance and chromaticity, but very different, up to a factor of 2, in the sextupole strength needed to compensate for the chromaticity. The configuration with the least sextupole strength places the SD next to the main bend and the SF at the outside of the UC.

In [9] it has been shown, that the distribution of the deflection angle between the UC and the DSC is of minor importance with regard to the emittance and α_c. In an optimal configuration of both cells, only a few pm can be gained in the emittance.

Therefore, the position of the magnets and all important magnet parameters of the UC can be determined from the phase conditions of the HOA, the goal emittance and α_c, and the goal to keep non-linear fields low. This guarantees a solution, under the given boundary conditions, close to the optimum. For the resulting β-functions, a suitable DSC has to be developed.

CONSTRUCTION OF THE DISPERSION SUPPRESSION CELL

The optimal conditions to seek low emittance in the DSC have been discussed in [9]. The best practical results with regard to the non-linear behavior have been achieved by designing the DSC as close as possible to the UC, preserving the phase relation between the sextupoles. To this end, the suppression of the dispersion must be mainly achieved by variation of the dipole parameters, i.e. the reverse bend angle (and therefore the DSB-angle, to keep the total deflection) and the length of the final bend. Minor adjustments of the RB field can be used to achieve a flat vertical β_y-function. Figure 4 shows a typical result.
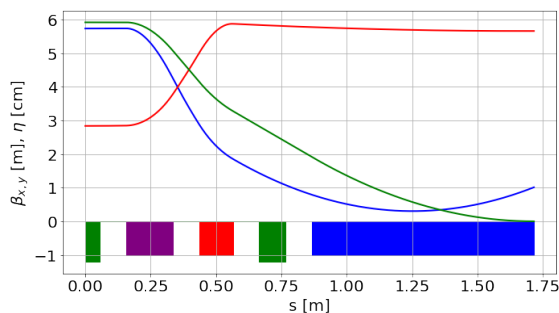
Figure 4: Typical DSC with dispersion suppression using mainly dipole parameters. β_x: blue, β_y: red, η_x: green. Magnet color code as above.

MATCHING THE STRAIGHT SECTION

The Twiss parameters at the end of the DS-bend must now be matched to the center of the straight section. A simple scan over doublet-, triplet- or quadruplet solutions can seek an overview of the options for matching. For BESSY III the design goal is 3 m β-functions in both planes at the center of the straight section with a length of 5.6 m. The only possible matching was achieved using 4 quadrupoles. The exact value of the β-functions is later sacrificed to achieve the desired working point, without changing the optimized UC and DSC parameters.

NON-LINEAR ASPECTS

The non-linear behavior of a lattice is governed by the resonance driving terms. One of the goals of the design process was to keep the unavoidable chromatic sextupole strength as low as possible, as the terms of the geometric as well as the amplitude-dependent driving terms include the integrated sextupole strength. Low sextupole fields keep the necessary higher-order corrections low.

The sum of the absolute chromatic sextupole strength can be calculated and compared to the achieved emittance, normalized by the square of the energy. For rough orientation, Table 3 compares the chromatic sextupole strength for a few cases. The necessary chromatic sextupole strength of BESSY III lies only 10 % over that of MAX 4, despite the much lower emittance, and is ≈ 70 % of that of SLS 2. Of course, a green field design has the advantage of not being limited by an existing beamline geometry and tunnel.

The periodicity of phase advance between the sextupole is disrupted due to the straight section. Therefore it makes

Table 3: Chromatic Sextupole Strength

|	ε	E	ε/E^2	$\Sigma(b_3 * L)$
	pm	GeV	pm/GeV²	1/m²
MAX 4	336	3.0	37.3	5180
SLS 2	123	2.4	21.4	8148
BESSY III	99	2.5	15.8	5742
Soleil	81	2.75	10.7	20278

sense to allow for some variation in the sextupole strength. Different schemes of grouping the chromatic schemes can be realized. Usually, the best results are reached by separating the sextupoles in the DSC. In order to get a realistic estimate of the momentum acceptance and the dynamic aperture without immense tracking effort, only momenta and amplitudes that correspond to a tune shift smaller than $|0.1|$ in both planes are considered stable, resulting in minor reductions when tracking with errors. Figure 5 shows the difference in momentum acceptance (left) and in dynamic aperture (right) between a symmetric scheme with 2 chromatic sextupole families and with different settings in the DSC.

There is a 5 % increase in momentum acceptance and the dynamic aperture is almost doubled. Separation into different families of the chromatic sextupoles is one of the most efficient knobs to improve the non-linear behavior of the lattice.
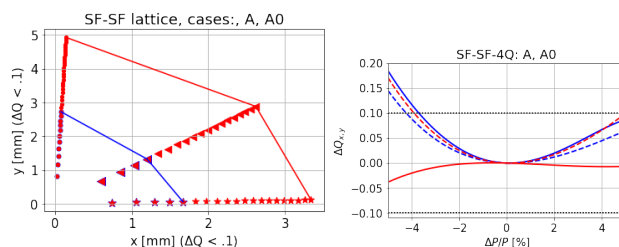
Figure 5: left: tune shift with momentum, 3.8 % for 2 families of chromatic sextupoles (blue) and 4.0 % with 4 families (red); right: dynamic aperture for the same cases, $\Delta Q < |0.1|$

CONCLUSION

HZB introduces a design procedure for MBA lattices, that develops the lattice in a deterministic way, rather than using resource-intensive optimizers. By applying the insights of the HOA and the reverse bend, and trying to minimize the sextupole fields, the unit cell is fixed to a large extent. The dispersion suppression cell is designed as close as possible to the unit cell. The mapping of the boundary conditions of the DSC onto the conditions at the center of the straight section is only possible with 4 quadrupoles in BESSY III. The resulting sextupole strength is small, and even without additional harmonic sextupoles or octupoles, the design criteria for the momentum acceptance can be exceeded. The lattice needs a modified injection straight with an increased β_x-function unless vertical injection is considered.

This lattice is considered a baseline lattice. From here optimizations including the introduction of further non-linear components like harmonic sextupoles or octupoles, technical adaptions, and computer-based optimization schemes will be applied for further improvements. Due to the well-optimized starting point, this process is expected to be fast.

A further advantage of this approach is, that it provides knowledge of the interplay between different parameters and the trade-offs for pushing certain parameters to the limit. Contrary to common practice, it turned out that combined function magnets are not the best choice for MBA lattices, as long as reverse bends can be utilized.

REFERENCES

[1] S. Leemann *et al.*, "Beam dynamics and expected performance of Sweden's new storage-ring light source: MAX IV", *Phys. Rev. Spec. Top. Accel. Beams*, vol. 12, p. 120701, 2009. doi:10.1103/PhysRevSTAB.12.120701

[2] L. Liu *et al.*, "Preliminary Sirius commissioning results", in *11th Int. Particle Accelerator Conf. (IPAC'20)*, Caen, France, May 2020, paper MOVIR06. doi:10.18429/JACoW-IPAC2020-MOVIR06

[3] S. White, *et al.,* "Commissioning and restart of ESRF-EBS", in *Proc. 12th Int. Particle Accelerator Conf. (IPAC'21)*, Campinas, Brasil, May 2021, paper MOXA01. doi:10.18429/JACoW-IPAC2021-MOXA01

[4] A. Streun, "The anti-bend cell for ultralow emittance storage ring lattices", *Nucl. Instrum. Methods Phys. Res., Sect. A*, vol. 737, pp. 148–154, 2014. doi:10.1016/j.nima.2013.11.064

[5] J. Bengtsson and A. Streun, "Robust design strategy for SLS-2", Paul Scherrer Institut, Villigen, Switzerland, SLS2-BJ84-001-2, Jun. 2017.

[6] J. Bengtsson, "The sextupole scheme for the Swiss light source (SLS): An Analytical Approach", Paul Scherrer Institut, Villigen, Switzerland, SLS note 9-97, Mar. 1997.

[7] P. Goslawski *et al.*, "A highly competitive non-standard lattice for a 4th generation light source with metrology and timing capabilities", in *Proc. 67th ICFA Advanced Beam Dynamics Workshop on Future Light Sources (FLS'23)*, Lucerne, Switzerland, Aug. 2023, paper TU1B1, this conference.

[8] B. Kuske, M. Abo-Bakr, and P. Goslawski, "Basic design choices for the BESSY III MBA lattice", in *Proc. 13th Int. Particle Accelerator Conf. (IPAC'22)*, Bangkok, Thailand, Jun. 2022, paper MOPOTK009. doi:10.18429/JACoW-IPAC2022-MOPOTK009

[9] B. Kuske and P. Goslawski, "Further aspects of the deterministic lattice design approach for BESSY III", in *Proc. 14th Int. Particle Accelerator Conf. (IPAC'23)*, Venice, Italy, May 2023, paper WEPL039, to appear in the proceedings.

DESIGN OF A 166.6 MHz HOM-DAMPED COPPER CAVITY FOR THE SOUTHERN ADVANCED PHOTON SOURCE*

Junyu zhu[†,1], Xiao Li[1], Jiebing Yu[1], Zhijun Lu[1],
Institute of High Energy Physics, Chinese Academy of Sciences, Beijing, China
[1]also at Spallation Neutron Source Science Center, Dongguan, China

Abstract

The Southern Advanced Photon Source (SAPS) aims to achieve ultra-low emittances and is expected to adopt low-frequency cavities (< 200 MHz) to accommodates on-axis injection. This paper focuses on the design of a 166.6 MHz HOM-damped normal conducting (NC) cavity for the SAPS. We propose a novel approach to achieve efficient HOM damping by optimizing the lowest frequency HOM and implementing a beam-line absorber in a coaxial resonant NC cavity. Notably, unlike beam-line absorbers for conventional NC cavities, the presence of a large beam tube in a coaxial resonant cavity does not affect the accelerating performance. This enables effective HOM damping while maintaining a high shunt impedance in a NC cavity. The numerical simulation results show that a compact copper cavity with effective HOM damping and excellent RF properties has been achieved.

INTRODUCTION

The Southern Advanced Photon Source (SAPS), planned for construction in the southern region of China, aims to become an advanced fourth-generation light source in the world. Its main parameters are listed in Table 1[1-2]. The recent lattice design of SAPS has successfully achieved a natural emittance of 32.5 pm, with an effective DA of 5 mm (horizontal) and 4 mm (vertical). Such a small DA is not enough for traditional off-axis injection schemes, which typically requires a DA of the order of 10 mm [3]. The on-axis longitudinal accumulation scheme is attractive due to its less demanding dynamic aperture requirement and the exempt from full-charge bunch delivery. However, a lower frequency RF system is required for a large separation between RF buckets since the state-of-art kicker has a total width of a few nanoseconds. In addition, lower frequency RF systems also have the advantages of low cost for RF power amplifiers and large acceptance, and have been used in many facilities, such as ILSF [4], MAX IV [5], Solaris [6], etc. Considering the technology readiness of 500 MHz HOM damped cavities and the fast kicker, a frequency of 166.6 MHz can be chosen for the fundamental cavity and 500 MHz for the third harmonic cavity.

Both normal conducting (NC) and superconducting (SC) options have been considered for the fundamental cavities during the design phase. The main parameters of these options are listed in Table 2. Due to the large RF power requirement and relatively small voltage requirement of SAPS, the number of cavities in the two schemes is very

close. However, the NC option offers cost savings of at least 40% in construction expenses and requires less space in the straight section, which is valuable for synchrotron light sources. Compared with the SC option, the NC case can save at least 40% of the construction expenses and need less space of straight section, which is very precious for the synchrotron light sources. Furthermore, the NC scheme can enhance system stability by adding an additional cavity and can continue to operate even if one set of RF systems fails, although this is expensive for the SC option. Therefore, we decided to develop a HOM damped 166.6 MHz compact NC cavity for the SAPS, although the 166.6 MHz SC cavity has successfully developed in our institute [7].

Table 1: Main Parameters of SAPS

Parameter	Value
Beam energy (E_0)	3.5 GeV
Circumference	810 m
Natural emittance ($\varepsilon_{natural}$)	32.5 pm-rad
Energy loss per turn	0.898 MeV
Synchrotron tune (Q_s)	0.709E-03
Betatron tunes v_x/v_y	81.23/ 64.18
Momentum compaction (α_p)	1.37E-05
Damping time (x/y/z)	18.1/28.1/19.3ms

Table 2: NC and SC Options for the 166.6 MHz RF System

Parameter	NC	SC
Frequency	166.6 MHz	
Total RF power	778 kW	
Total RF voltage	2.0 MV	
Number of cavities	5	4
Cavity voltage/MV	0.4	0.5
Cavity length/m	~ 1.0	3.0
Total cavity wall loss/kW	110	~0.4
Total RF power/kW	906	778
Total AC power/MW	1.776	1.756

RF CAVITY DESIGN

Due to the low RF frequency, the implementation of cylindrical or spherical shapes for the cavity geometry would lead to an overly large design. Therefore, a quarter-wave cavity was chosen for the 166.6 MHz NC cavity. In an ideal quarter-wave cavity, the resonant frequencies of eigenmodes induced by a coaxial structure are $f_n =$

$(2n + 1) \cdot c/(4l)$ (n = 0,1, 2, …). Thus, the frequency of the first HOM is three times that of the fundamental mode. However, in actual cavities, a large accelerating gap is required to achieve an accelerating voltage of several hundred kV or more, which cannot be neglected and results in a reduced frequency gap between the first HOM and the fundamental mode. Furthermore, as the cavity diameter increases, the frequency of HOMs becomes closer to the fundamental mode due to the large accelerating gap, thus limiting the improvement of cavity performance as the diameter increases.

The first several HOMs caused by coaxial structure are mainly monopole, whose electronic fields along the axis are shown in Fig. 1. Although they are affected by the acceleration gap, their frequency and electromagnetic field are still dominated by the coaxial structure. According to the coaxial line principle, the electric field at the open end is the smallest and the shunt impedance is near zero if the cavity length is equal to an integer multiple of the half wave of HOM. With this concept, we can optimize the shunt impedance of the first while simultaneously improving the performance of the fundamental.
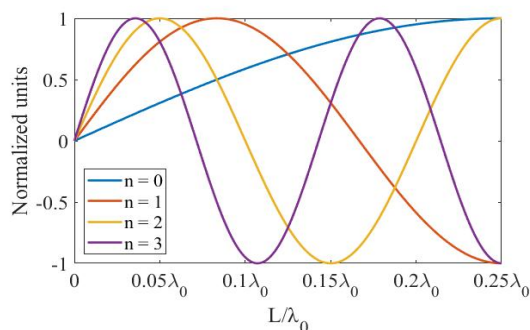

Figure 1: The electric field distribution of the first several HOMs along the axis.

The RF design and optimization process considered several key constraints. Firstly, to ensure practicality, the outer conductor diameter and length are kept below 1.0 m and 0.45 m, respectively. Secondly, the peak surface electric field (E_p) at the design voltage (V_c = 600 kV) is limited to 20 MV/m, which is 1.5 times the Kilpatrick breakdown limit at 166.6 MHz. A reasonable field enhancement factor (bravery factor) of up to 2 is applied, based on the experiences of other manufacturers and researchers, considering proper cleaning, heat treatment, and cavity baking [8]. Thirdly, to facilitate effective HOM damping through a beam-line absorber, the frequency of the first dangerous TM-like mode and TE-like mode should exceed 500 MHz and 400 MHz, respectively, ensuring a considerable frequency separation from the fundamental mode.

The optimized shunt impedance is approximately 8 MΩ (calculated as $R_s = V^2/P$), enabling the attainment of an accelerating voltage surpassing 600 kV, while sustaining a cavity power dissipation of 45 kW. These performance characteristics surpass those of cavities with similar structures. The first HOM, a monopole mode, exhibits a frequency of about 420 MHz, and its shunt impedance is optimized to be almost zero by matching the cavity's length

to its half-wavelength. Consequently, the next HOM becomes the nearest dangerous HOM, with a substantial frequency separation from the fundamental mode. The frequency of the first dangerous TM-like mode and TE-like mode is 504 MHz and 441 MHz, respectively. The main parameters are listed in Table 3.
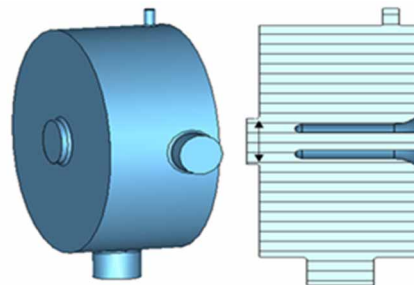
Figure 2: Cavity geometry and its cross-sectional view.

Table 3: Main Parameters of the 166.6 MHz NC Cavity

Parameter	Value
Frequency(f_0)	166.6 MHz
Cavity length (main body)	362 mm
Cavity diameter (no ports)	410 mm
Accelerating gap length	80 mm
Enlarged tube diameter	160mm
R/Q	257Ω
Shunt impedance $R_{sh}=V^2/(P_{in})$	7.76 MΩ
Quality Q	30200
Kilpatrick (k_p)	1.33
Frequency of nearest TM_like mode	504 MHz
Frequency of nearest TE_like mode	441 MHz

The cavity features multiple ports on its outer conductor, serving different purposes. One DN144 port is designated for the power input coupler, which utilizes a coaxial loop-type coupler with an alumina ceramic window. To accommodate frequency variations caused by temperature shifts, fabrication tolerances, and beam loading, two tuning plungers were designed. One plunger is manually operated, while the other is automatic. Each plunger can adjust the resonant frequency by approximately 200 kHz. The manual plunger sets the resonant frequency of cavity prior to operation, while the automatic plunger employs a stepper motor to adjust the resonant frequency during operation.

HOM INVESTIGATION AND DAMPING

Intense beam bunches in a storage ring can excite HOMs that may cause longitudinal and transverse coupled-bunch instabilities (CBI) by coupling the motion of different bunches. To maintain beam stability and prevent CBI, the HOM impedance of RF cavity must be damped below the CBI threshold level. The longitudinal and transverse CBI threshold of SAPS are 2.0 kΩ·GHz and 70 kΩ/m, respectively, which are calculated using the classic analytic formulas in the literature [9] according to the parameters in the literature [1].

67th ICFA Adv. Beam Dyn. Workshop Future Light Sources
ISBN: 978-3-95450-224-0

FLS2023, Luzern, Switzerland

JACoW Publishing

ISSN: 2673-7035

doi:10.18429/JACoW-FLS2023-WE4P33

(a)

(b)
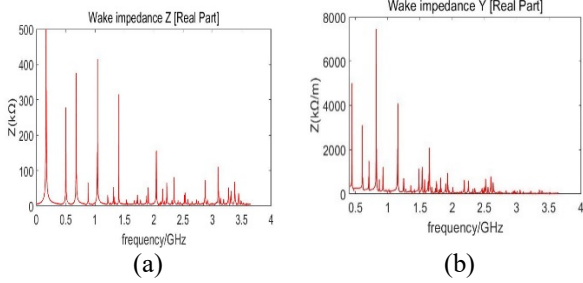
Figure 3: (a)Longitudinal HOM impedance spectrum of the bare cavity. (b) Transverse HOM impedance spectrum of the bare cavity.

The impedance spectrum of HOMs in the cavity was calculated by using CST Microwave Studio and Particle Studio, as shown in Fig.3. Only HOMs with frequencies below the beam tube cutoff were considered because those above will propagate out of the cavity. The beam-pipe radius at both ends of the cavity is 31.5 mm, and its cutoff frequency is 3.65 GHz for the TM mode and 2.8 GHz for the TE mode. The impedances of most HOMs are above the CBI threshold of SAPS.

A beam absorber scheme was proposed for the NC cavity, as shown in Fig.4. Notably, this scheme is uncommon in NC cavities because increasing the beam tube aperture to extract the HOMs can substantially affect the performance of copper cavities with a hollow structure. Nevertheless, it is a viable option for coaxial structure NC cavities since their impedance is primarily determined by the internal and external radius and length of the cavity, and less by the size of the tube outside the cavity. Moreover, due to a large frequency separation between the first HOM and the fundamental mode, combined with the ability of the NC cavity to withstand power losses of several hundred watts with minimal impact on performance, allows for the absorber to be positioned near the cavity, resulting in higher absorption efficiency. Finally, a beam-line ferrite damper with a diameter of 456 mm is employed to damp the HOM, and a transition section of 150 mm is used to attenuate the accelerating mode, as shown in Fig. 5. The absorbing material used here for the HOM-damped cavity is ferrite-C48 with a thickness of 4 mm [10]. To reduce processing costs, the entire material-type structure was replaced with a solution involving small pieces spliced together. The cavity iris, with a 160 mm aperture diameter, facilitates HOM field propagation and fundamental mode rejection. Additionally, a taper with a length of 100 mm and a radius of 31.5 mm at the exit is used to reduce the low loss factor.
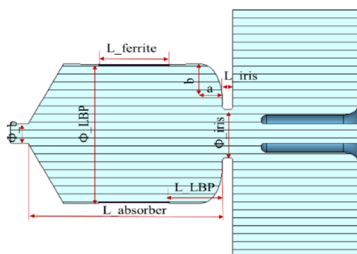
With the beam-line ferrite damper, the cavity impedance spectrum is illustrated in Fig.5. The results indicate that the longitudinal and transverse HOMs have impedances of less than 2.0 kΩ and 50 kΩ/m, respectively. The impedance and quality factor Q_0 of the fundamental mode are reduced by approximately 1% due to the absorber, which is negligible. Therefore, the loss power caused by the absorber is less than 500 W when the cavity dissipates power at the design value of 45 kW.

(a)

(b)
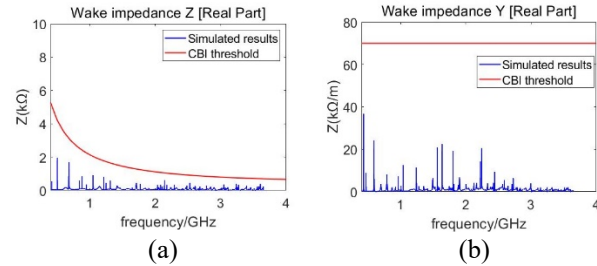
Figure 5: (a) Longitudinal HOM impedance spectrum of the 166.6 MHz cavity with absorber. (b) Transverse HOM impedance spectrum with absorber of the 166.6 MHz cavity with absorber.

THERMOMECHANICAL SIMULATION AND DESIGN

Thermal analyses of the cavity were performed using the ANSYS software, based on a maximum cavity dissipation power of 45 kW, corresponding to a 600 kV accelerating voltage along the cavity gap. In coaxial cavity structures, most of the power loss occurs on the inner conductor. To address this issue, a spiral-shaped water-cooled structure was designed for the inner conductor, with 12 cooling pipes placed inside the cavity mantle. The cooling pipes for the inner conductor and cavity mantle have diameters of 15 mm and 10 mm, respectively. The total volume flow rate was calculated to be 80 L/min, with a coolant velocity of 1.5 m/s, and a constant water temperature of 22°C was assumed. The simulation results indicated that the maximum temperature reached approximately 50°C, as shown in Figure 8, with a maximum thermal stress of 60 MPa. The multi-physical field analysis showed that this stress would result in a maximum thermal deformation of 0.11 mm and a frequency change of 90 kHz. However, with the tuners having an adjustment range of 400 kHz, the thermal deformation and frequency change values are acceptable.

Figure 4: Cavity with beam-line HOM absorber.
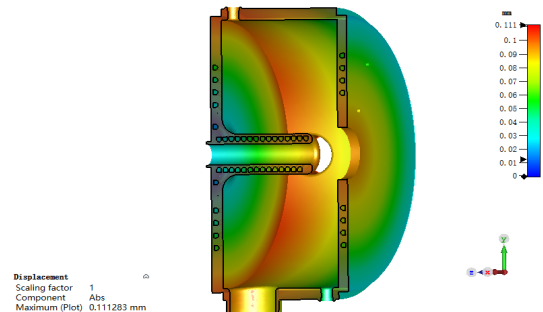
Figure 6: Cavity deformation as a result of thermal loss.

The heat of the HOM absorbers is caused by the fundamental mode and the HOMs. The fundamental mode brings no more than 500 W of thermal power when operating at the design value. The total power of the HOMs be obtained by Eq. (7).

$$P_{HOM} = k_{HOM} \cdot q \cdot I_b \tag{7}$$

where the P_{HOM} is the HOM power, k_{HOM} is the loss factor of the HOMs, q is the bunch charge, and I_b is the beam current. The loss factor is calculated to be 1.94 V/pC for HOMs with a natural bunch length of 5.06 mm, and the HOM power is about 3.2 kW. Considering the fundamental loss power caused by the absorber and redundancy, the maximum heat load of the absorber in the design is 5 kW. The simulation results indicate that the maximum temperature of the ferrite does not exceed 54 °C under the condition that the temperature difference between the inlet and outlet water does not exceed 7 °C, as shown in Fig.7.
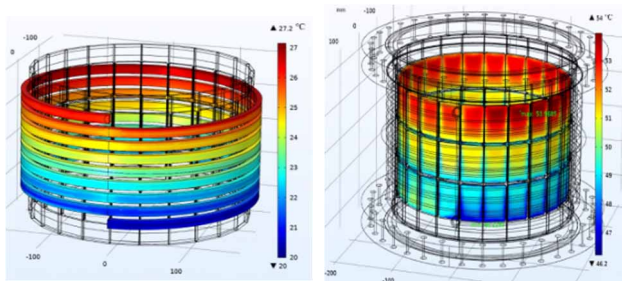
Figure 7: (a) Temperature distribution of the cooling pipe. (b) Temperature distribution of the ferrite.

CONCLUSION

This paper presents a novel approach to achieve effective HOM damping by optimizing the lowest frequency HOM and implementing a beam-line absorber in a coaxial resonant NC cavity. Unlike conventional NC cavities, by increasing the beam tube aperture in a coaxial resonant cavity to extract the HOMs does not compromise the accelerating performance, enabling efficient HOM damping while maintaining a high shunt impedance. Numerical simulations demonstrate that the 166.6 MHz HOM-damped NC cavity achieves a fundamental mode impedance of approximately 8 MΩ, which is superior to existing cavities with similar structure. The longitudinal and transverse HOM impedances are damped to below 2.0 kΩ and 50 kΩ/m, respectively, meeting the requirements for SAPS applications.

REFERENCES

[1] Y. Han *et al.*, "Preliminary study of the on-axis swap-out injection scheme for the southern advanced photon source", in *Proc. 12th Int. Particle Accelerator Conf. (IPAC'21)*, Campinas, Brazil, May 2021, pp. 1447-1449. doi:10.18429/JACoW-IPAC2021-TUPAB044

[2] X. Liu *et al.*, "Preliminary design of the full energy linac injector for the southern advanced photon source", in *Proc. 12th Int. Particle Accelerator Conf. (IPAC'21)*, Campinas, Brazil, May 2021, pp. 1454-1457. doi:10.18429/JACoW-IPAC-2021-TUPAB046

[3] G. Xu, J. Chen, Z. Duan, and J. Qiu, "On-axis Beam Accumulation Enabled by Phase Adjustment of a Double frequency RF System for Diffraction-limited Storage Rings", in *Proc. 7th Int. Particle Accelerator Conf. (IPAC'16)*, Busan, Korea, May 2016, pp. 2032–2035 . doi:10.18429/JACoW-IPAC2016-WEOAA02

[4] S. Ahmadiannamin *et al.*, "Design of 100 MHz RF cavity for the storage ring of the Iranian Light Source Facility (ILSF)", *Nucl. Instrum. Methods*, vol. 981, p. 164529, Aug. 2020. doi:10.1016/j.nima.2020.164529

[5] Å. Andersson *et al.*, "The 100 MHz RF system for the MAX IV storage rings", in *Proc. 2nd Int. Particle Accelerator Conf. (IPAC'11)*, San Sebastián, Spain, May 2011, pp. 193-195, paper MOPC051.

[6] A. I. Wawrzyniak *et al.*, "Solaris a new class of low energy and high brightness light source", *Nucl. Instrum. Methods*, vol. 411, pp. 4–11, 2017. doi:10.1016/j.ni-mb.2016.12.046

[7] P. Zhang *et al.*, "Development and vertical tests of a 166.6 MHz proof-of-principle superconducting quarter-wave beta= 1 cavity", *Rev. Sci. Instrum.*, vol. 90, p. 084705, 2019. doi:10.1063/1.5119093

[8] J. Bahng, E.-S. Kim and B.-H. Choi, "Design study of a radio-frequency quadrupole for high-intensity Beams", *Chin. Phys. C*, vol. 41. No. 7, pp.142-150, Jul.2017 . doi:10.1088/1674-1137/41/7/077002

[9] D. Einfeld, M. Plesko, and J. Schaper, "First multi-bend achromat lattice consideration", *J. Synchrotron Radiat.*, vol. 21, no.5, pp. 856–861, Sep. 2014. doi:10.1107/s160057751-401193x

[10] H. Hahn, E. M. Choi, and L. Hammons, "Ferrite-damped higher-order mode study in the Brookhaven energy-recovery linac cavity", *Phys. Rev. Accel. Beams,* vol. 12, p. 021002, Feb. 2009. doi:10.1103/PhysRevSTAB.12.021002

THE CRYOGENIC UNDULATOR UPGRADE PROGRAMME
AT DIAMOND LIGHT SOURCE

Z. Patel*, W. Cheng, A. George, S. Hale, M. Marziani, A. Ramezani Moghaddam, M. Reeves,
G. Sharma, S. Tripathi, Diamond Light Source Ltd., UK

Abstract

Diamond Light Source has installed four 2 m long, 17.6 mm period Cryogenic Permanent Magnet Undulators (CPMUs) as upgrades for crystallography beamlines since 2020, with two more planned within the next year. The CPMUs provide 2 - 3 times more brightness and 2 - 4 times more flux than the pure permanent magnet (PPM) devices they are replacing. They have been designed, built, and measured in-house. All four have a 4 mm minimum operating gap and are almost identical in their construction: the main difference being an increase in the number of in-vacuum magnet beam support points from four to five, between CPMU-1 and CPMUs 2 - 4, to better facilitate shimming, particularly at cold temperatures. The ability to shim at cryogenic temperatures necessitated the development of an in-vacuum measurement system. The details of the measurement system will be presented alongside the mechanical and cryogenic design of the undulators, including issues with the magnet foils, and the shimming procedures and tools used to reach the tight magnetic specifications at room temperature and at 77 K.

INTRODUCTION

Diamond Light Source has 24 straight sections, all of which are filled. With the exception of creating new straight sections, as with the installation of a DDBA cell [1], or replacing a sextupole magnet with a short wiggler [2], upgrading of existing insertion devices is the next major step in improving the existing machine for the beamlines.

CPMUs have become an attractive prospect as insertion devices since the manufacture of praseodymium material magnets. The remanence of PrFeB and PrNdFeB magnets increases when cooled to the cryogenic temperature of liquid nitrogen (77 K), unlike NdFeB magnets which undergo spin reorientation at 150 K [3]. Therefore, cryogenic cooling allows for a shorter period device while achieving the same, or stronger, magnetic field. An increase in the number of magnetic periods of an insertion device over the same length results in an increase in the radiation flux and brightness for the beamlines. Four in-house designed, built, and measured CPMUs have been installed at Diamond Light Source over the three years 2020 - 2022, with one new CPMU planned for installation this year, and two to be re-worked to overcome an issue with the magnet beam foil discussed later in this paper.

_____
* zena.patel@diamond.ac.uk

MAGNETIC AND MECHANICAL DESIGN

The magnetic design was developed to increase the brightness and flux of several of the Diamond crystallography beamlines (I03, I04, I11, I24, and VMXm). The design was modelled in Radia [4] using PrNdFeB magnets and vanadium permendur pole pieces, the details of which can be found in [5]. A 17.6 mm period was used for all CPMUs, chosen to cover a suitable x-ray energy range (5 - 30 keV) for the beamlines using the existing Diamond ring and the proposed Diamond-II ring.

The mechanical structure is based on the Diamond third-generation in-vacuum undulator (IVU) structure [6], shown in Fig. 1. Two out-of-vacuum beams move vertically along the two main columns of the structure by way of slides on linear guide rails. Two in-vacuum magnet girders, populated with magnets and poles, are attached to the beams by columns. A 100 μm CuNi foil is placed over the magnets and poles and attached by spring tensioners at the ends of the girders in order to reduce the wakefields produced by the electron beam as it traverses the undulator [7].
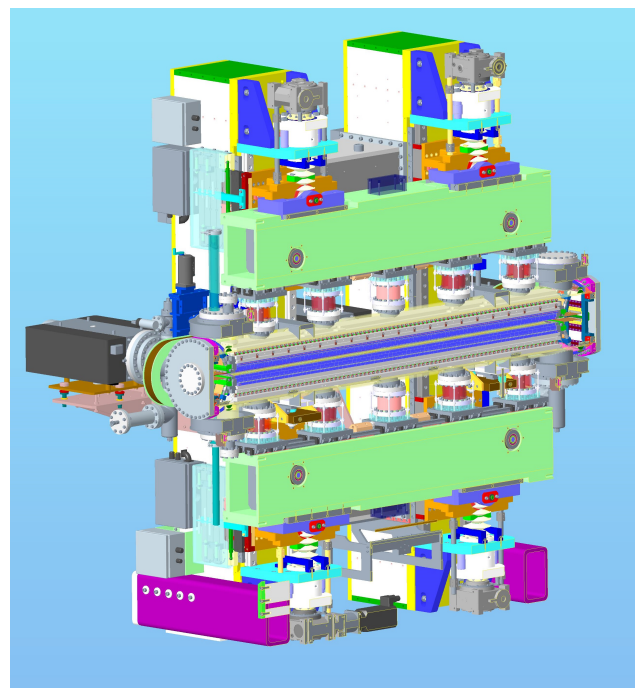

Figure 1: Model of CPMU-3 with the vacuum chamber cut away. The beams are light green with the bellows of the columns shown in red.

Cooling pipes are welded to the magnet beams in order to cool the magnets using a recirculating LN$_2$ cryocooler, supplied by FMB Oxford. The CPMUs typically reach 77 K

(LN$_2$ temperature) within 6 to 7 hours, with the cold mass acting as a cryo-pump. There is an 8 mm reduction in the length of the aluminium girders due to contraction upon cooling which is why the columns are mounted on slides. There is also a ~30% increase in force on the CPMU structure compared to a standard IVU, from 16 kN to 21 kN at a 4 mm gap, due to the increased magnet force when the magnets are cooled. Finite Element Analysis (FEA) in ANSYS [8] showed the standard structure was capable of withstanding the increased forces.

The motion control of the CPMU structure is the same as standard in-vacuum devices: 4 independent axes each with a linear encoder. CPMUs 1-3 use a Delta Tau Geo brick motion controller whereas CPMU-4 uses the newer Omron CK3M controller due to obsolescence of the former. The gap can be varied from 4 mm to 29 mm as well as tilt, taper, and individual axis and girder movements.

Design Evolution

The original builds of CPMU-1 and CPMU-2 were made with triplet (pole-magnet-pole), shown in Fig 2, and singlet (magnet) holders. These CPMU builds progressed to magnetic measurements, at which stage it was discovered that the holders did not retain the positions of the poles well enough. There was also an issue with the cold measurement system Hall probe beam deforming at cold temperatures at the same time. Therefore, the holder design was simplified to a doublet (magnet-pole) to simplify the pole clamping, and made 30% narrower to allow more room in the vacuum chamber for a thicker Hall probe beam. The doublet holder design has been used for all in-house built CPMUs at Diamond.
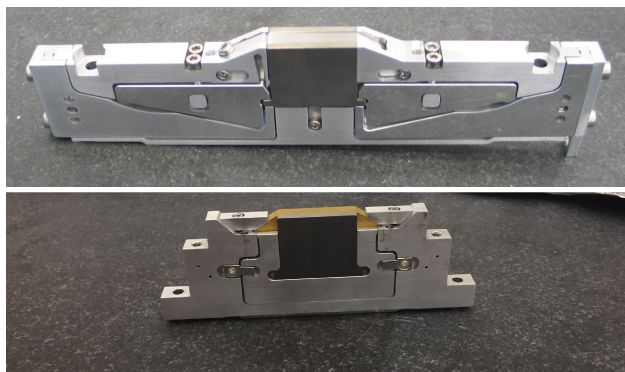

Figure 2: Above: The triplet holder initially used for CPMUs 1 and 2. Below: The doublet holder used for CPMUs 1-5.

The first CPMU had only 4 columns. Upon cooling the CPMU it was found that four columns was too few to correct the device satisfactorily. Following some FEA work, the number of columns was increased to five for the subsequent CPMUs. The addition of further columns had diminishing returns in reducing the girder deformation. Using an odd number of columns also meant that the centre columns could be fixed and the girders would contract equally around the centre columns upon cooling, rather than the unequal contraction around the off-centre fixed columns of CPMU-1.

MAGNETIC ASSEMBLY AND SHIMMING

Opt ID [9] is used to sort the magnets based on Helmholtz coil measured data. The magnetic assembly procedure has evolved during the last five CPMUs and has now been simplified to: assembling the magnets and poles onto the girders with nominal shim, measuring the heights and adjusting the shim until both magnets and poles are within $\pm 20\,\mu m$ tolerance (typically less than $\pm 10\,\mu m$ is achieved). This is the procedure CPMU-5 has recently undergone, where room temperature shimming has proved successful. CPMUs 1 - 4 were assembled in magnet-only configuration with the assumption that correcting a magnet-only device would leave minimal pole correction needed. However, it was found that pole height is the dominating factor in magnetic errors of the device, and any errors in the magnets are easily compensated by pole height and tilt corrections.

Once assembled, the CPMU is aligned to the out-of-vacuum measurement bench, consisting of a Hall probe and flipping coil. Column shimming is first performed to straighten the long-range undulation of the peak magnetic field, B$_p$. In-situ pole shimming is then used to reduce local errors in B$_p$, reducing trajectory and phase errors; the two main figures of merit for undulator performance. Pole height and tilt can be adjusted in micron steps, limited to a maximum of $50\,\mu m$ to avoid large step changes in height which can cause ripples on the CuNi foil, causing impedance to the beam, and to avoid large peak-to-peak deviations in the field, causing an increase in the local phase error. The final magnetic correction at room temperature is made with the addition of magic finger magnets, placed at the ends of the girders, to reduce field integrals and, therefore, the impact of the undulator on the storage ring.

COLD MEASUREMENT SYSTEM

Once the shimming of the CPMU at the out-of-vacuum bench is complete, the magnet girders are installed in the vacuum chamber, along with the cold in-vacuum measurement system in order to measure and shim the CPMU while cold. As discussed earlier, when the CPMU cools down to 77 K the force between the two magnet girders increases. This causes deflection of the unconstrained sections of the girders (between the column positions), which can be corrected for using column shimming. The cold measurement system consists of a Hall probe and stretched wire for field mapping and field integral measurements respectively. The Hall probe has evolved from Arepoc and PT100 sensors mounted on 4 mm thick ceramic (CPMUs 1 - 3), to a SENIS S-type probe in a 4 mm thick epoxy glass holder (CPMU-4), to the same SENIS probe mounted on a 1 mm thick epoxy glass holder (to be used for CPMU-5), in order to take measurements at smaller gaps. The Hall probe experiences a 35 - 40° temperature drop during the 45 minute Hall scan, therefore it was necessary to calibrate the voltage sensitivity with temperature. More details on the Hall probes and temperature calibration may be found in [10].

67th ICFA Adv. Beam Dyn. Workshop Future Light Sources
ISBN: 978-3-95450-224-0

FLS2023, Luzern, Switzerland

JACoW Publishing
ISSN: 2673-7035

doi:10.18429/JACoW-FLS2023-WE4P36

The Hall probe is mounted on a carriage that moves along an aluminium beam on rails, driven by a pulley system coupled to an out-of-vacuum motor, shown in Fig. 3. The longitudinal position of the Hall probe is measured with a Renishaw laser tracker. The sag of the aluminium beam is measured by a Leica laser tracker and a compensation table is applied to the Geo brick motor controller to move the beam vertically to compensate the sag as the probe travels the length of the CPMU.

The RMS phase errors of the CPMUs increase at cold temperatures due to the girder deformation, as shown in table 1. Column shimming is performed to reduce the phase error to the required value.

Table 1: RMS phase errors of CPMUs 1 - 5 measured using the out-of-vacuum measurement bench at room temperature and the in-vacuum measurement system upon initial cooling to 77 K, and the final value at 77 K after column shimming.

CPMU Name	RMS phase error [deg.] at 5 mm gap		
	@296K	Initial@77K	Final@7K
CPMU-1	2.1	8.2	4.6
CPMU-2	2.3	7.5	3.7
CPMU-3	1.8	6.6	3.2
CPMU-4	2.1	10.3	3.2
CPMU-5	2.0	*to be measured*	
CPMU-1*	2.1	*to be measured*	

*reworked

INSTALLED PERFORMANCE

Upon installation, beam-based alignment is performed as with a standard IVU [11]. Energy scans, using the beamlines' double crystal monochromators, show that the flux has increased on all beamlines that have been upgraded by CPMUs. At the main energy of interest, 12.6 keV, the flux has increased by a factor of two on average. The flux gain is greater still for the higher harmonics (higher x-ray energies).

CuNi Foil Issues

Following installation and cool-down of CPMU-1, a restriction on the aperture was found, which limited the minimum gap to 6.5 mm, that then disappeared following two thermal cycles. A further thermal cycle for a cryocooler service caused it to reappear. The tension of the foil was thought to be the cause and it was therefore increased by 50% for CPMU-2. However, the aperture of both CPMU-1 and CPMU-2 have both been found to change with thermal cycling of their cryocoolers. While there is limited thermal cycling of CPMU-3 and CPMU-4, what evidence there is shows no restriction of their apertures. The main differences between CPMUs 1 and 2 and CPMUs 3 and 4 are the height of the poles relative to the magnets, and the method of foil fitting. The poles were initially set 0.1 mm proud of the magnets for the first two CPMUs, whereas in the latter two they
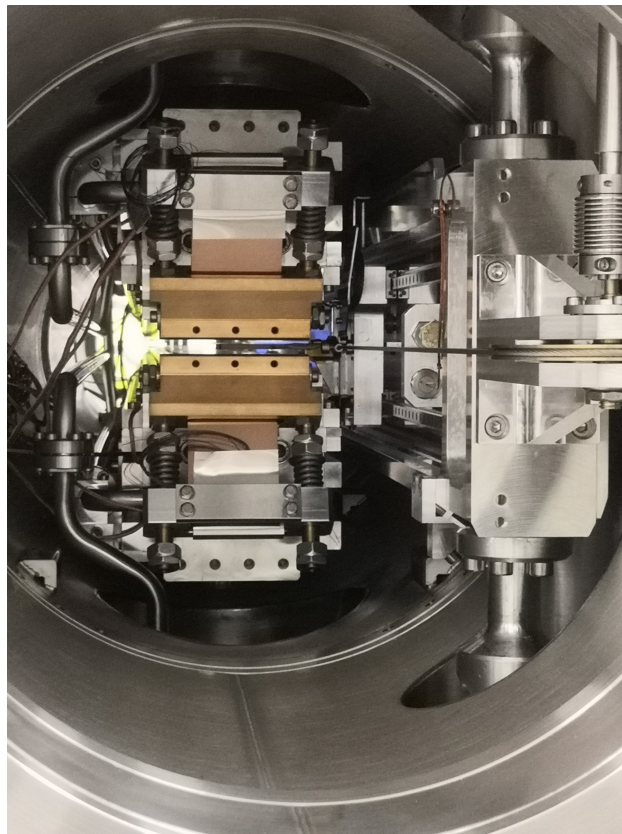
Figure 3: The cold measurement system Hall probe beam installed in the vacuum chamber alongside CPMU-1. The pulley system with its coupling to the out-of-vacuum motor is visible on the right. On the left the LN_2 pipes can be seen.

are set flush. The CuNi foil on CPMUs 1 and 2 was rolled over the magnets and poles and then tensioned, whereas for CPMUs 3 and 4 the foil was pre-stretched and placed over the magnets and poles before tensioning.

CPMU-1 has recently been removed from the storage ring and replaced by CPMU-3. CPMU-1 has been reworked, by removing the height offset of the poles and magnets, and pre-stretched foil will be attached at the appropriate assembly stage. It was clear from the visible burn marks that the original CuNi foil had bunched into the gap at the centre of the undulator. CPMU-2 will follow suit next year, and will be replaced with the reworked CPMU-1.

CONCLUSION

The cryogenic undulator upgrade programme at Diamond Light Source has largely been a success, increasing the flux on three beamlines over the energies of interest. However, the foil issue is still to be fully understood and overcome on CPMUs 1 and 2. While there is reticence regarding warming and cooling the CPMUs unnecessarily, further cooling cycles of CPMUs 3 and 4 for cryocooler maintenance will provide evidence that setting the pole heights flush with the magnets and/or the pre-stretching of foil is the required fix.

REFERENCES

[1] R. P. Walker *et al.*, "The Double-Double Bend Achromat (DDBA) lattice modification for the Diamond storage ring", in *Proc. IPAC'14*, Dresden, Germany, 2014, pp. 331-333. `doi:10.18429/JACoW-IPAC2014-MOPRO103`

[2] I. P. S. Martin, B. Singh, and R. Bartolini, "Impact of the DIAD wiggler and "missing-sextupole" optics on the Diamond storage ring", in *Proc. IPAC'10*, Melbourne, Australia, 2019, pp. 1581-1584. `doi:10.18429/JACoW-IPAC2019-TUPGW077`

[3] D. Goll, M. Seeger, and H. Kronmüller, "Magnetic and microstructural properties of nanocrystalline exchange coupled PrFeB permanent magnets", *J. Magn. Magn. Mater.*, vol. 185, issue 1, pp. 49-60, 1998. `doi:10.1016/S0304-8853(98)00030-4`

[4] RADIA, `http://www.esrf.eu/Accelerators/Groups/InsertionDevices/Software/Radia`

[5] G. Sharma *et al.* "CPMU development at Diamond Light Source", presented at IPAC'23, Venice, Italy, May 2023, paper MOPM096, to appear in the proceedings.

[6] Z. Patel, A. George, S. Milward, E. C. M. Rial, A. J. Rose, and R. P. Walker, "Insertion devices at Diamond Light Source: a retrospective plus future developments", in *Proc. IPAC'17*, Copenhagen, Denmark, 2017, pp. 1592–1595. `doi:10.18429/JACoW-IPAC2017-TUPAB116`

[7] J.-C. Huang, H. Kitamura, C.-H. Chang, C.-H. Chang, and C.-S. Hwang, "Beam-induced heat load in in-vacuum undulators with a small magnetic gap", *Nucl. Instrum. Methods Phys. Res., Sect. A*, vol. 775, pp. 162-167, 2015. `doi:10.1016/j.nima.2014.11.116`

[8] Ansys Mechanical 2020 R2

[9] J. Whittle *et al.*, "Using artificial immune systems to sort and shim insertion devices at Diamond Light Source", *J. Phys. Conf. Ser.*, vol. 2380, p. 012022, 2022. `doi:10.1088/1742-6596/2380/1/012022`

[10] Z. Patel *et al.*, "An in-vacuum measurement system for CPMUs at Diamond Light Source", presented at PAC'23, Venice, Italy, May 2023, paper MOPM095, to appear in the proceedings.

[11] O. Chubar *et al.*, "Spectrum-based alignment of in-vacuum undulators in a low-emittance storage ring", *Synchrotron Radiat. News*, vol. 31, no. 3, 2018. `doi:10.1080/08940886.2018.1460173`

LASER INTERFEROMETER FOR HALL PROBE ALIGNMENT AND MEASUREMENT OF UNDULATOR*

Saif Mohd Khan[†,1], Mona Gehlot[2], Shreya Mishra[3], Ganeswar Mishra[1]

[1]School of Physics, Devi Ahilya VishwaVidyalaya (DAVV), Indore, India

[2]Deutsches Elektronen-Synchrotron DESY, Hamburg, Germany

[3]Institute of Engineering and Technology (IET), DAVV, Indore, India

Abstract

In the Hall probe Magnetic measurement method the field mapping is done along the length of the undulator. The field integral and phase error computed from the field mapping works as the figure of merit of the undulator. In this paper, we discuss the working of a laser interferometer for precise Hall probe alignment. A new user friendly software based on MATLAB has been developed. The phase error and magnetic field integrals are calculated for both taper and untaper U50 undulator of the Laser and Insertion Device Application (LIDA) Laboratory.

INTRODUCTION

The Hall probe method is widely used measurement system for field integral and phase error calculations of undulators. In this method a Hall probe is moved on a moving sledge and the field is mapped along the undulator length. The measurement accuracy of the filed mapping gives precision in the field integral computation. For this purpose a position sensitive detection system is often used to calibrate the z-position of the Hall probe on the translation sledge [1, 2]. In this paper, we introduce additional laser interferometer system and compare the two methods.

LASER INTERFEROMETER ALIGNMENT AND MEASUREMENT

The experimental setup consists of a Hall probe sledge mounted on a motorized z-linear translation stage with a length of 2000 mm. The z-linear translation stage is driven by a stepper motor controlled by a single-axis motion controller. The controller operates using specialized software that enables the recording of multiple Teslameter channels at once. It is programmable to control the speed and direction of the sledge's movement, as well as the delay time and step length for measurements, which can be defined by the user. The control software allows the linear translation stage to move in both forward and reverse directions within a distance range of 2 μm to 2000 mm. The permissible speed of movement can reach up to 20 mm/s, and the system can be set to capture data with a delay time between 0 ms and 9999 ms for each measurement. To ensure accurate measurements of the magnetic field, it is crucial to maintain precise alignment of the Hall probe with the undulator axis. Any deviation from the desired position can introduce errors in the recorded data.

To verify the results of PSD, The Wollaston prism based laser interferometer is also implemented on the linear translation stage. The setup employs a laser as the primary light source. The light emitted by laser is directed towards a beam splitter. The transmitted light from the beam splitter is then passed through a polarizer. The polarized light emerging from the polarizer enters a Wollaston prism, a birefringent optical element. The Wollaston prism divides the incident light into two distinct rays based on their polarization characteristics: the ordinary ray (o-ray) and the extraordinary ray (e-ray). The retro reflector consists of two mirrors, both equipped with mounts on rotational stages featuring angular adjustment capabilities. These adjustments allow precise control over the tilt angles of the mirrors. By carefully adjusting the tilt angles of the mirrors in the retro reflector setup, the two reflected light rays combine at the Wollaston prism, resulting in constructive or destructive interference. The recombined light rays at the Wollaston prism pass through the polarizer and beam splitter once again facilitating the observation of the interference fringe pattern. The movement of the Wollaston Prism in vertical direction leads to shift in the interference pattern which is used to measure the misalignment of the Hall probe sledge on the linear translation stage. Laser interferometer assembly with Hall probe system shown in Fig. 1.
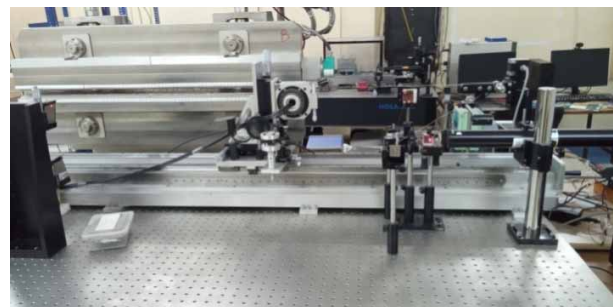
Figure 1: Laser Interferometer system on Hall probe bench.

RESULTS AND DISCUSSION

Throughout the entire length of the undulator, we carefully monitored the motion of the Hall probe with help of PSD. Our observations revealed that the Hall probe remained consistently positioned along the axis of the undulator, with a tolerance within the range of ±30 μm along the vertical direction presented in Fig. 2. The calibration curve of the laser interferometer was constructed as shown in Fig. 3 to facilitate the determination of transverse offset.
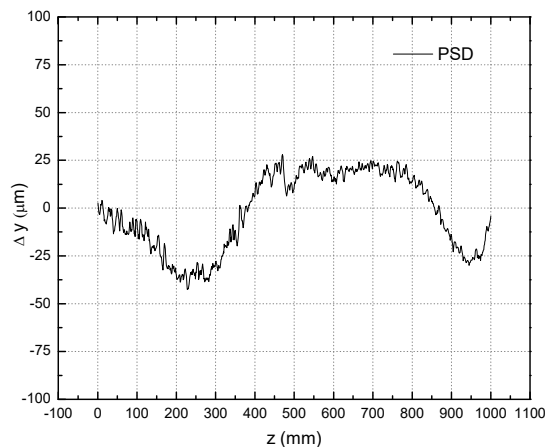
Figure 2: Misalignment captured by PSD.
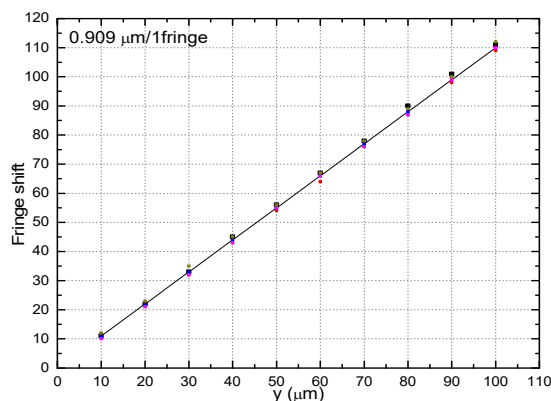
Figure 3: Calibration curve for laser interferometer.

We plotted the fringe shift against various transverse offsets while vertically displacing the interferometer. The slope of the curve represents the magnitude of fringe shift per unit transverse offset. Our analysis yielded a precise measurement of 0.909 microns per fringe shift as the transverse offset. The laser interferometer was systematically manoeuvred along the length of the undulator, utilizing the Hall probe sledge mounted on a linear translation stage. During the measurements, a comparison was made between the readings obtained from the laser interferometer and the PSD. It was observed that there existed a disagreement between the two measurements, with a range of ±0.5μm. Figure 4 shows the result obtained with laser interferometer.

Figure 5 presents the magnetic field measurement of untaper and taper gap undulator. The measurements by Hall probe were recorded at a step length of 1 mm for precise sampling of the magnetic field along the length of undulator, with a delay of 3000 ms between each reading ensured sufficient time for stabilization and minimized any potential interference between consecutive measurements. To calculate the magnetic field integrals, a newly developed user-friendly MATLAB code was utilized. Figures 6 and 7 show the first field integral and second field integral of magnetic field, respectively.
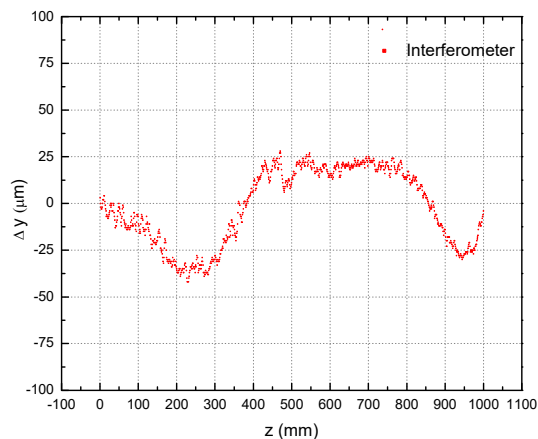
Figure 4: Misalignment captured by Laser interferometer.
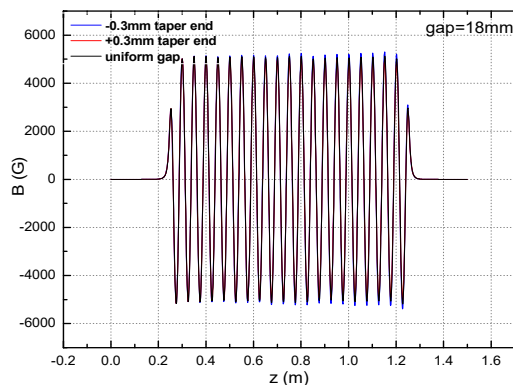
Figure 5: Magnetic field.
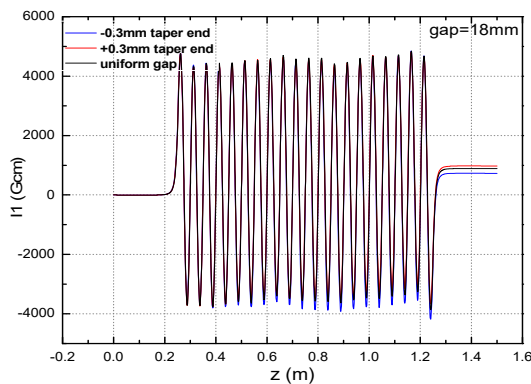
Figure 6: First field integral.
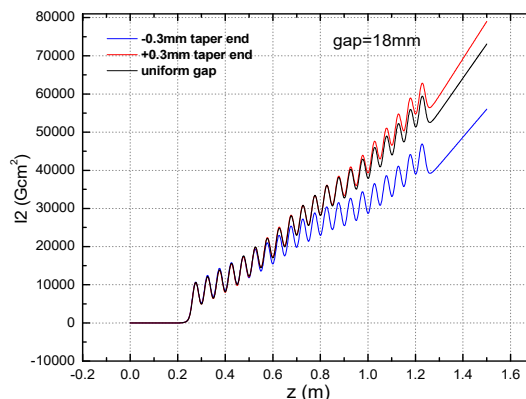
Figure 7: Second field integral.

In the stretched wire experiment, the measurement of the magnetic field integrals is conducted using a stretched copper litz wire consisting of 100 strands [3]. The wire undergoes multiple movements, and the measurements are averaged to obtain reliable results. Figures 8 and 9 shows the comparison between the measurement with Hall probe and stretched wire system for untaper gap undulator.
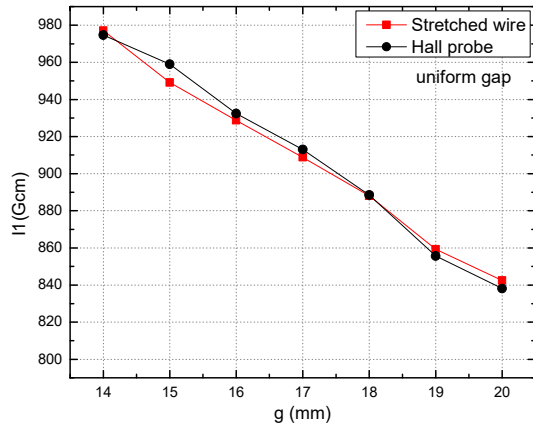
Figure 8: First field integral in uniform gap stretched wire measurement.
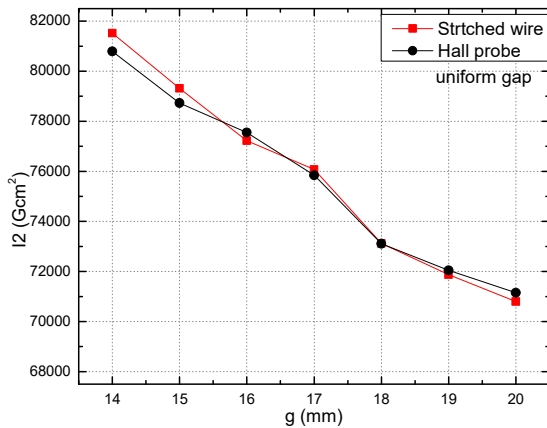
Figure 9: Second field integral in uniform gap stretched wire measurement.

Interestingly, both measurement methods yield closely matching outcomes in case of tapered gap [4]. The measurement is performed to tapered gap from -0.3mm to +0.3mm as shown in Figs. 10 and 11, respectively. Specifically, the first integral measured using the stretched wire exhibits a maximum difference of approximately2 Gcm, while the second integral shows a maximum discrepancy of approximately 100 Gcm^2.
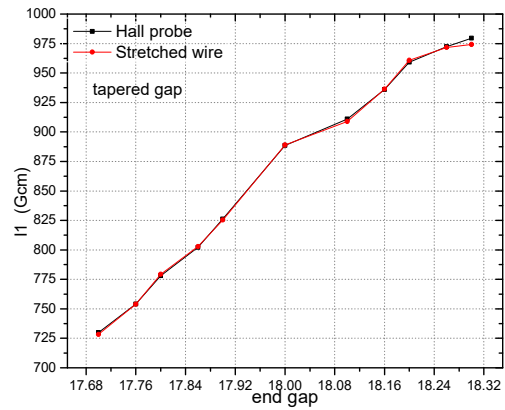
Figure 10: First field integral in taper gap stretched wire measurement.
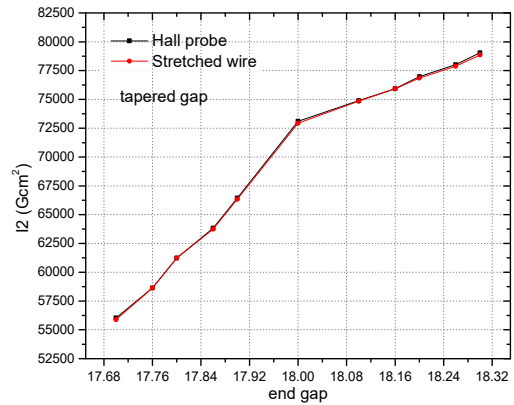
Figure 11: Second field integral in taper gap stretched wire measurement.

ACKNOWLEDGMENT

REFERENCES

[1] S. M. Khan *et al*., "Implementation of position measuring system for Hall probe alignment in undulator magnetic field measurement", in *Proc. 29th DAE-BRNS National Laser Symp. (NLS-29)*, RRCAT, Indore, India.

[2] S. M. Khan, G. Mishra, M. Gehlot, and H. Jeevakhan, "Hall probe magnetic measurement of 50 mm period PPM undulator", in *Proc. IPAC'22*, Bangkok, Thailand, Jun. 2022, pp. 2744-2746.
doi:10.18429/JACoW-IPAC2022-THPOPT064

[3] M. Gehlot, S. M. Khan, F. Trillaud, and G. Mishra, "Magnetic field integral measurements with stretched wire and Hall probe methods", *IEEE Trans. Magn.*, vol. 56, no. 5, 2020. doi:10.1109/TMAG.2020.2976031

[4] S. M. Khan, S. Mishra, and M. Gehlot, "Magnetic measurement of tapered gap U50 undulator", presented at IPAC'23, Venice, Italy, May. 2023, paper MOPM091, to appear in the proceedings.

PULSED WIRE MEASUREMENT OF
20 mm PERIOD HYBRID UNDULATOR*

Saif Mohd Khan[1,†], Ganeswar Mishra[1], Mona Gehlot[2]
[1]Laser & Insertion Device Application Laboratory (LIDA),
Devi Ahilya VishwaVidyalaya, Indore, India
[2]Deutsches Elektronen-Synchrotron DESY, Hamburg, Germany

Abstract

We investigate pulsed wire measurements of field integrals and phase error of a 20 mm-period, 500 mm-long undulator and discuss variation in performance with Hall probe data without any dispersion correction algorithm.

INTRODUCTION

The Pulsed wire method is alternate to Hall probe method and is preferred in in-vacuum, out-vacuum undulators with limited access. The pulsed wire technique finds potential applications in in-vacuum undulators and cryogenic undulators. The pulsed wire method is faster and suitable in detecting magnet position errors and replacing it. The pulsed wire technique with orthogonal pair of sensors can be utilized as similar to Hall probes with multi axis Hall sensors. Nevertheless, although the pulsed wire method proposed three decades back in 1988 and successfully improved over the years, the method needs to be carefully calibrated for wave dispersion & accurate pulse widths, sensor sensitivity and more importantly the tension in the wire in order that the method emerges as individual precision measurement system independent of the Hall probe method. The wire sag arises due to catenary weight of the wire and poses a serious threat for measurement of long undulators. The second important issue of concern is the dispersion associated with finite rigidity of the wire.

PULSED WIRE MEASUREMENT SYSTEM

The Hall probe and Pulsed wire magnetic bench have been described in Ref. [1]. A motorized linear translation stage with a Hall probe measures the magnetic field profile. The undulator length is 500 mm with 20 mm period length. The accuracy of the Hall probe position during the motion along the undulator length is measured by a position sensitive measuring detector system. The pulsar in the pulsed wire bench is a 50V-12A High Current Voltage Source (HCVS). Two CuBe wires of different diameters are used for the experiment. The 250 µm wire is used with a current of 5A in the wire. The 125 µm wire is used with 1.32 A for the experiment. A current probe measures the current in the wire. We use Tektronix make, Model No A622 AC/DC current probe for the measurement. The total wire length is 1660 mm and passes through the 500 mm length undulator on axis. The pulley end is 660 mm away from the undulator end. The fixed end is 500 mm away from the other undulator end. The wire

length in the arrangement is kept at 3.32 times the length of the undulator. The transverse wire displacement propagates along the wire as a wave longitudinally along both the directions and is detected by a laser-photodiode sensor located at the ends of the undulator. The wire displacement at the sensor for the first field integral is given by:

$$x(0,t) = -\frac{i_0 \Delta t_{short}}{2\upsilon\mu} I_1, \text{ where } \Delta t_{short} < \lambda_u / 2\upsilon \quad (1)$$

and i_0 is the amplitude (A) of the current pulse, υ is the velocity of the wave (m/s) in the wire, Δt is the pulse width (s), μ (kg/m) is the mass per unit length of the wire. Equation (1) is evaluated by looking at the wire displacement with a current of short duration applied to the wire. The wire displacement at the sensor for the second field integral is given by for a longer pulse:

$$X(0,t) = -\frac{i_0}{2\upsilon^2\mu} I_2, \text{ where } \Delta t > N\lambda_u / \upsilon \quad (2)$$

FIELD INTEGRAL MEASUREMENT

The first and second field integrals of U20 are measured by Hall probe [2]. The second field integral centroid is displaced from the axis by 500 Gcm². From the peak field data, first field integral (rms) is 732 Gcm and the second field integral (rms) reads 553 Gcm².

We choose tension at a preselect sag for the measurement. The second field integral from the pulsed wire data is captured at a tension of 22.9N as shown in Fig. 1. The sag with the 250 µm wire is 52 µm. The pulsed wire integral data is stretched beyond the Hall probe data implying that the pulsed wire is tension under-compensated. The tension is gradually increased. We define the tension compensated length as the difference in length of the und-
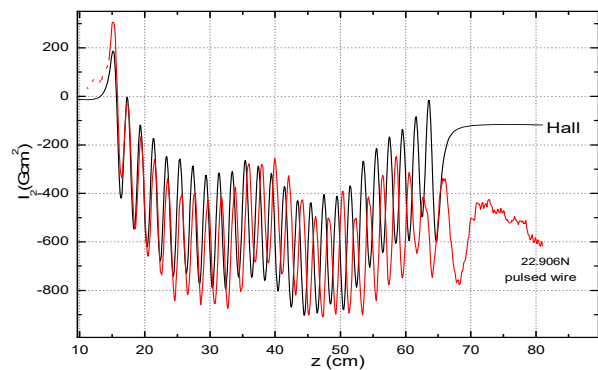
Figure 1: Second field integral at a wire tension.

ulator calculated by the Hall probe data and pulsed wire data. The minimum tension when it happens is called the optimum tension. The tension compensated length versus tension is shown in Fig. 2. The optimum tension for the 250 µm wire is 26.2N and for the 125 µm wire, it is 0.911 N. Beyond this point the wire is overcompensated with tension and then the pulsed wire result moves away from the Hall probe result. In Fig. 3, the field integral data is shown for the optimum tension and the pulsed wire data with overcompensated with tension. From the peak data, the second field integral (rms) reads from Fig.3 as 555 Gcm^2 and reaches an accuracy of 02 Gcm^2 between the two methods. The theoretical value of the velocity is 253.1 m/s. The experimental value of the velocity is 253.7 m/s. There is a difference between the theory and the measured is 0.2%. The long pulse is given by Eq. (2). With the measured value of the velocity the lowest pulse requirement is 1.97 ms. We vary the integral measurement with pulse width. The measurement gives good results at 4 ms. The second field integral is measured at 4 ms which is:

$$\Delta t_{long} = \alpha N \lambda_u / \upsilon$$

where α = 2.03. The measurement is repeated with 125 µm diameter wire. From the peak data, the field integral measures 554 Gcm^2 at the optimum tension of 0.911 N in Fig. 4. The pulse width for this measurement is 10.5 ms, α = 1.99. The theoretical value of the velocity is 95 m/s. The experimental measured value of the velocity is 94.86 m/s. There is a difference between the theory and the measured value is 0.15%.

The second field integral measured at the end of the undulator is seen at Fig. 5 for both the wire. The 125 µm wire pulsed wire data shows better result close to Hall probe data. At the optimum tension, the 125 µm wire gives the second field integral as 225 Gcm^2, the 250 µm wire reads as 650 Gcm^2 where the Hall probe reads the field integral as 125 Gcm^2.

The first field integral from Hall probe data and pulsed wire data with 250 µm wire is shown in Fig. 6. From the peak data, The Hall probe gives first field integral-rms data of 732 Gcm where the pulse wire data gives an rms value of 735 Gcm. Thus the accuracy is 3 Gcm between the two methods. The pulsed wire data is measured at 19.7 µs. The pulse requirement is given by Eq. (1). According to this at the measured value of the velocity of 253.7 m/s, the maximum value of the pulse requirement is 39.4 µs. The first field integral is measured at 19.7 µs which is:

$$\Delta t = \lambda_u / \alpha 2 \upsilon$$

where α = 2.00. The calculation for the first field integral is repeated for the 125 µm wire diameter in Fig.7. The field integral-rms measures 734Gcm at the optimum tension. The pulse width for the first field integral for 125-µm wire diameter is 50 µs and α = 2.10 .The end first field integral for the 250 µm wire from the Fig. 6 reads 85.5Gcm whereas with the 125 µm wire, this value is 24 Gcm as seen in Fig.7. The Hall probe data reads this value as 0.975 Gcm.
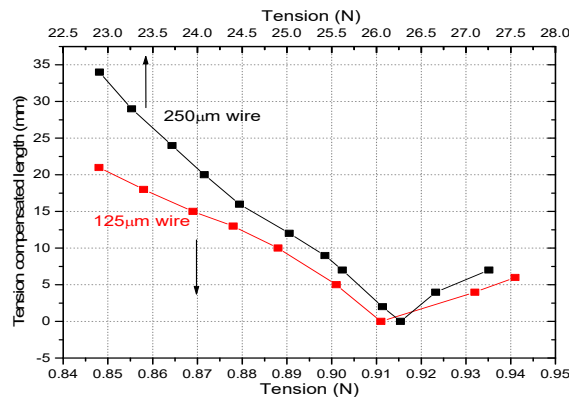
Figure 2: Calculation of optimum tension.
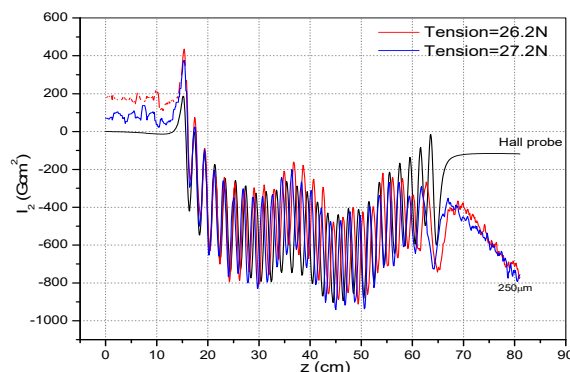
Figure 3: Field integral at the optimized wire tension 26.2N and higher than the optimized tension 27.2N for the 250µm wire.
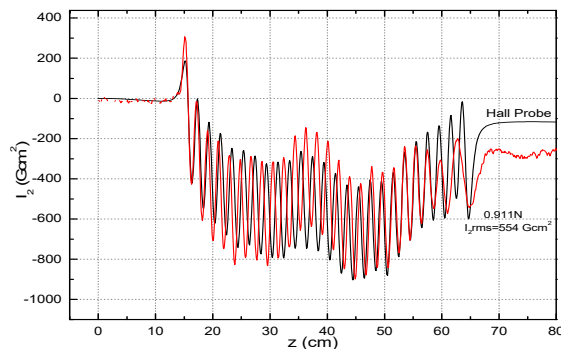
Figure 4: Second field integral at the optimized wire tension for the 125 µm wire.
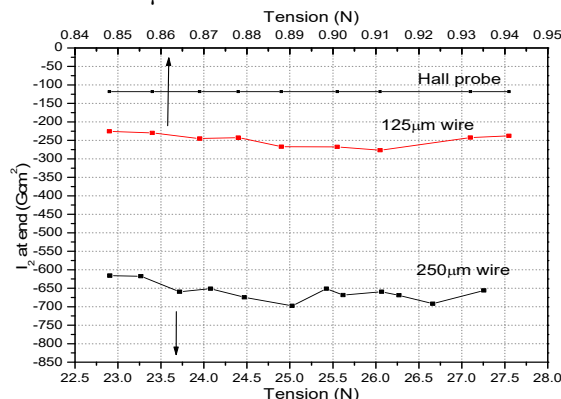
Figure 5: Second field integral measured at the end of the undulator.
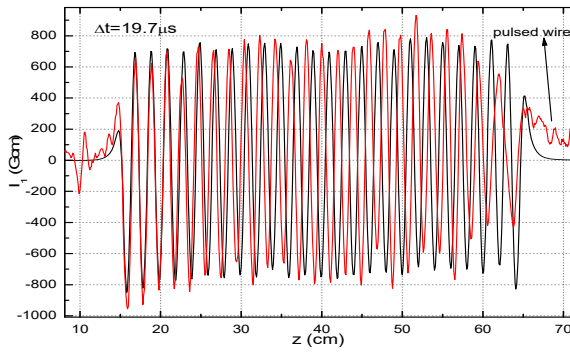
Figure 6: First field integral for the 250 μm wire.
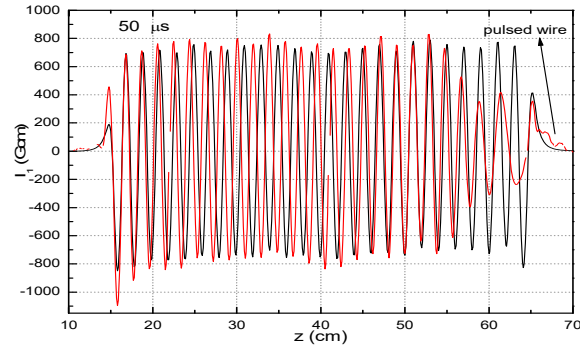
Figure 7: First field integral, 125 μm wire.

The phase error information is an important figure of merit of the undulator and is calculated from Eq. (3):

$$\phi(z) = \frac{2\pi}{\lambda}\left[\frac{z}{2\gamma^2} + \frac{\int(\frac{e}{\gamma mc}I_1)^2\,dz}{2}\right] \tag{3}$$

The numerical value of the phase integral (second term in Eq. (3)) and the phase error is an indication of the quality of the undulator. The optical phase advance is shown in Fig. 8 for the Hall probe data and for the two wire measurements. The slope of the optical phase measured by the Hall probe is 24.8 radian per meter.

The pulsed wire probe measures the optical phase advance with a higher slope of 25.5 radian per meter and 27.6 radian per meter for the 250 μm and 125 μm wires respectively. The phase error is calculated from the Fig.8 by a linear fit and is shown in Fig. 9. The Hall probe measurement gives information for the full length of the undulator, whereas the dispersion limited phase growth length inside the undulator is 433 mm and 406 mm for the 250 μm and 125 μm wire diameter respectively. The phase error calculation from the Hall probe data is 2.73 degree where the value reads as 5.25 degree from the pulsed wire data with the 250 μm wire diameter wire and 4.24 degree for the 125 μm wire diameter. The phase error is minimum at optimum tension and gives higher phase error value both at before and after this value as seen in Fig. 10.
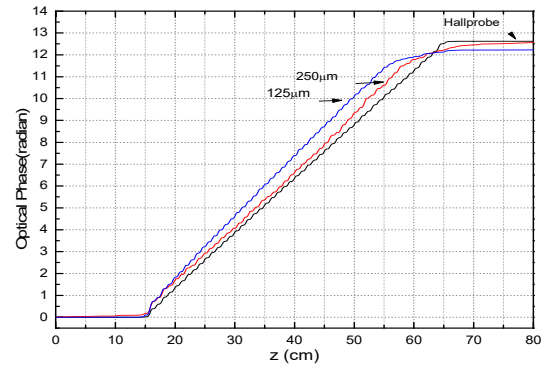
Figure 8: Optical phase advance in the undulator.
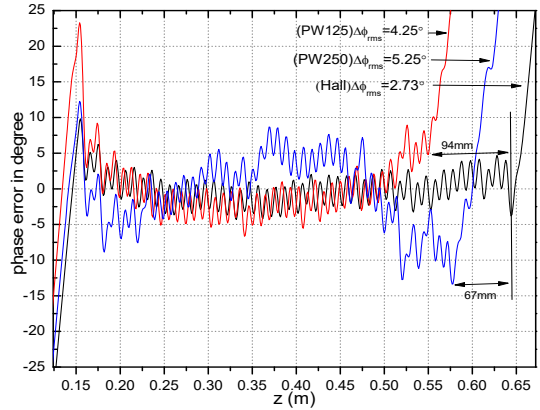
Figure 9: Phase error in degree.
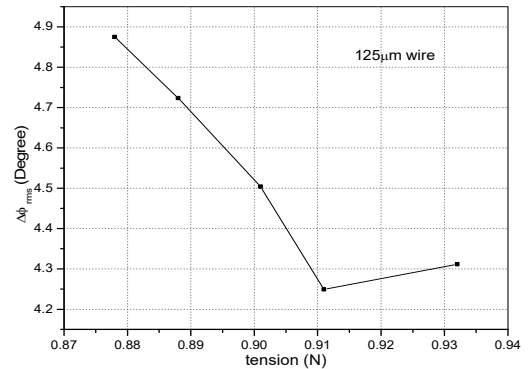
Figure 10: Phase error at the optimum tension.

ACKNOWLEDGEMENT

REFERENCES

[1] R. Khullar, S. M. Khan, G. Mishra, H. Jeevakhan, and M. Gehlot, "Laser instrumentation and insertion device measurement system", in *Proc. IPAC'22*, Bangkok, Thailand, Jun. 2022, pp. 2513-2516.
doi:10.18429/JACoW-IPAC2022-THPOST030

[2] G. Mishra, M. Gehlot, R. Khullar and G. Sharma, "Magnetic field integral requirements and measurement of 20-mm period hybrid undulator", *IEEE Trans. Plasma Sci.*, vol. 47, no.7, pp. 3182-3188. 2019.
doi:10.1109/TPS.2019.2919405

LARMOR RADIUS EFFECT ON IFEL ACCELERATOR WITH STAGGERED UNDULATOR

Roma Khullar, Government Holkar Science College, Indore, Madhya Pradesh, India
Saif Mohd Khan, G. Mishra, Deviahilya Vishwavidyalaya, Indore, Madhya Pradesh, India

Abstract

In this paper, the theory of inverse free electron (IFEL) accelerator using staggered undulator has been discussed. The important contribution of staggered undulator parameter and the finite Larmor radius effect on energy saturation, saturation length and accelerating gradient of the IFEL accelerator are included in the analysis. Considering the synchrotron radiation losses, the IFEL accelerator equations are derived.

INTRODUCTION

The inverse free electron laser (IFEL) accelerator is the most advance laser based accelerator scheme [1-6]. It has been demonstrated that the accelerating gradient is significantly larger than what we achieve with conventional IF accelerator [7-9]. In the IFEL accelerator the energy transfer is from the laser beam to electrons. In an IFEL relativistic particles are moving through an undulator magnetic field with an electromagnetic wave propagating parallel to the beam. The undulator magnets produces a wiggling motion in a direction parallel to the electric vector of the laser. Hence energy is transferred from wave to the particle, if the resonance condition $\lambda = \frac{\lambda_u}{2\gamma^2}(1 + K^2)$ satisfies where λ is the laser wavelength, λ_u is undulator wavelength and $K = \frac{eB_0\lambda_u}{2\pi mc^2}$ is undulator parameter. B_0 is the undulator magnetic field amplitude, 'm' is the mass of particle, 'c' speed of light. As the particle gain energy, the resonance condition of the free electron laser cannot be maintained for a long distance. The resonance condition can be maintained in two ways, firstly by changing the undulator period and secondly by changing the magnetic field of the undulator. The spectral properties of undulator radiation and the free electron laser gain in staggered undulator with the finite Larmor radius effect of electron are shown [10].

In this paper, we analyse the effect of Larmor radius on Inverse free electron laser accelerator with staggered undulator. We have obtained accelerator equation for inverse free electron laser accelerator. Synchrotron radiation losses are also included in the analysis. We have analysed the effect of Larmor radius on maximum energy gained by the electron and saturation length of the accelerator. Result and discussion of the analysis are given in the last section.

IFEL ACCELERATOR EQUATIONS

The motion and the energy change of relativistic electron in the presence of staggered array undulator and uniform magnetic field produced by a solenoid is calculated. The equation describing the motion of the electrons in the IFEL can be derived from the Lorentz equation of motion,

$$\frac{d\vec{\beta}}{dt} = \frac{e}{\gamma m_e c}\left[\vec{E}_L + \vec{\beta}\times\left(\vec{B}_L + \vec{B}_s\right)\right] \tag{1}$$

where B_L is the magnetic field of the laser and B_S is the magnetic field of the staggered undulator. e, m_e are the particle charge and mass respectively, c is the speed of light, $\gamma = (1 - \beta^2)^{-1/2}$ and $\beta = v/c$. We consider the magnetic field of a staggered array undulator with an axial magnetic field produced by a solenoid as

$$\vec{B}_s = [0, B_u(\sin\pi f/\pi f)\sin k_u z, B_0] \tag{2}$$

where λ_u is the undulator period with $k_u = 2\pi/\lambda_u$, $\omega_u = ck_u$, $f = \alpha/\lambda_u$, $\alpha = \lambda_u - d$ where 'd' is the width of the rectangular pole and 'α' is the pole to pole gap. The undulator field strength is derived from a solenoid and reads

$$B_u = 2B_o\big/\sinh\left(\pi g/\lambda_u\right)$$

where 'B_0' is the axial field strength derived from the solenoid and 'g' is the undulator gap. The electromagnetic wave propagating along the undulator is described by,

$$\vec{E}_L = \left[E_0\sin\psi, E_0\cos\psi, 0\right]$$
$$\vec{B}_L = \left[E_0\cos\psi, E_0\sin\psi, 0\right] \tag{3}$$

where $\psi = n(kz - \omega t)$ and $k = 2\pi/\lambda$, λ is wavelength of the laser. Using Eq. (1-3) for a staggered array undulator with an axial magnetic field, the electron velocity is given by,

$$\beta_x = \frac{\tilde{K}}{\gamma}\cos(\omega_u t) - \frac{K_L}{\gamma}\cos\psi + \beta_\perp\cos(\omega_u t) \tag{4a}$$

$$\beta_y = \beta_\perp\sin(\omega_u t) \tag{4b}$$

where the undulator and electromagnetic wave parameter is defined through

$$K = \frac{eB_u\lambda_u}{2\pi m_e c^2}, K_L = \frac{eE_L\lambda}{2\pi m_e c^2}, \tilde{K} = K\sin(\pi f)/\pi f$$

Substituting β_x and β_y from equations (4a) and (4b) into the relation $\beta^2 = 1 - \dfrac{1}{\gamma^2}$, we obtain the longitudinal velocity as,

$$\beta_z = \beta^* - \frac{\tilde{K}^2}{4\gamma^2}\cos 2(\omega_u t) - \frac{K_L^2}{4\gamma^2}\cos 2\psi \qquad (5)$$

Where

$$\beta^* = 1 - \frac{1}{2\gamma^2}\left[1 + \frac{\tilde{K}^2}{2} + \frac{K_L^2}{2} + \gamma^2 \beta_\perp^2\right]$$

Using Eqs. (4) and (5), the change in electron energy is given by,

$$\frac{d\gamma}{dz} = A\frac{\tilde{K}}{2\gamma}\sin(\xi)\sum_m\left[J_{m-1}(0,\chi) - J_{m+1}(0,\chi)\right] \qquad (6)$$

where

$$\chi = -\frac{n\tilde{K}^2 k}{8\gamma^2 k_u}$$

and phase term is

$$\xi = (nk + mk_u)\bar{z} - n\omega t \qquad (7)$$

$J_{m-1}(0,\chi), J_{m+1}(0,\chi)$ are generalized Bessel functions of first kind.

Using the properties of generalized Bessel function and for $m = 1$, Eq (9) reduced to

$$\frac{d\gamma}{dz} = \tilde{A}\frac{\tilde{K}}{2\gamma}[J_0(\chi') - J_2(\chi')] \qquad (8)$$

where $\tilde{A} = A\sin\xi$ and $\chi' = -\chi$

The resonance condition is read from Eq (7) by setting $d\xi/dz = 0$ as

$$\omega = \frac{2\gamma^2(\omega_u + \omega_c)}{\left[1 + \dfrac{\tilde{K}^2}{2} + \gamma^2 \beta_\perp^2\right]} \qquad (9)$$

For the electron trajectory such as given in Eq. (4) we get the synchrotron radiation loss term as,

$$\frac{1}{m_e c^2}\frac{dP}{dt} = \frac{1}{3}\frac{r_e}{c}\gamma^2\left[\omega_u^2 \tilde{K}^2 + 2\beta_\perp^2 \gamma^2 \omega_c^2\right] \qquad (10)$$

where $r_e = \dfrac{e^2}{m_e c^2}$ is the classical electron radius. Adding the radiation loss term and using resonance condition Eq (8) can be rewritten as,

$$\frac{d\gamma}{dz} = \tilde{A}\sqrt{\frac{\omega_u + \omega_c}{\omega}}[JJ] - \frac{2}{3}\frac{r_e}{c^2}\gamma^4\left[2\omega_u^2\frac{\omega_u + \omega_c}{\omega} + \beta_\perp^2 \omega_c^2\right] \qquad (11)$$

where $[JJ] = J_0(\chi') - J_2(\chi')$.

The solution for Eq. (11) is written as,

$$\gamma(z) = \gamma_\infty - [\gamma_\infty - \gamma_0]e^{-\frac{4F}{\gamma_\infty}(z-z_0)} \qquad (12)$$

where γ_0 is the initial energy of the electron,

$$F = \tilde{A}\sqrt{\frac{\omega_u + \omega_c}{\omega}}[JJ]$$

and

$$\gamma_\infty = \left[\frac{3\tilde{A}c^2\sqrt{\dfrac{\omega_u + \omega_c}{\omega}}[JJ]}{2r_e\left[2\omega_u^2\dfrac{\omega_u + \omega_c}{\omega} + \beta_\perp^2 \omega_c^2\right]}\right]^{1/4}$$

RESULTS AND DISCUSSION

We have analysed the staggered undulator with an axial magnetic field produced by a solenoid. The effect of synchrotron radiation losses derived in Eq.10 are included in the analysis. The relativistic Lorentz force equation is solved analytically for an electron beam having an initial finite perpendicular velocity. The electron entering the axial field executes Larmor motion. The Larmor motion is described by its Larmor radius defined as $r_L = \dfrac{c\beta_\perp}{\omega_c}$, where $c\beta_\perp$ is the initial transverse velocity and ω_c is the axial magnetic field strength. The effect of staggered undulator parameter and axial field on the performance of the IFEL accelerator is expressed in Eq. (12).

Figure 1 plots the accelerated energy for a 400 Giga Watt laser with 10.6 μm wavelength focused to a 240 μm spot size this gives an electric field strength of E=1.33×10⁶ statvolt cm⁻¹. Considering $r_e = 2.8179 \times 10^{-13}$ cm, $\tilde{A} = 667.686$ cm, $\lambda_u = 50$ mm, $\alpha = 1$ and $r_L = 300$ mm in Fig. 1. We calculate energy in GeV for different value of $\beta_\perp$ ranges from 0 to 0.1. As the value of $\beta_\perp$ increases the maximum energy gained by the electron decreases.
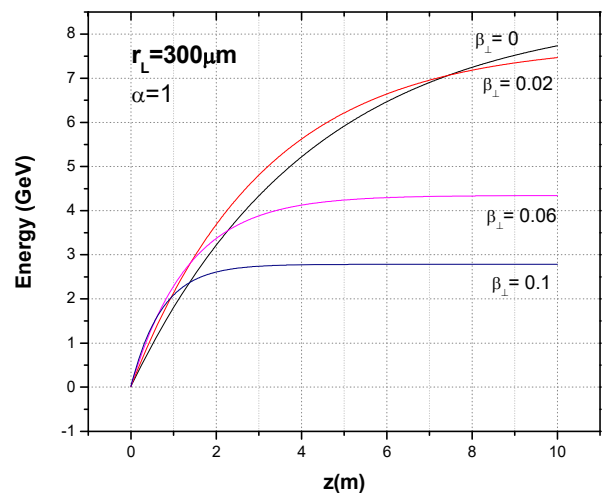
Figure 1: Electron energy vs distance for a fixed undulator wavelength.

The synchrotron radiation loss term decides the length of the IFEL accelerator. In Fig. 2 we plot the accelerating gradient in GeV/m vs $\beta_\perp$ for two different values of pole to pole gap 'α'. The accelerating gradient decreases as $\beta_\perp$ increases from 0 to 0.3. The fall in accelerating gradient is 76.8% for $\alpha = 1$ and 83.28% for $\alpha = 4$.

In Fig. 3 we describe the variation of saturation length in m vs $\beta_\perp$. The saturation length decreases with $\beta_\perp$ ranges from 0 to 0.3. For $\alpha = 1$ saturation length decreases by 95.14% and for $\alpha = 4$ saturation length decreases by 95.26%.
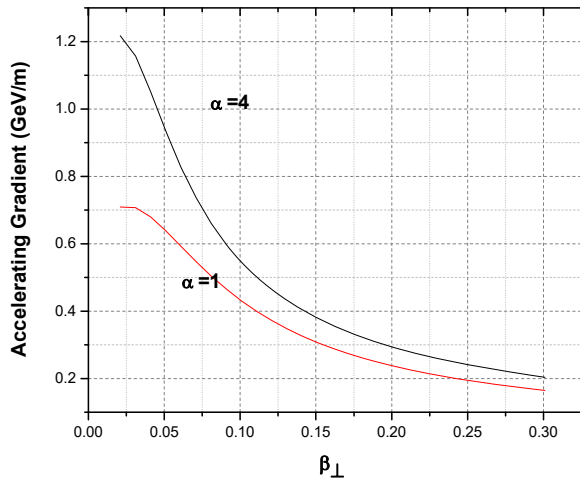
Figure 2: Accelerating gradient vs $\beta_\perp$.
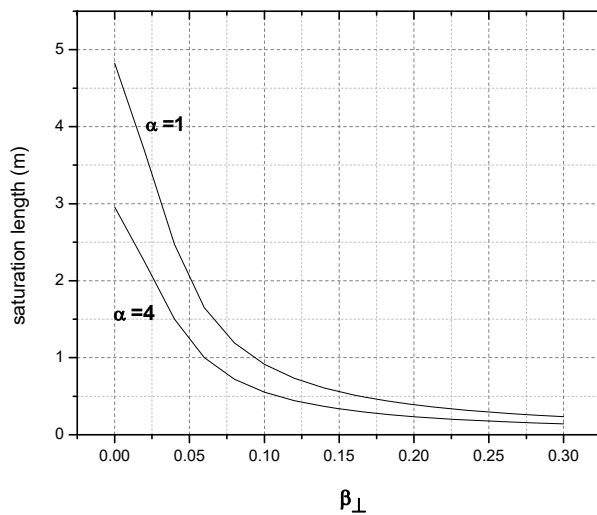
Figure 3: Saturation length vs $\beta_\perp$.

REFERENCES

[1] R .B. Palmer, *J. Appl. Phys.*, vol. 43, pp. 3014-3023, 1972.

[2] E. D. Courant, C. Pellegrini and W. Zakowicz, *Phys. Rev. A, Gen. Phys.*, vol. 32, no. 5, pp. 2813-2823, 1985.

[3] J. Duris, P. Musumeci, *et al.*, *Nature Com.*, vol. 5, p. 4928, 2014. doi:10.1038/ncomms5928

[4] J. P. Duris, P. Musumeci and R. K Li, *Phys Rev. Accel. Beams*, vol. 15, no. 6, p. 061301, 2012. doi:10.1103/PhysRevSTAB.15.061301

[5] R. Khullar and G. Mishra, *J. Synchrotron Radiat.*, vol. 25, pp. 1623-1626, 2018.

[6] R. Khullar and G. Mishra, *IEEE Trans. Plasma Sci.*, vol. 49, no. 2, pp. 729-733, 2021. doi:10.1109/TPS.2020.3046314

[7] S.G. Anderson, *et al.*, in *Proc. PAC'11*, NY, USA, Mar.-Apr. 2011, pp. 331-333, paper MOP127.

[8] A. Tremaine *et al.*, in *Proc. PAC'11*, NY, USA, Mar.-Apr. 2011, pp. 1-3, paper MOOBN2.

[9] C. Sung, S. Ya. Tochitsky, S. Richie, J. B. Rosenzweig, C. Pelligrini, and C. Joshi, *Phys. Rev. Spec. Top. Accel. Beams*, vol. 9, p. 120703, 2006. doi:10.1103/PhysRevSTAB.9.120703

[10] G. Mishra and A. Sharma, *Trans. on Plasma Sci.*, vol. 50, no. 12, pp. 4854-4859, 2022. doi:10.1109/TPS.2022.3223942

A BULK SUPERCONDUCTOR AND ITS APPLICATION TO INSERTION DEVICES*

T. Kii†, Institute of Advanced Energy, Kyoto University, Uji, Japan

Abstract

High-field short-period undulator will be one of the key technologies for the future light sources. Various approaches have been continued under the limitation of materials for permanent/superconducting magnets. The use of bulk superconductors is attractive because of their high current density in the presence of a high magnetic field. The critical current density for rare-earth barium copper oxide (REBCO) bulk superconductors exceeds 10 kA/mm^2 even at 10 K in a field range below about 3 T, and exceeds 20 kA/mm^2 at 4.2 K.

In order to utilize the relatively high current density in the bulk REBCO and to generate periodic magnetic field we proposed a staggered array bulk superconductor undulator. Recently, we have developed the third undulator prototype consisting of a 6 T solenoid and a 6 period bulk REBCO array, and successfully demonstrated periodic field amplitude of 2.22 T for period length of 10 mm and undulator gap of 4.0 mm at 7 K.

INTRODUCTION

Periodic alternating magnetic fields can be used in magnetic levitation systems, linear motors, undulators/wigglers in accelerators, and low-dimensional electron, spin systems for spin-state control in fundamental physics, etc.

Periodic magnetic fields can be generated relatively easily with strong neodymium permanent magnets. Stronger magnetic fields can be obtained by using commercially available superconducting wires. The critical density of commercially available superconducting wire is on the order of several kA/mm^2 at 4.2 K, and the strength of the periodic magnetic field is limited by this practical critical current density.

In order to generate stronger periodic magnetic field, we have to handle much higher current density than the practical SC wires. Focusing on the core of the superconducting wire, the critical current density is more than an order of magnitude higher than the effective engineering current density. For example, the engineering current density of NbTi and Nb$_3$Sn superconducting wires is limited to the order of a few kA/mm^2 due to the sheath required for wire fabrication, but the core parts have a critical current density of about 10 kA/mm^2. In the case of rare-earth barium copper oxide (REBCO) coated superconducting tapes, the critical current density of the superconducting thin-film layer can reach a few hundred kA/mm^2, but the thickness of the superconducting material layer is only a few micrometers and constitutes only a few percent of the total volume of the wire, resulting in an effective critical current density of the order of 1 kA/mm^2 as well as NbTi/Nb$_3$Sn.

On the other hand, the critical current density of bulk superconductors, which are formed from only superconductor materials in a bulk form, is lower than the superconducting part of wires and tapes, but the current density of the material is equal to the engineering current density. Critical current densities exceeding 10 kA/mm^2 at 4 K self-field have been achieved in the best performing rare-earth cuprate superconducting system. Therefore, the use of bulk superconductors potentially makes it possible to control magnetic fields using the superconducting current with current density that is one order of magnitude higher than that of commercial superconducting wires.

Therefore, we proposed [1] and demonstrated [2-4] a staggered array bulk superconducting undulator with periodically arranged bulk superconductors (Bulk HTS SAU), focusing on the high magnetic performance of rare earth cuprate superconductors. Recently, PSI started development for SwissFEL and Swiss Light Source 2.0 (SLS2.0) storage ring [5, 6].

In this study, a 6 T solenoid and a gadolinium barium cuprate (GdBaCuO) superconductor were used to generate and control periodic magnetic fields that significantly exceed the limits of permanent magnets and practical commercial wires.

BULK HTS SAU

The structural schematic drawing of a Bulk HTS SAU and the mechanism of periodic magnetic field generation are shown in Fig. 1.
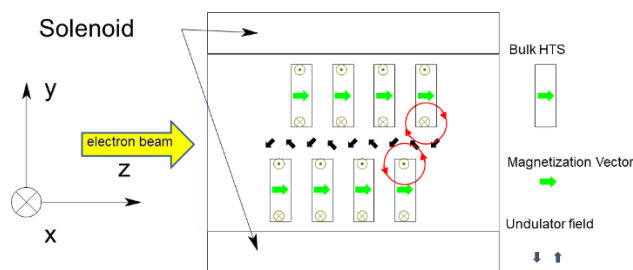
Figure 1: A schematic cross sectional view of a Bulk HTS SAU. When the magnetic field is changed by an external solenoid, a shielding current is induced inside the bulk HTS to cancel out the magnetic field change. The induced current produces a periodic alternating magnetic field along the z-axis.

When a magnetic field change is applied to the superconductor array installed in the solenoid, a shielding current is induced in each superconductor to cancel the magnetic field change. As a result, the large supercurrents, whose directions are different and having half a period offset from each other generate a strong periodic alternating magnetic field on the central axis.

Here I list the important differences from the case where the circulating current is realized by superconducting wires.

1. The current density of the bulk is one order of magnitude higher than that of the wire
2. The current path follows the bulk boundary, so the current can be bent at a steep angle without being limited by the minimum bend radius of the wire
3. The current flowing in each bulk cannot be controlled by an external power supply.

METHOD AND EXPERIMENT

The prototype undulator consists of a temperature controlled bulk superconductor array, a superconducting solenoid, and a 3D magnetic field scanning system on the beam axis. The bulk superconductor array consists of Nippon Steel QMG™ bulk GdBaCuO bulks and pure copper spacers. Figure 2 schematically shows the single unit of the assembled array.
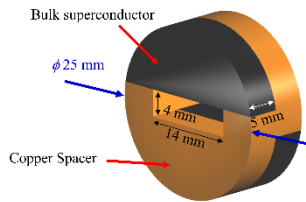
Figure 2: Schematic drawing of a single period of a bulk HTS array. It consists of an almost semicircular disk-shaped bulk superconductor and an almost semicircular pure copper spacer with a rectangular notch.

The undulator period is 10 mm, and the gap between the upper and lower arrays is 4 mm, and pure copper supports are used. The typical magnetic performance of the GdBaCuO superconductor was measured with PPMS using a micro specimen. At a temperature of 4 K, critical current density J_c of 20 kA/mm^2 was recorded [7].

The temperature of the bulk superconductor is monitored using a Cernox™ resistance temperature sensor attached to the end copper block. The bulk superconductor array is mounted in a pure copper sample holder and conductively cooled using a helium continuous flow cryostat. The temperature of the array is controlled by adjusting the helium flow rate and PID control of the heater output attached to the sample holder.

The external solenoid is a custom 6 T superconducting solenoid with a 10 cm diameter room temperature bore from Cryomagnetics. The magnetic field strength is 6.000 T at the center of the solenoid axis and 5.985 T at the edge of the array, 2.5 cm away from the center in the axial direction.

The magnetic field measurements are performed by scanning a Hall sensor array along the solenoid axis (z-direction), which can measure three-directional magnetic field components on the approximate center axis of a 4 mm × 14 mm rectangular cross-sectional space of the array inserted in a vacuum duct. It is estimated that the sensor element measuring the y-component was offset by about 0.2 mm, although no y-directional magnetic field was produced on the perfect central axis.

Figure 3 shows a photograph of the Hall sensor array. The Hall sensor array consists of three custom-made Arepoc model HHP-NU (1.5-300 K up to 5 T) 3 mm × 4 mm × 1 mm and one standard Arepoc model LHP-NU (1.5-300 K up to 30 T) 5 mm × 7 mm × 1 mm. Two elements for measuring the undulator magnetic field B_{und} are installed on the white ceramic plate so that the B_{und} component of the periodic magnetic field section and the B_{und} component of the edge leakage field can be acquired seamlessly in a short time.

Figure 3: Photograph of a Hall sensor array, which can measure three-component magnetic fields along the z-axis. The second and fourth Hall sensors from the left are used to measure the B_{und} component.

The Hall sensor array was fixed to the end of a 0.5 mm thick plastic rod and driven by a stepper motor with a linear motion actuator. The driving step along the z-axis was 0.2 mm and the total scanning distance was 66 mm.

The experiment was performed using the following so-called field cooling method: after applying an initial magnetic field of 6 T, the superconducting array was cooled to operating temperature. The magnetic field of the solenoid was then varied to induce a shielding current in each superconductor to generate a periodic magnetic field.

RESULTS AND DISCUSSION

The initial applied magnetic field was set to 6 T, and magnetic field changes of 3, 6, 9, and 12 T were applied at temperatures of 20 K, 10 K, and 7 K. The magnetic field in three directions along the z axis was measured. Figure 4 shows the measurement results when the magnetic field was changed from 6 to -6 T at 7 K.
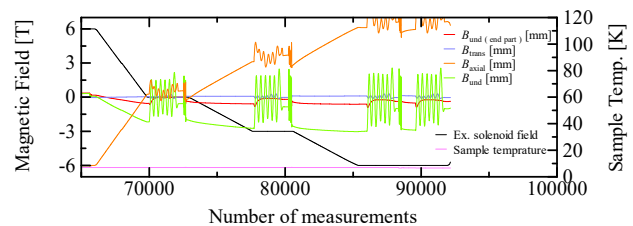
Figure 4: Results of undulator field measurements.

The relationship between the given magnetic field change and the undulator magnetic field B_{und} for each measurement is shown in Fig. 5; the B_{und} is the average of the magnetic field peak values of the 10 central peaks is adopted. For the peak field strength, a discrepancy was observed, with a variance of approximately 10%. This is due to the non-uniformity of the critical current properties of

the superconductor used in the array assembly. The bulk superconductor used in this experiment exhibited a variation of about 15%, according to the estimated magnetic field strength at a temperature of 77 K. The cause of the variation is thought to be due to the difference in critical current properties depending on the distance and angle from the seed crystal during the recrystallization process with the seed crystal during the synthesis of pseudo-single crystallized REBCO superconductors.
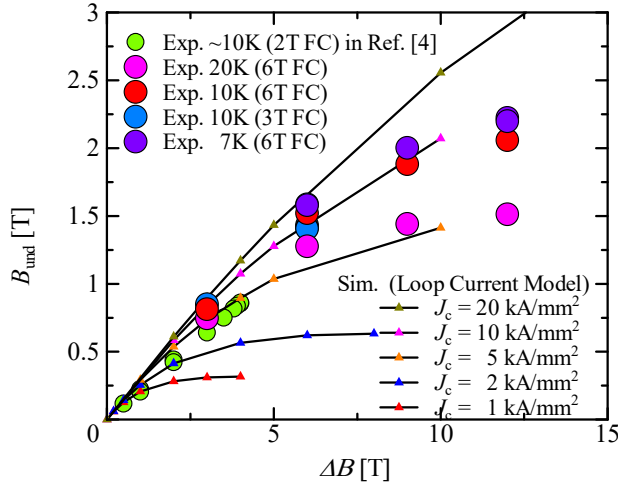
Figure 5: Relationship between undulator field and solenoid field change. As the field change is increased, the undulator field increases, but it gradually leaves the linear increase and tends to saturate.

The curves in Fig. 5 are the predicted results of the numerical model based on the loop current model developed by us [8]. Undulator magnetic fields of 2.22 T at 7 K, 2.06 T at 10 K, and 1.51 T at 20 K are observed. The undulator field strength tends to deviate from a linear trend at all temperatures, indicating that as the total amount of induced current in the superconductor increases, the induced current becomes more located closer to the center of the bulk, and when the entire bulk is filled with the shielding current, the undulator field saturates.

The experimental saturation characteristics are close to those predicted for about 5 k/mm^2 at a temperature of 20 K, and about 10 kA/mm^2 at 10 and 7 K. These critical current densities are consistent with the results of critical current characteristic measurements performed by PPMS for a small specimen [7].

For comparison with undulators using permanent magnets and superconducting wires, the magnetic field strength of various undulators with the horizontal axis as gap/period is shown in Fig. 6. The 2.22 T obtained at 7 K is approximately 3.1 times higher than the 0.71 T that can be generated by a cooled hybrid-type permanent magnet undulator, indicating that the Bulk HTS SAU can generate a much stronger period alternating magnetic field than conventional technologies. It also has an advantage of more than 25% over the superconducting wire type [9, 10]. Considering the advantages of small cold mass and significantly higher operating temperature than 4.2 K, the Bulk HTS SAUs are expected to have high potential as insertion devices for future light sources.
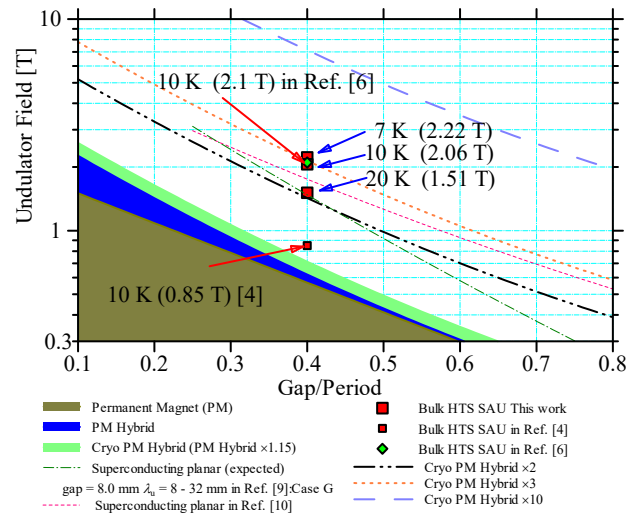
Figure 6: Comparison of undulator magnetic field strength of different types of undulators scaled by gap/period. Performance prediction curves for superconducting wire-wound planar undulators [9, 10], and characteristic curves for ×2, ×3, and ×10 based on the cryo hybrid permanent magnet type are also shown for comparison.

CONCLUSION

A new method for generating short-period, strong periodic magnetic fields using bulk superconductors has been presented. Bulk superconductors, which are composed entirely of superconducting materials, can handle current densities approximately 10 times higher than those of superconducting wires, which are expected to have high undulator fields. In this report, I attempted to generate a magnetic field using an array of bulk REBCO superconductors and a 6 T solenoid. The periodic magnetic field generation of 2.22 T is confirmed at a temperature of 7 K with a period of 10 mm and a gap of 4 mm. The results of the experiment show that the bulk superconductor has high potential as an insertion device for future light sources.

ACKNOWLEDGEMENTS

REFERENCES

[1] T. Kii et al., "Design study on high-TC superconducting micro-undulator", in Proc. 28th Int. Free Electron Laser Conf. (FEL '06), pp. 653-655, 2006.

[2] R. Kinjo et al., "A bulk high-TC superconductor staggered array undulator", in Proc. 30th Int. Free Electron Laser Conf. (FEL '08), pp.473-476, 2008.

[3] T. Kii et al., "Proposal of a bulk HTSC staggered array undulator", AIP Conf. Proc. (SRI '09), vol. 1234, pp. 539-542, 2010. doi:10.1063/1.3463261

[4] R. Kinjo et al., "Demonstration of a high-field short-period undulator using bulk high-temperature superconductor", Appl. Phys. Express, vol. 6, no. 4, p 042701, 2013. doi:10.7567/APEX.6.042701

[5] M. Calvi *et al.*, "A GdBCO bulk staggered array undulator", *Supercond. Sci. Technol.,* vol. 33, p. 014004, 2020.
doi:10.1088/1361-6668/ab5b37

[6] K. Zhang *et al.,* "Record field in a 10 mm period bulk high-temperature superconducting undulator", *Supercond. Sci. Technol.,* vol. 36, p. 05LT01, 2023.
doi:10.1088/1361-6668/acc1a8

[7] T. Kii *et al.*, "Low-temperature operation of a bulk HTSC staggered array undulator", *IEEE Trans. Appl. Supercond.*, vol. 22, no.3, p 4100904, 2012.
doi:10.1109/TASC.2011.2180498

[8] R. Kinjo *et al.*, "Numerical evaluation of bulk htsc staggered array undulator by Bean model", *in Proc. 31st Int. Free Electron Laser Conf. (FEL'09)*, pp. 746-749, 2009.

[9] P. Elleaume, J. Chavanne, and B. Faatz, "Design considerations for a 1 Å SASE undulator", *Nucl. Instrum. Methods,* vol. 455, no. 3, pp. 503-523, Dec. 2000.
doi:10.1016/S0168-9002(00)00544-1

[10] J.A. Clarke *et al.*, "Superconducting planar undulator development in the UK", *in Proc. 2nd Int. Particle Accelerator Conf. (IPAC'11)*, San Sebastián, Spain, pp. 3320-3322, 2011.

BI-PERIODIC UNDULATOR: INNOVATIVE INSERTION DEVICE FOR SOLEIL II

Angela Potet*, Frédéric Blache, Pascale Brunelle, Marie-Emmanuelle Couprie, Carlos De Oliveira, Arnaud Mary, Thibaut Mutin, Amor Nadji, Keihan Tavakoli, Olivier Marcouillé

Synchrotron SOLEIL, France

Abstract

SOLEIL II project aims at optimizing the production of photons by a modification of the present facility. The storage ring will be redesigned to reduce electron beam emittance and as a consequence increase photon beam brightness. The number of magnetic elements will be increased and the space reserved for insertion devices will be decreased by 30%. Among solutions of undulators fitting in a smaller space while maintaining the full spectral domain, the innovative and compact Bi-Periodic undulator allowing the use of two selectable magnetic periodicities by superimposition of magnets. The magnetic period can be switched from one value to its triple value by mechanical shift of magnetic arrays. A magnetic design has been performed and the construction of a prototype, including magnetic measurements and corrections, is under progress. The magnetic fields, the radiation produced and the electron beam dynamics will be considered to have a complete knowledge on this undulator.

INTRODUCTION

SOLEIL II [1] will lead to increase photon beam brightness. The storage ring presently composed of 16 cells and 3 straight section types will be redesigned to reduce electron beam emittance from 3.9 nm.rad to bellow 100 pm.rad. To achieve this reduction, the number of magnetic elements along the storage ring will be enlarged considerably. The consequence will be a reduction of the straight sections length reserved for the insertion devices. In present medium straight sections of 7 meters, the wide ranges of photons are obtained thanks to the longitudinal juxtaposition of two undulators with different magnetic periods. For the future ring, as straight section lenght is reduced to 4.2 or 3.7 meters, it will be impossible to iterate the same configuration to maintain the full spectral domain. Alternatives to combine several magnetic periods on a smaller space exist such as a dual undulalor with lateral shifting of two undulators [2], revolvers [3] with several indendepent magnetic structures of different periods arranged radially around the axis and a variable period helical undulator with tunable polarization [4] allows to modify the direction of the magnetization of the magnets by simple rotation of magnets. SOLEIL considers for its Upgrade DUAL, APPLE X [5] and BiPeriodic undulators. The Bi-Periodic solution is presented in this paper. This undulator is a device allowing the use of two selectable magnetic periodicities by superimposition of magnets. This technique permits to save half the longitudinal space previously required for SOLEIL I. The purpose of this study is to demonstrate the feasability of this system through simulations, construction of a prototype and tests on the present ring to validate its operation.

PRINCIPLE OF OPERATION

The Bi-Periodic undulator (Patent pending [6]) has a special arrangement of magnets allowing to switch from a magnetic period to its triple value by a longitudinal shift. It is based on the vertical superimposition of two magnetic systems in the Halbach configuration [7]. A system of magnets with a periodicity λ_0 is equipped vertically with an another array of magnets with triple periodicity $3\lambda_0$. This special arrangement of magnets enables to obtain two operating modes presented in Fig. 1. To alternate between the two periods, a phase shift system with a value of $3\lambda_0/2$ enables to obtain on the beam axis the cancellation of the vertical magnetic field of one period (red arrows) and the maximum value of the vertical magnetic field for the other period (green arrows).

(a) λ_0 mode

(b) $3\lambda_0$ mode
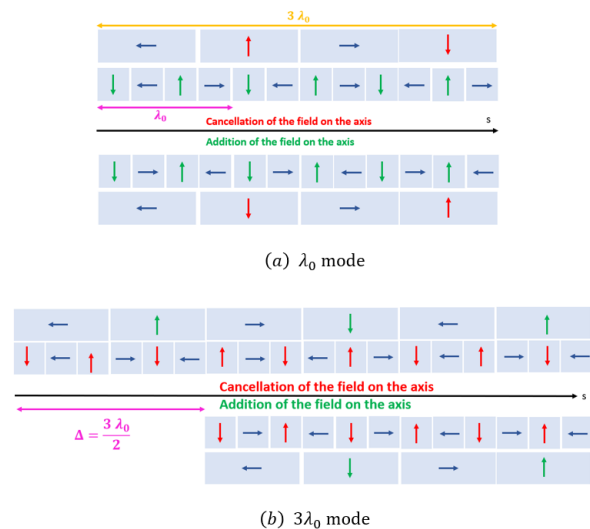
Figure 1: Configuration of magnet magnetization.

BI-PERIODIC PROTOTYPE DESIGN

The choice to make a design with a $\lambda_0 = 50$ mm period and its triple period of 150 mm was made to correspond to the needs of a potential beamline. NdFeB magnets were considered with a remanence of $B_r = 1.37$ T and a special trapezoidal geometry to facilitate the maintenance of the magnets on their supports.

---

* angela.potet@synchrotron-soleil.fr

Undulator Terminations

As such a magnetic configuration disturbs the trajectory of electrons passing through the undulator, termination elements must be designed. These modules are used to reduce the integrals of vertical and horizontal fields generated by the undulator which induce displacements (modification of the position and the angle at the exit of the undulator). In addition to the very special magnetic environment of the undulator, the constraint of reusing the same magnets as for the main part was imposed for delivery delay reason. Figure 2 shows a short model of the Bi-Periodic undulator equipped with terminaisons at entrance and exit in order to minimize the shifts in angle and in position for the first mode (λ_0). After correcting the perfect undulator, the corrected values at the exit on the axis at gap 15.5 mm are: $\Delta x, \Delta z < 1\ \mu$m and $\Delta x', \Delta z' \approx \pm 2.10^{-7}\ rad \approx \pm 0.019$ G.m. When phase shift is applied, this correction is no more optimal but will be completed by the storage ring orbit correction system.
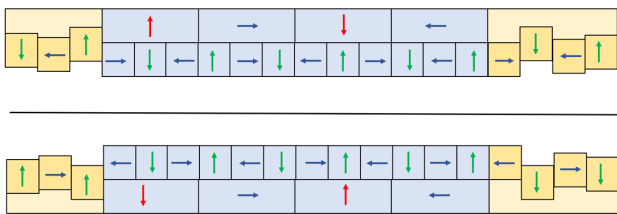
Figure 2: Configuration of magnets fot the λ_0 mode.

On Axis Magnetic Field

Magnetic design has been done using the RADIA program [8] (Python Version) to characterize the magnetic behavior of a perfect element with periodicity $\lambda_0 = 50$ mm et $3\lambda_0 = 150$ mm. One the axis, magnetic field was studied for the two operating modes at gap 15.5 mm (minimal gap allowed on the present storage ring), results are presented in Fig. 3.
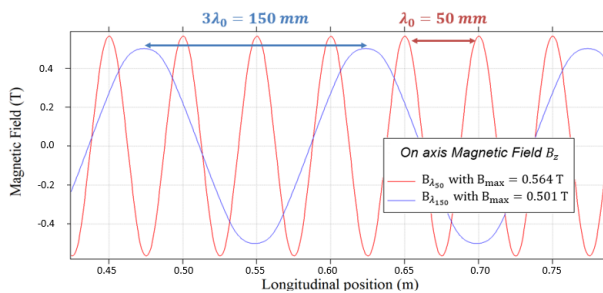
Figure 3: One axis magnetic field B_z at gap 15.5 mm: λ_0 mode in red (50 mm period appears) and $3\lambda_0$ mode in blue (150 mm period appears).

Off Axis Magnetic Field

The electrons that are moving away from the magnetic axis go closer to one of the two girders and the cancellation of the magnetic field coming from the non-active period on the axis is no more satisfied. The impact of a misalignment

on the magnetic field components is analysed via the magnetic field harmonic decompositions for different values of vertical positions in Fig. 4. A Fourier Transform treatment was applied in order to obtain the harmonic content of the magnetic fields for a misalignment of $z = 400\ \mu$m: frequency $\nu = 20\ \mathrm{m}^{-1}$ corrresponding to the period 50 mm and frequency $\nu = 6.66\ \mathrm{m}^{-1}$ corresponding to the period 150 mm. In 50 mm mode: A misalignment in z would induce the appearance of the 150 mm period initially absent in this mode. At off-axis, frequency corresponding to the period 150 mm $\nu_{6.66}$ emerges up to 2.8% of the main frequency ν_{20} corresponding to 50 mm period. In 150 mm mode: A misalignment in z would induce the appearance of the 50 mm period initially absent in this mode. At off-axis, frequency corresponding to the period 50 mm ν_{20} emerges up to 7.9% of the main frequency $\nu_{6.66}$ corresponding to 150 mm period. Off-axis field harmonic composition can induce the appearance of the frequency related to the non-selected period of the mode and can have an impact on the emmited synchrotron radiation.
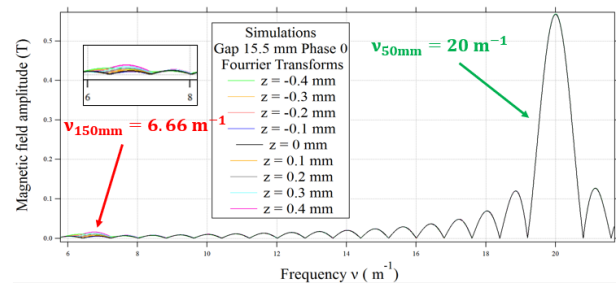
(a) λ_0 mode
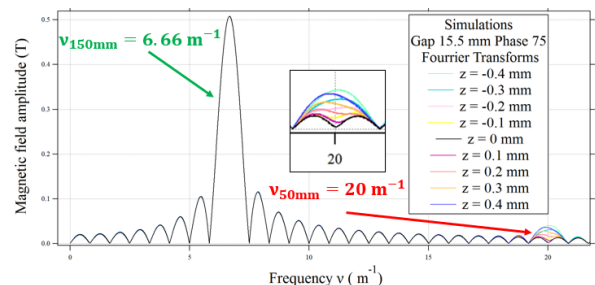
(b) $3\lambda_0$ mode

Figure 4: Magnetic field harmonic composition.

Beam Dynamics

From the second order angle kicks, representing the impact of the undulator magnetic field on angle of electrons, are deduced the tune variation (see Table 1). For the present SOLEIL ring, using the RADIA field map in the TRACY3 code [9]: The impact on the closed orbit (< 1 μm) is acceptable and there is no reduction of the Touschek lifetime.

Synchrotron Radiation

The synchrotron radiation emitted by this undulator on the present storage ring was calculated for each mode. At gap 15.5 mm, for $\lambda_0 = 50$ mm mode the fundamental energy

Table 1: Impact of magnetic field on betatron tune.

Period (mm)	$\Delta\nu_x$	$\Delta\nu_z$
$\lambda_0 = 50$	-0.0005	0.0020
$3\lambda_0 = 150$	-0.0010	0.0021

is E_{fund} = 320 eV and for λ_0 = 150 mm mode the fundamental energy is $E_{fund} = 18 eV$. The study of the spectrum versus vertical and horizontal position is also in progress with Spectra Software [10].

BI-PERIODIC PROTOTYPE CONSTRUCTION

A prototype of this new undulator is in phase of developpment, to experimentally study this configuration and especially to identify the possible technical constraints. Check that the magnetic axis of the two systems are indeed the same and that only one of the two periods can be selected on the magnetic axis with no contamination of the other are of priority importance. The goal is to characterize the system on the bench and then install it on the present SOLEIL storage ring to validate its operation.

Aluminium modules composed of 4 magnets were installed on an carriage allowing the phase shift and the variation of the gap (Fig. 5). The length of this system is 1.5 m.
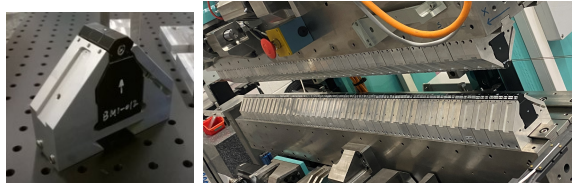
Figure 5: Module of magnets (left) and prototype installed on magnetic measurement bench (right).

Magnetic Measurement

An individual measurement of magnets delivered by the manufacturer (DAILYMAG) was made and average magnetization was deduced: for period λ_0 = 50 mm magnets average magnetization is Br_{avg} = 1.38 T and for λ_0 = 150 mm it is Br_{avg} = 1.42 T.

Magnetic measurements were performed on the prototype undulator to confirm the theoretical behavior. First of all, we calibrated the measuring bench equipped with Senis C-type Hall probe and flipping coil of copper wire. Measurements were made at different gaps in the two operating modes to compare the magnetic measurements to the simulations. Preliminary study of the magnetic field show that the general behavior of the field was identical, the shape of the magnetic field peaks and harmonic composition of magnetic field evolves in the same way according to the different gaps, phases and vertical positions z. Some differences were identified sush as difference between the simulated field and the measured field due to the magnetic defects of the magnets: the simulation fields are higher than the measured fields by less than 3%.

A shift in the magnetic axis between the simulations and the measurements was observed, a translation along z which can make think of a possible misalignment of the Hall probe. Magnetic measurements are underway to determine this magnetic axis and if this magnetic axis changes according to the gaps and the two modes of operation.

In parallel, support design of field terminaison modules was made and then built in our laboratories. The modules were then assembled on the undulator. A difference may appear between the simulation and the measurement so an additional correction using magic finger will be made to take into account the magnetic defects of the prototype.

CONCLUSIONS AND OUTLOOK

The first objective of a bi-periodic undulator is to replace two undulators by one which have the same spectral domain. In this purpose, a prototype has been designed and built to validate its operation and to identify the potential constraints. Present results are encouraging because magnetic measurement of prototype is in accordance with the simulations and we have possibility to select one of the two periods only. Magnet terminaisons to keep the electron beam on axis are installed. Magnetic correction will be finished to study the beam dynamics and the synchrotron radiation from the final measurements, to study impact of a misalignement on synchrotron radiation spectrum. Bi-Periodic prototype will be installed on the storage ring to study experimentally the impact on the beam dynamics and the characteristics of the photon radiation with a beamline. Following the theorical and experimental study of the Bi-Periodic prototype, cross version and APPLE X version are envisaged to produce soft X rays polarized photons for SOLEIL II.

REFERENCES

[1] A. Loulergue *et al.*, "TDR baseline lattice for the upgrade of SOLEIL", in *Proc. IPAC'22*, Bangkok, Thailand, Jun. 2022, pp. 1393–1396.
doi:10.18429/JACoW-IPAC2022-TUPOMS004

[2] T. Pedersen, "DUAL EPU Switchyard", presented at the Undulator Workshop for Multibend Achromat Rings and Free Electron Lasers (ID'17), Berkeley, CA, USA, May 2017.

[3] J. Grimmer, "Revolver undulators", presented at the Advanced Photon Source User Operations Meeting, Argonne National Lab, IL, USA 2014.

[4] P. Vagin, "Variable period helical undulator with tunable polarization", presented at the Undulator Workshop for Multibend Achromat Rings and Free Electron Lasers (ID'17), Berkeley, CA, USA, May 2017.

[5] T. Schmidt and M. Calvi, "APPLE X undulator for the Swiss-FEL soft x-ray beamline Athos", *Synchrotron Radiat. News*, vol. 31., no. 3, pp. 35–40, 2018.
doi:10.1080/08940886.2018.1460174

[6] O. Marcouille, A. Mary, M.-E. Couprie, and K. Tavakoli, *Onduleur bi-périodique, dispositif, installation et procédé associé*, Patent no. FR3125670, https://patents.google.com/patent/FR3125670A1/

[7] K. Halbach, "Design of permanent multipole magnets with oriented rare earth cobalt material", *Nucl. Instrum. Methods*, vol. 169, no. 1, pp. 1–10, 1980.
doi:10.1016/0029-554X(80)90094-4

[8] P. Elleaume, O. Chubar, and J. Chavanne, "Computing 3D magnetic field from insertion devices", in *Proc. PAC'97*, Vancouver, BC, Canada, May 1997, pp. 3509–3511.

[9] *A 6D True Symplectic Tracking Code*, SOLEIL version.

[10] T. Tanaka, "Major upgrade of the synchrotron radiation calculation code SPECTRA', *J. Synchrotron Radiat.*, vol. 28, no. 4, pp. 1267–1272, 2021. doi:10.1107/S1600577521004100

THE COXINEL SEEDED FREE ELECTRON LASER DRIVEN BY THE LASER PLASMA ACCELERATOR AT HZDR

M. E. Couprie[†], M. Labat, T. André, A. Berlioux, P. Berteaud, F. Blache, F. Bouvet, F. Briquez,
C. de Oliveira, J. P. Duval, Y. Dietrich, M. El Ajjouri, C. Herbeaux, N. Hubert, C. Kitégi, S. Lê,
B. Leluan, A. Loulergue, F. Marteau, M. H. N'guyen, D. Oumbarek-Espinos[1], D. Pereira,
J. P. Ricaud, P. Rommeluère, M. Sebdaoui, K. Tavakoli, M. Valléau, M. Vandenberghe, J. Vétéran,
Synchrotron SOLEIL, Saint-Aubin, France,
A. Ghaith, A. Irman, S. Bock, Y. Y. Chang, A. Debus, C. Eisenmann, R. Gebhardt, S. Grams,
U. Helbig, M. Kuntzsch, M. La Berge, R. Pausch, T. Püschel, S. Schöbel, K. Steiniger, P. Ufer,
U. Schramm, Helmholtz-Zentrum Dresden – Rossendorf (HZDR), Dresden, Germany.
S. Corde, J. Gautier, J. P. Goddet, I. Andriyash, O. Kononenko, G. Lambert, V. Malka[2], P. Rousseau,
A. Tafzi, C. Thaury, Laboratoire d'Optique appliquée (LOA), ENSTA Paris, CNRS, Ecole
Polytechnique, Institut Polytechnique de Paris, Palaiseau, France
E. Roussel, Univ. Lille, CNRS, UMR 8523–PhLAM, Lille, France
[1] present address: Institute of Scientific and Industrial Research, Osaka University, Ibaraki, Japan
[2] Present address: Department of Physics of Complex Systems,
Weizmann Institute of Science, Rehovot, Israel

Abstract

Laser Plasma Accelerators know a tremendous development these recent years. Being able to reach up to ~100 GV/m, they open new perspectives for compact accelerators. Their performance can be qualified by a Free Electron Laser (FEL) application. We report here on the COXINEL (COherent X-ray source INferred from Electrons accelerated by lasers) seeded FEL in the UV using high-quality electron beam generated by the 150 TW DRACO laser. We present the COXINEL line developed at Synchrotron SOLEIL (France), the first results when installed at LOA and the seeded FEL achieved at HZDR.

INTRODUCTION

The FEL [1] following the laser invention [2, 3] was developed from infra-red [4], visible [5], UV-VUV [6, 7] in oscillator and coherent harmonic generation, to X-rays in the Self-Amplified Spontaneous Emission (SASE) after demonstrations at long wavelengths [8, 9], thanks to the high-quality electron beams provided by state-of-the-art photo-injectors and accelerators. Longitudinal coherence is improved with external seeding [10] and self-seeding [11]. In the Laser Plasma Acceleration (LPA) concept [12], following the laser discovery, an ultrashort and intense laser focused in a gas cell/jet excites a plasma oscillation, leads to a strong longitudinal accelerating field. High power lasers using chirped pulse amplification [13] boosted experimental demonstrations with hundred MeV range beams with few percent energy spread [14-16]. It opened the hope for driving FELs with LPA [17, 18] considering the use of a 5 fs- 1 PW laser leading to electron beams with 1.74 GeV, 0.1 % energy spread, 10 µrad divergence, 20 µm beam size, 1 nC charge and 150 kA peak current. LPA now reaches ~100 GV/m accelerating field with up to 8 GeV energies [19], 0.4%–1.2% energy spread [20], nC charge [21,

† couprie@synchrotron-soleil.fr

22], few fs bunch duration [23], and low emittance (~mm·mrad) [24]. These features, even though not simultaneously achieved, get closer to the FEL application requirements. Indeed, the first LPA based FEL has been demonstrated at SIOM with state-of-the-art LPA performance at 27 nm in the SASE regime [25]. The second LPA driven FEL has been achieved on COXINEL at HZDR in the seeded configuration at 267 nm [26], enabling for an improved longitudinal coherence.

COXINEL LINE

The COXINEL line was designed in 2010 considering a 200 MeV electron beam with a 1 mrad RMS divergence, 1 µm RMS beam size, 3.3 fs RMS bunch length, 34 pC charge, 1 % energy spread, 1 mm·mrad normalised emittance. The divergence is handled via a strong transverse focusing [27, 28] at the gas jet exit to prevent chromatic emittance growth [29]. The large energy spread is mitigated by a magnetic chicane, reducing the slice one by its decompression factor while elongating the bunch and reducing the peak current accordingly. Thanks to this energy/position correlation introduced in the chicane, the electron beam transverse focusing and the light progress along the undulator can be synchronized (chromatic matching) [28]. Modelling include electron beam transport with collective effects (space charge, coherent synchrotron radiation) [30], FEL sensitivity to parameters [31], FEL radiation. The chicane induced energy chirp coupled with undulator dispersion leads to a red-shifted FEL [33], and inference fringes between the seed and the FEL appear.

The COXINEL equipment have been prepared. The magnetic elements include the QUAPEVA permanent magnet quadrupoles for the initial strong focusing, with gradients up to 200 T/m and 50 % variability [33-35], four chicane electromagnetic dipoles for the slice energy spread reduction and the seed mirror insertion, an electromagnetic

dipole dump, four electromagnetic quadrupoles for the chromatic matching and four electromagnetic correctors. Short period high field 2 m long undulators [36] are used: first the spare SOLEIL In Vacuum Undulator of 20 mm period (IVU20), replaced by a Cryogenic permanent Magnet Undulator of 18 mm period (CPMU18#2) [37, 38], and by the IVU20#8 for the HZDR (maximum deflection parameter K_u of 2.47 at 4 mm gap). Diagnostics include five motorized electron beam imagers, two Turbo Integrating Current transformers (ICTs) [39], a spectrometer and an UV - CCD camera collecting the radiation at the line exit with a lens doublet for imaging the radiation along the undulator. The different parts, including the mechanical and vacuum ones, have been pre-assembled and aligned on the girders [40-42].

COXINEL FIRST RESULTS AT LOA

The COXINEL has been installed and aligned in 2016 in Salle Jaune at LOA, for using the 60 TW, 800 nm, 30 fs FWHM Ti:Sapphire laser for the LPA. The electrons were generated mainly in the ionization injection scheme with the laser focused into a supersonic jet filled a gas mixture (99% Helium, 1% Nitrogen), leading to broad energy spectra with typical 3.5 mrad slice vertical divergence. The electron beam has been rapidly transported. A Beam Pointing Alignment Compensation method, using the transfer matrix response of the line in BETA [43] and the translation of the QUAPEVA magnetic axis enables to independently adjust the electron beam position and the dispersion [44]. The residual skew quadrupolar components of the QUAPEVAs have been corrected [45, 46]. A slit was then inserted in the chicane to reduce the electron beam energy spread [47]. Further LPA improvements enabled to limit the divergence and improve the charge density.

Following first LPA based undulator radiation measurements [48-50], the COXINEL undulator radiation has been characterized, first with its transverse pattern [44] and then with its spectrum, enabling to adjust the resonant wavelength with the undulator gap [51] and to control the line spectral bandwidth by adjusting the energy spread via the slit width in the chicane, showing a good agreement with electron beam transport and SRW undulator radiation simulations [53] and analytical expressions.

The electrons and the seed (High order Harmonics generated in Gas at 200 and 270 nm, EKSMA kit at 270 nm), were spatially overlapped (imaging in the undulator), spectrally tuned (spectrometer) and synchronised (photodiode, spatial interference, Hamamatsu FESCA streak camera). Despite the electron beam improvements (1.5 mrad divergence and 1.5 pC/MeV) thanks to a laser upgrade, its quality was still too far from the baseline reference parameters for achieving the seeded FEL demonstration at LOA.

COXINEL RESULTS AT HZDR

Feasibilities studies in 2020-2021 covered the adaptation to the infrastructure, new electron beam measurements at 200 MeV, the energy of interest for a seeded FEL at 270 nm on COXINEL, the adjustment of the electron beam

transport and FEL modelling with GENESIS [54], an upgrade of the QUAPEVAs for better vacuum compatibility and the construction of the IVU#8 undulator.

Figure 1: COXINEL line installed in HZDR LPA cave

The line was transported and installed in the HZDR cave in October 2021 (see Fig. 1), and aligned with a theodolite and a laser tracker, using the cross reference of the HZDR laser positions and fiducial SOLEIL ones.
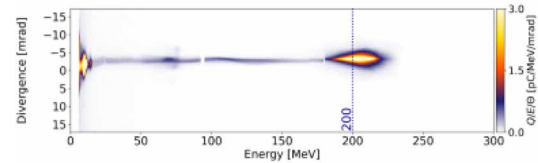
Figure 2: LPA e beam generated by the DRACO laser characterized on the magnetic spectrometer.

The HZDR LPA electron beam is operated with the 100 TW branch of the DRACO laser (30 fs FWHM, 2.1 J on target) in the tailored self-truncated ionization-induced injection [55] with 99 % He-1 % N_2 gas mixture, with a rather good charge and energy stability. Beam loading limits the energy spread to 6 % RMS at 188 MeV [21], a passive plasma lens by shaping the gas density profile keeps the divergence small (0.8 mrad in the horizontal plane), leading to 6.3 pC/MeV FWHM average charge density [26] (see Fig. 2), with a 14.8 fs FWHM estimated duration [23].
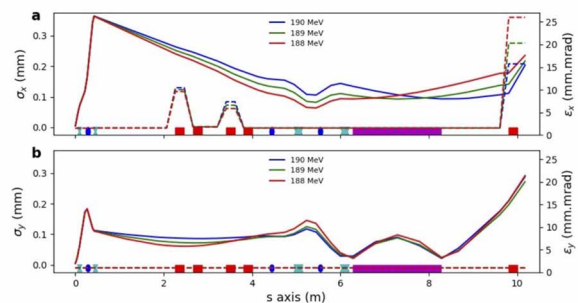
Figure 3: Electron beam envelops for different electron beam energies (ELEGANT simulations [56])

Electron beam was first transported in December 2021 (see envelops in Fig. 3) with up to 150 pC at the exit of the undulator. Undulator spontaneous emission was also measured, exhibiting the expected characteristics.

For the seed, a small fraction of the LPA driver laser is frequency tripled (EKSMA femtokit) with a group velocity compensation, spectrally and spatially filtered, stretched to 1 ps FWHM, resulting in a 3.9 nm (FWHM) bandwidth centered around 270 nm. It is injected with 0.8 μJ into the COXINEL line with an Al mirror, resulting in 0.5 μJ at the

undulator exit. The seed and undulator radiation are spectrally tuned looking at their spectra on the iHR320 Horiba-Jobin Yvon spectrometer, spatially overlapped by imaging in the undulator on a Hamamatsu ORCA-II UV camera and temporally synchronised with a FESCA 100 Hamamatsu streak camera from HZDR.
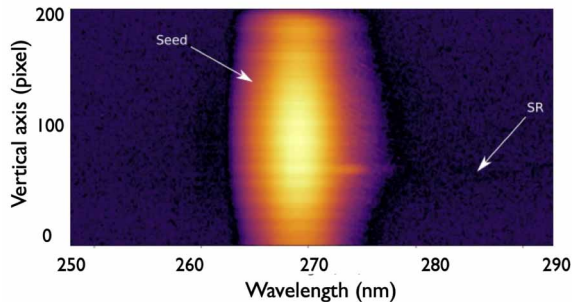
Figure 4: First seeded FEL signal.

During the first delay scan of FEL search in February 2022, the FEL signal was observed, as shown in Fig. 4 [26]. The FEL is red-shifted, as expected [32]. The FEL effect is confirmed by observing separately the seed, the spontaneous undulator radiation and the FEL, and by comparison with simulations. The quadratic charge dependence is confirmed. The FEL wavelength can be tuned with the undulator gap, but also with the delay because of the intrinsic red-shift and of the seed chirp. The expected fringes resulting from the phase-locked interference of the seed and the FEL are observed [26, 32], confirming the longitudinal coherence of the COXINEL seeded FEL. The FEL measurements have been reconfirmed during another experimental session in Nov. 2022.

CONCLUSION

We have demonstrated the first seeded LPA driven FEL on COXINEL installed at HZDR, evidencing longitudinal coherence [26]. Further electron beam improvements are foreseen for reaching shorter wavelengths.

ACKNOWLEDGEMENTS

REFERENCES

[1] J. M. J. Madey, "Stimulated emission of Bremsstrahlung in a periodic magnetic field", *J. Appl. Phys.*, vol. 42, no. 5, pp. 1906-1913, 1971. doi:10.1063/1.1660466.

[2] A. L. Schawlow and C. H. Townes, "Infrared and Optical Masers", *Phys. Rev. Lett.*, vol. 112, p. 1940. 1958. doi.org/10.1103/physrev.112.1940

[3] T. H. Maiman, "Stimulated emission of radiation in ruby", *Nature*, vol. 187, p. 493. 1960. doi:10.1038/187493a0.

[4] D. A. G. Deacon *et al.*, "First operation of a free-electron laser", *Phys. Rev. Lett.*, vol. 38, p. 892, 1977. doi:10.1103/physrevlett.38.892.

[5] M. Billardon *et al.*, "Optical frequency multiplication by an optical klystron", *Phys. Rev. Lett.*, vol. 51, p. 1652, 2014. doi:10.1103/physrevlett.51.1652.

[6] B. Girard *et al.*, "Optical frequency multiplication by an optical klystron", *Phys. Rev. Lett.*, vol. 53, p. 2405, 1984. doi:10.1103/physrevlett.53.2405.

[7] R. Prazeres *et al.*, "Coherent harmonic generation in the vacuum ultraviolet spectral range on the storage ring ACO", *Nucl. Instrum. Methods*, vol. 272, p. 68, 1988. doi:10.1103/PhysRevLett.114.050511

[8] A. L. Throop *et al.*, "Experimental results of a high gain microwave FEL operating at 140 GHz", *Nucl. Instrum. Methods*, vol. 272, p. 15, 1988. doi:10.1016/0168-9002(88)90187-8

[9] P. Emma *et al.*, "First lasing and operation of an ångstrom-wavelength free-electron laser", *Nat. Photonics.*, vol. 4, p. 641, 2010. doi:10.1103/PhysRevLett.114.050511

[10] L. H. Yu *et al.*, "High-gain harmonic-generation free-electron laser", *Science.*, vol. 289, no. 5, p. 5481, 2000. doi:10.1126/science.289.5481.932

[11] A. A. Lutman *et al.*, "Demonstration of single-crystal self-seeded two-color X-ray free-electron lasers", *Phy. Rev. Lett.*, vol. 113, no. 5, p. 254801, 2013. doi:10.1103/physrevlett.110.134801.

[12] T. Tajima and J. M. Dawson *et al.*, "Laser electron accelerator", *Phy. Rev. Lett.*, vol. 43, p. 267, 1979. doi.org/10.1103/PhysRevLett.43.267

[13] D. Strickland and G. Mourou, "Compression of amplified chirped optical pulses", *Opt. Commun.*, vol. 55, p. 447, 1985. doi:10.1016/0030-4018(85)90151-8

[14] S. P. Mangles *et al.*, "Monoenergetic beams of relativistic electrons from intense laser-plasma interactions", *Nature.*, vol. 431, p. 535, 2004. doi:10.1038/nature02939

[15] C. G. R. Geddes *et al.*, "High-quality electron beams from a laser wakefield accelerator using plasma-channel guiding", *Nature.*, vol. 431, p. 538, 2004. doi:10.1038/nature02900

[16] J. Faure *et al.*, "A laser-plasma accelerator producing monoenergetic electron beams", *Nature.*, vol. 431, p. 541, 2004. doi:10.1038/nature02963

[17] F. Grüner *et al.*, "Design considerations for table-top, laser-based VUV and X-ray free electron lasers", *Appl. Phys. B*, vol. 86, p. 431, 2007   . doi:10.1007/s00340-006-2565-7

[18] K. Nakajima *et al.*, "Towards a table-top free-electron laser", *Nat. Phys.*, vol. 4, p. 92, 2008. doi:10.1038/nphys846

[19] A. J. Gonsalves *et al.*, "Petawatt laser guiding and electron beam acceleration to 8 GeV in a laser-heated capillary discharge waveguide", *Phys. Rev. Lett.*, vol. 112, p. 084801, 2019. doi:10.1103/PhysRevLett.122.084801

67th ICFA Adv. Beam Dyn. Workshop Future Light Sources

ISBN: 978-3-95450-224-0

ISSN: 2673-7035

FLS2023, Luzern, Switzerland

JACoW Publishing

doi:10.18429/JACoW-FLS2023-TH2C1

[20] W. T. Wang *et al.*, "High-brightness high-energy electron beams from a laser wakefield accelerator via energy chirp control", *Phys. Rev. Lett.*, vol. 117, p. 124801, 2016. `doi:10.1103/PhysRevLett.117.124801`

[21] J. P. Couperus *et al.*, "Demonstration of a beam loaded nanocoulomb-class laser wakefield accelerator.", *Nat. Commun.*, vol. 8, p. 487, 2017. `doi:10.1038/s41467-017-00592-7`

[22] J. Götzfried *et al.*, "Physics of high-charge electron beams in laser-plasma wakefields", *Phys. Rev. Lett.*, vol. 114, no. 5, p. 050511, Feb. 1983. `doi:10.1103/PhysRevLett.114.050511`

[23] O. Zarini *et al.*, "Multioctave high-dynamic range optical spectrometer for single-pulse, longitudinal characterization of ultrashort electron bunches", *Phys. Rev. Accel. Beams*, vol. 25, p. 012801, 2022. `doi:10.1103/PhysRevAccelBeams.25.012801`

[24] G. R. Plateau *et al.*, "Low-emittance electron bunches from a laser-plasma accelerator measured using single-shot X-ray spectroscopy", *Phys. Rev. Lett.*, vol. 109, p. 064802, 2012. `doi:10.1103/PhysRevLett.109.064802`

[25] W. Wang *et al.*, "Free-electron lasing at 27 nanometres based on a laser wakefield accelerator", *Nature*, vol. 595, p. 516, 2021. `doi:10.1038/s41586-021-03678-x`

[26] M. Labat *et al.*, "Seeded free-electron laser driven by a compact laser plasma accelerator", *Nature Photon.*, vol. 17, p. 150, 2022. `doi:10.1038/s41566-022-01104-w`

[27] M. E. Couprie *et al.*, "Towards a free electron laser based on laser plasma accelerators", *Jour. Phys. B: At. Mol. Opt. Phys*, vol. 47, no. 23, p. 234001, 2014. `doi:10.1088/0953-4075/47/23/234001`

[28] A. Loulergue *et al.*, "Beam manipulation for compact laser wakefield accelerator based free-electron lasers", *New Jour. Phys.*, vol. 17, no. 2, p. 023028, 2015. `doi:10.1088/1367-2630/17/2/023028`

[29] K. Floettmann *et al.*, "Some basic features of the beam emittance", *Phys. Rev. Accel. Beams*, vol. 6, p. 034202, 2003. `doi:10.1103/PhysRevSTAB.6.034202`

[30] M. Khojoyan *et al.*, "Transport studies of LPA electron beam towards the FEL amplification at COXINEL", *Nucl. Instr. Meth. A.*, vol. 829, p. 260, 2016. `doi:10.1016/j. nima.2016.02.030i`

[31] M. Labat *et al.*, "Robustness of a plasma acceleration based Free Electron Laser", *Phys. Rev. Accel. Beams.*, vol. 21, p. 114802, 2018. `doi:10.1103/PhysRevAccelBeams.21.114802`

[32] M. Labat *et al.*, "Interferometry for full temporal reconstruction of laser-plasma accelerator-based seeded free electron lasers", *New Journ. Phys.*, vol. 22, no. 1, p. 013051, 2020. `doi:10.1088/1367-2630/ab6878`

[33] C. Benabderrahmane, M. E. Couprie, SOLEIL, F. Forest, O. Cosson Sigmaphi *et al.*, "Adjustable magnetic multipole", *Patent Europe.*, EP 3189715 B1, published 2018-06-13, 2018, `https://bases-brevets.inpi.fr/fr/document/EP3189715/publications.html`

[34] F. Marteau *et al.*, "Variable high gradient permanent magnet quadrupole (QUAPEVA),", *Appl. Phys. Lett.*, vol. 111, p. 25, 2017. `doi:10.1063/1.4986856`

[35] A. Ghaith *et al.*, "Tunable high gradient quadrupoles for a laser plasma acceleration based FEL", *Nucl. Instrum. Meth.*

A., vol. 909, p. 290, 2018. `doi:10.1016/j.nima.2018.02.098`

[36] A. Ghaith *et al.*, "Undulator design for Laser Plasma Based Free electron laser", *Phys. Rept.*, vol. 937, p. 2184, 2021. `doi:10.1016/j.physrep.2021.09.001`

[37] C. Benabderrahmane *et al.*, "Development and operation of a $Pr_2Fe_{14}B$ based cryogenic permanent magnet undulator for a high spatial resolution x-ray beam line", *Phys. Rev. Accel. Beams.*, vol. 20, p. 033201, 2017. `doi:10.1103/PhysRevAccelBeams.20.033201`

[38] M. Valléau *et al.*, "Development of Cryogenic Permanent Magnet Undulators at SOLEIL", *Synchrotron Radiat. News*, vol. 31, no. 3, p. 42, 2018. `doi:10.1080/08940886.2018.1460175`

[39] M. Labat *et al.*, "Electron and photon diagnostics for plasma acceleration-based FELs", *J. Synchrotron Radiat.*, vol. 25, no. 1, p. 59, 2018. `doi:10.1107/S1600577517011742`

[40] M. E. Couprie *et al.*, "Towards free electron laser amplification to qualify laser plasma acceleration", *Rev. Laser Eng.*, vol. 45, no. 2, p. 94, 2017.

[41] M. E. Couprie *et al.*, "An application of Laser Plasma Acceleration: Towards a Free Electron Laser amplification", *Plasma Physics & Controlled Fusion*, vol. 58, no. 3, p. 034020, 2016. `doi:10.1088/0741-3335/58/3/034020`

[42] M. E. Couprie *et al.*, "Towards a free electron laser using laser plasma acceleration on COXINEL", in *Proc. SRI'18*, Taipei, Taiwan, Jun. 2018, *AIP Conf. Proc..*, vol. 2054, no. 1, p. 030034, 2019. `doi:10.1063/1.5084597`

[43] J. Payet *et al.*, "BETA code", *CEA-Saclay* 2015, `http://irfu.cea.fr/Sacm/logiciels/index6.php`

[44] T. André *et al.*, "Control of laser plasma accelerated electrons for light sources", *Nat. Comm.*, vol. 9, p. 1334, 2018. `doi:10.1038/s41467-018-03776-x`

[45] D. Oumbarek-Espinos *et al.*, "Skew quadrupole effect of laser plasma electron beam transport", *Appl. Sci.*, vol. 9, no. 12, p. 2447, 2019. `doi:10.3390/app9122447`

[46] D. Oumbarek-Espinos *et al.*, "COXINEL transport of laser plasma accelerated electrons", *Plasma Physics & Controlled Fusion.*, vol. 62, no. 3, p. 034001, 2020. `doi:10.1088/1361-6587/ab5fec`

[47] E. Roussel *et al.*, "Energy spread tuning of a laser-plasma accelerated electron beam in a magnetic chicane", *Plasma Physics & Controlled Fusion*, vol. 62, no. 7, p. 074003, 2020. `doi:10.1088/1361-6587/ab8ca0`

[48] H. P. Schlenvoigt *et al.*, "A compact synchrotron radiation source driven by a laser-plasma wakefield accelerator", *Nat. Phys.*, vol. 4, p. 130, 2008. `doi:10.1038/nphys811`

[49] M. Fuchs *et al.*, "Laser-driven soft-X-ray undulator source", *Nat. Phys.*, vol. 5, p. 826, 2009. `doi:10.1038/nphys1404`

[50] M. P. Anania *et al.*, "An ultrashort pulse ultra-violet radiation undulator source driven by a laser plasma wakefield accelerator", *Appl. Phys. Lett.*, vol. 104, p. 264102, 2014. `doi:10.1063/1.4886997`

[51] A. Ghaith *et al.*, "Tunable high spatio-spectral purity undulator radiation from a transported laser plasma accelerated electron beam", *Sci. Rep.*, vol. 9, p. 19020, 2019. `doi:10.1038/s41598-019-55209-4`

[53] O. Chubar *et al.*, "A three-dimensional magnetostatics computer code for insertion devices", *J. Synchrotron Rad.*, vol. 5, p. 481, 1998. doi:10.1107/S0909049597013502

[54] S. Reiche *et al.*, "Genesis 1.3: a fully 3d time-dependent FEL simulation code", *Nucl. Instrum. Meth. A.*, vol. 429, no. 1-3, p. 243, 1999.
doi:10.1016/S0168-9002(99)00114-X

[55] A. Irman *et al.*, "Improved performance of laser wakefield acceleration by tailored self-truncated injection", *Plasma Physics & Controlled Fusion*, vol. 60, p. 044015, 2018.
doi:0.1088/1361-6587/aaaef1

[56] M. Borland, "Elegant: A flexible SDSS-compliant code for accelerator simulation", Argonne National Laboratory, IL, USA, 2000.

DEVELOPMENT OF LASER-DRIVEN PLASMA ACCELERATOR BASED UNDULATOR RADIATION SOURCE AT ELI-BEAMLINES

A. Molodozhentsev†, J. T. Green, A. Mondal, S. Maity, S. Niekrasz, E. Vishnyakov,
A. Jancarek, P. Zimmermann
Extreme Light Infrastructure ERIC, ELI-Beamlines, Dolni Brezany, Czech Republic

Abstract

A compact undulator radiation source based on a laser-driven plasma accelerator (LPA) is currently being commissioned at ELI-Beamlines (ELI-ERIC, Czech Republic). An intermediate goal of this activity is to deliver a stable and repeatable incoherent photon beam with a wavelength of about 4 nm to a user station. As a result of this development, the electron beam parameters will be improved, with the aim of producing a coherent photon beam, utilising a dedicated FEL undulator. An overview of the current status of the project (LUIS) is presented in this report, including the high-power high-repetition rate laser, the compact electron beam accelerator based on the laser-plasma interaction, and the electron and photon beamlines with relevant diagnostics. The challenges and future developments of the LUIS project, aimed at LPA-based EUV-FEL, will also be discussed.

INTRODUCTION

The scientific success and tremendous demand from the photon beam user community stimulate intensive research to find competitive approaches which would lead to a significant size and cost reduction of the instruments for both incoherent and coherent photon beams.

Constantly developing Laser Wakefield Acceleration (LWFA) techniques make it a very attractive candidate for novel, compact undulator radiation sources, especially in the light of recent progress in the laser technology [1], acceleration gain [2] and breakthroughs in electron beam quality improvement [3]. With the electron beam properties, obtained experimentally by different teams as the result of the laser-plasma interaction in the compact laser-plasma accelerator (LPA), a generation of the incoherent photon radiation in a compact undulator has already been demonstrated [4-6].

Nowadays main effort is concentrated on the improvement of the LPA-based electron beam quality to be able to use such a beam to generate a coherent undulator photon radiation utilizing the so-called Self-Amplified Spontaneous Emission (SASE) regime [7] of a Free Electron Laser (FEL). The novel LPA-based source of incoherent and coherent photon radiation has attracted interest for applications in medicine [8] and industry [9].

A compact LPA-based undulator radiation source (LUIS) is currently under development at ELI-ERIC in the Czech Republic. After the commissioning, it will bring to the user community a high repetition rate (50-100 Hz) of soft X-ray radiation aiming for high-temporal-resolution

pump-probe experiments, combined with XANES spectroscopy and high-resolution microscopy.

The main goal of this development is to improve the quality of the LPA-based electron beam to make this beam usable for not only for the incoherent regime but also for the coherent one in the extreme ultra-violet range of the radiation wavelength (for the fundamental harmonic). It will open the way to prepare the user-oriented compact LPA-based FEL, based on the 100 TW-class laser system with a repetition rate up to 100 Hz.

DEVELOPMENT AT ELI-BEAMLINES (ELI-ERIC)

The Extreme Light Infrastructure (ELI-ERIC) is the world's largest and most advanced high-power laser infrastructure and a global technology and innovation leader in high-power, high-intensity and short-pulsed laser systems. ELI-beamlines, as a part of ELI-ERIC, locates near Prague (Czech Republic). ELI-beamlines is a unique infrastructure in the field of photonic-based user-oriented research and the first large-scale facility in this worldwide domain. The specific nature of the ELI-beamlines user facility is its multi-disciplinary features, which open extremely wide opportunities for the user community to develop new secondary radiation and particle sources, creating new paths of applied and fundamental research, pushing the boundaries of science and technology.

Laser Development at ELI-beamlines

New LUIS-dedicated high-repetition high-power laser system is under development at ELI-ERIC (L2-DUHA laser) [10], based on the OPCPA technology, will deliver two pulses: the main laser pulse with energy of up to 5 J, 25 fs pulse duration and the wavelength of 820 nm, as well as the auxiliary laser pulse with the energy of a few mJ, 30 fs pulse duration and the wavelength of around 2.2 µm. The main laser pulse will be focused in the prefilled gas-cell (or preformed plasma channel) to produce a high-quality high-energy electron bunch. The auxiliary laser pulse will be used for the pump-probe experiments.

At the moment the LUIS technology is integrated with the L3-HALPS laser. This laser system currently operated at a 3.3 Hz repetition rate and provides a pulse with a central wavelength of 820 nm, 30 fs pulse duration and a pulse energy of up to 13 J with a possible upgrade up to 30 J. In the case of the L3-LUIS operation, the maximum pulse energy of the cropped laser beam is limited by 1.5 J (before the L3 upgrade) or 3.5 J after upgrade.

---
† Alexander.Molodozhentsev@eli-beams.eu

Both laser systems are suitable to accelerate the electron bunch with the parameters needed to generate the incoherent 'water-window' photon beam (the electron beam energy of 300-600 MeV and the bunch charge of the order of 50 pC).

Laser-Plasma Accelerator

Significant progress has been made to demonstrate to reach a few GeV energy of the electron beam using laser-plasma interaction [6], including machine learning [3] to produce stable and repeatable electron beams during the long-term continuous experimental activity.

Typical parameters, demonstrated recently by many groups, show that the electron beam with the energy of a few hundred MeV with the FWHM relative energy spread of 1-2% and the bunch charge of about 50 pC is achievable. However, the generation of high-quality electron beams still remains extremely challenging for a plasma-based accelerator.

The LPA electron beam quality depends strongly on the injection mechanism and its parametric dependence [11]. The self-truncated ionization-induced injection mechanism [12] in combination with the beam loading [13] and the energy chirp manipulation [14] is considered as the most promising technique for controlled injection and acceleration processes in the compact laser-plasma accelerator.

The LUIS setup at ELI-Beamlines is based on the LUX technologies, developed and tested at DESY in the collaboration between the University of Hamburg and ELI-Beamlines [4]. The compact laser-plasma accelerator, integrated into the LUIS Phase0 setup, is the gas-cell utilizing the 15 mm Sapphire capillary, which also can be used as the capillary with the preformed plasma for the laser guiding [15]. In the case of the gas-cell ('staged' LPA), the helium-nitrogen (90+10%) gas mixture will be utilized in the injection part of the gas-cell. In the acceleration part, pure helium gas with less pressure will be used. The results of the PIC-modelling will be published soon [16].

The performed LWFA PIC-simulations show [16] that the electron beam energy around 500-600 MeV can be obtained using the laser pulse energy of 1.5 J in the focus (laser intensity of 10^{19} W/cm^2) if the plasma density is around 1.6×10^{18} cm^{-3}. In this case, the FWHM relative energy spread is less than 5% and the FWHM transverse divergence is less than 1 mrad for the bunch charge of around 50 pC.

Such electron bunch can be used to generate the incoherent undulator radiation in the 'water-window' wavelength range, which is the intermediate goal of the LUIS development at ELI-Beamlines.

Incoherent Undulator Radiation Source

The incoherent LUIS setup at ELI-beamlines is based on the compact permanent-magnet undulator with the undulator period of 5 mm, the on-axis magnetic field of 0.6 T and the K-value of 0.28. The length of the undulator is 0.5 m. This unit will be placed at the end of a dedicated LUIS electron beam line. According to the LUIS commissioning plan, the electron beam line will be updated step-by-step

aiming for the setup, which will integrate all required components [17] to: (1) capture the electron beam from the LPA source; (2) clean the halo of the electron beam, caused by the chromatic aberration effect; (3) control the 'slice' energy spread (needed for the coherent FEL regime) and focus the electron beam in the undulator. The electron beam line will be equipped with relevant diagnostics to measure the main parameters of the beam along the beamline [18].

The strength of the focusing elements is optimized to transport the electron beam with the energy from 300 MeV to 600 MeV. If the charge of the electron beam, which is propagating along the undulator, is 30 pC the following parameters of the photon radiation will be obtained: the photon energy and corresponding photon wavelength in the range of 165 eV (7.5 nm)-658 eV (1.8 nm); the number of photons per pulse in the 0.1% bandwidth from 1.7×10^5 to 7.1×10^6; the peak brilliance at the peak current of the electron bunch from 4.8×10^{20} to 1.9×10^{21} photons/pulse/mrad^2/mm^2/0.1%bw, respectively. The expected RMS transverse size of the photon beam in the undulator is around 110 µm in both transverse planes with the RMS divergence of around 80 µrad.

In order to focus the photon beam in the sample location a focusing ellipsoidal mirror will be placed in a photon beam chamber with x6 demagnification in the aberration-corrected regime allowing a small focal spot of the photon radiation better than 20 µm with later reduction up to at least 5 µm [19]. The incoherent photon beam will be used for the user-oriented operation, using the following user-operation modes: (1) focused non-dispersed beam in combination with the pump-probe option; (2) defocused non-dispersed beam and (3) monochromatic photon beam.

Using the LWFA scaling laws [20] and existing experimental results [15] one can predict that by using the L2-DUHA laser system the electron beam energy of 1 GeV is achievable at the early stage of the L2-DUHA laser operation with the laser power of around 150 TW. The discharge plasma formation setup is under development at ELI-Beamlines, which can be used for the laser guiding and/or as an 'active' plasma lens [21] to focus the accelerated electron beam into an electron beam line, required to transport electrons from the compact laser-plasma accelerator up to the undulator line.

Coherent Undulator Radiation Source

The incoherent LUIS setup at ELI-Beamlines can be transferred to the coherent one if the electron beam quality at the undulator entrance fits the criteria for the SASE-FEL regime. We are aiming to use a hybrid-permanent-magnet-undulator (planar-HPMU) type [22] with the undulator period (λ_u) of 15 mm, the undulator parameter (K_u) of 1.0-1.5 (depending on the gap size) and the total length of 4 m. In the case of the electron beam energy of 350 MeV, the energy and the wavelength of the photon radiation (the fundamental harmonic) are 44.5 eV and 27.8 nm, respectively.

The free-electron lasing at 27 nm based on the laser-plasma accelerator was already demonstrated experimentally by the group from Shanghai Institute of Optics and

Fine Mechanics [23] by using the LPA-based electron bunch, propagating through 3 separated sections of the undulator with the length of 1.5 m each.

Using the 3D-model of the SASE-FEL regime ([24], [25]) we defined the parameters of the electron bunch, required to reach the saturation of the power of the photon radiation in one undulator unit ($L_{sat,3D} \sim 4m$). To get it, the electron beam energy should be around 350 MeV with the 'slice' RMS energy spread of less than 0.3 %. In addition, the transverse normalized RMS emittance should not exceed 0.3 π mm.mrad and the peak current has to be a few kA. The slice energy spread we are planning to control by utilizing the 'decompression-chicane' scheme [26], integrated into the dedicated electron beam transport [27]. Another possible approach to control the slice energy spread proposed recently is based on the usage of extra components, integrated into the electron beam line, in particular the X-band cavity [28] or the active plasma dechirper [29].

The initial RMS parameters of the LPA-based 350 MeV electron beam, which we used for our analysis, are based on the experimental results published recently [23]: the 'projected' relative energy spread is 0.5 %, the normalized emittance is 0.2 π mm.mrad, the transverse divergence is 0.5 mrad, the bunch length is 1 µm and the bunch charge is 40 pC (the corresponding peak current is 5.3 kA). Such a high initial peak current is required to provide the 'slice' peak current of the bunch in the undulator after the decompression. For such challenging initial parameters of the LPA electron bunch, the intrinsic growth of the normalized emittance [30] is negligible (the relative normalized emittance growth is less than 1% even after 20 cm for the bunch charge up to 75 pC).

For the comprehensive analysis, it is necessary to use the pre-simulation 6D particle distribution, obtained as the result of the comprehensive 3D simulations of the laser-plasma interaction and the laser wakefield acceleration.

The second effect which will lead to the dilution of the transverse emittance in addition to the space charge effect is the chromatic aberrations in the first block of the focusing elements. Comparison of the emittance growth in 3 possible combinations of the focusing elements, which can be utilized to capture the electron beam from the LPA-source, in particular: (1) triplet of the electro-quadrupole magnets; (2) combination of 2 permanent quadrupole magnets and one electro-quadrupole magnet [17] and (3) active plasma lens [21], shows that only the active plasma lens or the permanent quadrupole magnets should be used as the first block of the dedicated electron beam line for the compact LPA-based FEL setup.

The 'slice' energy spread control by using the 'decompression' chicane requires increasing bunch charge from LPA-source to get the peak current needed to get saturation of power of coherent photon radiation in one undulator unit with a length of 4 m. Nevertheless, collective effects [31] in the 'decompression' chicane with a relatively small bending angle ($R_{56} < 0.5$ mm) do not change significantly the electron beam parameters for the considered case.

At the same time, in order to clean the electron beam from the halo, caused by mainly the chromatic aberration

and space charge effect, it is necessary to use a collimator (transverse slits) placed near the undulator. It will improve the transverse quality of the electron bunch at the end of the dedicated beamline without reduction of the peak current leading to a reduction of the saturation length (see Fig.1).

After the proper analysis of the 'slice' parameters of the electron bunch at the end of the electron beamline, based on the active plasma lens as the first 'capture' element of the dedicated beam transport, the lasing and saturation in one undulator unit were verified using the SIMPLEX-code [32] in the case of the LPA-based EUV FEL. The saturation length as a function of the resulting 'slice' peak current is presented in Fig.1 for two cases: without collimator before the undulator ("red" line) and with collimator ("black" like).
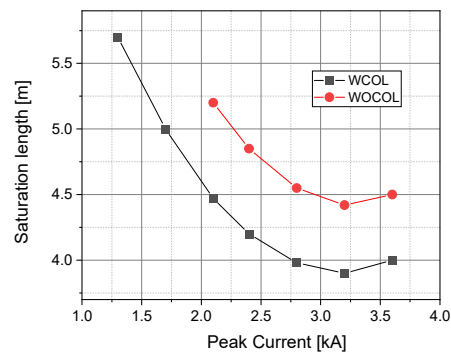
Figure 1: Dependence the saturation length on the peak current for the optimized decompressor parameters.

The saturation length is around 4m only in the case with the collimator if the "slice" peak current is around 3 kA. In order to get such a "slice" peak current the initial bunch charge should be around 60 pC. The bending angle of the dipole magnets in the decompression chicane should be around 0.9 degrees. The aperture of the collimator should be 0.8 mm. Comprehensive "Start-to-End" modelling is required to confirm the performance of the proposed setup.

CONCLUSION

Development of the incoherent undulator photon radiation source (LUIS), based on the compact high-repetition rate laser-plasma accelerator, is underway at ELI-Beamlines (ELI-ERIC). An upgrade of the LUIS technology to produce coherent EUV radiation using the SASE-FEL regime is in preparation aiming to achieve photon beam power saturation in the 4-m long undulator section. The main challenges of this project are the following: obtaining the required initial electron beam parameters from the modern LPA-based compact accelerator; maintaining the normalised emittance of the beam; controlling the 'slice' energy spread in combination with the beam charge; and matching and collimating the electron beam at the entrance of the undulator.

REFERENCES

[1] G. Mourou and T. Tajima, "The extreme light infrastructure: optics' next horizon", *Optics and Photonics News*, vol. 22, no. 7, p. 47, Jul. 2011. `doi: 10.1364/opn.22.7.000047doi`

[2] A.J. Gonsalves *et al.*, "Petawatt laser guiding and electron beam acceleration to 8 GeV in a laser-heated capillary discharge waveguide", *Phys. Rev. Lett.* vol. 122, no. 8, Feb. 2019. `doi:10.1103/PhysRevLett.122.084801`

[3] S. Jalas *et al*, "Bayesian optimization of a laser-plasma accelerator", *Phys. Rev. Lett.,* vol. 126, no. 10, p. 505, Mar. 2021. `doi:10.1103/PhysRevLett.126.104801`

[4] N. Delbos *et al*, "Lux-A laser-plasma driven undulator beamline", *Nucl. Instrum. Methods, Sect. A*, vol. 909, pp. 318–322, Nov. 2018. `doi:10.1016/j.nima.2018.01.082`

[5] T. Andre et al., "Control of Laser Plasma Accelerated Electrons for Light Sources", *Nature Communications*, vol. 9, p.1334, 2018. `doi:10.1038/s41467-018-03776-x`

[6] C. Schroeder *et al.,* "Application of laser-plasma accelerator beams to free-electron lasers", in: *Proc. of FEL'12*, Nara, Japan, 2012

[7] C. Pellegrini, "Design Considerations for a SASE X-ray FEL", *Nucl. Instrum. Methods, Sect. A*, 475 (2001) 1-12.

[8] F. Carrol *et. al.*, *Am. Jour. Roent.*, vol. 181, p. 1197, 2003. `doi:/10.2214/ajr.181.5.1811197`

[9] H.V. Gomez, "X-ray Computed Tomography for Dimensional Measurements", in *Proc. Digital Imaging Conference* USA, pp 44-57, 2016.

[10] T. Green *et al*, "L2-DUHA 100TW high repetition rate laser system at ELI-beamlines: Key design considerations", *Review of Laser Engineering*, vol. 49, pp. 106-109, 2021.

[11] V. Malka, "Plasma Wake Accelerators: Introduction and Historical Overview", in *Proc. of CAS-CERN Accelerator School: Plasma Wake Accelerators*, 2014. `doi:10.5170/CERN-2016-001.1`

[12] A. Irman *et al.*, "Improved performance of laser wakefield acceleration by tailored self-truncated ionization injection", *Plasma Physics and Controlled Fusion*, vol. 60(4), p. 044015, 2018

[13] M. Kirchen *et al.*, "Optimal beam Loading in a Laser-Plasma Accelerator", *Phys. Rev. Lett.* 126, 174801, 2021. `doi:10.1103/PhysRevLett.126.174801`

[14] W.T. Wang *et al.*, "High-brightness high-energy electron beams from LWFA via energy chirp control", *Phys. Rev. Lett.*, vol. 117, no. 12, Sep. 2016. `doi:10.1103/PhysRevLett.117.124801`

[15] K. Nakamura *et al.,* "GeV electron beams from a centimeter-scale channel guided laser wakefield accelerator", *Phys. Plasmas,* vol. 14, p. 056798, 2007. `doi:10.1063/1.2718524`

[16] S. Maity *et al.,* "Parametric Analysis of Electron Beam Quality in a Staged Lase,r Wakefield Acceleration Based on the Ionization Injection Mechanism", submitted for publication.

[17] A. Molodozhentsev *et al*, "Compact LWFA-based EUV-FEL: design constraints", *Instruments,* vol. 6, no. 1, p. 4, Jan. 2022. `doi:10.3390/instruments6010004`

[18] K. Kruchinin *et al.,* "Electron Beam Diagnostics Concept for the ELI-LUX Project", in *Proc. of IPAC18*, BC, Canada. `doi:10.18429/JACoW-IPAC2018-WEPAF057`

[19] E. Vishnyakov *et al.*, "Compact Undulator-Based Soft X-ray Radiation Source at ELI-Beamlines: User-Oriented Program", in *Proc. SPIE*, vol. 12582. `doi:/10.1117/12.2665377`

[20] W. Lu *et al*, "Generating multi-GeV electron bunches using single stage laser wakefield acceleration in a 3D nonlinear regime", *Phys. Rev. Spec. Top. Accel. Beams,* vol. 10, no. 6, Jun. 2007. `doi:10.1103/PhysRevSTAB.10.061301`

[21] J. van Tilborg *et al.*, "Active Plasma Lensing for Relativistic Laser-Plasma-Accelerated Electron Beams", *Phys. Rev. Lett.*, vol. 115, p. 181802, 2015. `doi:10.1103/PhysRevLett.115.184802`

[22] C.J. Milne *et al.*, "SwissFEL: the Swiss X-ray Free Electron Laser", *Appl. Sci ,* vol. 7, p. 720, 2017. `doi:10.3390/app7070720`

[23] W. Wang *et al.,* "Free-Electron Lasing at 27nm based on a Laser Wakefield Accelerator, *Nature*, vol. 595, 2021 . `doi:10.1038/s41586-021-03678-x`

[24] G. Dattoli *et al.*, "A Simple Model of Gain Saturation in High Gain Single Pass Free Electron Lasers", *Nucl. Instrum. Methods., Sect. A*, vol. 393, pp.133-136, 1997.

[25] M. Xie, LBNL-44381, CBP Note-323, 1999

[26] A. Maier *et al.,* *Phys.Rev.* X, vol. 2, p. 031019, 2012.

[27] A. Molodozhentsev, G. Korn, L. Pribyl and A. R. Maier, "LWFA-driven Free Electron Laser for ELI-Beamlines", in *Proc. FLS-18 Workshop*, Shanghai, China, Jun. 2018, pp. 62-67. `doi:10.18429/JACoW-FLS2018-TUA2WC02`

[28] S. Antipov *et al.*, "Design of a prototype laser-plasma injector for an electron synchrotron", *Phys.Rev.Accel.Beams*, vol. 24, p. 111301, 2021. `doi:10.1103/PhysRevAccelBeams.24.111301`

[29] A.F. Pousa *et al.*, "Energy Compensassion and Stabilization of Laser-Plasma Accelerators", *Phys.Rev.Lett.,* vol. 129, p. 094801, 2022. `doi:10.1103/PhysRevLett.129.094801`

[30] M. Migliorati *et. al.*, "Intrinsic normalized emittance growth in laser-driven electron accelerators", *Phys.Rev. ST Accel. Beams,* vol. 16, p. 011302, 2013. `doi:10.1103/PhysRevSTAB.16.011302`

[31] T. Limberg and M. Dohlus, "Impact of Optics on CSR-Related Emittance Growth in Bunch Compressor Chicanes", in *Proc. PAC'05*, Knoxville, TN, USA, May 2005, paper TPAT006.

[32] T. Tanaka, "SIMPLEX: simulator and postprocessor for free-electron laser experiments", *J. Synchrotron Radiat.*, vol. 22, no. 5, pp. 1319-1326, Aug. 2015. `doi:10.1107/S1600577515012850`

NOVEL X-RAY BEAM POSITION MONITOR
FOR COHERENT SOFT X-RAY BEAMLINES*

B. Podobedov[1,†], D.M. Bacescu[1], D. Donetski[2], C. Eng[1], S.L. Hulbert[1], K. Kucharczyk[2], J. Liu[2],
R. Lutchman[2], C. Mazzoli[1], C.S. Nelson[1], J. Zhao[2]

[1]Brookhaven National Laboratory, Upton, NY, USA
[2]Stony Brook University, Stony Brook, NY, USA

Abstract

A novel soft X-ray BPM (sXBPM) for high-power white beams of synchrotron undulator radiation is being developed through a joint effort of BNL/NSLS-II and Stony Brook University. In our approach, custom-made multi-pixel GaAs detector arrays are placed into the outer portions of the X-ray beam, and the beam position is inferred from the pixel photocurrents. Our goal is to achieve micron-scale positional resolution ~30 m away from the source, without interfering with user experiments, especially the most sensitive ones exploiting coherent properties of the beam. To this end, an elaborate mechanical system has been designed, fabricated, and installed in the 23-ID canted undulator beamline first optical enclosure (FOE), which allows positioning of the detectors with micron-scale accuracy, and provisions for possible intercepts of kW-level beam in abnormal conditions. Separately, GaAs detectors with specially tailored spectral response have been designed, fabricated, and tested in the soft and hard X-ray regions at two NSLS-II beamlines. This paper gives an overview of the sXBPM system and presents the first preliminary results from the high-power white X-ray beam.

INTRODUCTION

Non-invasive soft X-ray BPMs (sXBPMs) do not exist yet but are greatly desired for coherent soft X-ray beamlines. We are working to develop such sXBPM for high-power, white X-ray beams. In our approach [1], multi-pixel GaAs detector arrays are placed into the outer portions of X-ray beam, away from the undulator central cone. Beam position, together with other information, is inferred from the pixel photocurrents, see Fig. 1.

Potential advantages of this approach include much higher sensitivity of GaAs compared to metal blades used in conventional photoemission type XBPM designs for hard X-rays [2, 3]. Also, with pixelated detectors, we expect better positional resolution, spatial feature resolution, smaller systematic errors due to undulator gap changes (and phase changes for EPUs), and the ability to discriminate stray light from bending magnets and other sources. The last two are long-standing challenges for the conventional hard X-ray XBPMs (e.g., [4]).

The main challenges with our approach are that the device must have adequate responsivity in soft X-ray; it must withstand high power, potentially leading to elevated diode junction temperature and high pixel photocurrents, and it must reliably operate in UHV.

† boris@bnl.gov

The first goal of our R&D program to investigate this approach includes the design, fabrication, and demonstration of suitable performance of the detector arrays. The second goal is to design, fabricate, and install the sXBPM into the 23-ID FOE, where movable sXBPM detectors intercept the outer portions of white X-ray beam (Fig. 1) from two identical APPLE-II undulators (EPU49, L=2 m each, 2.5 m center-to-center spacing), nominally canted at 0.16 mrad. Each undulator serves as a primary radiation source for one of the two soft X-ray beamlines, CSX or IOS. Our final goal is to demonstrate micron-scale positional resolution of the sXBPM at the sampling rate of 10 Hz or higher for the undulator fundamental harmonic (E_1) tuned in the range of E_1=250-2000 eV covering the operating energy range of the beamlines.

Figure 1 shows the maximum expected power density at the sXBPM location from a single (downstream) undulator tuned to K=3.458 (E_1=250 eV) in linear horizontal polarization. Due to the FOE mask (fixed water-cooled aperture) ~1 m upstream of the sXBPM, the photons outside a ~5x10 mm^2 rectangle (shown in dash) are not accessible for detection. During user operations, the beam from the other undulator, independently tuned in the range of E1=250-2000 eV, is also present. In this (canted) configuration the two beams are displaced horizontally at the sXBPM location by about +/-2 mm with respect to the center of the mask. The photon beam can be further clipped by front-end (FE) slits, located in the ring tunnel ~7 m upstream of the sXBPM.

To install the sXBPM into an operating beamline our design must guarantee no interference with beamline operations under all possible scenarios. Therefore, the detectors are placed on movable blades, which can be completely removed (parked in the FOE mask shade) or positioned to intercept any desired fraction of the beam.
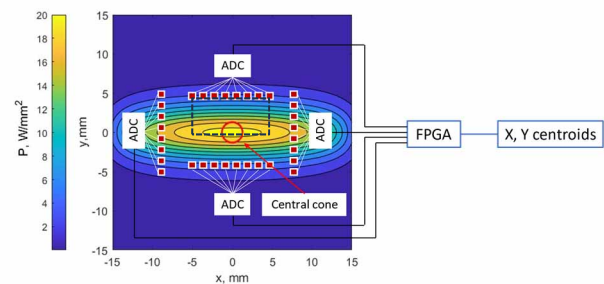
Figure 1: sXBPM concept (detector pixels shown overlaid on the X-ray power density distribution 26 m away from a single EPU in the non-canted configuration).

DETECTOR DEVELOPMENT

Details about detector development, fabrication, and testing can be found in Ref. [5]. Briefly, GaAs was selected due to mature material growth and processing technology, ability to operate at high current densities and elevated temperatures. Wafers were grown by solid-source Molecular Beam Epitaxy for the highest material quality and doping control. For studies, photodiode arrays with up to 64 pixels were fabricated with rectangular pixel sizes from 2x6 to 60x50 μm^2; round pixels were used in later designs (Fig. 2).
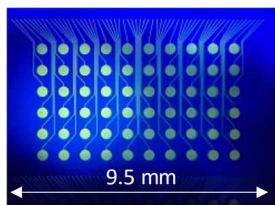
Figure 2: Diode array with contact pads before cleaving.

The sXBPM detectors must have spectral coverage (high responsivity) from ~650 eV to at least 2 keV, as defined by low-K undulator operation, where the intercepted power density is relatively small. At high K, high power is mainly coming from hard X-rays, even for the pixels positioned far away from the beam center (see figures in the accompanying talk). This regime requires low hard X-ray responsivity to maintain manageable photocurrent density levels. Such spectral response of the detector was accomplished by shallow p-n junction design.

The responsivity was measured with a high-power Ar-Ion laser in the visible range, as well as in two NSLS-II beamlines, one soft X-ray (23-ID-1, CSX) and one hard X-ray (4-ID, ISR). The required spectral response was confirmed.

Figure 2 shows one of the fabricated arrays targeted for white-beam installation: 60 mesa photodiodes with a 16-μm mesa diameter isolated by silicon nitride with 8-μm windows for the top metallization connecting the pixels of the linear array to 6 rows of 400-μm diameter contact pads. The distance from the mesa photodiode to the cleaved edge of the array was about 20 μm. The array length of ~1 cm matches the FE mask opening at the sXBPM location. The pixel spacing of 160 μm should allow one to resolve the expected shapes of the X-ray beam. Temporal variation of pixel photocurrents will be used to extract the beam centroid position vs. time.
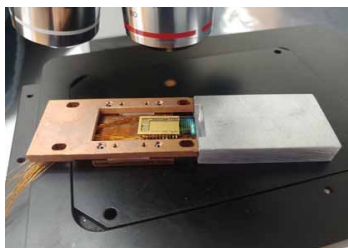
Figure 3: Detector assembly pre-alignment.

Special attention was given to the packaging of the detectors for the UHV operation. To bring the detected signals out-of-vacuum we went with individual Kapton-coated 120 μm diameter copper wires routed to the UHV feedthrough. Our first design assumed direct soldering to the contact pads, which turned out to be challenging due to tight space. We ended up wire-bonding the pixels to gold-plated pads of a ceramic carrier with wire leads (Fig. 3). The next design iteration had a ceramic interposer with two rows of gold-plated pads for wire bonds and three rows of pads for soldering wires.

The detectors operate in the photovoltaic mode (no DC bias) with transimpedance amplifiers for I-V conversion and 24-bit ADC USB5801 modules from Advantech are used for the data acquisition. Time domain multiplexing of the I-V converters is being added for the upcoming installation.

SXBPM DESIGN AND INSTALLATION

Mechanical design details can be found in Ref. [6]. The design had to address several unique challenges, including: 1) micron-level stability of the assembly, 2) management of the heat load from undulator X-ray beams (each EPU can radiate upwards of 3 kW), 3) assembly compactness to fit within the existing FOE, and 4) accessibility for modifications. All installations had to be carefully planned for machine shutdowns to not interfere with the user operations of the two 23-ID beamlines.
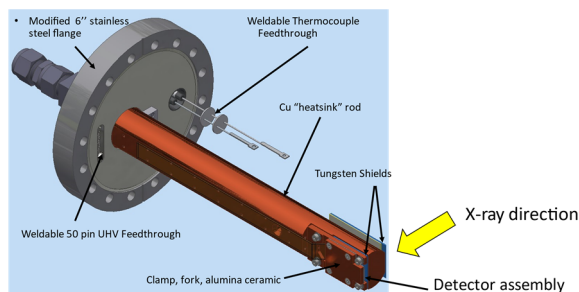
Figure 4: sXBPM blade assembly.

The sXBPM contains up to four water-cooled blade assemblies (Fig. 4), with their flanges mounted on bellows-coupled stepper-motor-driven linear manipulators, so that the blades can be inserted into the X-ray beam with sub-micron accuracy and resolution. Each blade assembly has a GaAs detector array mounted at the tip of the blade and aligned with respect to the tungsten shields upfront, such that only about a 50 μm-high area of the photodiode array is intercepting the X-ray beam. This limits the maximum heat power dissipation in the array itself to about 10 W, which is acceptable according to our thermal modeling.

The sXBPM 6-way cross is mounted on a high-stability Invar stand and is bracketed by two vacuum isolation valves. So far, only the top blade assembly with the detectors was installed and tested. A photo of the sXBPM as installed in 23-ID FOE is shown in Fig. 5.
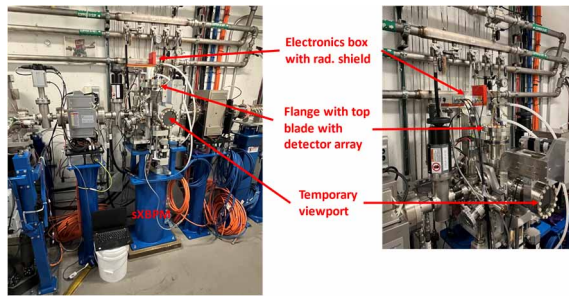
Figure 5: sXBPM installed in 23-ID FOE.

FIRST RESULTS

The top sXBPM blade equipped with a detector array was installed in May 2023. Only 4 array pixels were connected to the data acquisition electronics outside. After the installation, we were limited by the vacuum conditions, so, during user operations, the detector had to be parked in the shade of the FOE mask. However, during low-current machine studies, we were able to bring the detector out of the shade and scan it across the entire X-ray beam while varying the EPU gaps.
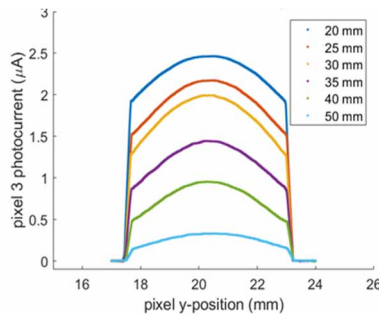
Figure 6: Vertical scans at different EPU2 gaps; I= 2 mA.

Figure 6 shows the photocurrent from one of the pixels recorded during these scans, when the upstream EPU gap was fully open, and the gap of the downstream EPU (EPU2) was varied in the [20-50] mm range, corresponding to the K parameter values of [2.6-0.4]. The 5-mm clipped width of all curves is due to the FOE mask vertical opening. Inside the opening, the signals traced the expected X-ray beam shapes, decreasing in intensity and narrowing with larger ID gaps. Importantly, no noise or parasitic signals were observed when the detector was positioned outside the FOE mask aperture.

Additional tests included closing the vertical FE slits and observing, as expected, further reduction of the intercepted beam height, as well as the observation of diffraction lobes near the projected edges of the slits (see talk).

As the sXBPM vacuum conditioning progressed, during high-current user operations we were able to bring the detector very close to the edge of the projected slits, so that the pixels were partially illuminated with diffracted X-rays. Even in these sub-optimal conditions, the pixel signals were clearly registering top-off injection transients, as well as tracking the EPU gap changes (see talk), which change the X-ray beam shape and intensity at the sXBPM detector location.

During the final days before the August 2023 machine shutdown the improved vacuum conditions have finally allowed us to bring the detector completely out of the shade. During user operations at 500 mA, the pixel signals were reading (depending on the EPU gap settings) up to ~120 µA with fairly low noise. They were changing, as expected, in response to the topoff injections, small orbit motions, EPU gap changes, etc. We are still performing a detailed comparison of the recorded data against the synchrotron radiation modeling which will be presented separately.

Figure 7 shows the signal from one of the pixels while the detector was extracted vertically upwards, in 50 µm steps, from the initial position ~1.4 mm away from the beam center. The signals were recorded at the sampling rate of 6 kS/s, and then each group of 512 samples was averaged, so the plotted sampling rate is ~12 Hz.

The 50-µm steps result in the corresponding step-wise reduction of the signal intensity seen in Fig. 7 as the detector moved vertically away from the X-ray beam center.
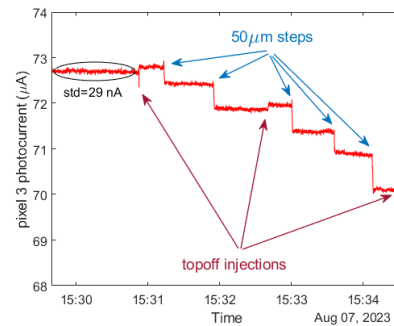
Figure 7: Pixel photocurrent during stepped extraction of the detector; I=500 mA, EPU2 gap at 30 mm.

Between the steps, the signal standard deviation is ~30 nA. Dividing this number by the current steps resulting from stepping the detector, measuring 0.35 to 0.74 µA in Fig. 7, we get that, depending on the detector location, the measured signal standard deviation is equivalent to a pixel rms motion ranging from 2 to 4 microns. These measurements give us a crude upper-bound estimate of the achievable positional resolution of the sXBPM. Based on these results, we are confident in meeting or exceeding our goal of micron-scale sXBPM resolution in the future, when we use symmetrically positioned arrays, multi-pixel X-ray beam position calculation algorithms, and optimized electronics.

CONCLUSION

Our R&D program investigates a novel approach to white-beam XBPMs targeting coherent soft X-ray synchrotron beamlines, where no other viable solutions exist.

To date, the required GaAs detectors have been designed, fabricated, and tested. Their responsivity from sub-keV to a few keV photon energies was accomplished with shallow p-on-n junction design. Detector arrays have been extensively characterized with a high-power Ar-ion laser, and then tested in a monochromatic beam at soft- and hard X-ray beamlines of NSLS-II. The sXBPM prototype with

a single detector array assembly was recently installed in the high-power X-ray white beam from two canted EPUs in the C23-ID straight. The device successfully resolved small beam and detector motions and gap-change-induced variations of X-ray beam shape during 500 mA user operations. To the best of our knowledge, this is the first successful attempt to use multi-pixel semiconductor detectors as diagnostics for high-power white-beam undulator radiation.

Our immediate future steps include the installation of a symmetric top-bottom sXBPM configuration with 25 wired pixels per blade and with optimized electronics. Studies of achievable X-ray beam position resolution and other XBPM performance metrics, as well as the optimization of beam position algorithms tailored to multi-pixel detectors, will follow.

Our longer-term plans include the investigation of sXBPMs with fixed-position detectors or with detectors combined with (adjustable) primary slits. Another promising direction includes analog-to-digital conversion performed in UHV immediately adjacent to the detector followed by a serial communication to the electronics outside, which should significantly reduce the number of signal wires needed to be brought out from the UHV volume. All of these potential upgrades are expected to reduce the cost of the device. Investigating designs tailored for hard X-ray beamlines is also an option.

We believe our innovative approach holds significant promise for enhancing synchrotron beamline and accelerator diagnostics, especially for highly coherent beams in future diffraction-limited light sources.

ACKNOWLEDGEMENTS

REFERENCES

[1] J. Liu *et al.*, "Progress towards soft x-ray beam position monitor development", in *Proc. IPAC'21*, Campinas, Brazil, May 2021, pp. 438-441.
doi:10.18429/JACoW-IPAC2021-MOPAB121

[2] E. D. Johnson and T. Oversluizen, "Compact high flux photon beam position monitor", *Rev. Sci. Instrum.*, vol. 60, no. 7, pp. 1947-1950, 1989. doi:10.1063/1.1140896

[3] D. Shu, B. Rodricks, J. Barraza, T. Sanchez, and T. M. Kuzay, "The APS X-ray undulator photon beam position monitor and tests at CHESS and NSLS", *Nucl. Instrum. Methods Phys. Res., Sect. A*, vol. 319, nos. 1-3, pp. 56–62, 1992.
doi:10.1016/0168-9002(92)90531-8

[4] G. Decker and O. Singh, "Method for reducing x-ray background signals from insertion device x-ray beam position monitors", *Phys. Rev. Accel. Beams*, vol. 2, no. 11, p. 112801, 1999.
doi:10.1103/PhysRevSTAB.2.112801

[5] D. Donetski *et al.*, "High power density soft x-ray GaA photodiodes with tailored spectral response", *Semicond. Sci. Technol.*, vol. 37, p. 085024, 2022.
doi:10.1088/1361-6641/ac7c88

[6] C. Eng, D. Donetski, J. Liu, S. Hulbert, C. Mazzoli, and B. Podobedov, "Mechanical design of a soft x-ray beam position monitor for the coherent soft x-ray scattering beamline", in *Proc. MEDSI'20,* Chicago, USA, Jul. 2021, pp. 56-58. doi:10.18429/JACoW-MEDSI2020-MOPC01

RADIATION PROTECTION ISSUES IN UNDULATOR UPGRADES FOR THE EUROPEAN XFEL*

A. Potter[†,1], A. Wolski[1], Department of Physics, University of Liverpool, Liverpool, UK

S. Liu, W. Decking, A. Leuschner

Deutsches Elektronen-Synchrotron - DESY, Hamburg, Germany

S. Casalbuoni, S. Karabekyan, H. Sinn, F. Wolff-Fabris

European XFEL GmbH, Schenefeld, Germany

F. Jackson[1], ASTeC, STFC Daresbury Laboratory, Daresbury, Warrington, UK

[1]also at the Cockcroft Institute, Daresbury, Warrington, UK

Abstract

European XFEL is the first free electron laser operating at MHz repetition rate with electron beam energy up to 17.5 GeV. The high repetition rate together with the high electron beam energy provides unique opportunities for users in different domains. To further extend the operation schemes, some upgrades have already been implemented and several more are planned. The advanced operation schemes may require devices inserted into the beam (e.g. slotted foil) or narrow vacuum chambers (e.g. corrugated structure, Apple-X undulator, superconducting undulator), and due to the high beam power, there are concerns about increased radiation loads. Therefore, simulations and measurements have been carried out to study the radiation dose rates that may be generated. We give an overview of the simulations and measurements for the case of the Apple-X undulators, and briefly consider the implications for other schemes.

INTRODUCTION

The SASE3 beamline [1] at the European XFEL (EuXFEL) delivers FEL beam in the photon energy range 0.25–3 keV. Photon pulses are generated by an electron beam with energy up to 17.5 GeV in a planar undulator, consisting of 21 modules each of length 5 m. To allow control of the polarisation of the X-ray beam, during the winter 2021/22 shutdown an Apple-X undulator (consisting of four modules each of length 1.98 m) was installed in the beamline following the planar undulator [2]. First lasing with the Apple-X undulator in place was achieved in early April 2022 [3]. However, after a short period of operation, faults began to occur with the linear and rotary encoders and cam movers used in the control of the magnet arrays in the Apple-X undulator. It was suspected that the damage was caused by spontaneous synchrotron radiation from the SASE3 planar undulator, and to prevent further damage the Apple-X undulators were removed in the summer shutdown 2022, and the new (narrower aperture) vacuum chamber in the Apple-X section was replaced by the original vacuum chamber. Simulation and experimental studies were begun to understand the cause of the radiation damage, and to plan potential mitigations to

allow reinstallation of the Apple-X: in this paper, we summarise the studies and outline the results. Other upgrades of EuXFEL, planned or in progress, also raise concerns regarding the effects of increased radiation loads on components in the machine, and we conclude this paper by considering briefly the lessons and implications of the Apple-X studies for these upgrades.

SYNCHROTRON RADIATION MODEL

The study reported here aimed to develop an understanding, through simulations and measurements, of the radiation loads on the Apple-X undulators in EuXFEL (in particular, the loads on the damaged encoders) arising from spontaneous synchrotron radiation from the SASE3 planar undulator. Note that it is assumed that FEL radiation from the undulator can be cleanly extracted along the beamline, and is therefore not included in this study: where we refer to synchrotron radiation in the present paper, it should be understood that (unless stated otherwise) the term refers only to spontaneous radiation. Following construction of a radiation model, the simulations can be developed to investigate possibilities for additional protection, allowing to reinstall the Apple-X undulators. As a first step, a model for the distribution of synchrotron radiation photons was constructed: this distribution was then tracked through a model of the machine (including detailed representations of relevant apertures and components) to the Apple-X undulators using a suitable simulation code, which can be used to estimate the radiation dose rates. We used analytical formulae verified with SPECTRA [4] for generating the photon distribution, and BDSIM [5] for the tracking simulations and radiation dose rate calculations.

For tracking photons in BDSIM, the initial distribution (at the mid-point of an undulator module) is modelled as a set of macroparticles over a 200×200 uniform grid of points in the transverse angular space, up to 0.5 mrad. The initial transverse spatial coordinates were assumed to be negligible, since the beam size towards the end of the undulator is dominated by the initial divergence. The electron beam emittance and energy spread are also neglected. Each macroparticle contains a number of photons with a range of energies: the number density and energy spectrum were calculated analytically as a function of angle using standard

---

Table 1: Parameters used to calculate the spontaneous radiation photon distribution in a SASE3 undulator module.

Parameter	Value
Electron beam energy	14 GeV
Bunch charge	250 pC
Average beam current	250 pA
Undulator period	68 mm
Number of periods per module	73
Undulator parameter, K	8.2

Figure 1: Dose rates in the copper absorbers (black), the planar undulators (red) and the Apple-X undulators (blue).

formulae (see, for example, Ref. [6]), and the results of the calculations were confirmed by comparison with simulations in SPECTRA. Relevant parameters are shown in Table 1. Note that constraints on machine operation (in particular, from simultaneous operation of hard and soft X-ray beam lines [1]) mean that the undulator parameter for SASE3 under normal operating conditions is relatively large, with the consequence that a large number of harmonics of the fundamental radiation frequency, extending to high photon energy, need to be included in the tracking. The electron beam current is an arbitrary parameter, since it is assumed that the radiation dose rates from simulation can simply be scaled to the actual beam current in machine operation.

RADIATION DOSE RATE SIMULATIONS

Having calculated the initial photon distribution in each module of the planar undulator, the distributions are tracked using BDSIM: this code provides a convenient tool for this purpose, since it also allows (through integration with GEANT4) modelling of the photon interactions with machine components. For the simulations, the machine model includes accurate representations of the vacuum chamber geometry and the photon absorbers designed to limit the synchrotron radiation impacting critical components such as the undulators. Photon absorbers, constructed of copper, are located after each module of the planar and Apple-X undulators. Simulations were performed under a variety of machine conditions: first, corresponding to the machine with the Apple-X undulator installed, to estimate the dose rates at key locations, and to allow comparison with dose rates monitored under standard machine operation; and second, with conditions corresponding to those used for more detailed dose rate measurements, performed following removal of the Apple-X undulators, and designed to provide data for validating the simulations.

Dose rates calculated using BDSIM with the Apple-X undulator installed are shown in Fig. 1. The results show dose rates building up along the initial section of the planar undulator, as expected from the divergence of the synchrotron radiation: the photons generated in an undulator module travel some tens of metres before photons reach the edge of the aperture in a photon absorber. Eventually, a balance is reached between the generation of new photons in successive undulator modules, and photons stopped by
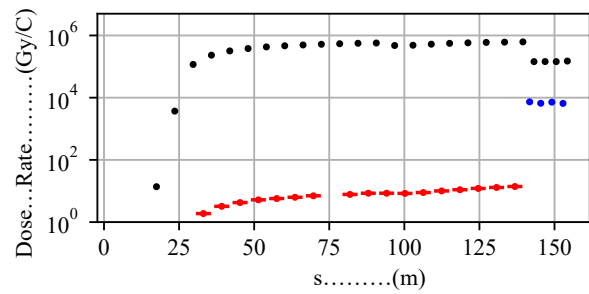
the absorbers. Significantly, the radiation dose rates in the Apple-X are larger by more than two orders of magnitude than the dose rates along the planar undulator: detailed inspection of results from photon tracking shows that this is due to the narrowing of the vacuum chamber aperture in the Apple-X, particularly in the horizontal dimension. The chamber in the planar undulator is elliptical to allow for efficient transport of synchrotron radiation (with a wide horizontal divergence) to the photon absorbers, but because of the geometry of the Apple-X devices, the chamber in these undulators is circular, with a narrow aperture.

The simulation model was used to investigate the effects of machine imperfections, including steering errors on the electron beam and alignment errors on the vacuum chamber and other components. The results suggested that under realistic assumptions for the scale of the errors, the effects of steering and alignment errors on the dose rates will be relatively small. The high dose rates observed in the Apple-X undulators come mainly from aperture limitations.

DOSE RATE MEASUREMENTS

In the winter shutdown 2022/23, after the Apple-X modules had been removed, the smaller vacuum chamber for the first Apple-X module was reinstalled to allow investigation of the radiation loads with the reduced aperture. Radiation dose rate measurements along the planar undulator and at the intended location of the Apple-X were made using MARWIN, a robot that can be driven along the accelerator tunnel (approximately 2 m from the beamline). MARWIN is equipped with a detector (LB6419) capable of measuring neutron and gamma radiation [7, 8]. To allow comparison with MARWIN data, iron blocks (width 0.1 m, height 0.5 m and length 1 m) were placed in the simulation along the beamline, 2 m from the beam: the dose rate in each block from synchrotron radiation (taking into account interaction with the vacuum chamber and photon stops) was calculated in BDSIM. Figure 2 shows a comparison between simulated and measured dose rates. The different colour lines show the dose rates with different sections of the planar undulator closed: the results from these measurements provide information on the contribution of different undulator sections to the radiation dose rates at the Apple-X.
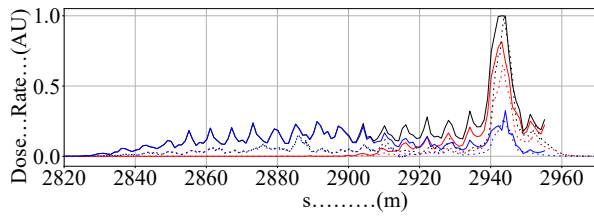
Figure 2: Normalised radiation dose rates simulations (solid) and measurements (dashed) for first 11 cells closed (blue), last 10 cells closed (red) and all cells closed (black).

The radiation dose rates along the beamline from the simulations are in good agreement with the MARWIN measurements. Good agreement is also found in comparing simulations with measurements made using fixed RADFETs [9], of dose rates at different points along the undulator beamline. Finally, simulations of the dose rates at the Apple-X location resulting from individual modules of the planar undulator are also in good agreement with measurements. Overall, the results provide confidence in the simulations as a means of developing a detailed understanding of the origins of the radiation loads on the Apple-X, and as a tool for investigating possible ways of enhancing the protection of the Apple-X undulators to prevent radiation damage.

MACHINE PROTECTION OPTIONS

Protecting the Apple-X from radiation resulting from photons generated in the planar undulator is a challenging problem for several reasons. First, constraints on the geometry limit options that would otherwise be attractive, such as increasing the vacuum chamber aperture in the Apple-X modules. Second, the high electron beam energy results in the production of a significant flux of high-energy (of order 1 MeV) photons from the planar undulator: such photons are highly penetrating, and difficult to stop using photon absorbers. Detailed inspection of simulations show that a significant contribution to dose rates on the Apple-X encoders comes from photons back-scattered from absorbers at the end of each module. Finally, the penetrating nature of high-energy photons also makes it difficult effectively to shield sensitive components.

Ideally, the radiation loads in the Apple-X should be reduced to levels comparable to those in the planar undulator (which has been operated for a number of years without problems from radiation damage). This would mean reducing the dose rates in the Apple-X by two orders of magnitude. To see whether this might be achieved by modifying the absorbers, simulations were carried out with the absorber aperture reduced (from 9 mm×8 mm elliptical, to 6 mm circular) in just the final two absorbers in the planar undulator and the four absorbers in the Apple-X section. It was found that although the dose rates in the Apple-X RADFETs and encoders were indeed reduced, the reduction was only about a factor of two, far short of the two orders of magnitude required. One possible reason for this is that photons back-scattered from the absorbers contribute to the radiation loads

on these components: reducing the aperture therefore has limited impact, and can even (under some conditions) make the situation worse.

To try to improve on the benefit from the aperture reduction in the absorbers, two further absorber modifications were investigated in simulation: first, increasing the narrow-aperture section length from 3 mm to 9 mm; and second, changing the material from copper to tungsten. As an additional option, the effect of lead shielding around the RADFETs and encoders was investigated. Results (shown in Table 2) suggest that some combination of changes (including shielding of sensitive components) would likely be needed to reduce the dose rates to safe levels.

Based on the simulation results, new absorbers (6 mm aperture and 15 mm length) were installed in the final two cells of the planar undulator, together with new, narrow-aperture quadrupole vacuum chambers (copper, 6 mm aperture, 150 mm length). Lead shielding (between 3 mm and 6 mm thickness) has also been added to the absorbers, to increase their effectiveness. Preliminary measurements (using MARWIN) show a reduction in dose rates by an order of magnitude in the region of the Apple-X undulators; results from detailed studies will be reported in due course, and will be used in planning the re-installation of the Apple-X undulators.

Table 2: Effect of modified photon absorbers on Apple-X radiation dose rates. The absorber aperture is 6 mm in all cases. Dose rates are expressed as a fraction of the rates with the current absorbers.

Absorber type/length	Shielding	Dose in first RADFET	Mean dose in encoders
Cu / 3 mm	No	0.726	0.680
Cu / 9 mm	No	0.262	0.565
Cu / 3 mm	Yes	0.170	0.629
W / 3 mm	No	0.031	0.071

IMPLICATIONS FOR OTHER UPGRADES

The tools and techniques used for the Apple-X studies build on and will support studies for other upgrades for Eu-XFEL that are planned or proposed. The experimental work to validate the simulations and the improved understanding of radiation issues generally will be of significant value. Simulations of radiation effects have already been reported for the slotted-foil scheme for generating short (femtosecond-scale) X-ray pulses [10]. Work is also in progress on a superconducting undulator to be installed after the current SASE2 undulator [11, 12]. In preparation for this upgrade, a test absorber with 4 mm aperture was installed downstream of the last modules in the present SASE2 undulator in the winter shutdown 2022/2023. Tests with electron beam were successful. Radiation sensitive detectors have been placed downstream and radiation effects on nearby devices are under investigation. Initial results show low radiation levels.

ACKNOWLEDGEMENTS

REFERENCES

[1] S. Liu *et al.*, "Parallel operation of SASE1 and SASE3 at the European XFEL", in *Proc. FEL'19*, Hamburg, Germany, Aug. 2019, pp. 25–28. doi:10.18429/JACoW-FEL2019-TUA01

[2] S. K. Karabekyan *et al.*, "SASE3 variable polarization project at the European XFEL", in *Proc. IPAC'21*, Campinas, Brazil, May 2021, pp. 1678–1680.
doi:10.18429/JACoW-IPAC2021-TUPAB122

[3] S. Karabekyan *et al.*, "The Status of the SASE3 variable polarization project at the European XFEL", in *Proc. IPAC'22*, Bangkok, Thailand, Jun. 2022, pp. 1029–1032.
doi:10.18429/JACoW-IPAC2022-TUPOPT014

[4] T. Tanaka, "Major upgrade of the synchrotron radiation code SPECTRA", *J. Synchrotron Radiat.*, vol. 28, pp. 1267–1272, 2021. doi:10.1107/S1600577521004100

[5] L.J. Nevay *et al.*, "BDSIM: An accelerator tracking code with particle–matter interactions", *Comput. Phys. Commun.*, vol. 252, p. 107200, 2020.
doi:10.1016/j.cpc.2020.107200

[6] A. Hofmann, *The Physics of Synchrotron Radiation*. Cambridge University Press, 2004.
doi:10.1017/CBO9780511534973

[7] A. Dehne, N. Möller, and T. Hermes, "MARWIN: Localization of an inspection robot in a radiation-exposed environment", *Adv. Sci., Technol. Eng. Sys.*, vol. 3, no. 4, 2018.
doi:10.25046/aj030436

[8] A. Klett, A. Leuschner, N. Tesch, "A dose meter for pulsed neutron fields", *Radiat. Meas.*, vol. 45, no. 10, pp. 1242-1244, 2010. doi:10.1016/j.radmeas.2010.06.008.

[9] F. Schmidt-Foehre, L. Froehlich, D. Noelle, R. Susen, and K. Wittenburg, "Commissioning of the new online-radiation-monitoring-Ssstem at the new european XFEL injector with first tests of the high-sensitivity-mode for intra-tunnel rack surveillance", in *Proc. IBIC'15*, Melbourne, Australia, Sep. 2015, pp. 585–589.
doi:10.18429/JACoW-IBIC2015-WECLA02

[10] A. Potter, B. Beutner, J. Branlard, A. Dehne, F. Jackson, S. Liu, N.J. Walker, A. Wolski, "Investigation of the beam losses and radiation loads for the implementation of a slotted foil at the European XFEL", in *Proc. FEL'22*, Trieste, Italy, Aug. 2022, pp. 2737–2740.
doi:10.18429/JACoW-FEL2022-WEP16

[11] S. Casalbuoni *et al.*, "European XFEL undulators - status and plans", in *Proc. IPAC'22*, Bangkok, Thailand, Jun. 2022, pp. 2737–2740.
doi:10.18429/JACoW-IPAC2022-THPOPT061

[12] S. Casalbuoni *et al.*, "Superconducting undulator activities at the European X-ray Free-Electron Laser Facility", *Frontiers in Physics* 11, 2023. doi:10.3389/fphy.2023.1204073

HOW CAN MACHINE LEARNING HELP FUTURE LIGHT SOURCES?

A. Santamaria Garcia*, C. Xu, L. Scomparin, E. Bründermann, M. Caselle, G. De Carne,
A.-S. Müller, Karlsruhe Institute of Technology (KIT), Karlsruhe, Germany

Abstract

Machine learning (ML) is one of the key technologies that can considerably extend and advance the capabilities of particle accelerators and needs to be included in their future design. Future light sources aim to reach unprecedented beam brightness and radiation coherence, which require challenging beam sizes and accelerating gradients. The sensitive designs and complex operation modes that arise from such demands will impact the beam availability and flexibility for the users, and can render future accelerators inefficient. ML brings a paradigm shift that can re-define how accelerators are operated. In this contribution we introduce the vision of ML-driven facilities for future accelerators, address some challenges of future light sources, and show an example of how such methods can be used to control beam instabilities.

INTRODUCTION

Frontier Accelerators

Both the photon science and high energy physics research communities generally aim at increasing the performance of accelerators, reduce their cost, and make them more power efficient. These goals are even more relevant for frontier particle accelerators, driven by ambitious research programs that require demanding beam parameters, often outpacing the progress of traditional accelerator technologies [1–3]. The current cost of frontier accelerators is estimated at more than 1 billion dollars, where larger facilities can cost up to 10 times more [4]. This cost is directly related to the technology these accelerators are based on, and can be reduced with advancements in such technology. Given the size, cost, and technological advancements required, frontier accelerators are one of the most challenging scientific endeavors.

The Potential of Machine Learning for Particle Accelerators

The potential of ML methods in accelerators was already identified back in 2018 [5], and their popularity has been rapidly increasing since then, as shown in Fig. 1.

This is due not only to the general rise in popularity of artificial intelligence (AI), but thanks to the continuous development of easily accessible ML software libraries and recent advances of ML methods, applied to a variety of fields. While interesting improvements have already been observed in existing accelerator facilities, particularly in tuning and optimization tasks [6, 7], a promising avenue for ML methods in accelerators is their potential to help overcome the challenges of frontier accelerators [8], which could become a liability in their development if unaddressed (e.g., technical impossibilities, insufficient beam availability, inefficient

---

* andrea.santamaria@kit.edu
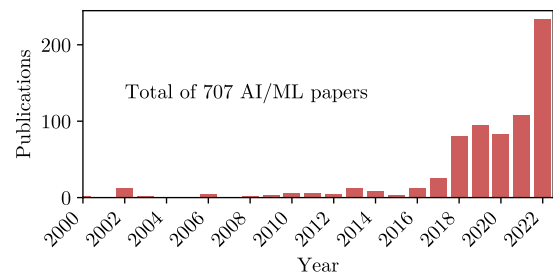
Figure 1: Number of publications with the words "machine learning" or "artificial intelligence" in the abstract, scraped from the JACoW database.

design). Some of the challenges that can be approached with ML are listed in Fig. 2, for different frontier accelerator design trends.
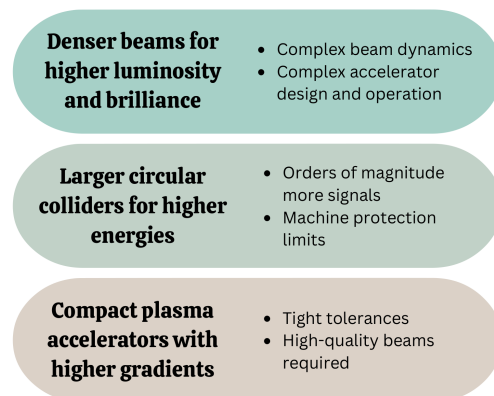
Figure 2: Some trends and related challenges of frontier accelerators.

ML methods can yield fast predictions at a reduced computational cost compared to analytical or classical numerical methods, can take into account the non-linear correlations in the data, and can adapt the predictions to the drifts in the machine state. These capabilities are highly desirable in accelerators since they open the door to a very robust and tailored online detection, prediction, optimization, and control. They can also help design future accelerators by alleviating the computational cost of numerical simulations and guiding the search for optimal parameters in a high-dimensional parameter space. Table 1 summarizes some applications of ML in current accelerators, split by the type of task. There are also numerous applications in particle physics that are not covered in this publication [9, 10].

Looking ahead into the future we can imagine a completely autonomous accelerator [11] where the operation is user-centric and guided by the changing demands of more complex and maybe ML-driven experiments. Such an accelerator would be energy responsible, with an automated

Table 1: Machine learning opportunities in particle accelerators (online and in simulation)

Task	Goal	Methods/Concepts	Examples[1]
Detection	Detect outliers and anomalies in accelerator signals for interlock prediction, data cleaning	• Anomaly detection • Time series forecasting • Clustering	• Collimator alignment • Optics corrections • SRF quench detection
Prediction	Predict the beam properties based on accelerator parameters	• Virtual diagnostics • Surrogate models • Active learning	• Beam energy prediction • Accelerator design • Phase space reconstruction
Optimization	Achieve desired beam properties or states by tuning accelerator parameters	• Numerical optimizers • Bayesian optimization • Genetic algorithm	• Injection efficiency • Radiation intensity
Control	Control the state of the beam in real time in a dynamically changing environment	• Reinforcement learning • Bayesian optimization • Extremum Seeking	• Trajectory steering • Instability control

[1] non-exhaustive

start-up and operation, failure and interlock prediction, virtual diagnostics, and intelligent control of beam dynamics phenomena (see Fig. 3).
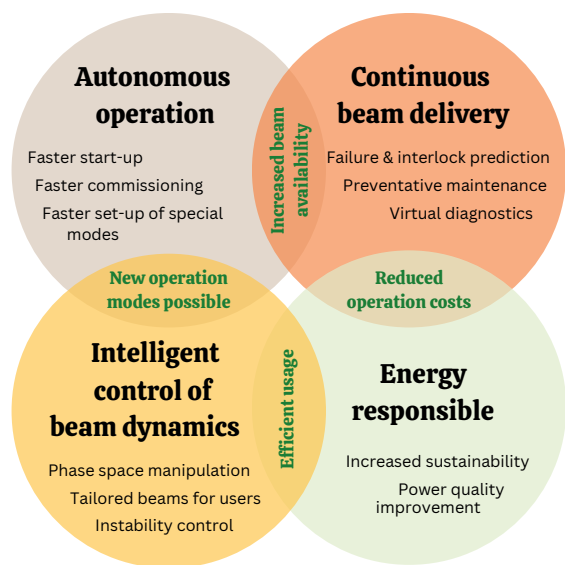
Figure 3: A vision for future accelerators, driven by ML methods.

On the one hand, this automation would increase the beam availability for users due to faster commissioning times, faster set-up of operation modes, interlock prediction, less destructive measurements thanks to virtual diagnostics, and the reduction in the mean time between failures thanks to preventative maintenance. On the other hand, an online targeted phase space manipulation could not only deliver tailored beams and radiation to the users, but also actively mitigate beam instabilities. Paired with the increased speed in accelerator operations, new special operation modes would also be accessible. Swift changes between these operation modes would be possible, with direct feedback from the sample position at a beamline. Finally, the reduction of the

mean time between failures and energy responsibility efforts would reduce the costs of operating an accelerator, making it more reliable and sustainable. More details about energy responsible accelerators are given in the following section.

Energy Responsible Accelerators

From a grid perspective, particle accelerators are electrical loads in the order of hundreds of MWs with stringent requirements on power quality and low flexibility in power demand. The electrical grid is experiencing an increased number of disturbances (faster, more frequent, and more severe) caused by a decreased system inertia and increased variability in the power production (i.e., renewables). In addition, the energy cost steeply increased in many countries due to ongoing geopolitical conflicts. In view of these trends, future accelerators can profit from being more energy-efficient and resilient to external disturbances. Some steps that can be taken in that direction are:

- Inclusion of renewable energy sources combined optimally with energy storage systems to maximize the local energy production over the absorption from the main grid.

- Use of alternative cooling sources, such as geothermal energy, to increase the cooling efficiency and reduce the dependence from the electrical grid.

- Implement flexibility options for accelerator operation, to enable fast load variations in case of emergency: data centers, cooling systems, experiment scheduling based on green power production have great potential to improve flexibility.

- Develop novel devices and systems that are able to decrease the energy usage during accelerator operations: solid state amplifiers, permanent magnets, efficient cryogenic systems, superconducting power supply and distribution.

A joint test field was created at KIT to address the energy efficiency challenge, merging the Karlsruhe Research Accelerator (KARA) and the Energy Lab 2.0, Europe's largest research infrastructure for renewable energy. This joint-lab is called KITTEN (KIT Testfeld für Energieeffizienz und Netzstabilität in großen Forschungsinfrastrukturen) and aims to research energy sustainable and resilient solutions for accelerators to reduce their carbon footprint. In the BMBF project "ACCelerator Energy System Stability - ACCESS" the real-time power consumption data from the accelerator will be fed to a digital twin that can emulate with high fidelity the accelerator power and energy dynamics during power systems studies. This will allow to test energy storage technologies or power electronics solutions in varying testing conditions without affecting the real hardware. In this context, the fast inference of ML methods can be used to provide important real-time insights, identify patterns, analyze trends, and predict control actions to make the accelerators more energy sustainable, efficient, and stable.

MACHINE LEARNING FOR LIGHT SOURCES

Storage Rings

The common desiderata for photon beams produced in 4th generation light sources (4GLS) are high brilliance and flux, coherent radiation, and tunability of wavelength, beam size, polarization, and time structure. Additionally, the beam has to be as stable in energy, intensity, position, and size as possible.

Operating with ultra-low emittances comes with various challenges [12], like for example a reduced lifetime due to an increased Touschek scattering effect. The Touschek scattering can be decreased using round beams, but flat beams have a higher coherence and brightness and are therefore preferred by the users. A multi-objective optimization algorithm can find a compromise between both, optimizing for both lifetime and brightness.

A stable beam size (source size) is also desired, as some experiments are highly sensitive to intensity fluctuations. Insertion device (ID) gap variations induce coherent tune shifts that translate into orbit distortions, caused by their integral field errors. This is usually compensated with local and/or global orbit and linear optics corrections schemes, but non-linear residual field errors persist and can significantly affect the quality of the beam. For example, residual skew quadrupole errors induce vertical beam size variations from undesired coupling, and residual higher-order components reduce the beam lifetime when the tune is near their resonance [13]. In both cases, the quadrupole strengths (skew or straight) can be used to change the optics and correct the betatron coupling or move the betatron tune away from resonances, respectively. ML methods have already been applied to this problem, where for example neural networks (NNs) were trained to predict the orbit distortion at 239 beam position monitors (BPMs) induced by 18 different ID gaps [14] and extremum seeking (ES) was used to tune skew

quadrupoles to minimize the vertical emittance [15]. A more detailed study can be found in Ref. [16], where beam size predictions were done with NNs and used as a feed-forward to stabilize the beam size. It was found that the levels of stability achieved were roughly one order of magnitude better than previously observed using model-based schemes, fulfilling the requirements for future light sources.

Storage rings can provide photons at MHz repetition rates but at a relatively low power. The intensity of the photons can be amplified by increasing the spatial coherence between the emitted waves, in which case the intensity will scale quadratically with the number of electrons at full coherence instead of linearly. This can be achieved by reducing the bunch length to the scale of the emitted wavelength or with the presence of substructures in a longer bunch, like the ones created by the microbunching instability (MBI). The MBI is a longitudinal collective instability that happens above a certain current threshold and is driven by the self-interaction of the bunch with its own wakefield. It results in the formation of substructures that emit bursts of coherent synchrotron radiation (CSR) [17]. These bursts happen at a particular frequency corresponding to the rate of growing and damping of the charge substructures, a periodic phenomenon driven by the non-equilibrium between the driving wake potential and radiation damping, diffusion, and filamentation mechanisms. This is observed as a partially periodic fluctuation of the CSR amplitude in time, and a growing and shrinking effect in longitudinal phase space. This bursting makes the CSR power considerably fluctuate on timescales that are difficult for users to average. Radio-frequency (RF) modulations can be used to stabilize the CSR power [18], but requires a more intelligent control than a simple feedback due to the continuously-evolving charge densities in longitudinal phase space. Studies have been carried out towards the control of the MBI with reinforcement learning (RL), and a summary is presented in the last section of this paper. Achieving control over the longitudinal phase space is particularly relevant for 4GLS, as they are mainly designed for beam brilliance optimization and lack pulse flexibility and variability for spectroscopy and timing experiments. Unprecedented control of pulse length and pulse repetition rate can make very flexible and tailored modes of operation possible. Additionally, such an intelligent feedback system can open the door to the control of other types of instabilities that deteriorate the beam quality and limit the bunch current range for stable operation, which is especially relevant in 4GLS where instabilities are more significant.

Reaching ultra-low emittances require stronger sextupole strengths for chromatic correction, which in turn reduce the dynamic aperture and therefore the transverse acceptance. For accelerators targeting two orders of magnitude reduction in emittance the injection needs to be done on-axis to avoid injection oscillations. Off-axis injection into storage rings with methods such as Bayesian optimization (BO) have already been successfully implemented in light sources [19], and similar or more advanced methods could assist novel injection schemes.

Special modes that are challenging to operate in existing machines can also be assisted by ML, like for example negative momentum compaction factor α_c operation. It is designed to increase the dynamic aperture by reducing the strength of the sextupoles and requires operation at negative chromaticities and α_c to avoid head-tail instabilities [20]. While the lifetime of this operation mode is lower than for positive α_c, it has a considerable bunch shortening effect that could be useful for particular experiments [21].

ML methods can certainly speed-up commissioning campaigns in any type of accelerator [19, 22], and more effort could be invested in developing an all-encompassing commissioning tool that leverages the advantages of ML.

Finally, ML can help in simulation by greatly reducing accelerator design stages and developing new optics. 4GLS have strongly nonlinear lattices where the optimization of the dynamic aperture and momentum acceptance is complex due to the dimensionality of the problem, the sensitive correlation among those parameters, and stringent constraints. Deep learning techniques have been developed to accelerate lattice evaluation for 4GLS [23], which allows a faster convergence to an optimal design. Accelerator design can be further sped-up by active learning, where the surrogate model is built iteratively with simulation points selected by a model that guides the parameter space exploration based on the uncertainty of the model (e.g., [24]).

Linear Accelerators

The existing and future free electron lasers (FELs) aim to reach a higher repetition rate and provide unprecedented precise control over the light pulses, such as sub-femtosecond pulses, higher peak power, flexible spectrum, and tunable polarization [25, 26]. As opposed to a storage ring, which can serve dozens of beamlines simultaneously, an FEL only have a handful of beamlines and requires special modes like multi-beam operation with a switchyard to provide the light to the beamlines simultaneously. Therefore, it is common that an FEL needs to switch operation modes multiple times a day to provide the light tailored to the requirement of user experiments. This necessitates methods and routines that can automate and speed up the process of setting up the accelerator for different operation modes. Various methods have been designed and applied to aid such tuning tasks, including the Nelder-Mead simplex algorithm, ES [27, 28], and robust conjugate direction search (RCDS) [29, 30]. An alternative approach, BO, is able to perform global optimization efficiently. It has been successfully tested at multiple FEL facilities for tasks like optics matching to SASE pulse energy optimization [31–33]. The BO algorithm can also be modified to incorporate correlations of the tuning parameters, safety constraints, and drifting systems, making it applicable to a wide range of daily accelerator tasks. Several software frameworks are developed collaboratively to provide a standardized implementation of the advanced optimization algorithms mentioned above and aid general accelerator tuning tasks [34–36]. Such frameworks simplify the sharing of models and algorithms across different facilities, helping the transition of state-of-the-art ML methods from research projects to operational tools.

Additionally, since FELs are single-pass accelerators and one bunch only radiates at a single beamline, they possess more freedom to modulate and tailor the pulses to the user requirements [37, 38]. With more ML-based tuning tools available for the operation of FLS, it can be expected that the machine operation modes will be dynamically changed, providing pulses according to the user's needs throughout the experiment.

In recent studies, RL proved to be able to solve various beam tuning tasks at simpler setups [39–41], outperforming existing numerical optimization methods. Once trained, the RL policy can also handle system drifts and be used as a continuous controller. With enough redundancy in the system, it can even deal with unexpected scenarios such as magnet power supply failures [42]. For future accelerators, it is foreseeable that RL methods will be deployed as robust controllers for complicated system dynamics, which will be otherwise challenging or not possible using conventional feedback controls.

Another challenge that future FELs face is diagnostic devices. Especially for the case of longitudinal phase space (LPS), existing diagnostics like transverse deflecting cavities are often destructive, lack resolution for ultra-short bunches, and need multi-shot measurements to reconstruct the full phase space information. ML methods, such as NNs, can be trained to provide rapid non-destructive predictions of the LPS [43, 44], which can have higher resolutions compared to the single shot measurements [45, 46]. The virtual diagnostics driven by the ML models can be used in combination with real diagnostics to provide higher-fidelity information on the electron bunch [47]. Future applications of ML-based virtual diagnostics are expected to drastically increase the information that can be obtained during operation to the full 6D phase space of the electron bunch and simultaneous prediction at various points along the accelerator.

The current X-ray free electron lasers (XFELs) are predominantly driven by RF-based accelerating structures, which places them among the largest facilities worldwide. There is active research to construct more compact XFELs by accompanying advanced accelerating schemes. The most promising one is the plasma-based accelerator (PBA), including the laser wakefield accelerator (LWFA) and plasma wakefield accelerator (PWFA) [48, 49]. The FELs impose stringent constraints on the upstream beam parameters like the energy spread and divergence, which remains an issue of PBAs. The acceleration process in plasma depends nonlinearly on a large number of parameters, which are evolving due to the dynamic nature of the plasma. An analytic solution is often not possible or not accurate enough, so online tuning of the input parameters is constantly required in operation. Methods such as genetic algorithms and BO have been successfully applied at LWFAs to improve various aspects of the electron bunch, increasing the bunch charge and the bunch energy, minimizing the energy spread, and reaching a more stable state [50–53]. In addition to online tuning,

67th ICFA Adv. Beam Dyn. Workshop Future Light Sources
ISBN: 978–3–95450–224–0

FLS2023, Luzern, Switzerland
ISSN: 2673–7035

JACoW Publishing
doi:10.18429/JACoW–FLS2023–TH3D3

Bayesian models and active learning can be used to build an accurate data-driven model using either the particle-in-cell (PIC) simulations or the experimental data [54–56]. This allows to identify the underlying correlation between the parameters, extract new knowledge from the physics process, and obtain an optimized set of design parameters trading off different objectives for future operation.

TOWARDS THE CONTROL OF THE MICROBUNCHING INSTABILITY AT KIT

The real-time control of the MBI with RL is actively being researched at the storage ring KARA. Due to the dynamically changing nature of the instability, classical feedback schemes are not able to provide the required level of control. RL is a powerful learning paradigm that is particularly well-suited to tackle control problems in large environments, can learn from experience without the need of a model of the dynamics, and can deal with delayed consequences. RL applications are very promising, but their deployment in accelerators is challenging and has been done only a handful of times. One of the difficulties of training RL agents is that they need numerous interactions with the environment to train, and this is too time-consuming to be done in low repetition rate accelerators. This is why the RL agents are usually pre-trained in simulation, although the transfer to the real accelerator can be problematic when the gap between the simulation and experiment is too large. In our case, the data is generated in the accelerator at a faster rate than in simulation, overcoming one of the main limitations of this method. The goal of this project is to control the radiation emitted by the MBI with RF modulations in order to stabilize and maximize the radiation power. This will be achieved with a control feedback loop, composed of the following elements:

- **CSR detection**: broadband Schottky diode.

- **Pulse digitization**: KAPTURE-2 board, a low-latency and high-throughput sampling system for continuous sampling of ultra-short pulses developed at KIT [57].

- **Data readout**: HighFlex 2, a custom modular readout card (Xilinx ZYNQ family).

- **Low-latency RL inference platform**: Xilinx Versal VCK190 evaluation board, where the KIT-developed KINGFISHER [58] platform allows to more easily train agents on the accelerator.

- **Feedback system**: low-level RF (LLRF) amplitude and phase modulation control, possible every six revolutions.

The KAPTURE-2 board has 8 parallel sampling channels with a sampling rate of 500 MS/s, designed for bunch-by-bunch diagnostics at synchrotron light sources. This high data throughput is handled by the Highflex 2 board, where the analog-to-digital converters (ADCs) samples are labeled with the bunch number information and optional metadata. These data are then sent to the Versal board through a high-speed fiber optic link, where the RL algorithm is implemented. This board combines an FPGA, an ARM processor, and programmable AI-engines, which are interconnected by a high-bandwidth Network-on-a-Chip (NoC) and allow full customization of the data flow. In this feedback system the more computationally heavy operations, namely feature extraction and agent inference, are carried out by the AI Engines, while the ARM processor runs the slow-control and the training algorithms as Petalinux applications. The system is designed as an experience accumulator, where the interaction of the RL agent with the accelerator is stored in the DDR memory. This data can then be used to train the model on several different platforms, ranging from the conventional CPU of a control room computer to a GPU equipped server, or to the ARM processor on a Versal board for cases with a particularly simple model, which would reduce the time needed for data access.

In order to influence the longitudinal beam dynamics the control feedback loop needs to act within a few synchrotron periods, imposing a latency constraint of tens of microseconds. This system was tested at KARA, showing a latency of 2.5 μs for inference [59].

Results

The feasibility of the MBI control with RL was first tested in simulation, with encouranging results [60].

Due to needed hardware and firmware modifications to the LLRF to accept the continuous signal generated by the RL agent, the testing of the feedback loop for MBI control was postponed. However, in order to already test the concept, the feedback loop was adapted to sample a BPM signal and the RL agent was designed to damp transverse oscillations with a stripline kicker, replacing the bunch-by-bunch feedback system. The RL agent was deployed in the Versal board and tested during beamtime without being previously trained. The agent learned purely through interaction with the machine in several episodes of 2048 turns, and was re-trained after every episode on the control room computers. The RL agent performed equally or better than the conventional feedback system, validating the design of the control feedback loop. The results will be summarized for publication.

SUMMARY AND OUTLOOK

ML methods are powerful tools that can improve the performance of existing accelerators and create a new generation of autonomous ones, helping future accelerators become viable and sustainable and changing the way they are operated. As shown in this contribution, ML is already being used by the accelerator community to solve a variety of problems, where an untapped wealth of applications remains to be discovered. More advanced concepts like explainability, robustness, safety, and uncertainty quantification will need to be considered, as well as hardware infrastructure upgrades, to make ML methods become regular tools in accelerators.

ACKNOWLEDGEMENTS

REFERENCES

[1] S. Gourlay *et al.*, *Snowmass'21 accelerator frontier report*, 2022. doi:10.48550/arXiv.2209.14136

[2] CERN Yellow Reports: Monographs, *Cern yellow reports: Monographs, vol. 1 (2022): European strategy for particle physics - accelerator R&D roadmap*, en, 2022. doi:10.23731/CYRM-2022-001

[3] R. W. Assmann *et al.*, *Eupraxia conceptual design report*, 2020. doi:10.1140/epjst/e2020-000127-8

[4] V. Shiltsev, "Particle beams behind physics discoveries," *Physics Today*, vol. 73, no. 4, 2020. doi:10.1063/pt.3.4452

[5] A. Edelen *et al.*, *Opportunities in machine learning for particle accelerators*, 2018. doi:10.48550/arXiv.1811.03172

[6] X. Huang, *Beam-based Correction and Optimization for Accelerators*. doi:10.1201/9780429434358

[7] Z. Geng and S. Simrock, *Intelligent Beam Control in Accelerators*. Springer Nature, 2023.

[8] C. Allaire *et al.*, "Artificial Intelligence for the Electron Ion Collider (AI4EIC)," in *Artificial Intelligence for the Electron Ion Collider*, 2023. doi:10.48550/arXiv.2307.08593

[9] A. Radovic, M. Williams, D. Rousseau, *et al.*, "Machine learning at the energy and intensity frontiers of particle physics," *Nature*, vol. 560, 2018. doi:10.1038/s41586-018-0361-2

[10] M. D. Schwartz, "Modern Machine Learning and Particle Physics," *Harvard Data Science Review*, vol. 3, no. 2, 2021. doi:10.1162/99608f92.beeb1183

[11] A. Eichler *et al.*, "First Steps Toward an Autonomous Accelerator, a Common Project Between DESY and KIT," in *Proc. IPAC'21*, Campinas, Brazil. doi:10.18429/JACoW-IPAC2021-TUPAB298

[12] R. Walker *et al.*, "Summary of Working Group B: Ring-Based Light Sources," in *Proc. FLS'18*, Shanghai, China. doi:10.18429/JACoW-FLS2018-FRA1PL02

[13] A. Papash *et al.*, "High order magnetic field components and non-linear optics at the ANKA storage ring," in *Proc. IPAC'17*, Copenhagen, Denmark, 2017. doi:10.18429/JACoW-IPAC2017-WEPAB011

[14] B. Veglia *et al.*, "Neural networks for ID gap orbit distortion compensation in PETRA III," presented at IPAC'23, Venice, Italy, May 2023, paper WEPA095, to appear in the proceedings.

[15] B. Veglia *et al.*, "Extremum seeking for accelerator optimisation," presented at IPAC'23, Venice, Italy, May 2023, paper MOPA137, to appear in the proceedings.

[16] S. C. Leemann *et al.*, "Demonstration of machine learning-based model-independent stabilization of source properties in synchrotron light sources," *Phys. Rev. Lett.*, vol. 123, p. 194 801, 19 2019. doi:10.1103/PhysRevLett.123.194801

[17] G. Stupakov and S. Heifets, "Beam instability and microbunching due to coherent synchrotron radiation," *Phys. Rev. ST Accel. Beams*, vol. 5, p. 054 402, 5 2002. doi:10.1103/PhysRevSTAB.5.054402

[18] A. Santamaria Garcia *et al.*, "Systematic study of longitudinal excitations to influence the microbunching instability at KARA," presented at IPAC'23, Venice, Italy, May 2023, paper WEPA018, to appear in the proceedings.

[19] C. Xu, T. Boltz, A. Mochihashi, A. Santamaria Garcia, M. Schuh, and A.-S. Müller, "Bayesian optimization of the beam injection process into a storage ring," *Phys. Rev. Accel. Beams*, vol. 26, no. 3, p. 034 601, 2023. doi:10.1103/PhysRevAccelBeams.26.034601

[20] P. Schreiber *et al.*, "Beam dynamics observations at negative momentum compaction factors at KARA," in *Proc. IPAC'22*, Bangkok, Thailand, 2017. doi:10.18429/JACoW-IPAC2022-THPOPT006

[21] P. Schreiber *et al.*, "Effect of negative momentum compaction operation on the current-dependent bunch length," in *Proc. IPAC'21*, Campinas, Brazil. doi:10.18429/JACoW-IPAC2021-WEPAB083

[22] J. Li *et al.*, "Particle swarm optimization algorithm applied in online commissioning at the MLS and BESSY II," in *Proc. IPAC'17*, Copenhagen, Denmark, 2017. doi:10.18429/JACoW-IPAC2017-THPAB008

[23] Y. Lu *et al.*, "Demonstration of machine learning-enhanced multi-objective optimization of ultrahigh-brightness lattices for 4th-generation synchrotron light sources," *Nuclear Instruments and Methods in Physics Research Section A: Accelerators, Spectrometers, Detectors and Associated Equipment*, vol. 1050, p. 168 192, 2023. doi:https://doi.org/10.1016/j.nima.2023.168192

[24] A. Oeftiger, A. Santamaria Garcia, S. Hirländer, and J. B. Lagrange, "Active Deep Learning for Nonlinear Optics Design of a Vertical FFA Accelerator," presented at IPAC'23, Venice, Italy, May 2023, paper MOPA137, to appear in the proceedings.

[25] T. Raubenheimer, W. Decking, L. Giannessi, and H.-S. Kang, "Summary Report: Linac-Based Light Sources," in *Proc. 60th ICFA Advanced Beam Dynamics Workshop (FLS'18), Shanghai, China, 5-9 March 2018*, Shanghai, China, 2018, pp. 199–201. doi:10.18429/JACoW-FLS2018-FRA1PL01

[26] N. Huang, H. Deng, B. Liu, D. Wang, and Z. Zhao, "Features and futures of X-ray free-electron lasers," *The Innovation*, vol. 2, no. 2, p. 100 097, 2021. doi:https://doi.org/10.1016/j.xinn.2021.100097

[27] A. Scheinker *et al.*, "Model-independent tuning for maximizing free electron laser pulse energy," *Physical Review Accelerators and Beams*, vol. 22, 8 2019. doi:10.1103/PhysRevAccelBeams.22.082802

[28] A. Scheinker, A. Edelen, D. Bohler, C. Emma, and A. Lut-man, "Demonstration of model-independent control of the longitudinal phase space of electron beams in the linac-coherent light source with femtosecond resolution," *Physical Review Letters*, vol. 121, p. 044 801, 4 2018. `doi:10.1103/PhysRevLett.121.044801`

[29] X. Huang, J. Corbett, J. Safranek, and J. Wu, "An algo-rithm for online optimization of accelerators," *Nuclear In-struments and Methods in Physics Research Section A: Accel-erators, Spectrometers, Detectors and Associated Equipment*, vol. 726, pp. 77–83, 2013. `doi:10.1016/j.nima.2013.05.046`

[30] Z. Zhang, M. Song, and X. Huang, "Optimization method to compensate accelerator performance drifts," *Physical Review Accelerators and Beams*, vol. 25, p. 122 801, 12 2022. `doi:10.1103/PhysRevAccelBeams.25.122801`

[31] J. Duris *et al.*, "Bayesian optimization of a free-electron laser," *Physical Review Letters*, vol. 124, 12 2020. `doi:10.1103/PhysRevLett.124.124801`

[32] J. Kirschner, M. Mutný, A. Krause, J.C. de Portugal, N. Hiller, and J. Snuverink, "Tuning particle accelerators with safety constraints using Bayesian optimization," *Physi-cal Review Accelerators and Beams*, vol. 25, p. 062 802, 6 2022. `doi:10.1103/PhysRevAccelBeams.25.062802`

[33] C. Xu *et al.*, "Bayesian Optimization for SASE Tuning at the European XFEL," presented at IPAC'23, Venice, Italy, May 2023, paper THPL028, to appear in the proceedings.

[34] I. Agapov, G. Geloni, S. Tomin, and I. Zagorodnov, "Ocelot: A software framework for synchrotron light source and fel studies," *Nuclear Instruments and Methods in Physics Re-search Section A: Accelerators, Spectrometers, Detectors and Associated Equipment*, vol. 768, pp. 151–156, 2014. `doi:10.1016/j.nima.2014.09.057`

[35] Z. Zhang *et al.*, "Badger: The Missing Optimizer in ACR," in *Proc. IPAC'22*, Bangkok, Thailand, 2022, paper TU-POST058, pp. 999–1002. `doi:10.18429/JACoW-IPAC2022-TUPOST058`

[36] R. Roussel *et al.*, "Xopt: A simplified framework for optimiza-tion of accelerator problems using advanced algorithms," pre-sented at IPAC'23, Venice, Italy, May 2023, paper THPL164, to appear in the proceedings.

[37] A. Marinelli *et al.*, "Multicolor operation and spectral con-trol in a gain-modulated x-ray free-electron laser," *Physical Review Letters*, vol. 111, p. 134 801, 13 2013. `doi:10.1103/PHYSREVLETT.111.134801`

[38] J. Duris *et al.*, "Tunable isolated attosecond X-ray pulses with gigawatt peak power from a free-electron laser," *Nature Photonics 2019 14:1*, vol. 14, pp. 30–36, 1 2019. `doi:10.1038/s41566-019-0549-5`

[39] V. Kain *et al.*, "Sample-efficient reinforcement learning for CERN accelerator control," *Physical Review Accelerators and Beams*, vol. 23, p. 124 801, 12 2020. `doi:10.1103/PHYSREVACCELBEAMS.23.124801`

[40] J. Kaiser, O. Stein, and A. Eichler, "Learning-based opti-misation of particle accelerators under partial observability without real-world training," in *Proceedings of the 39th Inter-national Conference on Machine Learning*, vol. 162, 2022, pp. 10 575–10 585. `https://proceedings.mlr.press/v162/kaiser22a.html`

[41] C. Xu *et al.*, "Beam trajectory cocntrol with lattice-agnostic reinforcement learning," in *Proc. IPAC'23*, Venice, Italy, 2023. `doi:10.18429/JACoW-IPAC2023-THPL029`

[42] J. Kaiser *et al.*, *Learning to do or learning while doing: Reinforcement learning and bayesian optimisation for online continuous tuning*, 2023. `doi:10.48550/arXiv.2306.03739`

[43] C. Emma, A. Edelen, M. J. Hogan, B. O'Shea, G. White, and V. Yakimenko, "Machine learning-based longitudinal phase space prediction of particle accelerators," *Physical Review Accelerators and Beams*, vol. 21, 11 2018. `doi:10.1103/PhysRevAccelBeams.21.112802`

[44] A. Hanuka *et al.*, "Accurate and confident prediction of elec-tron beam longitudinal properties using spectral virtual diag-nostics," *Scientific Reports*, vol. 11, p. 2945, 1 2021. `doi:10.1038/s41598-021-82473-0`

[45] J. Zhu, Y. Chen, F. Brinker, W. Decking, S. Tomin, and H. Schlarb, "High-fidelity prediction of megapixel longitu-dinal phase-space images of electron beams using encoder-decoder neural networks," *Physical Review Applied*, vol. 16, p. 024 005, 2 2021. `doi:10.1103/PhysRevApplied.16.024005`

[46] J. Kaiser, "Machine learning for combined scalar and spectral longitudinal phase space reconstruction," in *Proc. IPAC'23*, Venezia, 2023, pp. 4413–4416. `doi:10.18429/jacow-ipac2023-thpl019`

[47] J. Zhu, N. M. Lockmann, M. K. Czwalinna, and H. Schlarb, "Mixed diagnostics for longitudinal properties of electron bunches in a free-electron laser," *Frontiers in Physics*, vol. 10, p. 903 559, 2022. `doi:10.3389/FPHY.2022.903559`

[48] S. Corde *et al.*, "Femtosecond X-rays from laser-plasma ac-celerators," *Rev. Mod. Phys.*, vol. 85, pp. 1–48, 1 2013. `doi:10.1103/RevModPhys.85.1`

[49] W. Wang *et al.*, "Free-electron lasing at 27 nanometres based on a laser wakefield accelerator," *Nature*, vol. 595, pp. 516–520, 7868 2021. `doi:10.1038/s41586-021-03678-x`

[50] Z.-H. He, B. Hou, V. Lebailly, J. Nees, K. Krushelnick, and A. Thomas, "Coherent control of plasma dynamics," *Nature Communications*, vol. 6, p. 7156, 1 2015. `doi:10.1038/ncomms8156`

[51] S. J. D. Dann *et al.*, "Laser wakefield acceleration with ac-tive feedback at 5 hz," *Phys. Rev. Accel. Beams*, vol. 22, p. 041 303, 4 2019. `doi:10.1103/PhysRevAccelBeams.22.041303`

[52] R. J. Shalloo *et al.*, "Automation and control of laser wake-field accelerators using bayesian optimization," *Nature Com-munications*, vol. 11, pp. 1–8, 1 2020. `doi:10.1038/s41467-020-20245-6`

[53] S. Jalas *et al.*, "Bayesian optimization of a laser-plasma ac-celerator," *Physical Review Letters*, vol. 126, 10 2021. `doi:10.1103/PhysRevLett.126.104801`

[54] F. Irshad, S. Karsch, and A. Döpp, "Multi-objective and multi-fidelity Bayesian optimization of laser-plasma acceleration," *Physical Review Research*, vol. 5, p. 013 063, 1 2023. `doi:10.1103/PHYSREVRESEARCH.5.013063`

[55] A. F. Pousa *et al.*, "Bayesian optimization of laser-plasma accelerators assisted by reduced physical models," *Physical Review Accelerators and Beams*, vol. 26, p. 084 601, 8 2023.
doi:10.1103/PhysRevAccelBeams.26.084601

[56] M. Labat *et al.*, "Seeded free-electron laser driven by a compact laser plasma accelerator," *Nature Photonics*, vol. 17, pp. 150–156, 2 2023.
doi:10.1038/s41566-022-01104-w

[57] M. Caselle *et al.*, "KAPTURE-2. A picosecond sampling system for individual THz pulses with high repetition rate," *Journal of Instrumentation*, vol. 12, no. 01, p. C01040, 2017.
doi:10.1088/1748-0221/12/01/C01040

[58] L. Scomparin *et al.*, "KINGFISHER: A Framework for Fast Machine Learning Inference for Autonomous Accelerator Systems," in *Proc. IBIC2022*, Kraków, Poland.
doi:10.18429/JACoW-IBIC2022-MOP42

[59] L. Scomparin *et al.*, "A Low-Latency Feedback System for Electron Beam Control with Reinforcement Learning," presented at IPAC'23, Venice, Italy, May 2023, paper THPL027, to appear in the proceedings.

[60] T. Boltz, "Micro-Bunching Control at Electron Storage Rings with Reinforcement Learning," Ph.D. dissertation, 2021.
doi:10.5445/IR/1000140271

A COMPACT INVERSE COMPTON SCATTERING SOURCE BASED ON X-BAND TECHNOLOGY AND CAVITY-ENHANCED HIGH AVERAGE POWER ULTRAFAST LASERS

A. Latina*, V. Muşat, R. Corsini, L. A. Dyks, E. Granados, A. Grudiev, S. Stapnes,
P. Wang, W. Wuensch, CERN, Geneva, Switzerland
E. Cormier, G. Santarelli, LP2N, Talence, France

Abstract

A high-pulse-current photoinjector followed by a short high-gradient X-band linac and a Fabry-Pérot enhancement cavity are considered as a driver for a compact Inverse Compton Scattering (ICS) source. Using a high-power ultra-short pulse laser operating in burst mode in a Fabry-Pérot enhancement cavity, we show that outcoming photons with a total flux over 1×10^{13} ph/s and energies in the MeV range are achievable. The resulting high-intensity and high-energy photons allow various applications, including cancer therapy, tomography, and nuclear material detection. A preliminary conceptual design of such a compact ICS source and simulations of the expected performance are presented.

INTRODUCTION

In recent years, research and development of normal-conductive X-band accelerator technologies have seen tremendous progress in the context of the next generation of electron-positron linear colliders, where very high gradients are required to achieve the multi-TeV beam energy target for particle physics. The CLIC Study at CERN is the most notable example, where multi-bunch beams and accelerating gradients three to five times greater than those in currently operating linacs have been demonstrated in prototype accelerator structures [1].

During the last years, alongside X-band developments, laser technology has also undergone significant advancements, with high-power lasers becoming more readily available on the market. At the same time, to generate high-intensity photons, Fabry-Pérot enhancement cavities (FPCs) are becoming widely adopted in inverse Compton scattering sources, as reported in [2, 3].

There has been recent consideration for operating FPCs in pulsed (or burst) mode. FPCs operated in burst mode can achieve effective gains 2 to 3 orders of magnitude larger than in continuous mode, which is the commonly used operation mode in storage-ring-based sources. The operation of FPCs in burst mode is particularly well-suited for inverse Compton scattering sources based on X-band linacs as they have a lower repetition rate than storage rings or energy-recovery linacs [4] and allow for multi-bunch acceleration.

This paper presents the conceptual design of an ICS source based on X-band acceleration and external optical cavity enhancement in an optimised FPC operated in burst mode. By accelerating electrons to 240 MeV energy in less than 10 m,

our proposed ICS source could generate gamma photons with energies up to 2 MeV and unprecedented flux and brilliance values. High-quality gamma rays in the MeV energy range can have a wide range of applications in various fields, including material science [5], medicine [6], nuclear physics research [7], homeland security by nuclear resonance fluorescence inspection [8, 9], and nondestructive testing of industrial materials [10]. We named this apparatus HPCI-ICS, which stands for "High Pulse Current Injector driven Inverse Compton Scattering" source.

FACILITY DESCRIPTION

The High-Pulse-Current Injector consists of an S-band photoinjector operating at 3 GHz followed by a high-gradient X-band linac at 12 GHz and a short final focus preparing the beam for the interaction. The main parameters of the facility have been optimised along three axes: (1) ensure high RF power efficiency, (2) maintain beam stability in the linac by reducing the disruptive effects of wakefields, and (3) maximise the photon flux at the IP.

The result is a 12 m long setup that accelerates trains of 1000 electron bunches, each with 100 pC bunch charge, up to 240 MeV with a repetition rate of 100 Hz. These bunches are then collided with a laser beam stored in a burst-mode FPC. Table 1 summarises the main parameters of the facility. A short description of each subsystem is provided in the following sections.

Injector

The S-band photoinjector is similar to that of the CLEAR test facility at CERN [11]. The electrons are released from a photocathode due to the photoelectric effect induced by a UV laser. The single-bunch charge extracted from the cathode is 100 pC. A Cs_2Te cathode was selected due to the small spot size and the limited power required on the laser, thanks to the high quantum efficiency of this semiconductor. The photocathode is located at the centre of the half-cell of a 2.5-cell standing-wave electron gun with a cathode peak gradient of 90 MV/m, immersed in a solenoid field. The total length of the injector is 1.3 m, which accounts for diagnostics and trajectory correctors. Table 2 summarises the main parameters of the injector.

Linac

The X-band linac starts 1.3 m downstream of the cathode and operates at a repetition rate of 100 Hz with an average gradient of 35 MV/m. The linac consists of three X-band

---

* andrea.latina@cern.ch

Table 1: Main Parameters of the Proposed Facility

Electron Beam	Value	Unit
Energy	240	MeV
Single-bunch charge, Q	100	pC
Nb of bunches per train	1000	
Repetition rate, f	100	Hz
Bunch length, σ_t	< 300	µm/c
Bunch spacing	1/3	ns
Normalized transverse emittance, $\epsilon_{x,y}^N$	< 3	mm mrad
Colliding Laser		
Wavelength	515	nm
Pulse energy	10	µJ
Crossing angle	2	°
Outcoming Photons		
Compton edge	2.1	MeV
Total flux, $\mathcal{F}$	2.2×10^{13}	ph/s
Bandwidth (0.5 mrad)	2.0	%
Flux (0.5 mrad)	1.6×10^{12}	ph/s
Average Brilliance, $\mathcal{B}$	4.4×10^{13}	(1)
Peak Brilliance, $\hat{\mathcal{B}}$	3.9×10^{23}	(1)

(1) ph/(s mm^2 mrad^2 0.1%BW)

Table 2: Main Parameters of the HPCI Photoinjector

Parameter	Value	Unit
Gun gradient	90	MV/m
RF pulse length	1.5	µs
Electron energy	6.5	MeV
Norm. transv. emittance	< 4	mm.mrad
Bunch energy spread	0.5	%
Bunch length	1	ps
Total length	1.3	m

Table 3: Main Parameters of the HPCI Linac

Parameter	Value	Unit
Number of modules	3	
Nb of structures per module	4	
Average gradient	35	MV/m
Structure length	0.5	m
Energy gain per module	≈ 80	MeV
Final norm. transv. emittance	< 3	mm.mrad
Final bunch energy spread	0.3	%
Total length	8.3	m

Beam Delivery

A short beam delivery section (BDS), de-magnifying and preparing the beam for the collision, was designed using three quadrupole magnets within a total length of 2.7 m starting from the linac end. Upstream the interaction point (IP), a space $L^\star = 0.6$ m was considered to accommodate the interaction chamber (IC) and some diagnostics. A dipole downstream of the IC, necessary to dump the electrons after the collision, could be used for energy measurement.

The optics of the beam delivery system was determined through a numerical optimisation of the quadrupoles' position and strength, aiming at maximising the simulated flux using a realistic 6D phase space from the linac and a realistic simulation of the ICS process obtained with RF-Track [14]. Compared with a simplistic optimisation solely based on minimising the RMS beam size at the IP, our method brought a factor 2.5 increase in the outcoming photon flux. Table 4 summarises the main parameters of the BDS.

Table 4: Main Parameters of the HPCI Beam Delivery

Parameter	Value	Unit
Number of quadrupoles	3	
Distance to IP, $L^\star$	0.6	m
Beam size at IP, $\sigma_x^\star, \sigma_y^\star$	23, 47	µm
Total length	2.7	m

Fabry-Pérot in Burst Mode

A four-mirror Fabry-Pérot cavity was considered with a bow-tie geometry. An optimisation of the burst mode parameters and the geometry was performed following the procedure presented in [15], where a detailed description of the FPC parameters is given. Burst mode parameters were obtained by maximising the effective energy in the structure, $\mathcal{E}_{tot} = \epsilon_{eff} U$, where ϵ_{eff} is the cavity effective gain, and U is the laser macropulse energy. The cavity roundtrip length of 1 m was set to a sub-harmonic of the laser repetition rate, which matches the electron bunch spacing in the linac. The FPC optimisation showed that an effective energy of 6 J could be achieved using GHz-repetition-rate high-power lasers, such as kW-Flexiburst [16].

modules, each comprising four 0.5 m long structures and powered by an RF unit consisting of one single klystron and a pulse compressor. The RF pulse delivered by each unit allows the acceleration of trains up to 1000 bunches per train, with a bunch spacing of 1/3 ns. The three modules are distributed with spacing 70 cm, each space including a quadrupole doublet, one beam position monitor, and two trajectory correctors.

Building on the experience made in the context of CLIC, the single-bunch charge and the iris aperture of the X-band structures were carefully tuned to optimise the RF efficiency while controlling and limiting the impact of both short- and long-range wakefields using quadrupole focusing, BNS damping, and strong damping of the high-order-modes (HOM), like envisioned for the CLIC main linac accelerating structures [1, 12, 13]. Table 3 summarises the main parameters of the linac.

Table 5: Main Parameters of the HPCI Fabry-Pérot Cavity

Parameter	Value	Unit
Round-trip length	1	m
$2d_1$, $2d_2$, h, R	21.43, 28.54, 1.16, 21.46	cm
N_p, N_0, F	2292, 1298, 1000	
w_{0s}/w_{0t}	8.6/13.4	μm
Effective gain	264	
Effective energy	6	J

Start-to-End Simulation

Beam evolution simulations from the cathode to the inter-action point were performed using RF-track [14], a CERN-developed tracking code that can simulate beam transport under the simultaneous effect of space-charge forces, beam loading, and short- and long-range wakefields. The simu-lation was performed using 1D field maps of the gun, the solenoid, and the linac structures.

The evolution of kinetic energy, normalised transverse emittance, and beam size along the HPCI injector are shown in Fig. 1. As visible, an energy of approximately 240 MeV could be attained in less than 10 m from the cathode.
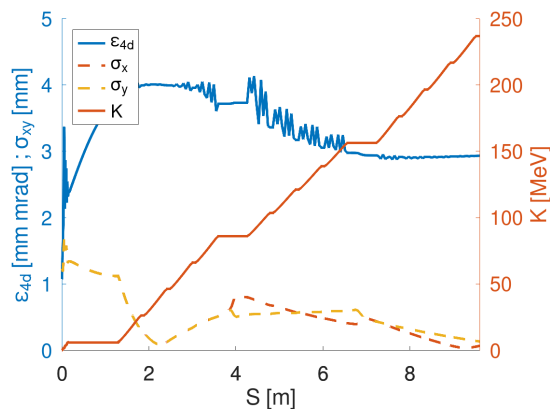
Figure 1: Evolution of the kinetic energy, the normalised transverse emittance, and the beam size along the HPCI facility, from the cathode to the linac end. The total length is 9.6 m.

The decrease of the transverse normalised emittance along the linac is related to an increase in the longitudinal emit-tance (not shown) due to the coupling between transverse and longitudinal planes in the accelerating structures. De-spite the increase in longitudinal emittance, the projected energy spread of the bunch remained below 1%, limiting the chromatic effects in the beam delivery system and still producing ICS photons with a bandwidth under 5%.

Factors such as the amplification of single-bunch jitter due to short-range wakefields and multi-bunch jitter due to HOM in the structures were computed, indicating that the beam is largely unaffected. A value of 1.0034 was obtained for the current set-up.

ICS PHOTON PERFORMANCE

Start-to-end simulations of the setup, including photon generation, were enabled by the recent integration into RF-Track of a module simulating the ICS process directly [17]. A benchmark against the established ICS code CAIN [18] was presented in [19]. The photon performance of the HPCI-ICS source is summarised in Table 1.

The flux of the scattered photons was maximised by op-timising both the electron and laser beamline. The elec-tron gun and linac parameters from Table 2 and Table 3 were tuned to provide a 240 MeV beam with low emittance and low energy spread. The final focusing consisting of a quadrupole triplet was optimised to provide the maximum number of scattered photons per bunch. By maximising the effective energy provided by an FPC with a finesse of 1000, and tuning the FPC's geometry to allow for a high macropulse energy, a total flux of 2.2×10^{13} ph/s was ob-tained. The low electron beam emittance allowed for an equivalently large brilliance.

Since the ICS photon energy depends on the emission angle, the scattered photon beam is typically collimated un-der a collection angle to achieve a small bandwidth. For a 240 MeV electron beam, the photon beam has a natural emission angle of around 2 mrad. To achieve a photon band-width of 2%, the emission angle was reduced to 0.5 mrad, as shown in Fig. 2.
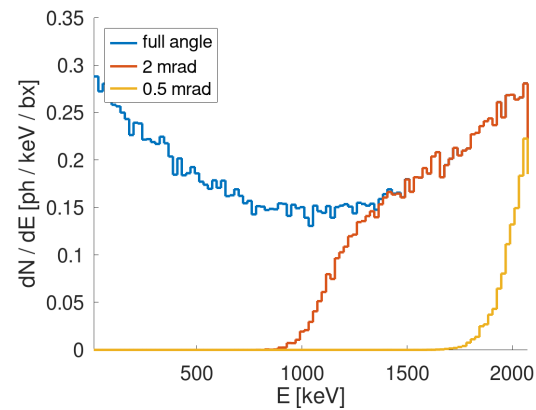
Figure 2: Scattered photon spectra from RF-Track, gener-ated by the HPCI-ICS source. The 0.5 mrad spectrum corre-sponds to an energy bandwidth of 2%.

CONCLUSIONS

This paper presents HPCI-ICS, an advanced conceptual design of a compact ICS source based on an S-band photoin-jector, an X-band linac, a short final focus, and a Fabry-Pérot cavity operating in burst mode, complemented by realistic beam dynamics and Compton scattering simulations. This ICS source has the potential to produce 2 MeV gamma rays with a flux of 2.2×10^{13} ph/s in less than 15 m, setting it among the most compact, high energy, and high flux source in the landscape of existing and designed ICS sources.

REFERENCES

[1] CERN, *CERN Yellow Reports: Monographs, Vol 2 (2018): The Compact Linear e+e- Collider (CLIC) : 2018 Summary Report*, 2018. `doi:10.23731/CYRM-2018-002`

[2] H. Kogelnik and T. Li, "Laser Beams and Resonators", *Applied Optics*, vol. 5, no. 10, 1966. `doi:10.1364/ao.5.001550`

[3] A. Latina *et al.*, "A Compact Inverse Compton Scattering Source Based on X-Band Technology and Cavity-Enhanced High-Average-Power Ultrafast Lasers", in *Proc. LINAC'22*, Liverpool, UK, Aug.-Sep. 2022, pp. 31–34. `doi:10.18429/JACoW-LINAC2022-MOPOJO09`

[4] K. Sakaue *et al.*, "Observation of pulsed x-ray trains produced by laser-electron Compton scatterings", *Review of Scientific Instruments*, vol. 80, no. 12, 2009. `doi:10.1063/1.3272789`

[5] R. W. Schoenlein *et al.*, "Femtosecond x-ray pulses at 0.4 Å generated by 90° Thomson scattering: A tool for probing the structural dynamics of materials", *Science*, vol. 274, no. 5285, 1996. `doi:10.1126/science.274.5285.236`

[6] M. Jacquet, "Potential of compact Compton sources in the medical field", *Physica Medica*, vol. 32, no. 12, pp. 1790–1794, 2016. `doi:10.1016/j.ejmp.2016.11.003`

[7] D. Habs, T. Tajima, J. Schreiber, C. P. Barty, M. Fujiwara, and P. G. Thirolf, "Vision of nuclear physics with photo-nuclear reactions by laser-driven γ beams", *European Physical Journal D*, vol. 55, no. 2, 2009. `doi:10.1140/epjd/e2009-00101-2`

[8] J. Pruet, D. P. McNabb, C. A. Hagmann, F. V. Hartemann, and C. P. Barty, "Detecting clandestine material with nuclear resonance fluorescence", *Journal of Applied Physics*, vol. 99, no. 12, 2006. `doi:10.1063/1.2202005`

[9] H. Lan *et al.*, "Nuclear resonance fluorescence drug inspection", *Scientific Reports*, vol. 11, no. 1, 2021. `doi:10.1038/s41598-020-80079-6`

[10] A. Kostenko *et al.*, "Three-dimensional morphology of cementite in steel studied by X-ray phase-contrast tomography", *Scripta Materialia*, vol. 67, no. 3, 2012. `doi:10.1016/j.scriptamat.2012.04.034`

[11] R. Corsini *et al.*, "First experiments at the CLEAR user facility", in *Proc. IPAC'18)*, Vancouver, BC, Canada, Apr.-May 2018, 2018, pp. 4066–4059. `doi:10.18429/JACoW-IPAC2018-THPMF014`

[12] H. Zha *et al.*, "Beam-based measurements of long-range transverse wakefields in the compact linear collider main-linac accelerating structure", *Phys. Rev. Accel. Beams*, vol. 19, p. 011 001, 1 2016. `doi:10.1103/PhysRevAccelBeams.19.011001`

[13] A. Novohatsky, V. Smirnovn, and V. Balakin, "VLEPP: Transverse beam dynamics", in *Proceedings of the 12th International Conference on High Energy Accelerators. Batavia; Illinois*, 1983, pp. 119–120.

[14] A. Latina, "RF-Track Reference Manual", CERN, Tech. Rep., 2020. `doi:10.5281/zenodo.3887085`

[15] V. Musat, A. Latina, E. Granados, E. Cormier, and G. Santarelli, "An Efficient Optimisation of a Burst Mode-Operated Fabry-Perot Cavity for Inverse Compton Scattering Sources", presented at the 67th ICFA Advanced Beam Dynamics Workshop on Future Light Sources (FLS'23), Lucerne, Switzerland, Aug.-Sep. 2023, paper TU1C1, this conference.

[16] H. Ye, L. Pontagnier, C. Dixneuf, G. Santarelli, and E. Cormier, "Multi-GHz repetition rate, femtosecond deep ultraviolet source in burst mode derived from an electro-optic comb", *Optics Express*, vol. 28, no. 25, 2020. `doi:10.1364/oe.409782`

[17] A. Latina and V. Musat, "An Inverse-Compton Scattering Simulation Module for RF-Track", presented at the 67th ICFA Advanced Beam Dynamics Workshop on Future Light Sources (FLS'23), Lucerne, Switzerland, Aug.-Sep. 2023, paper TU4P33, this conference.

[18] P. Chen, G. Horton-Smith, T. Ohgaki, A. W. Weidemann, and K. Yokoya, "CAIN: Conglomérat d'ABEL et d'Interactions Non-linéaires", *Nuclear Instruments and Methods in Physics Research, Sect. A*, vol. 355, no. 1, 1995. `doi:10.1016/0168-9002(94)01186-9`

[19] V. Mușat, A. Latina, and G. D'Auria, "A High-Energy and High-Intensity Inverse Compton Scattering Source Based on CompactLight Technology", *Photonics*, vol. 9, no. 5, p. 308, 2022. `doi:10.3390/photonics9050308`

RESEARCH ON BUNCH-BY-BUNCH POLARIZATION SWITCH MECHANISMS OF HIGH-REPETITION-RATE X-RAY FELs

Z. F. Gao, T. Liu, Shanghai Advanced Research Institute, Shanghai, China

Abstract

X-ray free electron laser (FEL) is one of the latest generation of high-quality accelerator-based light sources in the world. With the continuous development and improvement of magnetic dichroism, in order to meet the needs of various users, many mainstream X-ray FEL facilities in the world have been equipped with elliptically polarized undulators (EPUs) to realize polarization control. These schemes cannot switch the FEL polarization at a high speed, so it is difficult to meet the needs of high-frequency hard X-ray FEL facilities. This study aims to generate FEL radiation with different polarization states pulse by pulse on the first superconducting hard X-ray FEL facility under construction in China (SHINE), whose repetition rate will be up to 1 MHz. A new scheme is proposed combining a bunch-by-bunch phase shifter and several EPUs. Based on the parameters of FEL-II, the simulation results show that it is possible to produce X-ray pulses with higher than 85% circular polarization under SASE mode.

INTRODUCTION

Nowadays, several XFEL facilities around the world exploit circular polarization by employing Apple-type or Delta undulators as afterburner, such as Linac Coherent Light Source (LCLS), European XFEL, etc. [1, 2]. It's easy to reach as high as over 90% polarization degree for these EPU afterburner, but can hardly switch the polarization state at a high repetition rate, e.g more than 1 kHz. Another way to generate circularly polarized X-ray FEL is proposed by K.-J. Kim by using crossed-planar undulators (CPUs) as shown in Fig. 1 [3, 4]. In this case, the FEL polarization is significantly determined by the phase difference between horizontal and vertical radiation, which contributes to the possibility of fast arbitrary polarization switching. However, the circular polarization degree of the CPU radiation is theoretically limited to under 80% under SASE mode, much lower than EPU afterburner [5].

The scheme is based on the interference of horizontal and vertical radiation from two planar undulators in a crossed configuration. The CPUs serve as the afterburner, and a special bunch-by-bunch phase shifter is designed to change the phase difference rapidly. There will be 4 Apple-type undulators on FEL-II, 2 for horizontal radiation and 2 for vertical radiation, but only part of them will work meanwhile at a certain wavelength so as to reach a higher polarization degree. The phase shifter will be set between the horizontal undulators and vertical ones. It's also possible to make those Apple-type undulators generate left-handed and right-handed radiation, finally obtaining linear polarized radiation with different polarization directions.

BUNCH-BY-BUNCH PHASE SHIFTER

The bunch-by-bunch phase shifter consists of 4 kickers as shown in Fig. 2, with similar structure to normal phase shifters, usually called a chicane. The main parameters of the kickers are shown in Table 1, and the frequency and amplitude are adjustable continuously. It's apparently more difficult for kickers to achieve strong magnetic fields than normal dipoles, so the length of such a phase shifter is also much larger. In order to reduce the possible influence on the bunched electron beam, the whole length is limited under 2.5 m. The kickers operate on the 1 MHz continuous-wave (CW) electron beam, deflecting half of the bunches while allowing the rest of the beams to pass smoothly through the original trajectory. On the one hand, the parameters of the kickers make sure that the path length difference will offer enough phase difference (more than π) during the whole wavelength range. On the other hand, based on the existing conditions, these demands are not too high to be reached.

Table 1: Kicker Parameters

Parameter	Value	Unit
Beam energy	8	GeV
Max frequency	500	kHz
Working mode	bunch by bunch	
Effective length	300	mm
Deflection angle	25 −60	μrad

SASE FEL WITH THE PHASE SHIFTER

SASE starts from electron density shot noise and produces X-ray pulses with spiky temporal and spectrum profile, which leads to poor polarization purity [6, 7]. It can be improved by working under self-seeding mode, HGHG mode, or EEHG mode instead. Up to now, since seeded FEL is still much more complicated and difficult than SASE FEL in terms of high repetition, it's essential to generate FEL pulses with high polarization degree under SASE mode. Slight reverse tapering is used in the scheme to preserve the electron beam micro-bunching. Fewer planar undulators are on work than usual to prevent saturation, thus reducing the impact of phase difference.

As a numerical example, the three-dimensional FEL simulation is conducted by Genesis 1.3 using parameters of SHINE [8]. The main parameters of SHINE are listed in Table 2. The electron beams are chosen to be Gaussian profile and the radiation field file is obtained 100 m downstream of the last EPU.
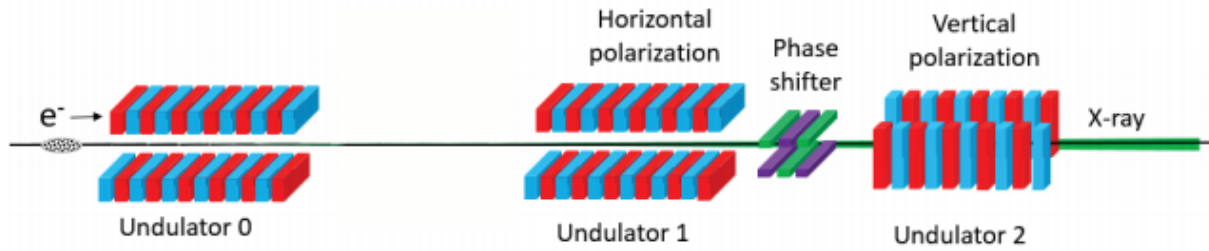
Figure 1: Layout of the scheme with CPU afterburner.
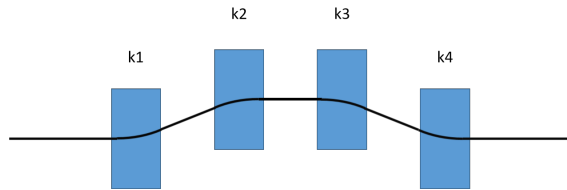
Figure 2: Layout of the bunch-by-bunch phase shifter.

Figure 3: The polarization degree at 1 nm. Blue:total polarization, green:45°/135° linear polarization, red:circular polarization, yellow: 0°/90° linear polarization.

As implied by the Stokes parameters, the vertically polarized laser should be matched to the horizontally polarized one in both intensity and phase in order to increase the polarization degree. So besides light intensity, it's also necessary to make both divergence angles similar. The first two EPUs are used to generate horizontal radiation, while the third EPU serves as the vertical radiation generator at 1 nm. As shown in Fig. 4, the polarization degree can be over 90%, with relatively similar light spots in both directions. The result is close to this when the radiation wavelength is set to 2.4 nm,, with 85% polarization degree. However, '2+1' mode is not suitable for 0.4 nm wavelength due to too large phase and intensity differences between horizontal and vertical radiation, and the polarization degree is under 80% as a result. It can be increased to 89% by adding the 4th EPU as a vertical radiator, as shown in Fig. 5.

Similarly, if the EPUs generate left-handed and right-handed FEL pulses, linearly polarized FEL radiation with almost the same polarization purity will be obtained, whose polarization direction rotates with the change of the phase shifter, just as shown in Fig. 3. The results seem not sensitive to different shot noise, only with a slight difference around 3%. The observation point has little impact on the results either, as long as it's 60-100 m downstream of the last EPU. The total length of the phase shifter determines the drift section between the 2nd and 3rd EPU, thus affecting the bunching factor of the electron beam as well as the beam trajectory in the downstream EPUs. If the length is limited between 2.1 m and 2.7 m, the polarization degree will remain over 80%.

CONCLUSION

In this paper, we propose to generate FEL radiation with different polarization states pulse by pulse, by means of a bunch-by-bunch phase shifter. A set of feasible parameters
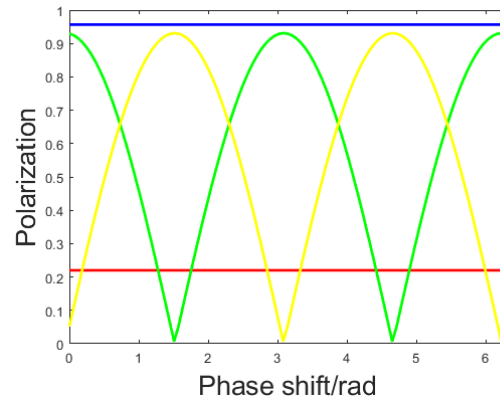
Table 2: SHINE Parameters

Parameter	Value	Unit
Beam energy	8	GeV
Repetition rate	1	MHz
Slice relative energy spread	0.01	%
Normalized emittance	0.45	mm · mrad
Peak current	1.5	kA
Bunch charge	100	pC
Undulator period	0.055	m
Undulator length per section	4	m

for the kickers have been put forward. Then, the parameters of SHINE FEL-II are used in the FEL simulations by means of Genesis 1.3. Based on the scheme of CPU afterburner, a series of simulations have been performed to obtain FEL radiation with polarization degree over 85%, even over 90% under certain circumstances. These simulations are all performed under SASE mode. Furthermore, the influence of different shot noise and observation point has also been evaluated, which makes little sense to the result. All these simulation results indicate that it's possible to realize high-repetition-rate polarization switch on an XFEL facility. The results will be even better under the seeding mode.
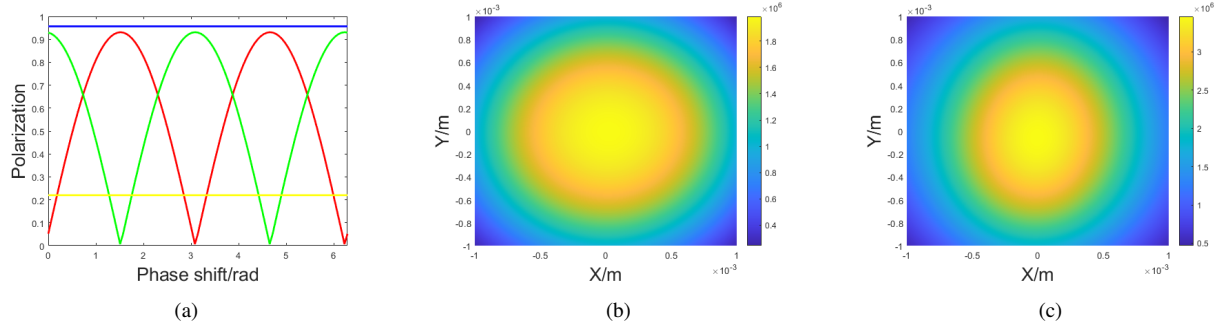
Figure 4: The polarization degree (a) and the radiation spots at 1 nm, (b) for horizontal radiation and (c) for vertical radiation. Blue:total polarization, green:45°/135° linear polarization, red:circular polarization, yellow: 0°/90° linear polarization.
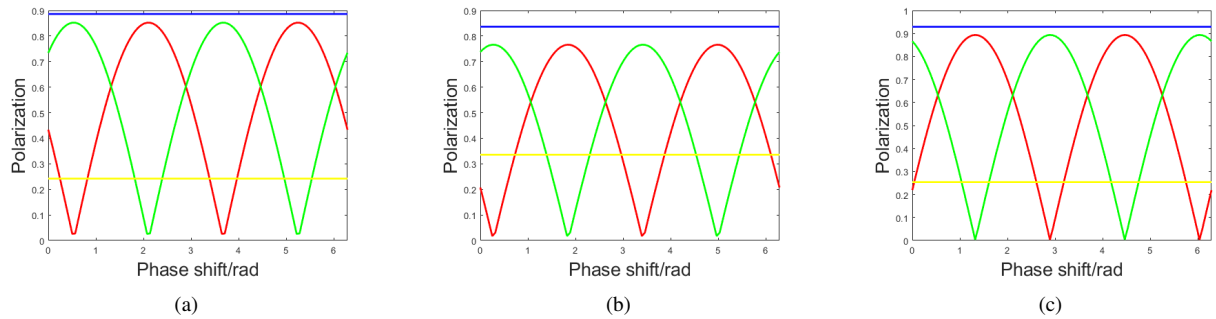
Figure 5: The polarization degree at 2.4 nm (a) and 0.4 nm, (b) for '2+1' mode and (c) for '2+2' mode. Blue:total polarization, green:45°/135° linear polarization, red:circular polarization, yellow: 0°/90° linear polarization.

REFERENCES

[1] A. A. Lutman, J. P. MacArthur, M. Ilchen, A. O. Lindahl, *et al.*, "Polarization control in an X-ray free-electron laser", *Nat. Photonics*, vol. 10, pp. 468–472, 2016. doi:10.1038/nphoton.2016.79

[2] P. Li, T. Wei, Y. Li, and J. Pflueger, "Magnetic design of an Apple-X afterburner for the SASE3 undulator of the European XFEL", *Nucl. Instrum. Methods Phys. Res., Sect. A*, vol. 870, pp. 103–109, 2017. 5 doi:10.1016/j.nima.2017.07.023

[3] K. J. Kim, "Polarization characteristics of synchrotron radiation sources and a new two undulator system", *Nucl. Instrum. Methods Phys. Res.*, vol. 222, nos. 1–2, pp. 11–13, 1984. doi:10.1016/0167-5087(84)90497-6

[4] L. Feng *et al.*, "Single-shot measurement of free-electron laser polarization at SDUV-FEL", *Chin. Phys. C*, vol. 39, no. 2, p. 028101, 2015. doi:10.1088/1674-1137/39/2/028101

[5] Y. Ding and Z. Huang, "Statistical analysis of crossed undulator for polarization control in a self-amplified spontaneous emission free electron laser", *Phys. Rev. Spec. Top. Accel. Beams*, vol. 11, no. 3, p. 030702, 2008. doi:10.1103/PhysRevSTAB.11.030702

[6] A. M. Kondratenko and E. L. Saldin, "Generation of coherent radiation by a relativistic electron beam in an ondulator", *Part. Accel.*, vol. 10, nos. 3–4, pp. 207–216, 1980.

[7] R. Bonifacio, C. Pellegrini, and L. M. Narducci, "Collective instabilities and high-gain regime free electron laser", *Opt. Commun.*, vol. 50, no. 6, pp. 373–378, 1984. doi:10.1016/0030-4018(84)90105-6

[8] S. Reiche, "GENESIS 1.3: a fully 3D time-dependent FEL simulation code", *Nucl. Instrum. Methods Phys. Res., Sect. A*, vol. 429, nos. 1–3, pp. 243–248, 1999. doi:10.1016/S0168-9002(99)00114-X

List of Authors

Bold papercodes indicate primary authors; ~~strike through/black~~ papercodes indicate **no submission received**

— A —

Abeghyan, S.	~~TH1D1~~
Abo-Bakr, M.	TU1B1
Aden, P.	TU4P13
Agapov, I.V.	~~M04B2~~
Aiba, M.	**M04B1**, TU4P26, ~~FR1M2~~
Aicheler, M.	~~WE2A4~~
Aksoy, A.	~~WE2A4~~
Al-Dmour, E.	~~TH4D1~~
Alesini, D.	~~WE2A4~~
Allaria, E.	~~M03A8~~, TU4P16
Andersson, Å.	M02L3
André, T.	TH2C1
Andriyash, I.A.	TH2C1
Angal-Kalinin, D.	TU4P13
Antipov, S.A.	~~M04B2~~
Apel, D.	WE1L4
Apsimon, Ö.	TU4P12
Aquila, A.	~~WE2C1~~
Arefiev, A.V.	~~TU1C3~~
Asaka, T.	TU3D4
Aßmann, R.W.	**M01L1**

— B —

Baader, J.E.	~~TH1D1~~
Bacci, A.	TU4P11
Bacescu, D.M.	TH3B2
Badano, L.	~~M03A8~~
Bahrdt, J.	~~TH3B1~~
Bai, Z.H.	**TU1B4**, WE4P21
Barbanotti, S.	~~TH1D1~~
Bazyl, D.B.	~~FR2M1~~
Benediktovitch, A.I.	~~WE2C1~~
Bengtsson, J.	TU1B1
Bergmann, U.	~~WE2C1~~
Berlioux, A.	TH2C1
Bernhard, A.	TU4P34
Berteaud, P.	TH2C1
Blache, F.	TH1D4, TH2C1
Bock, S.	TH2C1
Boin, M.	**WE1L4**
Borland, M.	~~TU3B4~~
Bostedt, C.	**~~TH2A0~~**
Bouchard, G.J.	~~TH1D3~~
Bouvet, F.	TH2C1
Braun, H.-H.	**FR2M2**
Brinkmann, R.	~~M04B2~~
Briquez, F.	TH2C1
Bründermann, E.	TU4P34, TH3D3
Brunelle, P.	TH1D4
Brynes, A.D.	**TU4P16**
Burrows, P.	TU4P19
Burt, G.	~~WE2A4~~

Byrd, J.M.	**WE1L3**, ~~TH1D3~~

— C —

Cao, J.S.	TU4P27
Carmignani, N.	**TU4P18**, **FR1M2**
Carver, L.R.	TU4P18
Casalbuoni, S.	~~TH1D1~~, TH3D2, ~~FR2M1~~
Caselle, M.	TH3D3
Castañeda Cortés, H.M.	~~WE2A4~~
Chang, Y.Y.	TH2C1
Chao, A.	**M02L2**, ~~TU1B2~~, TU4P28, TU4P29
Chao, H.-C.	**TU4P20**
Chavanne, J.	**M01L4**
Chen, G.	M04C2
Chen, H.B.	~~TH4D2~~
Chen, S.	WE4P14, **TU4P07**, **TU4P08**
Chen, Y.	**M01L3**, ~~TH2A2~~
Cheng, C.M.	WE4P20
Cheng, W.	WE4P36
Cheng, Y.-S.	WE4P19
Chiu, M.-S.	WE4P18, **WE4P19**
Cho, M.H.	**M03A6**
Chou, P.J.	WE4P18
Chung, T.Y.	WE4P20
Cinquegrana, P.	~~M03A8~~
Clarke, J.A.	TU4P13, ~~WE2A4~~, **FR2M1**
Cohen, I.	~~TU1C3~~
Cohen, T.	~~TU1C3~~
Collier, J.L.	TU4P13
Cormier, E.	TU1C1, TH4A2
Corsini, R.	TH4A2
Couprie, M.-E.	TH1D4, **TH2C1**
Croia, M.	~~WE2A4~~
Cudin, I.	~~M03A8~~
Cullinan, F.J.	**M02L3**, ~~FR1M2~~
Curatolo, C.	TU4P11
Czwalinna, M.K.	~~WE3D1~~

— D —

Danailov, M.B.	~~M03A8~~
D'Auria, G.	~~M03A8~~, ~~WE2A4~~
Davut, C.	**TU4P12**
De Carne, G.	TH3D3
De Ninno, G.	~~M03A8~~, **TU2A1**, TU4P16
de Oliveira, C.	TH1D4, TH2C1
Debus, A.D.	TH2C1
Decking, W.	~~TH1D1~~, ~~TH2A1~~, TH3D2
Delerue, N.	TU1C2
Delgiusto, P.	~~M03A8~~
Demidovich, A.A.	~~M03A8~~
Deng, H.X.	TU4P05, TU4P07, TU4P08, WE4P09, WE4P14
Deng, X.J.	~~TU1B2~~, **TU4P28**, **TU4P29**,

	TU4P30, TU4P31
Di Felice, M.	~~TH1D1~~
Di Mitri, S.	**M03A8**, TU4P16, **WE2A4**
Dietrich, Y.	TH2C1
Dijkstal, P.	~~TU2A3~~, ~~TH2A2~~
Ding, Y.	~~WE2A2~~
Diomede, M.	~~WE2A4~~
Donetski, D.	TH3B2
Drebot, I.	**~~M04C3~~**, TU4P11
Du, Y.C.	~~TH4D2~~
Duan, Z.	TU4P27
Dunham, M.	TU2A2
Dunning, D.J.	**TU4P13**, ~~WE2A4~~
Duval, J.P.	TH2C1
Dyks, L.A.	TH4A2

— E —

Eckoldt, H.-J.	~~TH1D1~~
Ego, H.	**TU3D4**
Eisenmann, C.	TH2C1
El Ajjouri, M.	TH2C1
El Khechen, D.	TU4P34
Eng, C.	TH3B2
Englisch, U.	~~TH1D1~~
Eom, I.	~~M03A6~~

— F —

Fedotov, A.V.	WE4P24
Felix, C.P.	WE4P19
Fell, B.D.	TU4P13
Feng, C.	**M03A9**, TU4P08, ~~WE3A4~~, WE4P15, ~~TH4A1~~, TU4P06
Ferran Pousa, Á.	~~M04B2~~
Ferrario, M.	~~WE2A4~~
Fielder, R.T.	**M04B3**, TU4P19
Fisher, A.S.	~~WE2A3~~
Frame, E.A.	M04C2
Fu, X.	TU4P07
Fuerst, J.D.	~~TH1D3~~

— G —

Gaebel, S.	~~TH3B1~~
Gallo, A.	~~WE2A4~~
Gamelin, A.	**M03B2**, M03B3
Gao, Z.F.	WE4P14, **TH4A4**
García-Moreno, F.	WE1L4
Garzella, D.	~~M03A8~~, TU4P16
Gassner, G.L.	~~TH1D3~~
Gautier, J.	TH2C1
Gebhardt, R.	TH2C1
Gehlot, M.	WE4P37, WE4P38
Geloni, G.	~~TU2A3~~, ~~TH1D1~~, ~~TH2A2~~
Genzel, C.	WE1L4
George, A.	WE4P36
Ghaith, A.	TH2C1
Giannessi, L.	~~M03A8~~
Giribono, A.	~~WE2A4~~
Gjonaj, E.	~~TH2A1~~

Gluskin, E.	~~TH1D3~~
Goddet, J.-P.	TH2C1
Gonnella, D.	**~~M03A3~~**, **~~TU3D1~~**
Goryashko, V.A.	~~WE2A4~~
Goslawski, P.	**TU1B1**, WE4P31, ~~TH3D5~~
Gottschlich, S.	~~TH3B1~~
Grabski, M.J.	**TH4D1**
Grams, S.	TH2C1
Granados, E.	TU1C1, TH4A2
Grattoni, V.	~~TH1D1~~
Grau, A.W.	~~TH1D1~~
Graves, W.S.	**TU1C4**
Grech, C.	~~TU2A3~~
Green, J.S.	TU4P13
Green, J.T.	TH2C2
Grimmer, S.	~~TH3B1~~
Grudiev, A.	TH4A2
Gu, D.	WE4P09, WE4P12, **WE4P13**
Gu, Q.	WE4P09
Gu, X.	WE4P24
Gubaidulin, V.	M03B2
Guetg, M.W.	~~TU2A3~~, ~~TH2A1~~, ~~TH2A2~~, ~~FR1M1~~
Guo, J.J.	~~TH2A1~~, **WE4P09**

— H —

Härer, B.	TU4P34
Halavanau, A.	~~TU2A4~~, **~~WE2C1~~**
Hale, S.H.	WE4P36
Hara, T.	~~M03A7~~
Hauberg, A.	~~TH1D1~~
He, D.Y.	TU4P27
He, P.	TU4P27
He, T.L.	WE4P21
Helbig, U.	TH2C1
Hellert, T.	**~~TU3B2~~**
Hemsing, E.	~~TH4A3~~, ~~FR1M1~~
Henderson, J.	TU4P13
Henstridge, M.	**~~WE2A3~~**
Heo, H.	~~M03A6~~
Herbeaux, C.	TH2C1
Hillert, W.	~~WE3A5~~
Hoffmann, M.C.	~~WE2A3~~
Holldack, K.	TU1B1
Hoummi, L.	TU4P18
Hsiao, Y.M.	WE4P20
Hua, J.F.	~~TH2C3~~, ~~TH4A1~~
Huang, N.	WE4P14
Huang, N.Y.	**WE4P18**
Huang, P.W.	~~TH4D2~~
Huang, W.-H.	TU1B2, TU4P28, ~~TH4D2~~
Huang, X.	**~~M03B1~~**
Huang, Y.-C.	**~~M04C1~~**, **~~WE2C2~~**, **~~FR1M3~~**
Huang, Z.	~~TU2A4~~, **~~WE1L2~~**, ~~WE2A3~~, ~~WE3A2~~, ~~TH1D3~~, ~~TH3D4~~, ~~TH4A3~~
Hubert, N.	TH2C1

Hüsges, Z.	TU1B1
Hulbert, S.	TH3B2
Husain, R.	**TU4P19**

— I —

Inagaki, T.	~~MO3A7~~, TU3D4, ~~FR1M1~~
Irman, A.	TH2C1
Ivanyushenkov, Y.	~~TH1D3~~
Iwai, E.	~~MO3A7~~

— J —

Jackson, F.	TH3D2
Jalas, S.	~~MO4B2~~
Jancarek, A.	TH2C2
Jankowiak, A.	TU1B1, ~~FR1M2~~
Jensch, K.	~~TH1D1~~
Ji, D.	TU3B3
Ji, H.F.	TU3B3, TU4P27
Jiang, Z.G.	TU4P05
Jiao, Y.	MO3B4, TU3B3, TU4P27
Jing, C.-J.	MO4C2
Jing, Y.C.	WE4P24

— K —

Kallestrup, J.	**TU4P26**
Kamm, P.H.	WE1L4
Kang, H.-S.	~~MO3A6~~
Kang, W.	TU4P27
Kang, Y.	TU4P06
Karabekyan, S.	TH3D2
Kasa, M.	~~TH1D3~~
Kayran, D.	WE4P24
Kewisch, J.	**WE4P24**
Khan, S.M.	**WE4P37**, **WE4P38**, WE4P39
Khullar, R.	**WE4P39**
Kiefer, K.	TU1B1
Kii, T.	**TH1D2**
Kim, K.-J.	**WE2A1**, ~~TH3B3~~
Kirchen, M.	~~MO4B2~~
Kitégi, C.A.	TH2C1
Klaus, M.	WE1L4
Kocharyan, V.	~~TU2A3~~
Kondo, C.	~~MO3A7~~
Kononenko, O.S.	TH2C1
Kraft, E.M.	~~TH1D3~~
Krasilnikov, M.	~~WE3A5~~
Krejcik, P.	**WE3D2**, ~~TH1D3~~
Krzywiński, J.	~~TU2A4~~
Kucharczyk, K.	TH3B2
Kuhn, C.	~~TH3B1~~
Kujala, N.G.	~~TU2A3~~
Kuntzsch, M.	TH2C1
Kuske, B.C.	TU1B1, **WE4P31**
Kuzikov, S.V.	MO4C2

— L —

La Civita, D.	~~TH1D1~~
Labat, M.	TH2C1
LaBerge, M.	TH2C1

Lam, B.	~~TH1D3~~
Lambert, G.	TH2C1
Latina, A.	TU1C1, **TU4P33**, ~~WE2A4~~, **TH4A2**
Lau, M.	**TU3D2**
Laube, F.	~~TH3B1~~
Le Flanchec, V.	TU1C2
Lê, S.	TH2C1
Lechner, C.	~~TU2A3~~, ~~TH1D1~~, ~~TH2A2~~
Lederer, S.	~~TH1D1~~
Leemann, S.C.	**TU3B1**, ~~FR1M2~~
Leemans, W.P.	~~MO4B2~~
Leluan, B.	TH2C1
Letrun, R.	**WE3A1**
Leuschner, A.	TH3D2
Li, F.	~~TH2C3~~, **TH4A1**
Li, J.	TU4P27
Li, J.Y.	TU3B3, TU4P27
Li, K.	~~TU2A4~~
Li, N.	TU3B3
Li, R.K.	~~TU1B2~~, **TH4D2**
Li, X.	MO3B4, WE4P33
Li, X.D.	TU4P05
Li, Y.	**TU1B3**
Li, Y.S.	**TH3B3**
Li, Z.Z.	~~TU1B2~~, TU4P28
Lilje, L.	~~TH1D1~~
Lindberg, R.R.	~~WE2A1~~, ~~TH3B3~~
Liu, B.	~~MO3A9~~, TU4P07, TU4P08, WE4P14
Liu, G.	WE4P21
Liu, J.	TH3B2
Liu, S.	**TU2A3**, ~~TH1D1~~, ~~TH2A1~~, TH3D2
Liu, T.	TU4P08, WE4P12, **WE4P14**
Liu, W.	**MO3B4**
Liu, X.	MO3B4
Liu, Y.-C.	**WE4P20**
Liu, Z.P.	**TU4P05**
Liuzzo, S.M.	TU4P18
Long, T.	~~MO1L3~~, ~~TU2A3~~
Lou, W.	TU2A2
Loulergue, A.	MO3B2, TU1B4, TH2C1
Lu, W.	~~TH2C3~~, ~~TH4A1~~
Lu, X.	MO4C2
Lu, X.H.	**TU3B3**, TU4P27
Lu, Z.J.	WE4P33
Lucas, T.G.	~~WE3A6~~
Lueangaramwong, A.	MO4B3
Luo, G.-H.	WE4P18, WE4P19
Luo, H.	**WE4P12**
Luo, H.W.	WE4P18
Lutchman, R.	TH3B2

— M —

MacArthur, J.P.	~~TU2A4~~
Maesaka, H.	~~MO3A7~~

Maier, A.R.	M04B2
Mainz, R.	WE1L4
Maity, S.M.	TH2C2
Majernik, N.	WE2C1
Malka, V.	TH2C1
Malygin, A.	TU4P34
Marangos, J.P.	TU4P13
Marchand, P.	M03B2, M03B3
Marchetti, B.	**TH1D1**
Marcouillé, O.	TH1D4, FR2M1
Marcus, G.	TU2A4
Margraf, R.A.	**TU2A4**
Marteau, F.	TH2C1
Martin, I.P.S.	TU4P19, TU4P20
Martinez de la Ossa, A.	**M04B2**
Mary, A.	TH1D4
Marziani, M.V.	WE4P36
Masciovecchio, C.	M03A8
Mathisen, S.L.	TU4P13
Mayes, C.E.	TU2A2
Mazzoli, C.	TH3B2
Meir, T.	**TU1C3**
Meng, C.	TU3B3, **TU4P27**
Meng, M.	WE4P09
Mercado, R.	WE4P36
Meseck, A.	TU1B1, **TH3B1**
Militsyn, B.L.	TU4P13, **TU3D5**, TU4P12
Min, C.-K.	M03A6
Mirian, N.S.	M04C3, TU2A3
Mishra, G.	WE4P37, WE4P38, WE4P39
Mishra, S.	WE4P37
Mo, Y.	WE4P21
Mohanty, S.K.	**WE3A5**
Molodozhentsev, A.Y.	**TH2C2**
Monaco, L.	WE3A5
Mondal, A.	TH2C2
Montironi, M.A.	TH1D3
Morgan, A.F.D.	M04B3
Mostacci, A.	WE2A4
Müller, A.-S.	TU4P34, TH3D3
Müller, R.	TU1B1
Muat, V.	**TU1C1**, TU4P33, TH4A2
Mutin, T.	TH1D4

— N —

Nadji, A.	TH1D4
Nadolski, L.S.	M03B2, TU1B4
Nagaoka, R.	M03B2, TU1B4
Naito, D.	M03B3
Nam, I.H.	M03A6
Nanni, E.A.	**TU3D3**
Nantista, C.D.	TH1D3
Nasse, M.J.	TU4P34
Nelson, C.S.	TH3B2
Nguyen, D.C.	TH1D3, **TU2A2**
Nguyen, F.	WE2A4
Nguyen, M.-H.	TH2C1

Niehues, G.	TU4P34
Niekrasz, S.N.	TH2C2
Nishimori, N.	TU3D4, FR2M1
Nuhn, H.-D.	TH1D3

— O —

Ohshima, T.	TU3D4
Oppelt, A.	WE3A5
Osaka, T.	TU2A4
Osterhoff, J.	M04B2
Oumbarek Espinos, D.	TH2C1

— P —

Pagani, C.	WE3A5
Pan, W.M.	TU4P27
Pan, Z.	**TU1B2**, TU4P28
Papash, A.I.	TU4P34
Park, J.	M03A6
Park, J.-W.	WE2A1
Park, S.H.	M03A6
Patel, Z.	**WE4P36**
Pausch, R.G.	TH2C1
Pellegrini, C.	WE2C1
Penco, G.	M03A8
Peng, Y.M.	TU3B3, TU4P27
Percival, S.S.	TU4P12
Pereira, D.	TH2C1
Perelmutter, L.	TU1C3
Permanyer, X.	TH1D3
Perosa, G.	TU4P16
Perron, T.P.	TU4P18
Petrillo, V.	TU4P11
Pinayev, I.	WE4P24
Piot, P.	**M04C2**, FR1M3
Pires, A.	**TU1C2**
Podobedov, B.	**TH3B2**
Pomerantz, I.	TU1C3
Potet, A.	**TH1D4**
Potter, A.T.	TH1D1, **TH3D2**
Power, J.G.	M04C2
Prat, E.	TH2A3, **FR1M1**
Püschel, T.	TH2C1
Puppin, A.	TU4P11

— Q —

Qi, Z.	TU4P08, WE4P14, **WE4P15**
Qian, H.J.	TU4P05
Qian, M.F.	TH1D3
Qin, W.	TU2A3, **TH2A1**
Qu, H.	TU4P27

— R —

Raimondi, P.	M02L1
Rainer, R.S.	TU1B3
Ramalingam, R.	TH1D1
Ramezani Moghaddam, A.	WE4P36
Rebernik Ribič, P.	M03A8
Reeves, M.	WE4P36
Reiche, S.	WE1L1, TH2A3

List of Authors

Rial, E.C.M.	~~TH3B1~~
Ricaud, J.P.	TH2C1
Robles, R.	~~TU2A4~~
Rochow, R.A.	~~WE2A4~~
Rohringer, N.	~~WE2C1~~
Rommeluère, P.	TH2C1
Roper, M.D.	TU4P13
Roques-Carmes, C.	**~~M01L2~~**
Rosch, R.	TU1C2
Rossetti Conti, M.	TU4P11
Rousseau, J.P.	TH2C1
Roussel, E.	TH2C1
Ruprecht, R.	TU4P34

— S —

Safranek, J.A.	~~M03B1~~
Sajaev, V.	**~~TU3B4~~**
Sakanaka, S.	M03B3
Sakdinawat, A.	~~TU2A4~~
Samsam, S.	TU4P11
Santamaria Garcia, A.	**TH3D3**
Santarelli, G.	TU1C1, TH4A2
Sato, T.	~~TU2A4~~
Sauerborn, M.K.	TU1B1
Schäfer, J.	TU4P34
Scheer, M.	~~TH3B1~~
Scheidt, K.B.	**TU4P17**
Schietinger, T.	**M03A2**
Schlarb, H.	**~~WE3D1~~**
Schlott, V.	**~~WE3D3~~**
Schnautz, T.	~~TH1D1~~
Schneidmiller, E.	~~TH2A2~~
Schnizer, P.	~~TH3D5~~
Schnorr, K.	~~TH2A3~~
Schöbel, S.	TH2C1
Scholz, M.	**~~M03A4~~**
Schramm, U.	TH2C1
Schreiber, S.	M03A5
Schuh, M.	TU4P34
Schulz, S.	~~WE3D1~~
Schwarz, M.	**TU4P34**
Schwarzkopf, O.	TU1B1
Scifo, J.	~~WE2A4~~
Scomparin, L.	TH3D3
Sebdaoui, M.	TH2C1
Seletskiy, S.	WE4P24
Serafini, L.	**TU4P11**
Serkez, S.	~~TU2A3~~, ~~TH1D1~~, ~~TH2A2~~
Sertore, D.	~~WE3A5~~
Shafqat, N.	~~M03A8~~
Shalloo, R.J.	~~M04B2~~
Sharma, G.	WE4P36
Shi, J.R.	~~TH4D2~~
Shim, C.H.	~~M03A6~~
Shiroyanagi, Y.	~~TH1D3~~
Shu, G.	TU4P05
Sigalotti, P.	~~M03A8~~

Sinn, H.	~~TH1D1~~, TH3D2
Smale, N.J.	TU4P34
Smaluk, V.V.	TU1B3
Snedden, E.W.	TU4P13
Song, Z.	~~TH4A1~~
Spataro, B.	~~WE2A4~~
Spezzani, C.	~~M03A8~~, TU4P16
Stapnes, S.	TH4A2
Steiniger, K.	TH2C1
Stephan, F.	~~WE3A5~~
Stupakov, G.	~~TH3D4~~, TU2A2
Sturari, L.	~~M03A8~~
Sudar, N.S.	**~~WE2A2~~**
Sulaiman Khail, W.	**~~TH3D5~~**
Sun, Y.	~~TU2A4~~

— T —

Tafzi, A.	TH2C1
Tamasaku, K.	~~TU2A4~~
Tanaka, H.	~~M03A7~~, TU3D4
Tang, C.-X.	~~TU1B2~~, TU4P28, ~~TH4D2~~
Tang, J.	**~~TH3D4~~**, **~~TH4A3~~**
Tang, J.Y.	**WE4P21**
Tangtartharakul, K.	~~TU1C3~~
Tavakoli, K.	TH1D4, TH2C1
Tavares, P.	M02L3
Thaury, C.	TH2C1
Thévenet, M.	~~M04B2~~
Thompson, N.	TU4P13, ~~WE2A4~~
Tian, S.K.	TU4P27
Tomai, T.	TU3D4
Touguet, J.	TU1C2
Tripathi, S.	WE4P36
Trovò, M.	~~M03A8~~
Tsai, C.-Y.	TU4P16, **TU4P31**, **WE3A3**
Tsai, H.-J.	WE4P18, WE4P19
Tseng, F.H.	WE4P18, WE4P19, WE4P20

— U —

Ufer, P.	TH2C1

— V —

Vaccarezza, C.	~~WE2A4~~
Valléau, M.	TH2C1
Vandenberghe, M.V.	TH2C1
Vannoni, M.	~~TH1D1~~
Vannozzi, A.	~~WE2A4~~
Vétéran, J.	TH2C1
Viefhaus, J.	TU1B1
Vishnyakov, E.	TH2C2
Völker, J.	TU1B1
Vogt, M.	**M03A5**
Volz, P.I.	~~TH3B1~~

— W —

Wagener, G.	WE1L4
Walsh, D.A.	TU4P13
Wan, J.	TU3B3
Wang, A.X.	WE4P21

List of Authors

Wang, D.	**M03A1**
Wang, G.L.	**TH2A3**
Wang, N.	TH3B4
Wang, P.	TH4A2
Wang, S.	M03B4
Wang, Z.	M03A9, **WE3A4**, WE4P09, WE4P12, WE4P13, TH4A1
Wei, B.F.	TU1B4
Wei, Y.	TU3B3
Welke, N.B.	WE2C1
Wesolowski, P.	TU4P34
White, S.M.	TU4P18
Wichmann, R.	TH1D1
Widmann, C.	TU4P34
Williams, P.H.	TU4P13
Wimpory, R.C.	WE1L4
Winkler, P.	M04B2
Wohlenberg, T.	TH1D1, TH2A1
Wolf, Z.R.	TH1D3
Wolff-Fabris, F.	TH3D2
Wolski, A.	TH3D2
Wu, X.W.	WE2A4
Wuensch, W.	WE2A4, TH4A2

— X —

Xiang, R.	**TH4D3**
Xiao, H.Y.	**TH2C3**, TH4A1
Xu, C.	TH3D3
Xu, D.	TU1B3
Xu, G.	TU3B3, TU4P27
Xu, H.S.	TU3B3, TU4P27, **TH3B4**
Xu, J.Y.	TH3B4

— Y —

Yakopov, M.	TH1D1

Yamaguchi, H.	TU3D4
Yamaguchi, T.	M03B3
Yamamoto, N.	M03B2, **M03B3**, FR1M2
Yan, B.Y.	TU4P07
Yan, J.W.	TU2A3, **TH2A2**, TH4A4
Yang, H.	M03A6
Yang, P.H.	WE4P21
Yu, J.B.	WE4P33

— Z —

Zagorodnov, I.	TH1D1, TH2A1
Zemella, J.	M03A5
Zhang, J.	TU4P27
Zhang, J.R.	TU4P27
Zhang, K.Q.	**TU4P06**, TU4P08, WE4P12
Zhang, M.	WE4P13
Zhang, T.L.	TH4A1
Zhang, X.-Y.	TH4D2
Zhang, Y.	WE3A3
Zhang, Z.	**WE3A2**, TH1D3, TH4A3
Zhao, J.	TH3B2
Zhao, Y.	M03B4
Zhao, Y.L.	TU3B3
Zhao, Z.	WE4P21
Zhao, Z.T.	M03A9, TU4P08, WE3A4, TH4A1
Zheng, L.M.	TH4D2
Zholents, A.	M03B1
Zhu, D.	TU2A4
Zhu, J.Y.	**WE4P33**
Zimmermann, F.	M04C3
Zimmermann, P.	TH2C2
Zimmermann, R.	TH1D1
Ziolkowski, P.Z.	TH1D1

Institutes List

Ankara University, Accelerator Technologies Institute
Golbasi, Turkey
- Aksoy, A.

ANL
Lemont, Illinois, USA
- Borland, M.
- Byrd, J.M.
- Chen, G.
- Fuerst, J.D.
- Gluskin, E.
- Ivanyushenkov, Y.
- Jing, C.-J.
- Kasa, M.
- Kim, K.-J.
- Lindberg, R.R.
- Lu, X.
- Park, J.-W.
- Power, J.G.
- Qian, M.F.
- Sajaev, V.
- Shiroyanagi, Y.
- Zholents, A.

ASU
Tempe, USA
- Graves, W.S.

BNL
Upton, New York, USA
- Bacescu, D.M.
- Eng, C.
- Fedotov, A.V.
- Gu, X.
- Hulbert, S.
- Jing, Y.C.
- Kayran, D.
- Kewisch, J.
- Li, Y.
- Mazzoli, C.
- Nelson, C.S.
- Pinayev, I.
- Podobedov, B.
- Rainer, R.S.
- Seletskiy, S.
- Smaluk, V.V.
- Xu, D.

CEA
Arpajon, France
- Pires, A.
- Rosch, R.
- Touguet, J.

CEA/DAM/DIF
Arpajon, France
- Le Flanchec, V.

CELIA
Talence, France
- Cormier, E.

CERN
Meyrin, Switzerland
- Corsini, R.
- Dyks, L.A.
- Granados, E.
- Grudiev, A.
- Latina, A.
- Mu at, V.
- Stapnes, S.
- Wang, P.
- Wu, X.W.
- Wuensch, W.
- Zimmermann, F.

Cockcroft Institute
Warrington, Cheshire, United Kingdom
- Angal-Kalinin, D.
- Apsimon, Ö.
- Clarke, J.A.
- Dunning, D.J.
- Henderson, J.
- Militsyn, B.L.
- Potter, A.T.
- Thompson, N.
- Williams, P.H.

Czech Republic Academy of Sciences, Institute of Physics
Prague, Czech Republic
- Molodozhentsev, A.Y.

DESY
Hamburg, Germany
- Agapov, I.V.
- Antipov, S.A.
- Aßmann, R.W.
- Barbanotti, S.
- Bazyl, D.B.
- Benediktovitch, A.I.
- Brinkmann, R.
- Chen, Y.
- Czwalinna, M.K.
- Decking, W.
- Dijkstal, P.
- Eckoldt, H.-J.
- Ferran Pousa, Á.
- Gehlot, M.
- Grech, C.
- Guetg, M.W.
- Guo, J.J.
- Hauberg, A.
- Jalas, S.
- Jensch, K.
- Kirchen, M.
- Kocharyan, V.
- Lederer, S.
- Leemans, W.P.
- Leuschner, A.
- Lilje, L.
- Liu, S.
- Long, T.

- Maier, A.R.
- Martinez de la Ossa, A.
- Mirian, N.S.
- Osterhoff, J.
- Qin, W.
- Ramalingam, R.
- Schlarb, H.
- Schnautz, T.
- Schneidmiller, E.
- Scholz, M.
- Schreiber, S.
- Schulz, S.
- Shalloo, R.J.
- Thévenet, M.
- Vogt, M.
- Wichmann, R.
- Winkler, P.
- Wohlenberg, T.
- Zagorodnov, I.
- Zemella, J.
- Zimmermann, R.

DESY Zeuthen
Zeuthen, Germany
- Krasilnikov, M.
- Mohanty, S.K.
- Oppelt, A.
- Qian, H.J.
- Stephan, F.

Devi Ahilya University
Indore, India
- Khan, S.M.
- Khullar, R.
- Mishra, G.

Devi Ahilya Vishwa Vidyalaya, Institute of Engineering & Technology
Indore, India
- Mishra, S.

DLS
Oxfordshire, United Kingdom
- Chao, H.-C.
- Cheng, W.
- Fielder, R.T.
- George, A.
- Hale, S.H.
- Husain, R.
- Lueangaramwong, A.
- Martin, I.P.S.
- Mercado, R.
- Morgan, A.F.D.
- Patel, Z.
- Ramezani Moghaddam, A.
- Reeves, M.
- Sharma, G.
- Tripathi, S.

Elettra-Sincrotrone Trieste S.C.p.A.
Basovizza, Italy
- Allaria, E.

- Badano, L.
- Brynes, A.D.
- Cinquegrana, P.
- Cudin, I.
- D'Auria, G.
- Danailov, M.B.
- De Ninno, G.
- Delgiusto, P.
- Demidovich, A.A.
- Di Mitri, S.
- Garzella, D.
- Giannessi, L.
- Masciovecchio, C.
- Penco, G.
- Rebernik Ribič, P.
- Rochow, R.A.
- Shafqat, N.
- Sigalotti, P.
- Spezzani, C.
- Sturari, L.
- Trovò, M.

ELI ERIC
Dolni Brezany, Czech Republic
- Jancarek, A.
- Maity, S.M.
- Mondal, A.
- Niekrasz, S.N.
- Vishnyakov, E.

ELI-BEAMS
Prague, Czech Republic
- Green, J.T.
- Zimmermann, P.

ENEA C.R. Frascati
Frascati (Roma), Italy
- Nguyen, F.

ENEA Casaccia
Roma, Italy
- Croia, M.

ESRF
Grenoble, France
- Carmignani, N.
- Carver, L.R.
- Chavanne, J.
- Hoummi, L.
- Liuzzo, S.M.
- Perron, T.P.
- Raimondi, P.
- Scheidt, K.B.
- White, S.M.

ESS
Lund, Sweden
- Permanyer, X.

Euclid Beamlabs
Bolingbrook, USA
- Jing, C.-J.
- Kuzikov, S.V.

EuXFEL

Schenefeld, Germany

- Abeghyan, S.
- Baader, J.E.
- Casalbuoni, S.
- Di Felice, M.
- Englisch, U.
- Geloni, G.
- Grattoni, V.
- Karabekyan, S.
- Kujala, N.G.
- La Civita, D.
- Lechner, C.
- Letrun, R.
- Marchetti, B.
- Serkez, S.
- Sinn, H.
- Vannoni, M.
- Wolff-Fabris, F.
- Yakopov, M.
- Yan, J.W.
- Ziolkowski, P.Z.

HIP

University of Helsinki, Finland

- Aicheler, M.

HUST

Wuhan, People's Republic of China

- Tsai, C.-Y.

HZB

Berlin, Germany

- Abo-Bakr, M.
- Apel, D.
- Bahrdt, J.
- Bengtsson, J.
- Boin, M.
- Gaebel, S.
- García-Moreno, F.
- Genzel, C.
- Goslawski, P.
- Gottschlich, S.
- Grimmer, S.
- Holldack, K.
- Hüsges, Z.
- Jankowiak, A.
- Kamm, P.H.
- Kiefer, K.
- Klaus, M.
- Kuhn, C.
- Kuske, B.C.
- Laube, F.
- Mainz, R.
- Meseck, A.
- Müller, R.
- Rial, E.C.M.
- Sauerborn, M.K.
- Scheer, M.
- Schnizer, P.
- Schwarzkopf, O.
- Sulaiman Khail, W.

- Viefhaus, J.
- Völker, J.
- Volz, P.I.
- Wagener, G.
- Wimpory, R.C.

HZDR

Dresden, Germany

- Bock, S.
- Chang, Y.Y.
- Debus, A.D.
- Eisenmann, C.
- Gebhardt, R.
- Ghaith, A.
- Grams, S.
- Helbig, U.
- Irman, A.
- Kuntzsch, M.
- Pausch, R.G.
- Püschel, T.
- Schöbel, S.
- Schramm, U.
- Steiniger, K.
- Ufer, P.
- Xiang, R.

IHEP

Beijing, People's Republic of China

- Cao, J.S.
- Duan, Z.
- He, D.Y.
- He, P.
- Ji, D.
- Ji, H.F.
- Jiao, Y.
- Kang, W.
- Li, J.Y.
- Li, J.
- Li, N.
- Li, X.
- Lu, Z.J.
- Meng, C.
- Pan, W.M.
- Peng, Y.M.
- Qu, H.
- Shu, G.
- Tian, S.K.
- Wan, J.
- Wang, N.
- Wang, S.
- Wei, Y.
- Xu, G.
- Xu, H.S.
- Xu, J.Y.
- Zhang, J.R.
- Zhang, J.
- Zhao, Y.L.
- Zhu, J.Y.

IHEP CSNS

Guangdong Province, People's Republic of China

- Liu, W.

- Liu, X.
- Lu, X.H.
- Yu, J.B.
- Zhao, Y.

ILE
Palaiseau Cedex, France
- Santarelli, G.

Imperial College of Science and Technology, Department of Physics
London, United Kingdom
- Marangos, J.P.

INFN- Sez. di Padova
Padova, Italy
- Curatolo, C.

INFN-Milano
Milano, Italy
- Bacci, A.
- Drebot, I.
- Rossetti Conti, M.
- Samsam, S.
- Serafini, L.

INFN/LASA
Segrate (MI), Italy
- Monaco, L.
- Pagani, C.
- Sertore, D.

JASRI
Hyogo, Japan
- Ohshima, T.
- Tomai, T.
- Yamaguchi, H.

JLab
Newport News, Virginia, USA
- Zhang, Y.

Karlsruhe Institute of Technology (KIT)
Eggenstein-Leopoldshafen, Germany
- De Carne, G.

KEK
Ibaraki, Japan
- Ego, H.
- Naito, D.
- Sakanaka, S.
- Yamaguchi, T.
- Yamamoto, N.

KIT
Karlsruhe, Germany
- Bernhard, A.
- Bründermann, E.
- Caselle, M.
- El Khechen, D.
- Grau, A.W.
- Härer, B.
- Malygin, A.

- Müller, A.-S.
- Nasse, M.J.
- Niehues, G.
- Papash, A.I.
- Ruprecht, R.
- Santamaria Garcia, A.
- Schäfer, J.
- Schuh, M.
- Schwarz, M.
- Scomparin, L.
- Smale, N.J.
- Wesolowski, P.
- Widmann, C.
- Xu, C.

Kyoto University
Kyoto, Japan
- Kii, T.

Lancaster University
Lancaster, United Kingdom
- Burt, G.

LBNL
Berkeley, California, USA
- Hellert, T.
- Leemann, S.C.

LNF-INFN
Frascati, Italy
- Alesini, D.
- Diomede, M.
- Ferrario, M.
- Gallo, A.
- Giannessi, L.
- Giribono, A.
- Scifo, J.
- Spataro, B.
- Vaccarezza, C.
- Vannozzi, A.

LOA
Palaiseau, France
- Andriyash, I.A.
- Gautier, J.
- Goddet, J.-P.
- Kononenko, O.S.
- Lambert, G.
- Rousseau, J.P.
- Tafzi, A.
- Thaury, C.

MAX IV Laboratory, Lund University
Lund, Sweden
- Al-Dmour, E.
- Andersson, Å.
- Cullinan, F.J.
- Grabski, M.J.
- Tavares, P.

Max Planck Institute for the Physics of Complex Systems
Dresden, Germany
- Rohringer, N.

Institutes List

MCL/ITRI
Hsinchu, Taiwan
- Felix, C.P.

Northern Illinois University
DeKalb, Illinois, USA
- Frame, E.A.
- Lu, X.
- Piot, P.

NSRRC
Hsinchu, Taiwan
- Cheng, C.M.
- Cheng, Y.-S.
- Chiu, M.-S.
- Chou, P.J.
- Chung, T.Y.
- Hsiao, Y.M.
- Huang, N.Y.
- Liu, Y.-C.
- Luo, G.-H.
- Luo, H.W.
- Tsai, H.-J.
- Tseng, F.H.

NTHU
Hsinchu, Taiwan
- Huang, Y.-C.

Oxford University, Physics Department
Oxford, Oxon, United Kingdom
- Burrows, P.

PAL
Pohang, Republic of Korea
- Cho, M.H.
- Eom, I.
- Heo, H.
- Kang, H.-S.
- Min, C.-K.
- Nam, I.H.
- Park, J.
- Park, S.H.
- Shim, C.H.
- Yang, H.

PhLAM/CERLA
Villeneuve d'Ascq, France
- Roussel, E.

PSI
Villigen PSI, Switzerland
- Aiba, M.
- Bostedt, C.
- Braun, H.-H.
- Kallestrup, J.
- Lucas, T.G.
- Prat, E.
- Reiche, S.
- Schietinger, T.
- Schlott, V.
- Schnorr, K.
- Wang, G.L.

QST
Sendai, Miyagi, Japan
- Asaka, T.
- Nishimori, N.

RIKEN SPring-8 Center
Hyogo, Japan
- Hara, T.
- Inagaki, T.
- Iwai, E.
- Kondo, C.
- Maesaka, H.
- Osaka, T.
- Tamasaku, K.
- Tanaka, H.

Sapienza University of Rome
Rome, Italy
- Mostacci, A.

SARI-CAS
Pudong, Shanghai, People's Republic of China
- Chen, S.
- Deng, H.X.
- Feng, C.
- Fu, X.
- Gu, D.
- Gu, Q.
- Jiang, Z.G.
- Liu, B.
- Liu, T.
- Luo, H.
- Meng, M.
- Qi, Z.
- Wang, Z.
- Zhang, M.
- Zhao, Z.T.

SINAP
Shanghai, People's Republic of China
- Guo, J.J.
- Kang, Y.
- Li, X.D.
- Liu, Z.P.
- Wang, D.
- Yan, B.Y.

SLAC
Menlo Park, California, USA
- Aquila, A.
- Bergmann, U.
- Bouchard, G.J.
- Ding, Y.
- Fisher, A.S.
- Gassner, G.L.
- Gonnella, D.
- Halavanau, A.
- Hemsing, E.
- Henstridge, M.
- Hoffmann, M.C.
- Huang, X.
- Huang, Z.
- Kraft, E.M.
- Krejcik, P.

Institutes List

- Krzywiński, J.
- Lam, B.
- Li, K.
- MacArthur, J.P.
- Marcus, G.
- Montironi, M.A.
- Nanni, E.A.
- Nantista, C.D.
- Nguyen, D.C.
- Nuhn, H.-D.
- Pellegrini, C.
- Robles, R.
- Safranek, J.A.
- Sakdinawat, A.
- Sato, T.
- Stupakov, G.
- Sudar, N.S.
- Sun, Y.
- Tang, J.
- Wolf, Z.R.
- Zhang, Z.
- Zhu, D.

SOLEIL
Gif-sur-Yvette, France

- André, T.
- Berlioux, A.
- Berteaud, P.
- Blache, F.
- Bouvet, F.
- Briquez, F.
- Brunelle, P.
- Couprie, M.-E.
- de Oliveira, C.
- Dietrich, Y.
- Duval, J.P.
- El Ajjouri, M.
- Gamelin, A.
- Gubaidulin, V.
- Herbeaux, C.
- Hubert, N.
- Kitégi, C.A.
- Labat, M.
- Lê, S.
- Leluan, B.
- Loulergue, A.
- Marchand, P.
- Marcouillé, O.
- Marteau, F.
- Mary, A.
- Mutin, T.
- Nadji, A.
- Nadolski, L.S.
- Nagaoka, R.
- Nguyen, M.-H.
- Oumbarek Espinos, D.
- Pereira, D.
- Potet, A.
- Ricaud, J.P.
- Rommeluère, P.
- Sebdaoui, M.
- Tavakoli, K.

- Valléau, M.
- Vandenberghe, M.V.
- Vétéran, J.

Soreq NRC
Yavne, Israel

- Cohen, T.

SSRF
Shanghai, People's Republic of China

- Chen, S.
- Feng, C.
- Gao, Z.F.
- Zhang, K.Q.

Stanford University
Stanford, California, USA

- Huang, Z.
- Margraf, R.A.
- Robles, R.
- Roques-Carmes, C.

STFC/DL
Daresbury, Warrington, Cheshire, United Kingdom

- Aden, P.
- Fell, B.D.

STFC/DL/ASTeC
Daresbury, Warrington, Cheshire, United Kingdom

- Angal-Kalinin, D.
- Castañeda Cortés, H.M.
- Clarke, J.A.
- Dunning, D.J.
- Henderson, J.
- Jackson, F.
- Mathisen, S.L.
- Militsyn, B.L.
- Percival, S.S.
- Roper, M.D.
- Snedden, E.W.
- Thompson, N.
- Walsh, D.A.
- Williams, P.H.

STFC/RAL
Chilton, Didcot, Oxon, United Kingdom

- Collier, J.L.
- Green, J.S.

Stony Brook University
Stony Brook, New York, USA

- Donetski, D.
- Kucharczyk, K.
- Liu, J.
- Lutchman, R.
- Zhao, J.

Tel Aviv University
Tel-Aviv, Israel

- Cohen, I.
- Meir, T.
- Perelmutter, L.
- Pomerantz, I.

TEMF, TU Darmstadt
Darmstadt, Germany
· Gjonaj, E.

The University of Liverpool
Liverpool, United Kingdom
· Potter, A.T.
· Wolski, A.

The University of Texas at Austin
Austin, Texas, USA
· LaBerge, M.

TRUMPF Huettinger GmbH
Freiburg, Germany
· Lau, M.

Tsinghua University
Beijing, People's Republic of China
· Zhang, T.L.

TUB
Beijing, People's Republic of China
· Chao, A.
· Chen, H.B.
· Deng, X.J.
· Du, Y.C.
· Hua, J.F.
· Huang, P.W.
· Huang, W.-H.
· Li, F.
· Li, R.K.
· Li, Z.Z.
· Lu, W.
· Pan, Z.
· Shi, J.R.
· Song, Z.
· Tang, C.-X.
· Xiao, H.Y.
· Zhang, X.-Y.
· Zheng, L.M.

UCLA
Los Angeles, California, USA
· Majernik, N.

UCSD
La Jolla, California, USA
· Arefiev, A.V.
· Tangtartharakul, K.

UMAN
Manchester, United Kingdom
· Davut, C.

Universita' degli Studi di Milano & INFN
Milano, Italy
· Petrillo, V.
· Puppin, A.

University of Cape Town
Cape Town, South Africa
· Marziani, M.V.

University of Chicago
Chicago, Illinois, USA
· Li, Y.S.

University of Chinese Academy of Sciences
Beijing, People's Republic of China
· Guo, J.J.

University of Hamburg, Institut für Experimentalphysik
Hamburg, Germany
· Hillert, W.

University of Nova Gorica
Nova Gorica, Slovenia
· De Ninno, G.

Università degli Studi di Milano & INFN
Segrate, Italy
· Pagani, C.

Università degli Studi di Trieste
Trieste, Italy
· Perosa, G.

Université Paris-Saclay, CNRS/IN2P3, IJCLab
Orsay, France
· Delerue, N.

Uppsala University
Uppsala, Sweden
· Goryashko, V.A.

USTC,SNST
Anhui, People's Republic of China
· Tang, J.Y.

USTC/NSRL
Hefei, Anhui, People's Republic of China
· Bai, Z.H.
· He, T.L.
· Liu, G.
· Mo, Y.
· Wang, A.X.
· Wei, B.F.
· Yang, P.H.
· Zhao, Z.

UW–Madison/PD
Madison, Wisconsin, USA
· Welke, N.B.

Weizmann Institute of Science, Physics
Rehovot, Israel
· Malka, V.

xLight
Palo Alto, USA
· Dunham, M.
· Lou, W.
· Mayes, C.E.
· Nguyen, D.C.
· Stupakov, G.

Zhangjiang Lab
Shanghai, People's Republic of China
· Guo, J.J.
· Huang, N.

Institutes List

Participants List

Participants List

— A —

Masamitsu **Aiba**
Paul Scherrer Institut
Switzerland

Deepa **Angal-Kalinin**
STFC
United Kingdom

Sergey **Antipov**
DESY
Germany

Öznur **Apsimon**
The University of Manchester and
Cockcroft Institute
United Kingdom

Felix **Armborst**
Paul Scherrer Institut
Switzerland

Ralph **Aßmann**
INFN
Italy

— B —

Johann **Baader**
European XFEL
Germany

Zhenghe **Bai**
National Synchrotron Radiation
Laboratory, USTC
China

Dmitry **Bazyl**
DESY
Germany

Joris **Beijers**
Pfeiffer Vacuum (Schweiz) AG
Switzerland

Simona **Bettoni**
Paul Scherrer Institut
Switzerland

François **Beutler**
Pfeiffer Vacuum (Schweiz) AG
Switzerland

Bolko **Beutner**
DESY
Germany

Nikos **Binkert**
TRUMPF Hüttinger GmbH + Co KG
Germany

Mirko **Boin**
Helmholtz Zentrum Berlin
Germany

Christoph **Bostedt**
Paul Scherrer Institut
Switzerland

Hans Heinrich **Braun**
Paul Scherrer Institut
Switzerland

Alexander **Brynes**
Elettra - Sincrotrone Trieste
Italy

Woo Jun **Byeon**
Pohang Accelerator Laboratory
South Korea

John **Byrd**
Argonne National Laboratory
United States

— C —

Manuel **Cargnelutti**
Instrumentation Technologies
Slovenia

Nicola **Carmignani**
ESRF
France

Sara **Casalbuoni**
European XFEL
Germany

Hung-Chun **Chao**
Diamond Light Source Ltd
United Kingdom

Alexander **Chao**
Stanford University
United States

Joel **Chavanne**
ESRF
France

Ye **Chen**
DESY
Germany

Si **Chen**
Shanghai Advanced Research Institute
China

Mau-Sen **Chiu**
National Synchrotron
Radiation Research Center
Taiwan

Myunghoon **Cho**
Pohang Accelerator Laboratory
South Korea

Jan **Chrin**
Paul Scherrer Institut
Switzerland

Jim **Clarke**
STFC
United Kingdom

Marie-Emmanuelle **Couprie**
SOLEIL
France

Paolo **Craievich**
Paul Scherrer Institut
Switzerland

Francis **Cullinan**
MAX IV Laboratory
Sweden

— D —

Sven **Dahl-Petersen**
Danfysik A/S
Denmark

Gerardo **D'Auria**
Elettra - Sincrotrone Trieste
Italy

Adrian **De Biase**
Swissvacuum Technologies SA
Switzerland

Giovanni **De Ninno**
Elettra Sincrotrone Trieste and
Nova Gorica University
Italy

Xiujie **Deng**
Tsinghua University
China

Simone **Di Mitri**
Elettra Sincrotrone Trieste
Italy

Philipp **Dijkstal**
Paul Scherrer Institut
Switzerland

Andreas **Dostmann**
VAT Vakuumventile AG
Switzerland

Illya **Drebot**
INFN-Milan
Italy

— E —

Hiroyasu **Ego**
KEK — High Energy Accelerator
Research Organization
Japan

— F —

Alessandro **Fabris**
Elettra - Sincrotrone Trieste
Italy

Chao **Feng**
Shanghai Advanced Research Institute,
CAS
China

Richard **Fielder**
Diamond Light Source Ltd
United Kingdom

— G —

Alexis **Gamelin**
SOLEIL
France

Romain **Ganter**
Paul Scherrer Institut
Switzerland

Zhangfeng **Gao**
Shanghai Advanced Research Institute,
CAS
China

Dan **Gonnella**
SLAC
United States

Paul **Goslawski**
Helmholtz-Zentrum Berlin
Germany

Marek **Grabski**
MAX IV-Lund University
Sweden

William **Graves**
Arizona State University
United States

Duan **Gu**
Shanghai Advanced Research Institute,
CAS
China

Marc **Guetg**
DESY
Germany

Junjie **Guo**
Shanghai Optoelectronic Science and
Technology Innovation Center
China

— H —

Daniel **Haas**
Pfeiffer Vacuum (Schweiz) AG
Switzerland

Aliaksei **Halavanau**
SLAC
United States

Ariel **Haymoz**
Swissvacuum Technologies SA
Switzerland

Changchao **He**
Shanghai Institute of Applied Physics
China

Thorsten **Hellert**
Lawrence Berkeley National Laboratory
United States

Erik **Hemsing**
SLAC
United States

Meredith **Henstridge**
SLAC
United States

Nicole **Hiller**
Paul Scherrer Institut
Switzerland

Yen Chieh **Huang**
National Tsing Hua University
Taiwan

NuanYa **Huang**
National Synchrotron
Radiation Research Center
Taiwan

Nanshun **Huang**
Shanghai Optoelectronic Science and
Technology Innovation Center
China

Zhirong **Huang**
SLAC
United States

Xiaobiao **Huang**
SLAC
United States

Riyasat **Husain**
Diamond Light Source Ltd
United Kingdom

— I —

Takahiro **Inagaki**
RIKEN SPring-8 center
Japan

— J —

Andreas **Jankowiak**
Helmholtz-Zentrum Berlin
Germany

— K —

Jonas **Kallestrup**
Paul Scherrer Institute
Switzerland

Simon **Keens**
Ampegon Power Electronics AG
Switzerland

Jorg **Kewisch**
Brookhaven National Laboratory
United States

Saif **Khan**
School of Physics, Devi Ahilya University
India

Toshiteru **Kii**
Institute of Advanced Energy,
Kyoto University
Japan

Kwang-Je **Kim**
Argonne National Laboratory
United States

J. Michael **Klopf**
Helmholtz-Zentrum Dresden-Rossendorf
Germany

Patrick **Krejcik**
SLAC
United States

Bettina **Kuske**
Helmholtz Zentrum Berlin
Germany

— L —

Andrea **Latina**
CERN
Switzerland

Marcus **Lau**
TRUMPF Hüttinger GmbH + Co. KG
Germany

Christoph **Lechner**
European XFEL
Germany

Simon **Leemann**
Lawrence Berkeley National Laboratory
United States

Ulf **Lehnert**
Helmholtz-Zentrum Dresden-Rossendorf
Germany

Eliane **Lessner**
Department of Energy
United States

Romain **Letrun**
European XFEL
Germany

Yongjun **Li**
Brookhaven National Laboratory
United States

Renkai **Li**
Tsinghua University
China

Fei **Li**
Tsinghua University
China

Shan **Liu**
DESY
Germany

Weihang **Liu**
Institute of High Energy Physics, CAS
China

Yi Chih **Liu**
National Synchrotron
Radiation Research Center
Taiwan

Bo **Liu**
Shanghai Advanced Research Institute,
CAS
China

Tao **Liu**
Shanghai Advanced Research Institute,
CAS
China

Zipeng **Liu**
Shanghai Optoelectronic Science and
Technology Innovation Center
China

Xiaohan **Lu**
Institute of High Energy Physics, CAS
China

Thomas **Lucas**
Paul Scherrer Institut
Switzerland

Hang **Luo**
SSRF
China

— M —

Urban **Maciej**
SENIS AG
Switzerland

Alan **Mak**
Daresbury Laboratory
United Kingdom

Evangelos **Makris**
Cosylab
Switzerland

Paolo **Manini**
SAES Getters S.p.A.
Italy

Bonfadini **Marco**
Swissvacuum Technologies SA
Switzerland

Olivier **Marcouillé**
SOLEIL
France

Rachel **Margraf**
Stanford University / SLAC
United States

Alberto **Martinez de la Ossa**
DESY
Germany

Cai **Meng**
Institute of High Energy Physics, CAS
China

Atoosa **Meseck**
Helmholtz-Zentrum Berlin,
JGU Mainz
Germany

Boris **Militsyn**
STFC ASTeC
United Kingdom

Sandeep **Mohanty**
DESY, Zeuthen
Germany

Alexander **Molodozhentsev**
ELI-ERIC / ELI-Beamlines
Czech Republic

Vlad **Musat**
CERN
Switzerland

— N —

Emilio **Nanni**
SLAC
United States

Alireza **Nassiri**
Argonne National Laboratory
United States

Dinh **Nguyen**
xLight, Inc.
United States

— O —

Anatoliy **Opanasenko**
Uppsala University
Sweden

— P —

Zhilong **Pan**
Tsinghua University
China

Chong Shik **Park**
Korea University
South Korea

Zena **Patel**
Diamond Light Source Ltd.
United Kingdom

Kevin **Pepitone**
ScandiNova Systems AB
Sweden

Philippe **Piot**
Northern Illinois University &
Argonne National Laboratory
United States

Abel **Pires**
CEA
France

Christian **Pirotte**
JEMA
Belgium

Boris **Podobedov**
Brookhaven National Laboratory
United States

Ishay **Pomerantz**
Tel Aviv University
Israel

Dragana **Popovic Renella**
SENIS AG
Switzerland

Angela **Potet**
SOLEIL
France

Eduard **Prat Costa**
Paul Scherrer Institut
Switzerland

— Q —

Weilun **Qin**
DESY
Germany

— R —

Pantaleo **Raimondi**
CERN
Switzerland

Del **Redfern**
Hitachi High Tech America Inc.
United States

Sven **Reiche**
Paul Scherrer Institut
Switzerland

Sebastian **Richter**
Paul Scherrer Institut
Switzerland

Charles **Roques-Carmes**
Stanford University
United States

Christoph **Ross**
AK Steel International B.V.
Germany Branch
Germany

Aimée **Ross**
ASML
Netherlands

Viviene **Rowland**
South African Radio
Astronomy Observatory
South Africa

— S —

Vadim **Sajaev**
Argonne National Laboratory
United States

Andrea **Santamaria Garcia**
Karlsruhe Institute of Technology
Germany

Bertus Kees **Scheidt**
ESRF
France

Thomas **Schietinger**
Paul Scherrer Institut
Switzerland

Holger **Schlarb**
DESY
Germany

Manfred **Schlicht**
Pfeiffer Vacuum (Schweiz) AG
Switzerland

Volker **Schlott**
Paul Scherrer Institut
Switzerland

Joachim **Schmidle**
W-IE-NE-R Power Electronics GmbH
Germany

Thomas **Schmidt**
Paul Scherrer Institut
Switzerland

Pierre **Schnizer**
Helmholtz Zentrum Berlin
Germany

Matthias **Scholz**
DESY
Germany

Markus **Schwarz**
Karlsruhe Institute of Technology
Germany

Xueyan **Shi**
Institute of High Energy Physics, CAS
China

Isleydys **Silva Torrecilla**
xLight Inc.
United States

Theo **Sinkovits**
SAES Rial Vacuum
Italy

Sasa **Spasic**
SENIS AG
Switzerland

Alexander **Stuck**
SENIS AG
Switzerland

Gennady **Stupakov**
xLight, Inc.
United States

Nicholas **Sudar**
SLAC
United States

— T —

Jingyi **Tang**
SLAC
United States

Jingyu **Tang**
University of Science and
Technology of China
China

Claude **Troesch**
JEMA
France

Cheng-Ying **Tsai**
Huazhong University of Science
and Technology
China

— V —

Rick **van den Berg**
Eindhoven University of Technology
Netherlands

Mathias **Vogt**
DESY
Germany

— W —

Jeffery **Wade**
ESRF
France

Weishi **Wan**
ShanghaiTech University
China

Jiuqing **Wang**
Institute of High Energy Physics, CAS
China

Guanglei **Wang**
Paul Scherrer Institut
Switzerland

Dong **Wang**
Shanghai Advanced Research Institute,
CAS
China

Zhen **Wang**
Shanghai Advanced Research Institute,
CAS
China

Jan Torben **Weber**
Pfeiffer Vacuum (Schweiz) AG
Switzerland

Sverker **Werin**
MAX IV-Lund University
Sweden

Michael **Wilde**
iseg Spezialelektronik GmbH
Germany

— X —

Rong **Xiang**
Helmholtz-Zentrum Dresden-Rossendorf
Germany

Yaozong **Xiao**
Shanghai Institute of Applied Physics,
CAS
China

Haisheng **Xu**
Institute of High Energy Physics, CAS
China

— Y —

Naoto **Yamamoto**
KEK
Japan

Jiawei **Yan**
European XFEL
Germany

— Z —

Frank **Zhang**
Australian Synchrotron
Australia

Kaiqing **Zhang**
Shanghai advanced research institute
China

Zhen **Zhang**
SLAC
United States

Zhentang **Zhao**
Shanghai Advanced Research Institute,
CAS
China

Qi **Zheng**
Shanghai Advanced Research Institute,
CAS
China

Junyu **Zhu**
Institute of High Energy Physics, CAS
China